

Shiwei Ma Li Jia Xin Li Ling Wang
Huiyu Zhou Xin Sun (Eds.)

Communications in Computer and Information Science

461

Life System Modeling and Simulation

International Conference on Life System Modeling and Simulation, LSMS 2014
and International Conference on Intelligent Computing
for Sustainable Energy and Environment, ICSEE 2014
Shanghai, China, September 20–23, 2014, Proceedings, Part I

Part 1

 Springer

Editorial Board

Simone Diniz Junqueira Barbosa

*Pontifical Catholic University of Rio de Janeiro (PUC-Rio),
Rio de Janeiro, Brazil*

Phoebe Chen

La Trobe University, Melbourne, Australia

Alfredo Cuzzocrea

ICAR-CNR and University of Calabria, Italy

Xiaoyong Du

Renmin University of China, Beijing, China

Joaquim Filipe

Polytechnic Institute of Setúbal, Portugal

Orhun Kara

TÜBİTAK BİLGEM and Middle East Technical University, Turkey

Igor Kotenko

*St. Petersburg Institute for Informatics and Automation
of the Russian Academy of Sciences, Russia*

Krishna M. Sivalingam

Indian Institute of Technology Madras, India

Dominik Ślęzak

University of Warsaw and Infobright, Poland

Takashi Washio

Osaka University, Japan

Xiaokang Yang

Shanghai Jiao Tong University, China

Shiwei Ma Li Jia Xin Li Ling Wang
Huiyu Zhou Xin Sun (Eds.)

Life System Modeling and Simulation

International Conference on Life System Modeling
and Simulation, LSMS 2014
and International Conference on Intelligent Computing
for Sustainable Energy and Environment, ICSEE 2014
Shanghai, China, September 20-23, 2014
Proceedings, Part I

Volume Editors

Shiwei Ma
Shanghai University, China
E-mail: masw@shu.edu.cn

Li Jia
Shanghai University, China
E-mail: jjali@staff.shu.edu.cn

Xin Li
Shanghai University, China
E-mail: lxli@staff.shu.edu.cn

Ling Wang
Shanghai University, China
E-mail: wangling@shu.edu.cn

Huiyu Zhou
Queen's University Belfast, UK
E-mail: h.zhou@ecit.qub.ac.uk

Xin Sun
Shanghai University, China
E-mail: xsun@staff.shu.edu.cn

ISSN 1865-0929

e-ISSN 1865-0937

ISBN 978-3-662-45282-0

e-ISBN 978-3-662-45283-7

DOI 10.1007/978-3-662-45283-7

Springer Heidelberg New York Dordrecht London

Library of Congress Control Number: 2014951539

© Springer-Verlag Berlin Heidelberg 2014

This work is subject to copyright. All rights are reserved by the Publisher, whether the whole or part of the material is concerned, specifically the rights of translation, reprinting, reuse of illustrations, recitation, broadcasting, reproduction on microfilms or in any other physical way, and transmission or information storage and retrieval, electronic adaptation, computer software, or by similar or dissimilar methodology now known or hereafter developed. Exempted from this legal reservation are brief excerpts in connection with reviews or scholarly analysis or material supplied specifically for the purpose of being entered and executed on a computer system, for exclusive use by the purchaser of the work. Duplication of this publication or parts thereof is permitted only under the provisions of the Copyright Law of the Publisher's location, in its current version, and permission for use must always be obtained from Springer. Permissions for use may be obtained through RightsLink at the Copyright Clearance Center. Violations are liable to prosecution under the respective Copyright Law.

The use of general descriptive names, registered names, trademarks, service marks, etc. in this publication does not imply, even in the absence of a specific statement, that such names are exempt from the relevant protective laws and regulations and therefore free for general use.

While the advice and information in this book are believed to be true and accurate at the date of publication, neither the authors nor the editors nor the publisher can accept any legal responsibility for any errors or omissions that may be made. The publisher makes no warranty, express or implied, with respect to the material contained herein.

Typesetting: Camera-ready by author, data conversion by Scientific Publishing Services, Chennai, India

Printed on acid-free paper

Springer is part of Springer Science+Business Media (www.springer.com)

Preface

The 2014 International Conference on Life System Modeling and Simulation (LSMS 2014) and 2014 International Conference on Intelligent Computing for Sustainable Energy and Environment (ICSEE 2014), which were held during September 20–23, in Shanghai, China, aimed to bring together international researchers and practitioners in the field of life system modeling and simulation as well as intelligent computing theory and methodology with applications to sustainable energy and environment. These events built on the success of previous LSMS conferences held in Shanghai and Wuxi in 2004, 2007, and 2010, and ICSEE conferences held in Wuxi and Shanghai in 2010 and 2012, and are based on large-scale RCUK/NSFC jointly funded UK–China collaboration projects on energy.

At LSMS 2014 and ICSEE 2014, technical exchanges within the research community take the form of keynote speeches, panel discussions, as well as oral and poster presentations. In particular, two workshops, namely, the Workshop on Integration of Electric Vehicles with Smart Grid and the Workshop on Communication and Control for Distributed Networked Systems, were held in parallel with LSMS 2014 and ICSEE 2014, focusing on the two recent hot topics on smart grid and electric vehicles and distributed networked systems for the Internet of Things.

The LSMS 2014 and ICSEE 2014 conferences received over 572 submissions from 13 countries and regions. All papers went through a rigorous peer review procedure and each paper received at least three review reports. Based on the review reports, the Program Committee finally selected 159 high-quality papers for presentation at LSMS 2014 and ICSEE 2014. These papers cover 24 topics, and are included into three volumes of CCIS proceedings published by Springer. This volume of CCIS includes 43 papers covering 11 relevant topics.

Shanghai is one of the most populous, vibrant, and dynamic cities in the world, and has contributed significantly toward progress in technology, education, finance, commerce, fashion, and culture. Participants were treated to a series of social functions, receptions, and networking sessions, which served to build new connections, foster friendships, and forge collaborations.

The organizers of LSMS 2014 and ICSEE 2014 would like to acknowledge the enormous contributions made by the following: the Advisory Committee for their guidance and advice, the Program Committee and the numerous referees for their efforts in reviewing and soliciting the papers, and the Publication Committee for their editorial work. We would also like to thank the editorial team from Springer for their support and guidance. Particular thanks are of course due to all the authors, as without their high-quality submissions and presentations the conferences would not have been successful.

Finally, we would like to express our gratitude to:

The Chinese Association for System Simulation (CASS)
IEEE Systems, Man and Cybernetics Society (SMCS) Technical Committee on
Systems Biology
IET China
IEEE CIS Adaptive Dynamic Programming and Reinforcement Learning
Technical Committee
IEEE CIS Neural Network Technical Committee
IEEE CC Ireland Chapter and IEEE SMC Ireland Chapter
Shanghai Association for System Simulation
Shanghai Instrument and Control Society
Shanghai Association of Automation
Shanghai University
Queen's University Belfast
Life System Modeling and Simulation Technical Committee of CASS
Embedded Instrument and System Technical Committee of China
Instrument and Control Society
Central Queensland University
Harbin Institute of Technology
China State Grid Electric Power Research Institute
Cranfield University

September 2014

Bo Hu Li
George W. Irwin
Mitsuo Umezu
Minrui Fei
Kang Li
Qinglong Han
Shiwei Ma
Sean McLoone
Luonan Chen

Organization

Sponsors

Chinese Association for System Simulation (CASS)
IEEE Systems, Man and Cybernetics (SMCS) Technical Committee on Systems
Biology
IET China

Organizers

Shanghai University
Queen's University Belfast
Life System Modeling and Simulation Technical Committee of CASS
Embedded Instrument and System Technical Committee of China Instrument
and Control Society

Co-Sponsors

IEEE CIS Adaptive Dynamic Programming and Reinforcement Learning
Technical Committee
IEEE CIS Neural Network Technical Committee
IEEE CC Ireland Chapter and IEEE SMC Ireland Chapter
Shanghai Association for System Simulation
Shanghai Instrument and Control Society
Shanghai Association of Automation

Co-Organizers

Central Queensland University
Harbin Institute of Technology
China State Grid Electric Power Research Institute
Cranfield University

Honorary Chairs

Li, Bo Hu (China)
Irwin, George W. (UK)
Umezu, Mitsuo (Japan)

Consultant Committee Members

Cheng, Shukang (China)	Xi, Yugeng (China)
Hu, Huosheng (UK)	Xiao, Tianyuan (China)
Pardalos, Panos M. (USA)	Xue, Yusheng (China)
Pedrycz, Witold (Canada)	Yeung, Daniel S. (Hong Kong, China)
Scott, Stan (UK)	Zhao, Guangzhou (China)
Wu, Cheng (China)	

General Chairs

Fei, Minrui (China)	Li, Kang (UK)
---------------------	---------------

International Program Committee

Chairs

Han, Qinglong (Australia)	McLoone, Sean (UK)
Ma, Shiwei (China)	Chen, Luonan (Japan)

Local Chairs

Chen, Ming (China)	Luk, Patrick (UK)
Chiu, Min-Sen (Singapore)	Park, Poogyeon (Korea)
Ding, Yongsheng (China)	Peng, Chen (China)
Fan, Huimin (China)	Su, Zhou (Japan)
Foley, Aoife (UK)	Yang, Taicheng (UK)
Gu, Xingsheng (China)	Zhang, Huaguang (China)
He, Haibo (USA)	Yang, Yue (China)
Li, Tao (China)	

Members

Albertos, Pedro (Spain)	Chen, Rongbao (China)	Fu, Jingqi (China)
Cai, Zhongyong (China)	Cheng, Wushan (China)	Gao, Shouwei (China)
Cao, Jianan (China)	Deng, Jing (UK)	Gao, Zhinian (China)
Chang, Xiaoming (China)	Deng, Li (China)	Gu, Juping (China)
Chen, Guochu (China)	Ding, Zhigang (China)	Gu, Ren (China)
Chen, Jing (China)	Du, Dajun (China)	Han, Liqun (China)
Chen, Qigong (China)	Du, Xiangyang (China)	Han, Xuezheng (China)
Chen, Weidong (China)	Emmert-Streib (Frank (UK)	Harkin-Jones, Eileen (UK)

He, Jihuan (China)	Luo, Qingming (China)	Wen, Guihua (China)
Hu, Dake (China)	Maione, Guido (Italy)	Wen, Tieqiao (China)
Hu, Guofen (China)	Man, Zhihong (Australia)	Wu, Jianguo (China)
Hu, Liangjian (China)	Marion, McAfee (Ireland)	Wu, Lingyun (China)
Hu, Qingxi (China)	Naeem, Wasif (UK)	Wu, Xiaofeng (China)
Jiang, Ming (China)	Ng, Wai Pang (UK)	Wu, Zhongcheng (China)
Jiang, Ping (China)	Nie, Shengdong (China)	Xi, Zhiqi (China)
Kambhampati, Chandrasekhar (UK)	Ochoa, Luis (UK)	Xu, Daqing (China)
Keane, Andrew (Ireland)	Ouyang, Mingsan (China)	Xu, Sheng (China)
Konagaya, Akihiko (Japan)	Piao, Xiongzhu (China)	Xu, Zhenyuan (China)
Lang, Zi-Qiang (UK)	Prasad, Girijesh (UK)	Xue, Dong (China)
Li, Donghai (China)	Qian, Hua (China)	Yang, Hua (China)
Li, Gang (China)	Qu, Guoqing (China)	Yang, Wankou (China)
Li, Guozheng (China)	Ren, Wei (China)	Yang, Yi (China)
Li, Tongtao (China)	Rong, Qiguo (China)	Yao, Xiaodong (China)
Li, Wanggen (China)	Shao, Chenxi, (China)	Yu, Ansheng (China)
Li, Xin (China)	Shen, Chunshan (China)	Yu, Jilai (China)
Li, Xinsheng (China)	Shen, Jingzi (China)	Yuan, Jingqi (China)
Li, Zhicheng (China)	Song, Zhijian (China)	Yue, Dong (China)
Lin, Haiou (China)	Song, Yang (China)	Zhang, Bingyao (China)
Lin, Jinguo (China)	Sun, Guangming (China)	Zhang, Peijian (China)
Lin, Zhihao (China)	Sun, Xin (China)	Zhang, Qianfan (China)
Liu, Guoqiang (China)	Teng, Huaqiang (China)	Zhang, Quanxing (China)
Liu, Mandan (China)	Tu, Xiaowei (China)	Zhang, Xiangfeng (China)
Liu, Tingzhang (China)	Verma, Brijesh, (Australia)	Zhao, Wanqing (UK)
Liu, Wanquan (Australia)	Wang, Lei (China)	Zheng, Qingfeng (China)
Liu, Wenbo (China)	Wang, Ling (China)	Zhou, Huiyu (UK)
Liu, Xinazhong (China)	Wang, Mingshun (China)	Zhou, Wenju (China)
Liu, Zhen (China)	Wei, Hua-Liang (UK)	Zhu, Qiang (China)
Luo, Wei (China)	Wei, Kaixia (China)	Zhu, Xueli (China)
Luo, Pi (China)		Zhuo, Jiangang (China)
		Zuo, Kaizhong (China)

Organizing Committee

Chairs

Jia, Li (China)
Wu, Yunjie (China)

Cui, Shumei (China)
Laverty, David (UK)

Members

Sun, Xin (China)

Liu, Shixuan (China)

Niu, Qun (China)

Special Session Chairs

Wang, Ling (China)

Ng, Wai Pang (UK)

Zhang, Qianfan (China)

Yu, Jilai (China)

Publication Chairs

Zhou, Huiyu (UK)

Li, Xin (China)

Publicity Chairs

Wasif, Naeem (UK)

Deng, Jing (UK)

Deng, Li (China)

Secretary-General

Sun, Xin (China)

Liu, Shixuan (China)

Niu, Qun (China)

Registration Chairs

Song, Yang (China)

Du, Dajun (China)

Table of Contents

The First Section: Biomedical Signal Processing, Imaging, and Visualization

A Preprocessing Method of EEG Based on EMD-ICA in BCI.....	1
<i>Banghua Yang, Liangfei He, Qian Wang, Chunting Song, and Yunyuan Zhang</i>	
Real-Time 3D Microtubule Gliding Simulation.....	13
<i>Greg Gutmann, Daisuke Inoue, Akira Kakugo, and Akihiko Konagaya</i>	
Research on Novel Optimization SIFT Algorithm Based Fast Mosaic Method.....	23
<i>Lisheng Wei and Shengwen Zhou</i>	
Investigation of Mental Fatigue Induced by a Continuous Mental Arithmetic Task Based on EEG Coherence Analysis.....	33
<i>Lanlan Chen, Yu Zhao, Jian Zhang, and Junzhong Zou</i>	
An Automatic Pulmonary Nodules Detection Method Using 3D Adaptive Template Matching.....	39
<i>Jing Gong, Ting Gao, Rui-Rui Bu, Xiao-Fei Wang, and Sheng-Dong Nie</i>	
A 3D Adaptive Template Matching Algorithm for Brain Tumor Detection.....	50
<i>Xiao-Fei Wang, Jing Gong, Rui-Rui Bu, and Sheng-Dong Nie</i>	
Influence of Conduit Angles on Hemodynamics of Modified Blalock-Taussig Shunt: Computational Analysis of Patient-Specific Virtual Procedures.....	62
<i>Jinlong Liu, Qi Sun, Mitsuo Umezue, Yi Qian, Haifa Hong, Zhou Du, Qian Wang, Yanjun Sun, and Jinfen Liu</i>	
Method for Detecting Gaze Direction Based on Eyes Moving Trend....	72
<i>Qijie Zhao, Hui Shao, Xudong Zhang, and Dawei Tu</i>	
Gait Pose Estimation Based on Manifold Learning.....	82
<i>Fan Zhao, Shiwei Ma, Zhonghua Hao, and Jiarui Wen</i>	
Method of CT Pulmonary Vessel Image Enhancement Based on Structure Tensor.....	91
<i>Rui-Rui Bu, Yuan-Jun Wang, Jing Gong, Xiao-Fei Wang, and Sheng-Dong Nie</i>	

An Improved Orthogonal Matching Pursuit Algorithm for Signal Reconstruction in Wireless Body Sensor Network 101
Rui Jiang, Yongsheng Ding, Kuangrong Hao, and Shiyu Shu

Calibration Method of Stereo Microscope Based on Depth Correction... 109
Yigang Wang, Gangyi Jiang, Mei Yu, and Shengli Fan

A Prediction Model of Rectum's Perceptive Function Reconstruction Based on SVM Optimized by ACO 121
Peng Zan, Yutao Ai, Jie Zhao, and Yong Shao

A New Polynomial Hybrid Reflection Model Based on Perspective Projection 129
Jiyuan Cai, Lei Yang, Ning Zhang, and Yanyun Ren

The Second Section: Computational Methods and Intelligence in Modeling Genetic and Chemical Networks and Regulation

An Improved Bayesian-Based Wavelet Package Denoising Method for Data Reconciliation to Coking Chemical Process 137
Shengxi Wu, Qiang Ye, Kai Shen, and Xingsheng Gu

Colored Petri Nets-Based Biological Network Reconstruction for Systems Biology 150
Fei Liu, Zhifa Hu, and Ming Yang

Online Anomaly Detection Method Based on BBO Ensemble Pruning in Wireless Sensor Networks 160
Zhiguo Ding, Minrui Fei, Dajun Du, and Sheng Xu

The Third Section: Computational Methods and Intelligence in Organism Modeling

The Hemodynamic Comparison of Different Carotid Artery Bifurcation Angles Based on Patient-Specific Models 170
Yuqian Mei, Matthias Müller-Eschner, and Duanduan Chen

Design and Implementation of a Plant Morphology Modeling System Based on Evolutionary Strategy 178
Weilong Ding, Chen Hu, Fuli Wu, and Nelson Max

The Fourth Section: Computational Methods and Intelligence in Modeling and Design of Synthetic Biological Systems

Numerical Simulation of the Nutrient Limitation in the Yangtze River Estuary	188
<i>Hao Liu, Wen-Shan Xu, Hong-Xuan Kang, Bao-Shu Yin, and De-Zhou Yang</i>	
Dynamic Analysis of Circular Engineered Cardiac Tissue to Evaluate the Active Contractile Force	198
<i>Zhonggang Feng, Tatsuo Kitajima, Tadashi Kosawada, Takao Nakamura, Daisuke Sato, and Mitsuo Umezumi</i>	
Real-Time Hand Gesture Recognition for Robot Hand Interface	209
<i>Xiaomeng Lv, Yulin Xu, and Ming Wang</i>	

The Fifth Section: Computational Methods and Intelligence in Biomechanical Systems, Tissue Engineering and Clinical Bioengineering

The Application of Computational Chemistry and Chemometrics to Developing a Method for Online Monitoring of Polymer Degradation in the Manufacture of Bioresorbable Medical Implants	215
<i>Darren A. Whitaker, Fraser Buchanan, Domhnall Lennon, Mark Billham, and Marion McAfee</i>	
Modeling and Simulation of the Neural Control on OSAS with Fluid-Structural Interaction Method	226
<i>Qiguo Rong, Shuang Ren, and Qihong Li</i>	

The Sixth Section: Intelligent Medical Apparatus and Clinical Applications

Circulation System Modelling with National Implantable Ventricular Assist Device (NIVAD): Hydrodynamic Characters, Hemolysis Test in Vitro and Animal Experiments	234
<i>Tieyan Li, Liang Ye, Rong Lu, Huimin Fan, and Zhongmin Liu</i>	
Fused Visualization for Large-Scale Blood Flow Dataset	246
<i>Kun Zhao, Naohisa Sakamoto, and Koji Koyamada</i>	

The Seventh Section: Modeling and Simulation of Societies and Collective Behaviour

The Research on Agent-Based Simulation Oriented to Emergency Management 256
Zhichao Song, Yuanzheng Ge, Hong Duan, and Xiaogang Qiu

A Research on Human Cognitive Modeling in Rumor Spreading Based on HTM 268
Xiangchen Li, Xi Chen, and Wei Wang

Knowledge Based Modeling Method of Artificial Society Oriented to Emergency Management 278
Peng Zhang, Laobing Zhang, Zongchen Fan, and Xiaogang Qiu

A Kinetic Modeling for Radiotherapy Mechanisms with Gene-Environment Network (GEN) Framework 288
Jin-Peng Qi, Jie Qi, Fang Pu, and Ying Zhu

The Eighth Section: Innovative Education in Systems Modeling and Simulation

Identification of MIMO Neuro-fuzzy Hammerstein Model with Noises . . . 298
Li Jia, Xunlong Li, and Min-Sen Chiu

A Virtual Training and Evaluation Platform for Electric Wheelchair Drivers 307
Li Liu, Jingchuan Wang, and Weidong Chen

Research of Damage Imaging Algorithm in Plate Based on Signal Magnitude 319
Cong Luo, Peijiang Li, Xiaojin Zhu, and Fei Deng

DES Algorithm Realization in Asynchronous Circuit Using Four-Phase Bundled-Data 329
Jingjing Liu, Guanghua Chen, Shiwei Ma, Weimin Zeng, and Mingyu Wang

Integrated Neurofuzzy-JITL Model and Its Application in Batch Processes 339
Zhao Fu and Li Jia

The Ninth Section: Data Analysis and Data Mining of Biosignals

MongoDB Improves Big Data Analysis Performance on Electric Health Record System 350
Wei Xu, Zhonghua Zhou, Hong Zhou, Wu Zhang, and Jiang Xie

The Tenth Section: Feature Selection

Survey of Multi-sensor Image Fusion	358
<i>Dingbing Wu, Aolei Yang, Lingling Zhu, and Chi Zhang</i>	
An Novel Quality Classification for Ring Die Pellet	368
<i>Kun Zhang, Minrui Fei, Jianguo Wu, and Peijian Zhang</i>	
Stereo Matching for Binocular Underwater Images Using SURF Operator and Epipolar Restriction	378
<i>Nengjun Wang, Bin bin Peng, Daqi Zhu, and Pengfei Xu</i>	
Seedling Image Segmentation and Feature Extraction under Complicated Background	387
<i>XiaYan Lu, Xin Li, YuShen Chai, and Xiang Li</i>	

The Eleventh Section: Robust Optimization and Data Analysis

Survey of Indoor Positioning Technologies and Systems	400
<i>Lingling Zhu, Aolei Yang, Dingbing Wu, and Li Liu</i>	
Robust H_∞ Control for Discrete-Time Systems with Uncertain Packet Dropouts Probabilities	410
<i>Ying Zhou, Chenjie Ma, Jiangnan Cao, and Qiang Zang</i>	
Effect of Environment on Prey-Predator Systems with Numerical Simulation	420
<i>Qing Fang and Xiao-Yu Zhang</i>	
Author Index	425

A Preprocessing Method of EEG Based on EMD-ICA in BCI

Banghua Yang, Liangfei He, Qian Wang, Chunting Song, and Yunyuan Zhang

Department of Automation, School of Mechatronics Engineering and Automation, Shanghai
Key Laboratory of Power Station Automation Technology, Shanghai University, Shanghai
200072

yangbanghua@shu.edu.cn, heliangfei126@126.com,
lvmaogui123@163.com

Abstract. In order to remove artifacts automatically and effectively from the Electroencephalography (EEG) in Brain Computer Interfaces (BCIs), a new preprocessing algorithm called EMD-ICA (Empirical Mode Decomposition, Independent Component Analysis) is explored. The EMD-ICA method includes the following steps: Firstly, EEG signals from single or multiple channels are decomposed into a series of intrinsic mode functions (IMFs) using EMD. Each IMF can be approximately used as an input channel of the ICA, and these IMFs constitute the input matrix of the ICA. Then, the input matrix is separated into a set of statistics independent components (ICs) by ICA. Furthermore, each of statistics ICs is analyzed by using the method of sample entropy to automatically determine whether it is artifact signal. Finally, the ICs determined as artifacts are eliminated and the remaining ICs are reconstructed. The reconstructed EEG is used in the following feature extraction and classification. To evaluate the effect of the proposed method, common spatial patterns (CSP) and support vector machine (SVM) algorithm are used to extract and classify the EEG data from two datasets. The experimental results show that the proposed method can remove various kinds of artifacts effectively, and improve the recognition accuracy greatly.

Keywords: Brain Computer Interface (BCI), Empirical Mode Decomposition and Independent Component Analysis (EMD-ICA), Electroencephalography (EEG).

1 Introduction

Brain computer interfaces (BCIs) are systems that provide an alternative pathway for their users to transmit information to external world, which has become an assistive tool for neuromuscular disordered people's communication and control [1]. Electroencephalography (EEG) might be the most widely used brain imaging modality for noninvasive BCI, because EEG can capture a fast dynamics of brain information processing at a high temporal resolution. However, it is known that EEG has low spatial resolution and high noise level, which make it challenging to extract

useful information from EEG signals for BCI applications [2]. EEG pre-processing is to eliminate noise to improve the quality of the EEG. It plays an important role on the BCI research. However, many of the preprocessing techniques require minimal number of channels (>6) [3, 4] to work well. In general, increasing the number of channels may improve the processing effect. But the increase of number of channels used in preprocessing techniques not only extends the processing time but also brings noise form non-related channels. Therefore, it is meaningful to propose a preprocessing method that can remove artifacts effectively using less than six channels or even a single channel.

At present, the commonly used methods for pre-processing contains: (1) Wavelet Transform (WT), (2) Principle Component Analysis (PCA), (3).Independent Component Analysis (ICA). ICA is a blind source separation (BSS) technique that can extract the relevant information buried within noisy signals and allow the separation of measured signals into their fundamental underlying independent component(IC) [5]. ICA has already been quite broadly applied to the analysis of biomedical signals, such as analysis of EEG [6]. However, ICA requires minimal number of channels to work well. Furthermore, ICA needs visual inspection to select components manually for correction [7]. Empirical mode decomposition (EMD) is a kind of self-adapting signal processing method and it is very suitable for dealing with nonlinear and non-stationary signals [8]. EMD can broke complex signals down into a set of IMF (Intrinsic Mode Functions), each IMF can be seen as a sub-channel for the input of ICA. The sub-channels are combined into the input matrix of ICA. EMD decomposes a channel into several sub-channels, which results in more input channels for ICA under the certain number of raw EEG. That is also to say that EMD can improve the performance of ICA in case of reducing the number of raw EEG channels required by ICA.

In this paper, a new EMD-ICA method for removing artifacts in EEG data is proposed, which combines EMD and ICA. The advantage of EMD, compared to WT, is that the EMD is a data driven algorithm. This means that it decomposes a signal in a natural way without prior knowledge about the signal of interest embedded in the data series. The ICA algorithm used in this study is FastICA. FastICA has the advantage of fast convergence and good separation. The EMD is employed to decompose the EEG signal into a series of physically meaningful IMFs. These IMFs are used as input of ICA to extract ICs. Then, sample entropy is used to automatically find out the artifact components among these ICs. Finally, EEG is obtained by reconstructing non-artifactual components. The EMD-ICA method can effectively remove artifacts just using a small number of raw EEG channels.

2 EMD-ICA Methodology

2.1 Introduction of EMD

The EMD is a signal-dependent decomposition. It can decompose a time series into waveforms which are modulated in amplitude and frequency [9]. The iterative extraction of these components is based on the local representation of the signal.

With the EMD, the signal is decomposed into a set of IMFs, which are a kind of complete, adaptive and almost orthogonal representation for the analyzed signals. More precisely, $X_l(t)$ is used to denote the EEG signal from channel l ($l=1,2,\dots,L$), L is the total number of channels). If $X_l(t)$ is input signal, then EMD decomposes the $X_l(t)$ into intrinsic mode functions denoted by $\{d_i(t)\}_{i=1}^N$ such that:

$$X_l(t) = \sum_{i=1}^N d_i(t) + r(t) \quad (1)$$

Where $r(t)$ denotes the residual monotonic function which reflects the average trend with in the original one signal. In order to get meaningful estimation of instantaneous frequency, the IMF should be designed as close symmetric around the local mean and their number of extrema and zero-crossing must be equal or differ at most by one . The IMFs can be obtained by shifting process, described as:

- 1 Find all extrema (minimum & maximum) of $X_l(t)$
- 2 Interpolate (using cubic spline interpolation) between maximums (minimums) to obtain signal upper envelope $e_u(t)$ (a lower envelop $e_l(t)$)
- 3 Calculate the local mean $m(t) = (e_u(t) + e_l(t)) / 2$
- 4 Subtract $m(t)$ from $X_l(t)$ to construct oscillating signal $h(t) = X_l(t) - m(t)$
- 5 If $h(t)$ satisfies all stopping conditions, $d(t) = h(t)$ becomes an IMF; otherwise repeat step1 by setting $X_l(t) = h(t)$

After the shifting, $X_l(t)$ is decomposed into a set of IMFs denoted by $\{d_1(t), d_2(t), \dots, d_n(t)\}$. n is the number of IMFs. Let $D(t) = [d_1(t), d_2(t), \dots, d_n(t)]$ and $D(t)$ is used as an input matrix of following ICA.

2.2 Introduction of ICA

ICA is a BSS technique for separating multivariate observed random data into mutually statistically non-Gaussian ICs. ICA can work well without any information about the mixing matrix. The time varying observed signals (mixed signals) are denoted by $D(t) = (d_1(t), d_2(t), \dots, d_n(t))^T$ and the source signals consisting of ICs by $S(t) = (s_1(t), s_2(t), \dots, s_m(t))^T$ and therefore

$$D(t) = AS(t) \quad (2)$$

Then there exists a de-mixing matrix W such that

$$S(t) = WD(t) \quad (3)$$

The object of ICA is to find W . ICA is actually an optimization problem, depending on objective function and optimization algorithm. In this paper, according to negentropy maximum criterion [10], the objective function is defined by

$$C(s) = \sum_{i=1}^m J(s_i) \quad (4)$$

Where $s_i = w_i D(t)$, $J(s_i) \approx \rho(E\{G_i(s_i)\} - E\{G_i(v)\})^2$, ρ is a positive constant, $\{G_i(\bullet)\}$ is a non-quadratic function, $E\{\bullet\}$ is a mean function and v is a Gaussian variable having zero mean and unit variance.

FastICA is one of the more popular and referenced ICA techniques which is based on its own unique fast fixed-point iterative algorithm. Using newton iteration method and choosing an initial weight vector W , the basic form of FastICA iteration algorithm is as follows:

$$W = E\{DG(W^T D)\} - E\{G'(W^T D)\}W \quad (5)$$

$$W = W / \|W\| \quad (6)$$

The algorithm calculates until convergence. The ICs denoted by $S(t) = (s_1(t), s_2(t), \dots, s_m(t))^T$ separated by FastICA will be analyzed by the following method of sample entropy.

2.3 Introduction of Sample Entropy

To assess EEG complexity, sample entropy has been introduced. It can be used for short, noisy time series. It measures the irregularity of a time series and does not involve the construction of the attractor. Sample entropy eliminates self matches and has the advantage of being less dependent on time series length and more consistent when comparisons are made over a broad range of conditions [11]. Thus sample entropy is used to measure complexity of EEG. Most of structures of EEG artifacts are relatively simple, such as power frequency interference, electrooculography (EOG), and electromyography (EMG). The sample entropy of those artifacts is small. However, the sample entropy of real EEG is large. Thus the sample entropy can be used to automatically identify common EEG artifact ingredients. Below is a brief description of the sample entropy.

Consider the time series $s_i(t)$ decomposed by ICA, $i = 1, 2, 3 \dots m$. The two input parameters p and r are chosen, where p is the vector length and r is the criterion of similarity. Let the p samples beginning at sample $s_i(t)$ be denoted by the vector $v_{i,p}(i) = [s_i(t), s_i(t+1), \dots, s_i(t+p-1)]$ and consider the set of all

vectors of length p within $s(n)$, that is $[v_{i,p}(1), v_{i,p}(2), \dots, v_{i,p}(N-p)]$. Let us define

$$B_{i,p} = \frac{n_{i,p}'(r)}{N-p-1} \quad (7)$$

Where $n_{i,p}'(r)$ is the number of vectors that are similar to $v_{i,p}(i)$, given the similarity criterion r , excluding self-matching. Similar calculations are carried out for each i , with $i=1, 2, 3 \dots N-p$. The function $B_p(r)$ is then defined as the average of the function $B_{i,p}(r)$

$$B_p(r) = \frac{\sum_{i=1}^{N-p} B_{i,p}(r)}{N-p} \quad (8)$$

Similarly let $B_{i,(p+1)}(r)$ defined as

$$B_{i,(p+1)}(r) = \frac{n_{i,(p+1)}'(r)}{N-p-1} \quad (9)$$

Where $n_{i,(p+1)}'(r)$ is the number of vectors in the sequence $[v_{i,p+1}(1), v_{i,p+1}(2), \dots, v_{i,p+1}(N-p)]$ that are similar to $v_{i,p+1}(i) = [s(i), s(i+1), \dots, s(i+p)]$, given the similarity criterion r , excluding self-matching. Similar calculations are carried out for each i , with $i=1, 2, 3 \dots N-p$. The function $B_{(p+1)}(r)$ is then defined as the average of the function $B_{i,(p+1)}(r)$.

The statistic $SampEn(p, r, N)$ is then defined by

$$SampEn(p, r, N) = -\ln(B_{p+1}(r) / B_p(r)) \quad (10)$$

Fig.1 shows the $SampEn$ of different signals. The $SampEn$ of the power frequency interference and EOG are 0.2572, 0.6241 respectively, which are much smaller than the $SampEn$ of real EEG with the value of 1.6135. The $SampEn$ of the above ICs are calculated respectively. The $SampEn$ of these ICs can be denoted by $SampEn = \{SampEn_1, SampEn_2, \dots, SampEn_m\}$. Then, $SampEn$ is used to differentiate artifacts components among ICs.

2.4 EMD-ICA Method

The flow chart for EMD-ICA method is illustrated below in Fig.2.

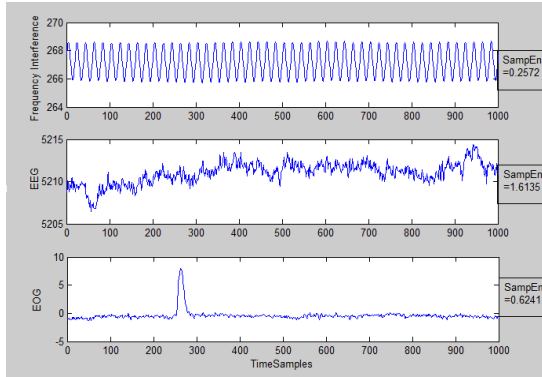


Fig. 1. SampEn of different signals

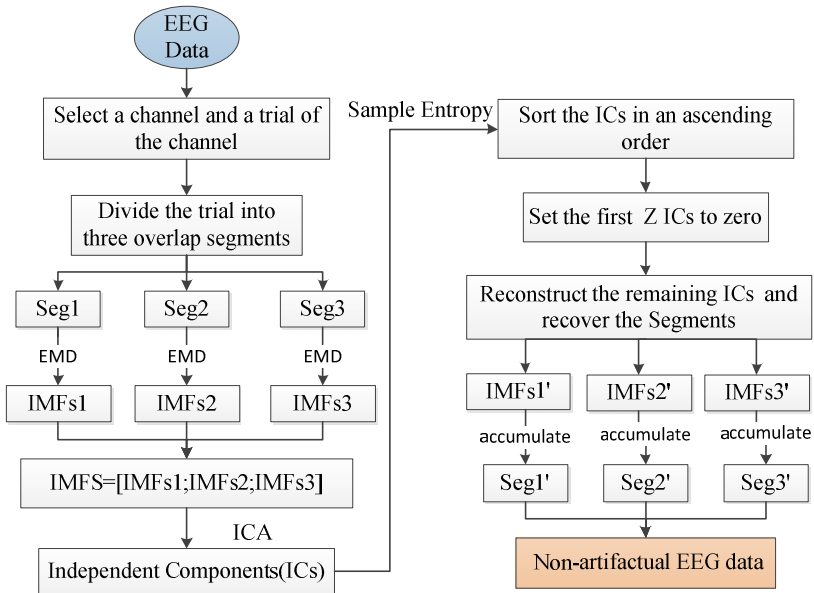


Fig. 2. Flow chart for EMD-ICA

The procedure of EMD-ICA for extracting and removing the artifact just using a single channel is summarized as follows:

- 1 Select EEG channel related closely with motor imagery. In this paper, CZ is selected.
- 2 Select one trial from a set of training trials.
- 3 Divide the trial into three overlap segments (Seg1, Seg2, and Seg3). The Fig.3 below shows how the three segments are divided.
- 4 Decompose each Seg_i , $i = 1, 2, 3$ into a set of IMF using EMD. Each set of

IMFs constitutes a matrix. The matrix can be denoted by $D_i(t) = [d_{i1}(t), d_{i2}(t), \dots, d_{in}(t)]$ $i = 1, 2, 3$. Where n is the number of

IMFs. We define $d_{i5}(t) = \sum_{j=5}^n d_{ij}(t)$. Then $D_i(t)$ can be expressed as

$$D_i(t) = [d_{i1}(t), d_{i2}(t), \dots, d_{i5}(t)].$$

5 Then FastICA is employed to separate $D(t) = [D_1(t), D_2(t), D_3(t)]$ into a set of statistics (ICs), denoted by $S(t) = [s_1(t), s_2(t), \dots, s_m(t)]$ where m is the number of ICs.

6 Calculate the sample entropy of each $s_i(t)$, $i = 1, 2, \dots, m$. Then a *SampEn* matrix denoted by

$$SampEn = \{SampEn_1, SampEn_2, \dots, SampEn_m\}$$
 can be obtained.

According to the *SampEn*, ICs are sorted in an ascending order.

$$S'(t) = [s_1'(t), s_2'(t), \dots, s_m'(t)].$$

7 The first Z ICs are determined as artifacts according to our experience.

8 Set the first Z ICs to zero from $S'(t)$ That is, $s_1'(t), s_2'(t), \dots, s_z'(t) = 0$.

9 The remaining ICs $s_{z+1}'(t), s_{z+2}'(t), \dots, s_m'(t)$ are reconstructed as $D_{i(reconstructed)}(t)$, denoted by

$$D_{i(reconstructed)}(t) = [d_{i1}'(t), d_{i2}'(t), \dots, d_{i5}'(t)].$$

10 Recover Seg_i' by accumulating component $d_{ij}'(t)$. $Seg_i' = \sum_{j=1}^5 d_{ij}'$.

11 Seg_i' ($i = 1, 2, 3$) are constituted into a non-artifact trial.

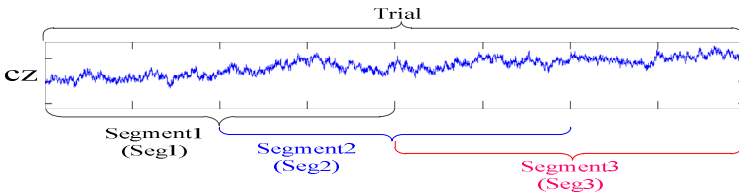


Fig. 3. Selection process of the three Segments

With the method of EMD-ICA, artifacts among the EEG are removed. Following, data from 2008 BCI Competition and our laboratory are used to validate the effect of EMD-ICA.

3 Preparation

3.1 Dataset 1—2008 BCI Competition Data

Dataset 1 used in the study is the publicly available dataset used for BCI Competition IV, which was launched on July 3rd 2008. Dataset 1 was recorded from 7 healthy subjects. For each subject, the two classes of motor imagery were selected from the three classes of left hand, right hand, and foot imagery. EEG signals were recorded from 59 channels, which positioned over sensorimotor areas densely. The signals were band-pass filtered between 0.05 and 200Hz and then sampled at 100Hz. More details are described in [12].

3.2 Dataset 2—Our Laboratory Data

Dataset 2 was from the authors' laboratory experiments. The authors recorded EEG signals using a 16-channel electrode cap. The EEG amplifier was a high-precision biological amplifier developed by Tsinghua University. The EEG signals were transformed by a 24-bit A/D converter and then collected through EEG signal acquisition software. The sampling frequency was 100 Hz. In this experiment, each of seven healthy subjects was asked to complete 60 trials in each session. Each trial included a 4 s left or right hand imagination task. There were eight sessions for each subject and then eight data sets for each subject were obtained.

3.3 Feature Extraction and Classification Method

The common spatial patterns (CSP) method is a widely used spatial filtering technique that can extract discriminative features for EEG-based BCI classification tasks [13]. The support vector machine (SVM) is one of the best-known techniques for its good theoretic foundations and high classification accuracy. It has been used extensively in biomedical signal analysis, speech recognition and face recognition [14]. In this paper, the method of EMD-ICA described in 2.4 is applied into the dataset2 described in 3.2 to get a non-artifact EEG dataset. Then, the CSP is used to extract six-dimensional feature of non-artifact EEG dataset. A SVM classifier is used to classify the features extracted by the CSP.

4 Results and Discussions of EMD-ICA

A trial from dataset 1 is randomly selected, and then the trial is used as the input of EMD-ICA described in 2.4. Fig. 4 shows the processing results of the trial. Fig. 4 (a) shows the raw EEG data of CZ channel. It is obvious that the raw data contains

many artifacts. Fig.4 (b) shows the ICs of CZ channel. IC 1 and IC 3 can be seen as EOG artifacts, while IC 7 can be seen as ECG. The sample entropies of these ICs (marked by bold red line) are showed in Table 1. It can be seen that the sample entropies of ICs that identified as artifacts are smaller than those of other ICs. Fig.4 (c) shows the reconstructed non-artifactual EEG components of CZ channel. Compared with Fig.4 (a), EOG, and ECG have been significantly removed.

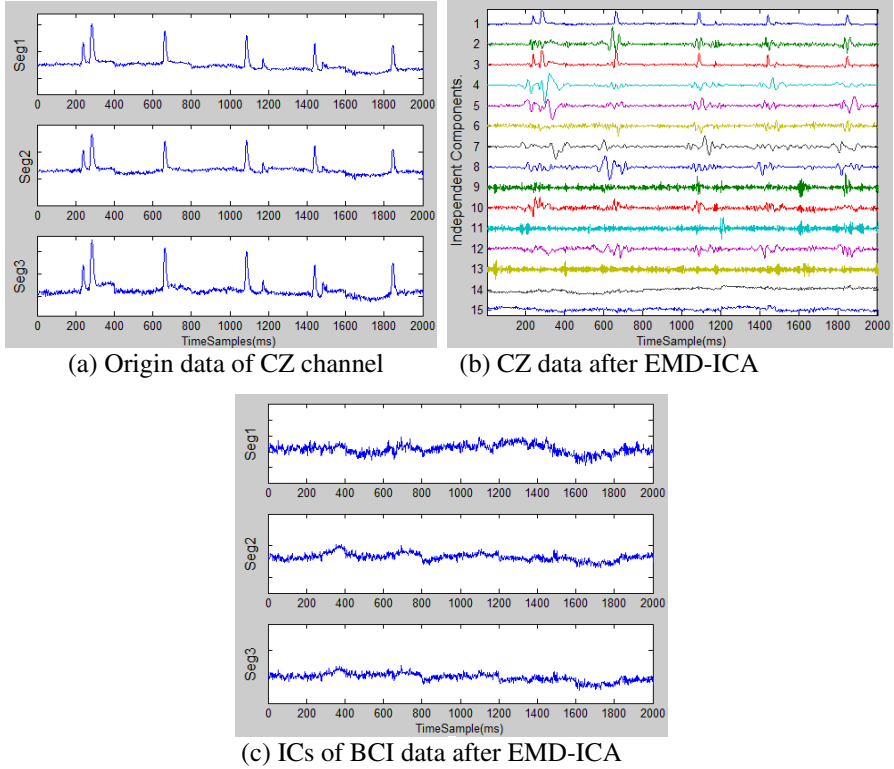


Fig. 4. Processing result of dataset 1

Table 1. Sample Entropy of ICs

ICs	1	2	3	4	5	6	7	8
<i>SampEn</i>	0.3505	0.5835	0.3205	0.7591	0.5518	1.0399	0.5419	0.5624
ICs	9	10	11	12	13	14	15	
<i>SampEn</i>	1.9504	1.9317	1.897	1.1469	0.8530	1.2542	0.7570	

Fig.5 shows the results of a random trial from dataset2 after the processing of EMD-ICA described in 2.4. Similar to Fig.4, Fig.5 (a), Fig.5 (b) and Fig.5 (c)

describe the raw EEG data, ICs separated by ICA and the reconstructed non-artifactual EEG components respectively. It can be seen from Fig.5 (a) that the raw EEG is covered by power frequency. In Fig.5 (b), IC 7, IC 10 and IC12 can be seen as frequency artifacts, while IC 5 can be seen as EMG artifact. Fig.5 (c) shows that Frequency and EMG artifacts are significantly removed automatically.

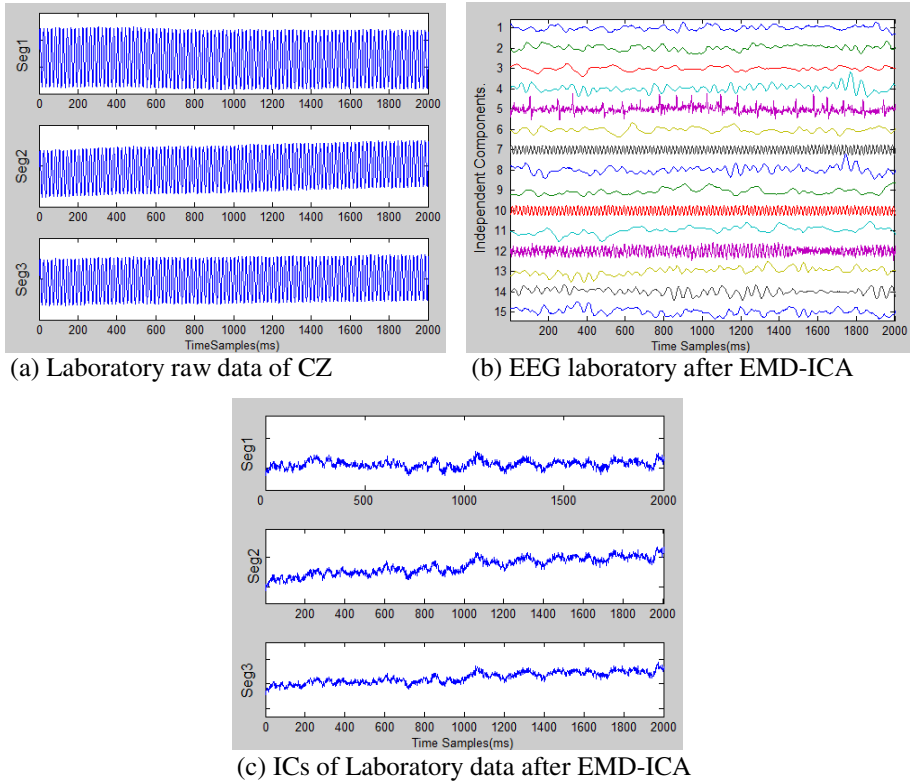


Fig. 5. Processing result of dataset 2

The processing results showed in Fig.4 and Fig.5 are from a random trial respectively. The left trials were also processed, and similar results were obtained. In addition to the comparison of results showed above, recognition accuracy is also used to evaluate the effect of the proposed method. Here the CSP is used for feature extraction and the SVM for classification. The details of the CSP and the SVM are described in 3.3. Dataset 2 is processed by EMD-ICA and ICA respectively just using a single channel. In the case of 5-fold cross-validation, the recognition accuracies are shown in Table 2. The result shows that the EMD-ICA leads to a higher 14% and 13% recognition accuracy than that of the raw EEG and ICA respectively.

Table 2. Recognition accuracy of different methods with single channel

Method	Recognition Accuracy						
	Subject1	Subject2	Subject3	Subject4	Subject5	Subject6	Subject7
None	0.50	0.52	0.51	0.52	0.53	0.53	0.54
ICA	0.51	0.52	0.52	0.54	0.54	0.53	0.54
EMD-ICA	0.62	0.65	0.71	0.67	0.68	0.67	0.66

Furthermore, the effect of the EMD-ICA is studied in the case of three channels. The result is showed in Table 3. What can be learned from the Table 3 is that the EMD-ICA leads to higher 17% and 4% recognition accuracy than that of the raw EEG and ICA respectively.

Table 3. Recognition accuracy of different methods with three channels

Method	Recognition Accuracy						
	Subject1	Subject2	Subject3	Subject4	Subject5	Subject6	Subject7
None	0.51	0.53	0.54	0.53	0.52	0.53	0.54
ICA	0.64	0.63	0.70	0.66	0.68	0.67	0.65
EMD-ICA	0.66	0.71	0.70	0.68	0.72	0.69	0.74

5 Conclusion

In this paper, a new method for automatically removal artifacts in EEG data based on EMD-ICA is presented. From the experiment results, the proposed method not only can remove the artifacts effectively but also can reduce the number of the raw EEG channels. The EMD-ICA can lead to higher 14% and 13% recognition accuracies than those of the raw EEG and ICA respectively in the case of just using a small number of channels, and higher 17% and 4% by using three channels. Thus, the EMD-ICA provides a foundation for online and practical application.

Acknowledgments. This project is supported by National Natural Science Foundation of China (60975079, 31100709), Innovation project of Shanghai Education Commission(11YZ19), Shanghai University, "11th Five-Year Plan" 211 Construction Project.

References

1. Wei, H., Pengfei, W., Liping, W.: A Novel EMD-Based Common Spatial Pattern for Motor Imagery Brain-Computer Interface. In: Proceedings of the IEEE-EMBS International Conference on Biomedical and Health Informatics (BHI 2012), Hong Kong and Shenzhen, China, January 2-7, pp. 216–219 (2012)

2. Hassan, A., Xiaomu, S.: A Study of Kernel CSP-based Motor Imagery Brain Computer Interface Classification. In: 2012 IEEE on Signal Processing in Medicine and Biology Symposium (SPMB), pp. 1–4. IEEE Press, New York (2012)
3. Azzerboni, B., Foresta, F.L., Mammone, N.: A new approach based on Wavelet-ICA algorithms for fetal electrocardiogram extraction. In: 13th European Symposium on Artificial Neural Networks, pp. 193–198. D-side Publication, Bruges (2005)
4. Jui, C., WeiYeh, L., Ju, H.: An Online Recursive ICA Based Real-time Multi-channel EEG System on Chip Design with Automatic Eye Blink Artifact Rejection. In: 2013 International Symposium on VLSI Design, Automation, and Test, Taiwan (2013)
5. Xiaojing, S., Yantao, T., Yang, L.: Feature Extraction and Classification of sEMG Based on ICA and EMD Decomposition of AR Model. In: 2011 International Conference on Electronics, Communications and Control (ICECC), pp. 1464–1467. IEEE Press, Ningbo (2011)
6. Soomro, M.H., Badruddin, N.: A Method for Automatic Removal of Eye Blink Artifacts from EEG Based on EMD-ICA. In: 9th IEEE International Colloquium on Signal Processing and its Applications, pp. 129–134. IEEE Press, Malaysia (2013)
7. Mijović, B., Vos, M.D., Gligorijević, I.: Combining EMD with ICA for Extracting Independent Sources from Single Channel and Two-Channel Data. In: 32nd Annual International Conference of the IEEE EMBS, pp. 5387–5390. IEEE Press, Argentina (2010)
8. Simon, R.H.D., Christopher, J.J.: Novel use of Empirical Mode Decomposition in single-trial classification of Motor Imagery for use in Brain-Computer Interfaces. In: 35th Annual International Conference of the IEEE EMBS, pp. 5610–5613. IEEE Press, Osaka (2013)
9. Abdollah, A., Amin, J.M., Hassan, M.: A Survey on EMD Sensitivity to SNR for EEG Feature Extraction in BCI Application. In: 2010 5th Cairo International Biomedical Engineering Conference, Cairo, pp. 176–179 (2010)
10. Huang, L., Wang, H.: Reducing the Computation Time for BCI Using Improved ICA Algorithms. In: Guo, C., Hou, Z.-G., Zeng, Z. (eds.) ISSN 2013, Part II. LNCS, vol. 7952, pp. 299–304. Springer, Heidelberg (2013)
11. Lei, W., Guizhi, X., Jiang, W.: Motor Imagery BCI Research Based on Sample Entropy and SVM. In: 2012 Sixth International Conference on Electromagnetic Field Problems and Applications, Dalian, pp. 1–4 (2012)
12. Benjamin, B., Guido, D., Matthias, K.: The non-invasive Berlin Brain-Computer Interface Fast acquisition of effective performance in untrained subjects. *J. NeuroImage* 37, 539–550 (2007)
13. Yan, L., Yasuharu, K.: A real-time BCI with a small number of channels based on CSP. *J. Neural Computing and Applications*. 20, 1187–1192 (2012)
14. He, X., Wei, S., Zhiping, H., Cheng, C.: A Speedup SVM Decision Method for Online EEG processing in Motor Imagery BCI. In: 2010 10th International Conference on Intelligent Systems Design and Applications, ISDA 2010, Cairo, pp. 149–153 (2010)

Real-Time 3D Microtubule Gliding Simulation

Greg Gutmann¹, Daisuke Inoue², Akira Kakugo^{2,3}, and Akihiko Konagaya¹

¹Department of Computational Intelligence and Systems Science,
Tokyo Institute of Technology, Yokohama 226-8502, Japan

²Faculty of Science, Hokkaido University, Sapporo 060-0810, Japan

³Graduate School of Chemical Sciences and Engineering, Hokkaido University,
Sapporo 060-0810, Japan

Abstract. A microtubule gliding assay is a biological experiment observing the dynamics of microtubules driven by motor proteins fixed on a glass surface. When appropriate microtubule interactions are set up on gliding assay experiments, microtubules often organize and create higher-level dynamics such as ring and bundle structures. In order to reproduce such higher-level dynamics *in silico*, we have been focusing on making a real-time 3D microtubule simulation. This real-time 3D microtubule simulation enables us to gain more knowledge on microtubule dynamics and their swarm movements by means of adjusting simulation parameters in a real-time fashion. One of technical challenges when creating a real-time 3D simulation is balancing the 3D rendering and the computing performance. GPU programming plays an essential role in balancing the millions of tasks, and makes this real-time 3D simulation possible. By the use of GPGPU programming we are able to run the simulation in a massively parallel fashion, even when dealing with more complex interactions between microtubules such as overriding and snuggling.

Keywords: Microtubule Gliding Assay, real-time 3D simulation, CUDA, DirectX.

1 Introduction

Microtubules and motor proteins reside in cells and act as transporters moving vesicles, granules, organelles like mitochondria, and chromosomes, as well as being a support structure for the cytoskeleton. They even play a part in cell division and cell motility. Recently, because of all the significant rolls microtubules play within molecular robotics, they are a topic of great research interest [1].

In order to analyze the dynamic behavior of microtubules, microtubule gliding assays have been proposed [2-6]. In gliding assays, microtubules run over a glass surface coated with motor proteins when they are dosed with ATP. The dynamical behavior of microtubules can be observed and captured by high resolution optical microscopes, often a succession of images are taken and then converted into video data.

One promising way to understand the video data, is a reproduction of the microtubule dynamics by means of a computer simulation [7,8]. However, conventional microtubule

simulations are primarily numerical or simulating only a single microtubule visually. These models are limited and cannot reflect microtubule interactions or swarm interactions visually that the proposed 3D microtubule simulation is able to do. To our knowledge, there is no example of any currently existing visual simulations that handle more than a single microtubule, typically in real-time fashion.

This paper focusses on the IT technology which enables the real-time 3D microtubule simulation, including complex interactions such as snuggling and overriding of microtubules. General-purpose computing on graphics processing units (GPGPU) plays an essential role to increase simulation performance. GPGPU is also effective for balancing the rendering and computing performance necessary for real-time simulations. This simulation is a helpful tool that creates good visuals for displaying microtubule dynamics; but more importantly it will become our platform to gain more understanding on microtubule swam behavior in the future.

The organization of this paper is as follows. Firstly, section 2 briefly introduces microtubule gliding assay. Section 3 and 4 describes methods and implementation of real-time 3D simulation, respectively. Then, section 5 reports performance evaluation of our prototype. Finally, section 6 concludes our prototype implementation and future works.

2 Microtubule Gliding Assay

The following figures show the movement of microtubules on a substrate. As shown in figure 1, the microtubules move by being pushed along by the motor proteins (kinesin) attached to the surface. Figure 1 also shows how two microtubules can come together: we refer to this phenomenon as “snuggling” in this article. Figure 2 (b) is also real image data, and is an example of overriding microtubules. These different types of interactions can occur when microtubules come close together, but while at a distance the microtubule’s movement seems random. These varying types of movements are what the 3D microtubule gliding simulation aims at recreating.

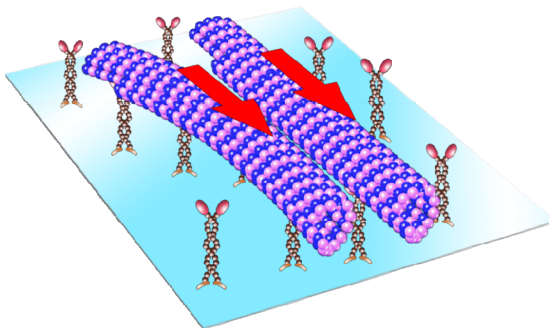


Fig. 1. 3D drawing of microtubule gliding assay

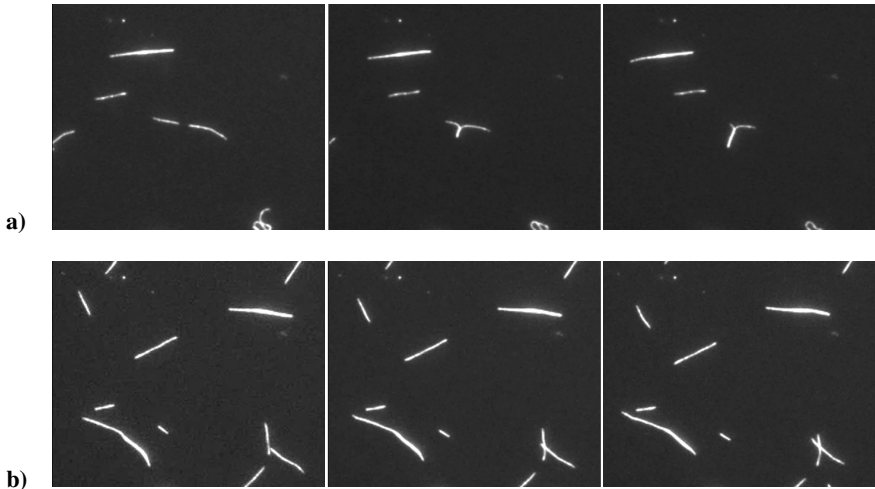


Fig. 2. Image data from a microtubule gliding assay: (a) showing snuggling, and (b) showing a cross over

3 Real-Time 3D Simulation

The main issue when creating a real-time simulation is dealing with the sheer number of calculations that are required to happen in real-time. By combining the two technologies DirectX, offering highly optimized 3D rendering algorithms, and CUDA, offering the ability to currently run around 2500 concurrent processes at a time per graphic processing unit (GPU) card, a real time 3D simulation has been performed on a standard gaming computer.

3.1 Features of Microtubule Gliding Simulation

The underlying framework for the 3D simulation has been created. The current features are: *Contained movement, variable or random length microtubules, segment following, variable turning rates and angles, parallel joining and following (when snuggling), and vertical avoidance (when overriding)*. These initial movements are fairly simple visually but have a great computational cost when dealing with interactions such as snuggling and overriding, as seen in figure 3. Whereas simulating a single microtubule is fairly trivial, simulating a large number becomes a non-trivial problem. When simulating a large number of microtubules, such as hundreds and thousands, both computational power, as mentioned, and the added complexity of swarm like integrations need to be considered. Treating all of the microtubules as independently acting agents adds both complexity and simplicity within parallel algorithms.

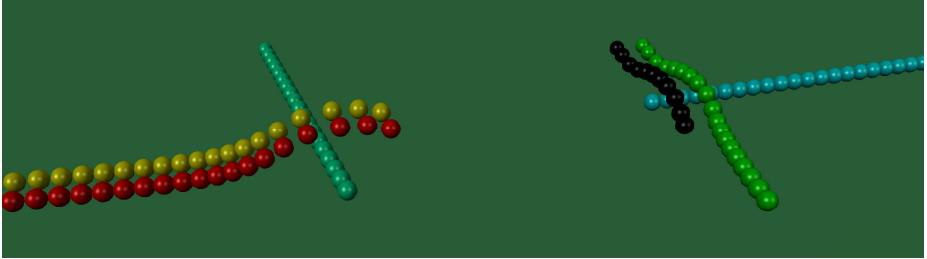


Fig. 3. An example image taken from the simulation showing overriding

3.2 Performance and Control

When large numbers of microtubules move together, systematic flows often form. One of our goals is the reproduction of the systematic flows by adding logic that controls on an individual microtubule. In comparison to creating global logic to control all microtubules, controlling them on an individual basis creates a far more realistic simulation because there is rarely an overseeing form of logic controlling processes in life. The simplicity comes in when working on some of the parallel algorithms. By having all independent agents parallel processes are more easily divided. This added simplicity in coding still has its limitations though, which are mostly due to hardware. In order to optimize the code to utilize the hardware there is still a great deal more complexity versus writing code in a serial fashion.

Despite the running of the simulation being done on an individual microtubule basis, there are certain calculations that can occur globally such as pre- and post-processing which occur around the logic and value updates of the microtubule. Our pre-processing consists of calculations that are used to populate values in a much greater degree of parallelism prior to the simulation than would be possible during the main update. These values may already be available to a microtubule in a real situation therefore does not interfere with the realism of the simulation. The post-processing is mainly for analysis of the current state of the simulation and therefore does not pose any threat of interfering with the validity. The analysis may consist of statistics about the state of the simulation, and can be used to quantify the observations made for information gathering or for further adjustment of the simulation.

The simulation also allows for random lengths to be chosen on run time. This allows for the use of input data files to set the microtubule lengths. The purpose of this is to use the findings of microtubule image processing data to setup the simulation and recreate the most realistic scenario possible or to test the simulation's accuracy against recorded findings. As a side note, it is unlikely that the simulation will exactly mimic recorded findings, as random movement is random. The goal is to simulate the general behavior, so when comparing the simulation to the experimental data, the goal is to have similar observable mechanics.

3.3 Simulation Features

As well as focusing on the performance and control, another aspect being looked at is making the simulation customizable and flexible. If a simulation targets at one specific goal, it is very difficult to use for other purposes. Flexibility is important because it is not reasonable to assume only one issue will ever be looked at. Then usability and clarity is important because it is difficult to change the simulation later on.

The final feature is having a degree of live interaction with the simulation. Interaction allows for testing many more situations much more quickly than modifying the program each time. Interaction could be initial settings or live interaction. For example, it is thought that the total energy changes types of movement. Therefore by adding the ability to add energy to simulation, this can be theoretically tested in many different situations quickly within the live computer simulation. Also, microtubule swarm movements such as turbulence and other organized movement can be tested. The goal of the live interaction is only to act as a catalyst for major changes in the group of microtubules being simulated.

4 Implementation

The main program runs using DirectX to create and update the scene. The data and calculations are handled either entirely on the CPU, or the data is initialized on the CPU and then transferred to the GPU to be handled in CUDA after that point in parallel, on the GPU.

4.1 CPU

Within the CPU code the microtubule segment object is responsible for initializing all of the microtubule segments for both versions, CPU and GPU. Also, this data class holds all of the algorithms required for the simulation; however the CPU computation in this project was only used for testing purposes, because initial algorithm debugging would be far more difficult in CUDA C.

4.2 GPU

When using GPU, data is initialized on the CPU then transferred to the GPU. After being transferred, the only modifications to the data that take place are on the GPU; therefore the data is only shared with the CPU and never transferred back to the GPU again. This cuts the data movement in half. The full process is shown graphically in figure 4. Then once on the GPU each segment gets its own dedicated process on the GPU, for a high degree of parallelism.

4.3 Parallel Algorithms

The main movement update function, step 4 in figure 4, has four tasks. The first two tasks handle microtubule overriding. The next task handles microtubule snuggling. Then, the last one updates the segment position using the previously updated states.

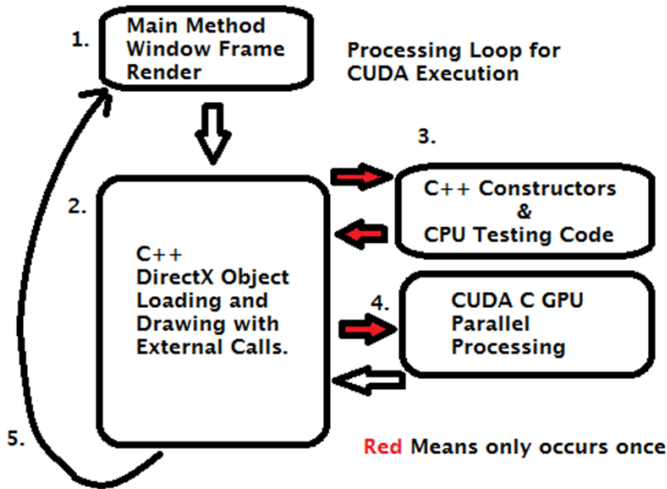


Fig. 4. Main processing loop when running the GPU version

The initial algorithms are considered to be pre-processing, this is because they calculate and update states of objects in the simulation but are not responsible for any movement or changes in the simulation. The first task runs a parallel sort on all of the segments. This is so that the second task only needs to search a fraction of the segments when each microtubule searches for other segments.

The parallel movement paring method runs through the head nodes and checks their distance and angle to each other. If they are within the specified distance and at an angle of 40 degrees or less, they join together, that is, snuggling occurs. This algorithm runs in parallel with a thread count equal to the microtubule count divided by two. The algorithm can achieve the maximum number of threads that can be used for comparisons at one time while avoiding memory collisions.

Lastly but most importantly, the main movement step handles which functions are called on which segments. Each microtubule is made up of segments. Each has a head segment and a variable number of body segments. If the segment being updated is a body segment, than it will update its direction to point at the segment in front of it, then move forward. If it is a head segment it may move in the environment naturally, follow in parallel to another microtubule or avoid another microtubule using overriding.

5 Performance Evaluation

In order to demonstrate the effectiveness of our approach, a performance comparison was done between our parallel GPU version and a non-parallel CPU version. From the figures below it can be seen that by using the parallelism of a GPU for calculations, the performance of the simulation is dramatically increased. The figures

below show a range of test cases from 50 to 1024 microtubules. The performance gains due to the GPGPU processing are impressive compared to standard CPU computing as seen in figure 5. As the test cases grow the gains from GPGPU processing continue to increase fairly consistently until reaching a 13x performance gain when simulating 1024 microtubules, as seen in figure 6.

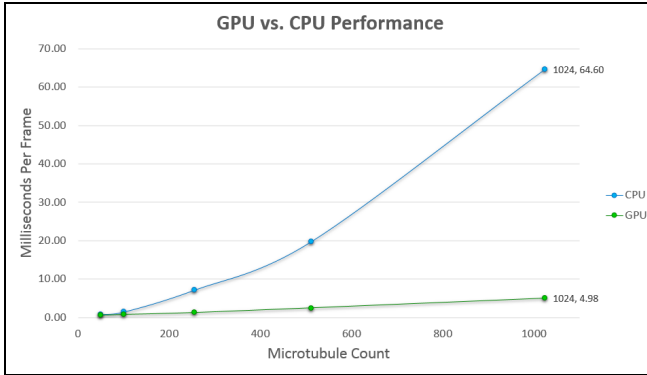


Fig. 5. GPGPU vs. CPU performance comparisons: In green is the GPU a GTX Titian, and in blue is the CPU an Intel i7-4770k. This figure shows the separation in update times between the two pieces of hardware as the test case size increase.

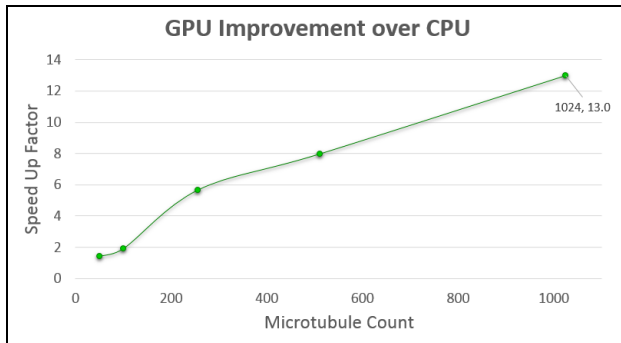


Fig. 6. GPU improvement over CPU: This figure shows the performance difference between the GPGPU computing and standard CPU computing. As the test case size increases the performance speed up improves in a linear like fashion.

The goal is to simulate enough microtubules to create the more complex microtubule dynamics; however while maintaining around or above 30 FPS, frames per second. The frame rate, or update rate, of the program is a very important detail because around 30 FPS is needed to create fluid looking visuals. 30 FPS comes from the standard TV broadcasting NTSC-M which uses a frame rate of 29.97 often referred to as 30 FPS. As seen in figure 7 the GPU version successfully maintains the needed frame rates. To better illustrate the challenges with parallel programming

figure 8 shows the average function count used for different segment counts. As can be seen, the function count is exponential in relation to the segment count. Thus as larger test cases are used more complex algorithms are needed to organize the number of functions into parallel threads on the GPU card. Future versions under development are working to address this issue, to reduce the number of calculations and threads needed per microtubule.

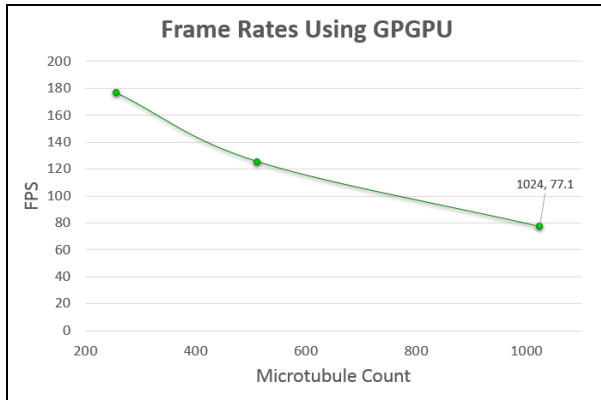


Fig. 7. Frame rates using GPGPU: This figure shows the frame rates at the upper end of the test cases with the GPU model. At lower microtubule counts the frame rates are well above the needed rate to create fluid looking motion.

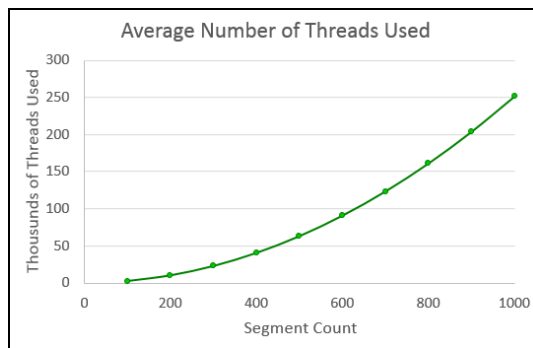


Fig. 8. Average number of threads used: Small segment count test cases are shown

6 Conclusion

Our primary goal of the 3D simulation to run in real-time has been accomplished by using GPU technologies such as DirectX and CUDA to handle the massive number of calculations. By the use of DirectX, the simulation is able to run efficiently in 3D. Then, the use of CUDA in the program offers a large amount of head room for current

and future calculations without negatively affecting the simulation speed. Also, the current model is very similar to what has been observed in experiments, qualitatively. The current model has already partially reproduced the behavior of microtubule gliding assay by means of a chain model of microtubules, with a randomly moving microtubule head followed by body chains. It also recreates the snuggling effect, parallel movement, overriding effect, and avoidance depending on the crossing angles of microtubules.

The primary advantage of creating a real time simulation that can run on a standard computer is that scientists will be able to locally, cost-effectively and rapidly test many varying situations. The current disadvantage is the limitation on the number of microtubules that can be simulated in real-time. Some may want to test hundreds of thousands to millions of microtubules; creating scalability to this extent will be a topic of future research for the project.

As the simulation advances our future work will consist of adding more complex dynamics such as: the creation of microtubule flows, ring movement, organized flows, turbulence and movements with additive properties between microtubules. Also, to best represent the true dynamics we will use molecular dynamics, such as thermodynamics, for reproducing the more complex interactions.

Acknowledgements. This work was supported by a Grant-in-Aid for Scientific Research on Innovation Areas “Molecular Robotics” (No. 24104004) of The Ministry of Education, Culture, Sports, Science, and Technology, Japan.

References

1. Murata, S., Konagaya, A., Kobayashi, S., Saito, H., Hagiya, M.: Molecular Robotics: A New Paradigm for Artifacts. *New Generation Computing* 31(1), 27–45 (2013)
2. Howard, J., Hudspeth, A.J., Vale, R.D.: Movement of microtubules by single kinesin molecules. *Nature* 342, 154–158 (1989)
3. Bohm, K.J., Stracke, R., Muhlig, P., Unger, E.: *Nanotechnology* 12, 238–244 (2001)
4. Fischer, T., Agarwal, A., Hess, H.: A smart dust biosensor powered by kinesin motors. *Nat. Nanotech.* 4, 162–166 (2009)
5. Akira, K., Jian, P.G., et al.: Formation of ring-shaped assembly of microtubules with a narrow size distribution at an air–buffer interface. *Soft Matter* 8, 10863–10867 (2012)
6. Inoue, D., Kabir, A.M.R., Mayama, H., Gong, J.P., Sada, K., Kakugo, A.: Growth of ring-shaped microtubule assemblies through stepwise active self-organisation. *Soft Matter* 9, 7061–7068 (2013)
7. Kraikivski, P., Lipowsky, R., Kierfeld, J.: Enhanced Ordering of Interacting Filaments by Molecular Motors, *Phys. Rev. Lett.* 96, 258103 (2009)
8. Kong, K.Y., Marcus, A.I., Giannakakou, P., Alberti, C., Wang, M.D.: A Two Dimensional Simulation of Microtubule Dynamics. In: *Proc. of the 5th Inter. Conf. on Information Technology and Application in Biomedicine*, pp. 461–462 (2008)
9. Sherrod, A., Wendy, J.: *Beginning DirectX 11 Game Programming*, Boston: Course Technology PTR, Print (2011)

10. Luna, F.D., Dulles, V.A.: Introduction to 3D Game Programming with DirectX 11, Mercury Learning & Information (2012, Print)
11. Kabir, A.M.R., Inoue, D., Kakugo, A., Kamei, A., Gong, G.P.: Prolongation of the Active Lifetime of a Biomolecular Motor for in Vitro Motility Assay by Using an Inert Atmosphere. *Langmuir* 27(22), 13659–13668 (2011)

Research on Novel Optimization SIFT Algorithm Based Fast Mosaic Method

Lisheng Wei^{1,2} and Shengwen Zhou¹

¹ School of Electrical Engineering, Anhui Polytechnic University, Wuhu 241000, China

² School of Mechatronics and Automation, Shanghai University, Shanghai 200072, China

Lshwei_11@163.com

Abstract. For SIFT(Scale Invariant Feature Transform) has poor real-time and low match rate problem in large-scale image registration, a improved registration algorithm based on SIFT algorithm is proposed in this paper, which down-sample the large-scale image with Cubic interpolation algorithm, and under the restriction that the minimum size of down-sampling image should be meet image registration requirement. We can calculate the transformation matrix of down-sampling image with SIFT algorithm, and then we can get transformation matrix of original large-scale image through the relationship of transformation matrix between down-sampling image and original image, so the registration of large-scale image can be got more rapidly. The experiment results show the effectiveness and feasibility of the proposed method.

Keywords: SIFT, Image matching, Image Stitching, down-sample.

1 Introduction

Image registration is the process that match and superposition two or more image which is obtained at different times, different sensor or under different conditions, it is widely used in the field of remote sensing data analysis, computer vision, image processing, etc[1-2]. Currently, many researchers focus on image registration techniques, and achieved fruitful results [3-11].

SIFT algorithm is proposed by Lowe in 1999[3], which has proved to be robust against rotation, affine, scaling, light changes. However, SIFT algorithm has a lot of redundant feature points and consume long time for large-scale image, which greatly restrict it's application in the real-time requirement situation. So, how to realize more real-time of SIFT has attract the focus of the domestic and foreign scholars [4-10].Li Fangfang select the size of Gaussian kernel adaptively, and then construct small-surface triangulation for small panel differential registration[5]; Xiong Ziming improved SIFT by combine SIFT and Harris algorithm, took Harris feature points in place of SIFT key-points, and adopt PCA (Principle Component Analysis) to reduce the dimension of descriptor, this method greatly improved the efficiency of registration[7]; Sukthankar reduce the dimension of descriptor from 128 to 20 by PCA method, which greatly cut down time-consuming[8].

As above descript, they focus on the improvement of key-point extraction or match method, and achieve great result. Base on their study, a new method which focuses on

the image relationship between image size and the number of key-point, and the relationship of transformation matrix between down-sampled image and original one. In this paper, key-point and transformation matrix can be got from down-sampling image, and then transformation matrix of original large-scale image can be got according to the relationship of two matrixes, so we can get a real-time image registration of our original image.

2 Down-Sample Image Preprocess

Feature extraction and matching with traditional SIFT algorithms for a large size image is time-consuming. The image down-sampling pre-process combine with cubic interpolation algorithm is proposed in this paper to reduce the image size, and the numbers of key-points are also reduced, as the result the registration of two images can consume less time. For the same image ,the experiment has proved that the number of key-points is proportional to the size of the image, how can we reduce the image size as small as possible while the effect of the image registration does not affected is became the focus of this paper. As we know, image registration transformation matrix H contains 8 unknown parameters, at least 4 pairs of matching points are needed to calculate them, so the size of down-sampled image should not be too small, we need set a limit to it. Then the feature extraction and matching process of SIFT algorithm can be done under down-sampled image, so we can calculate transformation matrix of two down-sampled images by using they matched points. However, we want to get the registration of two original large-size images, so we also need to know transformation matrix of two original images. In this paper, according to the intrinsic relationship of original image and its down-sampling one, the relationship between two transformation matrixes is established, so transformation matrix of original large-size images can be got. This method can reduce the number of key-points, and speed up the original SIFT algorithm. The specific flow chart of algorithm is shown in Fig.1.

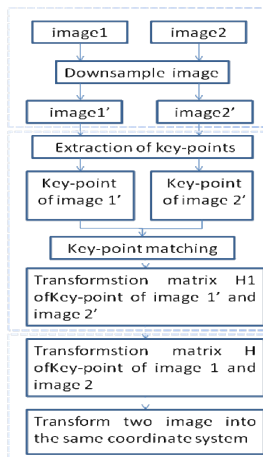


Fig. 1. The flow chart of improved registration algorithm based on SIFT algorithm

As flow chart shown in Figure 1, the improved algorithm can be divided into three parts: 1) down-sampling the original images; 2) Feature extraction and matching of down-sampled image and calculate the transformation matrix of down-sampled images; 3) Solving the transformation matrix between the original images, base on the intrinsic relationship between original image transformation matrix and down-sampled image transformation matrix, then realize the original image registration.

2.1 Down-Sample Image

The transformation matrix of images contains 8 parameters, as (1) shown:

$$H = \begin{bmatrix} a & b & c \\ d & e & f \\ g & h & 1 \end{bmatrix} \quad (1)$$

image rotation, displacement and affine transformation can be achieved through this parameters, and then turn the two image into the same coordinate system. To solve the transformation matrix parameters, we need at least four pairs of correct matching points. As we know, a large number of redundant key-points will be generated when using the original SIFT algorithm, and it is a time-consuming process. In the paper [13], Author compared image registration accuracy and time consuming under different interpolation methods and down-sampling multiple, and find that the time consumption can be reduced at least 20% -30% when down-sampling the original image to 80%-90% and the result can meet the requirements of registration accuracy. Under the condition of meeting the requirements of registration accuracy, reducing the size of original image as small as possible by down-sampling the rows and columns of image in same proportion is proposed in this paper. Found through experiments, generally, the requirements of Vision and image registration accuracy can be satisfied when the number of match points more than 40.

2.2 SIFT Key-Point Extraction

SIFT algorithm simulates human vision at different distances through multi-scale space approach, and constructs feature descriptors by using neighborhood information of feature points, so it could be rotation invariant. Concrete steps of extracting SIFT key-point are as follows:

1) Detection of Scale-Space Extreme

To ensure the stability of the key-points of the image scaling, it is necessary to extract key-points from the Gaussian scale-space image. As paper [3] show, Gaussian convolution kernel is the only linear kernel, two-dimensional scale space is defined as function $L(x, y, \sigma)$:

$$L(x, y, \sigma) = I(x, y) * G(x, y, \sigma) \quad (2)$$

$$G(x, y, \sigma) = \frac{1}{2\pi\sigma^2} e^{-\frac{(x^2+y^2)}{2\sigma^2}} \quad (3)$$

where $I(x, y)$ is input image, $*$ is the convolution operation, $G(x, y, \sigma)$ is Gaussian function with variable scale .

DOG (Difference of Gaussian) function which is defined as the difference of two nearby scale image in scale space:

$$\begin{aligned} D(x, y, \sigma) &= (G(x, y, k\sigma) - G(x, y, \sigma)) * I(x, y) \\ &= L(x, y, k\sigma) - L(x, y, \sigma) \end{aligned} \quad (4)$$

where k is multiplicative factor of two nearby scale image in scale space.

DOG function is proposed by LOWE, and has been proved can get more stable key-points. Images to be registered can be continuously filtered by different scale of Gaussian kernel and down-sampled, then form groups of different sizes Gaussian blur images, Gaussian pyramid and Difference of Gaussian pyramid can be constructed by this Gaussian blur images. In Gaussian differential space, each sample point of image is compared with its 8 neighborhood points and 9 neighbors in scale above and below, if the point is maxima or minima, then this points are selected as candidate key-points. To ensure the accuracy and stability of image registration, some feature points with low contrast ratio and unstable edge response points must be removed. .

2) The Local Image Descriptor

The key-point descriptor can be obtained by the statistics of gradient information, the main direction of each key-point is obtained according to the gradient direction histogram of each feature point neighborhood. The key-point is treated as the center of image, and then rotates the image to the main direction of the key-point. Take $16 * 16$ pixels around each key-point as the key-point neighborhood, then apart it into $16 * 4 * 4$ pixels sub-blocks, then 8-direction gradient orientation histogram can be calculated for each sub-block, so each key-point will get $4 * 4 * 8 = 128$ dimensional vector, which is also called SIFT feature descriptor, as figure 2 show.

3) Key-Point Match

The nearest neighbor distance algorithm (NN) is widely used to match key-points from different images, which compares the ratio of nearest neighbor Euclidean distance of a sample feature points and sub-neighborhood Euclidean distance of it to the threshold r_0 , of matching feature points.

Let $X_1 = (x_1, x_2, x_3, \dots, x_{128})$, $Y_1 = (y_1, y_2, y_3, \dots, y_{128})$ be two 128 dimension key-point descriptor:

$$d = \sqrt{(y_1 - x_1)^2 + (y_2 - x_2)^2 + \dots + (y_{128} - x_{128})^2} \quad (5)$$

$$r = \frac{\text{nearest neighbor Euclidean distance}}{\text{subneighborhood Euclidean distance}} < r_0 \quad (6)$$

When the ratio r small than threshold r_0 , the two points are considered to be a pair of matching point, generally, the value of r_0 is 0.8.

4) Accurate Match and Transformation Matrix

The transformation H with 8 parameters is used for image registration, as follow:

$$H = \begin{bmatrix} a & b & c \\ d & e & f \\ g & h & 1 \end{bmatrix} \quad (7)$$

Let (x, y) 、 (\hat{x}, \hat{y}) be a pair of correct match points, so the following formula can be satisfied:

$$\begin{bmatrix} \hat{x} \\ \hat{y} \\ 1 \end{bmatrix} = \begin{bmatrix} a & b & c \\ d & e & f \\ g & h & 1 \end{bmatrix} \times \begin{bmatrix} x \\ y \\ 1 \end{bmatrix} \quad (8)$$

We need at least 4 match points to calculate 8 parameters of H , a large number of key-points will be got from nearest neighbor distance algorithm, but a lot of error matching points still exist in it, and it will lead to great deviation. RANSAC (random sample consensus) algorithm widely used to removal mismatching points and effective for parameters estimation, so we use it for 8 parameters estimation.

3 Relationship of Image Transformation Matrix

From now on, we have down-sampled the original image, and get the transformation matrix (H_1) of down-sampled image base on SIFT algorithm, but registration result of down-sampled images has small size and low pixels, which is hard to meet the practical needs, so we need to perform image registration on the original images. First of all, the relationship between original transformation matrix H and down-sampled transformation matrix H_1 is needed. We have get down-sample transformation matrix H_1 as above describe, then we can calculate the original transformation matrix H by the relationship between two matrix base on down-sample factor p , so we can realize coordinate transformation between two original images.

If (x_1, y_1) 、 (\hat{x}_1, \hat{y}_1) is a pair of match point from down-sampled image, we define H_1 as follow:

$$H_1 = \begin{bmatrix} a_1 & b_1 & c_1 \\ d_1 & e_1 & f_1 \\ g_1 & h_1 & 1 \end{bmatrix} \quad (9)$$

Thus

$$\begin{bmatrix} \hat{x}_1 \\ \hat{y}_1 \\ 1 \end{bmatrix} = \begin{bmatrix} a_1 & b_1 & c_1 \\ d_1 & e_1 & f_1 \\ g_1 & h_1 & 1 \end{bmatrix} \times \begin{bmatrix} x_1 \\ y_1 \\ 1 \end{bmatrix} \quad (10)$$

So

$$\hat{x}_1 = \frac{a_1 \cdot x_1 + b_1 \cdot y_1 + c_1}{g_1 \cdot x_1 + h_1 \cdot y_1 + 1}, \quad \hat{y}_1 = \frac{d_1 \cdot x_1 + e_1 \cdot y_1 + f_1}{g_1 \cdot x_1 + h_1 \cdot y_1 + 1} \quad (11)$$

$$a_1 \cdot x_1 + b_1 \cdot y_1 + c_1 - g_1 \cdot x_1 \cdot \hat{x}_1 - h_1 \cdot y_1 \cdot \hat{x}_1 = \hat{x}_1 \quad (12)$$

$$d_1 \cdot x_1 + e_1 \cdot y_1 + f_1 - g_1 \cdot x_1 \cdot \hat{y}_1 - h_1 \cdot y_1 \cdot \hat{y}_1 = \hat{y}_1 \quad (13)$$

Let (x, y) (\hat{x}, \hat{y}) be a pair of match point from original image, and

$$H = \begin{bmatrix} a & b & c \\ d & e & f \\ g & h & 1 \end{bmatrix} \quad (14)$$

Thus

$$a \cdot x + b \cdot y + c - g \cdot x \cdot \hat{x} - h \cdot y \cdot \hat{x} = \hat{x} \quad (15)$$

$$d \cdot x + e \cdot y + f - g \cdot x \cdot \hat{y} - h \cdot y \cdot \hat{y} = \hat{y} \quad (16)$$

If (x_1, y_1) 、 (\hat{x}_1, \hat{y}_1) are two points zoomed with parameter p from (x_1, y_1) 、 (\hat{x}_1, \hat{y}_1) coming from original image, so

$$x_1 = p \cdot x, \quad y_1 = p \cdot y, \quad \hat{x}_1 = p \cdot \hat{x}, \quad \hat{y}_1 = p \cdot \hat{y} \quad (17)$$

Combine equation(12) (13) (17) , so

$$a_1 \cdot x + b_1 \cdot y + \frac{c_1}{p} - g_1 \cdot p \cdot x \cdot \hat{x} - h_1 \cdot p \cdot y \cdot \hat{x} = \hat{x} \quad (18)$$

$$d_1 \cdot x + e_1 \cdot y + \frac{f_1}{p} - g_1 \cdot p \cdot x \cdot \hat{y} - h_1 \cdot p \cdot y \cdot \hat{y} = \hat{y} \quad (19)$$

Then, according to (15) (16) (18) (19) :

$$H = \begin{bmatrix} a_1 & b_1 & c_1/p \\ d_1 & e_1 & f_1/p \\ g_1 p & h_1 p & 1 \end{bmatrix} \quad (20)$$

4 Experiment and Result

The platform used is memory 2G, window XP operating system, CPU 3.3GHZ, Matlab 7.0. Three groups of image are used in Fig.2, the size of them are 1296×968、830×620、384×640 respectively.

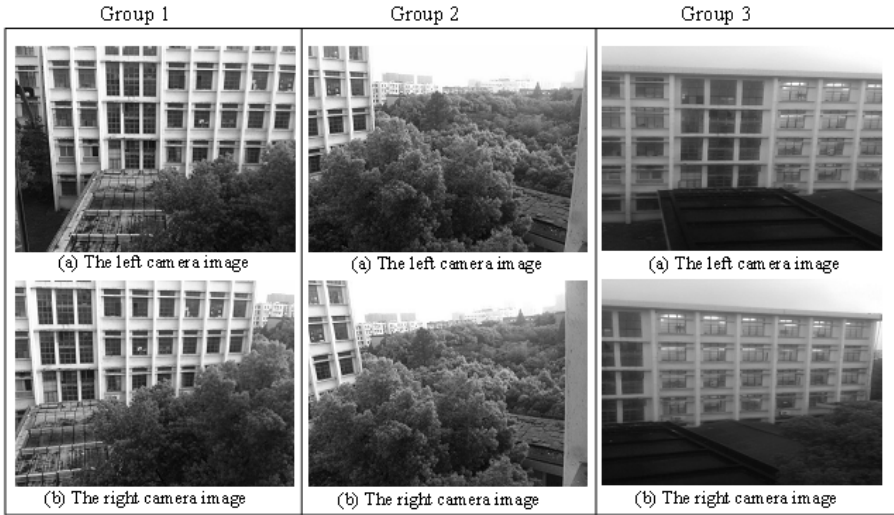


Fig. 2. The original image

Image size has great influence on the number of key-point, the influence of scaling factor p on the number of match point are following as:

Table 1. The influence of scaling factor on the number of match point

Scale(p)	0.08	0.1	0.15	0.2	0.3	0.4	0.5
Group1	13	23	59	101	171	281	356
Group2	7	15	35	79	184	397	652
Group3	<4	7	20	40	57	91	101
Scale(p)	0.6	0.7	0.8	0.9	1	1.1	1.2
Group1	472	579	672	723	757	1017	1121
Group2	1046	1456	1851	2361	2606	3221	3547
Group3	147	147	165	186	185	174	175

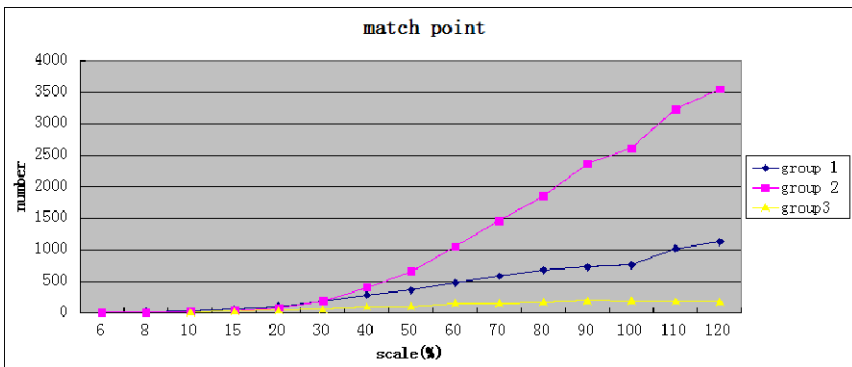


Fig. 3. The influence of scaling factor on the number of match point

Table 2. The influence of scaling factor on SIFT and match time

Scale(p)	0.08	0.1	0.15	0.2	0.3	0.4	0.5
Group1	0.893	0.876	1.188	1.156	1.844	2.281	3.374
Group2		0.657	0.719	0.797	1.156	1.36	1.797
Group3		0.562	0.593	0.688	0.782	0.938	1.203
Scale(p)	0.6	0.7	0.8	0.9	1	1.1	1.2
Group1	4.578	5.891	7.937	10.703	12.891	21.265	28.813
Group2	2.515	3.36	4.062	5.157	5.953	7.297	8.297
Group3	1.25	1.468	1.749	2.063	2.485	2.703	3.048

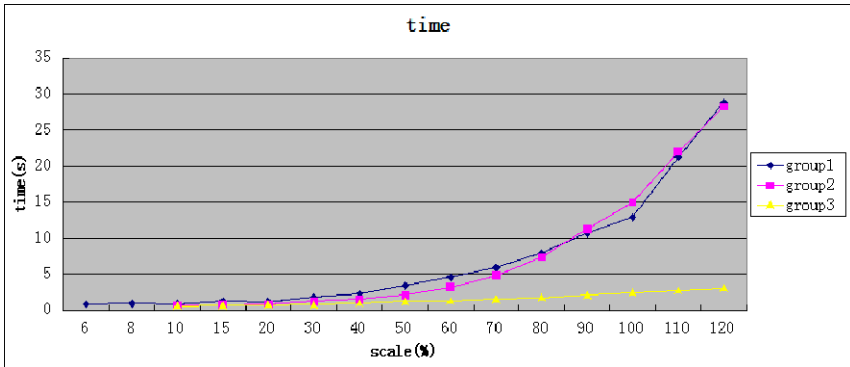


Fig. 4. The influence of scaling factor on SIFT and match time

As Fig.3 showing, the image size and the number of match point will increase or reduce following the down-sample factor p , as Fig.4 showing, consumption of time is also rise following the down-sample factor p , so reduce the size of image by down-sampling original image can reduce time consuming, but there will not enough matching point to calculate the conformation matrix when the size of image is too small. It has been proved that the registration accuracy has positively related to the number of matching points, so when down-sampling image size, the registration accuracy will decline. So how to solve the balance between registration accuracy and time-consuming is the main research in this paper. As experiment showing, more than about 40 matching-points can satisfy the requirements of visual accuracy, at that time, the down-sampling factor p of this three group image is 0.15\0.2\0.3, and the size of them is 194×145\66×124\115×192, the time consumption of image registration is far less than original image registration, it does not change much when down-sampling continues. In summary, down-sampling the large scale image with the constrain of image size can meet the requirements of balance between time consuming and Visual effects. The above experiment demonstrate that constrain size of image row or column in the range of 110-190 can meet this requirements well.

Following experiment down-sampling the three group of original image with the constrain of 180, as table3 and fig.8 show, this method show good result.

$$p = 180 / \min(m, n, k, l) \quad (21)$$

where $(m, n), (k, l)$ are row and column of two original image.

Table 3. The contrast between the original algorithm and the improved algorithm

		P(%)	Number of match point	Time consuming(s)
Group1	Optimization SIFT	0.185	159	2.045
	Tradition SIFT	1	2238	45.859
Group2	Optimization SIFT	0.29	167	1.986
	Tradition SIFT	1	2607	21.704
Group3	Optimization SIFT	0.47	116	1.991
	Tradition SIFT	1	185	3.827

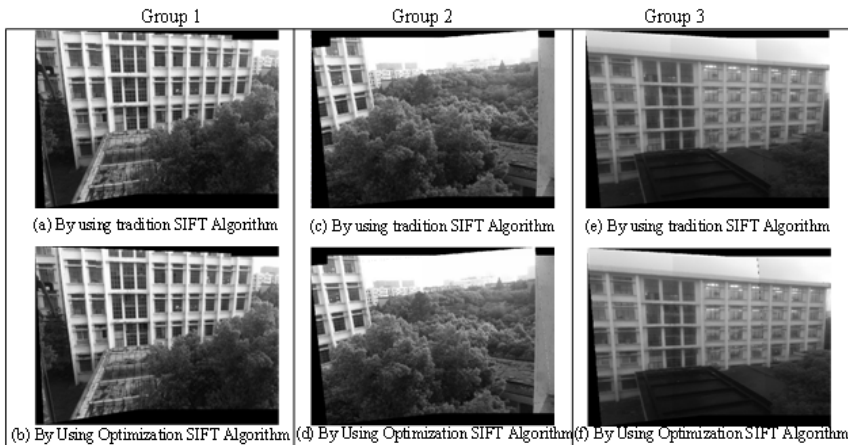


Fig. 5. The contrast between original algorithm and improved algorithm

5 Conclusions

The improved image registration algorithm based on SIFT algorithm is proposed in this paper, which down-sampling the original image under the constrain of the min size of image. In this paper the constrain we select is 180, which is based on the experiment we did in section 4, in this case we wan keep the balance of time consuming and registration accuracy. This improvement can be meet the need of real-time image process better than traditional SIFT algorithm. As the experiment show, this improved algorithm can be more highly real-time while satisfying the requirement of registration accuracy.

Acknowledgments. This work was supported by National Natural Science Foundation of China under grant 61203033, Anhui Provincial Natural Science Foundation under grant 1208085QF124, and National Student Innovation, Entrepreneurship, and Training Plan Foundation of China under grant 201210363061.

References

1. Xiong, L.: A survey of image matching in computer vision. *Journal of Hubei University Technology* 21(3), 171–173 (2006)
2. Qi, Z., Cooperstock, J.R.: Toward Dynamic Image Mosaic Generation With Robustness to Parallax. *IEEE Transactions on Image Processing* 21(1), 366–378 (2012)
3. Lowe, D.: Distinctive image features from scale-invariant keypoints. *International Journal on Computer Vision* 60(2), 91–110 (2004)
4. Wang, H., Wang, C., Li, P.: Review of multi-source remote sensing image techniques registration. *Computer Engineering* 37(19), 17–21 (2011)
5. Li, F., Xiao, B., Jia, Y.: Improved SIFT algorithm and its application in automatic registration of remotely-sensed imagery. *Geomatics and Information Science of Wuhan University* 34(10), 1245–1249 (2009)
6. Quelhas, P., Monay, F., Odobez, L.M.: D. Gatica-Perez, T. Tuytelaars, L. Van Gool.: Modeling scenes with local descriptors and latent aspect. In: *Proceedings of the Tenth IEEE International Conference on Computer Vision, ICCV 2005* (2005)
7. Xiong, Z., Wan, G.: Unmanned aerial vehicle serial image automatic registration base on improved SIFT algorithm. *Journal of Geomatics Science and Technology* 29(2), 153–156 (2012)
8. Ke, Y., Sukthankar, R.: PCA-SIFT: A more distinctive representation for local image descriptors. In: *Proceedings of the Conference on Computer Vision and Pattern Recognition, Washington, USA*, pp. 511–517 (2004)
9. Zhu, Z., Shen, Z., Luo, J.: Parallel remote sensing image registration based on improved SIFT point feature. *Journal of Remote Sensing* 15(5), 1024–1031 (2011)
10. Yu, L., Dai, Q.: Improved SIFT Feature Matching Algorithm. *Algorithm. Computer Engineering* 37(2), 210–212 (2011)
11. Zheng, Y., Huang, X., Feng, S.: An Image Matching Algorithm Based on Combination of SIFT and the Rotation Invariant LBP. *Journal of Computer-Aided Design & Computer Graphics* 22(2), 286–292 (2010)

Investigation of Mental Fatigue Induced by a Continuous Mental Arithmetic Task Based on EEG Coherence Analysis

Lanlan Chen^{*}, Yu Zhao, Jian Zhang, and Junzhong Zou

Key Laboratory of Advanced Control and Optimization for Chemical Processes,
Ministry of Education, East China University of Science and Technology,
130 Meilong Road, Shanghai 200237, P.R. China
chenlanlan104@gmail.com

Abstract. In the present study, twelve volunteers were participated in a 2 h continuous mental arithmetic task without any break, which was designed to induce mental fatigue. The negative influence was investigated through EEG coherence, which was used as a measure of synchronization of different underlying brain regions. It was observed that the sustained mental task led to increased EEG coherence, which did not result in more efficient performance. The change of EEG coherence was widespread not limited to specific brain regions or frequency bands. The variation of EEG coherence combined with behavior performance validated the impact of mental fatigue caused by a continuous mental task.

Keywords: mental fatigue, continuous mental arithmetic task, EEG signals, coherence analysis.

1 Introduction

When people concentrate for a long time to accomplish a repetitive task, they feel fatigued. This kind of fatigue is not necessarily physical but it may affect a person's normal activity. Mental fatigue is a very common phenomenon in modern society and sustained mental work is an important determinant of depressive disorders even accidents [1-3]. Concerning the influence of mental fatigue on daily life, less attention has been paid to the neuro-cognitive mechanisms underlying the effects of mental fatigue.

Previous studies have obtained some generally accepted concepts on arousal and fatigue. One of the most common findings of EEG studies is a shift from fast, low amplitude waves to slow, high amplitude waves when the level of alertness drops. Some of the studies analyzed the amount of theta and alpha power as indexes of fatigue level that subjects experienced [4].

These studies mainly focused on the impact of mental fatigue by using electroencephalogram (EEG). However, current analysis like EEG power estimator

^{*} Corresponding author.

reflects the power of neural activity in single brain site. While complementary information about brain functional organization during the mental task processes should be extracted from different brain regions. The information processed in separate brain regions is supposed to be integrated through synchronous activity of different neural clusters ranged in different brain areas [5-6].

Recent studies have used EEG coherence analysis to investigate functional changes in different situations. Some studies have analyzed EEG coherence during monotonous driving [7-8]. Inter-hemispheric coherent value in the alpha band showed significant difference between the earlier and later driving stages and coherence value in all frequency bands showed slightly increasing throughout driving sessions [7]. However, inconsistent results were reported with a reduction of inter-hemispheric qEEG coherence during the accomplishment of a motor task [8]. Portella's result should be interpreted carefully because the analysis was limited within the theta band. In the present study, EEG coherent estimators are analyzed as the biomarkers for the increasing mental fatigue which is induced by 2 h continuous mental calculation task. The major issue in the present study is to investigate whether the observed influence of mental fatigue is related to changes of neural dynamics of brain. Chen et al. (2010) limited their analysis of brain activity in that study to EEG power spectrum components which indicated a shift into slow frequency bands at occipital region with increasing mental effort [9]. The most important task in the present study is to explore the change of EEG coherent related with mental fatigue.

2 Materials and Methods

2.1 Subjects and Tasks

Twelve healthy male students participated in this experiment with an average age of 22.5 years old. All subjects were reported to have good sleep before the experiment days and were instructed to abstain from prescription medication, alcohol and caffeine 24 hours before experiments. Subjects were settled in a dimly lit, sound attenuated, electrically shield room. The experiments were performed according to the Declaration of Helsinki.

To induce mental fatigue, two-hour continuous mental calculation task without any break was designed. Subjects were instructed to perform the mental calculation continuously without any break and execute the task with maximum effort as quickly and correctly as possible. The content of mental arithmetic was 0~99 two-digit integer addition. For the convenience of further analysis, the 2 h continuous calculation task was divided into four stages each lasting half an hour and named as S1, S2, S3, and S4 respectively.

2.2 Behavioral Performance

During the whole process of mental task, several performance estimators including correct answers, reaction time, and standard deviation of reaction time were recorded and averaged each half an hour interval. Behavioral results were subjected to paired sample T tests to make comparisons between different time intervals.

2.3 EEG Acquisition

During the implement of fatigue task, eight-channel EEG signals were simultaneously acquired. Electrodes were placed according to the standard 10-20 system and positioned at Fp1, Fp2, F3, F4, Fz, Cz, O1, and O2 against ipsilateral earlobe electrode as shown in Fig.1a. The electrical impedance was under 10 kOhms for all electrodes. EEG was amplified by a digital EEG machine (Nihon-Koden EEG 2110) with the sampling frequency of 200 Hz, a low-frequency cut-off of 0.5Hz, and a high-frequency cut-off of 30Hz.

2.4 EEG Spectral Coherence

Coherence, defined as the cross-spectrum between two signals normalized by their power spectra, was calculated for the two types of trials separately between eight electrode positions. This resulted in 28 electrode pairs as displayed in Fig.1b. Coherence was determined within four specific frequency bands: delta, theta, alpha and beta.

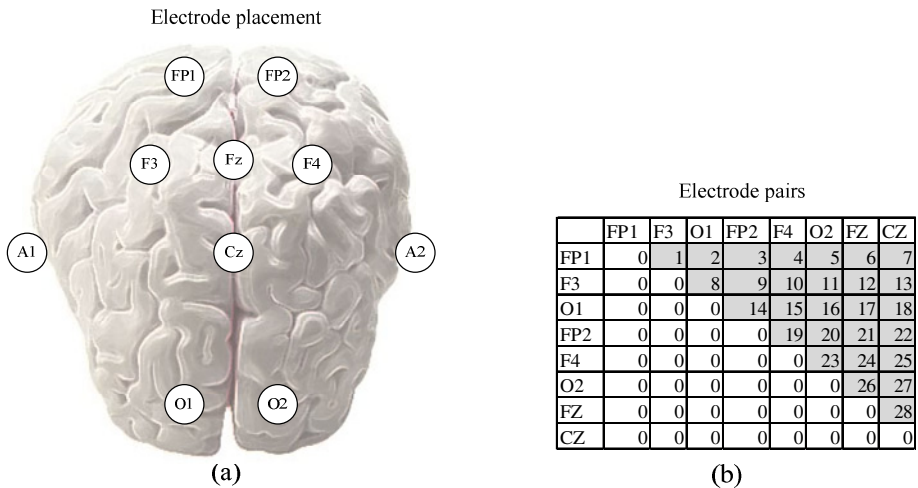


Fig. 1. Electrode placement and electrode pairs

3 Results

3.1 Behavior Performance

The global mean value of performance estimators displayed a clear deterioration during the continuous mental arithmetic task as shown in Fig.2. Paired sample T test between the last and the initial calculation stages was analyzed. The results reflected subjects made less correct answers with longer reaction time and larger S.D. of reaction time at the last calculation session (reduction of correct answers = 49.7, $p < 0.001$; increase of RT = 0.24 sec, $p = 0.003$; increase of RTSD = 0.41 sec, $p = 0.006$).

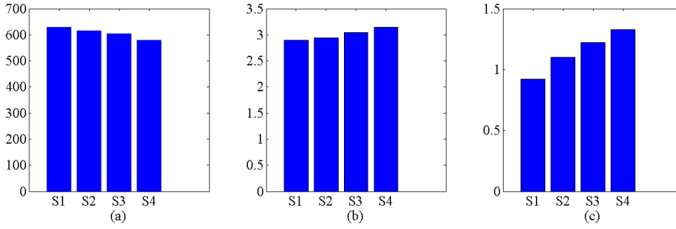


Fig. 2. Calculation performance for the four time intervals of mental task. (a) Correct answers (b) Reaction time (c) S.D. of reaction time.

3.2 EEG Coherence Analysis

The coherent difference between the last and the initial calculation stages was significant. As evident from Fig. 3, an increase of coherence at S4 stage was observed compared to that at the initial stage S1. Another piece of evidence came from the results of paired sample T comparisons. From Table 1, electrode pairs presenting significant difference between the last and initial stage were listed within four basic frequency bands. Most of the electrode pairs showed significant increase at the last stage compared with that of the initial stage.

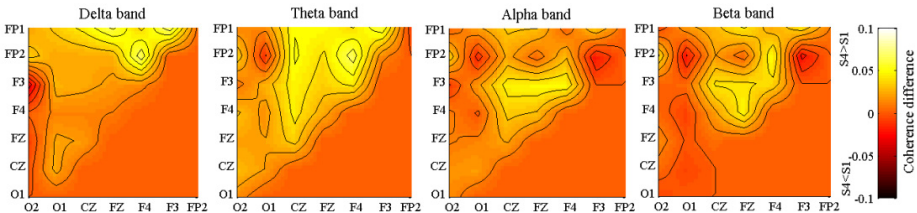


Fig. 3. Coherence difference between the last (S4) and initial (S1) time stages. Color bar displays the specific magnitude.

Table 1. Electrode pairs presenting significant difference between the last and initial time interval during mental task. Paired sample T test was used to make comparisons between time intervals. Significance level ($p < 0.05$) was analyzed.

Frequency band	Electrode pair
Delta band	Fp1-Fz;Fp2-F4;Fp1-Cz;Cz-O1;F3-O2*
Theta band	Fp1-Cz;Fp2-Cz;F3-Fz;F4-Fz;F3-F4;F3-Cz;F4-Cz;Fz-Cz;Cz-O2;Fp2-O2
Alpha band	Fp1-Cz;F3-Fz;F4-Fz;F3-Cz;F4-Cz
Beta band	Fp1-Cz;F4-Fz;F3-F4;Fp2-O2

The electrode pair without asterisk represents the coherence at the last stage (S4) was greater than that of the initial stage (S1) at a significance level $p < 0.05$; the electrode pair with an asterisk means the coherence at S4 was less than that of S1 with $p < 0.05$.

4 Discussions

Previous literature reports changes of EEG frequency bands are highly related to decrement performance caused by fatigue [1, 3]. EEG especially occipital alpha rhythm and frontal midline theta rhythm can be used to evaluate human's arousal level which is usually referred together with drowsy and mental fatigue [4]. This research supports the previous findings on EEG spectrum analysis and designs a continuous mental arithmetic task to induce mental fatigue. The timing of the experiment task is based on the basic rest-activity cycle which states an approximate 1.5 hour rhythm of arousal.

The purpose of this study is to explore whether the influence of mental fatigue is related to neural network dynamics. The present study used EEG coherence as a measure of synchronization of brain activity. Coherence of two EEG signals recorded from spatially separated scalp electrodes estimates the similarity of waveform components generated by the mass action of neurons in underlying cortical regions [10-12]. Our results observed increased neuronal activity and stronger synchronization at the end of 2 h continuous mental task, which did not result in more efficient performance. At the last calculation stage (from 1.5 h to 2 h), the deterioration on all performance estimators (correct answers, reaction time, and S.D. of reaction time) was significant, which can be viewed as a sign for mental fatigue. The increase in neural activity with increasing mental fatigue indicates the alteration of cerebral function organization under less alert even drowsy states. The changes of coherence were widespread since all frequency bands of EEG presented increased connectivity after long mental task.

Our previous studies on EEG power indicated a shift from fast to slow band and larger amplitude of slow waves especially theta wave during mental effort [9]. As coherence is influenced by both phase coupling and power changes, the increase of slow power may encounter with the parallel increase of brain network connectivity in the lower band [13]. Our results were consistent with these findings in Sauseng's research. In this research, the deteriorated performance and increased EEG coherence indicates a mental fatigue status after 2 h continuous mental arithmetic task and it is suggested to have a timely break to prevent mental disorders and accidents caused by fatigue.

5 Conclusions

Mental fatigue caused by sustained mental task is a serious problem in modern society. This research explored the variation of behavior performance and EEG coherence during a continuous mental arithmetic task. Increased coherence was

observed at the last stage of mental task accompanied with a decrement of calculation performance, which indicated a mental fatigue status. The change of EEG coherence observed in the present research was widespread not limited to specific brain regions or frequency bands.

Acknowledgments. This work is partly supported by National Natural Science Foundation of China No.61201124 and Fundamental Research Funds for the Central Universities WH1114028.

References

1. Azarnoosh, M., Nasrabadi, A.M., Mohammadi, M.R., Firoozabadi, M.: Investigation of mental fatigue through EEG signal processing based on nonlinear analysis: Symbolic dynamics. *Chaos Soliton. Fract.* 44, 1054–1062 (2011)
2. Folkow, B.: Mental stress and its importance for cardiovascular disorders: physiological aspects, ‘from-mice-to-man’. *Scand Cardiovasc J.* 35(3), 163–172 (2001)
3. Baker, K., Olson, J., Morisseau, D.: Work practices, fatigue, and nuclear power plant safety performance. *Human Factors* 36(2), 244–257 (1994)
4. Klimesh, W.: EEG alpha and theta oscillations reflect cognitive and memory performance: A review and analysis. *Brain Res. Rev.* 29, 169–195 (1999)
5. ten Caat, M., Lorist, M.M., Bezdan, E., Roerdink, J.B., Maurits, N.M.: High-density EEG coherence analysis using functional units applied to mental fatigue. *J. Neurosci. Methods* 171(2), 271–278 (2008)
6. Lorist, M.M., Bezdan, E., ten Caat, M., Span, M.M., Roerdink, J.B., Maurits, N.M.: The influence of mental fatigue and motivation on neural network dynamics: An EEG coherence study. *Brain Res.* 1270, 95–106 (2009)
7. Portella, C.E., Silva, J.G., Machado, S., Velasques, B., Bastos, V.H., Ferreira-Vorkapic, C., Terra, P., Lopes, V., Cagy, M., de Carvalho, E., Orsini, M., Basile, L., Piedade, R., Ribeiro, P.: EEG spectral coherence inter and intrahemispheric during catching object fall task. *Arq. Neuropsiquiatr* 65(1), 63–67 (2007)
8. Jap, B.T., Lal, S., Fischer, P.: Inter-hemispheric electroencephalography coherence analysis: assessing brain activity during monotonous driving. *Int. J. Psychophysiol* 76(3), 169–173 (2010)
9. Chen, L.L., Sugi, T., Shirakawa, S., Zou, J.Z., Nakamura, M.: Integrated design and evaluation system for the effect of rest breaks in sustained mental work based on neurophysiological signals. *Int. J. Control Autom.* 8(4), 862–867 (2010)
10. French, C.C., Beaumont, J.G.: A critical review of EEG coherence studies of hemisphere function. *Int. J. Psychophysiol* 1(3), 241–254 (1984)
11. Shaw, J.C.: Correlation and coherence analysis of the EEG: A selective tutorial review. *Int. J. Psychophysiol* 1(3), 255–266 (1984)
12. Wada, Y., Nanbu, Y., Koshino, Y., Shimada, Y., Hashimoto, T.: Inter- and intrahemispheric EEG coherence during light drowsiness. *Clin. Electroencephalogr* 27(2), 84–88 (1996)
13. Sauseng, P., Klimesch, W., Schabus, M., Doppelmayr, M.: Fronto-parietal EEG coherence in theta and upper alpha reflect central executive functions of working memory. *Int. J. Psychophysiol.* 57(2), 97–103 (2005)

An Automatic Pulmonary Nodules Detection Method Using 3D Adaptive Template Matching

Jing Gong, Ting Gao, Rui-Rui Bu, Xiao-Fei Wang, and Sheng-Dong Nie*

School of Medical Instrument & Food Engineering, University of Shanghai for Science and
Technology, Shanghai 200093, China
nsd4647@163.com

Abstract. This paper proposes a fast and robust computerized scheme for automatic detection of pulmonary nodules by using 3-dimensional adaptive template analysis. First, lung lobes are segmented clearly via the 3D region growing algorithm and then a number of regions of interest (ROIs) are extracted by using OTSU threshold segment algorithm. Second, to establish adaptive template for every ROI, a novel template matching technique is applied. Third, the similarity between the 3D adaptive template and pulmonary nodule candidate image is calculated by utilizing Normal Cross Correlation (NCC) algorithm. Finally, data, which are collected from Lung Image Database Consortium (LIDC) image dataset and Shanghai Lung Hospital, are selected to validate the efficiency of this algorithm. Results show that this proposal algorithm can detect the pulmonary nodule accurately. The sensitivity of former datasets is 95.29% and the false positive rate is 12.90%, while the sensitivity of later datasets is 87.82% and false positive rate is 18.68%. In conclusion, the underlying algorithm is effective and robust.

Keywords: Pulmonary nodule detection, template matching, 3D adaptive template matching.

1 Introduction

Lung cancer is becoming the leading cause of cancer-related death worldwide. The most realistic remedy of lung cancers is to identify the pulmonary nodules in early stages [1]. As regular chest X-rays produce less detailed images, this technique is not recommended in lung cancer screening plans for early detections. In general, a successful screening program can help lung cancer detection in early stage, for instance, the low-dose CT examination meeting a certain criterion has been recommended for a specific group of people with smoking history. However, reducing X-ray dose can lead to the degradation of spatial resolution and increase the risk of missing detection of pulmonary nodules, such as, the ground-glass opacity nodules. To overcome this problem, the computer aided detection (CAD) technique is applied to avoid missing of suspicious nodules.

* Corresponding author.

With the popularization of the low-dose CT screening, many researchers have taken enthusiasm to revisit the development of CAD technologies in chest CT images over the past several years [1-2]. The computerized CAD algorithms were mainly implemented with either the classification approach in statistics or a template matching method. Thanks to the development of statistics, classification based detection approach has attracted a considerable interest in medical pattern recognition, where pulmonary nodules in CT images were detected by using classifiers. A number of classification algorithms have been exploited to detecting pulmonary nodules, for example, feed forward neural networks (NN), support vector machines (SVM), naive Bayes (NB) and logistic regression (LR) methods [3], yet all lacking a rigorous study for anatomical features of lung CT image. Thus, their achievable system's sensitivity was often below 90% with an unacceptable false-positive rate in practice [4].

Motivated by the progress in the template matching method, a number of researchers have endeavored to exploit the template-based methods because of these approaches' high true-positive (TP) rates and low computational cost [5]. The template-based methods preserve both the image inherited textures and detail anatomical structures. Lee *et al* exploited a novel template matching CAD technique based on a genetic algorithm (GA) [5]. The genetic template matching algorithm later was extended to solving both 2D and 3D deformable template matching problems [6-8] and a spherical enhancement method has been used to reduce false positive rate significantly [16,17]. In general, 3D ROIs are extracted with the serial slices and then the ROIs are categorized according to their morphologies by applying a nodule template method. To establish a robust system, the multi-scale active appearance models are carefully designed to the framework of template matching [15].

Table 1. Review for the nodule detection employing template matching method

(NG symbols not given)

Author	No. of datasets	No. of slices	Slice thickness(mm)	No. of nodules	Nodules diameters(mm)	Sensitivity	FP
Lee [5]	20	557	NG	98	5-30	72%	89.67%
Farag [8]	NG	200	NG	130	NG	82.3%	9.2%/slice
Farag[10]	NG	NG	NG	NG	NG	95.65 %	87.1%
Osman[12]	6	160	5.625-18.75	6	3.5-7.3	100%	83% 0.46%/slice
PengWang[15]	12	742	3	47	4-20	100%	30.43%
Dehmeshkij[16]	70	16800	0.5-1.25	178	3-20	90%	14.6/scan 0.06/slice

The CAD technique adopting template matching methods is only applicable to detect solid nodules. This is because that most of solid nodules are encompassed well-defined boundaries and feasible to be distinguished. Thus, the template matching methods have been well studied in computer assisted detection for solid nodules in CT

images [14]. However, those computerized detection algorithms are most evaluated with the testing data lacking of clinical cases and rigorous gold standard in practice, showing in Table 1. In general, the template matching methods can be addressed to solve most problems in pattern recognition. A critical challenge for template matching is that there are no fixed templates to meet most of the practical problems, and these templates can only be applied in special situation. Therefore, most of the template-based lung nodule detection techniques select spherical or elliptic templates to match the lung nodule intensity distribution which follows *Gaussian* function.

However, these techniques usually use shape-fixed templates in the case of 2D space and are lacking of robustness for nodule detection. In order to circumvent above problems, we apply an adaptive template matching method in the case of 3D space over a large-scale CT dataset. In this work, we employ an automatic 3D template matching algorithm to detect pulmonary nodules effectively.

This paper is organized in the following way: Section 2 describes the detection method including lung parenchyma segmentation, ROI extraction, and 3D adaptive template matching method; Experiments, conclusions and discussions are displayed in Section 3.

2 Materials and Methods

2.1 Image Database

Computed tomography (CT) can help visualize small volume and low-contrast nodules by decreasing the thickness of slices and the interval between consecutive slices. CT is preferable for the preliminary detection of lung nodules comparing with other lung imaging methods. Lung CT images can be found in public and private databases. There are a number of popular public lung nodule databases including: Early Lung Cancer Action Program (ELCAP) Public Lung Image Database, Lung Image Database Consortium (LIDC) in National Imaging Archive, and Medical Image Database.

In order to test our detection method through clinical data, we select the image data acquired from LIDC and the Department of Radiology, Shanghai Pulmonary Hospital. LIDC database contains 155 CT image series including 238 nodules and datasets from Shanghai Pulmonary Hospital is made up of 66 CT image series including 85 nodules. The CT slice thickness of these data is ranging from 0.45mm to 3mm. All pulmonary nodules with diameter 3-20 mm in the databases are diagnosed by four experiment pulmonary doctors.

2.2 Algorithm Flow

The work flows of traditional template matching method and adaptive template matching method is shown in Fig.1. There are five major steps of the traditional method (Fig.1 (a)): pre-processing, parenchyma segmentation, templates design,

template matching process and detection result output. In the processing flow template designing plays a crucial role. Therefore, this paper proposes an adaptive template to improve the detection accuracy and the detection flow is displaying in Fig.1 (b). With this process flow, we can detect pulmonary nodules automatically and efficiently. The details of this detection algorithm will be given in the following chapters.

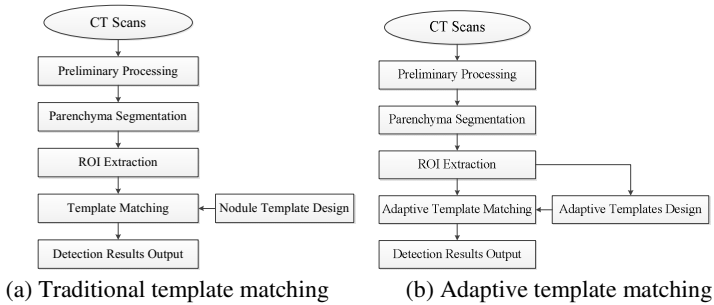


Fig. 1. Flowchart of 3D template matching methods

2.3 Parenchyma Segmentation

In order to reduce complexity of computation and improve matching accuracy, the parenchyma fields are isolated according to the following steps:

- (a) Apply a nonlinear operation to de-noise the "salt and pepper" noise (Fig. 2(a)).
- (b) Otsu's threshold segment algorithm [18] is used to get a binary image (Fig. 2(b)).
- (c) Morphological open and close operations are applied on binary image and parenchyma mask is obtained (Fig. 2(c)).
- (d) Mark the lung parenchyma regions, get the parenchyma mask by using 3D region growing algorithm, and fill the holes in the masks (Fig. 2(d)).
- (e) Mask on the original image with parenchyma masks gained in step (d) (Fig. 2(e)).

After segmenting lung parenchyma, we can obtain lung parenchyma image in each layer. Then, the lung parenchyma is reconstructed and reconstructed lung parenchyma is shown in Fig.3.



Fig. 2. Lung parenchyma segmentation

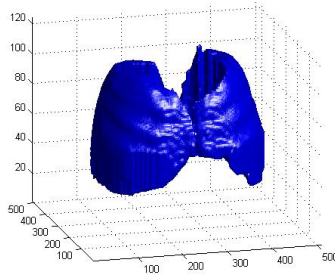


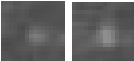
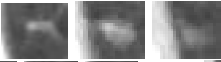
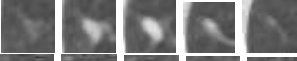

Fig. 3. Reconstruction of the lung parenchyma

2.4 ROI Extraction

In this section, firstly we abstract regions of interest in the lung parenchyma which are pulmonary nodule candidates. And adaptive template analysis will be applied on each ROI. ROI extraction helps reduce a lot of calculations and make this system a real effective one.

First, threshold segmentation is applied to exact the high level gray value parts, which contain arteries, veins, bronchi and a few lung abnormalities. Then, some experiments are taken to obtain the statistic information of nodules in LIDC database [19]. In the examples in Table 2, we can obviously figure that nodules have totally different gray value distribution, which has no pattern to follow; meanwhile, nodules can also connect with lung wall (case B) and vessel (case C). Therefore, it is very hard to separate regions of nodules just by using threshold segmentation. But we can use threshold segment algorithm with a small threshold to obtain the original regions of interests which include nodules. Analyzing the maximum gray value, minimum gray value and average gray value of 76 nodules in LIDC database, which is judged by gold standard, the most suitable threshold value 0.38 is derived to get the preliminary ROIs.

Table 2. The gray values of lung nodules segmented with gold standard

Case NO.	Nodule Image	Maximum gray value	Minimum gray value	Average gray value
A		0.388	0.303	0.333
B		0.872	0.756	0.812
C		0.899	0.757	0.813
D		0.538	0.235	0.393

Second, morphological processing is used to reduce the amount of ROIs. A 3D ball with diameter 2mm is applied for morphological open processing to extract ROIs more accuracy.

Finally, the ROIs with diameter bigger than 20mm will be removed. This action will not influence the sensitive rate of our detection system and decrease the calculation complexity for further steps. Fig.4 shows the results of ROI extraction in each step.



Fig. 4. (a) Lung parenchyma image (b) Threshold segmentation image (c) Morphological processing image (d) Ultimate ROIs mask

2.5 Adaptive Template Matching

The flowchart of ROI adaptive template designing is shown in Fig.5. Firstly, ROIs' masks are obtained through the ROI extraction process (Fig. 6(a)), and then these masks are masked with the original image (Fig. 6(b)). Secondly, high intensity region of each slice is extracted (Fig. 6(c)) and the centroids of these high intensity regions are sought (Fig. 6(d)). And then, the principal direction normal vector of each ROI's centroid is drawn. Meanwhile, the middle slice of each 3D ROI is used to simulate the gray distribution of the 3D template. The detail steps are as follow:

(a) Select the middle slice of ROIs as the information source, called "A". (Fig.7 (a))

(b) Find the high gray value points of each slice, and sign the center line of A (Fig. 7 (b)). Calculate the average gray value of the center line points on A, signed as parameter q_{\max} . Calculate the average gray value of edge points on A, signed as parameter q_{\min} . Calculate the average radius of A, signed as parameter R.

(c) Compute the gray distribution of the template image at the center line position. If define $T_1(x_1, y_1)$ as one point located in T (Signed as template image), then we can calculate the average gray value of point's (x_1, y_1) 8 neighbors on A, and reduce it through Gaussian gradient using slice thickness as the parameter S (Fig. 7 (c)). Equation (1) displays the detail computational procedure.

$$\left\{ \begin{array}{l} M = \begin{bmatrix} (x_1-1, y_1-1) & (x_1, y_1-1) & (x_1+1, y_1-1) \\ (x_1-1, y_1) & A_1(x_1, y_1) & (x_1+1, y_1) \\ (x_1-1, y_1+1) & (x_1, y_1+1) & (x_1+1, y_1+1) \end{bmatrix} \\ \rho = R(\ln(q_{\max}) - \ln(q_{\min}))^{-\frac{1}{2}} \\ T_1(x_1, y_1) = \overline{M} \times e^{\frac{S}{\rho}} \end{array} \right. \quad (1)$$

(d) Dispose all the points not located at the center line with following steps. If $T_2(x_2, y_2)$ is one point located in T (Signed as template image), then we can find the point $O(x_3, y_3)$, which is nearest to center line point $A_2(x_2, y_2)$ on A in the same slice. Calculate the distance between A_2 and O, signed as D. Find the point $Q(x_4, y_4)$ on the extend line of OA_2 , ensuring $OQ = OT_2$. Obtain the gray value of Q, and reduce it

through Gaussian gradient using slice thickness as the parameter S (Fig. 7(d)). Equation (2) displays the detail computational procedure.

$$\left\{ \begin{aligned} D &= (x_3 - x_2)^2 + (y_3 - y_2)^2 \\ P^2 &= D^2 + S^2 \\ \frac{P}{D} &= \frac{x_4 - x_2}{x_3 - x_2} = \frac{y_4 - y_2}{y_3 - y_2} \\ \rho &= R (\ln(q_{\max}) - \ln(q_{\min}))^{-\frac{1}{2}} \\ T_2(x_2, y_2) &= Q(x_4, y_4) \times e^{(\frac{S}{\rho})^2} \end{aligned} \right. \quad (2)$$

(e)Set template image T as the new information source A'. And then repeat the steps (b) to (e) to obtain other slices' gray distribution of the template until meeting the termination criterion that diameter of new slice is smaller than 1mm (Fig. 7(e)).

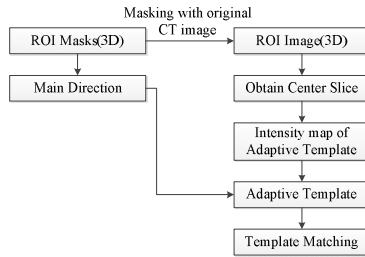


Fig. 5. Workflow of adaptive template matching

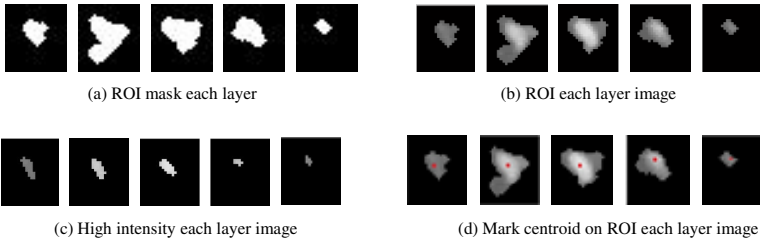


Fig. 6. ROI each layer image

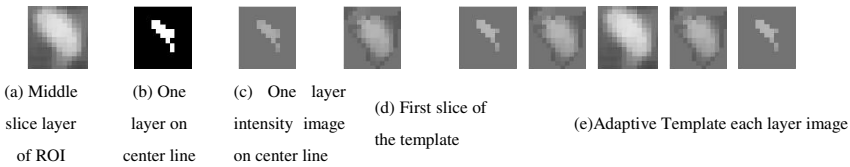


Fig. 7. Establishing adaptive template

In general, the similarity is estimated by correlation coefficient and diversity factor. Fast template matching algorithm NCC (Normalized Cross Correlation), SAD (Sum of Absolute Differences) and SSD (Sum of Squared Differences) are the most widely used, and the equations is given by equation (3)-(5). NCC is the measure by correlation coefficient, while SAD and SSD measure by the diversity factor. The NCC, SAD and SSD value are range from 0 to 1. For the NCC algorithm, the higher computed value is, the more similar, but for SAD and SSD algorithm, the lower computed value is, the more similar.

$$NC(x, y) = \frac{\sum_{i=1}^a \sum_{j=1}^b S(x+i, y+j)T(i, j)}{\sqrt{\sum_{i=1}^a \sum_{j=1}^b S^2(x+i, y+j) \sum_{i=1}^a \sum_{j=1}^b T^2(i, j)}} \quad (3)$$

$$SAD(x, y) = \frac{1}{ab} \sum_{i=1}^a \sum_{j=1}^b |S(x+i, y+j) - T(i, j)| \quad (4)$$

$$SSD(x, y) = \frac{1}{ab} \sum_{i=1}^a \sum_{j=1}^b [S(x+i, y+j) - T(i, j)]^2 \quad (5)$$

3 Results and Discussion

3.1 Experimental Results and Discussion

To validate this algorithm's performance we select MATLAB (Matrix Laboratory) as the image processing programming tools. Experiments has been tested on a computer with Intel® Core(TM) i6-2450M 22.5Ghz CPU and 6GB RAM. To compare experimental performance of our adaptive analysis method with that of Peng Wang *et al.*'s method [15] and, parameters of computer consumption and accuracy are taken into consideration.

Firstly, we choose a typical dataset of solid nodules with diameter 6mm to test the time consumption of different template matching algorithms. Here we select a series of 3 mm thick image slices to test the algorithms' performance, and the result indicates that time consumption of this paper's algorithm is only half of the 3D GATM method. To prove the high efficiency of our system, we list the time consumption of both. All the algorithms are tested by one typical series with 267 images and results are shown in Table.3.

Table 3. Time consumption test result

Template	Time consumption(s)
GATM of 6mm template	34.56
3D Adaptive template	12.56

Secondly, the 3D adaption template algorithm is experimented automatically on 299 datasets to detect pulmonary nodules. And 3 different styles 3D templates with diameter 6mm, 9mm and 12mm are established to imitate the 3D GATM method of Peng Wang *et.al.* [15]. Meanwhile, traditional template matching method and adaptive template matching method are tested on the same datasets.

The evaluation standards of this pulmonary nodules detection method include the Accuracy, Sensitivity, False Negative (FN) and False Positive (FP). The detail equations are shown below. Here, TP represents the true positive rate, meaning detection result is same as doctor diagnosis standard. FP means that detection result is wrong, viz. different from the diagnosis standard. FN means that our system has not detected the nodules which are given in doctor diagnosis standard. A method with high value of accuracy rate, sensitivity rate and low FP rate represents a good detection method.

$$\text{Accuracy} = \frac{TP+TN}{TP+TN+FP+FN} \quad (6)$$

$$\text{Sensitivity} = \frac{TP}{TP+FN} \quad (7)$$

$$\text{FalsePositiveRate} = \frac{FP}{TP+FP} \quad (8)$$

3.2 ROC Curve

ROC (receiver operating characteristic) curve analysis is a statistics method and has been widely applied in clinical diagnosis and analysis experiment. Horizontal coordinate of ROC curve denotes specificity and ordinate coordinate denotes Sensitivity. The area under the ROC curve reflects performance of the detection algorithm; viz. the larger, the better. If A_z represents the region areas under ROC curve, its value is between 0 and 1.

Analyzing ROC curve of the detection algorithm in this paper (Fig.8), we can reach the conclusion that 3D adaptive template matching algorithm is much better than the traditional detection algorithm in detection effectiveness.

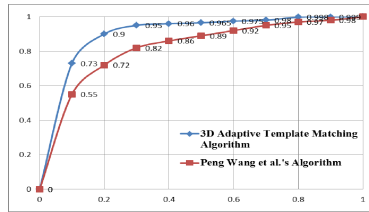


Fig. 8. ROC curve of experiments

4 Conclusion

The datasets employed in this paper are diagnosed by more than 4 experiment doctors, containing 1025 nodules with diameter 3-30mm. The data, which are collected from Lung Image Database Consortium (LIDC) image dataset and Shanghai Lung Hospital, are utilized to validate this algorithm's efficiency with a performance. The sensitivity of former datasets is 95.29% and the false positive rate is 12.90%, while the sensitivity of later datasets is 87.82% and false positive rate is 18.68%.

Due to the experimental result, 3D adaptive template matching method achieves high sensitivity rate comparing with the traditional template matching method [15]. The FP rate is 12.90% (0.54% per slice), also better than the traditional method. The experimental results display effectiveness and robustness of the underlying algorithm.

The experimental results show that 3D adaptive template analysis method can be used to detect nodules in CT images with a high sensitivity and little computer consumption. However, higher accuracy system with lower FP rate is still our further study's focus.

Acknowledgement. The research was sponsored by the National Natural Science Foundation of China (60972122), the Innovation Fund Project For Graduate Student of Shanghai (JWCXSL1402), the Natural Science Foundation of Shanghai (14ZR1427900).

References

1. Lee, S.L.A., Kouzani, A.Z., Hu, E.J.: Automated detection of lung nodules in computed tomography images: A review. *J. Machine Vision and Applications* 23, 151–163 (2012)
2. Messay, T., Hardie, R.C., Rogers, S.K.: A new computationally efficient CAD system for pulmonary nodule detection in CT imagery. *Medical Image Analysis* 14, 390–406 (2010)
3. Saba, L., Caddeo, G., Mallarini, G.: Computer-aided detection of pulmonary nodules in computed tomography: analysis and review of the literature. *Journal of Computer Assisted Tomography* 31, 611–619 (2007)
4. Choi, W.J., Choi, T.S.: Genetic programming-based feature transform and classification for the automatic detection of pulmonary nodules on computed tomography images. *Information Sciences* 212, 57–78 (2012)
5. Lee, Y., Hara, T., Fujita, H., Itoh, S., Ishigaki, T.: Automated detection of pulmonary nodules in helical CT images based on an improved template-matching technique. *IEEE Transactions on Medical Imaging* 20, 95–604 (2001)
6. Shi, Z.G., Zhao, M.H.: A Computer Aided Pulmonary Nodule Detection System Using Multiple Massive Training SVM. *Applied Mathematics & Information Sciences* 3, 1165–1172 (2013)
7. Choi, W.J., Choi, T.S.: Automated pulmonary nodule detection based on three-dimensional shape-based feature descriptor. *Computer Methods and Programs in Biomedicine* 3, 37–54 (2014)
8. Farag, A.A., El-Baz, A., Gimelfarb, G., El-Ghar, M.A., Eldiasty, T.: Quantitative nodule detection in low dose chest CT scans: new template modeling and evaluation for CAD system design, *Medical image computing and computer-assisted intervention: MICCAI... In: International Conference on Medical Image Computing and Computer-Assisted Intervention*, vol. 8, pp. 720–728 (2005)
9. Farag, A., et al.: Modeling of the lung nodules for detection in LDCT scans, *Conference proceedings: Annual International Conference of the IEEE Engineering in Medicine and Biology Society. In: IEEE Engineering in Medicine and Biology Society Conference*, pp. 3618–3621 (2010)

10. Farag, A.A., Graham, J., Elshazly, S., Farag, A.: Data-Driven Lung Nodule Models for Robust Nodule Detection in Chest CT. In: ICPR 2010 20th International Conference on Pattern Recognition, pp. 2588–2591 (2010)
11. Hong, H., Lee, J., Yim, Y.: Automatic lung nodule matching on sequential CT images. *Computers in Biology and Medicine* 38, 623–634 (2008)
12. Osman, O., Ozekes, S., Ucan, O.V.: Lung nodule diagnosis using 3D template matching. *Computers in Biology and Medicine* 37, 1167–1172 (2007)
13. Nie, S.D., Li, L.H., Chen, Z.X.: Pulmonary nodule segmentation algorithm based on three-domain mean shift clustering. *Journal of East China Normal University (Natural Science)* (2008)
14. Nie, S.D., Sun, X.W., Chen, Z.X.: Progress in Computer-Aided Detection for Pulmonary Nodule Using CT Image. *Chinese Journal of Medical Physics* (2009)
15. Wang, P., De Nunzio, A., Okunieff, P., O’Dell, W.G.: Lung metastases detection in CT images using 3D template matching. *J. Medical Physics* 34, 915 (2007)
16. Dehmeshki, J., Ye, X., Casique, M.V., Lin, X.Y.: A Hybrid Approach for Automated Detection of Lung Nodules in CT Images. In: 3rd IEEE International Symposium on Biomedical Imaging: Macro to Nano, pp. 506–509 (2006)
17. Messay, T., Hardie, R.C.: A new computationally efficient CAD system for pulmonary nodule detection in CT imagery. *J. Medical Image Analysis* 14, 390–406 (2010)
18. da Silva Sousa, J.R.F.: Methodology for automatic detection of lung nodules in computerized tomography images. *J. Computer Methods and Programs in Biomedicine* 98, 1–14 (2010)
19. Wang, Q.Z., Kang, W.W.: Computer-aided detection of lung nodules by SVM based on 3D matrix patterns. *J. Clinical Imaging* 37, 62–69 (2013)

A 3D Adaptive Template Matching Algorithm for Brain Tumor Detection

Xiao-Fei Wang, Jing Gong, Rui-Rui Bu, and Sheng-Dong Nie*

Institute of Medical Imaging Engineering, University of Shanghai for Science and Technology, Shanghai 200093, China

Abstract. This paper presents a three-dimensional adaptive template matching algorithm to detect brain tumors from Magnetic Resonance Images quickly. First, skull and other non-brain tissues were removed by the improved BET algorithm. Then we extracted the structures that contain all small tumors as ROIs (Region of Interest). After that, we screened all the ROIs by the circular degree and other features. Then a three-dimensional template was created conformed to tumor characteristics for each ROI. Finally, the three-dimensional templates were marched with the original images to calculate the similarity coefficient. Then the threshold was determined according to the matching characteristic. After that, the three-dimensional ROI with the similarity coefficient which was higher than the threshold value was marked as the tumor region. To evaluate the performance of the algorithm, 23 clinical cases which contain 124 tumors (3mm-15mm) in different size was used to test the system, using ROC (Receiver Operating Characteristic) curve to analysis the test results. According to the ROC curve, the positive rate reach 88.7097% and the false position rate is 16.03%. Compared to other template matching methods, the algorithm provided has been significantly improved.

Keywords: Magnetic Resonance Imaging, brain tumor, template marching, adaptive, detection.

1 Introduction

Brain tumors can be divided into primary tumors and metastases. Metastases which are multiples of the primary tumors originating in the other parts of the body and then transferred to brain through the blood cells and lymph channels, which are multiples of the primary tumors. Brain metastases of primary sites of lung, breast, gastrointestinal cancer and renal cell carcinoma is a common, which accounted for 16% ~ 25% of brain metastases from breast cancer, brain metastasis of lung cancer accounted for 30%~40%.

Brain tumors, particularly metastatic tumors grow very fast, its average volume doubling time was only 25 days. If don't take appropriate treatment promptly, the patient's survival is generally not more than half a year on average. It can be able to

* Corresponding author.

quickly lead to the deaths. The tumor cells spread to the brain will ground, interfere with even damage the normal brain tissue, which caused a series of symptoms, such as headache, epilepsy, aphasia, hemianopsia, nausea, paralysis, etc.[1]. Brain metastases tumor may make patients feel fatigue, also can cause memory disorders of patients, which reduces the patients' quality of life. If brain tumors can be early detected, and carries on the treatment, which can effectively prolong patients' survival time, improve the quality of life of patients.[2][3][4]

At present, magnetic resonance imaging (MRI) can carry on an effective diagnosis to the brain. In order to diagnose of brain tumors early, the whole brain need to be scanned with MRI thin layer, which will produce a large number of MRI images. Due to brain tumor is small (less than 10 mm) at the early stage, even on the contrast-enhanced magnetic resonance images, the contrast of early tumor and surrounding tissue is not obvious, also only on high-resolution images appear in three or four layer thickness, which makes clinical misdiagnosis easily. In addition, identifying smaller brain tumor correctly from a lot of MRI images, is also very difficult for the radiologist, especially after a long time reading, a radiologist will inevitably produce visual fatigue, easy to miss small lesions.

The development of computer aided detection (Computer-Aided Detection-CAD) technology, which laid a foundation for solving the problem of the early diagnosis of brain tumors. Numerous studies have demonstrated that CAD can effectively alleviate the radiologist read burden, improve its diagnostic accuracy. In recent years, CAD has been played a more and more important role in breast cancer, lung cancer and colorectal cancer early diagnosis [5] and there are a large number of literature reports, but in the early diagnosis of brain tumor research at home and abroad related reports. Moreover, although the CAD technology has great progress in recent ten years, the progress still exist many problems [6]: lack of specificity, high false positive. With the existence of these problems, on the one hand, CAD (including the FDA certification of commercial CAD) have not been promoted and popularize applied; On the other hand, due to the application prospect, more scholars were also attracted be involved in the study of CAD.

Automatic detection of brain tumors based on MRI brain images method basically has the following two kinds: the method based on template matching [7][8] and the method based on classifier[9][10]. Detection method based on classifier step is various, involved in the large and complex image processing algorithms. By the reports of the literature at home and abroad, the sensitivity of the method based on classifier is not too high (about 80%), false positive rate is low (typically around 10%). Yang et al [10] detect metastatic tumor from 3D magnetic resonance brain black blood rushed sequence with template matching, the sensitivity was 81.1%, the paper did not provide a false positive data; Robert D. et al [7] detected brain tumors on T1 weighted images with 3D template matching method. Take some offset to different size of the templates to make more templates to solve the problem of tumor offset. The sensitivity was 86.29% and false positive was 40.5%; Nie Sheng Dong et al [8] relies on the establishment of different size more 3D template to improve the detection rate of tumor, and reduce false positives. The sensitivity was 80.65%, the false positive was 22.5%. Although the detection method based on template matching is simple, fast, high

sensitivity, but this method has generally high rate of false positives (generally more than 20%), and the detection results has a high dependency to the designed template type, to detect all lesions, must design a variety of templates to cover all tumor forms. However to form variety of brain tumors, irregular geometry, boundary fuzzy design all possible tumor template is impossible. Even can design templates that enough to traverse the search tumor, it will cost a lot of computation time. Therefore, in view of the present problems of based on template matching algorithm to detect brain tumors, this paper proposes an adaptive template matching method. Therefor the detection speed and sensitivity can be improved and the false positive can be reduced.

2 Algorithm Flow

This method changes the traditional way of building templates, after splitting out parenchymal, extract contains all the interested area of the brain as a candidate for lesions through simple morphology processing first; Then build 3D template for each of the interested region respectively; According to the matching algorithm to calculate the interest area with the corresponding template matching coefficient, and to determine the coefficient of threshold to mark the tumor area. Figure 1 is the flow chart of adaptive 3D template matching algorithm.

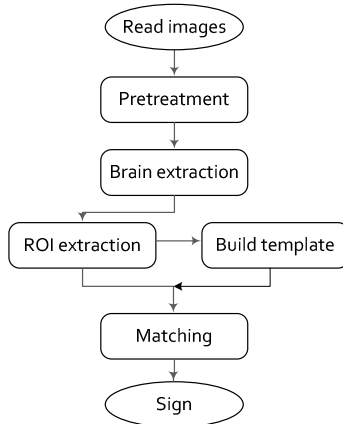


Fig. 1. The flow chart of adaptive 3D template matching algorithm

Main steps of 3D adaptive template matching algorithm:

- (1) Pretreatment: In order to enhance the signal-to-noise ratio, increase the contrast. This article take the pretreatment is to filter the noise reduction operation, and then make gray-scale map, the image grayscale readjust to achieve the display all of the structure under the premise of contrast enhancement.

- (2) Brain extraction: Using the improved BET algorithm for an initial coarse segmentation, make the border be initial boundary of second BET algorithm, accurate extract the brain again.
- (3) ROI extraction: This paper uses the method of top-hat, Un-Sharp Masking-USM sharpening, canny operator edge detection method to extract the ROI in the brain parenchyma.
- (4) Build template: According to ROI to build the corresponding 3D tumor template. Take any 2D ROI as the center slice, its center for the center of tumor template, build 3D tumor template.
- (5) Match algorithm: Normalized Cross Correlation - NCC algorithm was used to calculate the similarity of template and interested area.

The advantage of the adaptive template matching algorithm proposed is: specific form template don't need to be built at first (such as spherical or ellipsoidal model) so that false positive can be reduce effectively; Second, each template match only interested in the corresponding area, no necessary to spend a lot of time on the 3D data sets traversal searching for each template. [7]

2.1 Brain Extraction

Accurately segmented brain parenchymal from the MRI images is one of the key steps of the method. Skull interference must be avoid when extracted ROI from the parenchymal. Therefore, extract brain from MRI brain images accurately helps to improve the accuracy of the final detect results and reduce false positive. A large number of brain extraction method reported at home and abroad in recent years, the most widely used method is BET algorithm which has better effect.[11]

During the process of using BET algorithm, BET has good effect for the normal brain without tumors, but the effect of the BET for the brain with tumors is not very ideal. This paper improved the existing BET algorithm. BET algorithm, in fact, extracts the brain by boundary evolution. The effect of the algorithm is good for the brain without distractions, but is not ideal for the brain with tumors. Its basic reason is the unreasonable force u_3 , as shown in formula (1).

$$u_3 = f \times Sn \quad (1)$$

f in the formula (1) is associated with the contour evolution speed coefficient. Sn is the direction. Sn points to the pedal of current evolution to the two attachment points. In figure 2(a), O is the contour center. P_i is the contour boundary point. When the contour evolution to obstacles, contour began to appear changes as shown in figure 2(a). The reason is that the force u_3 and u_2 has the same direction, just different value. So in the next iteration, P_2 , P_4 and P_3 will be to the opposite direction, which leads to contour points more and more chaos, appear as shown in figure 2(b). So in this paper, the force u_3 has been changed, make it directs to the center of the contour, and the contour smoothing force u_2 was simplified.[12]

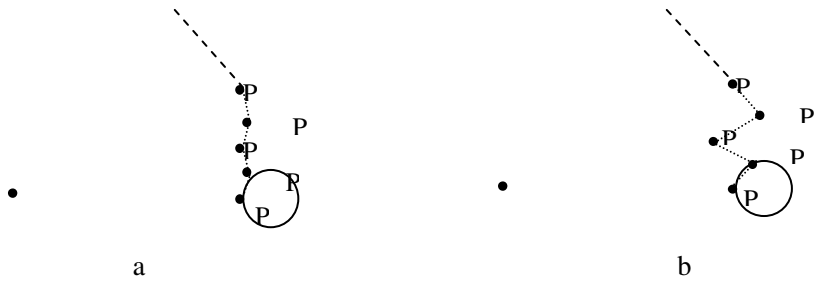


Fig. 2. Contour evolution to obstacles

Brain extraction method in this paper is: first, choose the middle slice of sequence image as the initial slice, an improved BET algorithm is applied, to obtain rough boundary $B_0(mid)$, as shown in figure 3(a); Second, $B_0(mid)$ will be took as the initial boundary using the improved BET algorithm again, for the middle slice of accurate boundary $B(mid)$, as shown in figure 3(c); Then, further to reduce $B(mid)$ a certain proportion to its center (shrink 10%) of this article. Make it as the initial boundary of the two adjacent layers, and BET algorithm to obtain accurate boundary, again. Finally, the steps in the cycle until completion of the all layers are divided. The segmentation process is as follows:

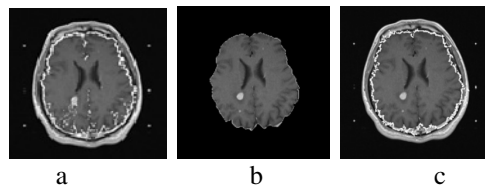


Fig. 3. Process of brain extraction (a) First rough boundary (b) First extraction result (c) Accurate extraction result

2.2 ROI Extraction

When extracting ROI, all brain tumors must be extracted as a candidate for lesions. Due to the human eye is more sensitive to the boundary information and contrast, clinicians were first observed that where exists significant difference with the surrounding structure, and then according to the rich medical knowledge to judge whether the structure of the exception. In order to ensure all anomaly area will be extracted, usually adopt a variety of methods of combining the interested region extraction, in the method of a single threshold and edge detection method is difficult to obtain satisfactory results. On the basis of the experiment many times, top-hat transform, the sharpening mask, canny operator algorithm of edge detection method were adopted in this paper.

First, the background is filled with the average gray level of brain tissue, as shown in figure 4(a). Different sizes of circular structure element was defined, then top-hat transform was used to enhance the comparison of background and interested area,

as shown in figure 4(b). On the basis of top-hat transformation Un-sharp Mask was applied, as shown in figure 4(d). The algorithm principle is that the filtered image multiplied by sharpening coefficient is added to the original image, achieve sharpening effect, as shown in formula (2) :

$$y(n, m) = x(n, m) + \lambda z(n, m) \quad (2)$$

In the formula (2), $x(n, m)$ is the input image, $y(n, m)$ is the output image, and $z(n, m)$ is the correct signal, typically computed by high-pass filter from the input image. λ is used as a scaling factor to control the effect of enhancement. In this paper, the image after using Gaussian filter from the original image was minus to achieve high-pass signal $z(n, m)$. After that, canny edge detection method was used to enhance the weak boundary, then the boundary was timed and added to the original image, as shown in figure 4(d). Then get the binary image, as shown in figure 4(e). Adjust the size of hat structural elements and extract again, as shown in figure 4(f). After many times extraction, binary image can be got as shown in figure 4(g). The experimental results show that this method can effectively extract the ROIs.

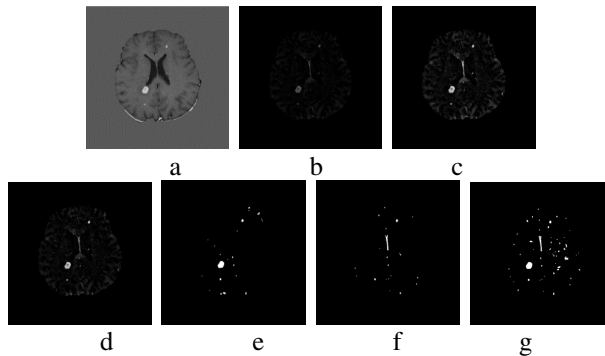


Fig. 4. ROI extraction (a) Original image with background (b) Result of top-hat transform (c) Result of USM (d) Result of canny edge detection enhancement (e) Result of masking the binary image (f) Many times extraction (g) Result

2.3 Build 3D Template

In the template matching algorithm, usually calculated according to the prior knowledge of the template meet spherical Gaussian distribution [7][13]. An important feature of spherical Gaussian template is center distance equal to the template of gray level is equal. The reason is that in the process of continuous tumor growth, the points with the same distance to the center are often in the same growth stage. According to this characteristic, a 2D ROI was used as the center layer to build the 3D model, based on the center of the center layer 3D template center, as shown in figure 5:

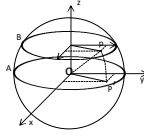


Fig. 5. Tumor model

In figure 5 A is a selected ROI, O is the center of A . p' is a point on A , build a plane XOY based on A plane, plane XOY normal to the Z axis of the 3D coordinate system. B in figure is calculated by A 3D template in A parallel to A plane, p is a point in planar B with corresponding point p' on plane A , namely to meet:

$$\text{pix}(p) = \text{pix}(p') \tag{3}$$

From p' to p :

$$|op| = |op'| \tag{4}$$

$$B(x, y) = A \left(\frac{\sqrt{x^2 + y^2 + z^2}}{\sqrt{x^2 + y^2}} \cdot x, \frac{\sqrt{x^2 + y^2 + z^2}}{\sqrt{x^2 + y^2}} \cdot y \right) \tag{5}$$

$$B \left(\frac{\sqrt{x^2 + y^2 - z^2}}{\sqrt{x^2 + y^2}} \cdot x, \frac{\sqrt{x^2 + y^2 - z^2}}{\sqrt{x^2 + y^2}} \cdot y \right) = A(x, y) \tag{6}$$

Formula (6) can be used to calculate the 3D model, z is the space from B to the center slice. The ROI and the corresponding template are shown in figure 6. Two 3D model built from two 2D ROIs are shown in figure 6(a) and figure 6(b). The neighbor slices in the original data field of 3D model in figure 6(b) are shown in figure 6(c). Attach to the established 3D template with the same data field information can be achieved with a thick layer as shown in figure 6(d) 3D template.

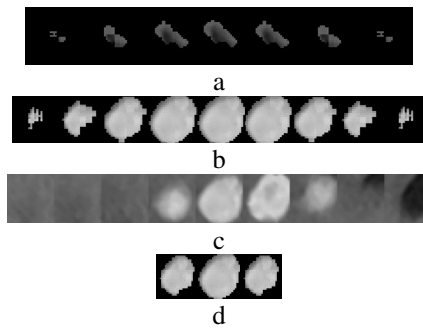


Fig. 6. Template and ROIs (a),(b) 3D template (c) The neighbor slices in the original data field of 3D model in figure 6(b) (d) Attach to the established 3D template with the same data field information

2.4 Matching Algorithm

Template and the corresponding region in the original data filed are computed as two dimensional vectors \bar{T} and \bar{S} . Then calculate the cosine of two vectors as the coefficient of similarity.

$$\cos\langle\bar{T},\bar{S}\rangle = \frac{\bar{T}\cdot\bar{S}}{|\bar{T}|\cdot|\bar{S}|} \tag{7}$$

$$\cos\langle\bar{T},\bar{S}\rangle = \frac{\sum_{k=1}^n \sum_{j=1}^m \sum_{i=1}^l T(i,j,k)\cdot S(i,j,k)}{\sqrt{\sum_{k=1}^n \sum_{j=1}^m \sum_{i=1}^l T(i,j,k)^2} \cdot \sqrt{\sum_{k=1}^n \sum_{j=1}^m \sum_{i=1}^l S(i,j,k)^2}} \tag{8}$$

When the similarity coefficient closer to 1, the similarity degree is higher, is equal when the similarity coefficient is 1. In the process of matching, to establish each template and the corresponding location in the 3D data field data matching.

2.4.1 Background Padding

Template background is the other areas except tumor section in the template. In the process of matching, add background information to the established 3D template plays an important role reduce false positives of test method. In the case of not adding background information, some non-tumor tissues such as low signal of the outer body of the structure of the coefficient of similarity may be high and misdiagnosed as tumor; Some smaller radius of tumor tissues due to its radius is less than the thickness, as shown in figure 7(a), 7 (d), established a template (figure 7 (e), figure 7 (h)) only one layer by the slice of thick, if you don't consider the template background when matching, the similarity coefficient of ROI and the template will reach 1. If you don't add the template of background information, therefore, is likely to lead to false positive results. Figure 7 is the average gray level for the template to add interest area 50% brain tissue (the average gray level than the tumor area around 50% lower than the average gray level) as the background and the original image.

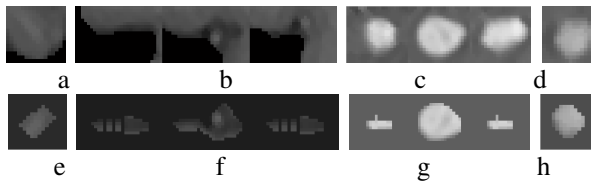


Fig. 7. Template and original image (a),(b) Non-tumor (c),(d) Tumor

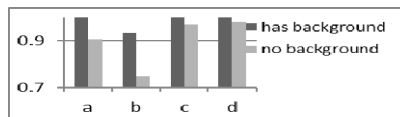


Fig. 8. Similarity coefficient with and without background in figure 9

The original image of ROI shown in figure 7(a), (b), (c), (d), the template of ROI shown in figure 7(e), (f), (g), (h). Non-tumor structures are shown in (e), (f). Tumor structures are shown in (g), (h). The similarity coefficient with and without background is shown in figure 8. As shown in figure 8, the background has little effects to tumor structures, but more to the non-tumor structures.

3 Experiment and Discussion

3.1 Experimental Data and Environment

Test data from Shanghai pulmonary hospital clinical cases of Simens 1.5T MRI scanner was used to detect the performance of the algorithm. Under the guidance of a radiologist, 23 T1 sequence images containing brain tumors were used to experiment. 23 cases including 124 different sizes (3 mm to 15 mm) of brain tumors, each contains 50 layers image, image size is 512 * 512 pixels, the image layer are 3 mm thick. In this paper, experimental environment for MATLAB2012, 2.0 GHz processor, 32 GB of memory (DDR3 1333 MHZ), 64-bit Windows 7 operating system.

3.2 ROC Curve Analysis

ROC curve was used to evaluation algorithm performance. ROC curve is a function curve of detection threshold. It directly reflects the brain tumor detection sensitivity and the relationship between the rate of false positives. False positive rate was used as abscissa of ROC curve, the sensitivity rate as the ordinate.

$$\text{Positive rate : } TP = \frac{TN}{SN} \quad (9)$$

$$\text{False positive rate : } FP = \frac{FN}{FN + TN} \quad (10)$$

TN is the number of correct detection, SN is the total number of tumor, FN is the number of false detection. The ROC curve tend to the upper left, the bigger the area under the curve, the greater the performance. Below is the test data of ROC curve:

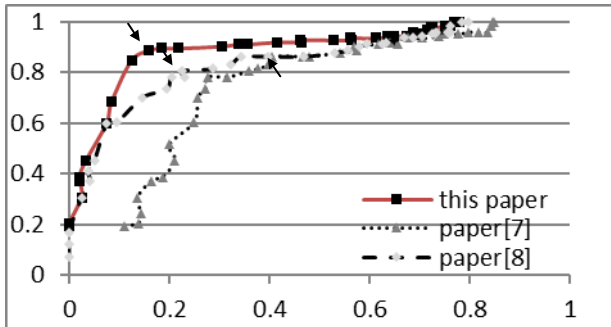


Fig. 9. ROC curve

3.3 Discussion

As shown in figure 9 that, this method has a good detection performance. Under the condition of the high sensitivity rate, the false positive rate drops rapidly. The point marked by the arrow closest to the ideal point (0, 1) is the best threshold point. The threshold condition sensitivity rate was 88.7097% (110/124) and 16.03% false positive (21/(110+21)). Compared with our previous studies [8] performed greater improvement. Literature [7] use the template with some offset to the center to overcome cancer center offset, therefore also brought more false positive results, and the detection time growth; Literature [8] build more fixed size of the template to detect tumor to reduce false positives, but consumed more time. And this method is not based on fixed size of template for the 3D data field in the form of traversal search, thereby greatly reducing the test time, and the template form and size as depending on the ROI, enables the template to cover more tumor, so as to improve the sensitivity, reduces the false positive.

Table 1. Comparison data

Method	Positive	False positive	Time
Proposed	88.7097%(110/124)	16.03%(21/131) 0.0287 per image	32.3s/case
Literature[7]	86.29%(107/124)	40.5%(73/180) 0.1 per image	193s/case
Literature[8]	80.65%(100/124)	22.5%(29/129) 0.0402 per image	350s/case after optimize 84.5s/case

Experimental result shows that compared with the paper published at home and abroad in recent years, the algorithm in this paper has been improved significantly. Ensured a high sensitivity and reduce the false positives, detection speed is also improved significantly.

4 Summary and Outlook

As the detection experiment shown that the brain lesions or other organizations, such as brain abscesses, cerebral hemorrhage, infarcts, sinus and carotid artery branch [8] and other vascular structures, is the main cause of false positives. As shown in figure 10(a), 1 is brain vena cava, in figure 10(b), 2,3 is middle cerebral artery, 4 in figure 10(c) is middle cerebral artery, 5, 6 is the former arteries, 7, 8 is choroid plexus. These small lesions or structure, its neighbor had little influence on itself, so the matching coefficient is often high. But compared with tumor exist obvious irregularity, the boundary is not smooth, and lesion often present boundaries relatively smooth round sphere [14]. According to the high circular degree features of tumor that the simple filtering part axle ratio relatively high area, effectively reduce the false positive rate. In subsequent work, more features can be calculated in the process of testing [15][16] and the use of classifier to template matching results are classified again, in order to further reduce the false positives.

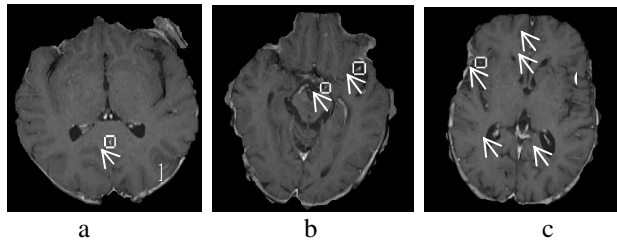


Fig. 10. Possible false positive (a) 1 is brain vena cava (b) 2,3 are brain middle artery (c) 4 is brain middle artery, 5, 6 are front middle artery, 7, 8 are choroid plexus

Acknowledgement. The research was supported by the National Natural Science Foundation of China (60972122), the Innovation Fund Project For Graduate Student of Shanghai (JWCXSL1402), the Natural Science Foundation of Shanghai (14ZR1427900).

References

1. Falk, M.R., Angelina, B.B., Iris, E., et al.: Stereotactic radiosurgery for the treatment of brain metastases. *J. Radiotherapy and Oncology* 91(1), 67–74 (2009)
2. Charles, J., Vecht, H.H.R., Evert, M., Noordijk, et al.: Treatment of single brain metastasis: radiotherapy alone or combined with neurosurgery. *J. Annals of Neurology* 33(6), 583–590 (2004)
3. Julio Sánchez de Cos, M., Agustín, S.G., Ma, V.M., et al.: Non-small cell lung cancer and silent brain metastasis Survival and prognostic Factors. *J. Lung Cancer* 63(1), 140–145 (2009)
4. Tomofumi, N., Tetsuya, U., Masahiro, K., et al.: Early detection of metachronous brain metastases by biannual brain MRI follow- up provide patients with non-small cell lung cancer with more opportunities to have radiosurgery. *J. Clin. Neurol Neurosurg.* 112, 770–774 (2010)
5. Lee, S.L.A., Kouzani, A.Z., Hu, E.J.: Automated detection of lung nodules in computed tomography images: A review. *J. Machine Vision and Applications*, 1–13 (2010) (in press)
6. Nie, S.D., Sun, X.W., Chen, Z.X.: Progress in Computer-Aided Detection for Pulmonary Nodule Using CT Image. *J. Chinese Journal of Medical Physics* 26(2), 37–41 (2009)
7. Robert, D., Ambrosini, W.P., Walter, G.: O'Dell: Computer-aided detection of metastatic brain tumors using automated three-dimensional template matching. *J. Journal of Magnetic Resonance Imaging* 31(1), 85–93 (2010)
8. Nie, S.D., Liu, X.S., Sun, X.W., et al.: Computer-aided Detection of Brain Metastases Using MR Images. *J. Chinese Journal of Biomedical Engineering* 29(5), 677–682 (2010)
9. Assefa, M., Faye, I., Malik, A.S., et al.: Lung nodule detection using multi-resolution analysis. In: 2013 ICME International Conference Complex Medical Engineering (CME), pp. 457–461 (2013)
10. Yang, S.W., Nam, Y., Kim, M.O., et al.: Computer-Aided Detection of Metastatic Brain Tumors Using Magnetic Resonance Black-Blood Imaging. *J. Investigative Radiology* 48(2), 113–119 (2013)

11. Smith, S.M.: Fast robust automated brain extraction. *J. Human Brain Mapping* 17(3), 143–155 (2002)
12. Jiang, S.F., Wang, W.H., Feng, Q.J., et al.: Automatic Extraction of Brain from Cerebral MR Image Based on Improved BET Algorithm. *Journal of Image and Graphics* 14(10), 2029–2034 (2009)
13. Farjam, R., Hemant, A., Parmar, D.C.N., et al.: An approach for computer-aided detection of brain metastases in post-Gd T1-W MRI. *J. Magnetic Resonance Imaging* 30, 824–836 (2012)
14. Lignelli, A., Khandji, A.G.: Review of Imaging Techniques in the Diagnosis and Management of Brain Metastases. *J. Neurosurg. Clin. N. Am.* 22(1), 15–25 (2011)
15. Wu, P., Xie, K., Zheng, Y.P., et al.: Brain Tumors Classification Based on 3D Shape. *J. Advances in Intelligent and Soft Computing* 160, 277–283 (2012)
16. Dahab, D.A., Samy, S.A.G., Gamal, M.S., et al.: Automated Brain Tumor Detection and Identification Using Image Processing and Probabilistic Neural Network Techniques. *J. International Journal of Image Processing and Visual Communication* 1(2), 1–8 (2012)

Influence of Conduit Angles on Hemodynamics of Modified Blalock-Taussig Shunt: Computational Analysis of Patient-Specific Virtual Procedures

Jinlong Liu^{1,*}, Qi Sun¹, Mitsuo Umezu², Yi Qian³, Haifa Hong¹, Zhou Du¹,
Qian Wang⁴, Yanjun Sun¹, and Jinfen Liu¹

¹ Department of Cardiothoracic Surgery, Shanghai Children's Medical Center, Shanghai Jiao Tong University School of Medicine, 1678 Dongfang Road, 200127, Shanghai, China

² Center for Advanced Biomedical Sciences, TWIns, Waseda University, TWIns 03C-301, ASMeW Lab, 2-2 Wakamatsucho, Shinjuku 162-8480, Tokyo, Japan

³ Australian School of Advanced Medicine, Macquarie University, North Ryde 2109, Sydney, NSW, Australia

⁴ Department of Medical Imaging, Shanghai Children's Medical Center, Shanghai Jiao Tong University School of Medicine, 1678 Dongfang Road, 200127, Shanghai, China
liujinfen2007@aliyun.com

Abstract. Currently, the modified Blalock-Taussig (mB-T) shunt is the most preferred surgery served as the first step of the staged procedures in the treatment of cyanotic congenital heart defect. A Gore-Tex conduit is used to surgically connect the systemic and pulmonary circulations. In the present study, we report on three-dimensional (3D) hemodynamic analysis of the effects of conduit anastomosis angles on hemodynamics of the mB-T shunt. We constructed a patient-specific 3D model after the mB-T shunt based on medical images and employed computer-aided design to reconstruct two new models with different anastomosis angles. The local pressure, blood flow distribution and wall shear stress were calculated. The results suggest the scheme of vertical anastomosis angle of the conduit on the pulmonary artery can increase the blood flow distribution from systemic circulation to two lungs and blood flows more smoothly in the conduit. The results are well congruent with our clinical experience. This indicates the numerical methods may be applied to investigate hemodynamics of the mB-T shunt for different surgical schemes.

Keywords: Modified Blalock-Taussig shunt, Computational fluid dynamics, Computer-aided Design, Hemodynamics, Congenital heart defect.

* Corresponding Author.

1 Introduction

Since Blalock and Taussig introduced the classical form of a systemic-to-pulmonary procedure with cutting off the subclavian artery in 1945 [1], various modifications have been made to improve this kind of surgical method [2]. However, a modified form of this procedure, called the modified Blalock-Taussig (mB-T) shunt, is the most preferred procedure in clinical applications over the past decades [3, 4]. It is widely used as the first-staged procedure of surgical management for the children with cyanotic congenital heart defects. The mB-T shunt is an effective procedure to increase pulmonary blood flow by the end-to-side anastomosis of the subclavian artery (or the innominate artery) and the pulmonary artery through a Gore-Tex conduit. This surgical connection allows the blood from the systemic arteries flow into the lungs to improve the oxygen saturation of the arterial blood.

The outcomes of the mB-T shunt have improved in the past years and satisfied results are achieved in clinic. However, some complications were reported due to the complex blood flow created by the systemic pulmonary connection through the conduit, including the distortion of the pulmonary arteries, formation of post-operative thrombosis and unbalanced distribution of blood flow to two lungs. These problems are partly related to the implantation of the conduit for the improper choice of anastomosis position or angles in surgeries.

Recent development of the techniques in medical image-based computational fluid dynamics (CFD) and computer-aided design (CAD) makes it possible to perform patient-specific virtual procedures to quantitatively investigate blood flow in vitro before operations. Different surgical schemes can be designed and compared for the evaluation of operative features. A series of related information of hemodynamics can be predicted in detail to help clinicians for surgical decision-making, such as pressure drop, wall shear stress (WSS), and the distribution of blood flow. Liu et al. [5] applied the method to study the hemodynamics of distal aortic arch recoarctation following the Norwood procedure to seek for the best timing of surgical repair. CAD was used to simulate seven stages of increasing stenosis and analyzed the corresponding hemodynamics by CFD calculations. Sun et al. [6] employed the technique of CAD to design different types of total cavopulmonary connections (TCPC) with dual superior venae cavae (SVC), considering different sites for anastomosis from venae cavae to pulmonary arteries (PAs), and compared hemodynamic features in these virtual operative designs by CFD analysis.

In the present study, we used the technique of medical image-based CAD to perform virtual procedures of the mB-T shunt by adjusting the angles of conduit implantation with considering patient-specific anatomical structures. Two three-dimensional (3D) vascular geometries were constructed based on the analysis of the patient's original mB-T shunt. A computational hemodynamic system that validated in our previous studies of Norwood Procedure [7, 8] was applied to perform CFD calculations and analyze the local hemodynamics. The aim of this study was not only to disclose the patient-specific hemodynamic features at the connection area of the mB-T shunt, but also to predict the potential influence of the conduit implantation angles on hemodynamics of the mB-T shunt.

2 Materials and Methods

2.1 Clinic Data Acquisition and Patient-Specific Model Generation

Clinical studies were done around the second-staged procedure with the permission of the parents of a 12-month-old child that had undergone the mB-T shunt at five months old by using a conduit of 4 mm in diameter to surgically connect the innominate artery and pulmonary artery. Protocols were approved by the local institutional review board and regional research ethics committee of Shanghai Children's Medical Center (SCMC) Affiliated Shanghai Jiao Tong University School of Medicine.

To generate the 3D geometric model of patient-specific mB-T shunt, a series of continuous 0.625 mm-thick CT images with 512×512-pixel field of view defined the anatomies of the thorax were acquired by a 16-slice multi-detector row enhanced CT scanner (Bright Speed Elite, GE Medical System, General Electric, America). Medical imaging software RealINTAGE[®] (KGT Co. Tokyo, Japan) compiled and reconstructed the 3D vascular geometry. Details of our method for 3D model reconstruction were reported previously [5]. Due to the pulmonary atresia of the child, only the left ventricle provided blood flow to the body through the ascending aorta (AAo). The blood in pulmonary arteries was provided by the flow distributed from the systemic circulation through a surgical implanted conduit. Fig.1 depicts the 3D reconstructed vascular geometry of the patient-specific mB-T shunt.

The mass flow at the AAo was acquired by echocardiography in real time with electrocardiogram (ECG). The distribution of blood pressure measured during the second-staged procedure at the left pulmonary artery (LPA) and the right pulmonary artery (RPA), respectively, were stored in ASCII format for CFD simulation.

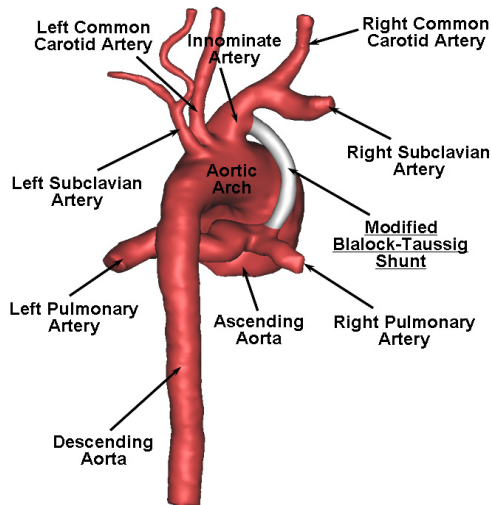


Fig. 1. Reconstruction of 3D patient-specific vascular geometry from original CT images

2.2 Model Rebuilding

Model rebuilding was done by the analysis of patient-specific anatomical structures of arteries in the mB-T shunt. To make new models, the implantation angles of conduit were adjusted based on clinical requirements considering that no kinking should be generated in the conduit. During this process, we applied the commercial software Materialise[®]-Mimics 12.0 to complete the 3D geometry separation, angle modification and model reassemble. Two parameters, θ_1 and θ_2 , were defined for the accurate control of the angle adjustment. The θ_1 was used to describe the angle between the innominate artery and the conduit, and θ_2 was employed to express the angle created by the anastomosis of the conduit and pulmonary artery. Two new virtual models were rebuilt for the CFD analysis in the present study, which expressed two possible surgical designs of the patient-specific mB-T shunt.

Compared with the original model, Model 1 adjusted θ_1 from 90° to 60° , and kept the same degree of θ_2 . Model 2 modified θ_2 from 120° to 90° , and kept θ_1 with the same degree of the original model. We examined the patient-specific anatomical structures and found that the two models with above angles represented the two extreme conditions of conduit implantation without generating kinking in this patient. Other possible implantation angles should be in the range of 60° - 90° for θ_1 and 90° - 180° for θ_2 in the procedure of the patient-specific mB-T shunt. Figure 2 compared the models with the changes of anastomosis angle.

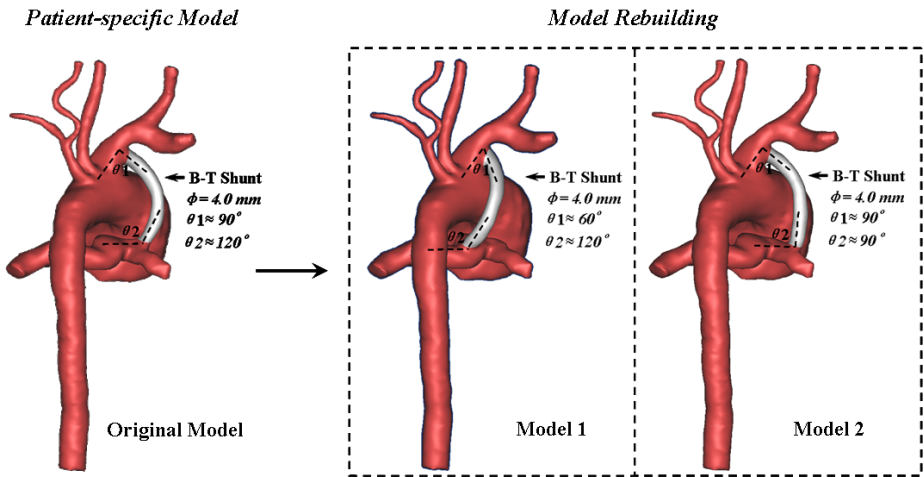


Fig. 2. Two virtual models constructed by computer-aided design with the changes of anastomosis angle

2.3 CFD Analysis

2.3.1 Governing Equations

The equations governing blood flow are the 3D incompressible Navier-Stokes (N-S) equations, which were described as below,

$$\begin{cases} \frac{\partial}{\partial t}(\rho u_i) + \frac{\partial}{\partial x_j}(\rho u_i u_j) = -\frac{\partial p}{\partial x_i} + \frac{\partial}{\partial x_j} \left[\mu \left(\frac{\partial u_i}{\partial x_j} + \frac{\partial u_j}{\partial x_i} \right) \right] + f_i \\ \frac{\partial \rho}{\partial t} + \frac{\partial}{\partial x_j}(\rho u_j) = 0 \end{cases} \quad (1)$$

where $i, j=1, 2, 3$, x_1, x_2 , and x_3 , represent coordinate axes, u_i, u_j are velocity vectors, p is pressure, μ is viscosity, ρ is density, and t is time. The term f_i expresses the action of body forces.

Because arteries are large relative to individual blood cells [9] and shear rates are greater in larger arteries [10], we assumed blood to be a Newtonian fluid with constant density ($\rho = 1060 \text{ kg m}^{-3}$) and viscosity ($\mu = 4.0 \times 10^{-3} \text{ Pa s}$) and the body forces were omitted.

We calculated the Reynolds numbers based on blood flow at the anastomosis of the mB-T shunt in one cardiac cycle, and found the maximum value was closed to 5000. Accordingly, the blood flow should be the turbulence flow in the patient-specific vascular geometry. The most widely validated turbulence model, the standard $k-\varepsilon$ model, was employed to solve the complex flows [11].

The flow distribution ratio (FDR) was defined to evaluate the balance of blood distribution between systemic and pulmonary circulations in the three models. The equation for FDR is given by:

$$FDR = \frac{Q_{outlet}}{Q_{inlet}} \times 100\% \quad (2)$$

where Q_{outlet} is the flow in the LPA, RPA, descending aorta (DA), left subclavian artery (LSA), right subclavian artery (RSA), left common carotid artery (LCCA), right common carotid artery (RCCA) and Q_{inlet} is the inflow at the AAO.

2.3.2 Mesh Generation

The grid-generation software, ANSYS[®]-ICEM 14.0 was applied to discretize the computational domain of the three models for CFD calculations. A combination of tetrahedral grids in the interior and five-layer body-fitted prismatic grids in the near-wall regions was employed for numerical solution of the equations governing blood motion.

To find the best mesh for CFD analysis, grid-independent verification were performed in our previous study and found that grid numbers of about one million would make the most efficient mesh in calculation of aortic flow [8]. Table 1 lists the mesh information for each model, including the patient-specific 3D model.

Table 1. Mesh information for each model

Model	Original Model	Model 1	Model 2
Total Nodes	565,394	559,954	566,504
Total Elements	1,503,964	1,490,333	1,507,513

2.3.4 Boundary Conditions

Due to the pulmonary atresia, the AAO was the only inlet of blood flowed into the arteries. To fully develop the flow boundary layer, the inlet domain was extended upstream to twenty times the size of the AAO. The pulsatile mass flow, measured by echocardiography in real-time with an electrocardiogram recorder, was imposed as the inflow conditions on the extended inlet.

At the outlet of the DA, LSA, LCCA, RCCA, and RSA, we extended sixty times of vessel diameter in a normal direction to allow sufficient recovery of blood pressure in each branch. A zero pressure gradient was used at these outlets. The estimated pressure wave reflections from peripheral vessels at diastolic phase proposed in our previous study of Norwood procedure [7] was applied to model cardiovascular flow. The pressure waves in pulmonary arteries, which were considered to be greatly affected by respiration and blood flow pulsation [12], were measured at the LPA and RPA during the patient's second-staged procedure. These profiles were imposed as the pressure outlet conditions in calculations. To avoid the influence of boundaries, we used same conditions at the inlet and outlet to predict hemodynamic features in the three models.

2.3.5 Calculation

CFD calculations were performed on the finite volume solver package, ANSYS®-FLUENT 14.0, to solve the turbulence flow inside the connection area of the mB-T shunt. For the simulation, we assumed vascular walls were rigid and impermeable, with no-slip boundary conditions. For convergence criteria, the relative variation of the quantities between two successive iterations was smaller than the pre-assigned maximum, 10^{-5} . We chose a second-order upwind scheme for discretization of the governing equations and all calculations were converged to 10^{-6} .

Simulations were run for three consecutive cardiac cycles to yield stable and precise periodic results, and the results of the last cycle were used for hemodynamic analysis.

3 Results

Fig.3 depicts the contour plots of the total pressure and WSS. Fig.3 (a) displays the results when the AAO's mass flow arrived at systolic peak. In the patient-specific model, there is a high pressure drop in the mB-T shunt at systolic peak, approximately 60 mmHg. Relatively low pressure area is observed at the connection area between the conduit and the PA. In Model 1, due to the sharp angle of θ_1 , a relatively high pressure drop is found at the connection area of the IA and conduit. Compared to the patient-specific model, almost the same value of pressure drop is observed at the anastomosis of the PA and conduit. When the θ_2 changes from 120° to 90° in Model 2, the total pressure drop decreases inside the conduit. There is approximately 50 mmHg at systolic peak.

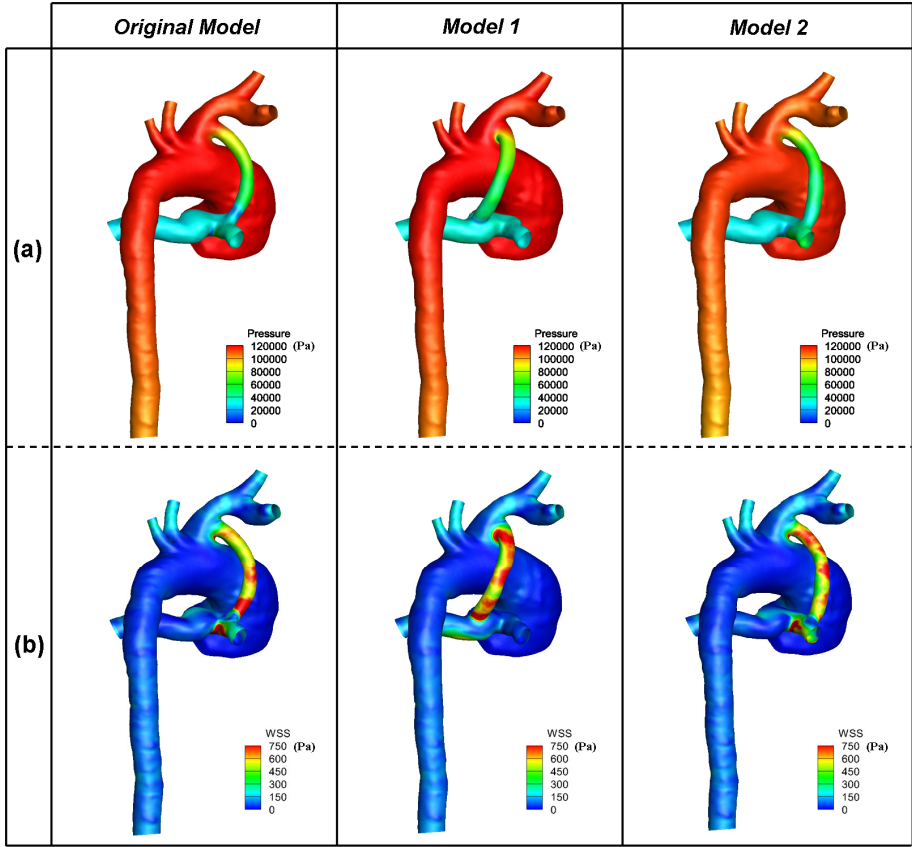


Fig. 3. The contour plots of the total pressure (a) and WSS (b) at systolic peak

WSS, as one of the most important hemodynamic indicators, is related to the remodeling process in the arterial walls and thrombosis formation. Fig.3 (b) displays the distribution of WSS. High values of WSS appear in the conduit and the orifice of the mB-T shunt at the PA in the patient-specific Model. When the θ_1 decreased from 90° to 60° in Model 1, the value of WSS increased sharply at the connection area of the IA and conduit. Large areas of high WSS distribution are observed inside the conduit in Model 1. This indicates that blood flow has accelerated and become more unstable and complex. Due to the restriction of the conduit, blood flow collides directly to the PA. High values of WSS are found at the orifice of conduit to PA. In Model 1, the areas of high values of WSS primarily located at the LPA, while they are mainly distributed at the RPA in the patient-specific model and Model 2.

We calculated the distribution ratio of mass flow at each branch. Table 2 shows these results of the three models respectively. With the decrease of the θ_1 , the mass flow distributed to the PA was declined around 6% of inflow in Model 1. Blood flow to the body through the DA increased by 3.42%. The flow distribution ratios in other branches have some increase. When the θ_2 changed from 120° to 90° in Model 2, a little increase of mass flow passed through the mB-T shunt, with 45.14% of the inflow distributed to the PA and the amount of blood to the DA decreased by 2.4%.

Table 2. The proportion of blood flow distribution (%)

	Original Model	Model 1	Model 2
mB-T shunt	42	37.61	45.41
DA	45	48.42	42.6
LSA	2.5	2.69	2.26
RSA	4.2	4.53	4.01
LCCA	3	3.2	2.86
RCCA	3.3	3.55	3.13

Note: The proportion of the mB-T Shunt expresses the ratio of blood flowed into pulmonary artery passed through the conduit.

4 Discussion

Since the hearts are dysfunctional among the cyanotic CHD patients needed to perform the mB-T shunt, little pressure drop, high WSS and small changes of the blood flow distribution are all important for the survival of the suffering weak hearts and post-operative recovery. Minimizing these factors by optimizing the anastomosis configurations is crucial in the clinical practice.

In the present study, we virtually rebuilt two models by using CAD to adjust the conduit anastomosis angles based on the patient-specific vascular geometry after the procedure of the mB-T shunt. In model 1, we adjusted θ_1 to its minimum angle. The outside wall of the conduit touched the surface of AAO without a kinking created. In model 2, we modified θ_2 to 90° . The conduit was vertically anastomosed on the PA. The angle was considered the optimal angle in the procedure of mB-T shunt based on our clinical experience. The effects of the anastomotic shape, which were considered to have influence on the hemodynamics in procedure, did not take into account in the present study. We kept same anastomotic shape in the process of model rebuilding.

Studies suggested that when the value of Q_p/Q_s (where Q_p was the flow distributes to pulmonary arteries through the conduit, and Q_s was the flow distributes to systemic circulation) reached between 0.5 and 1 [13], the maximal oxygen delivery would be achieved in the systemic-to-pulmonary procedure. We calculated value of Q_p/Q_s and found they were 0.724, 0.603 and 0.823 in three models, respectively. This indicated Model 2 with the conduit vertically anastomosed on the PA can delivery more oxygen in the arterial blood to alleviate cyanosis. The result was well congruent with our clinical experience. Model 1 was the worst design when θ_1 to its minimum angle.

The understanding of pathophysiological changes in the formation of thrombosis and occlusion is critical to improve surgical design of the mB-T shunt. Studies have shown a strong correlation in the magnitude of WSS, endothelial cell function, and vessel wall remodeling [14, 15]. High WSS can damage the endothelial layer of blood vessels. Moreover, low WSS coincided with areas of low flow velocity is considered to promote platelet activation, which is one of the reasons for causing shunt thrombosis and occlusion [16]. In Model 1, relatively high WSS was observed inside the conduit and the bottom of the LPA. It meant large damage of the

endothelial layer of blood vessels may be created in the LPA when the θ_1 was decreased. Due to the change of flow direction, low WSS was generated in the RPA. Although some areas of high WSS were also found inside the conduit in patient-specific model and Model 2, the region of high WSS appeared in PA is smaller comparing to Model 1. This implied relatively small range of damage of the endothelial layer may be made in the PA. As a result, the risk of the formation of thrombosis and occlusion was reduced. Accordingly, the decline of θ_1 can increase the WSS along the conduit and the change of θ_2 can control the distribution area of high WSS in the PA.

5 Conclusion

In the present study, the technique of CAD was used to adjust the anastomosis angles between the IA or PA and the conduit to virtually simulate two different surgical schemes. By the analysis of the distribution of pressure, WSS and flow ratio, the scheme of vertical anastomosis angle of the conduit on the PA was thought to be the optimal design of the procedure to increase the blood flow distribution from systemic circulation to two lungs and blood flows more smoothly in the conduit. The results are well congruent with our clinical experience. The studies of virtual procedure and its hemodynamic analysis are helpful in the surgical design of the mB-T shunt.

6 Conflict of Interest Statement

The authors of this manuscript have no conflicts of interest to disclose.

Acknowledgment. The authors wish to thank Prof. Mitsuo Umezu and Prof. Yi Qian for many fruitful discussions and suggestions arisen during the preparation of this work. This work was supported by the National Nature Science Foundation of China (No. 81070133. P.I.: Jinfen Liu and No. 81100117. P.I.: Qi Sun), Project funded by China Postdoctoral Science Foundation (No. 2013M530200. P.I.: Jinlong Liu), and the fund of The Shanghai Committee of Science and Technology (No. 134119a3900. P.I.: Yanjun Sun).

References

1. Blalock, A., Taussig, H.B.: The Surgical Treatment of Malformations of the Heart in Which there is Pulmonary Stenosis or Pulmonary Atresia. *JAMA* 128, 189–202 (1945)
2. Rodríguez, E., Soler, R., Fernández, R., Raposo, I.: Postoperative Imaging in Cyanotic Congenital Heart Diseases: Part 1, Normal findings. *Am. J. Roentgenol.* 189, 1353–1360 (2007)
3. de Leval, M.R., McKay, R., Jones, M., Stark, J., Macartney, F.J.: Modified Blalock–Taussig shunt: Use of the Subclavian Artery Orifice as Flow Regulator in Prosthetic Systemic Pulmonary Artery Shunts. *J. Thorac. Cardiovasc. Surg.* 81, 112–119 (1981)

4. Garson, A., Bricker, J.T., Fisher, D.J., Neish, S.R.: *The Science and Practice of Pediatric Cardiology*, 2nd edn. Williams & Wilkins, Baltimore (1998)
5. Liu, J.L., Qian, Y., Itatani, K., Murakami, A., Shiurba, R., Miyaji, K., Miyakoshi, T., Umezu, M.: Image-Based Computational Hemodynamics of Distal Aortic Arch Recoarctation Following the Norwood Procedure. In: 4th International Congress on Image and Signal Processing, pp. 318–323. IEEE Press, New York (2011)
6. Sun, Q., Liu, J.L., Qian, Y., Zhang, H.B., Wang, Q., Sun, Y.J., Hong, H.F., Liu, J.F.: Computational Haemodynamic Analysis of Patient-specific Virtual Operations for Total Cavopulmonary Connection with Dual Superior Venae Cavae. *European Journal of Cardio-Thoracic Surgery* (2013), doi:10.1093/ejcts/ezt394
7. Liu, J.L., Qian, Y., Itatani, K., Miyakoshi, T., Murakami, A., Ono, M., Shiurba, R., Miyaji, K., Umezu, M.: An Approach of Computational Hemodynamics for Cardiovascular Flow Simulation. In: ASME-JSME-KSME 2011 Joint Fluids Engineering Conference, pp. 1449–1456. American Society of Mechanical Engineers (2011)
8. Qian, Y., Liu, J.L., Itatani, K., Miyaji, K., Umezu, M.: Computational Hemodynamic Analysis in Congenital Heart Disease: Simulation of the Norwood Procedure. *Ann. Biomed. Eng.* 38, 2302–2313 (2010)
9. McDonald, D.A.: *Blood Flow in Arteries*. Edward Arnold Ltd. (1974)
10. Fung, Y.C.: *Biomechanics*. Springer-Verlag (1981)
11. Launder, B.E., Sharma, B.I.: Application of the Energy Dissipation Model of Turbulence to the Calculation of Flow near a Spinning Disc. *Letters in Heat Mass Transfer* 1, 131–138 (1974)
12. Marsden, A.L., Vignon-Clementel, I.E., Chan, F.P., Feinstein, J.A., Taylor, C.A.: Effects of Exercise and Respiration on Hemodynamic Efficiency in CFD Simulations of the Total Cavopulmonary Connection. *Ann. Biomed. Eng.* 35, 250–263 (2007)
13. Barnea, O., Santamore, W.P., Rossi, A., Salloum, E., Chien, S., Austin, E.H.: Estimation of Oxygen Delivery in Newborns with a Univentricular Circulation. *Circulation* 98, 1407–1413 (1998)
14. Adel, M.M., Seth, L.A., Seigo, I.: Hemodynamic shear stress and its role in atherosclerosis. *JAMA* 282(21), 2035–2042 (1999)
15. Gimbrone, M.A., Resnick, N., Nagel, T., Khachigian, L.M., Collins, T., Topper, J.N.: Hemodynamics, Endothelial Gene Expression, and Atherogenesis. *Ann. N. Y. Acad. Sci.* 811(1), 1–10 (1997)
16. Odum, J., Portzky, M.D., Zurakowski, G., Wernovsky, R.P., Burke, R.P., Mayer, J.E., Castaneda, A.R., Jonas, R.A.: Sternotomy Approach for the Modified Blalock-Taussig Shunt. *Circulation* 92, II256–II261 (1995)

Method for Detecting Gaze Direction Based on Eyes Moving Trend

Qijie Zhao^{1,2,*}, Hui Shao¹, Xudong Zhang¹, and Dawei Tu^{1,2}

¹ School of Mechatronics Engineering and Automation, Shanghai University, China

² Shanghai Key Laboratory of Manufacturing Automation and Robotics, Shanghai, China
zqj@staff.shu.edu.cn

Abstract. Eye gaze plays a very important role in identifying human's attention, so it has been considered to be applied in human computer interaction, and one of the main factors in hindering eye gaze application is the complexity of systems and detection method of gaze direction. To build up an eye gaze tracking human-computer interaction system with simple infrastructure and good usability, a kind of gaze direction evaluating approach based on eyes moving trend has been proposed, and the eyes image and feature information are respectively captured and extracted with a Web camera and a computer, and the quantity of eyes moving trend is defined by the ratio of the distances from iris center to the both corners in one eye. Moreover, the image processing algorithms have been provided to detect the characteristics in the image of eyes area, and the eye corners equivalent position detection method has been put up with respect to the shape of eye corners. Some experiments have been done in the test system, and the results show that the proposed methods and algorithms can meet the communication demands for different subjects in multi type work conditions; after completing the initialization, the subjects can freely interact with the computer in a certain work range, and there is no need to frequently calibrate the work parameters, so the limitations to the subjects have been decreased and the system is easy to use, furthermore, it provides a new way for eye gaze tracking technology applied for caring the old and the disability.

Keywords: eye gaze tracking, human computer interaction, eye moving trend, gaze direction, detection algorithm.

1 Introduction

Eye gaze tracking technology has a wide range of application, such as in psychology research, behavioural analysis, caring the old and the disability, human-computer interaction [1, 2]. In the field of caring the old and the disability, for those disabled people who lose their language competence and Body movement ability, the eye gaze tracking technology could help them express their desire by moving eyes and build the bridge of communication between patients and medical workers. Therefore, eye

* Corresponding author.

gaze tracking technology has attracted much attention in the field of caring the old and the disability.

The main methods for detecting eye gaze direction include Contact Lens, Electromagnetic Coil, Corneal Reflection, Electro-Oculography (EOG), Infrared TV Method and so on[3,4]. Most methods based on machine vision processing algorithm are unconstrained, non-wear and non-contact. They are the ideal methods for the caring the old and the disability auxiliary system. One of the most widely used methods is Pupil corneal reflection [5, 6]. By detecting the displacement which is auxiliary light's reflection point on the corner comparing with Pupil center, this method could estimate the gazing direction as eyes turn around. But it is unreliable when the relative position of user's head, camera and interaction interface is changing and needs to calibrate frequently. Some scholars put forward collecting a large number of samples training methods, such as, regression model [7, 8] and support vector machine (SVM) [9], wearing helmet reduce fixed related parameters calibration method [10, 11], adjust the camera parameters [12] and head motion compensation algorithm of image magnification [13], adopting the method of multiple cameras and auxiliary light source and so on [14-16], to solve this kind of problem. They perform well under some special conditions, but those kinds of systems are not fit for the physical disabled because of its complicated construction and tedious calibration process.

Based on the above analysis, this paper proposes a new gaze direction detecting algorithm. The method extracts the feature information respectively by a Web camera and a computer, and takes eye characteristics instead of external identifiers, such as auxiliary light source, as the reference to recognize the gazing direction. For example, iris center, corner feature points around eyes and parameters such as distance ratio based on these feature could serve as criterion for gaze direction detection algorithm. In this way can we reduce the restrictions for the user at a great extent, and offer help to explore establishing a simple structure and feasibly tracking man-machine interactive system.

2 Estimation of Gaze Direction

In the eye tracking human-computer interaction system(shown as Fig.1(a)), when the subject gazes at different target areas on the interactive interface, we could collect and extract eye feature information using a web camera and information processing algorithm and then achieving gaze direction estimation. When the eye opens (shown as Fig.1 (b)), pupil and iris are exposed between the eyelids. Then we can establish XOY coordinates on the eye image, defining $P_C(X_C, Y_C)$ as the center of iris, $P_L(X_L, Y_L)$ as the left canthus and $P_R(X_R, Y_R)$ as the right. Also, we take H_L and H_R as the distance between left or right canthus (P_L/P_R) and center of iris (P_C) respectively. Then we could get the relations as follow:

$$H_L = |P_C P_L| = \sqrt{(X_C - X_L)^2 + (Y_C - Y_L)^2} \quad (1)$$

$$H_R = |P_C P_R| = \sqrt{(X_C - X_R)^2 + (Y_C - Y_R)^2} \quad (2)$$

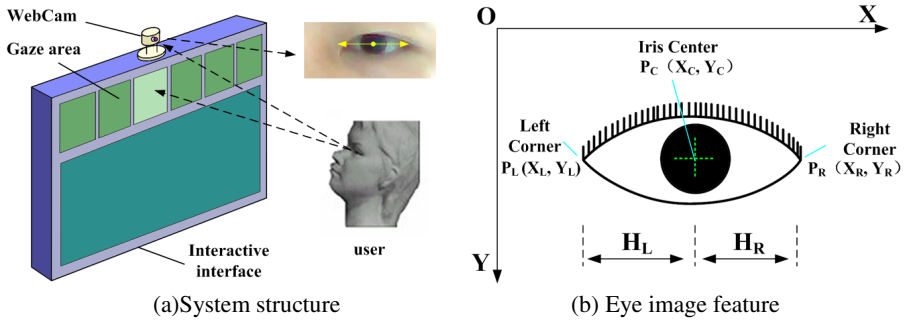


Fig. 1. Eye gaze tracking human-computer interaction system

When gaze direction turns to the left, iris moves to left relative to the eye socket and the position of left or right canthus is fixed. Fig.2 (a) presents the eye state diagram. H_L' stands for the distance between left canthus and iris center, decreases comparing with H_{L0} in the initial state shown as Fig.2 (b). And it increases for the distance between right canthus and iris center H_R' comparing with H_{R0} in the initial state shown as Fig.2 (b). So H_L'/H_R' reduces more significantly than H_{L0}/H_{R0} . In a similar way, when the gaze direction (shown in 2(c)) turns to right, H_L'/H_R'' increases more significantly than H_{L0}/H_{R0} . Therefore, the eye moving trend can be expressed by H_L/H_R . Then we define $R(P_i)$ as eye moving trend of any point P_i on the interface of eye gazing. $H_L(P_i)$, $H_R(P_i)$ respectively stands for the displacement between iris center and canthus. The eye moving trend $R(P_i)$ could be expressed as

$$R(P_i) = H_L(P_i) / H_R(P_i) \tag{3}$$

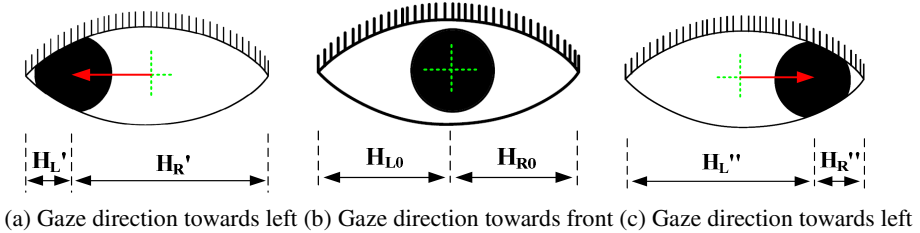


Fig. 2. Analysis of eye moving trend

During the process of human computer conversation in the eye tracking human-computer interaction system, what subject gazing at is a certain point P_{ij} of a target area D_i on the interface. Shown as Fig.3, P_{iL1} , P_{iL2} are any point of the left and right border line of the target area D_i , so when subject gazes at P_{ij} , P_{iL1} , P_{iL2} , the eye moving trend is:

$$\begin{cases} R(P_{ij}) = H_L(P_{ij}) / H_R(P_{ij}) \\ R(P_{iL1}) = H_L(P_{iL1}) / H_R(P_{iL1}) \\ R(P_{iL2}) = H_L(P_{iL2}) / H_R(P_{iL2}) \end{cases} \quad (4)$$

According to the definition of the eye moving trend and position of P_{ij} , P_{iL1} , P_{iL2} on the target area D_i , when subject gazes at the target area D_i , $R(P_{ij})$, $R(P_{iL1})$ and $R(P_{iL2})$ have a relation as followed:

$$R(P_{ij}) \in [R(P_{iL1}), R(P_{iL2})] \quad (5)$$

Combining with the interface design method of the eye tracking human-computer interaction system, we can use equation (4) to confirm the range of the eye moving trend in any target area on the interaction interface. When we gaze at the content on the interaction interface, the current ocular parameter and eye moving trend could be collected and extracted in real-time by web camera and computer. On the basis of equation (5), we could judge the current target area we gaze at, which is also the eye gazing direction.

3 Implementation of Detection Algorithm

In view of the proposed gaze direction estimation method, we use image processing algorithms to extract and calculate the ocular parameters of eye moving trend. And $I(x,y)$ is define as eye area binarization image when the iris is not obscured (shown as Fig.4). The whole information of the image is located in the range of $[x1,x2]$ and $[y1,y2]$. And $g(x,y)$ is a mark image of $I(x,y)$. Pixels are the pixels set of $p(x, y)$ built by black area which comes from the iris and canthus on the image.

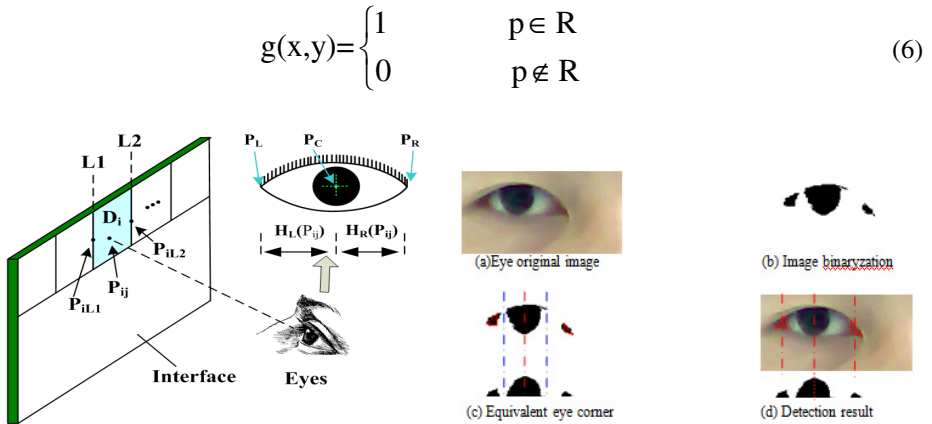


Fig. 3. Gaze a certain area of interactive interface Fig. 4. Process of feature extraction

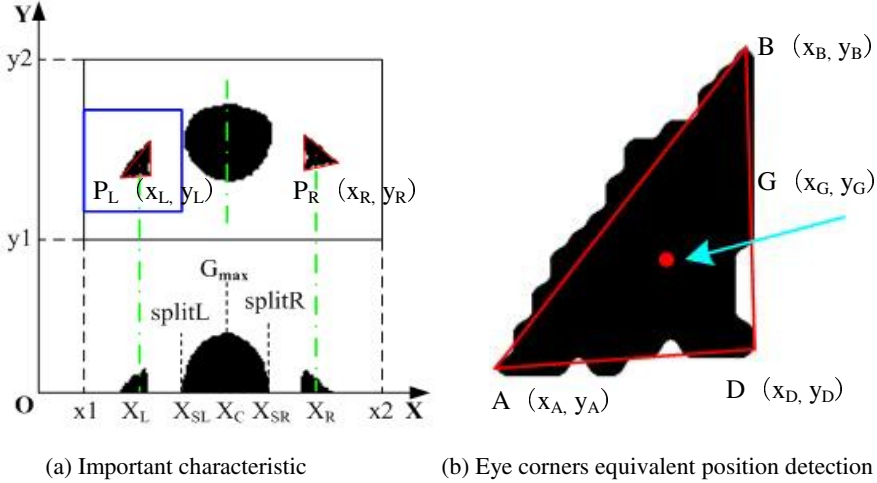


Fig. 5. Detection of characteristic parameter

In order to compile the information of iris and canthus area, we do a integral along the Y direction for the information of $g(x,y) = 1$ of the image, noted as:

$$f_k = \sum_{j=y1}^{y2} g(i_k, j) \tag{7}$$

$x_C = \{i_k \mid f_k = G_{max}, i_k \in (x1, x2)\}$, which is the correspondence of the global integrating maximum values $G_{max} = \max\{\sum_{j=y1}^{y2} g(i_k, j)\}$, is x-coordinate of the center of iris. Then we do integral for the area of $i_k < x_C$ and $i_k > x_C$ and compare respectively. So we affirm the two closet local minimum which is on the both side of global maximum values G_{max} to distinguish the image area of left and right canthus, marking as *splitR* and *splitL*.

$$splitR = \min\{\sum_{j=y1}^{y2} g(i_k, j) \mid i_k < x_C\} \tag{8}$$

$$splitL = \min\{\sum_{j=y1}^{y2} g(i_k, j) \mid i_k > x_C\} \tag{9}$$

The respective corresponding x-coordinate of *splitR* and *splitL* are

$$x_{SR} = \{i_{k1} \mid f_k = splitR\}, \quad x_{SL} = \{i_{k2} \mid f_k = splitL\}.$$

In order to reduce the influence of canthus's shadow and noise, we put forward the eye corners equivalent position detection method on the basis of the shape feature of canthus approximate triangle. In the image area of left and right canthus defined by $i_k < x_{SR}$ and $i_k > x_{SL}$, we scan the first black point ($g(x,y)=1$) by column from the left to right, and mark the location as $A(x_A, y_A)$; afterwards, marking the location as $B(x_B, y_B)$ which be scanned by row from the top to the bottom; and then get the first the black point $D(x_D, y_D)$ through scanning by row whose range is starts from the (x_B, y_A) and bigger than $(x_B + x_A)/2$ to $(y_B + y_A)/2$. By the knowledge of triangle-center, we get the equivalent canthus points $G(x_G, y_G)$ as

$$x_G = \frac{x_A + x_B + x_D}{3} \quad (10)$$

$$y_G = \frac{y_A + y_B + y_D}{3} \quad (11)$$

Through the above detection algorithm, we can ascertain the left and right equivalent canthus $P_L(x_L, y_L)$, $P_R(x_R, y_R)$. Combining with equation (1) ~ (5) to calculate the value of eye moving trend, we could identify the gaze direction.

Fig.5 is an example of the detection algorithm for information processing. It divides the threshold of the original eye image (Fig.5 (a)) into binary image (Fig.5 (b)) which contains iris and canthus information. With the characteristic parameters detection and triangle canthus of equivalent estimation algorithm, we can calculate the parameters of eye moving trend for the iris and canthus (Fig.5(c)). Fig.5 (d) presents result of the example. Three red dotted lines from left to right respectively represent left and right eye equivalent P_R, P_L and the iris center PC location. Using the equation (1) ~ (3), we can get H_L, H_R and eye moving trend $R = H_L / H_R$.

4 Experiments

According to the proposed gaze direction evaluating approach and detecting algorithm, we set up a experimental system which mainly consists of a USB interface Web camera, computer and interactive interface. And Fig. 6(a) presents the system. The hardware of interactive interface is a 17inch monitor, meanwhile, the information of interface is composed of multiple target areas expressing certain meanings and L1~L5 are the boundaries of target areas D1~D4 (see Fig.6 (b)). In the process of system parameters initialization, eyes gazed different target points on the boundaries. We repeatedly carried out experiments to record eye characteristic parameters and compute eyes moving trend. Finally, we could get eyes moving trend scope $R(D_i)$ of gazing every target area. Table 1 presents the experimental initialization information.

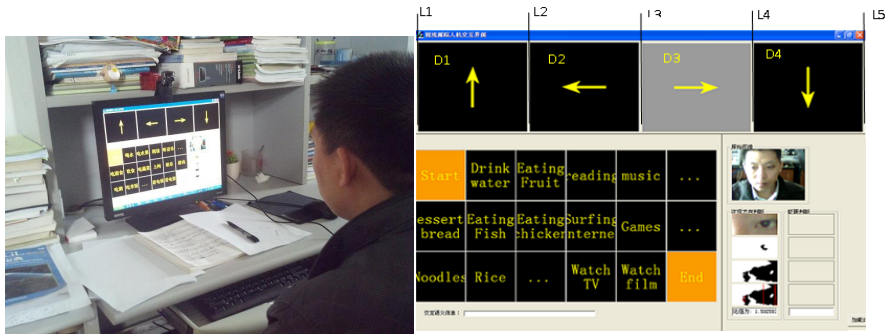


Fig. 6. (a) experiment environment; (b) Interactive interface

During human-computer interaction, when subject gazed the objects on interactive interface, we obtained the current eye moving trend values using detecting algorithm. Then the values were compared with that of initialization. So we could find and activate eyes gaze object regions. The current twinkling object region activated (Fig.6 (b)) was the area that subject interested in.

Table 1. The information of system initialization

	L1	L2	L3	L4	L5
R(P _{Li})	0.658	0.872	1.060	1.431	1.889
R(D _i)	D1[0.658,0.872)	D2[0.872,1.060)	D3[1.060,1.431)	D4[1.431,1.899]	

Table 2. Experiment data of eyes moving trend

Participants	Distances from eyes to interface	Average of R(D1)	Average of R(D2)	Average of R(D3)	Average of R(D4)
Subject1	Z1=400mm	0.801	1.041	1.359	1.886
	Z2=500mm	0.779	0.984	1.228	1.626
	Z3=600mm	0.816	1.033	1.281	1.569
	Z4=800mm	0.866	1.045	1.177	1.617
Subject2	Z1=400mm	0.693	0.976	1.291	1.788
	Z2=500mm	0.724	1.016	1.266	1.744
	Z3=600mm	0.698	0.972	1.259	1.484
	Z4=800mm	0.745	1.021	1.171	1.461
Subject3	Z1=400mm	0.671	0.887	1.279	1.664
	Z2=500mm	0.665	0.878	1.063	1.591
	Z3=600mm	0.668	0.955	1.092	1.450
	Z4=800mm	0.803	1.011	1.133	1.517

In order to analysis feasibility of detecting algorithm, many laboratorial experimenters respectively kept different working distances away from interactive interface and gazed different object regions (D1~D4) on the interface. Table 2 and Fig.7 present eyes moving trend detecting results of part experiments.

Seeing from detecting results, the proposed eye corners equivalent position detection method obviously accurate fixed on eye corners position (the red triangles and dotted lines). And the method is not susceptible influenced by eye corners edge shadow and noise. It can apply to different subjects with diverse eye corners features.

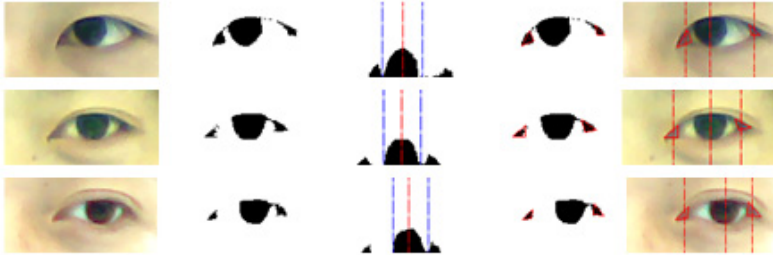


Fig. 7. Eye regions feature detecting process

Combining Table 1, Table 2 and the recorded experiment data, we performed further analysis. Fig.8 (a) presents the analysis results that different subjects gazed different target areas at same working distance. As can be seen from the figure, although eye moving trend values existed certain differences when three subjects gazed different object regions, they all fall into eye moving trend initialization scopes determined by the top and bottom red borderlines.

Fig.8 (b) presents the analysis results that different subject's gazed same region at different distance. According to the results, we can realize that the eye moving trend values of shorter working distance spread relatively divergence. And the values tend to concentration with the increase of working distance, but eye moving trend values are all in the regions determined by top and bottom red borderlines. The results showed that the proposed method allowed user free motion in lager area and system could still regular function. On the basis of Ergonomics knowledge, the distance of subject and computer interface is more appropriate among 350mm~1000mm. Subject will feel uncomfortable no matter it is excessive far or near.

According to above experiment and analysis, we propose methods for detecting gaze direction to judge eye moving trend in the way of distance ratio. By the camera imaging principle, the distances from iris center to the both corners will change, so long as the distance between subject and interactive interface changes. However, the changing distance from subject to interface has no obvious effect on distance ratio. The proposed method applies to eye gaze tracking human-computer interaction system. It can achieve different users gazing diverse objects at different places. And subjects can move freely in larger area after working parameters determined by initialization. The method is feasibility. In addition, the proposed method has some

limitations, such as, the detection of eye moving up and down trend is not obvious and the proposed feature detection algorithm is not precise enough. Particularly, the application of high resolution about major interface object regions should be emphasized in the future.

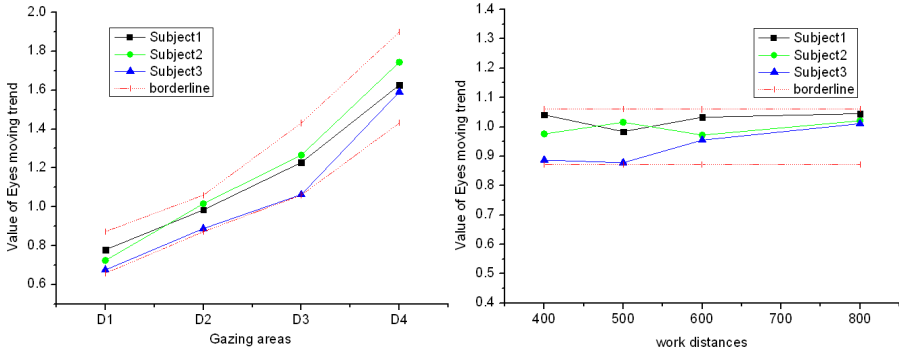


Fig. 8. (a) Different subjects gazing different regions at the same position; (b) Different subjects gazing the same region at different position

5 Conclusions

Eye gazing tracking technology applying for caring the elder and the disability, can set up a communication bridge between patients and medical workers by the interactive interface. Consequently, it enhances the nursing effects for the disabled. Considering the problems in the application of eye gaze tracking human-computer interaction system, such as, limitations to subject and demarcating frequently, this paper proposed a kind of gaze direction evaluating approach based on eyes moving trend, and the quantity of eyes moving trend is defined by the ratio of the distances from iris center to the both corners in one eye. Besides, eye currently gazing object is judged by the quantity of eyes moving trend. Moreover, on the aspect of gaze direction evaluating approach, the image processing algorithms have been provided to detect the characteristics in the image of eyes area, and the eye corners equivalent position detection method has been put up with respect to the shape of eye corners. Furthermore, we carried out experiments using a low cost Web camera and a computer. Then the recorded data was analyzed. Seeing from the analysis results, we found that the gaze direction detecting method applying to human-computer interaction system could meet different subjects working under various conditions. After completing the initialization, the subjects can freely interact with the computer in a certain work range, and there is no need to frequently calibrate the work parameters, so the limitations to the subjects have been decreased and the system is easy to use, furthermore, it provides a new way for eye gaze tracking technology applied for caring the old and the disability.

Acknowledgements. This work was supported by National Natural Science Foundation of China (No. 61101177).

References

- [1] Hutchinson, T.E., White, K.P., et al.: Human-computer interface using eye-gaze input. *IEEE Transactions on System, Man, and Cybernetics* 19(6), 1527–1534 (1989)
- [2] Majaranta, Kari-Jouko: Twenty Years of Eye Typing: Systems and Design Issues. In: *Proceedings of Eye Tracking Research and Applications (ETRA 2002)*, New Orleans LA, pp. 15–22 (2002)
- [3] Hansen, D.W., Ji, Q.: In the Eye of the Beholder: A Survey of Models for Eyes and Gaze Pattern Analysis and Machine Intelligence. *IEEE Transactions on Pattern Analysis and Machine Intelligence* 32(3), 478–500 (2010)
- [4] Morimoto, C.H., Mimica, M.R.M.: Eye Gaze Tracking Techniques for Interactive Applications. *Computer Vision and Image Understanding* 98(1), 4–24 (2005)
- [5] Sigut, J., Sidha, S.-A.: Iris Center Corneal Reflection Method for Gaze Tracking using Visible Light. *IEEE Transactions on Biomedical Engineering* 58(2), 411–419 (2011)
- [6] Nouredin, B., Lawrence, P.D., Birch, G.E.: Online Removal of Eye Movement and Blink EEG Artifacts Using a High-Speed Eye Tracker. *IEEE Transactions on Biomedical Engineering* 59(8), 2103–2110 (2012)
- [7] Williams, O., Blake, A., Cipolla, R.: Sparse and Semi-supervised Visual Mapping with the S3GP. In: *Proceedings of IEEE Computer Society Conference on Computer Vision and Pattern Recognition*, vol. 1, pp. 230–237 (2006)
- [8] Zhu, Z., Ji, Q.: Eye and Gaze Tracking for Interactive Graphic Display. *Machine Vision and Applications* 15(3), 139–148 (2004)
- [9] Zhu, Z.W., Ji, Q., Bennett, K.P.: Nonlinear Eye Gaze Mapping Function Estimation via Support Vector Regression. In: *Proceedings of IEEE Conference on Pattern Recognition*, vol. 1, pp. 1132–1135 (2006)
- [10] Shen, H.P., Feng, H.J., Xu, Z.H.: Gaze Tracking System Based on Pupil Detection. *Journal of Optoelectronics Laser* 16(8), 961–964 (2005)
- [11] Zhao, X.C., Lu, Z.Y.: Eye Gaze Tracking System with Head Unfixed. *Journal of Nanjing University of Aeronautics & Astronautics* 42(4), 435–439 (2010)
- [12] Tu, D.W., Zhao, Q.J., Yin, H.R.: Eye-gaze Input System Being Adaptive to the User's Head Movement 25(6), 828–831 (2004)
- [13] Hang, Y., Wang, Z.L., Tu, X.Y.: Development and Application of a Gaze-Tracking System Adapting to Natural Head-Movements. *Acta Electronica Sinica* 37(4), 764–770 (2009)
- [14] Kondou, Y., Ebisawa, Y.: Easy Eye-Gaze Calibration using a Moving Visual Target in the Head-Free Remote Eye-Gaze Detection System. In: *Proceedings of IEEE Conference on Virtual Environments, Human-Computer Interfaces, and Measurement Systems*, pp. 145–150 (2008)
- [15] Hennessey, C., Lawrence, P.: Noncontact Binocular Eye-gaze Tracking for Point-of-gaze Estimation in Three Dimensions. *IEEE Transactions on Biomedical Engineering* 56(3), 790–799 (2009)
- [16] Reale, M.J., Canavan, S., Yin, L.: A Multi-Gesture Interaction System Using a 3-D Iris Disk Model for Gaze Estimation and an Active Appearance Model for 3-D Hand Pointing. *IEEE Transactions on Multimedia* 13(3), 474–4866 (2011)

Gait Pose Estimation Based on Manifold Learning

Fan Zhao^{1,2}, Shiwei Ma^{1,2,*}, Zhonghua Hao^{1,2}, and Jiarui Wen^{1,2}

¹ Shanghai Key Laboratory of Power Station Automation Technology

² School of Mechatronic Engineering & Automation, Shanghai University, NO.149,
Yanchang Rd. 200072 Shanghai, China
masw@shu.edu.cn

Abstract. A manifold learning based approach for gait pose estimation is proposed in this paper. It consists of two manifold learning based dimension reductions and three mapping functions based on General Regression Neural Network (GRNN). A model of various people walking gait is built so as to find the correspondence between a new gait pose image and the model. The reduced low-dimensional data can be used to realize the mapping between 2D gait pose model and 3D body configuration. When inputting a 2D gait pose image, it can provide the corresponding pose image in the model which can be used to carry out the mapping by the trained GRNN. Simulated experiments manifested the effectiveness of the approach.

Keywords: Pose estimation, manifold learning, dimension reduction, GRNN.

1 Introduction

Estimation 3D human pose from 2D image is a challenging task in the field of machine learning and computer vision. The first problem is the high dimensionality of both the input 2D images and the 3D body configuration. The second is the congruent relationship between them. In the last decades, works have been done such as tracking the human body and recovering the 3D body posture to realize the goal of visual surveillance, human-machine interface, computer animation, virtual reality, etc. Researchers have been increasingly interested in studying the human pose estimating based on manifold learning.

As one of the core technology in human body pose, manifold learning was born to overcome the “curse of dimensionality”. Manifold learning can compute the low-dimensional representations of high-dimensional observations. Many methods have focused on the view variation since the manifold distributions are highly variable among different viewpoints. One is to separating view factors from mapping functions using a tensor decomposition[1][2]. This approach tries to extract the influence of viewpoint changes from coefficients in mapping functions between the 3D body configuration manifold and visual input. However, This approach does not guarantee a unique mapping between an input image and a corresponding 3D body pose.

* Corresponding author.

Another is to extract the influence of viewpoint changes from coefficients in mapping functions between the 3D body configuration manifold and visual input[3][4]. This method performs well in estimate the 2D images. However, it uses the data of one person to train the mapping process which cannot guarantee the generalization of different people.

2 Proposed Method

The approach we proposed in this paper is a unique mapping from 2D gait pose images to 3D body configuration. In the training course, a gait pose model of different walking people is built in the first place, the model is built based on six individuals' walking gait pose. Then we use the gait pose model to train the mapping between 2D images and 3D body configuration. Generalized Regression Neural Network (GRNN) method is employed so as to efficiently learn several different mapping functions. In the testing course, an image of walking people is regarded as the input data, we match the test image to one certain image inside of the 2D gait pose model. Then the trained mapping networks can be used to mapping from a 2D gait pose image to a 3D body configuration image. Figure 1 shows the framework of the proposed method. Fig. 1.(a) shows the training course of the proposed method. Fig. 1.(b) shows the testing course of the proposed method.

When comes a 2D test image, it can be matched to one certain pose image in the 2D model, the match method is based on the inter frame difference method. The matched 2D model image is used to mapping to 3D body configuration image based on the trained networks. Thus, the 2D test image is corresponded to its 3D body configuration.

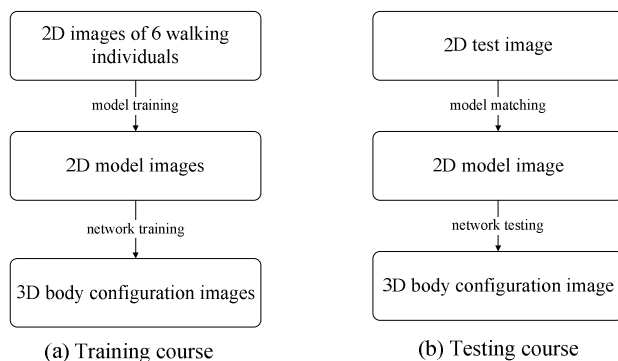


Fig. 1. Framework of the proposed method

3 Gait Pose Model

We use the 2D gait pose images of six individuals to train the gait pose model. Each of the walking action contains 30 frames, and every image is processed to silhouette image. All of the 2D images are synthesized images generated with Poser 7[5].

Despite the high dimensionality of both the human body configuration space and the visual input space, many human activities lie on low-dimensional manifolds. As one of the most classic method of linear dimension reduction, Principal Component Analysis[6] (PCA) aims to reduce the dimensionality of the input data of a large number of interrelated variables, while retaining the interrelatedness present in the low-dimensional target data as much as possible.

PCA is a linear transformation that transforms the data to a new coordinate system such that the new set of variables, the principal components, are linear functions of the original variables, are uncorrelated, and the greatest variance by any projection of the data comes to lie on the first coordinate, the second greatest variance on the second coordinate, and so on. In practice, this is achieved by computing the covariance matrix for the full data set. Next, the eigenvectors and eigenvalues of the covariance matrix are computed, and sorted according to decreasing eigenvalue.

Given the high-dimensional observation data of the processed silhouette image of six different walking people, $X = \{x_1, x_2, \dots, x_n\}$, x_i is the training sample. Our goal is to obtain the orthonormal vector v_1, v_2, \dots, v_d as low-dimensional orthogonal basis, thereby reducing the coordinates in low-dimensional space of high-dimensional data.

We adopt PCA method to train the gait pose model as follows,

a) Calculation of the mean value of observation data

$$u = \frac{1}{n} \sum_{i=1}^n x_i. \quad (1)$$

b) Calculation of the covariance matrix

$$C = \frac{1}{n} \sum_{i=1}^n (x_i - u)(x_i - u)^T. \quad (2)$$

c) Calculation of the orthonormal eigenvector v_1, v_2, \dots, v_d corresponding to the top d of maximum eigenvalue $\lambda_1, \lambda_2, \dots, \lambda_d$ of matrix nC .

d) Modeling of the training data

$$M = \frac{1}{n} \sum_{i=1}^d \lambda_i v_i. \quad (3)$$

Then the gait pose model containing 30 frames of people walking pose is built.

4 Learning Mapping Function

After building the gait pose model, we learn the mapping function from the 2D silhouette gait pose model image to 3D body configuration data getting from CMU Motion Capture dataset[7][8]. The 3D body configuration consists of 30 frames of data point set that can be observed from 360 degrees. Just like the 2D image dataset, 3D dataset also have the problem of dealing with high dimensional data, so we apply a nonlinear dimension reduction of manifold learning, ISOMAP[9], to overcome the ‘‘curse of dimensionality’’.

ISOMAP builds on classical MDS[10] but seeks to preserve the intrinsic geometry of the data, as captured in the geodesic manifold distances between all pairs of data points. ISOMAP is distinguished by its use of the geodesic distance induced by a neighborhood graph embedded in the classical scaling, and this is done to incorporate manifold structure in the resulting embedding.

The complete ISOMAP algorithm has three steps as listed below,

- a) Use K nearest neighbors to determine neighbors points on the manifold M based on the Euclidean distances $d_x(i, j)$ between pairs of points i, j .
- b) Estimate the geodesic distances $d_M(i, j)$ between all pairs of points on the manifold M by computing their shortest path distances $d_G(i, j)$ in the graph G .
- c) Apply classical MDS to the matrix of graph distances $D_G = \{d_G(i, j)\}$, constructing an embedding of the data in a d -dimensional Euclidean space Y that best preserves the manifold's estimated intrinsic geometry.

Two manifolds are learned to reduce the dimension of the input 2D image data and the 3D body configuration data using ISOMAP. Then we use a General Regression Neural Network (GRNN)[11] to build the mapping functions. The GRNN function is defined by the following equations,

$$\hat{Y}(X) = E(Y|X) = \frac{\sum_{i=1}^n Y_i \exp(-\frac{D_i^2}{2\sigma^2})}{\sum_{i=1}^n \exp(-\frac{D_i^2}{2\sigma^2})}. \quad (4)$$

where $D_i^2 = (x - x_i)^T (x - x_i)$, Y_i is the actual output of i in a training dataset, and σ is a smoothing parameter. We define error function to adjust the smoothing parameter σ by using the Mean Squared Error (MSE),

$$e = \hat{Y}(X_i) - Y(X_i). \quad (5)$$

where $\hat{Y}(X_i)$ is the estimated vector of the input vector X_i , $Y(X_i)$ is the actual vector of the input vector X_i , and the error e present the forecasting error of GRNN. The smoothing parameter is chosen when the error reaches its minimum value.

Following is the GRNN mapping function we defined in this paper,

$$M(P) = G(P, T). \quad (6)$$

where $M(P)$ is the estimating vector of an input vector presenting an image, and $G(P, T)$ is the GRNN net function. P is an input vector and T is an output vector.

With learned data of 2D gait pose model manifold M_i and 3D body configuration manifold M_b , we can mapping from the 2D silhouette images of gait pose

model to 3D body configuration by using three GRNN. Figure 2 shows the mapping network.



Fig. 2. The mapping network using GRNN

Given the silhouette images of 2D gait pose model X_i and its manifold M_i , we build a network to mapping them.

$$N_1 = G(X_i, M_i). \quad (7)$$

Given the manifold M_i of 2D gait pose model and the manifold M_b of 3D body configuration, we build a network to mapping them.

$$N_2 = G(M_i, M_b). \quad (8)$$

Given the 3D body configuration X_b and its manifold M_b , we build a network to mapping them.

$$N_3 = G(M_b, X_b). \quad (9)$$

So far, the training of the network is done. When comes a 2D image input, we mapping it with the three networks step by step, thus can gain the corresponding 3D body configuration.

We define the estimation error function as below,

$$E = \sqrt{\sum_{j=1}^n (x'_{ij} - x_{ij})^2}. \quad (10)$$

Where x'_{ij} is the estimated 3D body configuration data of 2D image data x_i , x_{ij} is the 3D body configuration data of 2D image data x_i , and n is the dimension of x_i .

5 Experiments

Six individuals' gait pose series including three male people and three female people are used to build the model generated with Poser 7[5], shows in Fig. 3. Each series of walking gait pose includes 30 frames. All of the 2D synthesized images are processed to silhouette images so as to build pose gait model.

Gait pose images of a man and a woman which are not involved in building the model were used to test our proposed way, shows in Fig. 4. Each row represents the test images of the same gait pose, the matched 2D model images, and the mapped 3D body configuration images of a man and a woman. The first column and the forth column are the original 2D images of the test man and woman, the second column and the fifth column are the matched images of the input test images in the 2D gait pose model, the third column and the sixth column are the mapped 3D body configuration images of the 2D model images.



(a) First frame of six individuals



(b) 30 frames of one individual

Fig. 3. Individuals of experiment generated with Poser 7

Both the test images and the model images are processed to silhouette images. A test image is subtracted from each of the 30 model images, the minimum value of the 30 subtraction is chosen as the matched result of the two images. The two images of the matched result represent the same gait pose. The mapping between 2D model images and 3D body configuration is based on the 3 networks we have built above.

As is shown in Fig. 4, different people of same gait pose image can match to the same model image representing its gait and each gait pose image can find its corresponding 3D body configuration. Experiments indicate that the changes in legs affect the result mostly while the arm changes play a small role when estimating the gait pose.

The estimated error between the estimated body configuration and the original body configuration was calculated according to Eq.(10). The results are shown in Fig. 5. The lateral axis represents the 30 frames of the test individual while the vertical axis represents the value of the estimated error.

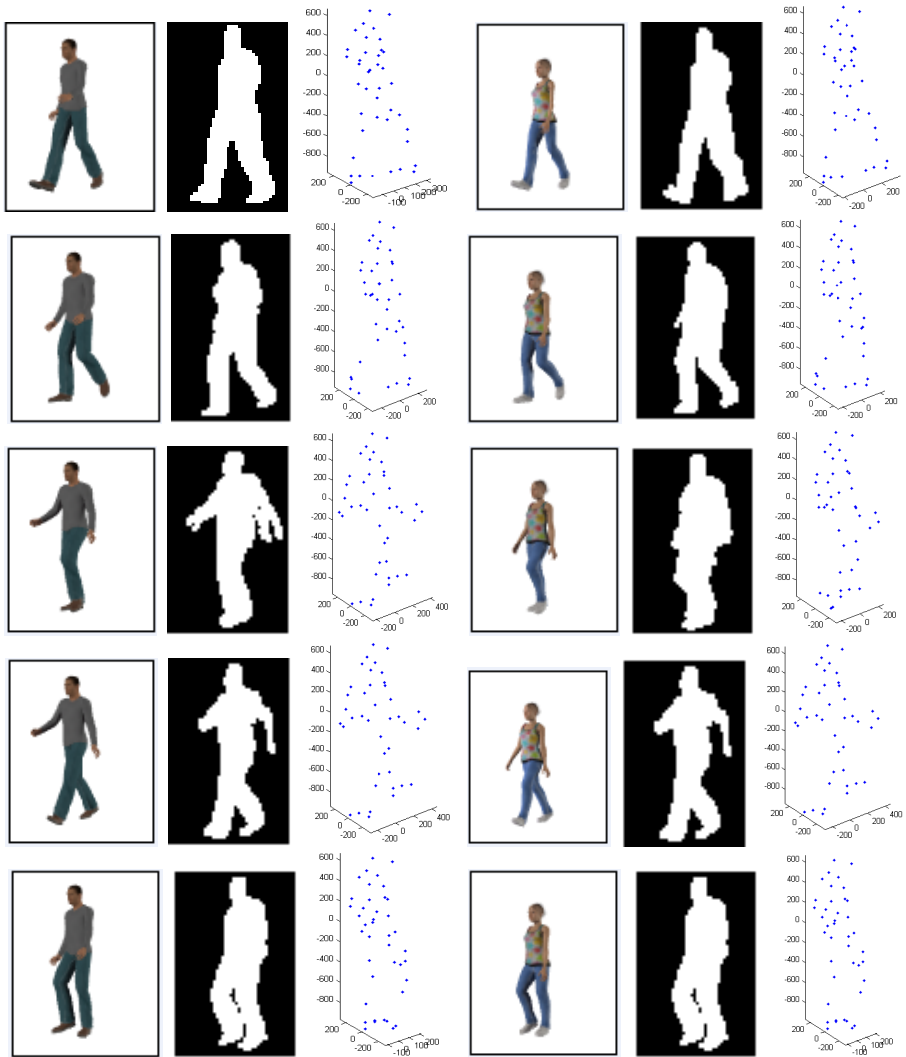


Fig. 4. Gait pose estimation of different people and different pose

The estimation error of the 3D body configuration shows the mapping result of each frame. As shown in figure 3(b), first three frames are the same with the last three frames, thus the estimation error of these frames are big. As the 2D images are processed to silhouette images which cannot tell the differences between the left and the right leg easily, the estimation error of these frames is big when the legs are overlapped.

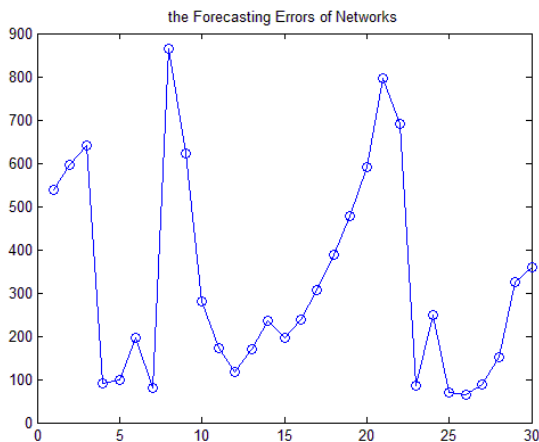


Fig. 5. The estimating error of the 3D body configuration

6 Conclusion

This work establishes a directly mapping between 2D gait pose model and 3D body configuration. It is a unique mapping so that each input 2D test image can find its gait pose in 3D body configuration through the GRNN mapping function. The walking pose images of six individuals guarantee the generalization of the model and the mapping guarantee its one-to-one correspondence. However, there are also some test frames that the method we proposed cannot deal with, that is because we use the silhouette images as our experiment data. Sometimes the left leg and the right leg cannot be distinguished correctly. The skin color of arms is considered to help figuring this out. The method we proposed in this paper estimates the gait pose of walking people. There are also more motions we can learn to mapping for realizing the pose estimation and motion analysis in the future.

Acknowledgments. This work was financially supported by the NSFC (61171145) and Shanghai Science and Technology Foundation (13510500400) and the Shanghai Educational Commission Foundation (12ZZ083).

References

1. Lee, C.S., Elgammal, A.: Modeling view and posture manifolds for tracking. In: IEEE 11th International Conference on Computer Vision, ICCV 2007, pp. 1–8. IEEE (2007)
2. Elgammal, A., Lee, C.S.: Tracking people on a torus. *IEEE Transactions on Pattern Analysis and Machine Intelligence* 31(3), 520–538 (2009)
3. Hur, D., Wallraven, C., Lee, S.W.: View invariant body pose estimation based on biased manifold learning. In: 2010 20th International Conference on Pattern Recognition (ICPR), pp. 3866–3869. IEEE (2010)

4. Hur, D., Wallraven, C., Lee, S.W.: Supervised manifold learning based on biased distance for view invariant body pose estimation. In: 2012 IEEE International Conference on Systems, Man, and Cybernetics (SMC), pp. 2717–2720. IEEE (2012)
5. <http://my.smithmicro.com/>
6. Abdi, H., Williams, L.J.: Principal component analysis. *Wiley Interdisciplinary Reviews: Computational Statistics* 2(4), 433–459 (2010)
7. Gross, R., Shi, J.: The cmu motion of body (mobo) database (2001)
8. <http://mocap.cs.cmu.edu/>
9. Tenenbaum, J.B., De Silva, V., Langford, J.C.: A global geometric framework for nonlinear dimensionality reduction. *Science* 290(5500), 2319–2323 (2000)
10. De Leeuw, J.: Applications of convex analysis to multidimensional scaling. Department of Statistics, UCLA (2011)
11. Specht, D.F.: A general regression neural network. *IEEE Transactions on Neural Networks* 2(6), 568–576 (1991)

Method of CT Pulmonary Vessel Image Enhancement Based on Structure Tensor

Rui-Rui Bu, Yuan-Jun Wang, Jing Gong, Xiao-Fei Wang, and Sheng-Dong Nie*

School of Medical Instrument & Food Engineering, University of Shanghai for Science and
Technology, Shanghai 200093, China
nsd4647@163.com

Abstract. This paper investigates an effective enhancement method for CT pulmonary vessel by using structure tensor. Firstly, based on a calculated image's structure tensor, the image's diffusion tensor is constructed. Then, the diffusion tensor is filtered with three different schemes. Finally, the result shows the effective of the proposed method. The synthetic dataset and CT Lung dataset from LIDC are used to verify this method's efficiency. The result shows the pulmonary vessels are enhanced and the images' contrast and SNR are improved. The enhancement method based on structure tensor is suitable for CT pulmonary vessel.

Keywords: Structure tensor, image enhancement, pulmonary vessel, anisotropic diffusion.

1 Introduction

The method of image expression which based on structure tensor has been successfully applied to image processing and computer vision, such as image's direction field, feature detection, image denoising and enhancement, etc. After the initial structure tensor was proposed by W.Forstner *et al.* [1], the structure tensor was applied by J.Bigun *et al.* [2] in calculating the image's direction and optical flow. Then, the linear structure tensor was changed to the nonlinear structure tensor with the method of Partial Differential Equation (PDE) by J.Weickert [3], which improved the accuracy of the edge and corner detection greatly. But due to the multiple iterations of the diffusion, the calculation speed of this method was limited. After then, the J.Weickert's algorithm was optimized by D.Kroon [4] with improving the calculation speed. In recent years, the structure tensor was also researched in different application fields by some researchers in our country. A trace-based nonlinear with a good robustness was proposed by Y. Zhong *et al.* [5] The anisotropic diffusion filter with optimal rotation invariance was used to enhance the 3D seismic imaging effectively by Y. Zhong *et al.* [6]. What's more, the structure tensor was applied in the image restoration to reduce noise and preserve image details at the same time [7]. Some researchers also used this method to reduce the image ambiguity of corner [8].

* Corresponding author.

It's helpful for doctors to identify vascular lesions easily and diagnose the vascular diseases accurately in the CT images by enhancing the blood vessel. Noises caused by volume effect in CT imaging can significantly degrade the contrast between blood vessels and other tissues. Moreover, a complex inherent structure or many vessel branches will cause blurring in vessel boundaries [9]. The enhancement method based on structure tensor uses eigenvectors and eigenvalues of the diffusion tensor to control the main directions of diffusion and the amount of diffusion in the corresponding direction, respectively. According to the relevant literatures, this enhancement method has been successfully involved into various areas like fingerprints, knit, seismic images [10], CT mandibular canal images [11] and ocular US images [12]. But this enhancement method hasn't been used in the CT pulmonary vessel processing. Therefore, a shipped version of this kind of method was proposed and cast in details.

2 Theory and Method

The flow diagram of the enhancement method based on structure tensor is as follows:

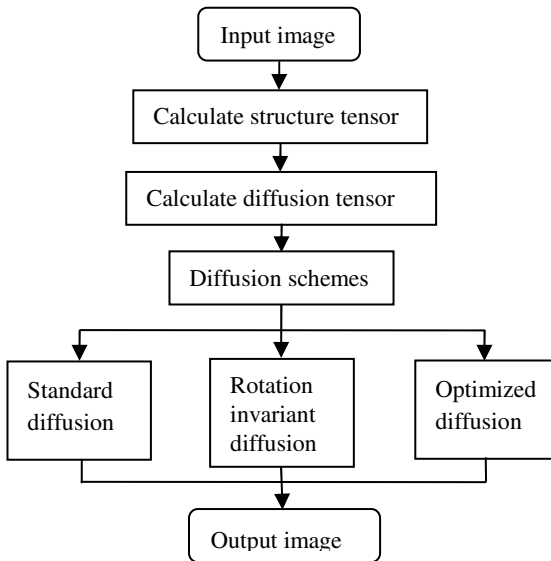


Fig. 1. The flow diagram of the enhancement method

2.1 Introduction of Structure Tensor

The diffusion model of structure tensor was proposed by J.Weickert:

$$\begin{cases} \partial_t u = \nabla \cdot (D \nabla u) & \Omega \times (0, \infty) \\ u(x, 0) = f(x) & \Omega \\ \langle D \nabla u, n \rangle = 0 & \Gamma \times (0, \infty) \end{cases}, \quad (1)$$

where $\{u(x, y, t), t \geq 0\}$ denotes a 2D image, D is the diffusion tensor, ∇u stands for the image gradient, Ω represents the rectangular image domain, n is the direction of exterior normal. Here $\partial_t u = \nabla \cdot (D \nabla u)$ can be specifically expressed by:

$$\frac{\partial u_{i,j}}{\partial t} = \text{div} \left(g \left(\sum_{k=1}^2 \sum_{l=1}^2 \nabla u_{k,l} \nabla u_{k,l}^T \right) \nabla u_{i,j} \right) \quad (i, j = 1, 2) . \quad (2)$$

The structure tensor $J = \nabla u_{k,l} \nabla u_{k,l}^T$ is the convolution of initial structure tensor and G_ρ is a Gaussian weighting function with sigma ρ :

$$J = G_\rho * ST(i, j) = G_\rho * (\nabla u_{i,j} \times \nabla u_{i,j}^T) = G_\rho * \begin{bmatrix} u_x^2 & u_{xy} \\ u_{xy} & u_y^2 \end{bmatrix} = \begin{bmatrix} u_{11} & u_{12} \\ u_{21} & u_{22} \end{bmatrix} . \quad (3)$$

The structure tensor combines the pixel information of other areas; therefore the direction and edge information are reflected better than the gradient representation.

The diffusion tensor $D = g \left(\sum_{k=1}^2 \sum_{l=1}^2 \nabla u_{k,l} \nabla u_{k,l}^T \right)$ which is a symmetric positive semi-definite 2×2 tensor can be written as $D = [w_1, w_2] \begin{bmatrix} \lambda_1 & 0 \\ 0 & \lambda_2 \end{bmatrix} \begin{bmatrix} w_1^T \\ w_2^T \end{bmatrix} = \begin{bmatrix} a & b \\ b & c \end{bmatrix}$. The local image orientations are given by the eigenvectors w_1 and w_2 . The average contrast in those directions is described by the eigenvalues $\lambda_1 \geq \lambda_2$. As we known, the Gaussian smoothing cannot adapt to the signal's change. To solve this problem, J.Weickert introduced a smoothing function $g(\cdot)$. In order to analyze easily, the diffusion tensor is rewritten to orthometric product:

$$D = V \text{diag}(g(\lambda_1), g(\lambda_2)) V^T = g(\lambda_1) w_1 w_1^T + g(\lambda_2) w_2 w_2^T, \quad (4)$$

where w_1 parallels to the gradient direction, while w_2 perpendiculars to the gradient direction. The anisotropic diffusion filtering can be achieved as long as $g(\lambda_1) \leq g(\lambda_2)$. Eigenvalues are given by:

$$\begin{cases} \lambda_1 = c_1 \\ \lambda_2 = \begin{cases} c_1 & \text{if } \mu_1 = \mu_2 \\ c_1 + (1 - c_1) \exp\left(-\frac{c_2}{(\mu_1 - \mu_2)^m}\right) & \text{else} \end{cases} \end{cases} . \quad (5)$$

The variable μ_1 and μ_2 are the eigenvalues of structure tensor J . λ_1 takes a smaller positive number to ensure the direction is perpendicular to the edge of the ridge with a small intensity. For λ_2 , it's increased with the increasing of $(\mu_1 - \mu_2)^m$. Therefore, there has a better enhancement effect along the edge of the ridge.

2.2 Diffusion Schemes

Model (1) is solved by the finite difference approximation. Here $\partial_t u = \nabla \cdot (D\nabla u)$ can be rewritten as:

$$u^{k+1} - u^k / \Delta t = \text{div}(D\nabla u^k) \Rightarrow u^{k+1} = u^k + \Delta t \text{div}(D\nabla u^k) , \quad (6)$$

where Δt is the iterative step, k denotes the iterations. Here $\text{div}(D\nabla u^k)$ is the discrete format of $\nabla \cdot (D\nabla u)$. Different discrete schemes are relative to the equation's stability and convergence, and affect whether the problem could be solved complexly or conveniently. Consequently, the final results of the iteration are affected by the discrete schemes. In the following, three different diffusion schemes are introduced including: the classically standard diffusion, J.Weickert's rotation invariant diffusion and D.Kroon's optimized diffusion.

(I) Standard Diffusion Scheme

The standard diffusion scheme belonging to explicit discrete is the easiest diffusion scheme which is easily affected by the iterations. In order to ensure the diffusion stability, only a small time step is allowed $\tau \leq 0.5/n$, with n the number of image dimensions. Discretized format is as follows [13]:

$$\begin{bmatrix} \frac{-b_{i-1,j} - b_{i,j+1}}{4} & \frac{c_{i,j+1} + c_{i,j}}{2} & \frac{b_{i+1,j} + b_{i,j+1}}{4} \\ \frac{a_{i-1,j} + a_{i,j}}{2} & \frac{a_{i-1,j} + 2a_{i,j} + a_{i+1,j}}{2} - \frac{c_{i,j-1} + 2c_{i,j} + c_{i,j+1}}{2} & \frac{a_{i+1,j} + a_{i,j}}{2} \\ \frac{b_{i-1,j} + b_{i,j-1}}{4} & \frac{c_{i,j-1} + c_{i,j}}{2} & \frac{-b_{i+1,j} - b_{i,j-1}}{4} \end{bmatrix} . \quad (7)$$

(II) Rotation Invariant Diffusion Scheme

J.Weickert showed that larger stencils than 3×3 in 2D are needed to fix the number of degrees of freedom of the kernel to allow rotation invariance, so he introduced a 5×5 stencil. The divergence operator equation $\text{div}(D\nabla u^k)$ in 2D can be written as:

$$\text{div}(D\nabla u) = \partial_x j_1 + \partial_y j_2 \quad (j_1 = a\partial_x u + b\partial_y u, j_2 = b\partial_x u + c\partial_y u) . \quad (8)$$

The image derivatives such as $\partial_x u$ are calculated by using the Sobel filter with values of Scharr, the same kernel is used to calculate the derivatives of the flux components.

(III) Optimized Diffusion Scheme

To solve the chessboard effect from the rotation invariant diffusion scheme, D.Kroon [4] proposed the optimized diffusion scheme which is as follows:

$$\begin{cases} \text{div}(D\nabla u) = \text{div}_1(D\nabla u) + \text{div}_2(D\nabla u) \\ \text{div}_1(D\nabla u) = (a * M_x + b * M_y) \cdot (u * M_x) + (b * M_x + c * M_y) \cdot (u * M_y) \\ \text{div}_2(D\nabla u) = au * M_{xx} + abu * M_{xy} + cu * M_{yy} \\ M_y = M_x^T, M_{yy} = M_{xx}^T \end{cases} . \quad (9)$$

The spatial kernels in 2D can be written as:

$$M_{xx} = \begin{bmatrix} p_1 & p_2 & p_3 & p_2 & p_1 \\ p_4 & p_5 & p_6 & p_5 & p_4 \\ -p_7 & -p_8 & -p_9 & -p_8 & -p_7 \\ p_4 & p_5 & p_6 & p_5 & p_4 \\ p_1 & p_2 & p_3 & p_2 & p_1 \end{bmatrix} M_{yy} = \begin{bmatrix} p_{10} & p_{11} & 0 & -p_{11} & -p_{10} \\ p_{11} & p_{12} & 0 & -p_{12} & -p_{11} \\ 0 & 0 & 0 & 0 & 0 \\ -p_{11} & -p_{12} & 0 & p_{12} & p_{11} \\ -p_{10} & -p_{11} & 0 & p_{11} & p_{10} \end{bmatrix} M_x = \begin{bmatrix} p_{13} & p_{14} & p_{13} \\ 0 & 0 & 0 \\ -p_{13} & -p_{14} & -p_{13} \end{bmatrix}$$

The kernel values $p = [p_1, \dots, p_{14}]$ can be found analytically or by numerical optimization. We choose numerical optimization, because it can optimize the whole process, while analytical derivation is only feasible for separate parts of the process, with simplifications such as ignoring numerical round of effects. The computed kernel values p [4] are:

$$0.008, 0.049, 0.032, 0.038, 0.111, 0.448, 0.081 \\ 0.334, 0.937, 0.001, 0.028, 0.194, 0.006, 0.948$$

2.3 Proposed Algorithm and Parameter Selection

Firstly, the original image is preprocessed by the Gaussian filter. Then, the image is enhanced with the method based on the structure tensor. The proposed algorithm consists of the following steps:

- (a) The original image I is input as the initial value of the iteration algorithm.
- (b) Set and initialize the diffusion time T .
- (c) Preprocess with Gaussian filter.
- (d) Calculate the structure tensor J , the eigenvalues and eigenvectors.
- (e) Calculate the diffusion tensor D .
- (f) Diffuse with three different schemes.
- (g) Judgment: if $t < T - 0.001$, then $t = t + \Delta t$, and then returns (c). Otherwise, the iteration will be ended, and then results will be output.

According to the literature [4] [11] [13], the standard deviation of the Gaussian filtering is $\rho = 1$. In the step of solving the diffusion tensor's eigenvalues, the parameters are $c_1 = 0.001$, $c_2 = e^{-10}$, $m = 1$, and the iteration's time step is $\Delta t = 0.2$. In this paper, 100 iterations were utilized to experiment.

3 Experiments and Results

In this section, the synthetic dataset and CT Lung images from LIDC were utilized to test the efficiency of our proposal method. Three different schemes were used, which including: the classically standard diffusion, J.Weickert's rotation invariant diffusion and D.Kroon's optimized diffusion. Two different ways were used to evaluate the

experimental results, the qualitatively and quantitatively. The quantitative evaluation indicator is SNR, and the corresponding definition is as follows:

$$SNR = 10 * \log_{10} \left(\frac{\sum_{i=0}^{m-1} \sum_{j=0}^{n-1} I^2(i, j)}{I(i, j) - K(i, j)^2} \right), \quad (12)$$

where I denotes the original image, K denotes the processed image, and $m \times n$ is the image size. The higher the SNR, the better the processed image.

3.1 Experiment of Synthetic Dataset

In this part, the size of the originally synthetic image we used is 673×583 . As shown in Fig.2, five objects were created to simulate different kinds of vessel structures, which resemble straight, varying diameter, curved, stenosed, and bifurcate vessels, respectively [14].

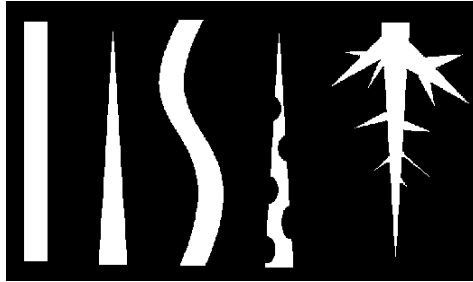


Fig. 2. The originally synthetic image

Different diffusion schemes were used to process these synthetic images. Results are shown in Fig.3~Fig.7.

As shown in Fig.3, (a) is the original image, (b)~(d) are the corresponding resultant images using standard diffusion scheme, rotation invariant diffusion scheme, and optimized diffusion scheme, respectively. The following figures (Fig.4~7) are arranged in the same way.

The qualitative analysis: The edges of straight blood vessels are blurred with the standard diffusion and have a better result with the optimized diffusion, showing in Fig.3. The varying diameter blood vessels can be changed uniformly with the optimized diffusion, showing in Fig.4. The edges of curved and stenosed blood vessels are smoothed with the rotation invariant diffusion and the optimized diffusion, but have no obvious effects with the standard diffusion, showing in Fig.5. For the bifurcations blood vessels, they are smoothed but blurred with the standard diffusion, while, they are smoothed well with the rotation invariant diffusion. But this diffusion cannot connect the small parted blood vessels. By contrast, the bifurcations blood vessels can be smoothed and connected meanwhile with the optimized diffusion. Overall, the optimized diffusion does best; the rotation invariant diffusion takes the second place and the standard diffusion works worst.

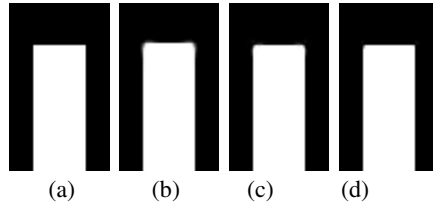


Fig. 3. Straight blood vessel

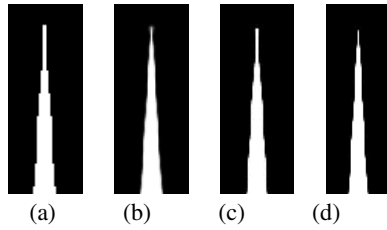


Fig. 4. Varying diameter blood vessel

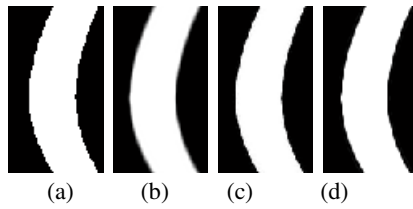


Fig. 5. Curved blood vessel

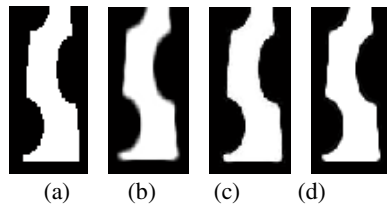


Fig. 6. Stenosed blood vessel

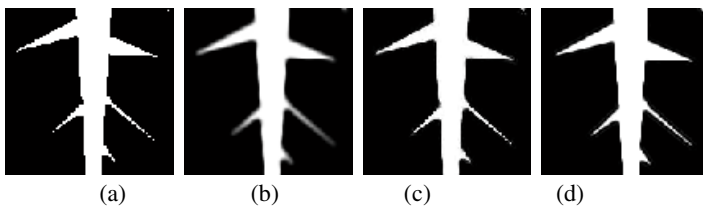


Fig. 7. Bifurcate blood vessel

3.2 Experiment of CT Lung Dataset

In this part, all test images were selected from Lung Image Database Consortium (LIDC) database.

As shown in Fig.8, according to the qualitative analysis, the image is smoothed with all the three diffusion methods. Besides structure of blood vessels are enhanced, some parted blood vessels are connected. And it is the optimized diffusion scheme enhances best. The described method to find the image structure orientations in this paper is comparable to the vesseness filter of Frangi *et al.* [15] Compared with the filter of Frangi, the method proposed in this paper has many advantages. Firstly, the diffusion filtering in this paper only uses one scale, while, Frangi uses a Gaussian scale space to find vessels of different sizes. Thus the method we described does not perform equally on lines of different widths and the calculation speed is improved. Secondly, the traditional Hessian filters are not good to preserve the junctions and local deformations. Thirdly, the described method has more advantages in enhancing both vascular branches and bifurcations. Fourthly, most details including local diameter variety and thin vessels are well preserved. Lastly, using the structure tensor to find the orientations is more robust against noise than the Hessian matrix used by Frangi [16].

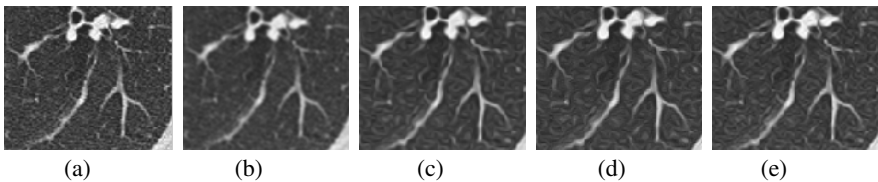


Fig. 8. The CT Lung dataset experiment result. (a) the original image; (b) the reprocessed image with Gaussian filter; (c) the standard diffusion scheme; (d) the rotation invariant diffusion scheme; (e) the optimized diffusion scheme.

As shown in Fig.9, according to the quantitative analysis, the images' SNR are increased with all the three diffusion methods in a short iteration. The rotation invariant diffusion's SNR is higher than the standard diffusion, but the optimized diffusion's SNR is the highest in these three diffusions. Thus the final result we can get is that the optimized diffusion does best, the rotation invariant diffusion takes the second place and the standard diffusion works last. The iterations should be controlled in an appropriate range; otherwise the image's SNR will be declined.

Besides the advantages we described above, the structure tensor based diffusion filtering always has the disadvantages. One obvious principle limitation of the structure tensors is that they cannot model complicated image structures, and therefore the multiple tensors are selected to describe the complex pulmonary vessel structures. Another limitation about this method is about the influence of iterations. The structure in the background will be over enhanced with the higher iterations. For different image structures, the iterations should be chosen different. Perhaps this described method has some other disadvantages we haven't discussed yet and the iterations' impact on background-image needs to be researched deeply in the future study.

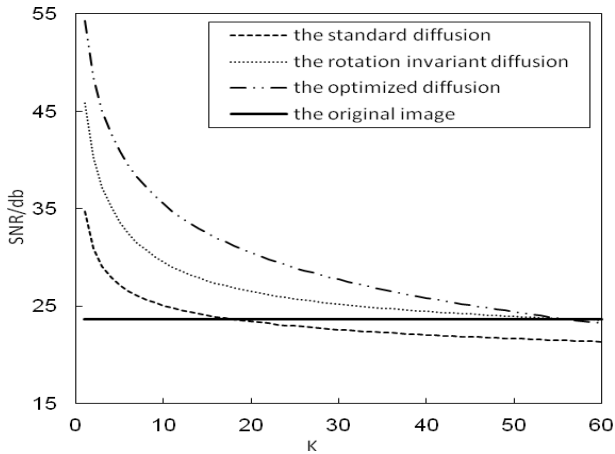


Fig. 9. Diagrams between the iterations of K and SNR

4 Conclusion

The paper proposes an effective enhancement method for CT pulmonary vessel by using the structure tensor. This method uses the structure tensor's eigenvectors to control the diffusion direction and the diffusion tensor's eigenvalues to control the direction's diffusion amount. In this paper, the synthetic dataset and CT Lung dataset from LIDC are utilized to test this method's efficiency by using three different schemes which including: the classically standard diffusion, J.Weickert's rotation invariant diffusion and D.Kroon's optimized diffusion. Experimental results are evaluated qualitatively and quantitatively. The results show that different schemes have different enhanced effects: the optimized diffusion does best, and then the rotation invariant diffusion; the standard diffusion works last. The pulmonary vessel is enhanced and the image's contrast and SNR are improved. Additionally, advantages and disadvantages of this described method are discussed. The advantages are the calculation speed and background noise are improved, the junctions and local deformations are preserved, both vascular branches and bifurcations are enhanced and most details including local diameter variety and thin vessels are well preserved. The disadvantages which require to be researched deeply in future are the description of the complex pulmonary vessel structures and the range's control of the iterations. Overall, the enhancement method based on structure tensor is suitable for CT pulmonary vessel.

Acknowledgement. The research was sponsored by the National Natural Science Foundation of China (60972122), the Innovation Fund Project For Graduate Student of Shanghai (JWCXSL1402) and the atural science Foundation of Shanghai(14ZR1427900).

References

1. Forstner, W., Gulch, E.: A fast operator for detection and precise location of distinct points, corners and centers of circular features. In: Proceedings of ISPRS Intercommission Workshop on Fast Processing of Photogrammetric Data, Interlaken, pp. 281–305 (1987)
2. Bigun, J., Granlund, G.H., Wilklund, J.: Multidimensional orientation estimation with applications to texture analysis and optic flow. *IEEE Trans. Pattern Analysis and Machine Intelligence* 13(8), 77–790 (1991)
3. Weickert, J., Romeny, B.M.T.H., Viergever, M.A.: Efficient and reliable schemes for nonlinear diffusion filtering. *IEEE Trans. Image Processing* 7(3), 398–410 (1998)
4. Kroon, D., Slump, C.H., Maal, T.J.J.: Optimized Anisotropic Rotational Invariant Diffusion Scheme on Cone-beam CT. *Med. Image Comput. Comput. Assist. Interv.* 13(3), 221–228 (2010)
5. Zheng, Y.H., Pan, Y., Wang, A.P., et al.: The Trace-Based Nonlinear Structure Tensor. *Journal of Computer-aided Design & Computer Graphics* 20(2), 259–266 (2008)
6. Zhong, Y., Wang, L.: Method of 3D seismic image enhancement based on structure tensor. *Computer Engineering and Design* 32(3), 1010–1013 (2011)
7. Wang, X.X., Li, L.G., Sun, W.: The Development of 3D Demonstration System Based on Web3D Engine. *Software Guide* 10(2), 152–154 (2011)
8. Liu, K., Su, B.Y., Zhao, X.J.: Image inpainting method based on structure tensor. *Journal of Computer Applications* 31(10), 2711–2713 (2011)
9. Lai, J., Xie, M.: Vascular segmentation for lung CT images based on fractional differential enhancement. *Journal of Computer Applications* 31(4), 1027–1113 (2011)
10. Chen, F., Li, J.Z., Li, D.D.: Applying Coherence Enhancing Diffusion to Seismic Image Sequences. *Chinese Journal of Computer* 27(7), 985–992 (2004)
11. Kroon, D., Slump, C.H.: Coherence Filtering to Enhance the Mandibular Canal in Cone-Beam CT Data. In: Annual Symposium of the IEEE-EMBS Benelux Chapter 2009, Enschede, The Netherlands, November 9–10, pp. 9–10 (2009)
12. Liu, Y.: Application of coherence-enhancing diffusion based on PDE in medical US image processing. D. Lanzhou Gansu, Lanzhou University, 1–53 (2009)
13. Welckert, J., Scharr, H.: A scheme for coherence-enhancing diffusion filtering with optimized rotation invariance. *Journal of Visual Communication and Image Representation* 13(2), 10–118 (2002)
14. Xiao, C.Y., Staring, M., Shamonin, D., et al.: A strain energy filter for 3D vessel enhancement with application to pulmonary CT images. *Medical Image Analysis* 15, 1–124 (2011)
15. Frangi, A., Frangi, R., Niessen, W., et al.: Multiscale vessel enhancement filtering. Springer Verlag, 130–137 (1998)
16. Good, W., Wang, X., Fuhrman, C.: Application of 3D geometric tensors for segmenting cylindrical tree structures from volumetric datasets. In: SPIE Conference Series, vol. 6512 (2007)

An Improved Orthogonal Matching Pursuit Algorithm for Signal Reconstruction in Wireless Body Sensor Network

Rui Jiang^{*}, Yongsheng Ding^{1,2,**}, Kuangrong Hao^{1,2}, and Shiyu Shu¹

¹ College of Information Sciences and Technology

² Engineering Research Center of Digitized Textile & Fashion Technology, Ministry of Education Donghua University, Shanghai 201620, P.R. China

ysding@dhu.edu.cn

Abstract. Energy efficiency is the primary challenge of wireless body sensor network (WBSN). Compressed sensing (CS) is a rapidly emerging signal processing technique that enables accurate capture and reconstruction of sparse signals from only a fraction of Nyquist Rate samples, significantly reducing the data-rate and system power consumption which solve the key issues in the WBSN. This paper proposes an improved CS-based Orthogonal Matching Pursuit (IOMP) algorithm in the WBAN. We evaluate the IOMP algorithm against the OMP algorithm from four aspects: compression ratio, percentage root-mean-square distortion, signal noise ratio and iterative times. Simulation results shows that, at the same compressed ratio, PRD SNR and iterative times of the proposed method are improved over those of the OMP algorithm.

Keywords: Wireless Body Sensor Network, Compressed Sensing, Orthogonal Matching Pursuit algorithm, Signal Reconstruction.

1 Introduction

In recent years, with the development of Wireless Sensor Network (WSN), Wireless Body Sensor Network (WBSN) has gained more and more attention by healthcare industry. The WBSN can be widely used in medical diagnosis, health restoration, etc. The WBSN is a small sensor network composed of some biosensors worn by a person or implanted in human body. These biosensors take charge of collecting, processing,

* This work was supported in part by the Key Project of the National Nature Science Foundation of China (No. 61134009), Program for Changjiang Scholars and Innovation Research Team in University from the Ministry of Education (No. IRT1220), Specialized Research Fund for Shanghai Leading Talents, Project of the Shanghai Committee of Science and Technology (Nos. 13JC1407500, 11JC1400200), Innovation Program of Shanghai Municipal Education Commission (No. 14ZZ067), and the Fundamental Research Funds for the Central Universities (No. 2232012A3-04).

** Corresponding author.

and transmitting vital biomedical signals, such as: blood pressure, electrocardiogram (ECG), body temperature, electroencephalography (EEG), blood oxygenation. In the WBSN, nodes are expected to perform energy-efficient and long-term acquisition of biomedical signals. Long-term real time monitoring will produce a huge amount of data consumed large energy while nodes transmitting the real time data. Energy consumption, computational costs and compression of biomedical signals are the three main constrains. It is very difficult to perform continuous monitoring or acquisition at a WBSN node. Therefore, finding a compression algorithm that could compress the acquired biomedical information at the biosensor nodes while still containing the relevant features of raw data is an important challenge.

Currently, more and more researches have been taken into account to reduce the energy consumption of the WBSN. A wireless autonomous spanning tree protocol for multi-hop body sensor network was proposed [1]. And a low power medium access control protocol for body-coupled communication networks was discussed [2]. Pennsylvania State University [3] applied Ultra-Wide-Band (UWB) technology to design the low-power transmitter for WBSN. The Chinese University of Hong Kong build hybrid body sensor network based on structure-based collaborative communication mechanism and carried out relevant research on Power Aware Medium Access Control for mobile WBSN. The Institute of Computing Technology, Chinese Academy of Science (ICT) used data fusion technology to build a new type of WBSN platform. Their methods reduce the energy consumption of transmitting procedure in the WBSN, but have not solved the issue from source side. As such, a new research idea for the WBSN proposed by Candes and Donoho, compressed sensing technology is as a new signal acquisition and encoding and decoding theory [4-5].

Compressed sensing theory suggests that a small number of random linear measurements from compressible or sparse signal contain enough information [6]. We can reconstruct the original signal from these measurements. Basically, many physiological signals such as ECG, EEG, blood pressure signals are sparse and compressible, can be reconstructed from bits of Gaussian random measurements by solving the norm optimization [7].

Greedy search algorithm had been proposed to solve the minimum l_1 norm optimization problem. OMP [8] is an iterative greedy search algorithm for sparse signal recovery. Needell et al. present a Regularized Orthogonal Matching Pursuit (ROMP) which can accurately reconstruct the sparse signal [9]. Donoho et al. propose Stagewise Orthogonal Matching Pursuit (StOMP) algorithm, which divides the iterative process into several stages [10]. These algorithms have a poor performance and require knowing the signal's sparsity. To reduce these disadvantages, we propose an improved Orthogonal Matching Pursuit (IOMP) algorithm in this paper. Simulation results show that the sample rate can be reduced to 30% of Nyquist Rate and reconstruction performance is better than OMP algorithm.

This paper is organized as follows. Section 2 briefly introduces the compressed sensing theory. Section 3 presents the IOMP algorithm. Section 4 gives the simulation results. Finally, conclusion is drawn in Section 5.

2 Compressed Sensing Theory

Suppose a signal $f(f \in R^N)$, the length is N , the sparse basis is $\psi_i(i = 1, 2, \dots, N)$, define $\Psi = [\psi_1 | \psi_2 | \dots | \psi_N]$, we can represent the signal f as follows:

$$f = \sum_{i=1}^N a_i \psi_i \text{ or } f = \Psi \alpha \tag{1}$$

where α is the $N \times 1$ vectors which contain N coefficients a_i . If the coefficients in equation (1) only have K ($N \gg K$) non-zero values and decay exponentially and approximate zero after sorting, the signal is called K -sparse in Ψ domain [4]. Useful information of sparse signal mainly focus on K dimension vectors instead of N dimension vectors, so when a biosensor is collecting data, it could acquire only K data from raw data. The acquisition is done by applying the measurement matrix to the original signal f , the model can be written as follows:

$$y = \Phi f = \Phi \Psi \alpha = \Theta \alpha \tag{2}$$

where y is the compressed data with M measurements, Φ is $M \times N$ measurement matrix with $M \ll N$, $\Theta = [\varphi_1 | \varphi_2 | \dots | \varphi_N]$ is called $M \times N$ sensing matrix with $M \ll N$. The measurement process is non-adaptive, because the measurement matrix does not depend on the original signal. It's very important to design a stable measurement matrix which ensures the salient information in the original signal is not damaged when the sparse signal is projected from the high-dimensional space onto low-dimensional space. Equation (2) is known as a Non-deterministic Polynomial (NP) hard problem, and has no definite solution. We could not recover the signal directly. However, the signal is K -sparse, if the sensing matrix Θ obeys Restricted Isometry Property (RIP), i.e., the sensing matrix satisfies:

$$1 - \delta_k \leq \frac{\|\Theta f\|_2^2}{\|f\|_2^2} \leq 1 + \delta_k \tag{3}$$

for all K -sparse vectors f , where δ_k is a constant with $\delta_k \in (0, 1)$, the coefficient K can be accurately reconstructed from the measurements y . When the measurement matrix Φ and the orthogonal basis Ψ are irrelevant, the sensing matrix Θ will satisfy RIP property. We could transfer the NP-hard problem to the following minimum l_1 norm optimization problem:

$$\min_{\alpha} \|\alpha\|_{l_1} \text{ s.t. } y = \Phi \Psi \alpha \tag{4}$$

When the compressed sensing theory is applied in the WBSN, signals are compressed on biosensors according to equation $y = \Phi f$, this stage consumes the chip energy of the WBSN. Signals are reconstructed on the remote healthcare center according to equation $y = \Theta \alpha$, this stage does not consume any energy of the WBSN.

3 An Improved Algorithm for Signal Reconstruction

3.1 Sparse Representation and Measurement of Signal

Because the precondition of compressed sensing theory is that the signal is sparse or compressible on some basis. If the signal only has K non-zero coefficients when projected onto orthogonal basis, it is a strictly sparse case. However, in most cases biomedical signals do not strictly satisfy sparse property. Thus only the appropriate orthogonal basis can ensure the accuracy of the signal recovery.

The original physiological signal is compressed through a linear projection according to equation (2). Whether the small amount of non-coherent projection contains enough information to reconstruct the original signal, it depends on measurement matrix that satisfies the RIP property. Currently, typical measurement matrixes which satisfy RIP property are Gaussian random matrix and Bernoulli random matrix.

a) Gaussian random matrix

$$G \in R^{M \times N} : G(i, j) = \frac{1}{\sqrt{M}} g_{ij}, g_{ij} \sim N(0,1) \quad (5)$$

where G is called Gaussian random matrix which comprises random independent and identically distributed (i.i.d.) entries. This is a strongly random measurement matrix, and has been validated to satisfy the RIP property [11]. Gaussian random matrix is irrelevant to most of the orthogonal sparse matrixes; therefore it can be used as the most common measurement matrix. When the signal is compressible with the length N and the sparsity K , the Gaussian random measurement matrix requires only $M \geq cK \log(N/K)$ measurements to accurately reconstruct the original signal, where c is a small constant.

b) Bernoulli random matrix

$$B \in R^{M \times N} : B(i, j) = \frac{1}{\sqrt{M}} b_{ij}, b_{ij} \sim \begin{bmatrix} 1 & -1 \\ 0.5 & 0.5 \end{bmatrix} \quad (6)$$

Bernoulli random measurement matrix is also a strongly random matrix [11].

3.2 An Improved Orthogonal Matching Pursuit algorithm

The OMP is an iterative greedy algorithm that selects at each step the dictionary element best correlated with the residual part of the signal. Then it produces a new approximant by projecting the signal onto the dictionary elements that have already been selected [8]. This ensures that the residual is orthogonal to the atoms that have already been chosen after iterations, so the algorithm converges faster.

However, this method also has following shortcomings. Firstly, we seek support atom mainly based on the maximum absolute inner product between atoms of sensing matrix and the residual. This method cannot guarantee the residual is decreasing at each step. To solve this problem, we propose a better method for atomic updates:

When selecting support atom, we should not only consider the maximum absolute inner product between atoms of sensing matrix and the residual, but also the previous inner product, which can be expressed as:

$$\zeta_t = \Theta^T r_{t-1} + \mu \zeta_{t-1} \tag{7}$$

where ζ is the new defined coherence parameter matrix, μ is weight coefficient, t represents the t -th iteration.

Secondly, OMP algorithm requires the receiver to know the sparsity of the original signal, which is hard to be achieved in the WBAN. For this problem, we propose a method that does not require knowing the sparsity of the original signal when we recover the original signal. The proposed IOMP algorithm is as follows:

Input: Sensing matrix Θ with $M \times N$ vectors, measurements y , error threshold e .

Output: The approximant \hat{f} of the original signal f .

Initialization: Initialize $t=1$ and set the initial residual $r_0 = y$, initial index set $\wedge_0 = \emptyset$, initial correlation $\zeta_0 = \emptyset$, and initial supporting matrix $S_0 = \emptyset$.

Main Iteration: Increase t by 1 and do the following steps:

Step1: Computing new defined correlation:

$$\zeta_t = \langle r_{t-1}, \varphi_j \rangle + \mu \zeta_{t-1} \tag{8}$$

where $\langle r_{t-1}, \varphi_j \rangle$ is the absolute inner product between atoms of sensing matrix and

the residual, μ is weight coefficient, $\mu = \frac{\|\langle r_{t-1}, \varphi_j \rangle\|}{\|\zeta_{t-1}\|}$, if $\mu > 1$, then $\mu = |\mu - 1|$.

Step 2: Find the subscript of matrix ζ_t of the maximum atom, namely:

$$\lambda_t = \arg \max_{j=1 \dots N} (\zeta_t) \tag{9}$$

Step 3: Update the index set $\wedge_t = \wedge_{t-1} \cup \{\lambda_t\}$ and the supporting matrix $S_t = [S_{t-1}, \varphi_{\lambda_t}]$.

Step 4: Use the least-squares minimization to get the approximate sparse coefficients $\hat{\alpha}$, update the residual $r_t = y - \Theta_t \hat{\alpha}$ and compute the relative

improvement of the residual $\left\| \frac{r_t - r_{t-1}}{r_{t-1}} \right\|_2$.

Step 5: If $\left\| \frac{r_t - r_{t-1}}{r_{t-1}} \right\|_2 < e$, stop, the approximant $\hat{f} = \Psi \hat{\alpha}$; Otherwise, do another iteration.

4 Simulation Results

To demonstrate the effectiveness of this method, we use blood pressure signal as the test signal f . The sparse matrix Ψ should be known at the receiver, if the signal f

is sparser in the Ψ domain than others, the reconstruction result will be much closer to the original signal. Therefore, the choice of sparse matrix Ψ affects the reconstruction and PRD significantly. In our simulation, we choose Fast Fourier Transform (FFT) orthonormal basis as the sparse basis Ψ , the sparse coefficients in FFT domain is shown in Fig. 2. We choose the Gaussian random matrix as the measurement matrix Φ . FFT orthonormal basis and Gaussian matrix satisfy RIP condition. Assuming the length of original signal in the WBAN is $L=512$, the number of row vectors in measurement matrix (i.e., the length of the transmission signal) is M . The performance of the IOMP algorithm is measured in terms of Compression Ratio (CR), Percentage Root-mean-square Distortion (PRD), Signal Noise Ratio (SNR) and Iterative times, CR, SNR and PRD can be drawn as follows:

$$CR = \frac{L-M}{L} \times 100 \quad (10)$$

$$SNR = -20 \log_{10}(0.01PRD) \quad (11)$$

$$PRD = \frac{\|x_{orig} - x_{rec}\|}{\|x_{orig}\|} \times 100 \quad (12)$$

where x_{orig} denotes the original signal and x_{rec} denotes the reconstructed signal.

Fig. 1 shows the sparse coefficients in FFT orthonormal basis domain, it is clear that the signal in FFT domain is sparse, and has only about 20 non-zero coefficients, which is much less than the length of the original signal, so we consider the blood pressure's useful information is concentrated in these 20 data. When the biosensor is acquiring, we only need to collect 20 data. This satisfies the premise of the compressed sensing theory, so we can reconstruct the original signal from a small number of these measurements.

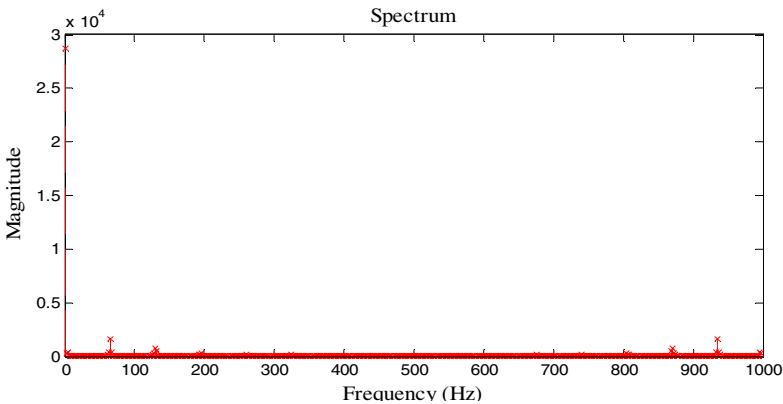


Fig. 1. The sparse coefficient in FFT orthonormal basis domain

As shown in Fig. 2 and Fig. 3, the proposed IOMP algorithm performs better than the OMP in both PRD and SNR. From the figures, we can see that as the number of measurements increasing, the value of PRD is decreasing and SNR is increasing.

When CR equals to 70, the original signal can be accurately reconstructed, that is to say, the biosensor in the WBAN only needs to transmit one third of the original data, thus the biosensor’s power consumption can be reduced to 30 percentage of original power consumption by applying CS theory.

Fig. 4 illustrates the comparison of iterative times for the OMP and the IOMP. Iterative times in the OMP is a constant, but in the IOMP, iterative times varies with CR, as the value of CR increasing, the iterative times is decreasing. Apparently, the IOMP is superior to the OMP.

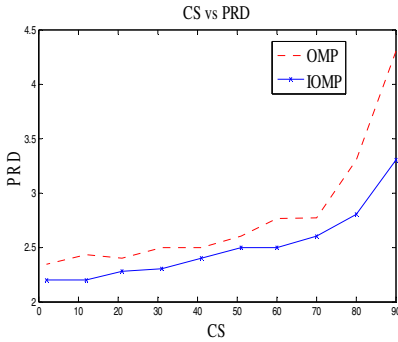


Fig. 2. PRD vs. CS for OMP and IOMP

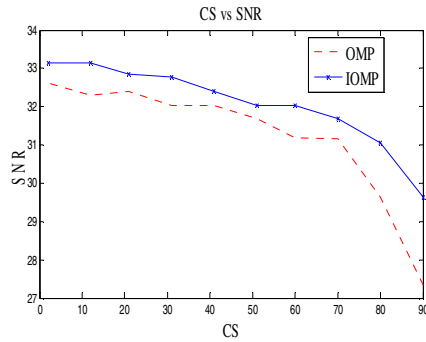


Fig. 3. SNR vs. CS for OMP and IOMP

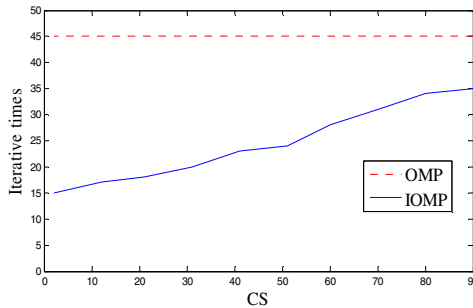


Fig. 4. Iterative times vs. CS for OMP and IOMP

5 Conclusions

This paper proposed an improved CS-based reconstruction algorithm in the WBAN. We evaluated this algorithm against the OMP from four aspects: compression ratio, percentage root-mean-square distortion, signal noise ratio and iterative times. Simulation results shows that, at the same compressed ratio, PRD SNR and iterative times of our proposed method are improved over those of the OMP algorithm.

However, despite the improved performance in terms of compressed ratio and PRD, the algorithm cannot process multi-dimensional signals. In the future, we will

concentrate on multi-dimensional signal reconstruction algorithms based on CS theory. We try to establish low power consumption systems for long-term real-time monitoring.

References

1. Braem, B., Latré, B., Moerman, I., et al.: The wireless autonomous spanning tree protocol for multihop wireless body area networks. In: 2006 Third Annual International Conference on Mobile and Ubiquitous Systems: Networking & Services, pp. 1–8. IEEE (2006)
2. Corroy, S., Baldus, H.: Low power medium access control for body-coupled communication networks. In: 6th International Symposium on Wireless Communication Systems, ISWCS 2009, pp. 398–402. IEEE (2009)
3. Ryckaert, J., Desset, C., Fort, A., et al.: Ultra-Wide-Band Transmitter for Low-Power Wireless Body Area Networks: Design and Evaluation. *IEEE Transactions on Circuits and Systems I: Regular Papers* 52(12), 2515–2525 (2005)
4. Donoho, D.: Compressed Sensing. *IEEE Transactions on Information Theory* 52(4), 1289–1306 (2006)
5. Balouchestani, M., Raahemifar, K., Krishnan, S.: Increasing the reliability of wireless sensor network with a new testing approach based on compressed sensing theory. In: 2011 Eighth International Conference on Wireless and Optical Communications Networks (WOCN), pp. 1–4. IEEE (2011)
6. Aeron, S., Saligrama, V., Zhao, M.Q.: Information Theoretic Bounds for Compressed Sensing. *IEEE Transactions on Information Theory* 56(10), 5111–5130 (2010)
7. Balouchestani, M., Raahemifar, K., Krishnan, S.: New Testing Method in Wireless Sensor Networks with Compressed Sensing Theory. In: 2011 International Conference on Computer Communication and Management (ICCCM 2011), vol. 5, pp. 1–6. IACSIT Press, Sydney (2011)
8. Tropp, J.: Greed is good: Algorithmic results for sparse approximation. *IEEE Transactions on Information Theory* 50(10), 2231–2242 (2004)
9. Needell, D., Vershynin, R.: Uniform uncertainty principle and signal recovery via regularized orthogonal matching pursuit. *Foundations of Computational Mathematics* 9(3), 317–334 (2009)
10. Donoho, D.L., Tsai, Y., Drori, I., Starck, J.L.: Sparse solution of underdetermined Linear equations by stagewise orthogonal matching pursuit (StOMP). *IEEE Transactions on Information Theory* 58(2), 1094–1121 (2012)
11. Baraniuk, R.: A lecture on compressive sensing. *IEEE Signal Processing Magazine* 24(4), 118–121 (2007)

Calibration Method of Stereo Microscope Based on Depth Correction

Yigang Wang^{1,2}, Gangyi Jiang^{1,*}, Mei Yu¹, and Shengli Fan^{1,2}

¹ Faculty of Information Science and Engineering, Ningbo University,
No.818, Fenghua Road, 315201 Ningbo, China

² Department of Information, Ningbo Institute of Technology, Zhejiang University,
No.1, Qianhu South Road, 315010 Ningbo, China
{wyg,victorfsl}@nit.zju.edu.cn, {jianggangyi,meiyu2}@126.com

Abstract. The use of stereo microscopes is on the rise in many biotechnology fields, but there are certain issues that are unique to binocular stereo microscopes, such as required calibrations, because a microscope's depth of focus is so small. In this paper, a new method that combines 2-D calibration and depth information is proposed to calibrate the binocular stereo microscope. First, based on the parameter estimate of a CCD or CMOS sensor, a calibration board is employed to acquire intrinsic and extrinsic parameters of the camera. Then, with images collected at different Z coordinates, the intrinsic and extrinsic parameters calibrated earlier are used to obtain the spatial coordinates of the calibration board by 2D reconstruction. Finally, a computed Z coordinate is compared with the actual Z coordinate in order to acquire the linear correction coefficient between the two and, thus, finish the final calibration. The experimental results show that the proposed method is both simple and practical, and the WCS (World Coordinate System) position recovered from the acquired calibration coefficient has an error of 0.0034mm along the X and Y axes and an error within 4.5% along the Z axis.

Keywords: Depth correction, calibration, stereo reconstruction, stereo microscope.

1 Introduction

Nowadays, binocular stereo microscopes have been widely used in more and more fields such as micromanipulator control, precision depth calculation and quality control. For example, stereo microscopes are indispensable for seed puncture injection control in agriculture, PCB quality control in industry and detection of cell phone camera module plastic parts [1-3]. Moreover, binocular stereo microscopes are employed in a variety of different fields, and the calibration of these microscopes is the first step in achieving the aforementioned objectives. With accurate calibration

* Corresponding author.

parameters, along with stereo matching and reconstruction, the accurate world coordinate of observed objects can be acquired. With an accurate world coordinate, it is possible to fulfill functions, such as stereo positioning, detection, measurement, and identification.

As for stereo camera calibration, the two monocular cameras are calibrated first, followed by the binocular cameras; this yields the relative position of the cameras. The monocular calibrations include those that are based on 1D, 2D, 3D, and other calibration objects. Based on 3D object shooting, Heikkilä et al presented a 4-step monocular calibration method [4]. Generally speaking, in 3D calibration, a certain, precise 3D object is needed; however, Wong et al presented a more flexible 3D calibration method, in which the camera was calibrated by utilizing the symmetry of everyday objects [5]. In addition, Ammi et al presented a calibration method based on virtual 3D objects for microscope calibration [6]. Recently, Li et al conducted an error analysis on the results of 3D calibration [7]. As for 2D calibration, however, Zhang presented a method using a checkerboard pattern to complete camera calibration, in which the depth is calibrated by making use of the changes of a checkerboard pattern in spatial position. This method macroscopically achieved great results [8]. Being aware in advance of relevant information of CCD or CMOS sensors (hereafter called imaging sensors), Tsai completed the calibration of intrinsic and extrinsic parameters of cameras through 2D imaging. Moreover, Han et al, on the condition of no calibration parameters, realized 3D re-construction of a final scene by capturing multiple 2D images [10]. Furthermore, in view of different calibration methods, Carlos et al presented a technique that used the optimal calibration condition to complete calibration when using 2D objects [11]. Based on the success of 2D calibration, Zhang again presented a method to complete calibration by one-dimensional objects, making object selection more open in addition to making experiments more convenient [12].

The most frequently used calibration methods from among those previously mentioned are those of Tsai and Zhang. In the microscope calibration field, however, new problems have arisen due to the existence of depth of field. If the calibration based on 3D objects were to be adopted, it would be necessary to prepare highly accurate 3D calibration objects. In effect, there would be a need to prepare a 3D lattice with center-to-center spacing of 0.01mm-0.1mm, which is more difficult to make and much more expensive than buying a stereo microscope. The calibration method based on 2D calibration objects or on one-dimensional calibration objects requires them to be placed at different positions. However, the microscopic depth of field is quite small, so a larger angle will render it nearly impossible to see the calibration objects in their entirety with any clarity, thus causing the calibration to fail. Similarly, self-calibration is impossible for stereo microscopes.

In analysis, the parameters that make accurate calibration impossible are primarily related to the actual depth in the limited depth of field. Therefore, this paper suggests a calibration method of binocular stereo microscopes based on depth correction. First, the binocular stereo microscope is calibrated for 2D calibration, with a predicted value given and in combination with actual camera information, to the depth parameter. Next in stereo reconstruction, the obtained depth information is compared with the actual information in order to produce a proportional relation. Experimental

results reveal that the method has, in reconstruction, an error of approximately 3.4% along the XY axis and approximately 4.5% along the Z axis.

2 Calibration Method of Stereo Microscope Based on Depth Correction

2.1 General Steps

Shown in Fig. 1 is a block diagram that details the depth correction-based calibration method of stereo microscopes that is introduced in this paper.

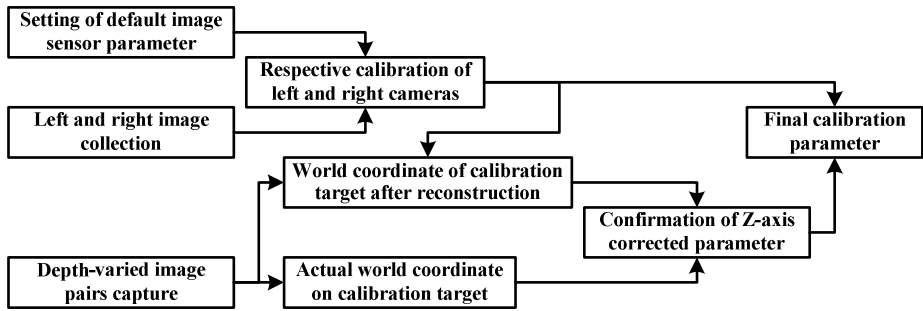


Fig. 1. Block diagram of algorithm of depth correction-based stereo microscope calibration method

First, the initial calibration of the left and right cameras uses a 2D calibration board to complete their calibration based on a default imaging sensor pixel pitch. Depth-varied image capture is used to gather image pairs of the calibration board at different Z coordinates within the range of depth of field and to complete the stereo reconstruction of the calibration board in combination with both the camera parameters and the image pairs acquired in the above steps. To confirm the correct parameters, compare the Z axis coordinate obtained from the reconstruction to the actual Z axis coordinate.

2.2 Monocular Camera Calibration

The observed object appears on a digital camera through a microscope’s objective lens; its underlying principle is similar to pinhole imaging, as shown below in Fig. 2. (x_w, y_w, z_w) is the 3D coordinate of point P in a world coordinate system. (x, y, z) is the coordinate of point P in a camera coordinate. The camera imaging plane, XO_1Y , is perpendicular to the optical axis OO_1 , and the OO_1 distance is the focal length f . (X_u, Y_u) is the ideal projection coordinate of point P on the camera imaging plane according to the pinhole imaging theory. (X_d, Y_d) is the actual projection coordinate on the camera imaging plane when factors like lens distortion are taken

into account. (X_i, Y_i) is the coordinate of (X_d, Y_d) in an image. Of the coordinates above, (x_w, y_w, z_w) , (x, y, z) , (X_u, Y_u) , and (X_d, Y_d) are usually given in millimeters, and (X_i, Y_i) is given in pixels. Imaging observed objects in a camera is essentially a process of turning (x_w, y_w, z_w) into (X_i, Y_i) .

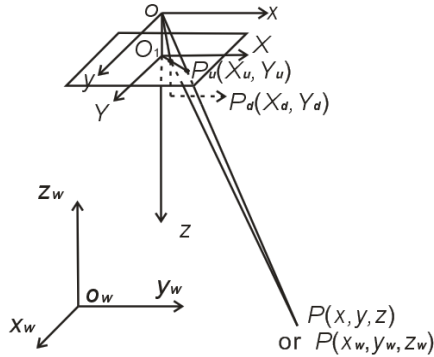


Fig. 2. Schematic diagram of digital camera imaging geometric model [9]

The followed formula 1 presents the relationship between the world coordinate, (x_w, y_w, z_w) and the pixel coordinate, (X_i, Y_i) .

$$z \begin{pmatrix} X_i \\ Y_i \\ 1 \end{pmatrix} = \begin{pmatrix} \frac{1}{d_x} & 0 & C_x \\ 0 & \frac{1}{d_y} & C_y \\ 0 & 0 & 1 \end{pmatrix} \begin{pmatrix} f & 0 & 0 & 0 \\ 0 & f & 0 & 0 \\ 0 & 0 & 1 & 0 \end{pmatrix} \begin{pmatrix} \mathbf{R} & \mathbf{T} \\ \mathbf{0}^T & 1 \end{pmatrix} \begin{pmatrix} x_w \\ y_w \\ z_w \\ 1 \end{pmatrix} = \mathbf{M}_1 \mathbf{M}_2 \begin{pmatrix} x_w \\ y_w \\ z_w \\ 1 \end{pmatrix} = \mathbf{M} \begin{pmatrix} x_w \\ y_w \\ z_w \\ 1 \end{pmatrix} \quad (1)$$

where, $\mathbf{R} = \begin{pmatrix} r_1 & r_2 & r_3 \\ r_4 & r_5 & r_6 \\ r_7 & r_8 & r_9 \end{pmatrix}$, $\mathbf{T} = \begin{pmatrix} T_x \\ T_y \\ T_z \end{pmatrix}$, d_x is the center-to-center distance of two

horizontal photo-sensitive cells of the camera's CCD or CMOS sensor. d_y is the center-to-center distance of two vertical photo-sensitive cells of the camera's CCD or CMOS sensor, and s_x is the uncertainty image scale factor. The formula above gives no consideration to distortion. In the formula, the \mathbf{M}_1 matrix is called the intrinsic matrix, \mathbf{M}_2 is the extrinsic matrix, and z is the Z axis coordinate of the camera coordinate system to which point P corresponds. The reason for the calibration is to determine the \mathbf{M} matrix. The parameters to be defined by calibration are \mathbf{R} , \mathbf{T} , f , s_x , and κ_1 [9].

2.3 Stereo Reconstruction

The process of reconstructing an object's prototype in a world coordinate system according to the left-right images captured by a digital microscope is known as stereo reconstruction. As shown in Fig. 3, point P in the world coordinate system forms an image p_L in the left-path graph; similarly, it forms an image p_R in the right. According to the principle of pinhole imaging, point P is also located at the connecting line of the left-path optical center O_L and its imaging point p_L in the left path. Likewise, point P is also situated at the connecting line of the right-path optical center O_R and its imaging point p_R in the right path. By learning the two straight line equations, P 's coordinate in the world coordinate system can be solved.

From the above formula, it follows:

$$z_{cL} \begin{pmatrix} X_{iL} \\ Y_{iL} \\ 1 \end{pmatrix} = \mathbf{M}_L \begin{pmatrix} x_w \\ y_w \\ z_w \\ 1 \end{pmatrix} = \begin{pmatrix} m_{11}^L & m_{12}^L & m_{13}^L & m_{14}^L \\ m_{21}^L & m_{22}^L & m_{23}^L & m_{24}^L \\ m_{31}^L & m_{32}^L & m_{33}^L & m_{34}^L \end{pmatrix} \begin{pmatrix} x_w \\ y_w \\ z_w \\ 1 \end{pmatrix} \quad (2)$$

$$z_{cR} \begin{pmatrix} X_{iR} \\ Y_{iR} \\ 1 \end{pmatrix} = \mathbf{M}_R \begin{pmatrix} x_w \\ y_w \\ z_w \\ 1 \end{pmatrix} = \begin{pmatrix} m_{11}^R & m_{12}^R & m_{13}^R & m_{14}^R \\ m_{21}^R & m_{22}^R & m_{23}^R & m_{24}^R \\ m_{31}^R & m_{32}^R & m_{33}^R & m_{34}^R \end{pmatrix} \begin{pmatrix} x_w \\ y_w \\ z_w \\ 1 \end{pmatrix} \quad (3)$$

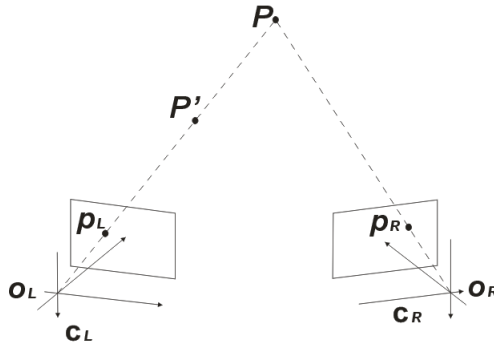


Fig. 3. Schematic diagram of stereo reconstruction

By arrangement, it follows the $O_L p_L$ equation (formula 4) and the $O_R p_R$ equation (formula 5). Solving the equations produces P 's coordinate in the world coordination system.

$$\begin{cases} (X_{iL}m_{31}^L - m_{11}^L)x_w + (X_{iL}m_{32}^L - m_{12}^L)y_w + (X_{iL}m_{33}^L - m_{13}^L)z_w = m_{14}^L - X_{iL}m_{34}^L \\ (Y_{iL}m_{31}^L - m_{21}^L)x_w + (Y_{iL}m_{32}^L - m_{22}^L)y_w + (Y_{iL}m_{33}^L - m_{23}^L)z_w = m_{24}^L - Y_{iL}m_{34}^L \end{cases} \quad (4)$$

$$\begin{cases} (X_{iR}m_{31}^R - m_{11}^R)x_w + (X_{iR}m_{32}^R - m_{12}^R)y_w + (X_{iR}m_{33}^R - m_{13}^R)z_w = m_{14}^R - X_{iR}m_{34}^R \\ (Y_{iR}m_{31}^R - m_{21}^R)x_w + (Y_{iR}m_{32}^R - m_{22}^R)y_w + (Y_{iR}m_{33}^R - m_{23}^R)z_w = m_{24}^R - Y_{iR}m_{34}^R \end{cases} \quad (5)$$

2.4 Correction of Depth Information

By directly making use of the method described in 2.1 for microscope calibration, even if there is an accurate parameter of sensor pixel pitch, the obtained result is only the accurate plane calibration data; however, the accurate depth recovery information cannot be calculated. Therefore, depth information can only be estimated, and thus, compared to reality, there are many errors. The solving processes involve linear equations. The depth recovery information obtained by the above method has a linear relationship with the actual depth, and the actual depth is acquired by motor motion. The following equation represents the relationship between the estimated depth and actual depth:

$$\begin{cases} \dots \\ Z'_{w1} = kZ_{w1} \\ Z'_{w2} = kZ_{w2} \\ Z'_{w3} = kZ_{w3} \\ \dots \end{cases} \quad (6)$$

where, k is the correction factor that is related to the uncorrected Z axis recovery coordinate, Z'_{wi} and the actual Z axis coordinate Z_{wi} .

Thus, we formulate a linear correction for the depth acquired by the steps listed above:

$$Z'_w = kZ_w \quad (7)$$

3 Experimental Results and Analysis

3.1 Experimental Platform, Calibration Board, and Experimental Procedure

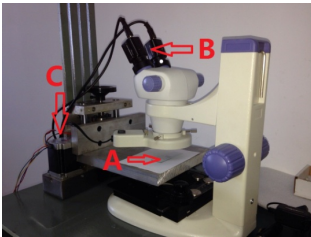
The experimental platform adopts the ZOOM460N stereo microscope manufactured by the Nanjing Wavelength Optics Co., Ltd. As shown in Fig. 4 (a), A is a calibration board under the microscope, B is two separate cameras for the two paths, and C is a

stepping motor which controls the platform where the calibration board moves up and down. First, an object passes under a large objective lens and then passes through two independent optical paths in order to form an image on their own camera to realize the stereoscopic effect. The camera is a Japanese Watec 902B, which is directly placed through an interface on the position of the observation eyepiece. By USB sampling, images of 704*576 per frame are acquired. The calibration target uses a 10mm*10mm calibration board, with the length and width divided into 100 equal squares (0.1mm*0.1mm in size), as shown in Fig. 4 (b), where the right squares are the calibration board.

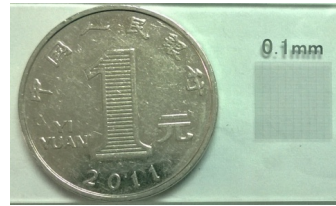
The motor goes 200 steps in a circle. The diameter ratio of the belt wheel connecting the motor and a ball screw is 1:2. Additionally, the screw pitch of the ball screw is 5mm. Thus, as the motor goes 5 steps, the platform's lifting height is 0.0625mm.

Upon placing the calibration board on the platform, a position is marked as the initial position, with a height of zero. That is, the Z axis measure is 0. Then, with 5 steps as a unit, walk 3 times clockwise to shoot 3 pairs of picture for both the left and right paths, and walk 3 times counterclockwise to shoot another 3 pairs of pictures. Finally, there are a total of 7 pairs of a picture, plus the initial position.

The 7 pairs of a picture correspond to a point's coordinates on the calibration board in the world coordinate system. The XY axis data are the same, and the difference is in the Z axis data. The gap of adjacent pairs is the difference of height, resulting from the 5 steps traveled by the stepping motor, which should be 0.0625 as calculated above.



(a)



(b)

Fig. 4. Stereo microscope and calibration board. (a) is a microscope used in this paper, and (b) is a calibration board.

3.2 Results and Analysis of Left-Right Monocular Calibration

The WATEC 902B camera's CCD is a half inch in size. The diagonal line of the actual light-sensing surface area is approximately 10mm long, and the sampled image is 704 pixels wide and 576 pixels high. Thus, the center-to-center distance of the horizontal and vertical photo-sensitive cells is about 0.011mm.

The left-path and right-path pictures shot under 0.7 magnitude by a stereo microscope are shown in Fig.5.

Upon selecting 100 corner points from both the left and right paths, the calibration results are as follows:

$$\mathbf{R}_L = \begin{pmatrix} -0.906942 & -0.114185 & -0.405485 \\ 0.121208 & -0.992591 & 0.008411 \\ -0.403442 & -0.041520 & 0.914063 \end{pmatrix}, \mathbf{T}_L = \begin{pmatrix} 8.954461 \\ 7.629249 \\ 226.445652 \end{pmatrix}$$

$$f_L = 422.202115, \kappa_L = -0.00003803818 \text{ } \circ$$

$$\mathbf{R}_R = \begin{pmatrix} -0.905128 & -0.080341 & -0.417479 \\ 0.090090 & -0.995927 & 0.003664 \\ 0.415484 & 0.040927 & 0.908679 \end{pmatrix}, \mathbf{T}_R = \begin{pmatrix} 8.153933 \\ 7.768442 \\ 222.573004 \end{pmatrix}$$

$$f_R = 428.551967, \kappa_R = 0.0001429197 \text{ } \circ$$

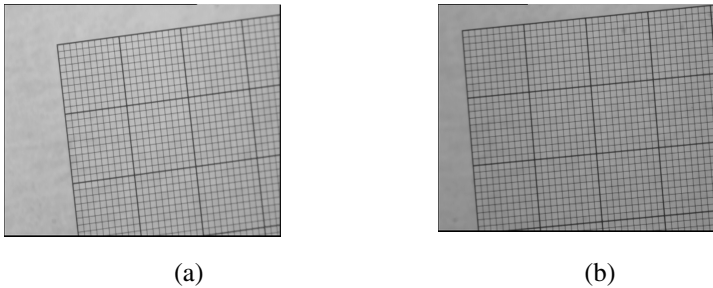


Fig. 5. Pictures shot under 0.7 magnitudes by a stereo microscope. (a) is the picture obtained from the left camera, and (b) is obtained from the right one.

Combing the calibration parameters, the coordinates of all corner points in the world coordinate system are mapped on the image coordinate so as to compare with the current actual image coordinate. The statistical error data is shown in Table 1.

Regardless of the Z axis depth correction, the results of the left-right images recovering on the world coordinate system are shown as Fig. 6, where the recovered points are blue and the original points, red.

Table 1. Measured data

	Group Number	$X_{new}-X_i$	$Y_{new}-Y_i$	Euclidean Distance
Left-path mean	100	0.0691	-0.0708	0.3637
Left-path variance	100	0.0423	0.1202	0.0388
Left-path mean	28×32	0.0675	-0.0790	0.3668
Left-path variance	28×32	0.0634	0.1147	0.0541
Right-path mean	100	-0.1171	0.0392	0.4633
Right-path variance	100	0.1097	0.1528	0.0610
Right-path mean	28×32	-0.1398	0.0393	0.4835
Right-path variance	28×32	0.0844	0.1849	0.0564

In the table, when the group number is 100, only the coordinates of the 100 points used for computing the camera parameter is compared. On the other hand, when the data is 28×32, the coordinates of all the selected corresponding corner points in the

left-right images is compared. X_{new} and Y_{new} are the image corner point coordinates mapped by the world coordinate system according to Formula (5) based on the computationally-acquired camera parameters. X_i and Y_i are the image corner point coordinates obtained from the corner point calculation. From Table 1, the Euclidean distance between the recovered corner point coordinate and the actual coordinate is within 0.36~0.48 pixels, subject to sub-pixel error range. In terms of variance, the variance of the Euclidean distance is within 0.36~0.48, which is not a great error on the whole.

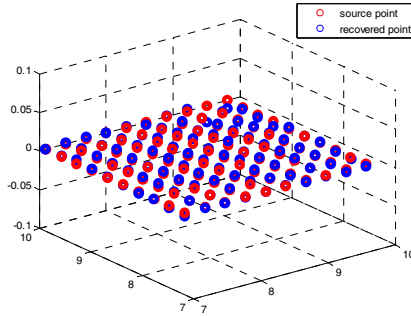


Fig. 6. Positions of the original points and recovered points

From Fig. 6, most points can recover nearly to the original position, and only a few points near (10, 10, and 0) have a great error. The Euclidean Distance error for both the 100 point pairs and for all point pairs is 0.0034mm.

Table 2. Plane Recovered Results

	Group Number	Xnew-X	Ynew-Y	Znew-Z	Euclidean Distance
Mean	100	5.4788×10^{-5}	3.4150×10^{-6}	0.0011	0.0034
Variance	100	1.1378×10^{-6}	2.8050×10^{-6}	1.1690×10^{-5}	5.4730×10^{-6}
Mean	28*32	-5.3500×10^{-6}	3.1171×10^{-5}	0.0013	0.0034
Variance	28*32	1.1725×10^{-6}	2.7557×10^{-6}	9.9962×10^{-6}	4.0255×10^{-6}

3.3 Depth Information Correction and Parameter Determination

The coordinate of the world coordinate system that is directly computed by using the above calibration parameters is accurate along the XY axis but is erroneous along the Z axis. As below shown in Fig. 7, the abscissa is the Z axis coordinate in the actual world coordinate system, and the ordinate is the average Z axis coordinate reconstructed according to the calibration parameter based on the 7 pairs of images. There is a quasi-linear relationship between the two. Therefore, a correction factor is introduced. In practical tests, the more heavily used interval is where the three middle points are located, which is known as the target depth: in this case, [-0.0625mm, 0.0625mm]. Thus, the correction factor value is set as 2.40.

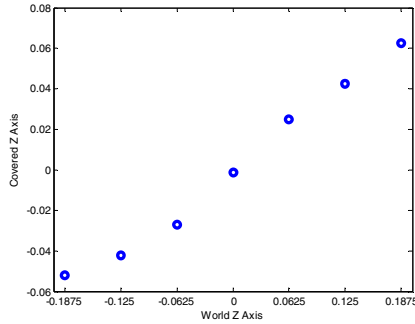


Fig. 7. Relationship diagram of the mean Z component in the world coordinate system and the mean recovered Z component

3.4 Results and Analysis of Stereo Reconstruction

Based on the calibration parameters, the above correction factor, and the acquired left-right microscopic images, the object in the world coordinate system will be reconstructed. Fig. 8 to Fig. 10 are the recovery images of the calibration board when the Z axis of the world coordinate system is at -0.0625mm, 0mm, and 0.0625mm.

From the figures above, the plane of the calibration board can be essentially recovered. The recovered Z axis coordinate and variance are shown in the table below. Except for a large error for a few of the coordinates located at the corner, the recovery of the plane is good on the whole. The Z axis error for position 3 is -4.43% and is 3.99% for position 5.

Table 3. Final Z Axis Recovery Results. AZM is the actual mean Z coordinate. AZV is the actual Z coordination variance. CZM is the current computed Z coordinate variance. CZV is the current computed Z coordinate variance. This data’s units are mm.

AZM	AZV	CZM	CZV
-0.0625	0	-0.0654	3.8903×10^{-5}
0	0	-0.0031	5.7578×10^{-5}
0.0625	0	0.0601	4.7872×10^{-5}

3.5 Summary

As seen in the final experimental results, the method proposed in the paper can complete effective calibration for small depth of field conditions and can recover the object’s actual coordinate in the world coordinate system. As illustrated in Fig. 8 to Fig. 10, the recovered data at the optic center is more accurate, but has a large error away from the optic center. This error is result of radial distortion.

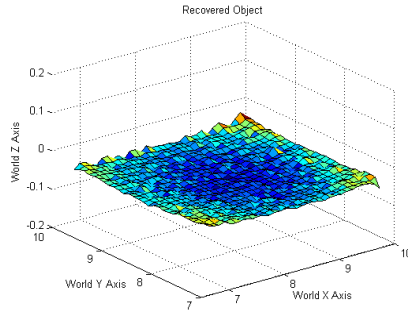


Fig. 8. Recovered calibration board plane of position 3, and the corresponding Z axis of the world coordinate is at -0.0625mm

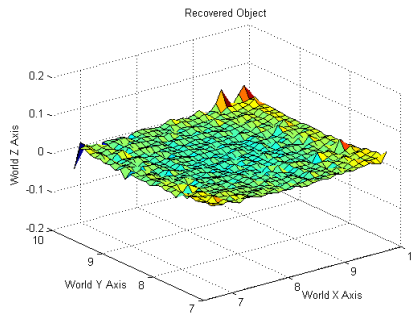


Fig. 9. Recovered calibration board plane of position 4, and the corresponding Z axis of the world coordinate is at 0mm

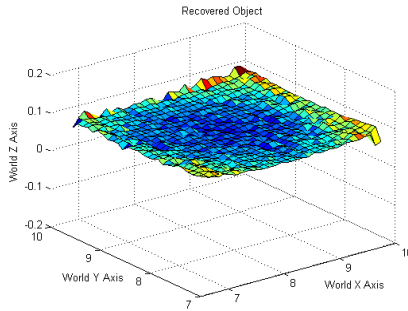


Fig. 10. Recovered calibration board plane of position 5, and the corresponding Z axis of the world coordinate is at 0.0625mm

4 Conclusion

Based on plane calibration, this paper proposes a new stereo microscope calibration process, which, via depth information correction, can finally realize the stereo reconstruction of a target image under a stereo microscope. This method has been shown to be a viable microscope calibration method, particularly as it bypasses the

conventional methods for calibration due to the small depth of field in stereo microscopes. Further confirming its reliability, the experimental results demonstrate that the method can effectively complete stereo reconstruction under a stereo microscope, with an error in reconstructed depth of approximately 4%. However, it is interesting to examine the reason that the relationship between the covered Z axis and the actual Z axis is not linear out of the range $[-0.0625\text{mm}, 0.0625\text{mm}]$. In the future, further studies will include methods for successfully running a stereo microscope under different magnitudes based on calibration parameter, along with compensation of radial distortion.

Acknowledgments. This work was supported in part by the Natural Science Foundation of China under Grant 61271270, U1301257 and 61311140262, and in part by the K. C. Wong Magna Fund in Ningbo University, and in part by the International Corporation Project of Ningbo under Grant 2013D10009.

References

1. Jahnisch, M., Schiffner, M.: Stereoscopic depth-detection for handling and manipulation tasks in a scanning electron microscope. In: IEEE International Conference on Robotics and Automation, pp. 908–913. IEEE Press, Orlando (2006)
2. Yamamoto, H., Sano, T.: Study of micromanipulation using stereoscopic microscope. IEEE T. Instrum. Meas. 51, 182–197 (2002)
3. Nakagawa, T., Hayashi, Y., Hatanaka, Y., Aoyama, A., Hara, T., Fujita, A., Kakogawa, M., Fujita, H., Yamamoto, T.: Three-Dimensional Reconstruction of Optic Nerve Head from Stereo Fundus Images and Its Quantitative Estimation. In: 29th IEEE International Conference on Engineering in Medicine and Biology Society, pp. 6747–6750. IEEE Press, Lyon (2007)
4. Heikkila, J., Silven, O.: A four-step camera calibration procedure with implicit image correction. In: IEEE Computer Society Conference on Computer Vision and Pattern Recognition, pp. 1106–1112. IEEE Press, California (1997)
5. Wong, K.Y.K., Mendonca, P.R.S., Cipolla, R.: Camera calibration from surfaces of revolution. IEEE T. Pattern Anal. 25, 147–161 (2003)
6. Ammi, M., Fremont, V., Ferreira, A.: Automatic Camera-Based Microscope Calibration for a Telemicromanipulation System Using a Virtual Pattern. IEEE T. Robot. 25, 184–191 (2009)
7. Li, K., Wang, Q., Wu, J., Yu, H.Y., Zhang, D.S.: Calibration error for dual-camera digital image correlation at microscale. Opt. Laser. Eng. 50, 971–975 (2012)
8. Zhang, Z.Y.: A flexible new technique for camera calibration. IEEE T. Pattern Anal. 22, 1330–1334 (2000)
9. Tsai, R.Y.: A Versatile Camera Calibration Technique for High-Accuracy 3d Machine Vision Metrology Using Off-the-Shelf Tv Cameras and Lenses. IEEE J. Robot. Autom. 3, 323–344 (1987)
10. Mei, H., Kanade, T.: Multiple motion scene reconstruction with uncalibrated cameras. IEEE T. Pattern Anal. 25, 884–894 (2003)
11. Ricolfe-Viala, C., Sanchez-Salmeron, A.J.: Camera calibration under optimal conditions. Opt. Express. 19, 10769–10775 (2011)
Zhang, Z.Y.: Camera calibration with one-dimensional objects. IEEE T. Pattern Anal. 26, 892–899 (2004)

A Prediction Model of Rectum's Perceptive Function Reconstruction Based on SVM Optimized by ACO

Peng Zan, Yutao Ai, Jie Zhao, and Yong Shao*

Department of Automation, College of Mechatronics Engineering and Automation,
Shanghai University; Shanghai Key Laboratory of Power Station Automation Technology,
Shanghai, China
shaoyong@shu.edu.cn

Abstract. In order to solve the problem that rectal pressure signal typically has complicate nonlinear and non-stationary signal characteristics. In this paper, our model uses wavelet packet to extract feature vectors and classifies them based on SVM. In our model, we choose RBF kernel function which has been proved has best discrimination for rectal pressure signals in the experiments. At the same time, in order to acquire higher accuracy, ACO is introduced to find the optimal value of parameters. We compare the prediction accuracy of SVM with different kernel functions. The results show that when we input parameters which were optimized by ACO into SVM, it acquires the highest classification accuracy and has preferable predication performance. So we can conclude that the proposed method is an effective way to rebuild patients' rectal perception function.

Keywords: artificial anal sphincter, support vector machine, optimal wavelet packet, ant colony optimization.

1 Introduction

Using artificial anal sphincter analog normal function of body's anal sphincter is an important treatment for anal incontinence. Clinically proven, it can save peoples' lives. However, existing artificial anal sphincter has many defects. The most serious drawback is that patients who use the product can't feel the volume of dung in their bodies, as the result they can't defecate under control. For the purpose to solve this problem, how to rebuild rectal perception function becomes the major bottleneck of the artificial anal sphincter research. Owing to rectal pressure signal typically has nonlinear non-stationary and nonlinear signal characteristics. It can hardly acquire ideal effect using traditional methods.

SVM (Support Vector Machine) is based on the statistical learning theory. It has been shown to be one of the best methods for classification problems [1, 2]. It was firstly introduced for nonlinear function estimation and nonlinear function estimation classification and is further investigated by many others. Currently, successful implementations of SVM classifiers have been reported in various applications [3, 4].

* Corresponding author.

ACO (Ant Colony Optimization) is a metaheuristic for discrete optimization problem based on population, which is inspired by the natural metaphor of real ant colony [5]. The feature of the ACO different from other methods is that it can be flexible for many different problems' formulation; implemented easily and the most important is that it can escape the local optima of the given problems [6]. The purpose of our study is to use wavelet packet combine with SVM which is optimized by ACO recognizes and classifies rectal pressure signal. In our experiments, we use HAPC as the index of rectal pressure signals. As rectal perception function rebuilding is achieved, showing that the proposed method is effective to rebuild patients' rectal perception function.

2 Artificial Anal Sphincter

Bowel incontinence is due to the loss of control over the rectal sphincter. This lack of muscle control can occur by reason of nerve medication, damage and even surgery. Although there are variety of methods to treat the disease such as sphincteroplasty and colostomy, most of them have some deficiencies. In recent years, using artificial anal sphincter rectum take the place of anal sphincter becomes an important means of treating the malady. It can improve the quality and extend patients' lives. Artificial anal sphincter rectum consists of holdback structure, reservoir and micro pump, as illustrated in figure 1.

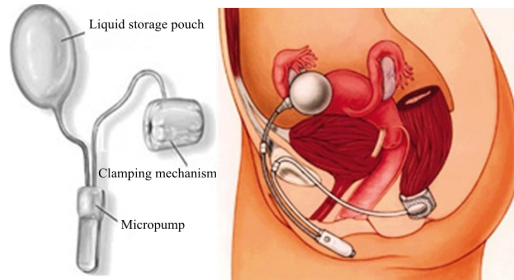


Fig. 1. The structure of artificial anal sphincter

Shanghai Jiaotong university has designed a feedback artificial anal sphincter. A pressure sensor has been installed in the traditional structure. The device predicts defecation by judging whether the pressure's value reach the "threshold". According to the research, the "threshold" generally is 7.3kPa [7]. However, because the form of this method is unitary; the technology is backward and intestinal pressure signal has non-stationary random characteristic, it's hard to make the right judgments in time.

3 Rectal Sensation Prediction Model

Medical research shows that high-amplitude propagated contractions (HAPC) is a high-amplitude and long-time contraction wave that can be used to determine if person

needs to defecation. In our research, we exploit HAPC as the judgment and wavelet packet is used to extract feature vectors of rectal pressure signals. Subsequently, we classify them based on SVM optimized by ACO. The implementation process can be shown as follow:

(1) We firstly conduct the intestinal pressure signals which were automatically detect by the biological feedback from artificial anal sphincter system using wavelet packet transform with four layer decomposition and reconstitution.

(2) Then we extract the value of mean coefficient and energy of subspace which was reconstructed above construct multidimensional vector space as the input of SVM. Meanwhile, ACO is used to optimize the parameters of SVM.

(3) We lastly judge if patients need to defecation based on whether the intestinal pressure signals contain HAPC. If the result is positive, we set alarm to inform patients to prepare.

Figure 2 illustrates inside flowchart of the prediction model.

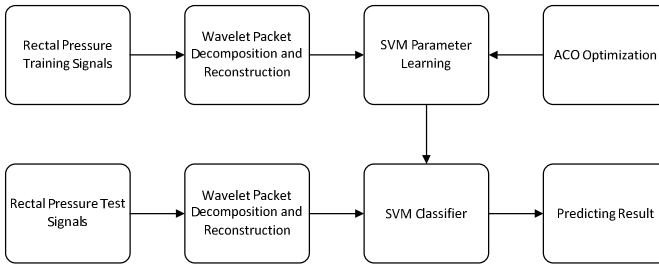


Fig. 2. Prediction model of rebuilding rectal sensation

4 Rectum's Perceptive Function Rebuilding Algorithm

4.1 Feature Vector Extraction Using Optimal Wavelet Packet

Thanks to wavelet packet analysis theory, we can extract the energy of each layer based on the multilayer signal analysis. What follows next we can classify and analyze the local rectum pressure signals very accurate [8].

The extraction procedure is as follow [9]:

(1) Firstly, we utilize wavelet packet decompose the rectal pressure signals into 4 layers. Then we reconstruct the coefficients of each sample's subspace denote $W_j^m (m = 0, 1, 2, \dots, 2^j - 1)$.

(2) The coefficients mean of wavelet packet's subspace $ME_{j,m}$ are being calculated. Meanwhile the energy of wavelet packet's subspace is counted according to the following formula

$$E_{j,m}^n = \sum_k (d_j^m(k))^2 \tag{1}$$

(3) Lastly, we extract $ME_{j,m}$ and $E_{j,m}$ which are acquired in step 2 as the feature vector of rectal pressure signals to constitute the feature vector space.

4.2 Support Vector Machine

Suppose sample set is $(x_i, y_i), i=1, \dots, n, x \in R^n$, suppose n is classification dimension and $y \in \{1, -1\}$ meet the conditions

$$y_i[(k \cdot x_i) + b] - 1 \geq 0, \quad i=1, \dots, n \tag{2}$$

The value of the classification interval is equal $2/\|k\|$. We know the classification interval get the maximum means $\|k\|/2$ get the minimum.

In order to change optimal classification problem into dual problem, Lagrange optimization method is introduced. Then we get

$$E(\alpha) = \sum_{i=1}^n \alpha_i - \frac{1}{2} \sum_{i,j=1}^n \alpha_i \alpha_j y_i y_j (x_i \cdot x_j) \tag{3}$$

Which is meet the conditions

$$\sum_{i=1}^n \alpha_i y_i = 0, \quad \text{and} \quad \alpha_i \geq 0, \quad i=1, \dots, n \tag{4}$$

For nonlinear problems, it can be converted into linear problems that in high-dimensional space and find optimal classification surface by transform the space

$$E(\alpha) = \sum_{i=1}^n \alpha_i - \frac{1}{2} \sum_{i,j=1}^n \alpha_i \alpha_j y_i y_j K(x_i, x_j) \tag{5}$$

Here $K(x_i, y_i) = \Phi(x_i)$ is kernel function.

Then the classification function is

$$f(x) = \text{sgn}(\sum_{i=1}^n \alpha_i^* y_i K(x_i, x) + b^*) \tag{6}$$

In order to find a balance between generalization performance and experience risk in SVM, relaxation factor ζ_i has been introduced. Constraint $y_i[(k \cdot x_i) + b] - 1 \geq 0, i=1, \dots, n$ is changed to $y_i[(k \cdot x_i) + b] - 1 + \zeta_i \geq 0, i=1, \dots, n$. Meanwhile, we join penalty term $C \sum_{i=1}^n \zeta_i$ into the minimize value $\frac{1}{2} \|k\|^2$. So Wolf dual problem can be described as:

$$\text{Maximize:} \quad E(\alpha) = \sum_{i=1}^n \alpha_i - \frac{1}{2} \sum_{i,j=1}^n \alpha_i \alpha_j y_i y_j K(x_i, x_j) \tag{7}$$

$$\sum_{i=1}^n y_i \alpha_i = 0, \quad 0 \leq \alpha_i \leq C \quad i=1, \dots, n \tag{8}$$

4.3 Optimize the Parameters of SVM Based on ACO

Ant colony algorithm (ACO) is a novel simulated evolutionary algorithm which is first proposed by Italian scholars in the 1990s. ACO belong to a kind of swarm intelligence algorithm that has good robustness, good positive feedback characteristics and the advantages of parallel search. In this paper, we treat the parameter selection of SVM as

a parametric optimization problem. Then we establish the objective function based on the combination of these parameters. Ant colony optimization algorithm is used to search the optimal objective function value and finally get the right combination of parameter values [10]. In our model we choose RBF which is the most common kernel function of SVM. So there are two parameters σ , C . What we want to do is improve the distinguish rate by optimize σ , C using ACO. The specific algorithm steps are described below:

Setp1: Parameter initialization

(1) We firstly give initial value of parameters (σ , C) to each ant;

(2) After learning training set by SVM based on initialize parameters (σ , C) we can get the error model of SVM

$$Er(i) = | Y_{tra} - Y_{rea} | \tag{9}$$

Here Y_{tra} is the value of training samples, Y_{rea} is the value of real samples.

(3) When ant is at position i , its pheromone can be described as

$$J_0(i) = \alpha^{Er(i)} \tag{10}$$

Here, we set $\alpha=3$, so we know as the smaller the error is the bigger the pheromone are according to formula (10).

Step 2: The pheromones are updated constantly due to the ants search in global and local space constantly. We can save the global optimal solution of each generation of ants.

(1)Based on the value of pheromone of each ant, we can acquire each ant's shift probability

$$P(i) = \frac{e^{J_0(BIndex) \cdot J_0(i)}}{e^{J_0(BIndex)}} \tag{11}$$

Here, BIndex is the ant which has the biggest pheromone.

(2) In order to prevent got local optimal solution, self-adaption method is utilized in this paper. The volatilization factor of pheromone has been set relatively small at the begging and increase constantly in the wake of increase of the number of ant evolution. The volatilization factor of pheromone can be described as

$$\rho = K * \frac{\log(9) * N}{e^{N_{max}}} \tag{12}$$

Here $K=0.1$, N is the present number of the evolve generation of ants. N_{max} is the max number of the evolve generation of ants.

(3) The global transfer factor P_0 is established based on the pheromone of ant: we suppose the number of ants is n , then we calculate the value of e^{-J_0} $i = 1, 2, \dots, n$, and arrange it in ascending order $J_i(j)$, $j = 1, 2, \dots, n$. When $N < \frac{N_{max}}{2}$ $P_0 = J_i(k)$, $k = \frac{2}{3}n$, on the contrary $P_0 = J_i(k)$, $k = \frac{1}{5}n$. If the transition probability is smaller then P_0 , ants search in local space, or ants search in global space. And because the pheromone of ant is increasing from enough small to enough large, algorithm can be prevented fall into local optima.

(4) The update rules of pheromone update based on SVM parameters optimized by ACO can be described as

$$J_{\phi}(i) = (1 - \rho) * J_{\phi}(i) + \Delta E(i) \tag{13}$$

Here $\Delta E(i) = \alpha^{-Er(i)}$.

(5) At the end of an iteration of work, we save the biggest pheromone and count the error based on the error model. At the same time the step turn to step 1 to continue.

(6) When the iteration fit the frequency we set. We find the optimal ant obtain the optimal parameters C and σ .

5 Experimental Analysis

5.1 Data Collection

Our experiments employ the biological parameters telemetry capsule which are provided by Shanghai Jiaotong university acquire rectal pressure signals from 10 healthy subjects with normal bowel function tests for 10 times. As 4 groups data are wrong, 52 groups are chosen as training data and left 44 groups are chosen as test data. This paper consider the rectal contraction pressure data which contains HAPC as the sign of defecation and denote as type "1"; on the contrary denote as type "0". The target of data processing is to identify the category in the original test samples correctly employing the training data, and calculate correct rate of the experiments as an indicator to assess the cons and pros of different methods.

5.2 Experiment of Signals Extraction

Our model selects “db4” as wavelet packet basis of wavelet packet decomposition. Four layer of wavelet packet decomposition are operated on 96 training and testing samples.

Fig. 3 shows the wavelet packet decomposition waveform of the rectal pressure signals.

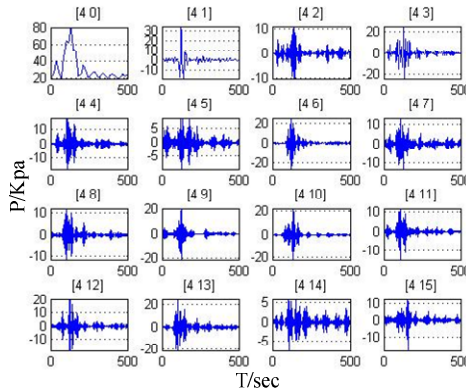


Fig. 3. Wavelet packet decomposition waveform of the rectal pressure signals

5.3 Data Analysis and Comparison for Prediction Model

RBF is chosen as the kernel function of SVM in our model. 52 training data extracted above are input into SVM to train the classifiers. With the default C and σ the prediction accuracy of the training prediction model is 86.36%. In order to improve the forecast accuracy of defecation, the parameters C and σ is optimized by ACO. We set there are 30 ants and give initial value $C=0.02$, $\sigma=0.7$, the maximum number of the evolve generation of ants is 100. Then we input 52 training data into SVM, and optimize the parameters follow the steps which are described in section 4. After C and σ have been operated by ACO we acquire the optimal parameters $C=0.03$, $\sigma=0.89$ as the RBF kernel function width and the penalty factor.

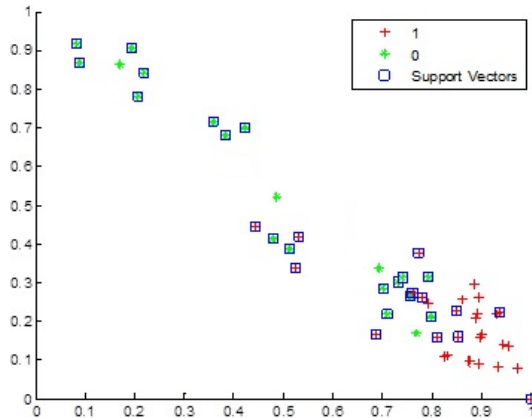


Fig. 4. SVM classification map of training samples

Fig. 4 illustrates the training data feature vector classification result and support vector of SVM.

For the purpose to proof our model is advanced, we select other three common kernel functions including linear kernel function, Sigmoid kernel function, polynomial kernel function and RBF function for pattern identification with the 44 groups of test data. And table 1 illustrates the classification rate of rectal pressure signals based on different kernel function.

Table 1. Prediction accuracy of SVM with different kernel functions

kernel function	polynomial	linear	Sigmoid	RBF
Test sample number	44	44	44	44
Correct prediction	39	35	36	41
Prediction accuracy	88.63	79.55	84.09	93.18

In table 1 we can conclude that using RBF kernel function optimized by ACO gets the highest rates reaching to 93.18%. It manifests that our model is an ideal model for reconstructing rectum's perceptive function.

6 Conclusion

Because typical rectal pressure signals are non-stationary, nonlinear and limited-sample, how to extract and classify feature vectors of rectal pressure signals accurately and efficiently becomes a bottleneck for reconstructing human rectal perception function. In this paper, we propose a prediction model of rectum's perceptive function that employs wavelet packet analysis to extract feature vectors, and uses SVM optimized by ACO to classify the extracted feature vectors. The model basically reconstructs patients' rectal perception function with only 96 groups of data. We can conclude that it is an effective model for reconstructing rectal perception function and has good application prospects.

Acknowledgments. This work was supported by National Natural Science Foundation of China (No. 31100708 and 31370998).

References

1. Shalev-Shwartz, S., Singer, Y., Srebro, N., et al.: Pegasos: Primal estimated sub-gradient solver for SVM. *Mathematical Programming* 127(1), 3–30 (2011)
2. Chiranjib, K., Purkait, P., Chakravorti, S.: Wavelet-Aided SVM tool for impulse fault identification in transformers. *IEEE Transactions on Power Delivery* 3(21), 1283–1290 (2006)
3. Pal, M., Foody, G.M.: Feature selection for classification of hyperspectral data by SVM. *IEEE Transactions on Geoscience and Remote Sensing* 48(5), 2297–2307 (2010)
4. Alonso, I.P., Llorca, D.F., Sotelo, M.Á., et al.: Combination of feature extraction methods for SVM pedestrian detection. *IEEE Transactions on Intelligent Transportation Systems* 8(2), 292–307 (2007)
5. Dorigo, M., Birattari, M.: Ant colony optimization. *Encyclopedia of Machine Learning*, pp. 36–39. Springer, US (2010)
6. Hsiao, Y.T., Chuang, C.L., Chien, C.C.: Ant colony optimization for best path planning. In: *IEEE International Symposium on Communications and Information Technology, ISCIT 2004*, vol. 1, pp. 109–113. IEEE (2004)
7. Li, Z.Z.: *New Sphincter Development based on Wireless communication and Wireless energy supply*. Shanghai Jiaotong University (2007) (in Chinese)
8. Zhou, R., Bao, W., Li, N., et al.: Mechanical equipment fault diagnosis based on redundant second generation wavelet packet transform. *Digital Signal Processing* 20(1), 276–288 (2010)
9. Jiang, E.Y., Zan, P., Zhu, X.J., Shao, Y., Wang, X.H.: Rectal perception function rebuilding based on wavelet packet analysis and support vector machine. *Yingyong Kexue Xuebao/Journal of Applied Sciences* 30(5), 538–544 (2012)
10. Zhuang, Y., Bai, Z.L., Xu, Y.F.: Research on Parameters of Support Vector Machine Based on Antcolony algorithm. *Journal of Computer Simulation* 28(5), 216–219 (2011) (in Chinese)

A New Polynomial Hybrid Reflection Model Based on Perspective Projection

Jiyuan Cai, Lei Yang, Ning Zhang, and Yanyun Ren

Shanghai Key Laboratory of Power Station Automation Technology,
School of Mechatronics Engineering and Automation, Shanghai University,
Yan-chang Road 149, Shanghai, 200072, China
yangyoungya@sina.com

Abstract. Reflectance model is an important concept in computer vision. Most classical reflection models based on orthogonal projection with Lambert reflection model assumptions don't correspond to the real imaging process. This paper proposed a new polynomial hybrid reflection model based on perspective projection. The imaging process of camera is simulated by the proposed reflection model with perspective projection. Then non-negative least squares algorithm (NNLS) is used to estimate parameters of the proposed reflectance model by using pixels values in image of some known 3-D shape object. At last, synthesis images produced by the proposed model and existing ones are compared with the real captured images by camera. Experimental results showed that the proposed reflectance model is more accurate than the Lambert model and Phong models under perspective projection.

Keywords: Perspective projection, reflectance model, parameters measurement, non-negative least square regression algorithm.

1 Introduction

Light reflectance models have shown great interest in the computer vision community. Image is a physical form to represent visual information. To know the intrinsic properties of image generation and carried information, appropriate mathematical model should be used to characterize the imaging process. The basic form of the mathematical model is the imaging geometry model which is used to describe how to form the 2D images from 3D world. Recently, Shape-From-Shading (SFS) gets great improvements and rapid developments in methodology and application. SFS is a method to reconstruct 3D surface height from a single image, but it needs to know the relationship between 2D image and 3D surface. In the 1970s, SFS is first introduced by Horn to solve a radiation equation which relates reflection map and image brightness [1]. The seminal work of Horn is followed by many works in this field which assumed Lambertian diffuse reflectance [2]. Then the most commonly used model was derived by Phong approximately forty years ago [3][4]. The Phong model is a simple representation that can simulate the specular reflection of shiny surfaces, but it is not accurate in the sense of representing the true reflection behavior of surfaces [5].

Various kinds of reflection models are put forward and valid method for reliability analysis are provided. In particular, a hybrid reflection model is proposed and least square regression algorithm is used to estimate the ratio of diffuse and specular reflection [6]. But the reflection model is based on orthogonal projection. Orthogonal projection is a kind of ideal assumption in compute vision. However, the actual imaging relation is under perspective projection which creates the sense of distance. In recent years, the research of SFS models based on perspective projection has been made gradually, such as face reconstruction [7], reconstruction of organs [8][9], and digitization of documents [10][11].

In this paper, a new polynomial hybrid reflection model based on perspective projection is proposed. The imaging process of camera is simulated by the proposed reflection model. Then non-negative least squares algorithm (NNLS) is used to estimate parameters of the proposed reflectance model by using pixels values in image of some known 3-D shape object. At last, synthesis images produced by the proposed model and existing ones are compared with the real captured images. Numerical comparing results showed that the proposed reflectance model is accurate.

2 General Polynomial Hybrid Reflection Model

In order to research the polynomial hybrid reflection model based on perspective projection and use non-negative least squares method (NNLS) to estimate parameters, we give general polynomial reflection model firstly. When light is reflected at an opaque surface, it can be described by bidirectional reflectance distribution function (BRDF) as

$$f(\theta_i, \phi_i; \theta_o, \phi_o) = \frac{\partial L_o(\theta_o, \phi_o)}{\partial L_i(\theta_i, \phi_i)}. \quad (1)$$

where $\partial L_i(\theta_i, \phi_i)$ is the illumination in the (θ_i, ϕ_i) direction onto the object surface. And $\partial L_o(\theta_o, \phi_o)$ is the reflecting brightness viewed from (θ_o, ϕ_o) direction. It is a four-dimensional function that expresses the ratio of reflected radiance towards a viewing direction to the irradiance from an incoming direction. In SFS situation, following assumptions are usually used. Firstly, the light is assumed to be a point light source located in infinite position [12][13]. Its direction is n_i in image center coordinates. Secondly, camera should be put into the origin and make sure observation direction is $n_o = (0, 0, -1)$. So the radiance of reflected light in the viewing direction n_o is

$$L(n_i, n_o) = \int_{\omega} f(n_i, n_o) L_i(\omega) d\omega = f(n_i, n_o) E \max\{0, n_i \cdot n\}. \quad (2)$$

where E is the light strength and w is outgoing direction depends on (θ_i, ϕ_i) .

As we know, the characteristic of most practical object is hybrid. In other words, the real surface neither is completely diffuse reflection nor specular reflection mostly. In 1991, Tagare proposed a hybrid model that consists of three components (a diffuse lobe, a specular lobe, and a specular spike) [14][15]. With a smart set of principal direction p_i , a general non-Lambertian model can be described as

$$R_{hybrid} = \sum_j p_j \Phi(\vec{p}_i * \vec{n}) + b. \tag{3}$$

where p_j is albedo derived by the directions of light source vector and observing camera vector, Φ is a monotonically increasing function, and b is a constant. Inspired by the reflectance model (3), a new polynomial hybrid reflection model based on orthogonal projection is proposed as

$$R_{hybrid} = d_0 \vec{n} * \vec{n}_i + \sum_{k=1}^{\infty} d_k (\vec{n} * \vec{n}_{spec})^k. \tag{4}$$

where d_0 can be considered as the ratio of diffuse reflection, k denotes the k th order mirror-like component and a series of constants d_k are the ratio of specular reflection. Each terms of (4) denotes all different degrees of specular reflectance components. When eq.(4) is used in practice, ∞ can be replaced by some positive integral N .

3 Hybrid Reflection Model under Perspective Projection

Generally, Lambertian model under orthogonal projection is used to simulate the imaging process, following reflectance map equation is established [1]

$$I = R = \frac{\vec{n} * \vec{n}_i}{|\vec{n}| |\vec{n}_i|} = \frac{pp_0 + qq_0 + 1}{\sqrt{p^2 + q^2 + 1} \sqrt{p_0^2 + q_0^2 + 1}}. \tag{5}$$

where $\vec{n}_i = (p_0, q_0, -1)$ denotes a known lighting source direction. Surface normal is denoted by $\vec{n} = (p, q, -1)$, $(p, q) = (\partial z / \partial x, \partial z / \partial y)$, and $z = z(x, y)$ is the surface equation in scene. Considering the near-scene imaging situation, perspective projection is better suited. The perspective projection is illustrated in Fig.1.

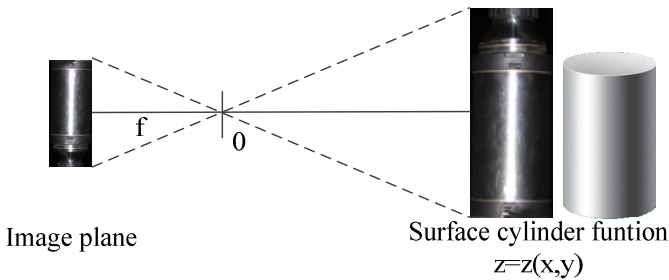


Fig. 1. The perspective projection imaging model

The 3-D surface of objective (such as cylinder in fig.1) in the scene is defined as $z = z(x, y)$, and pixel is denoted as (u, v) at imaging plane $z = -f$, where f is focus length. The perspective projection equations is

$$\frac{x}{u} = \frac{y}{v} = -\frac{z}{f}. \quad (6)$$

From Eq. (6), the image brightness equation of the model can be derived. In perspective projection, following relationships is obtained from Eq. (6),

$$\begin{cases} x = -u \frac{z}{f} \\ y = -v \frac{z}{f} \end{cases}. \quad (7)$$

And the surface S is parameterized such as

$$(x, y, z) = z(u, v) * \left(\frac{u}{f}, \frac{v}{f}, 1\right). \quad (8)$$

By using the partial derivative method and difference geometry theory, the normal of the surface is given by

$$\begin{aligned} \vec{n}(u, v) = \vec{S}_u \times \vec{S}_v &= \begin{vmatrix} i & j & k \\ \frac{\partial x}{\partial u} & \frac{\partial y}{\partial u} & \frac{\partial z}{\partial u} \\ \frac{\partial x}{\partial v} & \frac{\partial y}{\partial v} & \frac{\partial z}{\partial v} \end{vmatrix} = \begin{vmatrix} i & j & k \\ \frac{z_u u + z}{f} & \frac{z_u v}{f} & z_u \\ \frac{uz_v}{f} & \frac{z_v + z}{f} & z_v \end{vmatrix}. \quad (9) \\ &= \left(-f \frac{\partial z}{\partial u}, -f \frac{\partial z}{\partial v}, u \frac{\partial z}{\partial u} + v \frac{\partial z}{\partial v} + z(u, v)\right) * \frac{z(u, v)}{f^2} \end{aligned}$$

So the unit vector of the normal of the surface is as

$$\vec{n} = \frac{(-fz_u, -fz_v, uz_u + vz_v + z)}{\sqrt{(uz_u + vz_v + z)^2 + f^2(z_u^2 + z_v^2)}}. \quad (10)$$

where $(z_u, z_v) = (\partial z / \partial u, \partial z / \partial v)$. So the reflectance map equation of Lambertian model under perspective projection is concluded from Eq. (5) as

$$I(u, v) = \frac{\vec{n}_i * \vec{n}}{\|\vec{n}_i\| \|\vec{n}\|} = \frac{(u - fp_0) \frac{\partial z}{\partial u} + (v - fq_0) \frac{\partial z}{\partial v} + z}{\sqrt{p_0^2 + q_0^2 + 1} \sqrt{(f \frac{\partial z}{\partial u})^2 + (f \frac{\partial z}{\partial v})^2 + (u \frac{\partial z}{\partial u} + v \frac{\partial z}{\partial v} + z)^2}}. \quad (11)$$

Due to the assumption that object is in the camera shooting range and the distance between the camera and object is greater than the camera focal length, namely $z > F$. We let $Z(u, v) = \ln z(u, v)$, $\partial Z / \partial u = Z_u$, $\partial Z / \partial v = Z_v$ and we denote $z(u, v) > 0$, then we have

$$I(u, v) = \frac{(u - fp_0)Z_u + (v - fq_0)Z_v + 1}{\sqrt{p_0^2 + q_0^2 + 1} \sqrt{(fZ_u)^2 + (fZ_v)^2 + (uZ_u + vZ_v + 1)^2}}. \quad (12)$$

Eq. (12) can be further written as

$$I(u, v) = \frac{(u - fp_0)p + (v - fq_0)q + 1}{\sqrt{p_0^2 + q_0^2 + 1}\sqrt{(fp)^2 + (fq)^2 + (up + vq + 1)^2}}. \quad (13)$$

where $p = Z_u, q = Z_v$. Eq. (13) is a nonlinear partial differential equation named reflection map equation with Lambertain model under perspective projection.

The polynomial hybrid reflection model can be further established based on perspective projection by substituting Eq. (10) into model Eq. (4) such as

$$I = R_{hybrid} = d_0 \left(\frac{(-fz_u, -fz_v, uz_u + vz_v + z)}{\sqrt{(uz_u + vz_v + z)^2 + f^2(z_u^2 + z_v^2)}} \right)^T * \vec{n}_i \rightarrow \vec{n}_i^k + \sum_{k=1}^{\infty} d_k \left(\frac{(-fz_u, -fz_v, uz_u + vz_v + z)}{\sqrt{(uz_u + vz_v + z)^2 + f^2(z_u^2 + z_v^2)}} \right)^T * \vec{n}_{spec}^k. \quad (14)$$

The reflectance model Eq.(14) is function of \vec{n}, \vec{n}_i and \vec{n}_o . The coefficients denote the reflectance properties. If some $\vec{n}_1, \vec{n}_2, \dots, \vec{n}_M$ are M known directions of surface, from (14), (10) and (4), we get

$$\begin{bmatrix} I_1 \\ I_2 \\ \vdots \\ I_M \end{bmatrix} = \begin{bmatrix} (\vec{n}_1^T * \vec{n}_i) & (\vec{n}_1^T * \vec{n}_{spec})^1 & \dots & (\vec{n}_1^T * \vec{n}_{spe})^N \\ (\vec{n}_2^T * \vec{n}_i) & (\vec{n}_2^T * \vec{n}_{spec})^1 & \dots & (\vec{n}_2^T * \vec{n}_{spe})^N \\ \vdots & \vdots & \dots & \vdots \\ (\vec{n}_M^T * \vec{n}_i) & (\vec{n}_M^T * \vec{n}_{spec})^1 & \dots & (\vec{n}_M^T * \vec{n}_{spe})^N \end{bmatrix} \begin{bmatrix} d_0 \\ d_1 \\ \vdots \\ d_N \end{bmatrix}. \quad (15)$$

Then the coefficients of $R_{hybrid}(\vec{n}, \vec{n}_i, \vec{n}_o)$ can be estimated. In our experiment, a stainless steel cup with known shape (denoted by surface cylinder function) is used to determine the coefficients of (14) by non-negative least squares algorithm. And member of image pixel M is larger than the highest order of specular component. We write Eq.(15) in matrix form as

$$I = AD. \quad (16)$$

which can be solved by nonnegative least-squares curve fitting problems easily such as the following form [16]

$$\min \|A \cdot D - I\|_2^2, \text{ where } D \geq 0. \quad (17)$$

4 Experimental Results

To evaluate the performance of the proposed model based on perspective projection and compare the image generated from each model, we use criteria namely mean error (ME) and root square mean error (RS), which are defined as

$$ME = \frac{1}{M} \sum_{k=1}^M |R_{(k)} - I_{(k)}|. \quad (18)$$

$$RS = \sqrt{\frac{1}{M} \sum_{k=1}^M (R_{(k)} - I_{(k)})^2}. \quad (19)$$

Figure 2(a) is a real captured image of stainless steel cup which is cylinder shape. In camera center coordinates system, the light is located in 3 meter distance from the cup, and the diameter of the cylinder is 10 cm. In our experiments, N is set as 100. $\{d_0, d_1, d_2, \dots, d_N\}$ are calculated by using non-negative least squares algorithm and we get $\{d_0 = 0.1133, d_{10} = 0.0070, d_{11} = 0.2904, d_{40} = 0.2186, d_{100} = 0.3899\}$, and other coefficients are zero. The synthesis images using proposed reflectance model, hybrid model and Lambertian model are shown in Figs. 2(b)—(d). Figure 3 shows the gray intensities of Figs. 2(a)—(d) along the surface directions. Figure 4 shows the intensity errors of Figs. 2(b)—(d) compared with the intensity of the original surface of Fig. 2(a). Table 1 lists the results using ME criteria Eq. (18) and RS criteria Eq. (19).

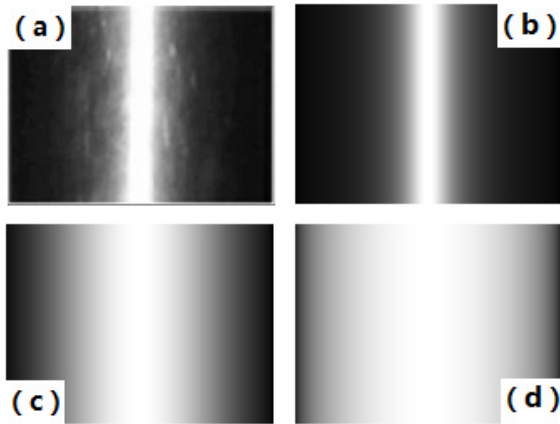


Fig. 2. (a) Real image of a metal cylinder. Composite images using (b) the proposed model, (c) hybrid model, and (d) Lambertian model under perspective projection

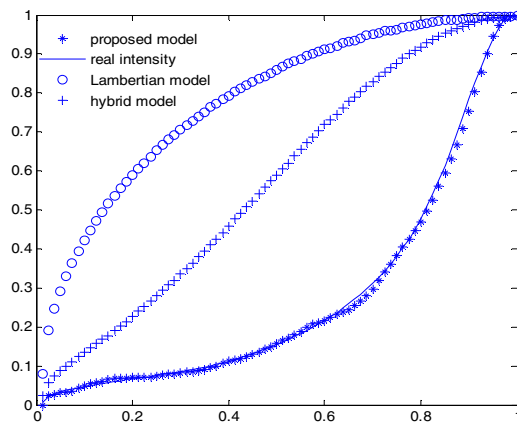


Fig. 3. Intensities of Figs. 2(a)—(d) along the surface directions

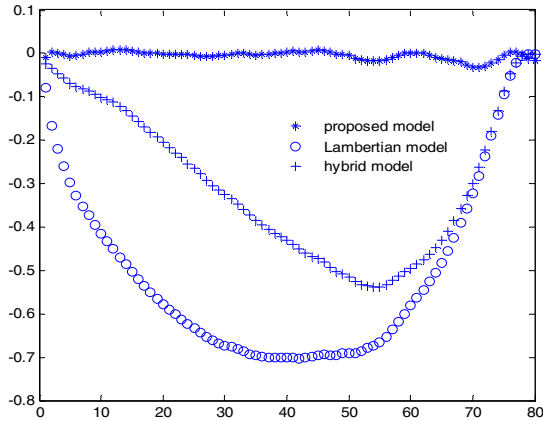


Fig. 4. Error of intensities compared with the original intensity of Fig. 2(a)

Table 1. Reflectance Maps of Three Models

Index	Proposed	Hybrid[15]	Lambertian[8]
ME	0.0069	0.2982	0.5042
RS	0.0101	0.3442	0.5461

From the fig.3, fig.4 and table 1, we can see that under perspective projection, the proposed reflectance model is more accurate than other models. It can describe the imaging process perfectly.

5 Conclusion

A new polynomial hybrid reflection model based on perspective projection is proposed. We use a nonlinear partial differential equation to simulate perspective projection and estimate the parameters of the proposed reflectance model by non-negative least squares algorithm. The results of these experiments show the proposed reflectance model is suitable for describing the real reflectance property. In addition, the proposed reflectance model may be used to help improve the accuracy of three-dimensional (3D) reconstruction based on shape from shading (SFS) which is under perspective projection.

Acknowledgements. The work is supported by the National Natural Science Foundation of China (61005015), the third National Post-Doctoral Special Foundation of China (201003280), Shanghai University 11th Five-Year Plan 211 Construction Project, and Shanghai Committee of Science and Technology, China (10DZ2273400), and 2011 Shanghai city young teachers subsidy scheme.

References

1. Horn, B.K.P.: Understanding Image Intensities. *Artificial Intelligence* 8(2), 201–231 (1977)
2. Horn, B.K.P.: *Robot Vision*. The MIT Press/McGraw-Hill Book Company (1986)
3. Phong, B.T.: Illumination for computer generated pictures. *Communications of the ACM* 18(6), 311–316 (1975)
4. University of Utah School of Computing,
<http://www.cs.utah.edu/school/history/#phong-ref.5>
5. Greenberg, D.P., Torrance, K.E., Shirley, P., et al.: A framework for realistic image synthesis. In: Whitted, T. (ed.) *Proceedings of the 24th Annual Conference on Computer Graphics and Interactive Techniques*, pp. 477–494 (1997)
6. Yang, L., Han, J.Q.: A polynomial hybrid reflection model and measurement of its parameters based on images of sample. *Chin. Opt. Lett.* 5(12), 683–686 (2007)
7. Prados, E., Faugeras, O.: Perspective Shape from Shading and viscosity solutions. In: *Proceedings of the 9th International Conference on Computer Vision*, vol. 2, pp. 826–831 (2003)
8. Tankus, A., Sochen, N., Yeshurun, Y.: A new perspective [on] Shape-from-Shading. In: *Proceedings of the 9th International Conference on Computer Vision*, vol. 2, pp. 862–869 (2003)
9. Tankus, A., Sochen, N., Yeshurun, Y.: Perspective Shape-from-Shading by Fast Marching. In: *Proceedings of the 2004 IEEE Computer Society Conference on Computer Vision and Pattern Recognition*, Washington, D.C., USA, pp. 43–49 (2004)
10. Courteille, F., Crouzil, A., Durou, J.D., Gurdjos, P.: Towards shape from shading under realistic photographic conditions. In: *Proceedings of the 17th International Conference on Pattern Recognition*, Cambridge, UK, vol. II, pp. 277–280 (2004)
11. Courteille, F., Crouzil, A., Durou, J.D., Gurdjos, P.: Shape from Shading for the digitization of curved documents. *Mach. Vis. Appl.* 18, 301–316 (2007)
12. Zhang, R., Tsai, P.S., Cryer, J.E., Shah, K.: Shape from Shading: A Survey. *IEEE Transactions on Pattern Analysis and Machine Intelligence* 21(8), 690–706 (1999)
13. Yang, L., Han, J.: Fast algebra algorithm of shape-from-shading with specular reflectance. *Chin. Opt. Lett.* 5(2), 204–207 (2007)
14. Tagare, H.D., de Figueiredo, P.: A theory of photometric stereo for a class of diffuse nonLambertian surface. *IEEE Trans. Pattern Anal. Mach. Intell.* 13(1), 133–152 (1991)
15. Cho, S.Y., Chow, T.W.S.: *Neural Computation* 14(11), 2751–2789 (2002)
16. Lawson, C.L., Hanson, R.J.: *Solving Least Squares Problems*. Prentice-Hall (1974)

An Improved Bayesian-Based Wavelet Package Denoising Method for Data Reconciliation to Coking Chemical Process

Shengxi Wu, Qiang Ye, Kai Shen, and Xingsheng Gu*

Key Laboratory of Advanced Control and Optimization for Chemical Processes,
Ministry of Education
East China University of Science and Technology, Shanghai 200237, PRC
Xingsheng Gu, No. 130 of Meilong Road, Shanghai 200237
xsgu@ecust.edu.cn

Abstract. Measurement data usually do not reflect actual chemical processes correctly because of inevitable errors in measurement, which is known as unbalance of measurement data. Data reconciliation and gross error detection are methods of processing measuring instruments that are inconsistent with mass and energy balances. At present, research on data reconciliation mainly focuses on the steady state model of the linear system. However, data reconciliation cannot be implemented in cases of sudden changes in production conditions, operations or instability, or discontinuous data acquisition. An improved Bayesian based on wavelet package denoising for data reconciliation is proposed. After a measurement signal is decomposed into a certain level, the optimal tree is selected with Bayesian classification. Bayesian classification was used to select the node of the optimal tree that would accelerate the calculation speed. The simulation and the coking chemical application show that the improved denoising method contributes to the effectiveness and efficiency of data reconciliation.

Keywords: Data reconciliation, data denoising, wavelet package, Bayesian, optimal tree, coking chemical.

1 Introduction

Measurement data in chemical processes include mass, flow, component, temperature, and pressure. Measurement data collected from chemical processes usually contain inaccurate and imperfect information because of disrepair, leak, and lack of measurements. Data reconciliation and gross error detection are methods of processing measuring instruments that are inconsistent with mass and energy balance.

Data reconciliation was studied under the assumption that the process data are stable. However, data cannot be reconciled under practical conditions despite the utilization of related software products because certain problems, such as fluctuations

* Corresponding author.

in the operation, multi-working conditions, and discontinuous data acquisition, would occur.

An efficient way of processing the historical data should be developed. A study of the denoising method of the Bayesian-based wavelet package revealed that the key in enhancing efficiency was extracting a certainty feature from the raw signal that is to obtaining the trend of historical data to eliminate the inherent system error. The wavelet package is the generalization of wavelets with signal analytical ability. Given the gross error in historical data, a non-Gaussian error would exist in multi-scale detail and approximation coefficients, which makes the distinction between the coefficient of non-Gaussian and the certainty feature.

To overcome these problems, an improved Bayesian-based wavelet package is proposed. This wavelet package would obtain the trend analysis of the historical data that reflects errors more precisely than measurement. This novel strategy includes two key points: (1) the decomposition is performed with a discrete wavelet package; and (2) the noise node is deleted based on a combination of local variance and Bayesian classification. With the application of filtered data, the traditional methods of gross error detection in statistical testing can now reconcile data more efficiently.

2 Review of Previous Work

Data rectification consists of three steps: data reconciliation, gross error detection, and redundancy analysis, of which gross error detection is the key step and is the most investigated among all steps.

The concept of data reconciliation has evolved since it was introduced by Kuehn and Davidson (1961). The criterion used back then was the least squares solution of the reconciled and measurement data under the constraints of mass balance and energy balance.

In certain practical situations, variance/covariance should be obtained from historical data to achieve dynamic data reconciliation. Almsy and Mah presented the calculation method of covariance with a constraint residual error. Using that method as basis, Chen and Morad presented the M estimator of variance (1999). Tona (2005) presented a moving horizon reconciliation with a moving time window approach. Based on the noise model and PCA, the process variable was decomposed by an orthogonal wavelet basis function. The coefficients that were less than the threshold were deleted to reduce random noise with a moving time window. The process data are assumed stable regardless whether a self-developed or a commercial software is used. The main problems that arise in practical application include fluctuations in the operation, multi-working conditions, and discontinuous data acquisition. To overcome these problems, the combination of a data denoising method and data reconciliation is used as the criterion based on historical data.

3 Data Reconciliation

3.1 Principle of Data Reconciliation and Gross Error Detection

In this article, all the measurement data were assumed reconciled, and all unmeasured data were assumed estimable. The reconciled data should be subject to mass balance,

energy balance, and chemical reaction principles. All these can be represented in a constraint equation defined as

$$F(\hat{x}, U) = 0 \quad (1)$$

where \hat{x} is the vector of measurement data, U is the vector of unmeasured data or data to be estimated, and F represents all the constraints. The data reconciliation can be represented as the least square solution between the measurement data and the reconciled data, as in

$$\min_{\hat{x}_i} \sum_{i=1}^n (\hat{x}_i - x_i)^2 / \sigma_i^2 \quad (2)$$

where x_i is the measurement data, \hat{x}_i is the reconciled data, and σ_i is the variance/covariance of the measurement error.

The effectiveness of data reconciliation depends on the measurement data distribution and the modeling of uncertain assumptions. If the gross error in measurement data is unknown, then the result of the data reconciliation might be invalid. The three usual ways of detecting gross error are

- 1) Theoretical analysis of all the factors that caused or produced gross error
- 2) Measurement and comparison of the same process by using different methods
- 3) Statistical hypothesis testing of the measurement data

The third method is the focus of this paper. The basic principle is to test the statistical hypothesis by the significance level of error.

3.2 Data Reconciliation and Gross Error Detection Based on Data Denoising Method

The proposed improved denoising with Bayesian of data reconciliation and gross error detection is shown in Figure 1. The advantage of such a method is the improved monitoring of the instrument's performance by using historical data. The addition of the data denoising method to data reconciliation and gross error detection solves several problems experienced in online applications, such as fluctuations in the operation, data loss, and leak loss, and improves the accuracy of data reconciliation. A novel Bayesian-based wavelet package is used to analyze the trend by using historical data, which can reflect the error of the data more accurately.

The main difference of the novel strategy from the traditional method is that the former obtains posterior Bayesian probability from the historical dataset by collecting data for a period of time. The present data are then decomposed by using a wavelet package. The local variance of each node is compared with the Bayesian probability in the historical data set to generate the optimal tree of the wavelet package. After mean squared error (MSE) evaluation, the reconciliation is enhanced by the improved stable data.

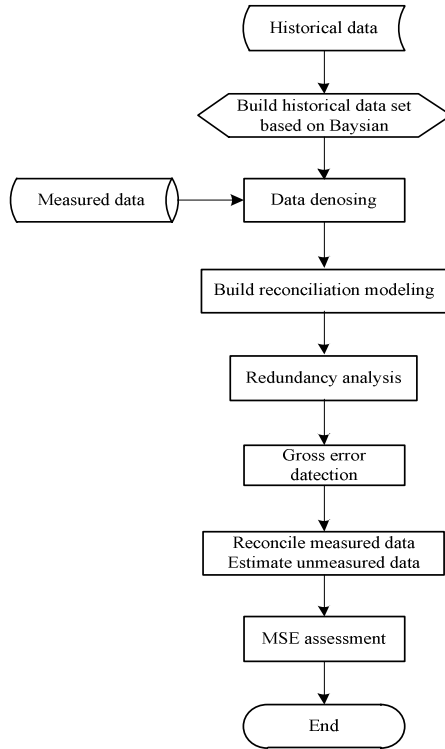


Fig. 1. Data reconciliation through a Bayesian-based wavelet package denoising method

4 Improved Filtering of the Wavelet Package for Data Reconciliation

4.1 Wavelet Decomposition and Reconstruction

Continuous wavelet transform is defined as Eq. (3), where CWT means continuous wavelet transform, which is expressed as $\psi(\tau, s)$.

$$CWT_x^\psi(\tau, s) = \psi_x^\psi(\tau, s) = \frac{1}{\sqrt{|s|}} \int x(t) \psi^* \left(\frac{t-\tau}{s} \right) dt \quad (3)$$

where τ and s represent the translation parameter and extension parameter, respectively; and $x(t)$ is the transformation equation defined as the mother wavelet.

The term wavelet means that a small wave is of limited length. The usual function of a wave is oscillating. The term mother wave means that all kinds of function waveforms were derived from one main function, that is, the mother wavelet is the prototype for producing other window functions. Some common mother wavelets are the Haar and db wavelets.

If a wavelet function satisfies Eq. (4), then the continuous wavelet transform becomes a kind of reversible transform that can be reconstructed, as shown in Eq. (5).

$$c_\psi = \left\{ 2\pi \int_{-\infty}^{\infty} \frac{|\hat{\psi}(\xi)|^2}{|\xi|} d\xi \right\}^{1/2} < \infty \tag{4}$$

$$x(t) = \frac{1}{C_\psi} \int_s \int_\tau \psi_x^\psi(\tau, s) \frac{1}{s^2} \psi\left(\frac{t-\tau}{s}\right) d_\tau d_s \tag{5}$$

where τ is the translation parameter, s is the extension parameter, and C_ψ is the constant in the wavelet transform depending on the mother wavelet. If C_ψ satisfies Eq. (4), then the signal of the time domain can be obtained with a wavelet reconstruction where $\hat{\psi}(\xi)$ is the FFT of $\psi(t)$, and Eq. (4) becomes $\int \psi(t) d_t = 0$.

4.2 Procedure of the Improved Wavelet Package Filtering

Unlike the standard method, a method which combines statistical features and the Bayesian principle is proposed in this paper, as shown in Figure 2. A certain particular

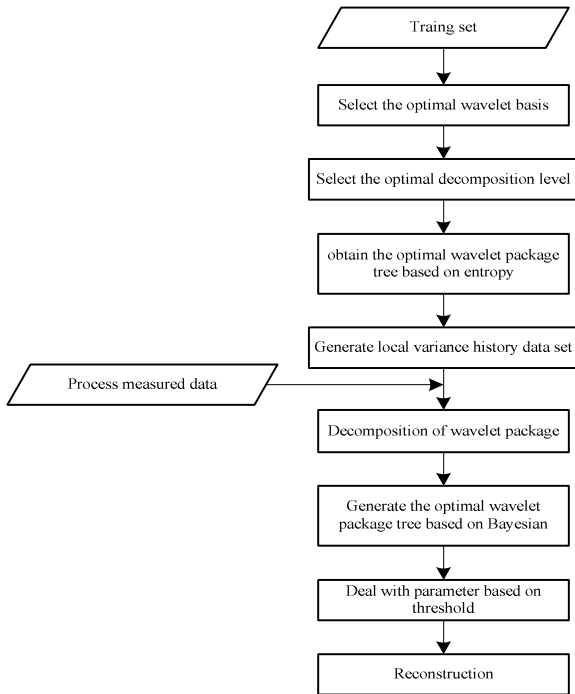


Fig. 2. Bayesian-based wavelet package denoising method

wavelet from a series of wavelet families should be selected as the mother wavelet. The optimal decomposition level is then selected according to the corresponding method. The optimal decomposition tree and the threshold value should also be selected and determined. Finally, the denoised signal is reconstructed, and the denoising performance is assessed based on Shannon's entropy. The application of Bayesian classification on the historical data enables Bayesian probability to determine whether a node is noise or not.

5 Bayesian-Based Wavelet Package Denoising Process

To demonstrate the proposed Bayesian-based wavelet package denoising process, simulation data were obtained from a certain coking chemical process. These data were then denoised based on the novel strategy provided as follows:

(Step 1) Select the wavelet basis for wavelet package decomposition.

The function of a discrete wavelet family is presented as

$$\psi_{mk}(t) = 2^{-m/2} \psi(2^{-m}t - k) \quad (6)$$

where $\psi(t)$ is the mother wavelet, m is the flexible coefficient, and k is the translation coefficient. Any signal can be decomposed into multi-scale form, which is defined as

$$y(t) = \sum_{m=1}^M \sum_{k=1}^N d_y(m, k) \psi_{mk}(t) + \sum_{k=1}^N a_y(L, k) \phi_{mk}(t) \quad (7)$$

where $d_y(m, k)$ is the wavelet coefficient or detail signal under scale m , $a_y(L, k)$ is the wavelet coefficient at the roughest scale, $\phi_{mk}(t)$ is the scaling function, and $\psi_{mk}(t)$ is the wavelet function.

Denoising performance has two key factors: to select which wavelet is the mother wavelet for the wavelet packet decomposition and determining the decomposition level of the wavelet packet. In this paper, the wavelet packet decomposition method was used to decompose under the predefined level 4. The average value η of the absolute value of the detail coefficient is calculated up to decomposition level 4. η represents the degree of similarity between the measurement data of the wavelet expressed and the original process. The selected process data in this paper are shown in the Table 1.

Table 1. Proper mother wavelet and value of η of measurement signals

measurement point	1	2	3	4	5
Best mother wavelet	db10	db10	Haar	bior6.8	Haar
η	1.4382e+06	7.2323e+05	4.2695e+05	2.1555e+05	5.0938e+04

The measurement data in Table 1 were obtained from a certain coking chemical plant. Measurement point 1 represents the flow of the TEXACO outlet. Measurement point 2 represents the flow of the shift converter outlet. Measurement point 3 represents the flow of the synthesizing tower inlet. Measurement point 4 represents the flow of shift converter inlet. Measurement point 5 represents the flow of the ice chest inlet.

(Step 2) Select the decomposition level

The above mentioned method cannot ensure the selection of the best decomposition level because the decomposition level is not always 4. The alternative wavelet would not always be effective at this decomposition level. Hence, Shannon’s entropy is used as the performance index of the decomposition level. The Shannon’s entropy H of a random variable $X = \{x_1, x_2, \dots, x_n\}$ is defined as

$$H(X) = E(I(X)) \tag{8}$$

where E is the expectation function and $I(X)$ is the quantity of information of X . If P is represented as the probability density function of X , then the Shannon entropy’s is defined as:

$$H(X) = \sum_{i=1}^n p(x_i)I(x_i) = -\sum_{i=1}^n p(x_i)\log_b p(x_i) \tag{9}$$

where b is the logarithm base, which is usually 2, the natural constant e , or 10. When $b = 2$, the unit of Shannon’s entropy is bit. When $b = e$, the unit of Shannon’s entropy is nat. When $b = 10$, the unit of Shannon’s entropy is dit. When $P_i = 0$, for some value i , the corresponding value $0\log_b 0$ is 0, and is the same as the extreme value.

(Step 3) Select the optimal tree based on the Bayesian principle

Clipping the original wavelet package tree is important in denoising the measurement data. The original wavelet package decomposition tree of measurement point 1 is shown in Figure 3.

Table 2. Best decomposition level of the measurement points

Measurement point	1	2	3	4	5
Best decomposition level	4	5	6	4	4

Clipping the wavelet package decomposition tree is tantamount to saving the effective node and deleting the node with the error. The clipped decomposition tree can then be reconstructed to obtain accurate measurement data. A performance index should be selected to determinate the validity of the node. Given that the average value of white noise is 0 and standard deviation is 1, the local standard deviation of each node is used to detect the white noise of the node.

The local standard deviation of the n th node of the k th signal is shown as

$$\sigma_n^k = \sqrt{\frac{1}{N_n - 1} \sum_{j=1}^{N_n} [c_n^k(j) - \mu_n^k]^2} \tag{10}$$

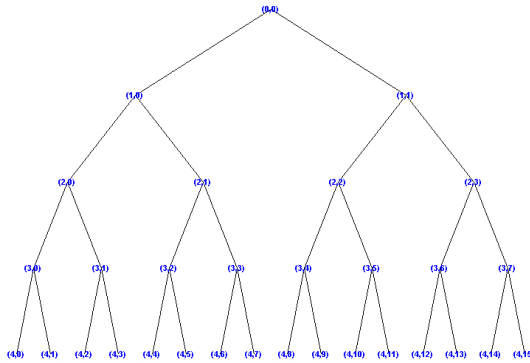


Fig. 3. Binary tree of measurement point 1 after decomposition

where μ_n^k represents the average value of the wavelet coefficient c_n^k of the n th node for the k th training signal, and N_n represents the length of the vector c_n^k .

Figure 4 shows the best tree of measurement point 1 after decomposition by using the local standard deviation and Bayesian criterion.

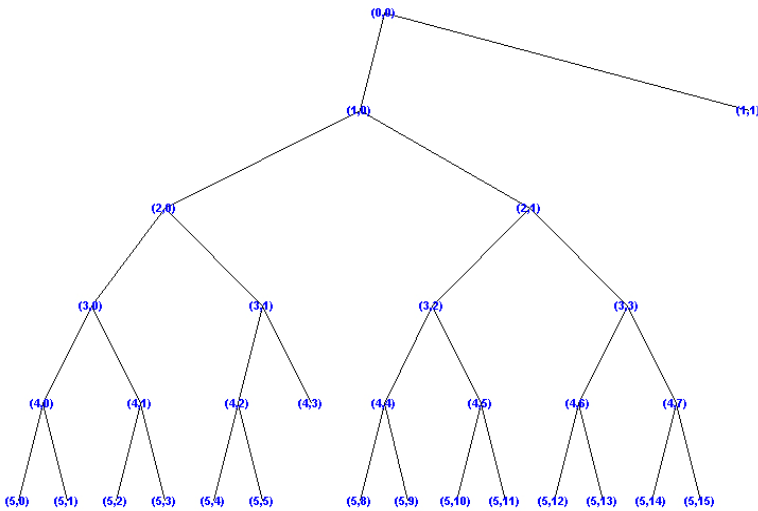


Fig. 4. Best tree of signal 1

(Step 4) Select the threshold

After Step 3, the best tree can be obtained by deleting the noise node. The decomposition coefficient of the saved node is limited by the threshold. The hard threshold can save the decomposition coefficients that are lower than the certain fixed value, whereas the soft threshold can contract all the saved coefficients based on linear criterion.

The soft threshold is defined as

$$u = \begin{cases} \text{sign}(v)(|v|-t), & \text{if } |v| > u \\ 0, & \text{otherwise} \end{cases} \tag{11}$$

where t is the threshold, and v is the wavelet coefficient. The hard threshold is defined as

$$u = \begin{cases} v, & \text{if } |v| > u \\ 0, & \text{otherwise} \end{cases} \tag{12}$$

Usually, the threshold is selected by considering the mathematical calculation aside from the feature of the data itself. Systemic prediction deviation occurs because of the signal error to the soft threshold. Although the prediction deviation can be insignificant, it results in inconsistency and instability in the hard threshold. Thus, a non-negative garrote threshold, which can maintain the advantage of the hard and soft thresholds, is proposed in this paper. It is defined as

$$u = \begin{cases} v - \frac{u^2}{v}, & \text{if } |v| > u \\ 0, & \text{otherwise} \end{cases} \tag{13}$$

(Step 5) Reconstruct the wavelet package

The decomposition coefficients were adjusted to the saved node, as shown in Table 3. The reconstruction of the wavelet package is the inverse of wavelet packet decomposition. The algorithm is shown as

$$\omega_{j,n}(k) = \sum_m \bar{h}(m-2k)\omega_{j+1,2n}(m) + \sum_m \bar{g}(m-2k)\omega_{j+1,2n}(m) \tag{14}$$

If the effectiveness of the training set is more satisfactory or better than the average of the training set, then the denoising parameters are obtained.

Poor performance may be due to the following:

- 1) The signal in the training set cannot include enough measurement data. More data, including various working conditions, are required to extend the training set.
- 2) The denoising parameters were selected independently, which cannot guarantee the optimal choice for the training set.

(Step 6) Evaluating the simulation result

The data in Tables 1 and 2 are used to analyze the signal. A correlation coefficient was considered as the deciding criterion and is shown as

$$CC = \frac{\sum_{i=0}^{N-1} (Y(i) - \bar{Y})(R(i) - \bar{R})}{\sqrt{\sum_{i=0}^{N-1} (Y(i) - \bar{Y})^2 \sum_{i=0}^{N-1} (R(i) - \bar{R})^2}} \tag{15}$$

CC is the correlation coefficient that can express the degree of similarity between denoised data and original data. The value of the variable decomposition level indicates the optimality of the selected wavelet and decomposition level. In this paper, the best tree with wavelet package is better than the tree with wavelet transform shown in Table 3.

Table 3. Correlation coefficient between denoised signals and raw signals

	Point 1	Point 2	Point 3	Point 4	Point 5
CC	0.9753	0.9857	0.9831	0.9781	0.9986

6 Simulation Study

6.1 Process Model

Figure 5 depicts the schematic drawing of the production process of a certain coking chemical plant.

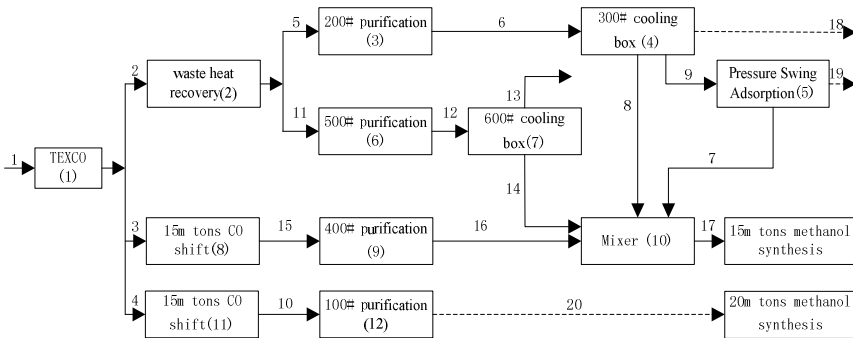


Fig. 5. Flow diagram of production line of a coking plant

The total flow rate balance was considered in the linear model, and a total flow rate balance equation was designed for each operational unit, which is a total of 12 balance equations. Each flow had 7 component balance equations. The component is equal to the product of the total flow rate and the corresponding component percent, that is, of the bilinear component.

6.2 Simulation Results and Evaluations

The case data were obtained from an 8-hour production process in a certain coking plant. The data were used in the integral form over time effect. Table 4 shows the result of data reconciliation after Bayesian-based wavelet package denoising (linear model). The result expresses the balance of the flow rate. The comparison between the measurement data and the reconciliation data is shown in Table 5.

The comparison between the data reconciliation based on Bayesian wavelet package performance and the classical method without wavelet denoising in the industrial application case is provided. The error in the example was assumed independent and subject to uncorrelated Gaussian distributions. The least squares linear programming of

Table 4. Total flow rate after reconciliation (linear model)

Flow No.	Flow before reconciliation (m3/h)	Flow after reconciliation (m3/h)
1	134623	134190
2	24847	24907
3	40615	40713
4	68960	68571
5	14533	14397
6	11765	11803
7	6200	1930
8	565	673
9	5000	4930
10	86864	84284
11	10314	10510
12	8349	8616
13	4400	4714
14	3949	3902
15	49206	49289
16	34303	34667
17	3653.2	41172
18	6200	6200
19	3000	3000
20	58004	58004

Table 5. Reconciliation result of different methods

filtering method	MSE	
	average value	standard deviation
no filtering	0.9991	0.0440
wavelet package	0.8465	0.0395
Bayesian-based wavelet package	0.8463	0.0044

Notes: MSE in the case is based on the average value and standard deviation of 512 measurement data. The decomposition level of wavelet package is 4.

MATLAB was used to resolve the optimization problem of data reconciliation. MSE, shown as Eq. (16), was used to evaluate the least squares expectations between the estimated value of the parameter and the true value of the parameter. A smaller value of MSE translates to more accurate reconciliation data.

$$MSE = \frac{1}{N} \sum_{i=1}^N \sqrt{(y_i - \hat{y}_i)^2 / \sigma_i^2} \quad (16)$$

Table 5 shows the comparison between the data reconciliation results based on variable methods. The results show that the reconciled data based on Bayesian wavelet package is closer to the measurement data. The influence of data fluctuation and instability decreased because of the use of the proposed denoising method.

7 Conclusions

With the consideration of the existence of unstable data in an industrial application, a novel strategy based on wavelet package and Bayesian classification is proposed to denoise process data for data reconciliation. This paper focused on how to remove the noise node of an optimal tree based on Bayesian classification. Sufficient historical data was used to acquire prior knowledge, which served as a criterion for identifying the noise node. Finally, the proposed Bayesian-based wavelet package for data reconciliation was implemented in an actual chemical process, and its application was analyzed extensively in this paper. Thus, the proposed method is proved to be effective for engineering practice.

Acknowledgments. This work was supported by Shanghai Natural Science Foundation (14ZR1409900), National Natural Science Foundation of China (61174040), the Basic Research Project of Shanghai Science and Technology Commission (12JC1403400), and the Shanghai Leading Academic Discipline Project (B504).

References

1. Kuehn, D.R., Davidson, H.: Computer control II, mathematics of control. *Chem. Eng. Prog.* 57(6), 44–47 (1961)
2. Almasry, G.A., Madh, R.S.H.: Estimation of measurement Error Variance From Process Data. *Industrial and Engineering Chemistry Process Design and Development* 23, 779–784 (1984)
3. Crowe, C.M., Garcia Campos, Y.A., Hrymak, A.: Reconciliation of Process Flow Rates by Matrix Projection. I. The Linear Case. *AIChE J.* 29(5), 881–895 (1983)
4. Tong, H., Crowe, C.M.: Detecting persistent gross errors by sequential analysis of principal components. *AIChE* 43(5), 1243–1249 (1997)
5. Narasimhan, S., Jordache, C.: *Data Reconciliation and Gross Error Detection: An Intelligent Use of Process Data*. Gulf Publishing Company, Houston (2000)
6. Romagnoli, J.A., Sanchez, M.C.: *Data Processing and Reconciliation for Chemical Process Operations*. Academic Press, London (2000)
7. Shuanghua, B., McLean, D.D., Thibault, J.: Auto associative neural networks for robust dynamic data reconciliation. *AIChE Journal* 53(2), 439–448 (2007)
8. Ruben, G., Biao, H., Xu, F., Aris, E.: Dynamic bayesian approach to gross error detection and compensation with application toward an oil sands process. *Chemical Engineering Science* 67, 44–56 (2012)
9. Hu, M., Shao, H.: Theory Analysis of Nonlinear Data Reconciliation and Application to a Coking Plant. *Ind. Eng. Chem. Res.* 45(26), 8973–8984 (2006)
10. Wu, S., Zhao, X., Gu, X.: Available estimation of measurement error variance/covariance and sequential compensating algorithm of gross error for data reconciliation. *Control Theory & Applications* 25(4), 717–722 (2008)
11. Bai, S., Jules, T., McLean, D.D.: Dynamic data reconciliation: alternative to kalman filter. *Journal of Process Control* (16), 485–498 (2006)

12. Bakshi, B.R., Bansal, P., Nounou, M.N.: Multiscale rectification of random errors without fundamental process models. *Comp. Chem. Eng.* 21, 1167–1172 (2007)
13. Nounou, M.N., Bakshi, B.R., Goel, P.K., Shen, X.: Improving Principal Component Analysis by Bayesian and Multiscale Estimation. In: *AIChE Annual Meeting*, Los Angeles, CA, Paper 252h (November 2000)
14. Tona, R.V., Benqlilou, C., Espun, A., Puigjaner, L.: Dynamic Data Reconciliation Based on Wavelet Trend Analysis. *Ind. Eng. Chem. Res.* 44(12), 4323–4335 (2005)

Colored Petri Nets-Based Biological Network Reconstruction for Systems Biology

Fei Liu, Zhifa Hu, and Ming Yang

Control and Simulation Center, Harbin Institute of Technology
Harbin 150001, China
liufei@hit.edu.cn

Abstract. The reconstruction of biological networks from experimental data is one of the most important challenges in systems biology. Currently, a network reconstruction algorithm for automatically generating possible Petri net models for a set of experimental data has been given; however, although it is interesting and helpful, it usually results in a number of possible models for a set of experimental data, and the resulted Petri net models are difficult to manage. In order to offer a compact representation of network reconstruction results, in this paper we propose to use colored Petri nets to model all possible networks for a set of experimental data. Specifically, we present a colored Petri nets-based network reconstruction algorithm and implement it in our modeling tool Snoopy. We also give an application of our algorithm by taking the sensory control of sporulation in *Physarum polycephalum* as an example.

Keywords: Systems biology, network reconstruction, colored Petri nets, *Physarum polycephalum*.

1 Introduction

Systems Biology [6] is an emerging scientific discipline in bioscience research, which aims to understand the behavior of a biological system at the system level by means of investigating the behavior and interactions of all of the components in the system. One of the most important challenges in systems biology is the reconstruction of biological networks from experimental data [9, 10]. Specifically, the network reconstruction problem aims to find all possible explanations (models or networks) of a set of experimental results or observations. In order to achieve this, a lot of work [1, 9–11] has been done. Among them, Marwan et. al. [1, 9, 10] developed a Petri nets-based network reconstruction algorithm for automatically generating possible Petri net models for a set of experimental data, which has gained much attention.

However, although it is interesting and helpful, it usually results in a number of possible networks with similar structure for a set of experimental data, and the resulted Petri net models are difficult to manage. In order to alleviate this process and offer a compact representation of network reconstruction results, in this paper, we build our work on [1, 9, 10] and propose to use colored Petri nets to model all possible networks for a set of experimental data.

Colored Petri nets [3, 5] are a colored extension of standard Petri nets [12], where a group of similar components are represented as one component, each of which is defined as and thus distinguished by a color. Colored Petri nets provide parameterized and compact representations of complex biological systems, while they do not lose the analysis capabilities of standard Petri nets. Using colored Petri nets, we can represent each possible (and similar) network as a color. As a result, we can use the structure of only one possible network and the defined colors to compactly represent all possibilities of a network reconstruction problem. We have developed a colored Petri net tool, Snoopy, to support the modeling of biological systems [4] and given a set of case studies [7].

This paper is structured as follows. Section 2 gives a brief introduction to colored Petri nets. After that, Section 3 presents a colored Petri net network reconstruction algorithm, followed by a case study and the conclusions.

2 Colored Petri Nets

2.1 Petri Nets

Petri nets [12] are weighted, directed, bipartite multigraphs, consisting of places, transitions and arcs that connect them. Places usually represent species or any kind of chemical compounds, e.g., genes, mRNA, proteins or proteins complexes, while transitions represent chemical reactions, e.g., association, disassociation, translation, transcription or translocation. For a chemical reaction, its precursors correspond to the preplaces of a transition while its products to the postplaces of the transition. The arcs are directed from places to transitions, or from transitions to places, and their weights indicate the multiplicity of each arc, reflecting e.g., stoichiometries of chemical reactions. The arc weight 1 is usually not labeled explicitly. A place may contain an arbitrary (natural) number of tokens, represented as black dots or a natural number. A distribution of tokens over all places of a Petri net represents a state of it, often called a marking.

A Petri net can be formally defined as $N = \langle P, T, F, W, M_0 \rangle$, where:

- P is a finite, nonempty set of places,
- T is a finite, nonempty set of transitions,
- F is a finite set of directed arcs, $F \subseteq (P \times T) \cup (T \times P)$,
- W is a function that assigns a positive integer in \mathbb{N}_+ to each arc in F , and
- M_0 is the initial marking, which assign to a place a non-negative integer in \mathbb{N}_0 .

A marking M is usually written as a row vector $M(P) = (M(p_1), M(p_2), \dots, M(p_m))$, where $P = \{p_1, p_2, \dots, p_m\}$, which defines a state $\chi \in \mathbb{N}_0^{|P|}$ of a system. $X \subseteq \mathbb{N}_0^{|P|}$ denotes the set of all possible states of a system. $C \in \mathbb{Z}^{|P| \times |T|}$ defines the incidence matrix of a net N , where \mathbb{Z} is the integer set,

$$C(p, t) = W(t, p) - W(p, t), p \in P, t \in T. \quad (1)$$

Further, we can divide the incidence matrix C into two matrices, namely, $C = C^+ - C^-$, where

$$C^+(p, t) = W(t, p), p \in P, t \in T, \tag{2}$$

$$C^-(p, t) = W(p, t), p \in P, t \in T. \tag{3}$$

Suppose $N = \langle P, T, F, W, M_0 \rangle$ is a Petri net and C is the incidence matrix of N . M is a marking of N . $t \in T$ is enabled if and only if the following condition is satisfied,

$$M^T \geq C^-(\bullet, t), \tag{4}$$

where M is written as a row vector indexed by P , and $C^-(\bullet, t)$ denotes the column to which transition t corresponds.

If t is enabled at marking M , it may fire and reach a new marking M' ,

$$M'^T = M^T + C\tilde{t}, \tag{5}$$

where \tilde{t} denoted a column vector indexed by T , where the element to which t corresponds is set to 1 and the others 0.

Furthermore, suppose σ is a transition occurrence sequence, and $\tilde{\sigma}$ is the column vector indexed by T , where the element to which $t \in T$ corresponds is set to the occurrence times of t in σ and the others 0. For example, assume $T = \{t_1, t_2, t_3\}$, and $\sigma = t_1 t_1 t_3$, which means that t_1 fires two times and t_3 one times, and then $\tilde{\sigma} = (2, 0, 1)^T$.

Now if a transition sequence σ is enabled at marking M , it may fire and reach a new marking M' ,

$$M'^T = M^T + C\tilde{\sigma}. \tag{6}$$

Fig. 1 gives two Petri net models, which model two biochemical reaction networks: (a) $P1+P2 \rightarrow P3$, and (b) $P1 \rightarrow P3$ and $P2 \rightarrow P3$, respectively. Three places P1, P2 and P3 represent three substrates, among which there are two reaction possibilities: only one reaction, represented by t1 in Fig. 1(a), and two reactions, represented by t1 and t2 in Fig. 1(b), respectively.

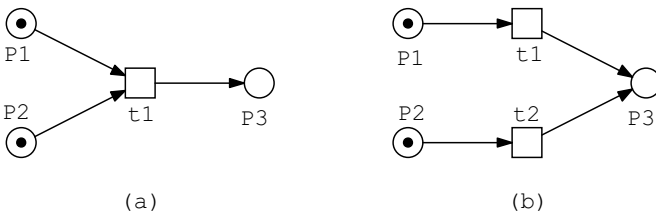


Fig. 1. Two Petri net models, which model two biochemical reaction networks: (a) $P1+P2 \rightarrow P3$, and (b) $P1 \rightarrow P3$ and $P2 \rightarrow P3$, respectively

2.2 Colored Petri Nets

Colored Petri nets (see Fig. 2 for an example) are additionally associated with a set of color sets. Each place is attached to a finite color set, e.g., each place in Fig. 2 gets a color set CS with two colors, 1 and 2. The tokens on a place are not an integer anymore but a multiset expression, and each token is distinguished by a color, e.g., the place P1 has two tokens, $1'1++1'2$, which means one token of color 1 and color 2, respectively. A transition is associated with a guard, which is a Boolean expression. The default guard “true” is usually not labeled. For example, the transition t1 has a guard, $[x = 1|x = 2]$, which means only if x equals 1 or 2, the expression is evaluated to true. The multiplicity of an arc is not an integer anymore, but a multiset expression, e.g., the arc from P1 to t1 has an expression x (an abbreviation of $1'x$). See [8] for the syntax of the expressions used in our colored Petri nets.

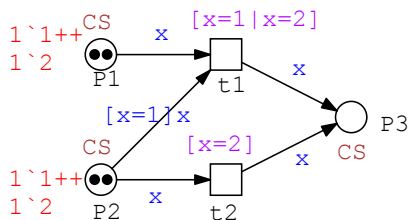


Fig. 2. A colored Petri net model obtained by folding the two Petri net models given in Fig. 1. The declarations: colorset CS = int with 1,2, and variable x :CS.

A colored Petri net can be formally defined as an eight-tuple, $N = \langle P, T, F, \sum, c, W, g, M_0 \rangle$ [7], where:

- $P, T,$ and F have the same meanings as those of standard Petri nets above,
- \sum is the set of color sets,
- c is a color function that assigns a color set $cs \in \sum$ to a place $p \in P,$
- W is a function that assigns to each arc $a \in F$ an multiset expression, which is a multiset on the color set of the corresponding place,
- g is a function that assigns a guard (Boolean expression) to each transition $t \in T,$ and
- M_0 is an initialization function that assigns to each place $p \in P$ a multiset expression, which is a multiset on the color set of the place.

Colored Petri nets can be (automatically) unfolded to uncolored Petri nets, and Petri nets can be (automatically or semi-automatically) folded to colored Petri nets. Therefore, the enabling and firing rules of colored Petri nets can be given similarly as we do for uncolored Petri nets.

3 Colored Petri Nets-Based Network Reconstruction

In this section, we present a colored Petri net network reconstruction approach to implementing the automatic generation of a colored Petri net from a group of possible Petri net models, see Fig. 3 for the general idea. That is, we first reconstruct Petri net models from experimental data using the method given in [1] and then construct colored Petri net models from Petri net models using the method given below. We will describe these two problems, respectively, as follows.

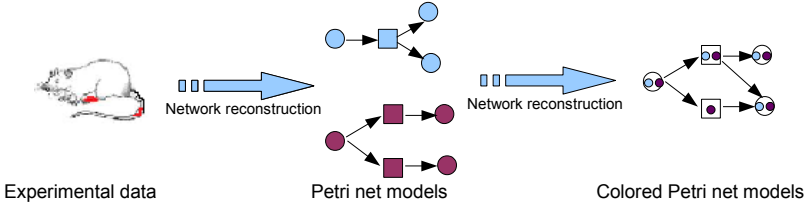


Fig. 3. Colored Petri nets-based network reconstruction process

3.1 Petri Nets-Based Network Reconstruction

The first step of the network reconstruction problem is to generate Petri net models from the given experimental data. For this, we use the network reconstruction algorithm given in [1, 2, 10]. In the following, we will briefly recall how it works.

In order to reconstruct a (Petri net) biological network $N = \langle P, T, F, W \rangle$, we first choose a set of components of interest, consisting of the place set P . We then perform an experiment in some state χ^0 (by external stimuli) to generate an initial state χ^1 , which reflects how the system reacts to the stimuli at certain time point. If we perform k experiments, we can obtain the following occurrence sequence,

$$X(\chi^1) = (\chi^0, \chi^1, \dots, \chi^k). \quad (7)$$

If we consider several initial states χ^1 , denoted by IS , we denote all the sequences by X' :

$$X' = \{X(\chi^1) | \chi^1 \in IS\}. \quad (8)$$

After that, the network reconstruction problem becomes how to generate $N = \langle P, T, F, W \rangle$, given (P, X') . To solve this, we first compute the changes of states (CoS) in the following way,

$$CoS := \{d^i = \chi^{i+1} - \chi^i | i > 0, \chi^i, \chi^{i+1} \in X(\chi^1), \chi^1 \in IS\}. \quad (9)$$

In order to find all the possible networks given (P, X') , we have to find all the possible incidence matrices $C \in \mathbb{Z}^{|P| \times |T|}$, such that

$$C\tilde{\sigma} = d, d \in CoS. \quad (10)$$

Algorithm 1. Colored Petri nets-based network reconstruction algorithm

Require: A set of possible Petri net models PMs, where each $PM = \langle P, T, F, W, M_0 \rangle$ **Ensure:** A colored Petri net model $CM = \langle Pc, Tc, Fc, \sum, Wc, gc, Mc_0 \rangle$

1. //to construct a basic colored Petri net model CM
 2. define a color set CS, and a variable x of CS;
 3. $\sum \leftarrow CS$;
 4. define a new color c in CS;
 5. randomly take a PM from PMs;
 6. **for** each $p \in P$ **do**
 7. assign CS to p ;
 8. assign $M_0(p)^c$ to p ;
 9. $Pc \leftarrow p$;
 10. **end for**
 11. **for** each $t \in T$ **do**
 12. assign $[x = c]$ to t ;
 13. $Tc \leftarrow t$;
 14. **end for**
 15. **for** each $a \in F$ **do**
 16. assign $[x = c]x$ to a ;
 17. $Fc \leftarrow a$;
 18. **end for**
 19. // to incrementally construct CM
 20. **for** each other PM in PMs **do**
 21. define a new color c in CS;
 22. **for** each p in PM **do**
 23. $Mc_0(p) \leftarrow Mc_0(p) + M_0(p)^c$;
 24. **end for**
 25. **if** $t \in PM$ exists in CM **then**
 26. $gc(t) \leftarrow gc(t)|x = c$;
 27. **for** each a that connects t **do**
 28. **if** a exists in CM **then**
 29. $Wc(a).pr \leftarrow Wc(a).pr|x = c$, where pr is the predicate part of a ;
 30. **else**
 31. $fc(a) \leftarrow [x = c]x$;
 32. $Fc \leftarrow a$;
 33. **end if**
 34. **end for**
 35. **else**
 36. $gc(t) \leftarrow [x = c]$;
 37. $Tc \leftarrow t$;
 38. **for** each a of t **do**
 39. $Wc(a) \leftarrow [x = c]x$;
 40. $Fc \leftarrow a$;
 41. **end for**
 42. **end if**
 43. **end for**
-

$\tilde{\sigma} \in \mathbb{Z}_0^{|T|}$ represents the occurrence times of the transitions in T and d means the state (marking) changes due to $\tilde{\sigma}$; see Equation 6. So if $\tilde{\sigma}$ and C are determined, the components T, F, W will be decided, that is, the whole network is generated. See e.g., [1, 2, 10] for more details.

3.2 Colored Petri Nets-Based Network Reconstruction Algorithm

Before giving the algorithm, we have to keep the following points in mind. That is, in the reconstruction of a biological network, the substrates (places) to be considered are fixed for all possible models, and the differences of these models lie in the reactions (transitions and arcs) [1]. The algorithm follows two steps, see Algorithm 1.

Firstly, we randomly choose a Petri net model PM from all possibilities (PMs) as the basic colored Petri net model, and define a color set CS with only one color c and a variable x of the color set CS. We then assign CS to each place, $[x = c]x$ to each arc, and $[x = c]$ to each transition of the basic model. As a result, we obtain a basic colored Petri net model, CM. See Lines 2-18. In fact, at this step, the obtained colored Petri net model CM can be exactly unfolded to the selected Petri net model, PM.

Secondly, for each of the other possibilities, denoted by PM, we add a new color c in CS and update the marking of each place (see Lines 20-24). For each transition t in PM, if t exists in CM, we update the guard of t in CM by adding a new OR (“|”) item, $x = c$, to the old guard $gc(t)$. In this case, for each arc a of t , if a exists in CM, we update the expression of a in CM by adding a new OR item $x = c$ to the predicate part, written as $Wc(a).pr$; otherwise, we add a new arc in CM with the expression $[x = c]x$ (see Lines 25-34). If t does not exist in CM, we add a new transition in CM with the guard $[x = c]$, and for each arc a of t , we add a new arc in CM with the expression $[x = c]x$ (see Lines 36-41). As a result, we obtain the final colored Petri net model of a network reconstruction problem.

4 Case Study

In this section, we give an application of our algorithm by taking the light-induced sporulation of *Physarum polycephalum* [2, 10] as an example. During the cell differentiation process, the sporulation of *Physarum polycephalum* is induced by irradiation with the far-red light (FR). The photoreceptor protein phytochrome (Pfr) that detects the far-red light can turn into its red light-absorbing form (Pr), which can go back to Pfr by the red light (RL). The light-induced reaction (LIR) can not be triggered if the organism is not starving. If the cell is fed with glucose, sporulation is prevented. Without glucose, the induced system goes to the committed state and sporulation takes place. Fig. 4(a) [2] illustrates a common network for this process. From this figure, we can see that we need to find the suitable reactions among three places (substrates), Pfr, Pr and RL (Fig. 4 (a)). Using the network reconstruction approach given in [2, 10], three possibilities (Fig. 4 (b)-(d)) are obtained. See [2, 10] for details.

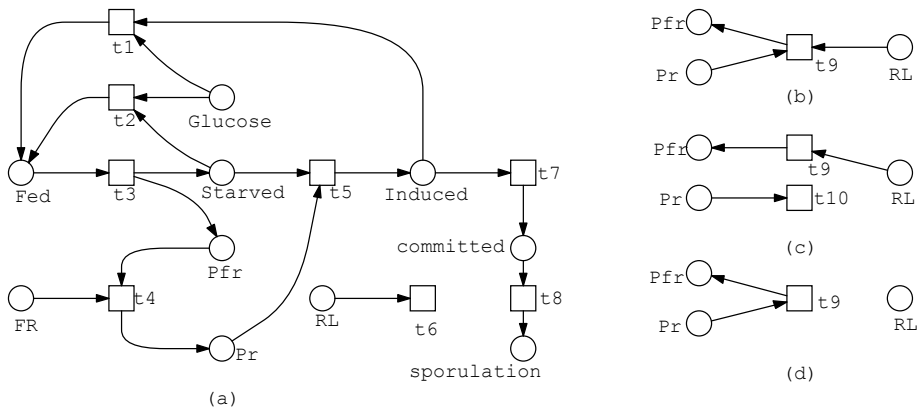


Fig. 4. A Petri net model for the sensory control of sporulation in *P. polycephalum* (a) and three possible subnetworks (b)-(d), which are adapted from [2].

Obviously, we can use colored Petri nets to model the whole system, illustrated in Fig. 5 with the algorithm given above. For readability, we use logic places to separate the main network and the possible networks. To do this, we define a color set CS with three colors, 1-3, to differentiate the three possibilities in (Fig. 4 (b)-(d)).

For each color, which represents one of the three possibilities, we can run animation or simulation to determine the most suitable network model. For example, if we set the rate functions of all transitions to 1, and one token for places, Fed, FR, RL and Glucose, respectively, we obtain one plot for colors 1-3, respectively, illustrated in Fig. 5. According to the plots, we may determine which of the three possibilities is appropriate.

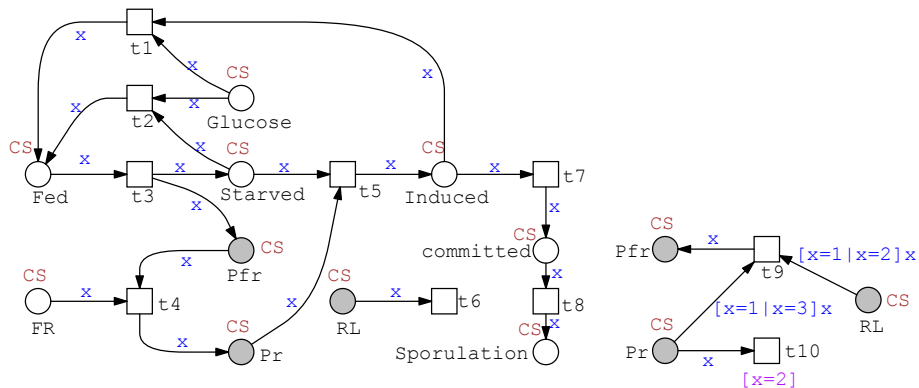


Fig. 5. A colored Petri net model for the sensory control of sporulation in *P. polycephalum* in Fig. 4. The declarations: colorset CS = int with 1-3, and variable x: CS. Logical nodes with identical names serve as connectors; they are multiple representations of the same node used for layout clarity.

5 Conclusions

Network reconstruction is a key problem in systems biology. A good network reconstruction method has to include two important points. First, we need to obtain all possible networks as accurate as possible. For this, the number of the resulted possibilities may be large and thus difficult to manage. So we have to face the second problem, how to increase the readability of the number of the resulted networks and manage them. In this paper, we have presented a colored Petri net-based network reconstruction method for systems biology based on the work of [1, 9, 10]. Using the strong modeling capability of colored Petri nets, we can offer a compact representation of a network reconstruction problem, which would be helpful for biologists to manage and analyze network reconstruction results.

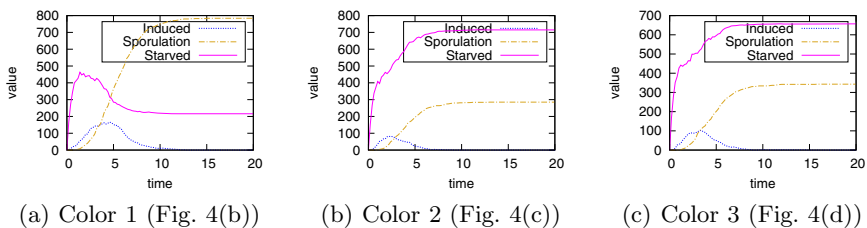


Fig. 6. Plots of three possibilities (colors) in Fig. 4. Each plot is an average run of 10000 stochastic runs.

We have implemented this algorithm in our colored Petri net tool, Snoopy. In a next step, we will continue to improve this algorithm and explore more biological problems that can be modeled by colored Petri nets in order to better support systems biology.

Acknowledgement. This work has been supported by Germany Federal Ministry of Education and Research (0315449H), and National Natural Science Foundation of China (61273226). We would like to thank Monika Heiner for many fruitful discussions.

References

1. Durzinsky, M., Marwan, W., Wagler, A.: Reconstruction of extended Petri nets from time-series data by using logical control functions. *Mathematical Biology* 66, 203–223 (2013)
2. Durzinsky, M., Wagler, A., Weismantel, R.: An algorithmic framework for network reconstruction. *Theoretical Computer Science* 412, 2800–2815 (2011)
3. Genrich, H.J., Lautenbach, K.: System modelling with high-level Petri nets. *Theoretical Computer Science* 13(1), 109–135 (1981)

4. Heiner, M., Herajy, M., Liu, F., Rohr, C., Schwarick, M.: Snoopy - a unifying Petri net tool. In: Haddad, S., Pomello, L. (eds.) PETRI NETS 2012. LNCS, vol. 7347, pp. 398–407. Springer, Heidelberg (2012)
5. Jensen, K.: Coloured Petri nets and the invariant-method. *Theoretical Computer Science* 14(3), 317–336 (1981)
6. Kitano, H.: Systems biology: A brief overview. *Science* 295(5560), 1662–1664 (2002)
7. Liu, F.: Colored Petri Nets for Systems Biology. Ph.D. thesis, Brandenburg University of Technology Cottbus (2012)
8. Liu, F., Heiner, M., Rohr, C.: Manual for colored Petri nets in Snoopy (2012), http://www-dssz.informatik.tu-cottbus.de/publications/btu-reports/Manual_for_colored_Petri_nets_2012_03.pdf
9. Marwan, W., Sujatha, A., Starostzik, C.: Reconstructing the regulatory network controlling commitment and sporulation in *Physarum polycephalum* based on hierarchical Petri net modeling and simulation. *Journal of Theoretical Biology* 236(4), 349–365 (2005)
10. Marwan, W., Wagler, A., Weismantel, R.: A mathematical approach to solve the network reconstruction problem. *Mathematical Methods of Operations Research* 67(1), 117–132 (2008)
11. Papin, J.A., Hunter, T., Palsson, B.O., Subramaniam, S.: Reconstruction of cellular signalling networks and analysis of their properties. *Nature Reviews Molecular Cell Biology* 6, 99–111 (2005)
12. Petri, C.A.: Kommunikation mit Automaten. Ph.D. thesis, Bonn: Institut für Instrumentelle Mathematik, Schriften des IIM Nr. 2 (1962)

Online Anomaly Detection Method Based on BBO Ensemble Pruning in Wireless Sensor Networks

Zhiguo Ding^{1,2}, Minrui Fei¹, Dajun Du¹, and Sheng Xu¹

¹ Shanghai Key Laboratory of Power Station Automation Technology, School of Mechatronics Engineering and Automation, Shanghai University, Shanghai, 200072 China

² College of Mathematics, Physics and Information Engineering, Zhejiang Normal University, Jinhua, Zhejiang, 321004, China

dingzhiguo@shu.edu.cn, mrfei@staff.shu.edu.cn,
{ddj559, xsheng1980}@163.com

Abstract. Online anomaly detection in wireless sensor networks (WSNs) has been explored extensively. In this paper, exploiting the spatio-temporal correlation existed in the sensed data collected from WSNs, an online anomaly detector for WSNs are built based on ensemble learning theory. Considering the resources constrained in WSNs, ensemble pruning based on bio-geographical based optimization (BBO) is conducted. Experiments conducted on a real WSN dataset demonstrate that the proposed method is effective.

Keywords: Online Anomaly detection, Ensemble pruning, Biogeography-based Optimization (BBO), Wireless sensor network (WSN).

1 Introduction

A wireless sensor network (WSN) typically consists of a large number of small, low-cost sensor nodes, which are integrated with sensing, processing and wireless communication capabilities [10], and have been received considerable attention for multiple types of applications. However, wireless sensor network are highly susceptible to suffer various kinds of failures, such as hardware malfunctions, energy depletion, and intrusion, etc, which results in the observations anomalous. Under the context of resource constraints in WSNs, identifying anomalies data timely becomes much more important, which can save the network resources and help decision-making swiftly.

Up to now, there are many anomaly detection techniques specifically developed for WSNs emerged [10]. Ensemble learning, as the first concerns method in machine learning community, has attracted many researchers attention. A large body of theoretical and empirical research shows that ensemble learning can improve the generalization performance. However, ensemble learning method requires build and store multiple detectors which incur large amount of computation and storage resource requirement. Consequently, ensemble pruning is a possible strategy to obtain the better (at least same) performance compared to the initial ensemble. From the perspective of resource saving in WSNs, the pruning [11] is a necessary strategy for anomaly detection in WSNs.

In this paper, considering the spatio-temporal correlation of sensed data in WSNs, a distributed anomaly detection method for WSNs is proposed based on the ensemble learning theory. In order to reduce the high communication requirements caused by broadcast multiple detectors, ensemble pruning based on the BBO [7] is used. The pruned ensemble detector is then used to detect anomalous data.

The remaining of this paper is organized as followed. In section 2, we presented our propose anomaly detection method; in section 3, experiment and results analysis are outlined; Conclusion is presented in section 4.

2 Proposed Online Anomaly Detection Method

2.1 Problem Statement

Generally, the WSNs is composed of a large amount of sensor nodes that can be self-organized into clusters. It can be represented as a graph $G=(V,E)$, where $V=\{v_1,v_2,\dots,v_{|V|}\}$ is a finite set of vertices and $E=\{e_1,e_2,\dots,e_{|E|}\}$ is a finite set of edges, vertex $(v_i,i=1,\dots,|V|)$ and edge $(e_i,i=1,\dots,|E|)$ refers to sensor nodes and the one-hop or multi-hop communication link reachable between sensor v_i and v_j , respectively.

In WSNs, some clusters are formed based on node geographical positions information. In order to concisely describe our proposed anomaly detection method, a relatively small sub-network consisted of some sensor nodes deployed densely is taken into account, which forms a cluster C_i consisting of one cluster head and a number of sensor node represented as CH_i and $N_{i,j}:j=1\dots|C_i|$, respectively.

For one cluster, $C_i=\{CH_i,N_{i1},\dots,N_{im}\}$, which represents a closed neighborhood of node $CH_i,N_{i,j}\in V$. Each sensor node in the sub-network at every time interval Δt measures a data vector. For the cluster head CH_i , the observation is $X^i=(x_1^i,x_2^i,\dots,x_d^i)$, where d denotes the dimension. For the j -th neighbor node, $N_{i,j}$, the observation is $X_k^i=(x_{k,1}^i,x_{k,2}^i,\dots,x_{k,d}^i)$. Each node in the cluster can do the same work and thus scales well to the whole WSNs.

2.2 Spatial and Temporal (Spatio-Temporal) Correlation of Sensed Dataset

For the sensed dataset, we analyzed the spatio-temporal correlation firstly, which will be used later to build online ensemble detector.

The sensor dataset collected is a time series dataset. A time series is a sequence of value $X=\{x(t),t=1\dots n\}$ which is a non-random order. For dataset collected form WSNs, Analysis these observations can help to understand the data trend over time and build the appropriate detector. Before training the detector, the foremost requirement is data pre-processing, some data processing method have been emerged and applied to sequence dataset. The commonly methods, such as polynomial fitting, moving averages, differencing, or double exponential smoothing, are used widely [9]. Considering the limited computation resources, one of efficient non-parametric technique, first

differencing, can be used to eliminate the trend and obtain a stationary time series in WSNs, which can be formulated as:

$$X' = \{x'(s, t) = x(s, t) - x(s, t - 1) : t = 2, 3 \dots n\} \tag{1}$$

Besides, the sensor nodes are always deployed with high density, consequently, the space redundancy existed. A data sequence, $X = \{x(s), s = 1 \dots m\}$, is collected from m sensor nodes with different neighbor locations at a time interval. This dataset can help to understand the spatial correlation structure of data and predict the data value at a location nearby

2.3 Proposed Ensemble Learning Method of Anomaly Detection in WSNs

Considering the spatio-temporal correlations that existed among sensor data and resource constraints in the WSNs, ensemble learning and ensemble pruning were adopted. Our proposed online anomaly detection method includes three parts, ensemble detector training, online anomaly detecting and detector updating, which is depicted in Fig. 1.

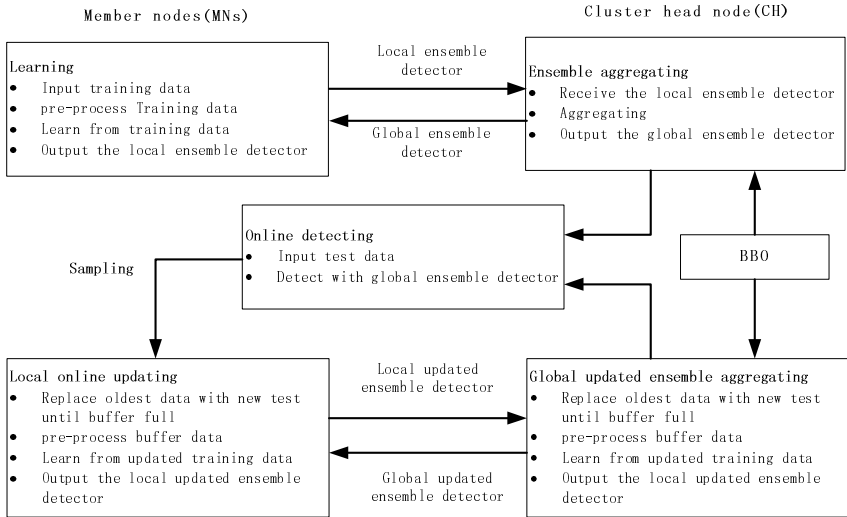


Fig. 1. Ensemble Anomaly Detection Method based on BBO pruning in WSNs

From the Fig. 1, we can see that our proposed method enables each sensor node to globally detect its every new observation normal or anomalous online. Here, distributed detecting is employed to achieve load (communication, computation and storage) evenly in the network and to prolong the lifetime of the whole network. This method can scale well with increase of number of nodes in WSNs due to its distributed processing nature. It has low communication requirements and does not need to transmit any actual observations between cluster head node and its member sensor node which save the communication resource significantly. Next, we described three important procedures mentioned above in detail.

(1) Building the initial Ensemble Detector

Considering the spatio-temporal correlation existed in sensed data in a given cluster, an initial ensemble is constructed by two steps. Firstly, a number of base detectors are firstly trained sequentially for each sensor nodes in a cluster (including the cluster head node itself); In order to build the ensemble detector, the history data are divided into the multiple chunks with the same size and each chunk is used to train a single detector. Because the data distribution maybe changed over time, the previous trained detector maybe useless for the future detection, what’s more, the limited memory resource in the sensor node is another constraint to storage too many previous detectors. In practice, according to the space of memory resource, only the latest multiple detectors are kept to build the initial ensemble for one sensor node.

Once the ensemble detector is built, various techniques can be employed to combine the results of each detector. The common used in literature is the majority vote (for classification problem) and weighted average (for regression problem). In our paper, the final ensemble detection result can be calculated by formula (2), w_i denotes weight coefficient, m denotes the number of node and n the number of individual detector of each node). In our paper, for simplicity, the simple average strategy ($w_i = 1$) is employed to combine the finally result.

$$f_{fm}(x) = \frac{1}{n * m} \sum_{i=1}^{n*m} f_i(x) * w_i \tag{2}$$

(2) Ensemble Pruning based on BBO search

Constrained by the limited communication and storage resource in sensor node, the ensemble pruning is necessary.

Given an initial ensemble anomaly detector, $E = \{AD_1, AD_2, \dots, AD_{n*m}\}$, AD_i is a trained anomaly detector; a combination method C , and a test dataset T . The goal of ensemble pruning is to find an optimal or sub-optimal subset $E' \subseteq E$ which can minimizes the generalization error. Let $f_{i,j}$ ($i=1, 2, \dots, m, j=1, 2, \dots, n$) be the fitness values measured by the general performance of the detectors, such as true positive rate, false positive rate, accuracy and diversity among different detector so on. Obviously, fitness value F , can be defined as formula (3) based on the results of testing data.

The final fitness function can be defined as:

$$Maximize(\sum_{i=1}^{n*m} f_i * w_i), \text{ s.t. } \sum_{i=1}^{n*m} w_i = 1. \tag{3}$$

BBO [7] is a population-based, global optimization method, which has some common characteristics similar to existing evolutionary algorithms (EAs), such as genetic algorithm (GA), particle swarm optimization (PSO), ant colony optimization (ACO) and so on. The details between BBO and these EAs can be seen in [7].

The pseudo-codes of ensemble pruning based on BBO can be described as follows. Here H indicates habit, HIS is fitness, SIV (suitability index variable) is a solution feature.

Algorithm: Ensemble Pruning BBO(E, T)

Input: E - initial ensemble anomaly detector, T - The number of maximization iteration

Output: E' - final ensemble anomaly detector

1: BBO parameter initialization

Create a random set of habitats (populations) $\{H_1, H_2, \dots, H_N\}$;

Compute corresponding fitness, i.e., HSI values;

2: Optimization search process

While (! T)

 Compute immigration rate λ and emigration rate u for each habitat based on HSI ;

 /* Migration */

 Select H_i with probability based on λ_i ;

 If H_i is selected

 Select H_j with probability based on u_j ;

 If H_j is selected

 Randomly select a SIV from H_j ;

 Replace a random SIV in H_i with one from H_j ;

 End if

 End if

 /* Mutation */

 Select an SIV in H_i with probability based on the mutation rate;

 If $H_i(SIV)$ is selected

 Replace $H_i(SIV)$ with a randomly generated SIV ;

 End if

 Re-compute HSI values;

End while

3: Ensemble pruning

Get the final ensemble of anomaly detector E' based on the habitats H_i^* with acceptable HSI .

(3) Online Update and Relearning

Distribution evolving is occurred possibly and detector updating is necessary. Online detector updating will be accompanied by a relearning procedure. In order to save the computation, communication and memory resources, a comprised strategy, i.e., sampling and delay strategy, was adopted [8]. Simply, a probability p can be specified, which samples the subsequent new observation as a training data for new detector. Here some heuristic rule should be employed to guide its value, for example, if the dynamics is relatively stationary, the small p should be used; otherwise, the big p should be chosen. When the buffer of a sensor node was replaced by the new data completely, online update is triggered and new detector is trained. The pseudo-codes of algorithm can be described as follows.

Algorithm: Online Updating (E' , p)

Input: E' - Current pruned ensemble anomaly detector, p - Sampling probability

Output: E^* - Updated pruned ensemble anomaly detector

For each sensor node

Retain the new observation with probability p ;

If buffer is replaced completely

Train new detector and transmit its summary to cluster head;

$E^* = \text{Ensemble_Pruning_BBO}(E', T)$

Broadcast E^* to its member sensor node for subsequent anomaly detection.

3 Experimental and Analysis

3.1 Dataset and Data Pre-processing

IBRL datasets [1] was used in our paper, which was collected using a WSN deployed in Intel Research laboratory at University of Berkeley and commonly used to evaluate the performance of some existing models [2][5][6][8]. This network consists of 54 Mica2Dot sensor nodes which were deployed in a period of 30 days from 29/02/2004 until 05/04/2004. Fig. 2 shows the location of each node in the deployment [5]. Four types of measures data, that is light, temperature and humidity as well as voltage, were collected by this network. Those measurements were recorded in 31s interval. Because the measurement variables have little changes over the time, this dataset is considered a type of static datasets for many researchers. In our experiments, to evaluate the anomaly detection algorithm, some artificial anomalies are created by randomly modify some observations [6].

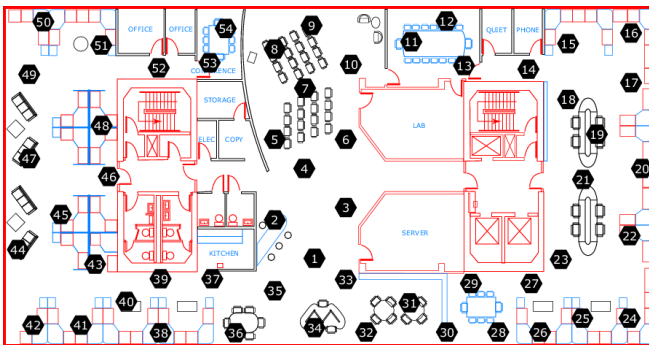


Fig. 2. Sensor nodes location in the IBRL deployment

In our experiment, a cluster (consisted of 4 sensor nodes, i.e., N7, N8, N9 and N10) and dataset (collected from these four nodes on 29th/02/2004) is chosen. The data

distribution can be seen in Fig. 3. From Fig. 3 an obvious fact is that data distribution in a cluster is almost same which are well proved that spatial correlation exists. There are some trivial differences largely due to packet loss. Following accepted practices, we replaced missing data points with the average values of the data points within a certain amount of time [2].

Because the IBRL dataset has no label attributes and regarded as all observation are normal, to evaluate the performance of our proposed method, some anomaly data points should be inserted. In our paper, a number of 30 data points of artificial anomalies for each sensor were injected consecutively in each dataset to calculate the true positive rate (TPR) and false negative rate (FNR) as well as detection accuracy (ACC). The anomalies were generated using a normal randomizer with slightly deviate statistical characteristics from the normal data characteristics [6].

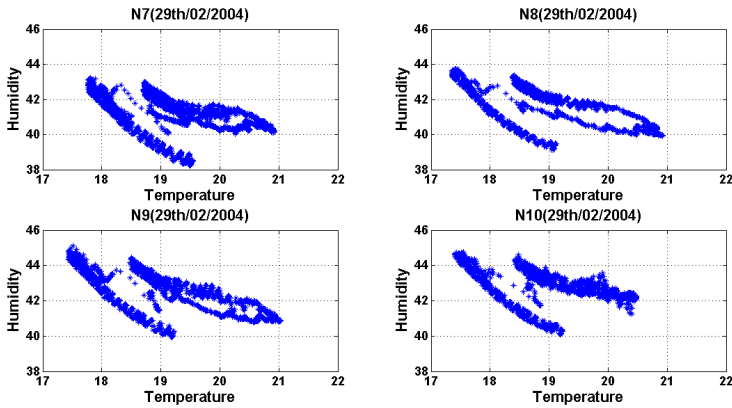


Fig. 3. The data distribution of Node 7, Node 8, Node 9 and Node 10 on Feb. 29, 2004

3.2 Performance Evaluation Metrics and BBO Parameters

In order to evaluate our proposed method, some commonly used performance evaluation metrics for anomaly detection are used in our paper, such as detection accuracy (ACC), true positive rate (TPR) and false positive/alarm rate (FPR). It was described as follows:

$$\text{Accuracy} = \frac{TP+TN}{TP+TN+FP+FN} \quad (4)$$

$$\text{TPR} = \frac{TP}{TP+FN} \quad (5)$$

$$\text{FPR} = \frac{FP}{FP+TN} \quad (6)$$

where TP means number of samples correctly predicted as anomaly class, FP means number of samples incorrectly predicted as anomaly class, TN means number of samples correctly predicted as normal class and FN means number of samples incorrectly predicted as normal class; Further, the TPR and FPR can be calculated by following formulas:

BBO is employed to prune the initial ensemble. For BBO parameter setting, the migration model is same as that present in [7], other parameters are set as: Habitat (population) size $S=30$, the number of *SIVs*(suitability index variables) in each island $n=\{20, 40, 60, 80\}$, maximum migration rates $E=1$ and $I=1$, and mutation rate $m=0.01$, λ, μ are the immigration rate and emigration rate, respectively. The elitism parameter $\rho=2$.

HIS (habitat suitability index) is a fitness function. Here, which is evaluated by *F-measure* (*F-score*), which is a measure of a test’s accuracy. It considers both the precision probability and recall probability of binary classification problem.

$$F - measure = \frac{(1 + \beta^2) precision * recall}{\beta^2 * precision + recall} = \frac{(1 + \beta^2) * TP}{(1 + \beta^2) * TP + \beta^2 * FN + FP} \tag{7}$$

F-measure can be interpreted as a weighted average of the precision and recall, the big *F-measure* means that the precision and recall are both big. Consequently, a good detector is analogous to a habitat with a high *HSI* which is included in the final ensemble detector, and a poor detector is analogous to a habitat with a low *HSI*, which may be discard from the finally ensemble detector. In our paper, the $\beta = 1$.

3.3 Results Presentation and Discussions

One class SVM, due to its attracting advantages, is especially favored by anomaly detection methods [3]. In our paper, it is used to train the base learner of anomaly detection. The dataset for each sensor node was divided into two parts: about 66% are used for training the local detector, the remainder is test set for evaluating our proposed method. Online Bagging [4] is used to build our initial ensemble detector. In our paper, three experiments are done, i.e., local ensemble anomaly detection only considering the temporal correlation of each sensor node, global ensemble anomaly detection considering the spatio-temporal correlation and the global pruned ensemble anomaly detection based on BBO. For the page limitation, only later two experimental results are presented in **Table 1** and **Table 2**, respectively.

Table 1 shows the global detection performance of each sensor node, Here, each member node sent its local ensemble detector to cluster head, combing with the cluster head itself built local ensemble detector, a global ensemble detector is built. Then cluster head broadcast this global ensemble detector, each member node use this global detector to online test the local observation.

Table 1. Global Detection Performance Based on Global-Ensemble Detector

Combined	N7			N8			N9			N10		
Ensemble Size	ACC	TPR	FPR	ACC	TPR	FPR	ACC	TPR	FPR	ACC	TPR	FPR
20	0.9467	0.8333	0.0486	0.9300	0.7778	0.0603	0.9467	0.7500	0.0423	0.9500	0.7857	0.0420
40	0.9700	0.7500	0.0208	0.9433	0.8333	0.0496	0.9710	0.8938	0.0246	0.9650	0.8929	0.0315
60	0.9700	0.8333	0.0243	0.9733	0.8889	0.0213	0.9800	0.9375	0.0176	0.9783	0.9357	0.0196
80	0.9817	0.9583	0.0174	0.9800	0.9444	0.0177	0.9767	0.9375	0.0211	0.9780	0.9714	0.0217

However, sending the local ensemble detector and global ensemble detector between member node and cluster head will arouse massive communication requirement. Consequently, despite the global ensemble detector has a good detection performance, it is impracticable in the real application due to communication cost. Here, ensemble pruning is activated based on BBO for global ensemble detector in cluster head, **Table 2** show the result of detection performance of pruned global ensemble detector. An obvious facts is that the size of global ensemble decreases sharply (at least 60%) and thus save communication resources to some extent, while the detector performance keep the same compared the initial global ensemble detector.

Table 2. Global Detection Performance Based on Global-Ensemble Detector of BBO Pruned

Ensemble	N7			N8			N9			N10		
	ACC	TPR	FPR	ACC	TPR	FPR	ACC	TPR	FPR	ACC	TPR	FPR
Size(BBO pruned)												
14	0.9480	0.8000	0.0458	0.9327	0.7667	0.0567	0.9500	0.8125	0.0423	0.9533	0.8571	0.0420
23	0.9710	0.7750	0.0208	0.9447	0.8000	0.0461	0.9733	0.9250	0.0239	0.9697	0.9143	0.0276
27	0.9713	0.8500	0.0236	0.9683	0.8333	0.0230	0.9810	0.9563	0.0176	0.9797	0.9357	0.0182
32	0.9820	0.9750	0.0177	0.9750	0.8333	0.0160	0.9820	0.9500	0.0162	0.9830	0.9786	0.0168

4 Conclusion and Future Work

Since the ensemble detector is verified to have better performance than single detector, in this paper, exploiting the spatio-temporal correlation existed in the sensed data collected from WSNs, an online ensemble anomaly detector method is proposed. Due to the computation and communication resource constrained in the WSNs, ensemble pruning is employed to identify the optimal subset of detectors based on BBO method. The experiment results on real dataset demonstrated our proposed method effective and efficient.

Acknowledgments. This work is supported by the National High Technology Research and Development Program of China (2011AA040103-7), the National Key Scientific Instrument and Equipment Development Project (2012YQ15008703), National Science Foundation of China (61104089), Science and Technology Commission of Shanghai Municipality (11jc1404000), Shanghai Rising-Star Program (13QA1401600).

References

1. Intel Berkely Reseach Lab (IBRL) dataset (2004), <http://db.csail.mit.edu/labdata/labdata.html>
2. Branch, J.W., Glannella, C., Szymanski, B., Wolf, R., Kargupta, H.: In-network Outlier Detection in Wireless Sensor Networks. *Knowledge and Information Systems* 34, 23–54 (2013)

3. Hejazi, M., Singh, Y.P.: One-class Support Vector Machines Approach to Anomaly Detection. *Applied Artificial Intelligence* 27, 351–366 (2013)
4. Oza, N.C.: Online Bagging and Boosting, Systems, man and cybernetics. In: 2005 IEEE International Conference on, pp. 2340–2345 (2005)
5. Rassam, M.A., Zainal, A., Maarof, M.: An Adaptive and Efficient Dimension Reduction Model for Multivariate Wireless Sensor Networks Applications. *Applied Soft Computing* 13, 1978–1996 (2013)
6. Rassam, M.A., Zainal, A., Maarof, M.: One-Class Principal Component Classifier for Anomaly Detection in Wireless Sensor Network. In: 2012 Fourth International Conference on Computational Aspects of Social Networks, New York, pp. 271–276 (2012)
7. Simon, D.: Biogeography-based Optimization. *IEEE Transactions on Evolutionary Computation* 12, 702–713 (2008)
8. Xie, M., Hu, J., Han, S., Chen, H.: Scalable Hyper-Grid KNN-based Online Anomaly Detection in Wireless Sensor Networks. *IEEE Transactions on Parallel and Distributed Systems* 24, 1661–1670 (2012)
9. Zhang, Y.: Observing the unobservable: distributed online outlier detection in wireless sensor networks, p. 174. University of Twente, The Netherlands (2010)
10. Zhang, Y., Meratnia, N., Havinga, P.: Outlier Detection Techniques for Wireless Sensor Networks: A survey. *IEEE Communications Surveys & Tutorials* 12, 159–170 (2010)
11. Zhou, Z.H., Tang, W.: Selective Ensemble of Decision Trees, Rough Sets, Fuzzy Sets, Data Mining, and Granular Computing, pp. 476–483. Springer (2003)

The Hemodynamic Comparison of Different Carotid Artery Bifurcation Angles Based on Patient-Specific Models

Yuqian Mei¹, Matthias Müller-Eschner^{2,3}, and Duanduan Chen^{1,*}

¹ Department of Biomedical Engineering, School of Life Science,
Beijing Institute of Technology, Beijing, China

² Department of Diagnostic and Interventional Radiology,
University Hospital Heidelberg, Heidelberg, Germany

³ Department of Radiology, German Cancer Research Center (dkfz), Heidelberg, Germany
duanduan@bit.edu.cn

Abstract. Carotid atherosclerosis is related to cerebrovascular diseases. The anatomic features of the carotid artery may influence the hemodynamics within the vessel and therefore stimulate atherosclerotic process. This paper establishes two three-dimensional patient-specific models of the carotid artery. By changing the bifurcation angle while keeping the physiological morphology of the carotid artery, we investigate the hemodynamic variations and discuss their relationships to atherosclerosis. The results indicate: (i) the volume flow rate ratio of internal-to-external carotid artery decreases while the external-to-common carotid artery angle and the internal-to-common carotid artery angle increase; (ii) the enlargement of the angle (either external-to-common carotid artery angle or internal-to-common carotid artery angle) can reduce the region of low time-averaged wall shear stress ($<0.3\text{Pa}$) on the affected internal or external carotid artery, a positive effect to protect further plaque formations; and (iii) changing of the bifurcation angle presents little effects on the velocity, pressure and wall shear stress distributions in the carotid artery.

Keywords: Carotid artery, bifurcation angle, computational fluid dynamics, hemodynamics.

1 Introduction

Atherosclerosis disease of carotid artery is an important cause of ischemic cerebrovascular events by either representing a source of embolism or locally occluding the internal carotid artery to the brain. The pathogenesis of atherosclerosis and plaques formation has been studied extensively [1-4]. From the physiological perspective, the risk factors related to atherosclerosis include age, sex, hypertension, smoking, and different levels of plasma concentrations of high density lipoprotein cholesterol, uric acid, apolipoprotein and so on [5, 6]. On the other hand, from the biomechanics perspective, the morphology of the blood vessels may induce different hemodynamic

* Corresponding author.

conditions in individual; indeed, previous studies indicate that the geometric feature of bifurcation plays an important role in atherosclerosis disease by influencing the flow condition [7-12]. Moreover, the hemodynamic parameters such as wall shear stress (WSS) has been confirmed highly related to the establishment of atherosclerosis as well [4]. Detailed instantaneous flow field data *in vivo* is difficult to be captured by present medical engineering technology. However, simulation method by computational fluid dynamics (CFD) can represent the real flow environment in the blood vessel and provide detailed quantitative information regarding the mechanical parameters related to atherosclerosis. In the current study, we reconstruct three-dimensional patient-specific models based on the CTA image datasets of two patients. The bifurcation angle is artificially enlarged to investigate its influence on the flow; while the physiological shape of the carotid arteries is maintained. Detailed flow and loading information are reported by solving the three-dimensional unsteady conservation equations of mass and momentum. Velocity, pressure, WSS and the time-averaged WSS are investigated; with the increase of the bifurcation angle, the variations of these physical parameters are discussed.

2 Methods

Institutional review board approval was obtained for this retrospective analysis. The two patients received multidetector computed tomography (MDCT). They were scanned with a Somatom Definition (Siemens Medical Systems, Erlangen, Germany). Scan and reconstruction parameters were as follows: 120kV, 120 ref. mAs, reconstructed slice thickness 1mm, reconstruction increment 0.7mm, pixel spacing 0.5x0.5mm and 90ml contrast medium (iomeprol with 350mg iodine per ml, Imeron 350, Bracco Diagnostics, Princeton, NJ, USA) with 50ml saline chaser.

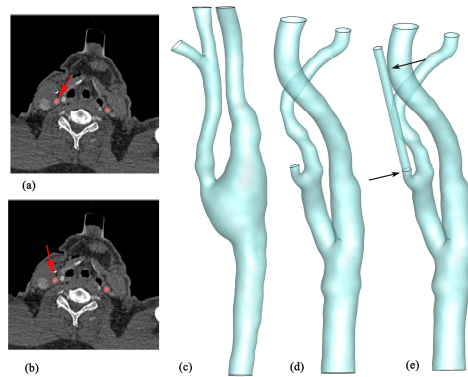


Fig. 1. Figure (a) and-(b) show one slice of the CTA datasets of patient I and II, respectively. The arrows are pointing at the selected carotid artery regions. (c) and (d) displays the reconstructed surface of patient I and II, respectively. And (e) displays the computational model of patient II by artificially extending the superior thyroid artery.

The segmentation and surface reconstruction of the carotid arteries were accomplished by a semi-automatic threshold-based segmentation tool (Amira 5.4, Visage Imaging Inc., USA). As shown in Figure 1a-b, regions of the carotid arteries have been selected in each cross-sectional image of the datasets. Geometries of the vessels were reconstructed, detailed views of which are displayed in Figure 1c-d. The superior thyroid artery in patient II has been artificially extended in order to reduce the pressure difference at the outlets of this artery and the external carotid artery (Figure 1e).

The angle of the internal-to-common carotid artery (named ‘ICAangle’) and that of the external-to-common carotid artery (named ‘ECAangle’) are defined as between the centerline of the common carotid artery and the centerline of the corresponding internal or external carotid artery, as shown in Figure 2a. The ICAangle and ECAangle are assigned in the range of 8-80° and 10.5-56.5°, respectively [14, 15].

The reconstructed geometries are meshed by ICEM CFD 14.0 (ANSYS 14.0 Inc, Canonsburg, USA) with tetrahedral elements in the core region and prismatic cells in the boundary layer near the vessel wall (8 layers of prismatic cells define the near-wall region). This results in a total of 1798519 cells and 1532691 cells for the models of patient I and patient II, respectively. Studies with finer grids (patient I: 4765582 cells; patient II: 5532688 cells) are conducted on the two models with original bifurcation angle, and the independency of grid is confirmed; thus, the baseline resolution of the grid is employed.

Numerical simulation was performed by a Finite Volume solver, CFD-ACE (ESI-Group, France) by solving the transport equations - the Navier-Stokes equations. The blood flow was treated as an incompressible and Newtonian with a density of 1050kg/m³ and a dynamic viscosity of 0.0035Pa·s [16-20]. A second order accurate discretization (central differences) was used to solve the flow velocity and a laminar model of the flow was applied during the computation [21, 22]. Algebraic MultiGrid acceleration was employed and the SIMPLEC-type pressure correction was used for pressure-velocity coupling [23, 24]. Pulsatile flow information was derived from the waveforms described in older human subjects [25]. Parabolic velocity profile was applied at the inlet of common carotid artery (CCA) [26], and the maximum velocity at the inlet along the centerline of CCA was calculated based on the instantaneous volumetric flow rate, as represented in Figure 3. Vessel boundaries were assumed non-compliant. No-slip boundary conditions were imposed at the walls, and zero-pressure boundary conditions were applied at the outlets of internal carotid artery (ICA), external carotid artery (ECA) and their branches.

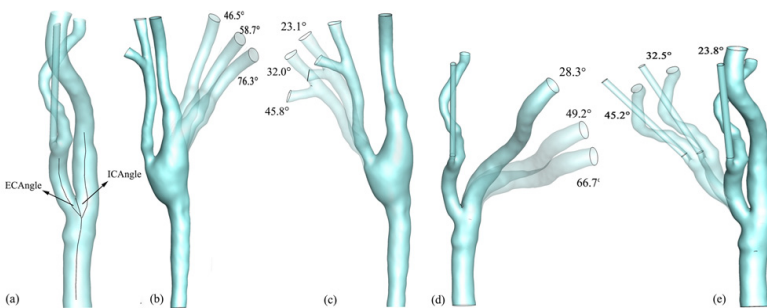


Fig. 2. (a) Rescripts the definition of ECAngle and ICAngle. (b-c) show the variations of ICA angle and ECA .angle of patient I and (d-e) present the same variations of patient II.

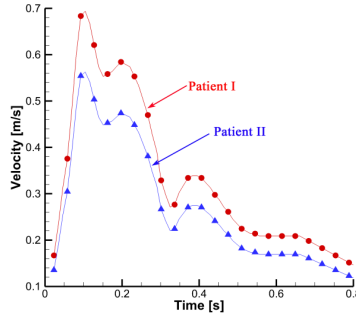


Fig. 3. The variation of the maximum velocity at the inlet for each model. displays the cross-sectional velocity profiles of the inlet at the common carotid artery.

3 Results and Discussions

The flow patterns, by drawing the streamlines, at systolic peak of patient I and II based on the original configurations of the carotid arteries are presented in Figure 4a-b. Fairly organized flow is presented throughout the vessel. Relatively high velocities (0.36–0.59 m/s) are shown along the centerline of CCA and ICA in both cases, indicating strong blood transports (with high flow rates) in these vessels. Relatively low velocities are presented at the carotid bulb in patient I, due to the widened shape of this region. By increasing the IC Angle and the EC Angle, the change of the flow condition in the carotid artery is trivial. The maximum variation of the velocity magnitude in the IC Angle altering models are 3.2% and 2.2% respectively for patient I and II; and the maximum variation of the velocity magnitude in the EC Angle altering models are 3.5% and 0.34% for patient I and II, respectively. Figure 4c-f, by drawing the streamlines, display the flow pattern at systolic peak of patient I and II when the maximum variation of the velocity magnitude presents.

In the study of pressure distribution, consistent to the flow patterns, relatively high pressure (220 Pa) is shown at the carotid bulb in patient I, where vortical flow with low velocities presents. However, in patient II, pressure gradually decreases along the stream path, from inlet at the CCA (about 290 Pa) to the outlets at ICA and ECA (zero pressure) and the pressure in the carotid bulb is about 250 Pa. The change of the pressure distribution in the carotid artery with increasing IC Angle and EC Angle is also small. The maximum variation of the pressure in the IC Angle altering models are 2.1% and 1.9% respectively for patient I and II; and that of the EC Angle altering models are 1.05% and 2.4% for patient I and II, respectively.

The WSS distribution at systolic peak is also studied. In the models with original bifurcation angle, the root of ICA and ECA is experiencing high WSS of about 9–13 Pa and relatively low WSS (0–1 Pa) is shown at the carotid bulb. The endothelial cells desquamated from the vessel wall has been identified at WSS levels exceeding 30 Pa while low levels WSS increased endothelin production [3, 27, 28]. In this study, the maximum WSS in all of the computational models is less than 20 Pa, while the low WSS presents at the carotid bulb, indicating the vulnerability of this region subject to

endothelin production. Variations of WSS are investigated in the models with changing ICAnge and ECAnge. Similar to the results of flow pattern (velocity magnitude) and pressure distribution, the maximum variation of the WSS is small (6.5Pa), indicating the enlargements of ICAnge and ECAnge have little effects on the velocity, pressure and WSS distributions in the carotid artery.

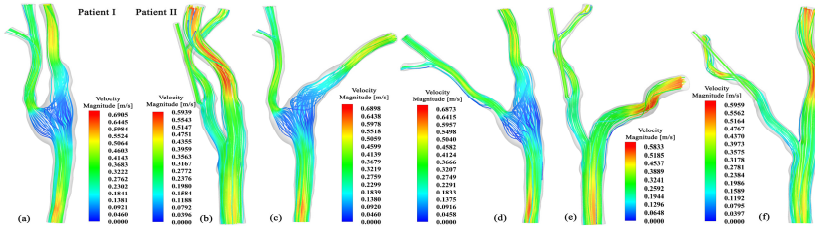


Fig. 4. The flow patterns at systolic peak of patient I and II (the original configurations) and the flow pattern at systolic peak of patient I and II when the maximum variation of the velocity magnitude.

To further investigate the influence of the bifurcation angles on the hemodynamics of carotid artery, we study the time-averaged WSS (TAWSS), which represents the effect of pulsatile flow-induced shear forces on the arterial walls. The TAWSS can be defined as $TAWSS = \left\| \frac{1}{T} \int_0^T \tau dt \right\|$, where T represents a cardiac cycle and τ denotes

the instantaneous WSS vector. Figure 5a-c and 5g-i display the TAWSS distributions for ECAnge changing models in patient I and ICAnge changing models in patient II, respectively, over a complete cardiac cycle. In order to clearly present the low TAWSS distribution, the color map is limited within the range of 0-1 Pa. The results show that low TAWSS (<0.3 Pa) is occurred in the carotid bulb; while, relatively high TAWSS (2.29Pa) is happened near the bifurcation. Low TAWSS less than 0.5Pa may stimulate atherogenic phenotype indicating a higher possibility for the formation of atheromatous plaques at the carotid bulb[32]. In patient I, with the increasing of ECAnge, the area of low TAWSS (about 0.125Pa) at the root of ECA is reducing (Figure 5a-c); while, in patient II, with the enlargement of ICAnge, the area of low TAWSS (0.147Pa) at the root of ICA is reducing. Correspondingly, the with the angle increasing, smoother streamlines are shown in these regions (Figure 5d-f and 5k-m shows the flow pattern at these regions for patient I and II, respectively). The results indicate that the enlargement of the ICAnge and ECAnge can reduce the region of low TAWSS on the affected internal or external carotid artery and therefore protect these regions from further plaque formations.

The volume flow rate of ICA and ECA at the proximal region over a cardiac cycle is investigated. And the ICA-to-ECA volume flow rate ratio is calculated in each model. Table 1 shows the magnitudes of changed ICAnge and ECAnge, and the volume flow ratios of the two patients. The results indicate the volume flow rate ratio of ICA-to-ECA decreases while the ICAnge and the ECAnge increase.

Table 1. The table below shows the magnitudes of changed angles and the volume flow ratios of the two patients

	Angle/ICA-to-ECA volume flow rate ratio	
	PatientI[angle°/flow rate ratio]	PatientII[angle°/flow rate ratio]
ECA-1	23.1/1.8617	23.8/3.6715
ECA-2	32.0/1.7841	32.5/3.6564
ECA-3	45.8/1.7573	45.2/3.6242
ICA-1	27.5/1.8778	28.3/3.4956
ICA-2	46.5/1.7565	49.2/3.4586
ICA-3	58.7/1.6959	66.7/3.4378
ICA-4	76.3/1.6867	--

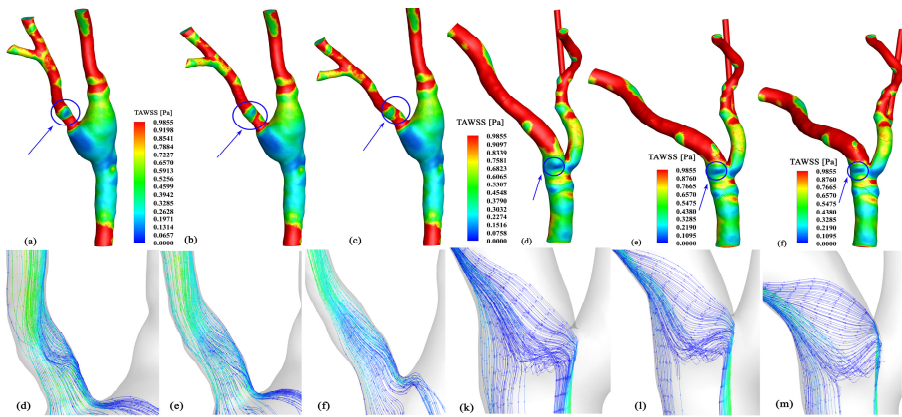


Fig. 5. (a-c, h-j) display the low TAWSS distribution changed regions where especially revealed by the velocity streamlines in the corresponding regions(d-f, k-m).

4 Conclusions

In this study, we establish three-dimensional patient-specific models based on the CTA image datasets of two patients and artificially enlarge the ICAngle and ECAngle to investigate their influence on the flow and other mechanical parameters. The physiological shape of the carotid arteries is well maintained at the same time, in order to produce a realistic simulation environment. Flow patterns, volume flow rate, and loading distributions are quantitatively analyzed and their variation with the enlargement of ICAngle and ECAngle of patient I and II is discussed. Our results indicate that: (i) the volume flow rate ratio of the internal-to-external carotid artery decreases while the ICAngle and ECAngle are enlarged; (ii) areas with low TAWSS on the angle-changing internal or external carotid artery is reduced with the increasing ICAngle or ECAngle, while, in the unaffected carotid artery branch, the hemodynamic parameters nearly remains unchanged; and (iii) the enlargement of ICAngle and ECAngle

present little effects on the variations of the velocity magnitude, pressure and WSS in the carotid artery.

Acknowledgements. This work is supported by the National Natural Science Foundation of China (31200704 and 81371647). DC would like to acknowledge the ESI Group and Mr. Xiangde Zhu for the use of CFD-ACE+, ANSYS Inc. for the use of ICEM, and Visage Imaging Inc. for the use of Amira.

References

1. Schmidt-Trucksäss, A., Huonker, M.: Assessment of atherosclerotic arterial changes in the carotid artery with noninvasive ultrasound. *Z Kardiol.* 81, 124–129 (2000)
2. Caroline Cheng, D.T., van Haperen, R., van der Baan, A., Grosveld, F., Daemen, M.J.A.P., Krams, R., de Crom, R.: Atherosclerotic Lesion Size and Vulnerability are Determined by Patterns of Fluid Shear Stress. *Circulation* 113, 2744–2753 (2006)
3. Dirksen, M.T., van der Wal, A.C., van den Berg, F.M., van der Loos, C.M., Becker, A.E.: Distribution of Inflammatory Cells in Atherosclerotic Plaques Relates to the Direction of Flow. *The American Heart Association* 98, 2000–2003 (1998)
4. Wakhloo, A.K., et al.: Hemodynamics of Carotid Artery Atherosclerotic Occlusive Disease. *Journal of Vascular and Interventional Radiology* 15(1), S111–S121 (2004)
5. Crouse, J.R., Toole, J.F., McKinney, W.M., Dignan, M.B., Howard, G., Kahl, F.R., McMahan, M.R., Harpold, G.H.: Risk factors for extracranial carotid artery atherosclerosis. *Stroke* 18, 990–996 (1987)
6. Willeit, J., Kiechl, S.: Prevalence and risk factors of asymptomatic extracranial carotid artery atherosclerosis. A population-based study. *Arteriosclerosis, Thrombosis, and Vascular Biology* 13(5), 661–668 (1993)
7. Peterson, R.E., Livingston, K.E., Escobar, A.: Development and distribution of gross atherosclerotic lesions at cervical carotid bifurcation. *Neurology* 10(11), 955–959 (1960)
8. Zarins, C.K., et al.: Carotid bifurcation atherosclerosis. Quantitative correlation of plaque localization with flow velocity profiles and wall shear stress. *Circulation Research* 53(4), 502–514 (1983)
9. Thomas, J.B., et al.: Variation in the carotid bifurcation geometry of young versus older adults: implications for geometric risk of atherosclerosis. *Stroke* 36(11), 2450–2456 (2005)
10. Resch, K.P.A.M.: Numerical flow studies in human carotid artery bifurcations: basic discussion of the geometric factor in atherogenesis. *J. Biomed. Eng.* 12, 111–123 (1990)
11. Landis, G.S., Faries, P.L.: A critical look at “high-risk” in choosing the proper intervention for patients with carotid bifurcation disease. *Semin. Vasc. Surg.* 20(4), 199–204 (2007)
12. Phan, T.G., et al.: Carotid artery anatomy and geometry as risk factors for carotid atherosclerotic disease. *Stroke* 43(6), 1596–1601 (2012)
13. Affeld, K., et al.: Variability of the Geometry of the Human Common Carotid Artery. A Vessel Cast Study of 31 Specimens. *Pathology - Research and Practice* 194(9), 597–602 (1998)
14. Goubergrits, L., et al.: Atherosclerosis in the human common carotid artery. A morphometric study of 31 specimens. *Pathol. Res. Pract.* 197(12), 803–809 (2001)
15. Goubergrits, L., et al.: Geometry of the human common carotid artery. A vessel cast study of 86 specimens. *Pathol. Res. Pract.* 198(8), 543–551 (2002)

16. Hayase, H., Tokunaga, K., Nakayama, T., Sugiu, K., Nishida, A., Arimitsu, S., Hishikawa, T., Ono, S., Ohta, M., Date, I.: Computational Fluid Dynamics of Carotid Arteries After Carotid Endarterectomy or Carotid Artery Stenting Based on Postoperative Patient-Specific Computed Tomography Angiography and Ultrasound Flow Data. *Neurosurgery* 68(4), 1069–1101 (2011)
17. Cebal, J.R., et al.: Blood Flow Modeling in Carotid Arteries with Computational Fluid Dynamics and MR Imaging. *Academic Radiology* 9(11), 1286–1299 (2002)
18. Xue, Y., Gao, P., Lin, Y., Dai, C.: Preliminary Study of Hemodynamics in Human Carotid Bifurcation by Computational Fluid Dynamics Combined with Magnetic Resonance Angiography. *Acta Radiol.* (7), 787–797 (2007)
19. Jou, L.-D., et al.: Wall Shear Stress on Ruptured and Unruptured Intracranial Aneurysms at the Internal Carotid Artery. *AJNR Am J. Neuroradiol* 29, 1761–1767 (2008)
20. Schirmer, C.M., Malek, A.M.: Wall Shear Stress Gradient Analysis within an Idealized Stenosis Using Non-Newtonian Flow. *Neurosurgery* 61, 853–864 (2007)
21. Xue, Y.J., et al.: Preliminary study of hemodynamic distribution in patient-specific stenotic carotid bifurcation by image-based computational fluid dynamics. *Acta Radiol.* 49(5), 558–565 (2008)
22. Younis, H.F., et al.: Hemodynamics and wall mechanics in human carotid bifurcation and its consequences for atherogenesis: investigation of inter-individual variation. *Biomech. Model Mechanobiol* 3(1), 17–32 (2004)
23. Lonsdale, G., Schuller, A.: Multigrid Efficiency for Complex Flow Simulations on Distributed Memory Machines. *Parallel Computing* 19(1), 23–32 (1993)
24. Vandoormaal, J.P., Raithby, G.D.: Enhancements of the Simple Method for Predicting Incompressible Fluid-Flows. *Numerical Heat Transfer* 7(2), 147–163 (1984)
25. Hoi, Y., et al.: Characterization of volumetric flow rate waveforms at the carotid bifurcations of older adults. *Physiol. Meas.* 31(3), 291–302 (2010)
26. Campbell, I.C., et al.: Effect of inlet velocity profiles on patient-specific computational fluid dynamics simulations of the carotid bifurcation. *J. Biomech. Eng.* 134(5), 051001 (2012)
27. Zarins, C.K., Giddens, D.P., Bharadvaj, B.K., Sottiurai, V.S., Mabon, R.F., Glagov, S.: Quantitative correlation of plaque localization with flow velocity profiles and wall shear stress. *Circ. Res.* 53, 502–514 (1983)
28. Augst, A.D., Ariff, B., McG Thom, S.A., Xu, X.Y., Hughes, A.D.: Analysis of complex flow and the relationship between blood pressure, wall shear stress, and intima-media thickness in the human carotid artery. *Am. J. Physiol. Heart Circ. Physiol.* 293, H1031–H1037 (2007)

Design and Implementation of a Plant Morphology Modeling System Based on Evolutionary Strategy

Weilong Ding^{1,2}, Chen Hu¹, Fuli Wu¹, and Nelson Max²

¹College of Computer Science & Technology, Zhejiang University of Technology, 310023, Hangzhou, China

²Department of Computer Science, University of California, 95616, Davis, USA
{wlding, chenhu, fuliwu}@zjut.edu.cn, max@cs.ucdavis.edu

Abstract. In order to improve the efficiency of virtual plant modeling based on L-systems, a plant morphology modeling system using an evolutionary strategy is designed and implemented. First the axiom and the productions of an L-system are mapped to chromosomes, and then the initial population is designed. Genetic operators are designed to generate the individuals of a new population. The fitness function considers two aspects: the plant outline, and the internal branching. Using the fitness function for evolution, the L-system's production rules for the target plants can be obtained. Key implementation techniques, function modules, and interfaces of the system are briefly introduced. Finally, the validity of the system is tested in detailed experiments.

Keywords: L-system, gene expression programming, genetic algorithm, plant morphology.

1 Introduction

Current research on virtual plants has involved the fields of computer science, applied mathematics, botany, biology and ecology. Virtual plant models can not only reproduce natural landscape, but also model the growth condition of plants under the influence of different physiological and ecological factors.

L-systems, which are effective approaches to model plant morphology [1], [2], are widely used to create virtual plant models. With the continuous development of L-systems, some plant modeling packages, which are based on, them have begun to appear. A common characteristic of this kind of software is that the user must know how to set up the parameters of the axioms and the productions before modeling. To simulate a target plant, an L-system needs dozens of production rules. Most of the rules and parameters are artificially determined by trial and error. Because you don't know what shapes will be produced by using the parameters you set up, to get the ideal target shape you need many iterations, so this manual method is blind and inefficient. Therefore, it is desirable to automatically obtain L-system rules and parameters to match the simulated target.

In this paper, we propose a plant morphology simulation algorithm based on an evolutionary strategy and develop a system based on the proposed algorithm. On the

basis of gene expression programming (GEP), the system first automatically obtains the production rules of the L-system, and then simulates the morphological structure of a specific plant. The system established in this paper does not need the user to control the L-system directly; the user need only choose one plant type from the templates provided by the system. Through the interactions between the user and the computer, the system can generate various plant shapes. The method overcomes the blindness and inefficiency of manipulating the L-system directly.

2 Related Work

To visually simulate plant morphology there are at present process-based methods, image-based methods, and reconstruction methods based on large-scale measurement data [3]. The process-based methods use a mathematical model to simulate plant growth or morphological characteristics, which include different types of L-systems, reference axis technology, dual-scale automaton model, fractal methods, iterated function systems and particle systems, etc. Although these models have their advantages, they all need to set up the rule parameters. The traditional methods of manual parameter acquisition are inefficient and difficult. Image-based modeling methods [4] directly construct 3D plant structure through the analysis and processing of one or more images of a plant. Compared with process-based or measurement-based methods, these methods are relatively simple, and the simulated plants they produce have a very strong sense of reality. However, these methods can only imitate a specific static plant; they are not suitable for simulating dynamic growth. Moreover, their modeling process requires a large amount of manual intervention. The advantage of the static structural model to simulate the shape of a plant [5] is its ability to accurately describe the morphology of specific plants, which can be used to study the quantitative and qualitative characteristic related to the plant spatial structure. However, these methods require lots of manual measurement data and a lot of time to process data.

The scholars of CIRAD studied a method to extract plant growth rules by using statistical analysis and pattern recognition, and applied it in a sub-system of the AMAP software, named AMAPmod [6]. Since the evolution of plant topological structure and the patterns or rules of geometry change are not known in advance and also are very complex, fully and accurately extracting plant growth rules needs other intelligent technologies, instead of simply relying on pattern recognition.

In order to simulate a specific 2D plant structure, papers [7], [8], [9] studied the problem of how to extract the production rules and axiom for a simple L-system. Since the simulated target is a simple 2D plant form, the chromosome encoding and genetic operation forms were quite simple. How to automatically evaluate the fitness of an individual in the system is a key problem. Ochoa [7] designed a specific fitness function, considering the height, left-right proportion, leaf area, structural stability, and bifurcation points of simulated plants. Using the distance from the simulated plants to a specified two-dimensional plant structure, Bian *et al.* [8], [9] designed a fitness function for two-dimensional simulation models. But evaluating the individual fitness

of a three-dimensional simulated plant was not considered in their studies. By using an evolutionary algorithm, Hemberg and O'Reilly [10] generated the production-rule set of a Map L-system to simulate the growth of 3D digital surfaces. Venter and Hardy [11] proposed a 3D plant simulation model based on genetic programming. The model uses a "genotype" which is expressed by an L-system to describe a specific plant shape, and then forms different "phenotypes" through the graphical interpretation of the L-system. The goal of their study is to obtain a large number of different plant shapes, and to avoid or reduce the complexity of setting up the parameters for the axiom and the productions of an L-system. Since there is no explicit optimization target, their model did not use a fitness evaluation function, so the best individual has to be chosen by man-machine interactions according to the visual effects of individual plants. Obviously, the search efficiency of this manual method is very low.

3 Evolution of L-System Rules Based on GEP

3.1 Genetic Encoding and Initial Population

An L-system is a string rewriting system. Its axiom and productions are composed of characters. Therefore, when the axiom and the productions of an L-system are mapped to chromosomes, symbols are mostly used to do the encoding for individual chromosomes [8, 9]. Some scholars integrated different encoding techniques in one chromosome. For example, Venter and Hardy [11] mixed the technique of symbol encoding with the technique of binary encoding. This hybrid encoding is convenient for the iteration of the L-system's string, and also uses the advantage of binary coded genes. Therefore, this paper also uses this hybrid chromosome coding method. Each individual is formed by chromosomes $\{c_0, c_1 \dots c_{nc-1}\}$, where nc represents the number of chromosomes. Each chromosome is also composed of multiple genes $\{g_0, g_1, \dots, g_{ng-1}\}$, where ng represents the total number of genes in each chromosome. Chromosome c_0 corresponds to the axiom while chromosomes c_1 to c_{nc-1} correspond to the productions of an L-system. Each gene consists of a head and a tail, respectively expressing the real character corresponding to the character set of L-system and the parameters corresponding to the character. In addition, terminal symbols, which are extra bits on the bit string defining the last parameter of the last gene, are added into each chromosome. The size of chromosomes can be changed and using of the terminal symbols will increase the diversity of the individuals.

The individual chromosomes in the initial population are designed through the random combination of characters. According to the rules of L-systems, some combinations may be illegal. If the individuals with illegal style are a large proportion in the population, the search space will become enormous and the efficiency will become very low. In order to improve the effectiveness of the solution space, we add some predefined chromosomes into the initial population. The production rules of those chromosomes are determined through a manual and qualitative way according to the structural characteristics of the target plants, rather than in a completely random manner. The remaining individual genomes are generated through the control of gene g_0 in each chromosome and the number of genes that can generate branches.

3.2 Design of Genetic Operators

We first randomly select an individual and then do some genetic operations, such as crossover, mutation, and transposition, so as to generate the individuals of a new population. By improving the strategy to eliminate the bad individuals, the effects of bad characters can be reduced and the efficiency of the algorithm can be improved.

As a basic genetic operation, crossover between the individuals of a population is used to exchange genes and generate new individuals. According to the difference of crossover positions on two chromosomes, there are some different kinds of gene exchange: one-point crossover, two-point crossover, three-point crossover, and genetic recombination. Genetic material is exchanged based on the unit of a gene, which avoids the separation of the head and the tail of a gene.

Transposition is the movement of a sequence of characters in a chromosome to other positions, which are located in the same chromosome. It has two forms: insertion and gene conversion. The former means that a short character sequence is randomly selected in a chromosome, and then the selected character sequence is used to replace another character sequence in the same chromosome. The latter means that a gene in a chromosome is transferred to the head of chromosome, while the positions of the other genes are moved backward. This operation is only for a single complete gene, to ensure the integrity of the genetic information.

For the evolutionary mechanism, if we consider only the operations of crossover and transposition, the population will become too similar, and have premature convergence, so that the optimal solution cannot be obtained. In order to avoid premature convergence, the mutation operation of the individuals should be taken to make the offspring genes change according to a small probability after the operations of crossover and transposition. The individuals will produce new characters through these changes.

3.3 Fitness Evaluation

A reasonable fitness function can guide the genome evolution, and avoid the loss of excellent individuals and premature convergence of the genetic algorithm. We need to judge whether an individual is similar to the target of plant to be simulated, in order to select a subset of the fittest individuals to produce the next generation. However, due to the complexity of structure of plants it is a challenging task to quantify the similarity between real plants and rebuilt 3D plant models, and then design an appropriate fitness function. In 1998, Ochoa [7] designed an evaluation function as a weighted mean of five elements of a virtual plant: plant height, proportion of left and right, leaf area, stability of the structure, and branching points. Bian et al. [8, 9] designed an individual fitness based on a distance function between the virtual plant and the 2D structure of the target plant. In this function, the number of organs, depth of branching and the distance between organs were considered. Zheng. [12] divided the structure of a tree into left tree, right tree, and middle tree, and then computed the difference of the number of child trees in each branching level using iteration. They took the total difference of branching as the difference of the two trees. The fitness

evaluation function from the studies mentioned above are all for 2D simulation models, and can not evaluate the fitness of 3D simulated plants.

Unlike in the above papers, in this paper we first calculate the similarity between the simulated plants and the real plants, and we consider both the plant outline and the inner details of the plant structures. The three-dimensional convex hull is used to represent the plant outline. In order to evaluate the similarity between the outlines of the real plants and the rebuilt 3D plant models, we compute the 3D convex hulls and project them in different directions to get 2D projections, and then calculate the 3D similarity based on the similarities of these 2D projections. Based on this idea, we designed a coarse-grained fitness function, *Rfitness*, to effectively evaluate the similarity between the simulated plants and the target plants just from the shape of the plant. On the other hand, we propose an algorithm to evaluate the similarity of morphology between the simulated plants and the target plants according to the internal branching structure, which is described by using of geometric attributes of plant organs and topological connections between different organs. These attributes and connections include the average branching angles on the stem, the ratios of cross-sectional area and diameters of the stem to the branches on main stem, the ratio of the plant's width to its height, and the average branching angles of 2nd level branches on 1st level branches. The similarities between these parameters can be calculated first, and then a similarity with a weighted average of these five aspects can be calculated. According to these calculated parameters, we designed a fine-grained fitness function, *Dfitness*, to evaluate the similarity of internal architectures between the simulated plants and the target plants.

Due to the complexity of the structure of plants, the method to calculate the similarity between different plants is also very complicated and needs a lot of words to explain clearly. Limited by the length of this paper, we will specifically explain the details of our method in another paper. Here we only present a brief formula combining these two kinds of fitness values to evaluate the fitness of an individual:

$$Fitness = \alpha * Rfitness + \beta * Dfitness \quad (1)$$

where α and β are empirical constants, which satisfy $\alpha + \beta = 1$. Combining these two fitness functions can help our system to find the optimal individuals, whose outline and internal topologies are both similar to the target plants, so as to generate a detailed simulation of a specific plant.

4 System Implementation

4.1 System Implementation Environment and Parameters Setting

Based on the above methods, we implemented an experimental program on Windows XP, with Visual C++ 2005 as IDE. The program is implemented in C++ with the OpenGL library. The experimental machine has 4GB RAM, an Intel Pentium D 2.67GHz CPU and an Nvidia GeForce 7300GT graphic card. The flowchart of the system is given in Fig. 1.

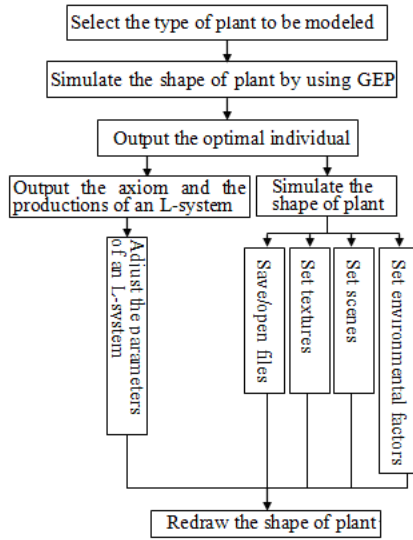


Fig. 1. The flowchart of the system

The number of individuals in the initial population (n_o), the number of chromosomes (nc), the number of genes in a chromosome (ng), the termination condition of evolution, the iteration number of an L-system, and the probabilities of crossover, transposition, and mutation are described in detail in Table 1.

Table 1. Parameters of the algorithm

initial population (n_o)	20
the number of chromosomes (nc)	4
the number of genes in a chromosome (ng)	6
the number of evolutionary generations	100
the iteration number	3
the probability of mutation (p_m)	0.02
the probability of Insert String (p_{is})	0.02
the probability of gene conversion (p_{gt})	0.02
the probability of one-point crossover (p_{1r})	0.2
the probability of two-point crossover (p_{2r})	0.2
the probability of three-point crossover (p_{3r})	0.2

4.2 Main Functions and Main Modules of the System

The system can not only simulate different types of plant morphology, but also simulate the change of plant shapes under the influence of different light environments and mineral resources. It provides a simple and practical plant morphological modeling software for the user. The system also provides various scenes and organ textures for the user to select. It can save the simulation results, as well as open saved plant

morphology files for further modification. The system can be applied to visual simulation, virtual scene generation, and three-dimensional animation. It consists of seven modules:

(1) Preprocessing module

In this module, users can select a predefined plant type as a simulation target. The system can extract the features of the target plant's outline and its internal branching structure.

(2) Genetic algorithm module

In this module, the genetic algorithm is used to create various individuals by using different genetic manipulations, including individual choice, transposition, crossover and mutation, and calculation of the individual fitness. When the algorithm reaches the termination condition after these genetic manipulations, the system invokes the morphology output to present the shapes of the best individuals.

(3) Morphology output module

This module is used to draw the shapes of plant morphology according to the rule parameters of the optimal individuals.

(4) Parameter modification module

This module allows the user to modify the parameters of the L-system so as to create ideal plant shapes.

(5) Graphics rendering module

The module is used to render the scene. The user can select various scenes and plant organ textures.

(6) Environmental factors setting module

The module can provide interfaces for the users to set up different lighting and distributions of the mineral resources, and let them observe the change of plant morphology in response to different environmental conditions.

(7) File management module

The module provides functions to save the parameters for the evolved individuals, and to open and redraw saved plant morphologies.

4.3 The Interface of the System

The interface of the system includes the unit for selecting the target plant type, the image display unit, the parameter modification unit, the environmental factor setting unit, and the file operations unit. For example, suppose a user wants to simulate a sympodial branching tree, whose shape is shown in Fig. 2. Aiming at this target, he first needs to select a module, which describes the features of sympodial branching from the predefined library of plant shapes. Then the system will generate a 3D plant morphology similar to the target plant and gives its parameters to the user. The user can modify these L-system parameters and the environmental factors of the scene to create different plant shapes. The system interface and simulated results are shown in Fig. 3. Through setting different environment factors, the simulated result will show different morphologies. When the user selects the effect of side light, the created plant shape will change accordingly under the influence of the light source position, as shown in Fig. 4. We modify the topological parameters of the branches according to

their positions on the tree. If the light source is on the left side of a tree, the length and the branching angles of branches on the left side will be increased within a certain range, while those on the right side will be decreased. But if the light is on the right side, the situation is just the opposite. The user can also choose an uneven distribution of resources to observe the distribution and growth conditions of individuals in a region. From these examples, we can see that the system can realistically simulate plant morphologies with different branched structures.



Fig. 2. Target tree

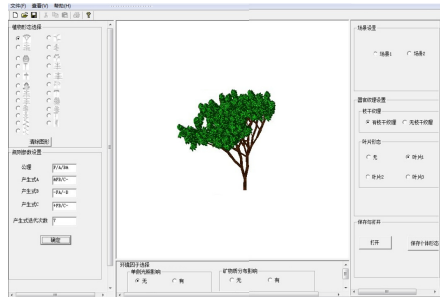


Fig. 3. System interface and simulated result



a) Left-side light b) Light from above c) Right-side light

Fig. 4. The effects of directional light on plant morphology

5 Discussion

Most current works that focus on the simulation of plant shape based on genetic algorithms do not have a specific plant shape to be simulated. The purpose of evolution is just to obtain a lot of different plant forms, since there is no explicit target form. What they did was just to reduce the complexity in the process of setting parameters of the axiom and the productions of an L-system. So they did not design any evaluation function to judge the individual fitness. The superior individuals which form a new population were chosen manually in every iteration step [11]. In terms of search efficiency, there are limitations in such selection methods, which are based on human visual impressions [13]. A reasonable fitness function can evaluate the merits of individuals automatically and also improve the efficiency of searching. Therefore, Christian Jacob [14], Ochoa [7], and Bian [8], [9] designed fitness functions to guide the evolution. But those fitness functions were only for the 2D simulation of plants, and did not consider 3D plant structure. In contrast to their fitness functions, we not only consider the plant outline, but also consider the inner details of the plant

structures, such as branching angles and diameters of the different organs. We designed a coarse-grained fitness function and a fine-grained fitness function, to evaluate respective aspects. Therefore, our method is suitable for dealing with 3D plants model and can obtain the best individuals easily and more accurately.

Our plant modeling methods also have some shortcomings. 1) In order to improve the effectiveness of the solution space, the method only designed twenty-three kinds of templates, and these are only for woody plants. Thus, our method can only simulate limited types of plant shape and is not suitable for simulating the shapes of the herbaceous plants. 2) It can only generate plant models which are similar to the target plants. Because plant structure is very complex, it is very difficult to design an ideal fitness function. The currently fitness function uses the similarity between real plants and the 3D reconstructed model. Complex 3D plant structures cause the similarity measure between plants individuals to also be complicated. Hence, we need to develop a simple and quick way to compare the similarity between real plants and 3D models. Then we can design a reasonable and efficient fitness function.

The authenticity of the visual effects should be reflected in four aspects: shape similarity, topology similarity, geometric similarity, and geometric detail realism. The plant shapes generated in this paper are similar to the simulated target in external morphology. But in the geometric details, the simulation results of our system is not visually satisfactory, since we neither add textures to leaves and bark, nor add the effects of shadows and other details. Thus we will do future work to compensate for these weaknesses. Nevertheless, our system can automatically seek out the plant shapes, which are similar to the target plants through an evolutionary algorithm. So the system can avoid the cumbersomeness and low efficiency of manually determining the axiom and production rules of an L-system.

6 Conclusion

In this article, a new system for simulating plant morphology based on evolutionary strategy is designed and implemented. The system does not need the user to manipulate the L-system directly, so it has the advantages of simple operation, strong interactivity, and wide range of applications, in contrast to traditional L-system-based plant simulation software.

In future work, we will study an optimized strategy for generating the initial population and further refine the design of the fitness function to more precisely simulate the target plants. We will also simulate the dynamic interaction between different environment factors and plant morphologies. Moreover, we also need to find suitable methods to simulate the shapes of herbaceous plants based on an evolutionary strategy.

Acknowledgements. This work was supported by the Natural Science Foundations of Zhejiang Province (LY14C130015).

References

1. Prusinkiewicz, P., Lindenmayer, A.: *The Algorithmic Beauty of Plants*. Springer, New York (1990)
2. Boudon, F., Pradal, C., Cokelaer, T., et al.: An L-System Simulation Framework for Modeling Plant Architecture Development Based on a Dynamic Language. *Frontiers in Plant Science* 3, 76 (2012)
3. Ding, W.L., Cheng, Z.J., Chen, M.Z.: Interactive Modeling Plant Architectures Based on Template Library. In: *Proceedings of the 2009 International Conference on Modeling, Simulation and Visualization Methods, Las Vegas*, pp. 121–126 (2009)
4. Tan, P., Fang, T., Xiao, J.X., et al.: Single Image Tree Modelling. *ACM Trans. Graph* 27(5), Article 108 (2008)
5. Zheng, B.Y., Shi, L.J., Ma, Y.T., et al.: The study of rice canopy field in-situ 3D digital and virtual layer. *Scientia Agricultura sinica* 42(4), 1181–1189 (2009)
6. Godin, C., Guédon, Y., Costes, E., et al.: Measuring and analyzing plants with the AMAPmod software. In: Michalewicz, M.T. (ed.) *Plants to Ecosystems Advances in Computational Life Sciences*, pp. 53–84. CSIRO, Melbourne (1997)
7. Ochoa, G.: On genetic algorithms and lindenmayer systems. In: Eiben, A.E., Bäck, T., Schoenauer, M., Schwefel, H.-P. (eds.) *PPSN 1998. LNCS*, vol. 1498, pp. 335–344. Springer, Heidelberg (1998)
8. Runqiang, B., Chen, P., Burrage, K., Hanan, J., Room, P., Belward, J.: Derivation of L-system models from measurements of biological branching structures using genetic algorithms. In: Hendtlass, T., Ali, M. (eds.) *IEA/AIE 2002. LNCS (LNAI)*, vol. 2358, pp. 514–524. Springer, Heidelberg (2002)
9. Bian, R.Q., Jim, H.N., Chiba, N.: Statistical data directed evolution of L-system models for botanical trees. In: *Proceedings of the 4th International Workshop on Functional-Structural Plant Models*, pp. 253–256 (2004)
10. Hemberg, M., O'Reilly, U.M.: Integrating generative growth and evolutionary computation for form exploration. *Genetic Programming and Evolvable Machines* 8(2), 163–186 (2007)
11. Venter, J., Hardy, A.: Generating plants with gene expression programming. In: *Proceedings of Afrigraph 2007*, pp. 159–167 (2007)
12. Zheng, M.R., He, Z.F.: Construction of virtual plants based on genetic algorithm with dual-scale automata. *Journal of Fuzhou University (Natural Science)* 38(2), 208–212 (2010) (in Chinese)
13. McCormack, J.: Aesthetic evolution of L-systems revisited. In: Raidl, G.R., et al. (eds.) *EvoWorkshops 2004. LNCS*, vol. 3005, pp. 477–488. Springer, Heidelberg (2004)
14. Jacob, C.: Genetic L-System Programming. In: Davidor, Y., Männer, R., Schwefel, H.-P. (eds.) *PPSN 1994. LNCS*, vol. 866, pp. 334–343. Springer, Heidelberg (1994)

Numerical Simulation of the Nutrient Limitation in the Yangtze River Estuary

Hao Liu¹, Wen-Shan Xu¹, Hong-Xuan Kang¹, Bao-Shu Yin², and De-Zhou Yang²

¹ College of Marine Sciences, Shanghai Ocean University, 999 Hu-Cheng-Huan Rd,
201306 Shanghai, China

² Key Laboratory of Ocean Circulations and Waves, Institute of Oceanology, CAS,
7 Nan-Hai Rd, 266071 Qingdao, China
haoliu@shou.edu.cn

Abstract. A Nutrient-Phytoplankton-Zooplankton-Detritus (NPZD) type of biogeochemical model is developed to investigate the nutrient limitation in the Yangtze River Estuary. By means of a series of numerical experiments, it is found that the phosphate limitation is dominant especially in the coastal region due to the large amounts of riverine nitrogen input. It is also found that the nutrient limitation tends to shift from the P-limitation to the N-limitation toward the offshore region, since the N/P ratio has decreased drastically in this sea region. The difference in the nutrient source may be responsible for shaping such nutrient limitation in the Yangtze River Estuary, since nitrogen mainly comes from the riverine input whereas phosphate mainly comes from either the regeneration process or the intrusion of the branch of the Kuroshio current.

Keywords: Biogeochemical model, nutrient limitation, phytoplankton, Yangtze River Estuary.

1 Introduction

Nutrients, like nitrogen, phosphate and silicon, are the essential nutrition elements for phytoplankton to grow, and construct the material basis of the primary production in the marine environment. The distribution and variation of these nutritive materials not only depend on the physical process, such as the transport and mixing of the water column, but also rely on the biogeochemical process happening between nutrient, phytoplankton, zooplankton and planktobacteria[1], [2]. In recent years, the nutrient flux into the sea increased drastically due to the human activity and the global climate change, and then led to the serious eutrophication and harmful algae bloom in the coastal area. How will the primary production and the biological resources respond to the nutrient variation? What is the relationship between the nutrient variation and the harmful algae bloom? All the relevant scientific problems invite the concern of the oceanographers. Changjiang is the largest river in China, and carries large amounts of nutrients into the Yangtze River Estuary annually. Therefore, understanding the nutrient dynamics (distribution and variation) is meaningful to prevent the marine environment from the further deterioration in this sea region.

It is generally believed that the biogeochemical variation of carbon, nitrogen and phosphorus follows the Redfield ratio (106:16:1) in the marine environment [3]. Currently, the Redfield theory is still used to examine the nutrient limitation, which means if the atomistic N/P ratio in seawaters exceeds 16, the algae growth is thought to be limited by the insufficiency of phosphorus; Vice versa. The hydrodynamics of the Yangtze River Estuary is characterized by the strong vertical mixing [4], which may lead the sediment to suspend, thus the turbid seawater further restricts the photo-production of algae. Additionally, the Changjiang Diluted Water carries large amounts of riverine nutrients into the sea annually [5], so it was generally believed that the phytoplankton growth may be more impacted by the weak light radiation due to the suspended sediment other than by the nutrient insufficiency in this sea region. The Yangtze River Estuary and its adjacent sea were well-known for the high primary production, so the nutrient limitation is less concerned previously. However, some recent observations and experiments have revealed that the nutrient limitation exist in this sea region, which is characterized by the phosphorus limitation onshore and the nitrogen limitation offshore [6]. In order to examine the relevant ecological process, a relatively complicated NPZD biogeochemical model is developed to reproduce the annual cycle and variation of the key biogenic elements. Moreover, a series of numerical experiments are designed and conducted to investigate the feature of the nutrient limitation in this sea region.

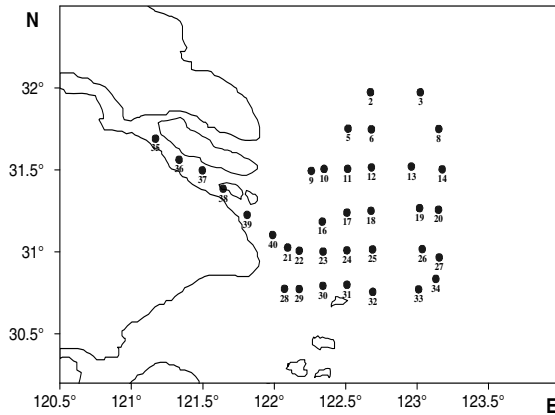


Fig. 1. Yangtze River Estuary and 40 sampling stations. It is noted that station 1, 4, 7 and 15 are not shown, since the data are problematic for these stations.

2 Model Description

The biogeochemical model used in this study belongs to the NPZD type. N indicates the nutrient including nitrate, ammonium, and phosphate. P indicates phytoplankton including diatom and dinoflagellate. Z indicates zooplankton which is the forcing term of the model. D is the biological detritus coming from the phytoplankton or zooplankton. The detailed relationships between seven biogenic elements are given in Fig.2

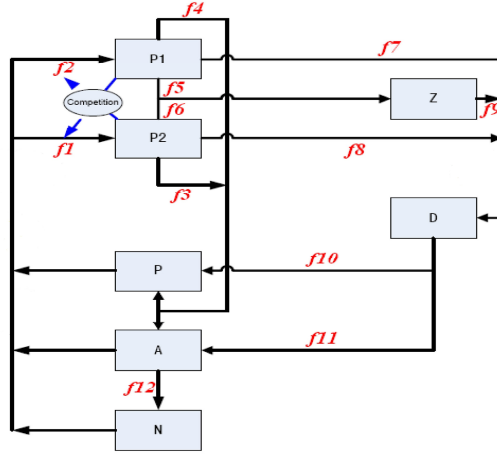


Fig. 2. Scheme of the biogeochemical model. The biogenic elements include three nutrients-nitrate (*N*), ammonium (*A*) and phosphate (*P*); two algae- diatom (*P*₁) and dinoflagellate (*P*₂); zooplankton (*Z*) and detritus (*D*). *f*₁ to *f*₁₂ represent the biogeochemical processes.

The biogeochemical processes can be formulated as follows.

$$\begin{cases}
 \frac{dP_1}{dt} = f_1 - f_3 - f_5 - f_7 - Exud \\
 \frac{dP_2}{dt} = f_2 - f_4 - f_6 - f_8 \\
 \frac{dZ}{dt} = Ass_{P_1-Z}f_5 + Ass_{P_2-Z}f_6 - f_9 - f_{10} \\
 \frac{dD}{dt} = f_7 + f_8 + f_9 - f_{11} \\
 \frac{dA}{dt} = (f_3 + f_4 + f_{10} + f_{11}) - k_1(f_1 + f_2) - f_{12} + IN_A \\
 \frac{dN}{dt} = f_{12} - k_2(f_1 + f_2) + IN_N \\
 \frac{dP}{dt} = [P : N](f_3 + f_4 + f_{10} + f_{11} - f_1 - f_2) + IN_P
 \end{cases} \tag{1}$$

In the above equation, *f*₁ and *f*₂ represent the growing process of diatom and dinoflagellate, respectively, which are influenced by theseawater temperature (*T*), the light radiation (*I*), the concentration of the suspended sediment and the nutrient.

$$\begin{cases}
 f_1 = r_{\max_P_1} r_T r_I \min((r_{Nitrate} + r_{Ammonium}), r_{Phosphorus}) r_{sus} P_1 \\
 f_2 = r_{\max_P_2} r_T r_I \min((r_{Nitrate} + r_{Ammonium}), r_{Phosphorus}) r_{sus} P_2
 \end{cases} \tag{2}$$

*F*₃ and *f*₄ represent the respiration process of diatom and dinoflagellate, respectively, which are taken as the exponential function of the seawater temperature based on the laboratory experiment [7].

$$\begin{cases} f_3 = r_r \exp(k_r T) P_1 \\ f_4 = r_r \exp(k_r T) P_2 \end{cases} \quad (3)$$

F_5 and f_6 represent the grazing process of zooplankton on diatom and dinoflagellate, respectively, and the so-called M-M formulation [8] is adopted.

$$\begin{cases} f_5 = g_{m_{-P_1}} \frac{P_1}{P_1 + K_{P_1}} Z \\ f_6 = g_{m_{-P_2}} \frac{P_2}{P_2 + K_{P_2}} Z \end{cases} \quad (4)$$

F_7 and f_8 represent the mortality process of diatom and dinoflagellate, respectively, and are formulated as follows.

$$\begin{cases} f_7 = r_m P_1 \\ f_8 = r_m P_2 \end{cases} \quad (5)$$

F_9 and f_{10} represent the zooplankton excretion and mortality processes, respectively, and are formulated as follows.

$$\begin{cases} f_9 = r_{r_Z} Z \\ f_{10} = r_{m_Z} Z^2 \end{cases} \quad (6)$$

F_{11} and f_{12} represent the remineralization and the nitrification processes, respectively, which can be expressed in the following form.

$$\begin{cases} f_{11} = r_{mine_A} (1 + \beta_{mine_A} \frac{T^2}{T_{mine_A}^2 + T^2}) D \\ f_{12} = r_{A_N} \exp(\beta_{A_N} T) A \end{cases} \quad (7)$$

Besides the biogeochemical processes, the term IN_A , IN_N and IN_P in Equation 1 indicate the nutrient sources, which reflect the influx of ammonium, nitrate and phosphate into the sea. The term $Exud$ indicates the sinking process of diatom, meaning the material outflow from the marine ecosystem. In order to guarantee the mass conservation for the ecosystem, it must have

$$\frac{dP_1}{dt} + \frac{dP_2}{dt} + \frac{dP}{dt} + \frac{dZ}{dt} + \frac{dD}{dt} + \frac{dA}{dt} + \frac{dN}{dt} = IN_P + IN_N + IN_A - Exud \quad (8)$$

The biological parameters appearing in the above equations are listed and illustrated in Table 1. The parameter value is crucial for the model results, so its choice is an important and difficult task. Unfortunately, the parameter measured or observed directly in this sea region is very scarce, so we have to use publications as reference. It should be stressed that as a process-oriented research, the annual variation of the biogeochemical processes is the major concern of this study, which means that the chosen parameters are not calibrated to match the observations purposely.

Table 1. Biological parameters

Parameter	Explanation	Value
$r_{\max_P_1}$	The maximum growth rate of diatom	1 d ⁻¹
$r_{\max_P_2}$	The maximum growth rate of dinoflagellate	0.6 d ⁻¹
r_l	Light influence on algae growth	By equation
r_T	Temperature influence on algae growth	By equation
r_{sus}	Concentration of SS on algae growth	By equation
r_r	Respiration rate of algae	0.138 d ⁻¹
$g_{m_P_1}$	Grazing rate of zooplankton on diatom	0.05 d ⁻¹
$g_{m_P_2}$	Grazing rate of zooplankton on dinoflagellate	0.1 d ⁻¹
r_m	Mortality rate of algae	0.05 d ⁻¹
r_{r_Z}	Excretion rate of zooplankton	0.03 d ⁻¹
r_{m_Z}	Mortality rate of zooplankton	0.01 d ⁻¹
$r_{\min e_A}$	Remineralization rate of detritus to ammonium	0.003 d ⁻¹
r_{A_N}	Nitrification rate of ammonium to nitrate	0.001 d ⁻¹
$Ass_{P_1_Z}$	Assimilation rate of zooplankton grazing on diatom	0.5
$Ass_{P_2_Z}$	Assimilation rate of zooplankton grazing on dinoflagellate	0.5
K_{P_1}	Half saturation constant of zooplankton grazing on diatom	0.068 mmol/m ³
K_{P_2}	Half saturation constant of zooplankton grazing on dinoflagellate	0.068 mmol/m ³
k_1	Uptake rate of ammonium by algae	2.0
k_2	Uptake rate of nitrate by algae	1.0
$T_{\min e_A}$	Temperature constant of remineralization	13
$\beta_{\min e_A}$	Temperature coefficient of remineralization	20
β_{A_N}	Temperature coefficient of nitrification	0.11

3 Simulation and Analysis

In order to compare and analyze the model results easily, the units of the biogenic elements are unified as mmol N/m³ except phosphate whose unit is mmol P/m³. The initial conditions of the biogenic elements are based on observations in winter. By averaging the data over 36 stations, the individual value of nitrate, ammonium, phosphate, diatom, dinoflagellate, zooplankton and detritus is 6.58, 2.63, 0.68, 0.02, 0.15, 0.01 and 0.01 mmol/m³ [9]. Considering the impact of the suspended sediment on the algae photoproduction, the measured concentration of SS (3.5 g/m³) is also adopted in the model run. As the standard model run, the external nutrient sources are not taken into account tentatively just to reproduce the annual cycle of the biogenic elements.

The model is run for 1200 days, and the simulation of the first year is neglected due to the model stabilization, and the results of the second and the third years are compared for analysis.

3.1 Annual Variation of the Nutrients, Phytoplankton and Zooplankton

Figure 3 shows the annual cycle of the nutrients, phytoplankton and zooplankton simulated by the standard model run. It is found that the highest level of nitrate appears in spring just before the onset of the algae bloom, whereas the highest level of ammonium appears in autumn just after the algae boom. It is generally believed that ammonium is preferentially consumed by algae compared to nitrate. Additionally, ammonium is also transferred to nitrate through the nitrification process, so the ammonium content always declines first compared to that of nitrate in the annual cycle. On the other hand, as soon as the algae bloom happens, the ammonium content begins to resume firstly due to the regeneration process. It is why the ammonium content returns to the highest level just after the algae bloom. Nitrate is generally called the new-nutrient, meaning that it is mainly made up from the external source, so its level declines to the lowest just after the algae bloom. Compared to the nitrogen, the phosphate variation is not marked. Just like ammonium, phosphate can also be regenerated in the marine environment; moreover, the rate of regeneration is quicker than that of ammonium [10]. On the other hand, algae consume phosphate generally according the Redfield ratio, which means that the consumed phosphate is about 1/16 of that nitrogen. The less consumption and the quick makeup lead to the small fluctuation in the annual cycle.

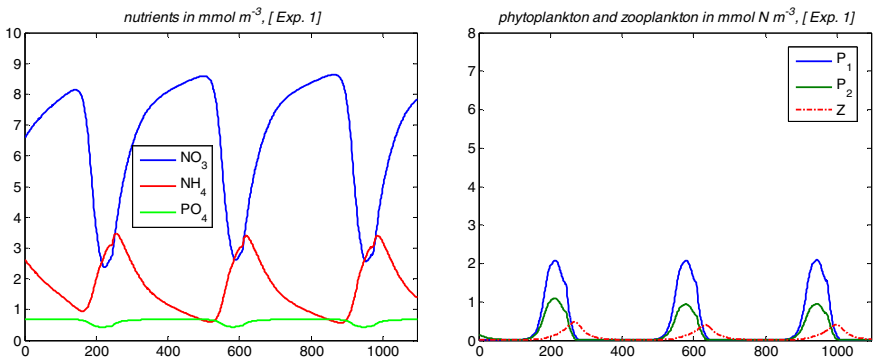


Fig. 3. The time series of nutrients (left plot) and planktons (right plot) based on a standard run

Figure 3 also shows the annual variation of planktons. It is found that the algae biomass reach the highest level after the spring bloom, since the nutrients, light radiation and seawater temperature are conducive to the phytoplankton growth. Thereafter, the algae biomass begins to decrease drastically for two reasons, namely the nutrient depletion and the grazing pressure from zooplankton. From Figure3 it is also found that the summit of the zooplankton biomass lags behind that of algae. In winter, the

low seawater temperature limits the algae activity though the nutrient content is sufficient, and it is why both the phytoplankton and zooplankton biomass decrease to the lowest level in the annual cycle.

3.2 Influence of the Suspended Sediment on the Nutrient-Phytoplankton Dynamics

Just as specified previously, the concentration of the suspended sediment is set as 3.5 g/m^3 in the standard model run. In this section, the clear seawater without the suspended sediment is presumed to examine the influence of the suspended sediment on the nutrient-phytoplankton dynamics. The model results are shown in Figure 4. Compared to the standard case, the phytoplankton biomass (no matter diatom or dinoflagellate) increases drastically, and meanwhile the nutrient consumption is also considerable. During the course of the algae bloom, the nutrient content may decline to 0 if the seawater is clear, which generally happens in the open ocean. In the coastal waters, the marine ecosystem is generally characterized by the high nutrient level and the low algae biomass, since the suspended sediment has effectively limited the algae photoproduction by weakening the light radiation.

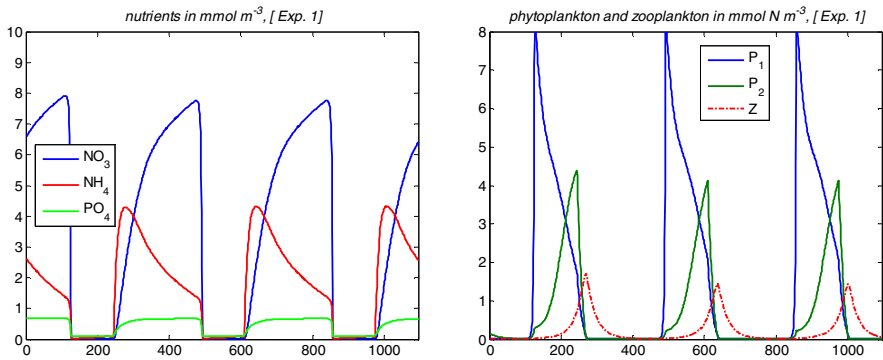


Fig. 4. The simulated time series of nutrients (left plot) and plankton (right plot) as the suspended sediment concentration is set to be 0

3.3 Numerical Experiments on the Nutrient Limitation

The nutrient enrichment experiment was generally used to examine the nutrient limitation in the genuine marine environment. However, the in situ nutrient enrichments may bring about the secondary pollution. In this study, the numerical nutrient enrichment experiment is designed and the model results are analyzed. In order to determine which nutrient may limit the algae growth, only one nutrient is added to the model as the external nutrient source in each model run. Table 2 lists the added nutrient concentration in each experiment: (1) without any nutrient addition (standard model run); (2) only ammonium added; (3) only nitrate added; (4) only phosphate added.

Table 2. Numerical experiments of the nutrient enrichment (mmol/m³)

Experiment	Nitrate	Ammonium	Phosphate
1	0	0	0
2	0	0.001	0
3	0.001	0	0
4	0	0	0.001

Figure 5 shows the annual variation of the nutrients simulated by different numerical experiments.

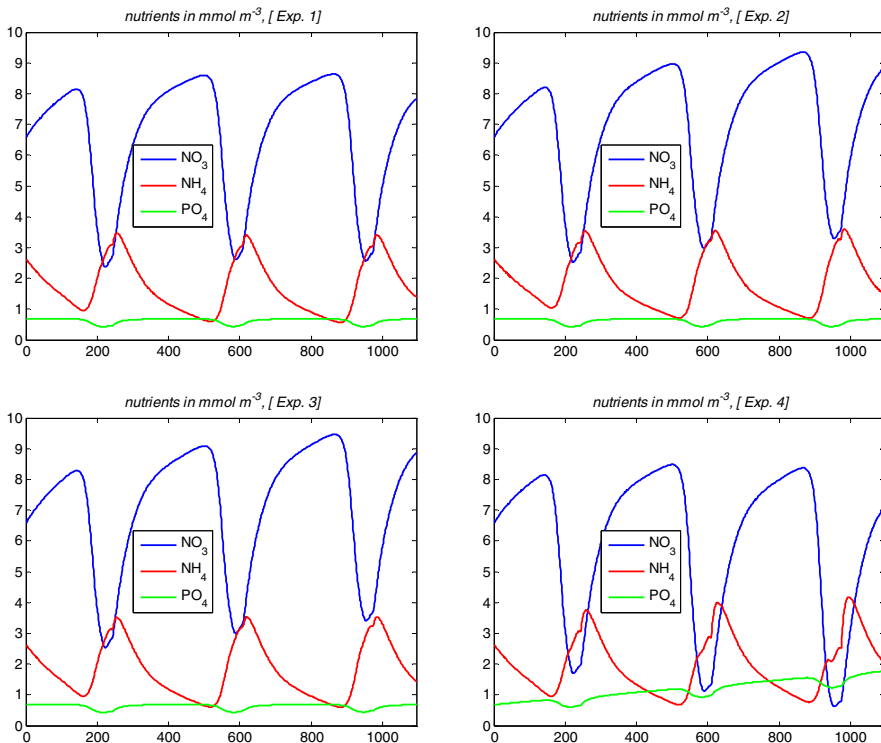


Fig. 5. The time series of the nutrients obtained from Exp.1 to Exp.4

Compared to the standard case which is characterized by the mass conservation, every enriched nutrient can enhance its content ultimately in the annual cycle. The exception is the ammonium enrichment, which can not only improve its own content, but also enhance the nitrate content due to the nitrification process. In addition, the phosphate enrichment can enhance the ammonium content and reduce the nitrate content simultaneously. It is an interesting phenomenon. Both ammonium and phosphate can regenerate from planktons, implying that the more plankton biomass create more phosphate and ammonium.

Figure 6 shows the annual variation of planktons simulated by different numerical experiments. It can be also found that the phosphate enrichment enhance the phytoplankton biomass markedly, and the ammonium and nitrate enrichments do not embody such an influence, implying that the phosphate limitation may be dominant in the standard case run, which agrees with the recent observations [5], [6].

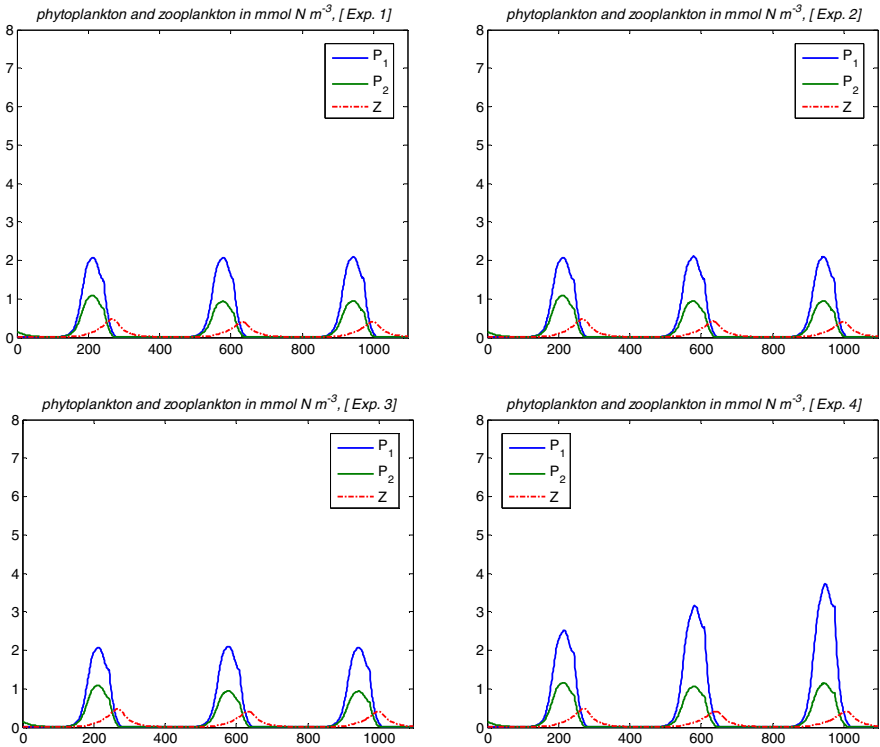


Fig. 6. The time series of phytoplankton and zooplankton obtained from Exp.1 to Exp.4

4 Discussion and Conclusion

In this study, a NPZD biogeochemical model is developed to simulate the annual variation of the key biogenic elements in the Yangtze River Estuary. The nutrient limitation is further investigated by a series of numerical nutrient enrichment experiment, and it is found that the phosphate limitation may be dominant in this sea region.

Given that the high level of N/P ratio is mainly induced by the riverine nutrients, the phosphate limitation concentrates in the coastal waters, especially in the region of the fresh water influence (RFWI). The recent investigation and simulation reveal that the phosphate content carried by the branch of Kuroshio Current into this region is much higher than the riverine phosphate carried by the Changjiang Diluted Water [11], so the nitrogen limitation may appear in the offshore region.

Admittedly, the model used in this study only belongs to the box type, in which the physical process is not considered tentatively. The further study is to develop a coupled bio-physical model to reproduce the biochemical process in the genuine physical background.

Acknowledgments. The work is financially supported by the Innovation Project of Shanghai Education Committee (12ZZ165) and the Special Project of Marine Strategy Guide, Chinese Academy of Sciences (XDA11020305.2).

References

1. Huang, X.P., Huang, L.M.: Several Progress of the Nutrient Dynamics in Estuary. *Journal of Huanghai and Bohai Seas* 19(4), 86–92 (2001)
2. Liu, H., Yin, B.S.: Numerical Investigation of Nutrient Limitations in the Bohai Sea. *Marine Environmental Research* 70, 308–317 (2010)
3. Redfield, A.C., Ketchum, B., Richards, F.A.: The Influence of Organisms on the Composition of Seawater. In: *The Sea 2*, pp. 26–77. Wiley Interscience, New York (1963)
4. Lü, X.G., Qiao, F.L., Xia, C.S., et al.: Upwelling off Yangtze River Estuary in Summer. *Journal of Geophysical Research* 111(C11S08), 1–19 (2006)
5. Chai, C., Yu, Z.M., Song, X.X., et al.: The Status and Characteristics of Eutrophication in the Yangtze River Estuary and the Adjacent East China Sea. *Hydrobiologia* 563, 313–328 (2006)
6. Zhang, J., Liu, S.M., Ren, J., et al.: Nutrient Gradients from the Eutrophic Changjiang Estuary to the Oligotrophic Kuroshio Waters and Re-evaluation of Budgets for the East China Sea Shelf. *Progress in Oceanography* 74(4), 449–478 (2007)
7. Liu, H., Yin, B.S.: Annual Cycle of Carbon, Nitrogen and Phosphorus in the Bohai Sea: A Model Study. *Continental Shelf Research* 27, 1399–1407 (2007)
8. Steel, J.H., Henderson, E.W.: The Role of Predation in Plankton Models. *Journal of Plankton Research* 4(1), 157–172 (1992)
9. Liu, H., Xu, W.S.: Study on the Nutrient Limitations in the Yangtze River Estuary. *Journal of Shanghai Ocean University* 22(5), 720–725 (2013)
10. Ryther, J.H., Dunstan, W.M.: Nitrogen, Phosphorous, and Eutrophication in the Coastal Marine Environment. *Science* 171, 1008–1013 (1971)
11. Yang, D.Z., Yin, B.S., Liu, Z.L., et al.: Numerical Study of the Ocean Circulation on the East China Sea Shelf and a Kuroshio Bottom Branch Northeast of Taiwan in Summer. *Journal of Geophysical Research* 116(C05015), 1–20 (2011)

Dynamic Analysis of Circular Engineered Cardiac Tissue to Evaluate the Active Contractile Force

Zhonggang Feng¹, Tatsuo Kitajima², Tadashi Kosawada¹, Takao Nakamura³,
Daisuke Sato³, and Mitsuo Umezu⁴

¹ Graduate School of Science and Engineering, Yamagata University, Japan

² Department of Electronic Systems Engineering, Malaysia-Japan International Institute of Technology, Malaysia

³ Graduate School of Medical Science, Yamagata University, Japan

⁴ Integrative Bioscience and Biomedical Engineering, Waseda University, Japan

Abstract. Circular engineered cardiac tissue was fabricated by embedding rat embryonic cardiomyocytes into collagen (type I) gels. The engineered tissue was set to a specific configuration and the spontaneous beat displacement at one site of it was measured. The active contractile force of the embedded cardiomyocytes was derived from the displacement data. In this process, the engineered tissue was constitutively modeled as three components in parallel: i.e., an active contractile component representing the cardiomyocyte contraction, a pre-force component representing the effects of gel compaction during the tissue fabrication, and a Kelvin model for the passive properties of the tissue. Dynamic analysis of the beat displacement allowed solving out the active contractile force. In addition, energy coefficient was defined to evaluate the pump function of the engineered tissue. It demonstrated that this approach can detect the active contractile force as small as ~ 0.01 mN and can sensitively reveal the change of the active contractile force under different culture conditions. Besides being an assay to evaluate the mechanical performance of engineered cardiac tissue, this novel method is particularly suitable to be used in pharmacological response testing of stem cell-derived cardiomyocytes under three-dimensional culture attributed to its high sensitivity and feasibility for continuous and in situ measurement.

Keywords: Active contractile force, cardiomyocytes, collagen gel, constitutive model, beat displacement, energy coefficient.

1 Introduction

Engineered cardiac tissue (ECT) provides a promising modality to the treatment of severe heart disease [1-3]. In the meanwhile, it can also be used as an in vitro model for pharmacologic testing and drug screen [4-6]. Therefore, measurement of the contractile force of ECT is not only an evaluation to its pump function but also an important procedure for the pharmacologic testing. And it is attractive if the force measurement can continuously monitor the cellular differentiation and drug response while keeping the ECT intact as cultured in CO₂ incubator. Measurement systems employing sensitive force transducers are often used [7-10]. Obviously, this kind of system is costly and may not be suitable for the continuous in situ measurement.

In this regards, vision-based force sensing is an attractive choice for its low-cost, continuity, and intactness to the samples. However, contractile force referred by the beat amplitude but lacking of accurate analysis on the mechanical characteristics of the constructs [11,12] is at best just quasi-quantitative. Most recently, contractile force measurement through monitoring the deflection of cantilever is reported [13, 14]. However, constraint of the gel compaction at the two ends of ECT slabs results into heterogeneity in the ECT; and in addition, beating deflection of the cantilever includes the overall dynamics of the cardiomyocytes-collagen gel-cantilever systems, which is not a direct measurement of the active contractile force exerted by the cardiomyocytes themselves.

In this paper, we provide a novel method to analyze the active contractile force in collagen gel-based ECT. This method fabricates ECT into a circular shape so as to ensure the homogeneity of the ECT and only needs to measure the beat displacement at one site on the ECT. The prerequisite to make this method feasible is to capture the mechanical characteristics of the collagen gel-based ECT in details as we have achieved [15-19]. Here we demonstrate that this method is precise and sensitive to evaluate the function of ECT.

2 Materials and Methods

Wistar rats were used in this study. All procedures in animal experiments followed the Guide for the Care and Use of Laboratory Animals of the National Institutes of Health, Bethesda, MD, USA, and were approved by the Animal Studies Ethics Committee of Yamagata University.

2.1 Fabrication of Circular ECT (CECT) and Measurement of Beat Displacement

Cardiomyocytes were harvested from 18-day-old rat embryos. The procedures are described in detail elsewhere [18]. When collagen solution is mixed with living cells and rendered to gelate, the gel will compact due to the interaction between the embedded cells and the collagen fibrils, which results in a condensed collagen matrix closing to native connective tissues. Fabrication of CECT was firstly reported by Zimmermann WH et al [20]. In this study, collagen-gel based CECT was created by using silicone rubber mold, details may refer to [15]. The spontaneously beating CECT was set in between two fixed silver pins as shown in Figure 1 and the beat displacement of the point at the top of the medial symmetric axis of CECT was videoed through a light microscope (Olympus X71 inverted microscope). The displacement of the point during one beat period was then measured frame by frame (60 frames per second) by using Adobe Photoshop CS6.

2.2 Constitutive Model of CECT

In order to quantitatively analyze the beat behavior of CECT, the mechanical characteristics of the CECT has to be understood firstly. Integrating our preceding experimental and theoretical studies on this subject [15-19], we propose a mechanical constitutive

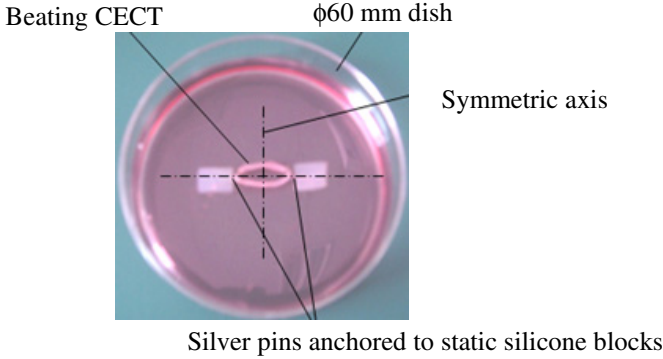


Fig. 1. A CECT set in culture dish

model as diagrammatically illustrated in Figure 2. It consists of an active force generator (σ_a) to represent the active contraction of the cardiomyocytes, a pre-force element ($\sigma_0 < 0$) to reflect the effect of the gel compaction during fabrication, and a Kelvin model (K_1, K_2, η) to represent the passive mechanical characteristics of the CECT. Hence, the tensile force (σ) in the CECT can be expressed as

$$\sigma = \sigma_a + \sigma_0 + K_1 \int_{-\infty}^t \psi(t-t') \cdot \varepsilon(t') dt', \quad (1)$$

$$\psi(t) = \frac{1}{\lambda_2} \left[-\frac{\lambda_1}{\lambda_2} \exp(-t/\lambda_2) + (\lambda_1 + \lambda_2) \delta(t) \right] \quad (2)$$

where $\lambda_1 = \eta / K_1$, $\lambda_2 = \eta / K_2$; t is time; and ε is the contractile strain.

2.3 Dynamics of the CECT Beating

The configuration of the CECT is schematically shown in Figure 3, where the displacement of top point A at the medial symmetric axis is measured. To analyze the dynamics of the CECT beating, we regard it as a simple beam [21] and further assume that (1) with comparison to normal stress σ , shear stress and moment at any cross-section can be neglected (refer to Discussion); (2) normal stress σ is uniform along the CECT.

As shown in Figure 3, at the relax state the central line of the CECT between two pins is approximated as an arc with radius R and chord L . Let $w_A(t)$ to be the displacement of point A at time t , under the above assumptions the following governing equation can be obtained through considering the movement of an infinitesimal (dx) symmetric to the medial symmetric axis (deduction in detail may refer to Appendix A).

$$-\pi\phi\sigma/R + 2D_f\rho_m\dot{w}_A(t) \Big| \dot{w}_A(t) \Big| = -\pi\phi\rho\ddot{w}_A(t), \quad (3)$$

where ϕ is the diameter of the CECT; D_f is the medium drag coefficient; ρ and ρ_m are the densities of the CECT and the medium, respectively; dot on $w_A(t)$ represents the derivative to time t . Medium drag coefficient D_f can be calculated by the following formulas [22]

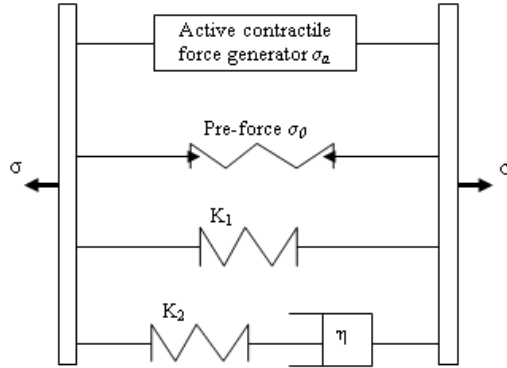


Fig. 2. The constitutive model of the CECT. It consists of three components, i.e., an active contractile element representing the cardiomyocytes contraction, a pre-force element representing the effects of gel compaction during fabrication, and a Kelvin model for the passive properties of collagen scaffold.

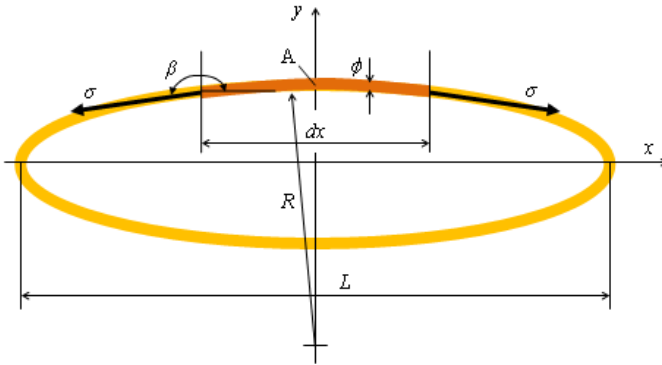


Fig. 3. Schematic drawing for the analysis of the dynamics of CECT

$$D_f = \begin{cases} \frac{8\pi}{R_e(2.002 - \ln(R_e))} & \text{(Lamb's formula as } R_e \leq 1.0) \\ (0.707 + 3.42R_e^{-1/2})^2 & \text{(Imai's formula as } 1.0 < R_e < 40.0) \end{cases} \quad (4)$$

where R_e is Reynolds number defined as

$$R_e = \frac{\rho_m \phi}{\mu} |\dot{w}_A(t)|, \quad (5)$$

where μ is the viscosity of the culture medium. Substituting equation (1) into (3) we obtain

$$\sigma_a = \rho R \dot{w}_A(t) + \frac{2R\rho_m}{\pi\phi} D_f \dot{w}_A(t) |\dot{w}_A(t)| - \sigma_0 - K_1 \int_{-\infty}^t \psi(t-t') \cdot \varepsilon(t') dt' \quad (6)$$

The contractile strain can be approximately expressed as (Appendix B)

$$\varepsilon = Cw_A(t); \quad C = -\frac{L}{3R^2 \arcsin(L/2R)}. \quad (7)$$

Since $w_A(t)$ is a periodic function and can be expressed in Fourier series, we finally obtain the equation to compute the active force (Appendix C)

$$\begin{aligned} \sigma_a(t) = & \rho R \ddot{w}_A(t) + \frac{2R\rho_m}{\pi\phi} D_f \dot{w}_A(t) |\dot{w}_A(t)| - \sigma_0 - (K_1 + K_2)Cw_A(t) + \\ & K_2 C \left[\frac{a_0}{2} + \sum_{n=1}^{\infty} \frac{1}{1 + 4\pi^2 f^2 \lambda_2^2 n^2} ((a_n - 2\pi f \lambda_2 n b_n) \cos(2\pi f n t) + \right. \\ & \left. (b_n + 2\pi f \lambda_2 n a_n) \sin(2\pi f n t)) \right] \end{aligned} \quad (8)$$

where f is the frequency of the spontaneous beating; a_0 , a_n , and b_n are the coefficients in Fourier series for $w_A(t)$. In practical computation n was taken up to 10 to get enough accuracy. Parameters used in the computation are listed in Table 1.

Moreover, we introduce the following energy coefficient

$$E_p = \frac{\frac{1}{2} \rho \dot{w}_A^2(t)}{\sigma_a(t) \varepsilon(t)}. \quad (9)$$

It is the kinetic energy of the CECT divided by the output of the active contractile force at beating. The kinetic energy i.e., the movement of the CECT, will push the fluid, if supposed to be sealed in the CECT, to eject it outside. Therefore, this index can be used to evaluate the pump function of the CECT.

Table 1. Parameters used in computing active contraction force

Substance physical properties	
ρ	$1.0 \times 10^3 \text{ kg/m}^3$
ρ_m	$1.0 \times 10^3 \text{ kg/m}^3$
μ_m	$1.0 \times 10^{-3} \text{ Pa-s}$
Circular tissue geometry	
L	$1.7 \times 10^{-2} \text{ m}$
ϕ	$5.0 \times 10^{-4} \text{ m}$
$Y(0)$	$1.2 \times 10^{-3} \text{ m}$
Passive constitutive model	
K_1	$6.5 \times 10^3 \text{ Pa}$
K_2	$10.2 \times 10^3 \text{ Pa}$
η	$2.0 \times 10^3 \text{ Pa-s}$

3 Results

To demonstrate the validity and the sensitivity of the method, we present the results from one gel under different culture conditions. At first, before medium change (performed every three days) the beating of the gel was videoed (data noted as “old medium” in Figure 4); then after medium change and cultured for one hour in the 5%-CO₂, 37°C incubator, the beating was taken again (noted as “new medium”); and at last the gel was cultured in a 60%-O₂, 5%-CO₂, 37°C incubator for another hour and

then the beating was videoed (noted as “new medium 60%-O₂”). It can be seen that the beat displacement obviously differs under different conditions (Figure 4a). New medium enhanced the beating significantly, and culture under high oxygen partial pressure affected the displacement pattern of the CECT.

The active contractile force (Figure 4b) was at several tens of μN in this experiment and had the following features. (1) The active force also quite differed under different conditions, and its waveform broadly resembled the displacement waveform; (2) at the beginning of the beating, active force was not zero but the pre-force σ_0 which was established during the recovery and static phase of the beating. When the active force was plotted against contractile strain (Figure 4c), it showed a hysteresis loop: the force at recovery phase was smaller than that at contraction phase. Moreover, because of the strain during the beating the contraction was more like under auxotonic condition rather than isometric; therefore, the force-strain plot also resembled the force-length plot of individual cardiomyocytes under auxotonic condition[23].

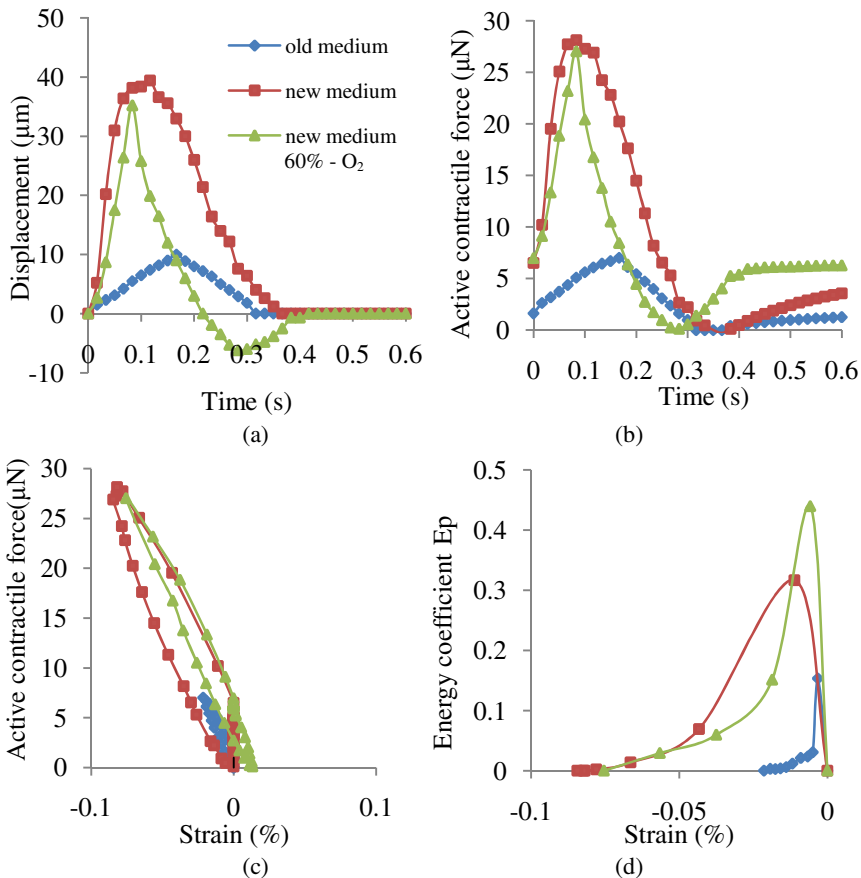


Fig. 4. Results of one CECT under different culture conditions; beat displacement (a), active contractile force profiles (b), active contractile force versus contractile strain (c), energy coefficient versus contractile strain (d).

The energy coefficient of the CECT was at the maximum at the beginning of the beating, but decreased abruptly as contraction going on (Figure 4d). Medium change improved this index substantially; high oxygen environment increased its starting value but brought rather more subsequent decay.

4 Discussion

In the dynamic analysis we assumed the CECT as a simple beam and neglected the shear stress and moment in cross-section. The ratio of length to the diameter of the cross-section is more than 30, the assumption of simple beam is thus reasonable. We have estimated the shear force and maximum moment in cross-section by means of classical beam theory supposing that the CECT deformed at the same extent under external medial concentrated loading. It turns out that the shear force is about $0.01 \mu\text{N}$ and the maximum moment at $0.1 \text{ nN}\cdot\text{m}$. Therefore the neglect is rational.

Pre-force σ_0 is introduced in the model because the collagen fibrils have been in the bent state due to the compaction during the CECT fabrication [16, 17]; due to this reason, σ_0 has negative values. This force is ultimately exerted by the populated cardiomyocytes and fibroblasts included as the cell harvest. We have developed a program to estimate the bending force imposed on the collagen fibrils from individual cells by employing fiber packing theory and network alteration theory for fibrillar networks [16, 17]; therefore, the σ_0 can be deduced. With the gel condition in this study, the σ_0 was estimated at several μN as having been used in this analysis. This quantity is affected by culture condition as well. Medium change enhances cellular activities and thus increases its value.

A new index, energy coefficient E_p , to evaluate the pump function of CECT is defined in this study. Coefficient of energy transfer to external work for native heart muscle expressed as the ratio of external work to myocardium oxygen consumption is around 0.4 [24]. The spontaneous beating of the CECT with new medium and at high oxygen partial pressure reached this value just at the beginning of the beating; after that the energy coefficient abruptly dropped (Figure 4d). This is because that as the beating going on, output of the active contraction is mainly consumed to deform the collagen matrix. For the same sake, it also has substantially low values under other culture conditions.

5 Conclusion

We present a novel method to analyze the contractile force of the ECT as its spontaneously beating. This method can detect as small as several μN of the active contractile force exerted by the cardiomyocytes in ECT, and quite sensitive to different culture conditions. Therefore, it is a sensitive assay to test pharmacological response of ECT, particularly for those with stem cell-derived cardiomyocytes. Furthermore, energy coefficient is defined to evaluate the pump function of CECT. The change of this new index during beating reveals the mismatch between the active contraction of the cardiomyocytes and the passive mechanical properties of the collagen matrix. Expected mechanical properties for the scaffold in creating ECT are proposed.

References

1. Eschenhagen, T., Zimmermann, W.H.: Engineering Myocardial Tissue. *Circ. Res.* 97, 1220–1231 (2005)
2. Shimizu, T., Yamato, M., Kikuchi, A., Okano, T.: Cell sheet engineering for myocardial tissue reconstruction. *Biomaterials* 24, 2309–2316 (2003)
3. Caspi, O., Lesman, A., Basevitch, Y., Gepstein, A., Arbel, G., Huber, I., Habib, M., Geps-tein, L., Levenberg, S.: Tissue engineering of vascularized cardiac muscle from human embryonic stem cells. *Circ. Res.* 100(2), 263–272 (2007)
4. Liau, B., Zhang, D., Bursac, N.: Functional cardiac tissue engineering. *Regen. Med.* 7(2), 187–206 (2012)
5. Tanaka, T., Tohyama, S., Murata, M., Nomura, F., Kaneko, T., Chen, H., Hattori, F., Ega-shira, T., Seki, T., Ohno, Y., Koshimizu, U., Yuasa, S., Ogawa, S., Yamanaka, S., Yasuda, K., Fukuda, K.: In vitro pharmacologic testing using human induced pluripotent stem cell-derived cardiomyocytes. *Biochemical and Biophysical Research Communications* 385, 497–502 (2009)
6. Mehta, A., Chung, Y.Y., Ng, A., Iskandar, F., Atan, S., Wei, H., Dusting, G., Sun, W., Wong, P., Shim, W.: Pharmacological response of human cardiomyocytes derived from virus-free induced pluripotent stem cells. *Cardiovasc. Res.* 91(4), 577–586 (2011)
7. Pillekamp, F., Reppel, M., Rubenchyk, O., Pfannkuche, K., Matzkies, M., Bloch, W., Sreeram, N., Brockmeier, K., Hescheler, J.: Force Measurements of Human Embryonic Stem Cell-Derived Cardiomyocytes in an In Vitro Transplantation Model. *Stem Cells* 25, 174–180 (2007)
8. Guo, X., Zhao, Y., Chang, H., Wang, C.: Creation of engineered cardiac tissue in vitro from mouse embryonic stem cells. *Circulation* 113(18), 2229–2237 (2006)
9. Kensah, G., Lara, A.R., Dahlmann, J., Zweigerdt, R., Schwanke, K., Hegermann, J., Skvorc, D., Gawol, A., Azizian, A., Wagner, S., Maier, L.S., Krause, A., Drager, G., Ochs, M., Haverich, A., Gruh, I., Martin, U.: Murine and human pluripotent stem cell-derived cardiac bodies form contractile myocardial tissue in vitro. *European Heart J.* 34, 1134–1146 (2013)
10. Tulloch, N.L., Muskheli, V., Razumova, M.V., Korte, F.S., Regnier, M., Hauch, K.D., Pabon, L., Reinecke, H., Murry, C.E.: Growth of engineered human myocardium with mechanical loading and vascular coculture. *Circ. Res.* 109(1), 47–59 (2011)
11. Stevens, K.R., Kreutziger, K.L., Dupras, S.K., Korte, F.S., Regnier, M., Muskheli, V., Nourse, M.B., Bendixen, K., Reinecke, H., Murry, C.E.: Physiological function and trans-plantation of scaffold-free and vascularized human cardiac muscle tissue. *Proc. Natl Acad. Sci. USA.* 106(39), 16568–16573 (2009)
12. Song, H., Yoon, C., Kattman, S.J., Dengler, J., Massé, S., Thavaratnam, T., Gewarges, M., Nanthakumar, K., Rubart, M., Keller, G.M., Radisic, M., Zandstra, P.W.: Interrogating functional integration between injected pluripotent stem cell-derived cells and surrogate cardiac tissue. *Proc. Natl Acad. Sci. USA.* 107(8), 3329–3334 (2010)
13. Hansen, A., Eder, A., Bonstrup, M., Flato, M., Mewe, M., Schaaf, S., Akshirlioglu, B., Schworer, A., Uebeler, J., Eschenhagen, T.: Development of a drug screening platform based on engineered heart tissue. *Circ. Res.* 107, 35–44 (2010)
14. Boudou, T., Legant, W.R., Mu, A., Borochin, M.A., Thavandiran, N., Radisic, M., Zandstra, P.W., Epstein, J.A., Margulies, K.B., Chen, C.S.: A microfabricated platform to measure and manipulate the mechanics of engineered cardiac microtissues. *Tissue Eng. Part A* 18, 910–919 (2012)

15. Feng, F., Seya, D., Kitajima, T., Kosawada, T., Nakamura, T., Umezu, U.: Viscoelastic characteristics of contracted collagen gels populated with rat fibroblasts or cardiomyocytes. *J. Artif Organs* 13, 139–144 (2010)
16. Feng, Z., Wagatsuma, Y., Kobayashi, S., Kosawada, T., Sato, D., Nakamura, T., Kitajima, T., Umezu, U.: Analysis of the Contraction of Fibroblast-Collagen Gels and the Traction Force of Individual Cells by a Novel Elementary Structural Model. In: *Proceedings of 35th Annual International Conference of the IEEE EMBS, Osaka, Japan*, pp. 6232–6235 (2013)
17. Feng, Z., Wagatsuma, Y., Kikuchi, M., Kosawada, T., Nakamura, T., Sato, D., Shirasawa, N., Kitajima, T., Umezu, M.: The mechanisms of fibroblast-mediated compaction of collagen gels and the mechanical niche around individual fibroblasts. *Biomaterials* (2014), <http://dx.doi.org/10.1016/j.biomaterials.2014.05.072> (online first)
18. Feng, Z., Matsumoto, T., Nakamura, T.: Measurements of the mechanical properties of contracted collagen gels populated with rat fibroblasts or cardiomyocytes. *J. Artif. Organs*. 6, 192–196 (2003)
19. Feng, Z., Yamato, M., Akutsu, T., Nakamura, T., Okano, T., Umezu, M.: Investigation on the mechanical properties of contracted collagen gels as a scaffold for tissue engineering. *Artif. Organs*. 27(1), 84–91 (2003)
20. Zimmermann, W.H., Schneiderbanger, K., Schubert, P., Didić, M., Münzel, F., Heubach, J.F., Kostin, S., Neuhuber, W.L., Eschenhagen, T.: Tissue Engineering of a Differentiated Cardiac Muscle Construct. *Circ. Res.* 90, 223–230 (2002)
21. Solecki, R., Conant, R.J.: *Advanced Mechanics of Materials*. Oxford University Press, Inc., New York (2003)
22. The Japan Society of Mechanical Engineers. *JSME Mechanical Engineer's Handbook, A5: Fluid Mechanics*. Published by the Japan Society of Mechanical Engineers, Tokyo (1986)
23. Iribe, G., Helmes, M., Kohl, P.: Force-length relations in isolated intact cardiomyocytes subjected to dynamic changes in mechanical load. *Am J. Physiol. Heart Circ. Physiol.* 292, H1487–H1497 (2007)
24. Kawaguchi, O., Huang, Y., Yuasa, T., Horam, C.J., Carrington, R.J., Zeng, B., Brady, P.W., Murase, M., Hunyor, S.N.: Improved efficiency of energy transfer to external work in chronic cardiomyoplasty based on the pressure-volume relationship. *J. Thorac. Cardiovasc Surg.* 115, 1358–1366 (1998)

Appendix A (Deduction of the Governing Equation)

As shown in Figure 3, at the relax state the central line of the CECT between two pins is approximated as an arc with radius R and chord L . Let $(x, y(x, t))$ to be the coordinates of the central line at time t , then $(x, y(0, t))$ is the coordinates of point A. Considering the movement of an infinitesimal dx symmetric to the medial symmetric axis, we can write the following equation by Newton's second law,

$$\begin{aligned}
 & 2\pi(\phi/2)^2 \sigma \sin \beta - D_f \phi dx \frac{1}{2} \rho_m \frac{d}{dt} y(0, t) \left| \frac{d}{dt} y(0, t) \right| \\
 & = \rho \pi (\phi/2)^2 dx \frac{d^2}{dt^2} y(0, t).
 \end{aligned}
 \tag{A1}$$

Since $\sin \beta \approx -\frac{dy}{dx} \Big|_{x=-\frac{dx}{2}} = \frac{dx}{2} \frac{d^2y}{dx^2} \Big|_{x=0}$, thus

$$\pi\phi\sigma y''(0,t) - 2D_f \rho_m \dot{y}(0,t) \Big|_{y(0,t)} = \pi\phi\rho \ddot{y}(0,t), \quad (\text{A2})$$

where prime and dot on $y(0,t)$ represent the derivative to x and time t , respectively. Let $(x, Y(x))$ is the coordinates of the central line of the CECT at relax state, thus

$$Y(x) = Y(0) + \sqrt{R^2 - x^2} - R \quad (\text{A3})$$

$w_A(t)$, the displacement of point A we have measured, is

$$w_A(t) = Y(0) - y(0,t), \quad (\text{A4})$$

so that $\dot{y}(0,t) = -\dot{w}_A(t)$, and $\ddot{y}(0,t) = -\ddot{w}_A(t)$. We assume that

$$u(x,t) = Y(x) + u(x)w_A(t) \quad \text{with } u(\pm \frac{L}{2}) = 0, \quad u(0) = -1. \quad (\text{A5})$$

Furthermore, we make interpolation for

$$u(x) = \frac{4}{L^2} (x - \frac{L}{2})(x + \frac{L}{2}), \quad (\text{A6})$$

then

$$y''(0,t) = Y''(0) + (8/L^2)w_A(t) \approx Y''(0) = -\frac{1}{R}. \quad (\text{A7})$$

Therefore, equation (A2) becomes

$$-\pi\phi\sigma/R + 2D_f \rho_m \dot{w}_A(t) \Big|_{\dot{w}_A(t)} = -\pi\phi\rho \ddot{w}_A(t), \quad (\text{A8})$$

which is the equation (3) in the main text.

Appendix B (Deduction of the Contractile Strain ε)

To obtain contractile strain of the CECT during its spontaneous beating, we need to calculate its contour length $S(t)$.

$$S(t) = \int_{-L/2}^{L/2} \sqrt{1 + y'(x,t)^2} dx \quad (\text{B1})$$

Substituting equations (A5) into the above equation and neglecting secondary infiniteness. The strain is defined as

$$\varepsilon = \frac{S(t) - S_0}{S_0}, \quad (\text{B2})$$

where S_0 is the contour length of the CECT at relax state. Substitute equations (A3) and (A6) into (B1) and (B2), we obtain

$$\varepsilon = -\frac{L}{3R^2 \arcsin(L/2R)} w_A(t) = C w_A(t), \quad (\text{B6})$$

which is the equation (7) in main text.

Appendix C (Computation of the Active Contractile Force σ_a)

Substitute equation (2) and (7) into (6), we have

$$\begin{aligned} \sigma_a = & \rho R \ddot{w}_A(t) + \frac{2R\rho m}{\pi\phi} D_f \dot{w}_A(t) |\dot{w}_A(t)| - \sigma_0 - (K_1 + K_2) C w_A(t) \\ & + \frac{K_1 \lambda_1 C}{\lambda_2^2} \int_{-\infty}^t w_A(t') \exp(-(t-t')/\lambda_2) dt', \end{aligned} \quad (C1)$$

Since $w_A(t)$ is periodic, it can be expressed in Fourier series as

$$w_A(t) = \sum_{n=-\infty}^{\infty} Q_n e^{i2\pi f n t} \quad (C2)$$

Therefore,

$$\begin{aligned} \sigma_a = & \rho R \ddot{w}_A(t) + \frac{2R\rho m}{\pi\phi} D_f \dot{w}_A(t) |\dot{w}_A(t)| - \sigma_0 - (K_1 + K_2) C w_A(t) \\ & + K_2 C \sum_{n=-\infty}^{\infty} \frac{1}{1 + i2\pi f \lambda_2 n} Q_n e^{i2\pi f n t} \end{aligned} \quad (C3)$$

Expressing the last term in real leads to

$$\begin{aligned} \sigma_a = & \rho R \ddot{w}_A(t) + \frac{2R\rho m}{\pi\phi} D_f \dot{w}_A(t) |\dot{w}_A(t)| - \sigma_0 - (K_1 + K_2) C w_A(t) + \\ & + K_2 C \left[\frac{a_0}{2} + \sum_{n=1}^{\infty} \frac{1}{1 + 4\pi^2 f^2 \lambda_2^2 n^2} ((a_n - 2\pi f \lambda_2 n b_n) \cos(2\pi f n t) + \right. \\ & \left. (b_n + 2\pi f \lambda_2 n a_n) \sin(2\pi f n t)) \right] \end{aligned} \quad (C4)$$

Real-Time Hand Gesture Recognition for Robot Hand Interface

Xiaomeng Lv, Yulin Xu, and Ming Wang

School of Mechatronic Engineering and Automation, Shanghai University,
Shanghai 200072, China
sdtalxm@163.com

Abstract. In this paper, a highly accurate real-time hand gesture recognition system is proposed and implemented. This system can drive a dexterous robot hand behave as humans do without motional sensors attached to humans. The gesture region is segmented from complicated background based on the depth image which is obtained from Kinect. The features, such as the number of fingers, the radians between fingers, are extracted to improve the rate of recognition effectively. Then template matching with the shortest distance was used to recognize the gesture. The result of recognition is sent to the lower computer via RS232. Finally, the five fingers dexterous hand can behave as what the humans do. It can be seen from the experiments that our system can track humans' hand gesture robustly and recognize more than 90 percent of the hand gestures of our depth image database.

Keywords: Gesture recognition, depth image, kinect, dexterous hand.

1 Introduction

The main input tools of the traditional computer interaction are keyboards, mouse, joysticks and so on. However, these tools are not easy to use in virtual reality environment which limit the freedom of hands. The gestures, gestures and voice are the most natural and intuitive manners for communicating. In recent years, more and more people attach importance to Natural Human Computer Interaction (NHCI) which leads to the rapid development of NHCI. Due to comply with interpersonal communication habits, the recognition of face, gesture and body posture have become an important issue of NHCI. Gestures are a common natural and intuitive way of communicating not only in daily life but also in virtual reality. Therefore, gestures become one of the favorite ways to interact. There's no denying that vision-based recognition is a challenging and multi-disciplinary research because of the diversity and ambiguity gestures.

Currently, the modeling based on the color of skin is widely used in gestures recognition. The region of hands is segmented through the color of skin. Common gesture recognition algorithm is HMM, SVW, BP, DTW and so on [1-4]. In 1991, the Fujitsu laboratory finished the recognition of 46 kinds of gestures [5]. Jintae Lee and Tosiyasu L. Kunii analyzed three-dimensional gesture automatically based on the dynamic image data acquired from camera. Then they extract the features of contour

boundary and got 27 parameters of hands. Finally, they finished the reconstitution of three-dimensional gestures [6]. Ren Hhaibin finished the recognition of 12 kinds of gestures based on Multi-state Gaussian probability model which was independent distribution [7]. Hardy Francke built a real-time gesture recognition system by using Boost classifier and Self-learning algorithm [8]. Yang Bo extracted the characteristics of the spatial relative density and knuckle relative spacing. The similarity of gesture feature vector is computed to recognize gestures [9]. Sheng-Yu Peng use Camshift to track hands. He also use PCA to recognize six kinds of gestures [10].

Vision-based gesture recognition process can be divided into three stages: gesture segmentation, feature extraction and gesture classification. According to the three stages, this paper presents that we can use depth image to recognize gestures which are in complex background. In depth images, pixel expresses the physical distance from objects to the camera. So we can finish gesture segmentation by setting the dynamic threshold of distance. The center of hand is extracted by using mathematical morphology and edge extraction algorithm. The features, such as outlines, the radian and number of fingers, are used to recognize gestures. Then we match with the self-organized image database in the method of the minimum distance. Finally, a dexterous hand with five fingers is controlled to behave as what he/she does accurately.

2 System Configuration

2.1 Image Acquisition

The image is acquired through the Kinect. There are three camera lens in Kinect, the left one is infrared emitters, the middle one is RGB camera, and the right one is IR CMOS camera. The infrared emitters and the IR CMOS camera constitute 3D depth sensors (Fig.1).

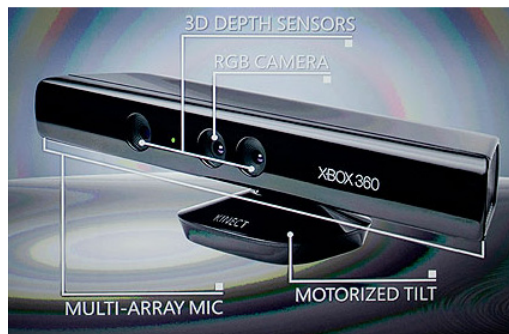


Fig. 1. Depth sensors-Kinect

Kinect uses Light Coding technology to detect the depth. Pixel in depth images expresses the physical distance from objects to the sensor. Pixel values will increase as the distance becomes larger. The actual detection distance of the camera is from 0 to 4096mm. The error range is 5mm when the distance is between 1200mm and 3600mm. Fig.2 is a typical depth image.



Fig. 2. Typical depth image

2.2 Hands Segmentation Based on the Threshold of Depth Image

Histogram statistics is used to segment the hand from complicated background. Histogram indicates the number of pixels which are in same gray levels, reflecting the frequency of each gray-scale image (Fig.3).

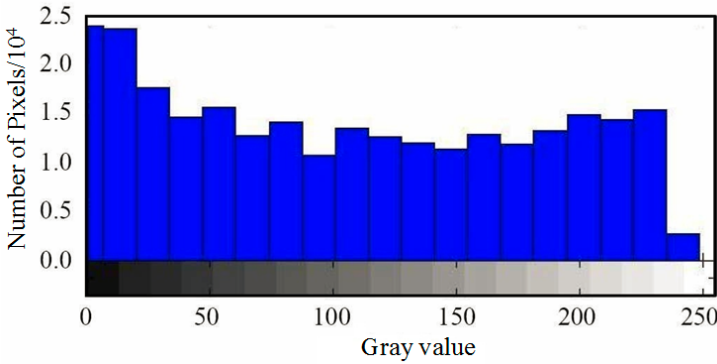


Fig. 3. Gray histogram

After the quantization of gray histogram, we can get the centroid of the hand region. The depth pixel value of the centroid is converted to space actual distance $d_{\text{Hand Center}}$. Then $d_{\text{Hand Center}}$ is the threshold for dynamic hand segmentation. The method of segmentation is shown in equation (1).

$$D_{hand}(x, y) = \begin{cases} 1, & d(x, y) \in (Z \pm \tau) \\ 0, & \text{otherwise} \end{cases} \quad (1)$$

Where: the $D_{hand}(x, y)$ is gesture area. $d(x, y)$ is actual depth value of the pixel(x,y). Z is dynamic threshold acquired from depth image.

There is noise in the binary image, so we need to conduct morphological filtering. The process is in Fig.4

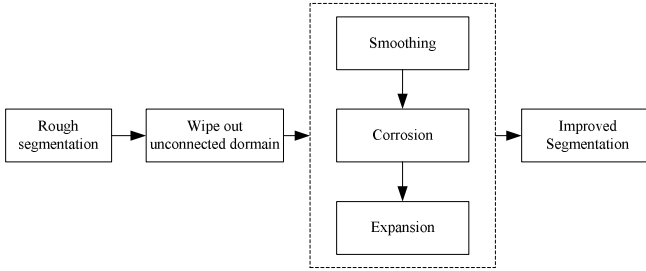


Fig. 4. Simulation model of PV system

2.3 Extraction of the Features about Hand Images

Gesture features have important influence on the recognition result. The common features are gray level, contour, border, region, etc. In this paper, we take the finger radian, interphalangeal radian, number of fingers as recognition features.

In Fig.5, we define the radian between A_1 and A_2 as finger radian. The radian between A_2 and A_3 is called interphalangeal radian.

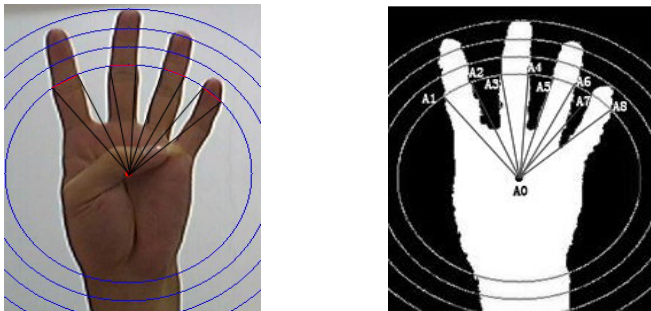


Fig. 5. Dividing of gesture

The following is feature extraction procedure.

(1) For the segmented binary image, using cvMoments structure to get distance parameter and gesture central point. In the two-dimensional image coordinates with coordinate axis X and axis Y, the two-dimensional p, q stage central moment and central point coordinate of region D are as follows:

$$\tilde{M}_{p,q} = \frac{1}{M_{0,0}} \int_D (x - \bar{x})^p (y - \bar{y})^q dx dy, \quad \bar{x} = \frac{M_{10}}{M_{00}}, \quad \bar{y} = \frac{M_{01}}{M_{00}}$$

Among them, $M_{0,0}$ is the two-dimensional 0 stage moments and the effective area of region D. (\bar{x}, \bar{y}) is the central point's coordinate value of region D.

(1) The maximum distance L between the edge of the hand gestures and the central point of the hand region is calculated. The circumcircles, with the central point as

the center and L value as the radius, are drawn. The circumcircles are divided equidistantly from inner to outer. This paper divides it in ten equal portions. Concentric circles, with $d=L/10$ and the central point of the gesture region as the center, are drawn. Define $i=1, 2, \dots, 10$ as the number of the layers. O_i is the circular trajectory of layer i .

(2) The circular finger radian and interphalangeal radian of layer i ($5 \leq i < 10$) are calculated. Using hand central point as the polar point of the polar coordinate. The changed points on the circular trajectory are traversed by polar coordinate style. The angle of the pixel points are recorded when they change. Then the finger radian and the interphalangeal radian are calculated.

(3) Radian number is the sum of the wrist and palm connection branches. The average value of the branches' width is calculated, based on the fact that the wrists are much wider than the fingers. The wrist is the widest place, and the others are the finger branches. So, the number of the branches is $N-1$. But the fingers differ in length. The fingers in out layers are less. So the finger's number is hierarchically record for recognition.

Finger radian, interphalangeal radian and the number of finger radian are hierarchical recorded and to be as the features for recognition.

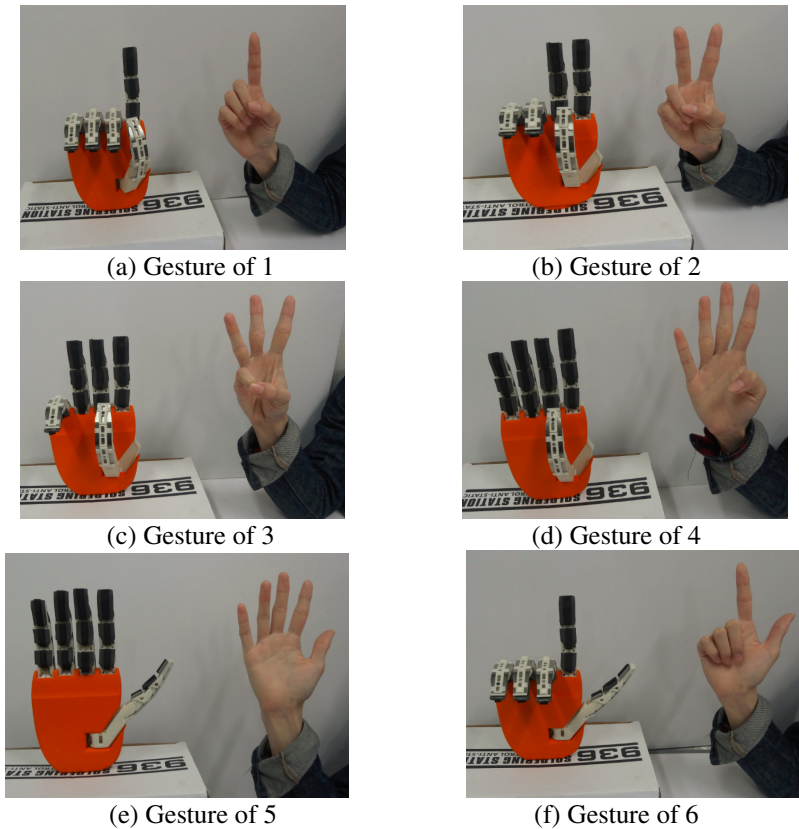


Fig. 6. Examples of the results

3 Experiments

Figure 6 shows the examples of the experimental results. Each result shows the controlled robot on the left side, and human hand on the right side of each snapshot. It can be understood that the human hand is estimated in high accuracy and the robot hand is controlled according to the gestures when the human hand change its gesture.

4 Conclusion

The accurate real-time hand gesture estimation can be applied in many systems, such as robot hand control which imitates the same motions as humans by self-observation, and human-machine interface by moving one's hand and fingers. Therefore we proposed this system and the method of robot hand control, by constructing the database where the sequence was previously sorted according to the feature of each image.

From numerous experiments, it can be seen that the proposed system performs with excellent accuracy.

References

1. Lee, J., Kunii, T.L.: Model based Analysis of Hand Posture. *Computer Graphics and Applications* 5(5), 77–86 (1995)
2. Nasser, H., Dardas, N.D.: Georganas: Real-Time Hand Gesture Detection and Recognition. *Computer Vision and Image Understanding* 60(11), 3592–3607 (2011)
3. Suk, H.I., Sin, B.K., Lee, S.W.: Hand gesture recognition based on dynamic Bayesian network framework. *Pattern Recognition* 43(9), 3059–3072 (2010)
4. Zhang, X., Chen, X., Li, Y.: A framework for hand gesture recognition based on accelerometer and EMG sensors. *IEEE Transactions on Systems, Man and Cybernetics, Part A: Systems and Humans* 41(6), 1064–1076 (2011)
5. Wachs, J.P., Kölsch, M., Stern, H.: Vision-based hand-gesture applications[J]. *Communications of the ACM* 54(2), 60–71 (2011)
6. Francke, H., Ruiz-del-Solar, J., Verschae, R.: Real-time hand gesture detection and recognition using boosted classifiers and active learning. In: Mery, D., Rueda, L. (eds.) *PSIVT 2007*. LNCS, vol. 4872, pp. 533–547. Springer, Heidelberg (2007)

The Application of Computational Chemistry and Chemometrics to Developing a Method for Online Monitoring of Polymer Degradation in the Manufacture of Bioresorbable Medical Implants

Darren A. Whitaker¹, Fraser Buchanan², Domhnall Lennon², Mark Billham², and Marion McAfee¹

¹ Centre for Precision Engineering, Materials & Manufacturing, Institute of Technology Sligo, Sligo, Ireland

² School of Mechanical & Aerospace Engineering, Queen's University Belfast, Belfast, UK

Abstract. Bioresorbable polymers such as PLA have an important role to play in the development of temporary implantable medical devices with significant benefits over traditional therapies. However, development of new devices is hindered by high manufacturing costs associated with difficulties in processing the material. A major problem is the lack of insight on material degradation during processing. In this work, a method of quantifying degradation of PLA using IR spectroscopy coupled with computational chemistry and chemometric modeling is examined. It is shown that the method can predict the quantity of degradation products in solid-state samples with reasonably good accuracy, indicating the potential to adapt the method to developing an on-line sensor for monitoring PLA degradation in real-time during processing.

Keywords: Bioresorbable polymer, PLA, IR spectroscopy, computational chemistry, chemometrics.

1 Introduction

Bioresorbable polymers are predicted to have a significant impact on modern medicine. They are increasingly being used to create temporary medical devices for implantation inside the human body. Such a device provides temporary mechanical support and/or other functions and break down over time into simple non-toxic products – ideally at the same rate that the body's own tissue regenerates. Drug-eluting bioresorbable medical implants are active implants that induce healing effects, in addition to their regular task of support. This effect is achieved by controlled release of active pharmaceutical ingredients (API) into the surrounding tissue as the polymer degrades.

The concept is being used or developed in a wide range of applications such as orthopaedics (fracture fixation plates, pins and screws, bone augmentation); surgery

(ligament repair, wound closure sutures, suture anchors, skin staples, adhesion barriers, drug delivery, antineoplastic delivery, ligating clips, hemostasis clips); stents, and tissue engineering.

However, high development and manufacturing costs have hindered growth of the industry. Bioresorbable polymers have a high cost and are difficult to process into the form required for the implant application. Usually some form of melt processing such as extrusion or injection molding is required, where the heating and shearing of the material tends to degrade the material. Currently, long and expensive trial and error periods are required to establish process settings for a new device and yet result in typical scrap rates of 25-30% - in many cases this is prohibitive to successful commercialisation. A major problem is the lack of information on key product properties during processing. Conventional polymer melt processing instrumentation consists largely of temperature and pressure sensors which give little insight on chemical changes to the material and are difficult to correlate to final product properties such as mechanical properties and biodegradation. Therefore, determination of product quality generally requires expensive and time-consuming off-line testing, resulting in long lead times and high rates of out of specification product.

In this work, the potential to use vibrational spectroscopy techniques together with chemometric modelling to analyse the degradation of a bioresorbable polymer is investigated. Such a method has the advantage of being possible to implement online during processing of the polymer and as such could provide real-time information on key product properties.

The remainder of the manuscript is organized as follows: first, a brief review is given of the effect of melt processing on the properties of PLA. Next the experimental thermal processing and characterization methods are described, followed by the computational chemistry techniques used to predict changes in the infra-Red (IR) spectra of the material when it undergoes degradation. This is followed by a description of the chemometric methods applied to develop a model relating polymer degradation to the experimentally acquired spectral data. The results are presented and discussed and finally some conclusions are posed on the future potential of the method to the manufacturing of bioresorbable medical devices.

2 Melt Processing of Bioresorbable Polymers

Melt processing steps, particularly extrusion or injection molding, are the most common techniques for the forming of bioresorbable polymers such as Polylactic Acid (PLA) into final products. PLA is susceptible to thermal degradation and it is suggested that the temperatures, and residence times should be kept low to avoid reduction of polymer molecular weight and the formation of monomers[1]. The generation of monomers (lactide) during processing accelerates hydrolytic degradation of the material and has a significant impact on the biodegradation rate and rate of loss of mechanical properties. It has been found that increasing shear can avoid the formation of monomer in the process [2, 3]. The processing of bioresorbables is significantly more complex than that of conventional engineering plastics, not only due to the sensitivity to

degradation, but also since it is almost impossible to use fillers or additives to aid processing since most of these are not approved for use in the human body. Further, the high sensitivity of the materials to processing factors can mean that the slight variations between batches of raw material can result in significant product deviations under the same processing conditions. Adjusting the process settings to compensate for the feed variations is not an easy task as 1) the properties of the feed material are not accurately known; and 2) the key resulting properties of the polymer melt cannot be determined online during processing.

In the next sections the ability to analyse thermal degradation – encompassing changes in Molecular weight and/or lactide content – using a vibrational spectroscopy method which can then be applied in process, is examined.

3 Experimental Section

Sample Preparation

Poly-L-Lactide (PLLA) (Purasorb (PL38) (Purac, Gorinchem, The Netherlands) samples were produced by compression moulding. Pellets were placed in the centre of a stainless steel frame with internal dimensions of 100 x 60 mm. Before compression was started, a sheet of parchment paper was placed above and below the frame which was then sandwiched between two plates of stainless steel, before being placed into the press. This was to ensure the material did not come into direct contact with the press. Pellets were compression moulded at a range of temperatures with different residence times (Table 1). All samples were held at a pressure of 10MPa to produce flat sheets at 1 ± 0.1 mm thickness.

Table 1. Parameters of processing for PLA samples

Sample	Temperature (°C)	Time (min)	Cooling Method	Notes
A	200	10	Crash Cooled	Annealed
B	200	10	Crash Cooled	
C	220	10	Crash Cooled	
D	240	10	Crash Cooled	
E	240	30	Slow Cooled	

Infrared Spectroscopy

Infrared spectra of the PLA samples were recorded on a Perkin-Elmer spectrum 100 using an ATR sampling accessory. The spectra were recorded over a wavenumber range of 600 – 4000 cm^{-1} , with a resolution of 4 cm^{-1} . A single spectrum was constructed from co-addition of 16 scans over the defined wavenumber range. Ten spectra were recorded from different places on the sample to account for any in sample variation which may be observed.

GC-MS

Gas Chromatography – Mass Spectrometry (GCMS) was carried out to quantify the lactide concentration in the PLLA samples.

A portion of the processed PLLA sample (*ca.* 1g) was dissolved in chloroform (18 mL). 2,4-dimethyl- γ -pyrone (1 mL, 10,000 ppm) solution was added. A portion of this solution (1 mL) was added to a mixture of acetone (3 mL) and cyclohexane (16 mL). This solution was filtered using a 0.45 μm syringe filter and presented for GC analysis.

Samples were run on a Varian 3900 gas chromatograph fitted with an Agilent DB-FFAP column coupled to a Varian Saturn 2100T mass spectrometer. 1 μL of the sample was injected into the injector port operating in splitless mode at 200 $^{\circ}\text{C}$, the column oven was set at 65 $^{\circ}\text{C}$ for 1 minute and then ramped at 30 $^{\circ}\text{C} \cdot \text{min}^{-1}$ to 250 $^{\circ}\text{C}$ where the temperature was held for 2 minutes. After 1 minute the split valve of the injector was operated to purge the injector port of any residual sample. Carrier gas used was helium at a continuous flow rate of 0.8 $\text{mL} \cdot \text{min}^{-1}$. Quantification was achieved by calculation of the relative response factors from a stock solution of lactide (10,000 ppm) and the internal standard (2,6-dimethyl- γ -pyrone, 10,000 ppm).

Computational Chemistry

Ab Initio calculations were performed using the GAMESS[4] suite of programs and utilizing the computational power of ICHEC's FIONN supercomputer. Calculations were typically carried out on two of FIONNs nodes (each node containing 2 x 12 Intel Ivy Bridge cores and 64 GB of RAM).

Calculations were carried out for; *r,r*- (or D-), *s,s*- (or L-) and meso-lactide and also for a PLA 3-mer (Figure 1). The three isomers of lactide (*r,r*-, *s,s*- and *meso*-) were calculated separately to identify any band contributions which may be assigned to the presence of a specific isomer. This is important as all three isomers may be present within the sample, so any quantification will need to take into account contributions from all three isomers.

Calculations were performed at the B3LYP level of theory using the correlation consistent polarized valence double-zeta basis set (CC-PVDZ) proposed by Dunning *et al*[5, 6]. The work flow consisted of three steps: first the geometry was optimized; second a hessian calculation was carried out to compute IR frequencies and to ensure that the optimized geometry was a stable configuration (no negative frequencies); thirdly a Raman calculation was carried out using the geometry and hessian from the second calculation.

Following this, a VSCF (at B3LYP and CC-PVDZ) calculation was carried out to treat the anharmonicity of the vibrational modes.

Spectral curves were constructed by adding a Lorentzian peak shape with a full width half maximum (FWHM) of 10-15 cm^{-1} to each transition, the sum of all the peaks were then calculated to display the computed trace[7, 8].

Chemometrics

Chemometrics were carried out using the R software[9] and RStudio as a graphical front end[10]. Linear discriminant analysis was carried out using the *lda* routine in the MASS package for R[11]. Data files were batch imported using custom written import routines. The aim of the chemometric analysis was to create a model which can classify the spectra based on the amount of degradation, or a model which can quantify the amount of lactide in the sample.

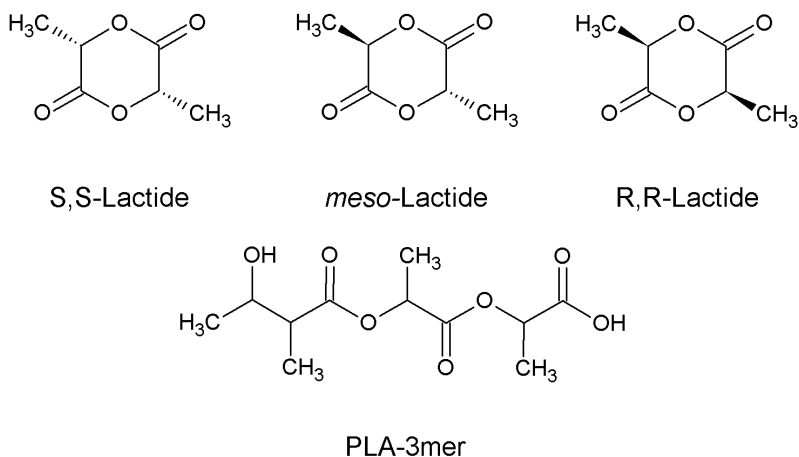


Fig. 1. Molecular structures of lactide isomers and a PLA trimer

4 Results and Discussion

The optimised structures (Figure 2) for the *s,s*-, and *r,r*-lactide molecules show a “chair” like conformation with both CH_3 groups adopting an axial position, whereas in the *r,s*-lactide one CH_3 group locates at the axial and the other at the equatorial position. Bond lengths (not shown) for the *r,r*-(or *s,s*) and *r,s*-lactide molecules are in agreement with published X-Ray data[12].

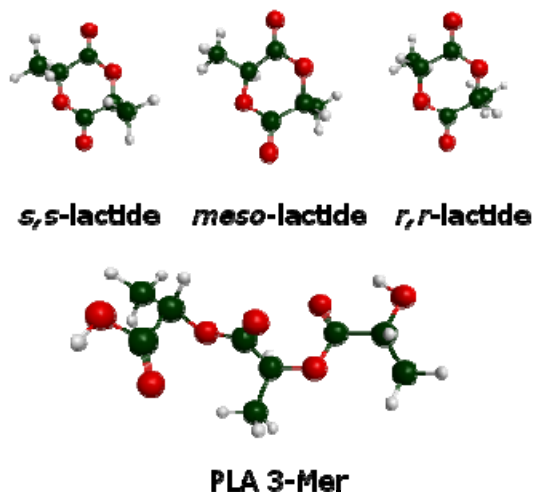


Fig. 2. Optimised structures of lactide isomers and a PLA trimer

As would be expected the calculated IR spectra of *r,r*- and *s,s*- lactide are identical, the spectrum of *r,s*-lactide however, differs slightly (Figure 3). The main differences are observed in modes relating to CH vibrations, this is due to the variation in local environments of the methyl groups. For example the *r,r*- and *s,s*-lactides show a single transition for the $\nu_{(\text{sym})}\text{CH}_3$ and the $\nu_{(\text{asym})}\text{CH}_3$ whereas the *r,s*-lactide shows two transitions for each mode, clearly due to the non-symmetric nature of the *r,s*-lactide molecule (Figure 4).

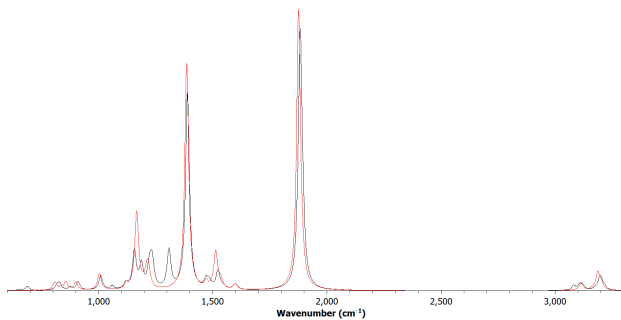


Fig. 3. Predicted IR spectrum of *meso*- (black) and *r,r*-/*s,s*-Lactide (red)

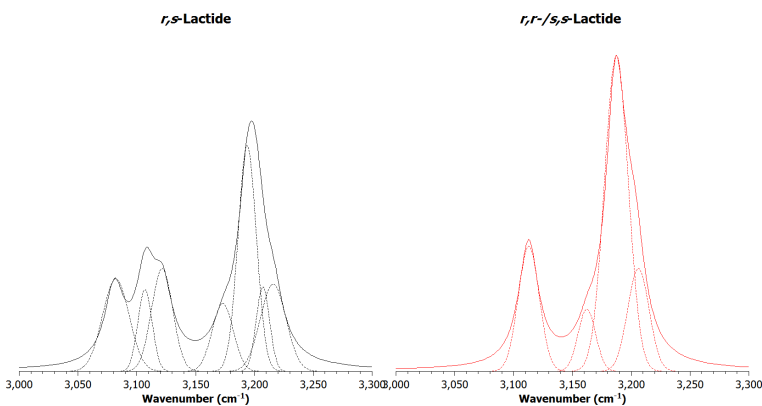


Fig. 4. CH stretching region of predicted spectra of lactide isomers displaying fitted peaks under curves (dotted)

These predictions display a relatively good agreement with experimental values (Figure 5) deviations are expected as the homochiral racemic sample is likely to contain small amounts of the heterochiral isomer (due to epimerisation during storage) which would result in peak broadening and shifting.

Chemometric analysis showed a reasonable separation between samples, which allowed classification boundaries to be observed. PCA was performed to reduce the dimensionality of the data, from this LDA was performed on the first 10 components. A plot of LD1 vs LD2 as a result of this shows clear separation between the samples.

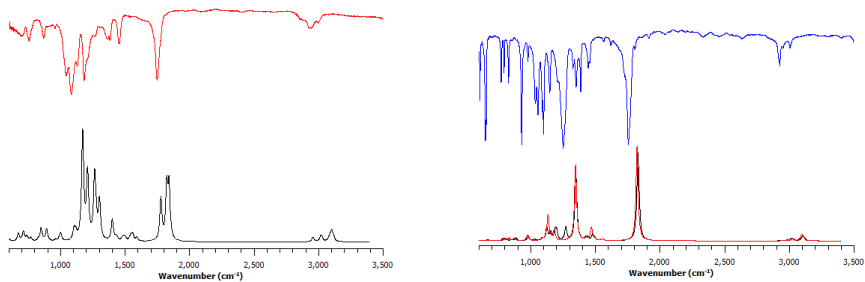


Fig. 5. Predicted (bottom) and experimental (top) spectra for a PLA trimer (left) and the lactide isomers (right)

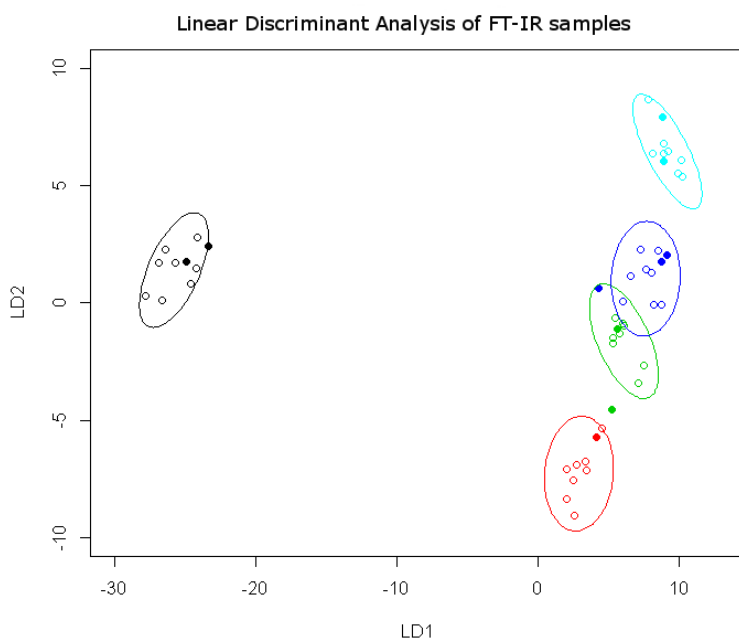


Fig. 6. LD1 vs LD2 for the IR spectra of processed PLA samples

Sample A (Figure 6, black points) was located the furthest away from the main cluster, this is likely owing to the difference in optical properties of this sample from the annealing process. Samples B, C, D, and E were clustered with minimal variation in LD1 but good separation from LD2. Two spectra of each sample were run through the model and all but two were correctly classified (Figure 6, filled circles).

Following a good separation, two quantitative models based on PLS analysis was built. One model used the whole spectrum and another focused on just the CH stretching region (as computations suggested variation would be seen here from increasing CH contributions from lactide as concentrations increased). GCMS results allowed quantification of lactide content in the processed samples (Table 2), these values were used to construct a model trained with a 30 spectra subset of the data (5 spectra from each sample) and then tested with the same sized subset. The model was able to predict the actual lactide content to within $<\pm 5\%$ in most cases, although some outliers were greater than this (Table 3). Overall performance (measured using the RMSEP values) of the model using just the CH stretching frequencies was better than the model using the full spectrum (Figure 7).

Table 2. Lactide content of samples

Sample	Lactide (w/w %)
A	0.12
B	0.07
C	0.09
D	0.24
E	1.20

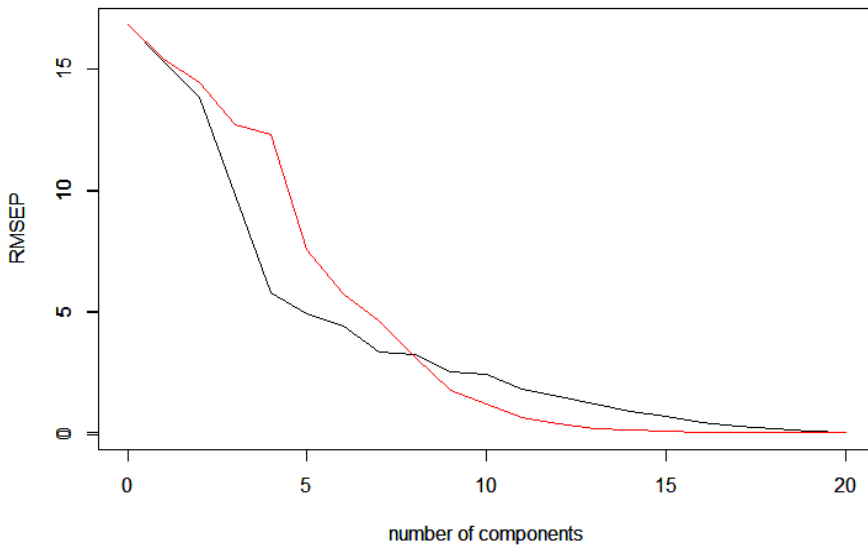


Fig. 7. RMSEP values for the PLS model. Model using whole spectrum (black) and model using CH stretching region only (red).

Table 3. Actual and predicted values from the PLS models

Lactide concentration	CH Stretching Region Model		Whole Spectrum Model	
	Predicted Concentration	Δ	Predicted Concentration	Δ
0.12	0.26	0.14	0.12	0.00
0.12	0.44	0.32	0.22	0.10
0.12	0.19	0.07	0.06	-0.06
0.12	0.18	0.06	-0.01	-0.13
0.12	0.16	0.04	0.15	0.03
0.07	-0.20	-0.27	0.01	-0.06
0.07	-0.09	-0.16	0.07	0.00
0.07	0.00	-0.07	0.06	-0.01
0.07	-0.08	-0.15	0.16	0.09
0.07	0.36	0.29	0.26	0.19
0.09	0.46	0.37	0.27	0.18
0.09	0.25	0.16	0.17	0.08
0.09	0.32	0.23	0.25	0.16
0.09	0.10	0.01	0.02	-0.07
0.09	0.09	0.00	0.13	0.04
0.24	0.08	-0.16	0.17	-0.07
0.24	0.21	-0.03	0.25	0.01
0.24	0.21	-0.03	0.21	-0.03
0.24	0.03	-0.21	0.05	-0.19
0.24	0.54	0.30	0.34	0.10
1.20	0.97	-0.23	0.93	-0.27
1.20	0.97	-0.23	0.92	-0.28
1.20	1.25	0.05	1.19	-0.01
1.20	1.19	-0.01	1.12	-0.08
1.20	1.07	-0.13	1.12	-0.08
0.12	0.26	0.14	0.12	0.00
0.12	0.44	0.32	0.22	0.10
0.12	0.19	0.07	0.06	-0.06
0.12	0.18	0.06	-0.01	-0.13
0.12	0.16	0.04	0.15	0.03

5 Conclusions

The initial work presented in this paper has centered on the construction of models which were able to classify PLA samples showing differing degrees of process induced degradation. This was extended to build a model which was able to predict the lactide content of the analysed sample with a relatively good degree of accuracy. The computational methodology employed was able to identify areas of the spectrum where sufficient variation due to process induced lactide may exist. When compared with a whole spectrum approach this significantly improved the predictive accuracy of the model

There are still improvements to be made, these are based on an improvement of data acquisition and an increase in data points / data classes made available for training the models. Additionally the models will be extended for use with other techniques which are perhaps more conducive to online monitoring (nIR and Raman spectroscopies), with the overall goal being a system which updates the user in real time which class the sample belongs to, with the possibility of providing an estimated lactide content.

Acknowledgements. The research leading to these results has received funding from the European Union's Seventh Framework Programme managed by REA-Research Executive Agency [http://ec.europa.eu/research/rea\(FP7/2007-2013\)](http://ec.europa.eu/research/rea(FP7/2007-2013)) under grant agreement n°605086 FP7-SME-2012. The Science Foundation Ireland (SFI) and Higher Education Authority funded Irish Centre for High End Computing (ICHEC) is acknowledged for access to computational facilities.

References

1. Taubner, V., Shishoo, R.: Influence of processing parameters on the degradation of poly(L-lactide) during extrusion. *J. Appl. Polym. Sci.* 79, 2128–2135 (2001)
2. Paakinaho, K., Ellä, V., Syrjälä, S., Kellomäki, M.: Melt spinning of poly(l/d)lactide 96/4: Effects of molecular weight and melt processing on hydrolytic degradation. *Polym. Degrad. Stab.* 94, 438–442 (2009)
3. Ellä, V., Nikkola, L., Kellomäki, M.: Process-induced monomer on a medical-grade polymer and its effect on short-term hydrolytic degradation. *J. Appl. Polym. Sci.* 119, 2996–3003 (2011)
4. Schmidt, M.W., Baldrige, K.K., Boatz, J.A., Elbert, S.T., Gordon, M.S., Jensen, J.H., Koseki, S., Matsunaga, N., Nguyen, K.A., Su, S., Windus, T.L., Dupuis, M., Montgomery, J.A.: General atomic and molecular electronic structure system. *J. Comput. Chem.* 14, 1347–1363 (1993)
5. Dunning, T.H.: Gaussian basis sets for use in correlated molecular calculations. I. The atoms boron through neon and hydrogen. *J. Chem. Phys.* 90, 1007 (1989)
6. Kendall, R.A., Dunning, T.H., Harrison, R.J.: Electron affinities of the first-row atoms revisited. Systematic basis sets and wave functions. *J. Chem. Phys.* 96, 6796 (1992)
7. Brauer, B., Pincu, M., Buch, V., Bar, I., Simons, J.P., Gerber, R.B.: Vibrational spectra of α -glucose, β -glucose, and sucrose: anharmonic calculations and experiment. *J. Phys. Chem. A.* 115, 5859–5872 (2011)

8. Pele, L., Šebek, J., Potma, E.O., Benny Gerber, R.: Raman and IR spectra of butane: Anharmonic calculations and interpretation of room temperature spectra. *Chem. Phys. Lett.* 515, 7–12 (2011)
9. R Core Team: R: A Language for Statistical Computing. R Found. Stat. Comput. (2013)
10. RStudio: RStudio: Intergrated Development Environment for R (2013)
11. Venables, W.N., Ripley, B.D.: *Modern Applied Statistics with S*. Springer, New York (2002)
12. Van Hummel, G.J., Harkema, S., Kohn, F.E., Feijen, J.: Structure of 3,6-dimethyl-1,4-dioxane-2,5-dione [D-,D-(L-,L-)lactide]. *Acta Crystallogr. Sect. B Struct. Crystallogr. Cryst. Chem.* 38, 1679–1681 (1982)

Modeling and Simulation of the Neural Control on OSAS with Fluid-Structural Interaction Method

Qiguo Rong¹, Shuang Ren¹, and Qihong Li²

¹ College of Engineering, Peking University, Beijing 100871, China

² Department of Stomatology, Afiliated Hospital of Academy of Military Medical Sciences, Beijing 100071, China

Abstract. Numerical simulation is an effective tool to study the biomechanical mechanism of the upper airway collapse, but few previous studies have considered the effect of the neural control. Based on a finite element model including airway, skull, neck, hyoid and soft tissue around the upper airway, the effect of the neural control on the upper airway collapse was studied with fluid-structure interaction method. Spring element was used to simulate the function of the muscle group. The results show that the strain concentration disappears and the airway resistance decreases during the apnea episode when the neural control exists, which means that the neural control reduces the deformation of airway successfully and avoids the risk of OSAS.

Keywords: Sleep apnea, Upper airway collapse, Fluid-structure interaction.

1 Introduction

Obstructive sleep apnea syndrome (OSAS) is a respiratory disease characterized by the upper airway collapses and reopens repeatedly during sleep. The collapsed airway restricts or even blocks the airflow totally until the obstructive site disappears. As a result, the OSAS patients suffer the frequent switch between asleep and aroused status, which leads to the severe somnolence in the daytime and cardiovascular or cerebrovascular disease.

In addition to abnormal anatomical structures, weak or absence of the neural control on respiration is also an important factor. Many studies have confirmed the important role of muscle excitability on respiration [1-9]. With the help of polysomnography, it can be found that neuromuscular myoelectricity around upper airway is higher for OSAS patients than normal person in the daytime while drops sharply during sleep especially rapid eye movement sleep. There exist several types of neurotransmitter distributed around the airway wall which function as receptors that can perceive the change of physical or chemical environment, such as pressure variation inside the airway or the fluctuation of oxygen saturation in blood. This information is transmitted by neurotransmitter to the respiratory central nervous system which is in control of the hypoglossal motor neurons that innervate the muscles associated with upper airway. In other words, the control strength of muscles on upper airway

varies with some physical and chemical parameters which reflect the breath state under normal circumstances.

The breathing process is in fact a mechanical problem with fluid and structure interaction. A three-dimensional finite element model of the upper airway was developed in [10]. It was also applied to study the effect of upper airway shape on OSAS [11]. The purpose of this paper was to study the effect of the neural control on OSAS by finite element method.

2 Method

The FE model includes skull, neck, hyoid, airway and the surrounding soft tissues, as shown in Fig. 1. The loading conditions, boundary conditions, and the material parameters are the same as in [10].

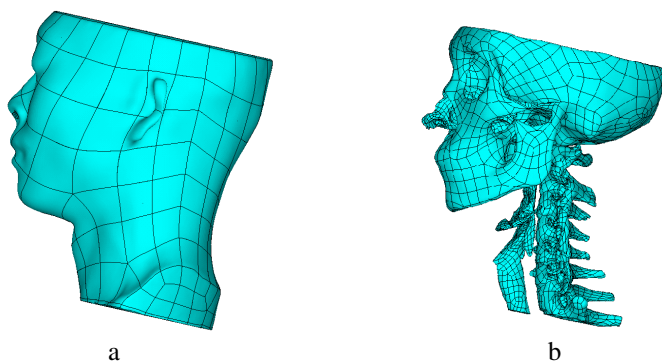


Fig. 1. Finite element model of the upper airway and the surrounding structures. a: the skin and soft tissues; b: the upper airway and bone structures.

A linear spring element was chosen to simulate the effect of the neural control. The spring elements were created directly by nodes. The stiffness matrix of element has only one component. The action force of the spring element depends on the relative displacement of the nodes. The directions of the muscles applied on the upper airway depend on the spatial distribution and attachments of the muscles. Whichever the force direction is, the final effect turns out to inhibit excessive contraction of the airway and retain regular conformation of the airway. Thus, the spatial distribution of the action forces wasn't taken into consideration in this study, and all spring elements are along the sagittal direction. The muscle group distributes just in front of the neck, so only the anterior wall of the airway will be exposed to muscle forces. The spring elements were applied on nodes of the airway from oropharynx to the anterior of the hyoid. The spring elements were shown in Fig. 2a. By now, there are no quantitative studies on muscle stiffness under the neural control during sleep. In this study, the force-displacement curve of the muscles was assumed nonlinearly, as shown in Fig. 2b.

The fluid-structure coupled simulation of respiratory process was carried out using FE software Adina, which offers a one-system program that specializes in fluid

structure interaction. The main principle of the coupled algorithm in Adina is that the displacement compatibility and the pressure equilibrium along the structure-fluid interfaces should be satisfied.

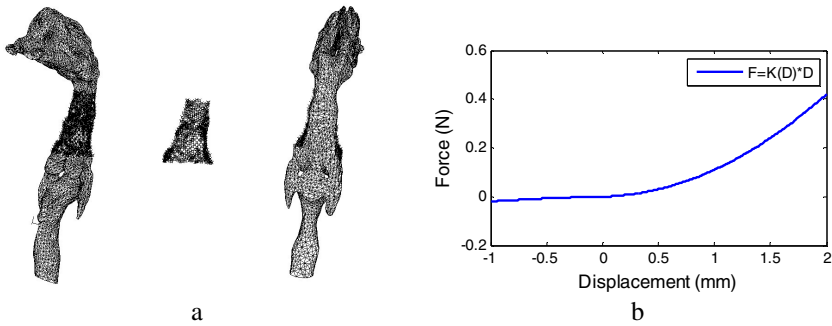


Fig. 2. The neural control of the upper airway. a: the position of spring elements; b: the force-displacement curve of the spring elements.

In view of the enormous degrees of freedom and the fluid-structural coupled algorithm, the equations for structural dynamics were solved with the sparse solver and the nonlinear finite volume equations for airflow were solved iteratively with Newton-Raphson method. The time step length is designed quite small at the beginning, for the purpose of obtaining a reasonable initial condition for the iteration in the transient analyses. However, the time step length depends on the pressure gradient variation, especially around the peak value as well as the moment when expiratory phase transits to inspiratory phase or in verse. Therefore, the time step length was artificially set only at the initial moment, and then was automatic regulated by the algorithm.

3 Results and Discussion

A cross section located on the oropharynx part was selected to describe the deformation of the upper airway. Fig. 3 shows that the airway model with spring elements contract less under the same negative pressure, and expanded less under the same positive pressure than that without spring elements. Therefore, the spring elements resist the excessive deformation of the airway. The posterior wall of the airway has no spring elements, consequently, there is no difference in the posterior walls of the airway between models with and without spring elements.

It should be noted that although deformation of the airway in sagittal direction decreased due to regulation of the spring elements, inward contraction of the sidewalls of the airway increased, especially under larger negative pressure during inspiration. Without regulation of the spring elements, serious inward collapse of the anterior wall of the airway led to increase of the curvature of the sidewalls of the airway, which in turn enhanced anti-bend stiffness of the sidewalls so that its inward collapse was not obvious. In the model with spring elements, reaction forces of the spring elements and bone tissue support the anterior and posterior walls of the airway respectively, yet the sidewalls lack support so as to have got obvious collapse.

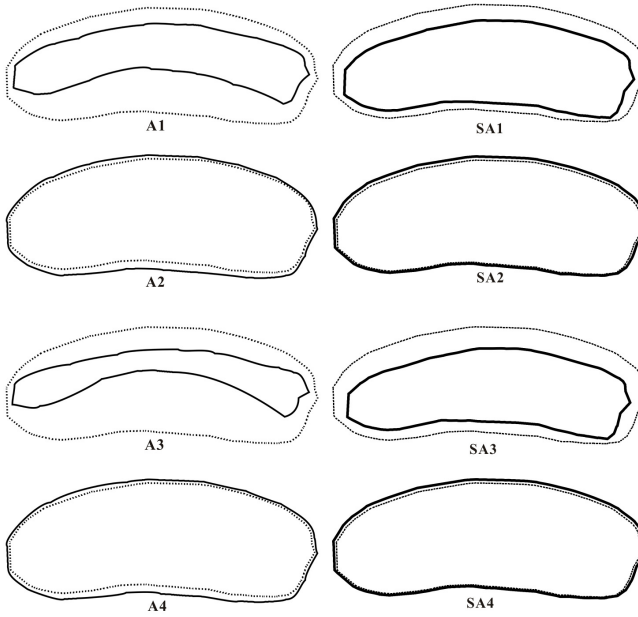


Fig. 3. Deformation of the airway section under sleep apnea pressure condition. Solid line: airway section before deformation; dotted line: airway section after deformation. A1-A4: results of the model without spring elements; SA1-SA4: results of the model with spring elements. Time and pressure of the sections: A1, SA1: T=1.7s, P=-3900Pa; A2, SA2: T=4.2s P=760Pa; A3, SA3: T=8.6s, P=-5500Pa; A4, SA4: T=10.5s P=780Pa.

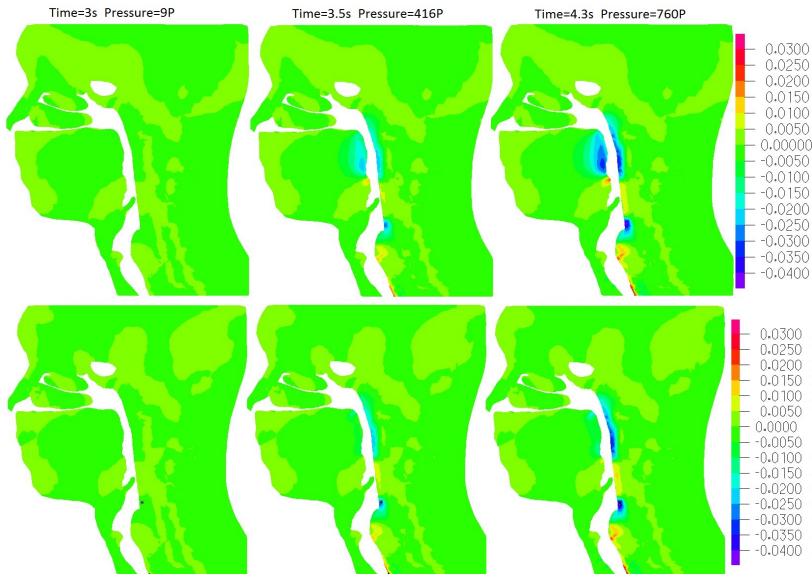


Fig. 4. Expiration: Strain distribution of solid model without (top) and with (bottom) spring elements during expiration in sagittal direction under sleep apnea pressure condition

A sagittal section was selected for analysis of stress and strain distribution. It can be seen from Fig. 4 and Fig. 5 that, in both inspiratory and expiratory phases, strain concentrations in the oropharynx and basement of the tongue disappeared after spring elements were added in the model. At the maximum magnitude of the negative pressure, the boundary of the airway didn't present obvious variations. There is no obvious difference in the strain distributions of the posterior wall of the airway between models with and without spring elements, which shows that spring elements only affect the anterior wall of the airway.

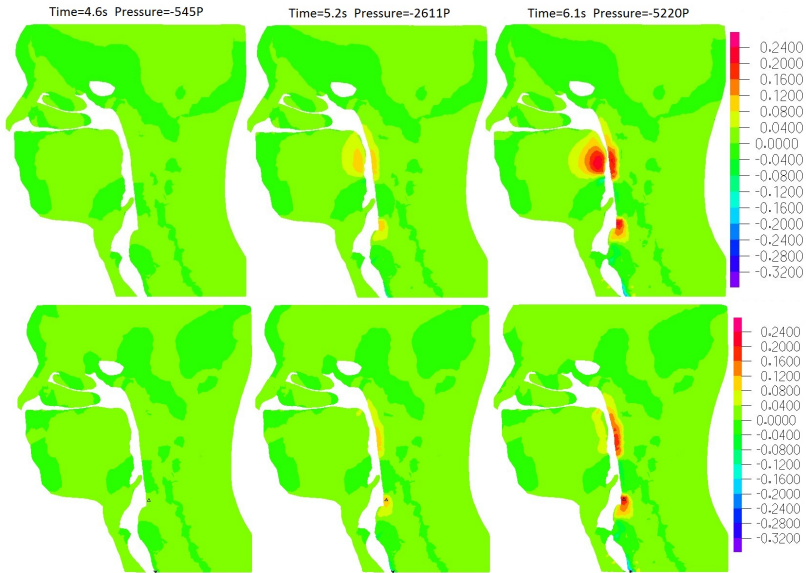


Fig. 5. Inspiration: Strain distribution of solid model without (top) and with (bottom) spring elements during inspiration in sagittal direction under sleep apnea pressure condition.

The air flows in the airway will be obstructed by deformed airway wall which produces flow resistance. The more serious the airway collapse, the larger resistance it generates to the airflow. Besides, the airflow gathers above the obstructive location after collapse of the airway, which in turn increases the pressure in the upper airway. As a result, resistance in the airway is relevant to both the oropharynx deformation and condition of the airflow, and it is also a reflection of breathing fluency. In this study, resistance of the airway is obtained by summing up resistance of every node on the oropharynx areas of the airway. The oropharynx is the most liable position to collapse, and resistance here indicates the general deformation and airflow status of the oropharynx. It can be seen from Fig. 6 that for the expiratory phase under positive pressure, the curves of resistance of the airway with and without spring elements are consistent. The reason lies in that during the expiratory phase, positive pressure expands the airway, and flow field grows, which decrease resistance of the airway wall to the airflow. The action force of the airflow passing the oropharynx to the airway

wall is mainly tangential force. Consequently, there is little difference of the airway expansion between models with and without spring elements, and the results of both models are the same during expiration. When it comes to inspiration phase, the airway without control of the spring elements shrinks inward, and airflow during inspiration applies on collapsed airway. Therefore, resistance of the airway increases as collapse gets larger under greater negative pressure. The spring elements significantly hinder collapse of the airway, which renders less airway resistance in the airway model with spring elements than that without, especially at the peak of the negative pressure.

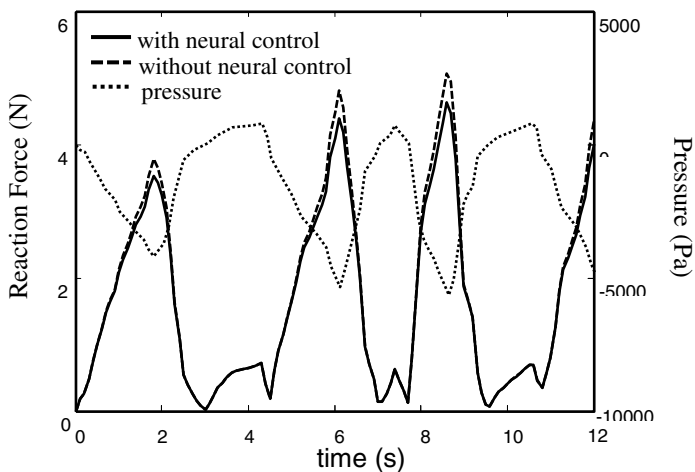


Fig. 6. Relationship of the resistance of the airway in oropharynx and the airway pressure

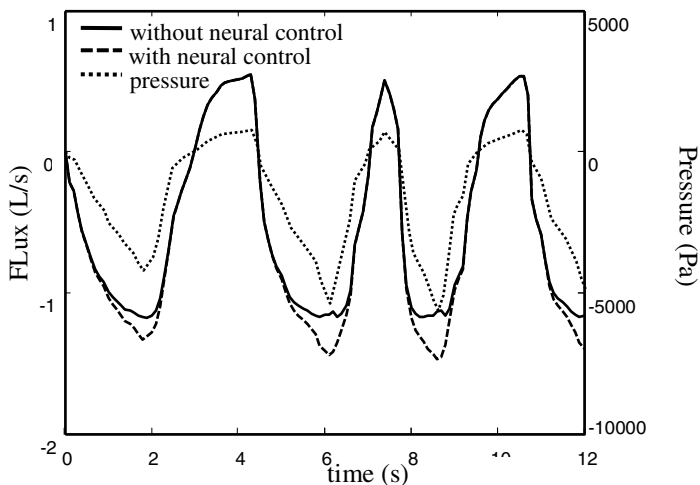


Fig. 7. Relationship of the flux of the horizontal cross-sectional area and the airway pressure under sleep apnea pressure condition

Flux of the section can be obtained by integration of velocity in the section. It can be seen from Fig. 7 that, similar to that of the airway resistance, the curves of the positive flux during expiration of the two models with and without spring elements are basically accordant. However, negative flux during inspiration is obviously higher in the airway model with spring elements than that without spring elements. This is due to that decreased collapse in the airway with spring elements sustains relatively normal configuration of the airway under negative pressure, which guarantees fluent pass of the airflow. During expiration, positive pressure in the airway is lower than the negative pressure, which doesn't induce obvious expansion of the airway. In such a situation, the spring elements don't restrict airway expansion strongly, and the sectional areas don't change obviously. Therefore, during expiration, there is little difference of the flux between the two models.

4 Conclusions

The respiratory neural control has great physiological significance to the normal respiration. Weak or loss of the neural control is one of the major causes of OSAS. In this paper, the effects of the neural control on resisting collapse of the airway were investigated by spring elements. It has been shown that under sleep apnea pressure, after adding spring elements to the airway model, strain concentrations in the oropharynx and basement of the tongue disappeared; resistance of the airway diminished; flux of the horizontal cross-sectional area increased at the peak of the negative pressure in the airway. This study reveals that regulation of spring elements effectively restrains the deformation of the airway, and in turn reduces the occurrence of OSAS. Although the spring elements can't perfectly reflect the mechanism of the regulation of the respiration nerve, it is a meaningful attempt to simulate the dynamic process of respiration using the FE models of OSAS.

Acknowledgements. This study was supported by Beijing Natural Science Foundation Grants 7133248 and 3122020.

References

1. Younes, M., Ostrowski, M., Thompson, W., et al.: Chemical Control Stability in Patients with Obstructive Sleep Apnea. *American Journal of Respiratory and Critical Care Medicine* 163, 1181–1190 (2001)
2. Jiang, C., Rojas, A., Wang, R., et al.: CO₂ central chemosensitivity: why are there so many sensing molecules? *Respiratory Physiology & Neurobiology* 145, 115–126 (2005)
3. Nattie, E.: CO₂ Brainstem chemoreceptors and breathing. *Progress in Neurobiology* 59, 299–331 (1999)
4. Mulkey, D.K., Stornetta, R.L., Weston, M.C., et al.: Respiratory control by ventral surface chemoreceptor neurons in rats. *Nature Neuroscience* 7, 1360–1369 (2004)
5. Horner, R.L.: The neuropharmacology of upper airway motor control in the awake and asleep states: implications for obstructive sleep apnoea. *Respiratory Research* 2, 286–294 (2001)

6. Haberthür, C., Fabry, B., Zappe, D., et al.: Effects of mechanical unloading/loading on respiratory loop gain and periodic breathing in man. *Respiration Physiology* 112, 23–36 (1998)
7. Steier, J., Jolley, C.J., Seymour, J., et al.: Increased load on the respiratory muscles in obstructive sleep apnea. *Respiratory Physiology & Neurobiology* 171, 54–60 (2010)
8. Chen, W.H., Ye, J.Y., Han, D.M., et al.: End-tidal carbon dioxide concentration monitoring in obstructive sleep apnea patients. *American Journal of Otolaryngology*, doi:10.1016/j.amjoto.2010.01.006
9. Kezirian, E.J., Boudewyns, A., Eisele, D.W., et al.: Electrical stimulation of the hypoglossal nerve in the treatment of obstructive sleep apnea. *Sleep Medicine Reviews* 14, 299–305 (2010)
10. Huang, R., Li, X., Rong, Q.: Control mechanism for the upper airway collapse in patients with obstructive sleep apnea syndrome: a finite element study. *Science China Life Sciences* 56(4), 366–372 (2013), doi:10.1007/s11427-013-4448-6
11. Rong, Q., Ren, S., Li, Q.: Effect of upper airway shape on obstructive sleep apnea syndrome: numerical simulation by fluid–structure interaction method. *Journal of Mechanics in Medicine and Biology* 13, 1340009 (2013), doi:10.1142/S0219519413400095

Circulation System Modelling with National Implantable Ventricular Assist Device (NIVAD): Hydrodynamic Characters, Hemolysis Test in Vitro and Animal Experiments

Tieyan Li, Liang Ye*, Rong Lu, Huimin Fan**, and Zhongmin Liu**

Department of Cardiac Surgery, Shanghai East Hospital Affiliated to Tongji University,
200120 Shanghai, China
frankfan@tongji.edu.cn, liu.zhongmin@tongji.edu.cn

Abstract. This study is to detect the flow field characters of NIVAD and the hemolysis test in vitro and to evaluate the hemodynamic performance and the influence on calves. The flow field characters of NIVAD were calculated by CFD. In hemolysis test in vitro, controlled flow of NIVAD 5 L/min and the out-flow tract pressure 100 mmHg, the plasma free hemoglobin (FHB) content and the hematocrit (HCT) were measured at 0, 0.5, 1, ...4 hours. Then NIH (Normal Index of Hemolysis) of NIVAD was calculated. In vivo experiments, NIVAD was implanted in 8 calves. Physiological index and biochemical data of serum were taken during the experiments. The nephograms show the speed and pressure change of NIVAD flow field by CFD. The hemolysis, which was evaluated by NIH was 0.065 ± 0.014 mg/L in vitro, by FHB was below 10 mg/dl in vivo. There was no obvious thrombus and adverse events on the animals and pumps. Biochemical data of serum evaluation showed that implantation of NIVAD in calves did not impair end organ function. Gross and microscopic sections of kidney, liver, and lung revealed no evidence of microemboli, edema or infarcts. The index of NIVAD satisfy the request of clinic use. The results of experiments in vitro and in vivo lay foundations for clinic use in future.

Keywords: Ventricular assist device, Computational Fluid Dynamics, Hemolysis, animal experiments.

1 Introduction

Every year a fifth of heart disease patients worldwide will suffer from heart failure [1]. Currently the treatments for heart failure are drugs, heart transplantation, ventricular assist devices (VAD) and others. Since clinical application of VAD in the 1960s, after a long time of research and development, the axial pump became a major method for treating heart failure. Several kinds of VAD have been applied for clinic applications all over the world, of which HeartWare, Berlin Heart Incor, DeBakey

* This author contributed equally to this work.

** Corresponding author.

VAD and so on are the best known. However, merely few VAD are used in China partly because of their high prices. Thus, it is imperative to develop a domestic VAD with our independent intellectual property rights, although the domestic research started much later in a very slow progress, and so far no commercial VAD is available for clinic applications. Over the last decade, the national implantable ventricular assist device (NIVAD) has been designed and developed by our group. In comparison to other blood pumps, NIVAD has a smaller design and lower rotating speed with sufficient flow [2].

The purpose of this study was to calculate the characters of flow field, evaluate the hemolysis in vitro using NIVAD, and to detect biocompatibility by monitoring hematology, chemistry blood, autopsy, postexplant device examination to improve pump and cannula design, resolve the animal model, provide feedback for surgeons to gain experience.

2 Flow Field Characters and Hydrodynamic Performance of NIVAD

2.1 Device Description

NIVAD is a miniaturized rotary blood pump with an outer diameter of 29.5 mm, a length of 76 mm, a weight of 158 g, a speed range of 5000-11000 rotations/min and max flow 9 L/min (100 mmHg). At the speed of 7500-8000 rotations/min and after-load 100 mmHg, a flow of 5 L/min can be delivered. The pump consists of a rotor driven by a brushless direct current (DC) motor, the housing of the rotor, the inflow inducer, the outflow wing-type diffuser and the big-small tandem impeller (Fig.1.a-b). The titanium wall and components inside the pump are coated by polyurethane heparin. This design uses an advanced fluid dynamics method and the efficiency is improved. Also we design a real-time flowmeter with 29.5×24 mm, weight 26.5 g which can detect the flow and pressure of the pump outflow based on Doppler principle. The whole pump is controlled by an intelligent monitor which can display the parameters of the pump and allow the management of the pump by varying the rotational speed. A mini battery with 55×57×150 mm and a weight of 1120 g, 24V 6A can supply power for 4-6 h continuously. The detailed design features of the NIVAD have been published previously [2-3].

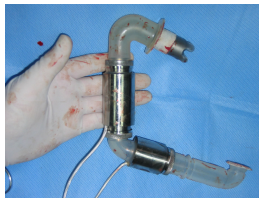


Fig.1a. National Implantable Ventricular Assist Device (NIVAD)

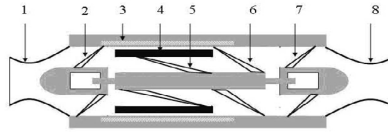


Fig.1b. 1-Inlet tie-in, 2-Inlet guide vane, 3-Motor stator, 4-Magnetic ring,5-Small impeller, 6-Big rotor, 7-Outlet guide vane, 8-Outlet tie-in

2.2 Hydrodynamic Performance

The different volume force loads in the blood pump circuit are simulated to obtain the blood pump hydrodynamic performance curve by Computational Fluid Dynamics (CFD). The volume forces are 50000 N/m³, 57000 N/m³, 60000 N/m³, the blood plasma accounts for 65% of the overall blood, and the red blood cells account for 35%. Fig.2 shows the calculated hydrodynamic performance curve, and also shows the design operating point (the flow rate is 5 L/min and the head is 100 mmHg). It can be seen from that figure that the calculated hydrodynamic performance of the blood pump basically meets the design conditions. It is shown that the flow rate is 5 L/min corresponding to the head of 102.24 mmHg based on the curve fitted results of the numerical simulation. The force load should be 58700 N/m³ according to the numerical simulation.

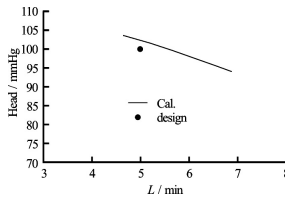


Fig. 2. Hydrodynamic performance curve of the blood pump

In order to analyze the relation between the blood pump performance and the blood components, the plasma with the overall proportion of 70%, 65% and 60% is assumed, respectively, for the volume force load of 58700 N/m³, and the three calculated results of the blood pump hydrodynamic performance are shown in table 1. It can be seen that the blood components affect the hydrodynamics performance of the blood pump very little.

Table 1. The blood pump hydrodynamic performance for different blood components

Plasma ratio (%)	Head (mmHg)	Flow rate (L/min)
70	102.33	4.96
65	102.24	5.00
60	102.24	5.03

2.3 Flow Field Characteristics

The simulation of flow field and interior structure of NIVAD is shown in Fig.3. As a whole, the interior flow field of NIVAD is smooth when rotation is 9000 rpm/min, head 100 mmHg and flow rate 7.7 L/min. The velocity and the pressure distribution in the internal flow field of the blood pump can be analyzed under the conditions of the volume force load of 58700 N/m^3 and the plasma ratio of 65%. Fig.4 and Fig.5 show the flow velocity distribution and the pressure distribution in the axial plane of the blood pump. From these figures it can be seen that the velocity is stable in the part from the impeller inlet to the small wheel of the blood region and the pressure distribution is relatively regular. But the flow field shows some disordered features and the pressure distribution has relatively large variations in the large wheel region and the outlet guide vane area.

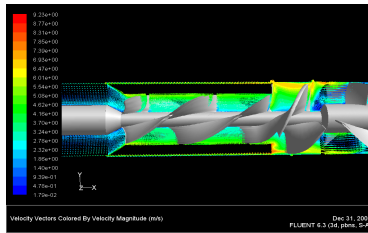


Fig. 3. Simulation of flow field and structure of interior NIVAD (Rotation 9000 rpm/min, Head 100 mmHg, Flow rate 7.7 L/min)

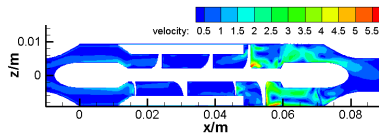


Fig. 4. Velocity distribution in axial flow field

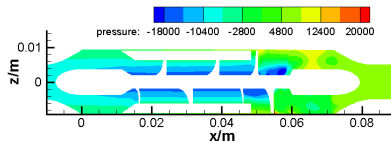


Fig. 5. Pressure distribution in the axial surface of the flow field

The characteristics of the flow fields in the small impeller region, the big impeller region and the outlet guide vane area are analyzed by taking the cross-sectional views. Fig.6 shows the three cross section locations. Fig.7-9 show the axial velocity and pressure distributions in the cross sections in the small impeller region, the big impeller region and the outlet guide vane area, respectively. From Fig.6, it can be seen that the axial velocity varies little in the small impeller region, the pressure distribution in

the circumferential direction varies relatively little, the isobar is in an annular shape, with a radical variation. This kind of flow field means a poor performance with respect to the blood hemolysis. From Fig.6, it can be seen that the flow direction in the small narrow gap between the motor stator and the magnetic wheel is opposite to the mainstream direction in the pump. The scouring effect will help to avoid the adverse effect due to the flow stagnation of blood. The large flow field in the big impeller region sees more chaos, the velocity ranges from 5.5 m/s to 3 m/s, with a reflux in the blade root hub. The flow field in this region shows a poor quality and the variations of velocity and pressure is relatively large.

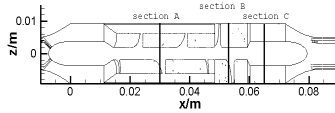


Fig. 6. The cross section location map

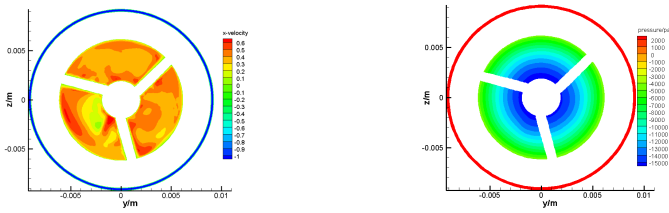


Fig. 7. The flow field distribution on the cross section of the small impeller region. *Left* is the axial velocity distribution. *Right* is the pressure distribution.

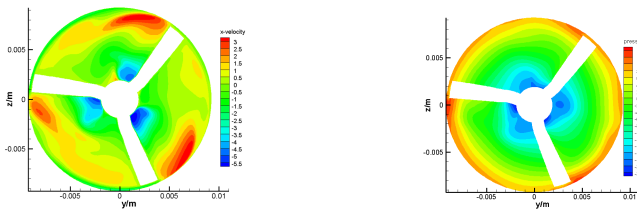


Fig. 8. The flow field distribution on the cross section of the big impeller region. *Left* is the axial velocity distribution. *Right* is the pressure distribution.

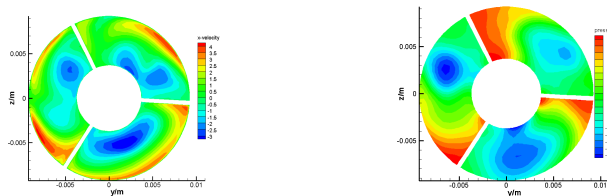


Fig. 9. The flow field distribution on the cross section in the outlet guide vane region. *Left* is the axial velocity distribution. *Right* is the pressure distribution.

3 Materials and Methods

3.1 Hemolysis Experiment in Vitro

The hemolysis test in vitro was designed as Fig.10. We simplify the physiological circulation system as atrium-ventricle-artery-vein-atrium. The medical blood container (FLY-2000K, FLY Medical, LTD. China) was used as atrium, NIVAD as ventricle and medical tube as vessel. An electronic thermometer (Darrcom JXB-178, China) was used to measure the temperatures of pump inflow and outflow. The real-time flowmeter was set on the outflow of NIVAD. The blood container was soaked in water which has a heater and a circulation to maintain a constant temperature of 37°C blood system.

Six hemolysis tests were taken. Each time, 2000 ml of calf blood was anticoagulated at the proportion of 1:9 with 3.8% sodium citrate. The flow was adjusted to 5L/min and the outflow pressure at 13.3 kPa (100mmHg) through the damper valve and rotational speed of NIVAD. Blood samples were taken before and 0.5, 1, 1.5 ... 4 h after NIVAD working. Free plasma hemoglobin (FHB) (SIGMA Diagnostics, St. Louis, MO) and hematocrit (HCT) were measured. During the same time, the unused calf blood was taken as control. The results were calculated as the average. Additionally NIH (Normal Index of Hemolysis) was calculated to evaluate the hemolysis.

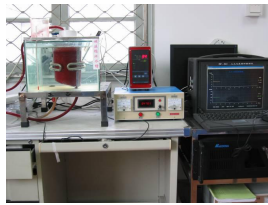


Fig. 10. Equipments of Hemolysis experiment in vitro

3.2. Experiment in Vivo

Animal care 8 healthy young male calves (weighing between 90 and 140 kg) were used in these experiments. All animals received humane care in compliance with the “Regulation to the Care and Use of Experimental Animals” (Beijing Council on Animal Care, revised 2006, China). Animal care and use committee of Tongji university approved all protocols used in the present study.

Surgical procedure and postoperative care Food was withheld from each calf 48 hours and water for 24 hours before induction of anesthesia. A standard anesthesia protocol was followed. Anesthesia was induced with glycopyrrolate (1 mg) and ketamine (5 mg/kg) intramuscularly (IM). A cuffed endotracheal tube and an orogastric decompression tube were inserted. General anesthesia was maintained with isoflurane (1.0-3.0%) in oxygen (40-100%). The anesthetized calf was then placed on the operating table in the right lateral decubitus position with preparation for a left thoracotomy. The left neck was incision and allowed two catheters to be inserted into the left jugular

vein for intraoperative blood test and carotid for monitoring arterial pressure and blood gas. The NIVAD was implanted through thoracotomy from the 4th intercostal space during cardiopulmonary bypass (CPB) at a body temperature of 30-32 °C (Fig.11). A silicone/polyester sewing cuff was sewn to the ventricular apex with pledgeted, coated, braided 2-0 polyester mattress sutures. The inflow cannula of NIVAD was inserted into the apex of the left ventricle and secured with cotton tape around the cuff and pump casing. The outflow cannula was connected to the descending aorta with a 4-0 propylene suture. Air was removed from the left ventricle, pump and graft. Once the calf's body temperature was normalized (37-39 °C), the calves were then slowly weaned from CPB [4]. After routine closure, the calf was transported to the intensive care unit of our animal facility and positioned in a sling within the stanchion for post-operative recovery (Fig.12). An infusion of dopamine (5 µg/kg/min) and heparin (0.01 µg/kg/min) was started upon the calf's arrival in intensive care [5]. Activated clotting time (ACT) was maintained at a value of 200-250 s throughout the whole observation period. Ceftazidime was given 4g bid intravenous during and after the operation. The calf was extubated once the swallowing reflex had returned and awareness was clear within 24h after the operation. As the animal became more alert, the sling was gently lowered and the calf positioned in sternal recumbency. Arterial blood gas measurements, hematologic and serum biochemical parameters, FHB, parameters of NIVAD and normal postoperative monitor were analyzed every 3h in the 1st day. From the 2nd day on, we implemented these everyday.

Pathology When animals were sacrificed, tissue samples were taken routinely. The hearts, kidneys, livers and lungs were evaluated macroscopically. The cannula and the pump were also examined to detect the thrombus.

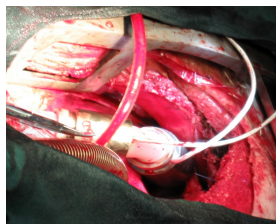


Fig. 11. The implantation of NIVAD



Fig. 12. Calf with NIVAD and recovery in postoperative period

4 Results

4.1 Hemolysis Results

During the 6 experiments in vitro, FHB varied from 1.7-40.2 mg/L and showed on an average rotation of 7800 r/min (Table.2, Fig.13). The temperature was changed from 0.5-1.3 °C between exit and entrance of NIVAD (Fig.14). The pump has certain damage to erythrocytes by shear not heating blood. Average of NIH was calculated from six hemolysis tests. Formulas as followed:

$$NIH \text{ (mg/L)} = \Delta FHB \times V \times (100 - Hct) / 100 \times 100 / (Q \times T)$$

ΔFHB = increase of plasma free haemoglobin concentration (mg/L) over the sampling time interval; V = circuit volume (L), Q = flow rate (L/min); Hct = hematocrit (%), and T = sampling time interval (min). During the 6 tests, the average of NIH is 0.065 ± 0.014 mg/L within the normal range 0.01-0.1 mg/L comparing to other VADs [6-9].

Table 2. The content of Plasma Free Hemoglobin (mg/L)

Group/ Time	0h	0.5h	1h	1.5h	2h	2.5h	3h	3.5h	4h
Hemolysis	1.7±	2.8±	8.5±	16.2±	25.03±	32.15±	36.17±	36.80±	40.27±
	1.05	1.87	6.16	12.37	15.88	15.68	15.89	15.80	14.88
Control	1.27±	1.23±	1.38±	2.78±	2.87±	3.48±	5.13±	5.83±	6.07±
	0.71	0.88	1.02	3.00	1.75	2.01	2.67	3.68	3.26

The hemolysis group is significant with the control group by analysis of variance ($P < 0.01$)

4.2 Experiment Results in Vivo

8 calves were implanted with NIVAD with all surviving beyond the perioperative period. The pumps ran continuously from 26 h to 132 h with sufficient flow (3.59-4.85 L/min) against mean AP 110-130 mmHg (Fig.15). Rotation and outflow fluctuated

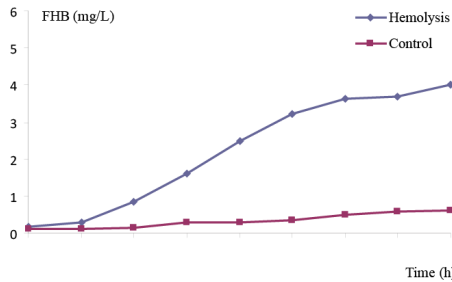


Fig. 13. Mean FHB in 6 Hemolysis tests in vitro

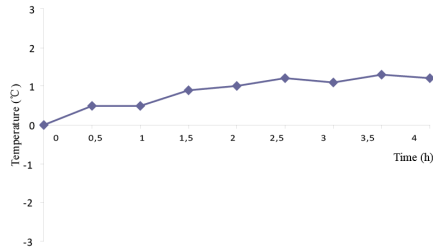


Fig. 14. The change of temperature during test

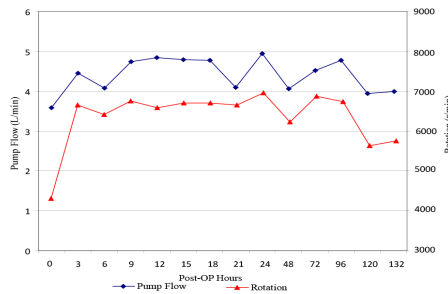


Fig. 15. The graph illustrates the mean values of RPM and outflow of NIVAD during 132 h in calves

from 24 h to 132 h because of some individual cases in which a flow disturbance was present. The overall level of pump rotation was stable at approximately 5500-6900 r/min.

Renal function (as measured by blood urea nitrogen-BUN and creatinine plasma level) and liver function (plasma bilirubin) remained normal. Creatinine, BUN and bilirubin increased in the postoperative observation period (Fig.16). The average daily FHB level varied from 4.3 to 9.1 mg/dl which was less than others' limit of 20 mg/dl [10-11].

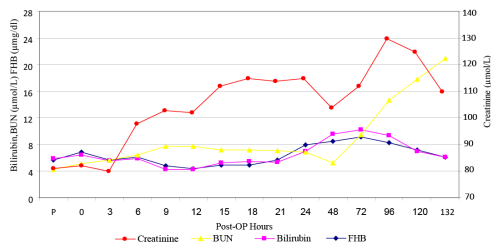


Fig. 16. The mean Creatinine, BUN, Bilirubin and FHB are illustrated of 8 calves up to 132h

After death of animals, autopsy was performed on every animal. Endocardial and myocardial contusions were seen in one animal and may have been related to negative pressure created by the high speed of the pump when the ventricular filling volume

was low (hypovolemia, bleeding, etc). There was no evidence of systemic thromboembolism in all calves. Similarly, disassembly of the pumps from these animals demonstrated no thrombi on inner surfaces and outflow grafts. The hearts, lungs, livers and kidneys of all calves were taken to pathology and electronic microscope analysis. There was no obvious hyperaemia and infarct in myocardium. The lungs showed no signs of pulmonary edema or atelectasis. The liver and both kidneys showed no infarcts. Electronic microscope of all the tissues showed no obvious damage at cell level.

5 Discussion

Ventricular assist device (VAD) has been shown to be effective for short-term therapy, as a bridge to heart transplantation and for permanent cardiac support. During the past decades, new generations of VAD were continuously developed. But in China, there was no domestic commercial VAD for the Chinese. Partly because of the high price of imported VADs, there were used by a few patients. Since 2001, our group has worked on and developed an axial pump NIVAD at Shanghai East Hospital [2-3, 12-14]. The third generation NIVAD is to date one of the smallest heart assist devices (diameter 29.5 mm, long 76 mm, weight 147 g). Preparation and implantation technique of the pump proved to be technically easy, safe, and reproducible. The small size of the pump can save intrathoracic space with minor displacement of the lung and may allow implantation of the pump even in thin adults or large children.

The studies of inner flow field by computational fluid dynamics (CFD) show that serious red blood cell damage may mainly occurs in the complex flow areas such as boundary separation, reversal, and leakage flow [2-3]. The whole inner flow field of NIVAD is smooth in the mass. The hemolysis tests *in vitro* show a good performance in hematology. The results of the hemolysis tests coincide with CFD. Although FHB rises significantly, it is related to the shear force of the impeller of NIVAD and is not caused by the heating of the pump. However the value of FHB and NIH was still in the allowed clinical range [6-9].

In vivo experiments, some degree of pump flow fluctuation is maintained because of the varying inflow pressures which result from ventricular contraction [5]. This varied inflow pressure increases flow from NIVAD. But the calves have generally shown no evidence of end-organ dysfunction or hypoperfusion attributable to flow fluctuation. However, little is known about the long-term physiologic effects of continuous axial flow perfusion. Main characteristics for a good blood pump are good results regarding thrombus and hemolysis. Hemolysis can be defined as FHB above 20 mg/dl *in vivo* [10-11]. During the animal experiments, results of hemolysis of NIVAD were acceptable when they were below 10 mg/dl. The risk of thromboembolic events in human VAD patients is at approximately 30%, despite all effort to achieve an effective anticoagulation [15-16]. In calves with VAD, the number of thromboembolic events is probably even higher than in humans caused by the calves' specific complex coagulation system. Despite so, thromboembolic events were successfully prevented in our studies *in vivo* by controlling the ACT constant at 200-250 s [17]. In evaluation of removed NIVAD, we didn't found thrombus inside the pump.

Complications related to late bleeding caused the death of some calves. This incident is not related to the device but may be related to the difficulty in maintaining coagulation parameters within a specified range in calves. The function of liver and kidney were good although creatinine, BUN and bilirubin in plasma rised postoperatively. But the parameters of hematology were still in the normal ranges. Their rising should be related to the trauma of operation. The pathology also confirmed that there was no edema or infarcts in these organs.

Our research still has some limitations. First, chronic animal experiments should be taken to evaluate long term effect on remote organs by NIVAD. Second, the NIVAD is designed to be used in patients with end-stage cardiac failure. Therefore, our present results, obtained in healthy animal models, may not be directly applicable to the clinical setting. This limitation might be addressed in the future by establishing an ischemic or heart failure animal model. Finally, we should pay more attention on animals recover and resume eating and drinking within 24h after surgery. This is an important factor in ruminants, because prolonged atony of the rumen will lead to the demise of the animal [18].

6 Conclusion

We can improve and develop the design of NIVAD in blueprint with CFD. While, we have established a reliable, reproducible calf model and hemolysis test in vitro for NIVAD. Additional chronic studies and pathologic animal model are acted. Repeated, success in vitro and vivo test of the NIVAD allows the pump to move forward into clinical trials.

Acknowledgment. This research was funded by China Postdoctoral Science Foundation funded Project (2014M551458), National High Technology Research and Development program of China (863 Program, Grant No.2007AA02Z439), Shanghai focus on specialties of medicine (ZK2012A27), Shanghai Municipal Science and Technology Commission projects (12441902500), Key Disciplines Group Construction Project of Pudong Health Bureau of Shanghai (Grant No. PKzxxq2010-01) and the program for outstanding medical academic leader of Shanghai (LJ06051).

References

1. Kwon, M.H., Moriguchi, J.D., Ardehali, A., et al.: Use of ventricular assist device as a bridge to cardiac transplantation: impact of age and other determinants on outcomes. *J. Tex. Heart. Inst.* 36, 214–219 (2009)
2. Fan, H.M., Hong, F.W., Zhang, G.P., et al.: Application of CFD techniques in the design and flow analysis of implantable axial flow blood pump. *J. Hydrodynamics* 22, 518–525 (2002)
3. Fan, H.M., Hong, F.W., Zhou, L.D., et al.: Design of implantable axial- flow blood pump and numerical studies on its performance. *J. Hydrodynamics* 21, 445–452 (2009)

4. Tuzun, E., Eya, K., Chee, H.K., et al.: Myocardial hemodynamics, physiology, and perfusion with an axial flow left ventricular aAssist device in the calf. *J. ASAIO* 50, 47–53 (2004)
5. Frazier, O.H., Cohn, W.E., Tuzun, E., et al.: Continuous-Flow total artificial heart supports long-term survival of a calf. *J. Tex. Heart. Inst.* 36, 568–574 (2009)
6. Hoshi, H., Shinshi, T., Takatani, S.: Third generation blood pumps with mechanical non-contact magnetic bearing. *J. Artif. Organs.* 30, 324–339 (2006)
7. Nojiri, C., Kijima, T., Maekawa, J., et al.: Development status of Terumo implantable left ventricular assist system. *J. Artif. Organs.* 25, 411–413 (2001)
8. Asama, J., Shinshi, T., Hoshi, H., et al.: A compact highly efficient and low hemolytic centrifugal blood pump with a magnetically levitated impeller. *J. Artif. Organs.* 30, 160–167 (2006)
9. Zhang, J., Gellman, B., Koert, A., et al.: Computational and experimental evaluation of the fluid dynamics and hemocompatibility of the CentriMag blood pump. *J. Artif. Organs.* 30, 168–177 (2006)
10. Fossum, T.W., Morley, D., Benkowski, R., et al.: Chronic survival of calves implanted with the DebaKey ventricular assist device. *J. Artif. Organs.* 23, 802–806 (1999)
11. Kerkhoffs, W., Schumacher, O., Meyns, B., et al.: Design, development, and first in vivo results of an implantable ventricular assist device, MicroVad. *J. Artif. Organs.* 28, 904–910 (2004)
12. Ye, L., Fan, H.M., Lu, R., et al.: Establishment of an animal model for implantable ventricular assist device. *J. Acta. Lab. Anim. Sci. Sin.* 17, 457–459 (2009)
13. Li, T.Y., Ye, L., Zhang, Z.G., et al.: The hemolysis research of the national implantable ventricular assist device. *J. Tongji. Uni (Med. Sci.)* 32, 47–50 (2011)
14. Fan, H.M., Lu, R., Liu, Z.M.: Experimental study of domestic implantable ventricular assist device. *J. Tongji. Uni (Med. Sci.)* 27, 6–9 (2006)
15. Kirklin, J.K., Holman, W.L.: Mechanical circulatory support therapy as a bridge to transplant or recovery (new advances). *J. Curr. Opin. Cardiol.* 21, 120–126 (2006)
16. Takahama, T., Kanai, F., Onishi, K.: Anticoagulation during use of a left ventricular assist device. *J. ASAIO* 46, 354–357 (2000)
17. Schmitto, J.D., Ortmann, P., Akdis, M., et al.: Miniaturized HIA microdiagonal pump as left ventricular assist device in a sheep model. *J. ASAIO* 54, 233–236 (2008)
18. Carney, E.L., Clark, J.B., Myers, J.L., et al.: Animal model development for the Penn State Pediatric ventricular assist device. *J. Artif. Organs.* 33, 953–957 (2009)

Fused Visualization for Large-Scale Blood Flow Dataset

Kun Zhao¹, Naohisa Sakamoto², and Koji Koyamada²

¹ Graduate School of Engineering, Kyoto University, Japan

² Institute for Liberal Arts and Sciences, Kyoto University, Japan

{zhao.kun, naohisas}@viz.media.kyoto-u.ac.jp,

koyamada.koji.3w@kyoto-u.ac.jp

Abstract. Recently, there is a big need for the fused visualization in medical simulation field (e.g., the large-scale blood flow dataset). That is because it is desirable and advantageous to fuse the different objects (e.g. the fusion of red blood cells and platelets) and analyze the relationship between them. Nevertheless, such a simulation data always results in a large-scale time-varying volume data, which make the fused visualization even more difficult. To solve this problem, a sorting-free rendering technique, Particle-based Rendering (PBR), is used to visualize the large-scale time-varying volume data. Because this method visualizes the volume data by generating opaque particles from the original volume data and projects these particles to the image plane, the visibility sorting is not needed. This makes the fusion of different objects and handling of large-scale volume data is very easy. Moreover, a time-varying visualization framework is developed to visualize the time-varying data in real time and analyze the dynamics of the time-varying data in detail. The designed system is applied to the large-scale blood flow dataset, and the experimental results show its efficiency.

Keywords: Fused visualization, time-varying visualization, large-scale volume data, particle-based rendering, medical visualization.

1 Introduction

Time-dependent simulations can be found in many scientific fields (e.g. computational fluid dynamics, electromagnetic field simulation or ocean prediction). A good visualization result for these time-dependent simulations is always needed to clearly show changes and variations over time. However, effective visualization of time-varying data is extremely difficult to achieve due to the complexity of illustrating multiple time-steps and clearly showing changes and variations over time.

Moreover, in some recent researches, the time-dependent simulations may also need to fuse different objects together to observe and analyze the relationship between these objects. This need is especially urgent for the medical simulation field [7]. Toward the multi-scale simulation for a human body, Sugiyama et al. [4] have developed novel numerical methods to simulate the time-dependent blood flow. To figure out the effect of the red blood cells on the platelet motion, the fusion of these two objects is needed. The spatial and temporal resolutions for the simulation data is also very high

so that the shape of the vesicles subjected to the linear shear flow can be represented. Such a large-scale time-varying volume data make the fused visualization becomes much more difficult.

To visualize such a huge size of volume dataset and perform the fusion of different objects, the traditional visualization is always based on the extracted surfaces (polygon) or 2D images to realize the fusion of different objects [5] [7] [8]. That is because different objects can also be converted into different surfaces, and the fusion of polygons and 2D images make the rendering be easy to be realized. However, a real fusion of different objects, including volume/surface, can provide a more realistic result for the positional information of these objects and can help the researchers to analyze the result more efficiently. At a result, a good rendering method is needed to render the time-varying volume data and also fuse different objects efficiently.

To solve this problem, we employ our particle-based rendering technique, which can handle large-scale volume datasets and easily fuse different objects, since it utilizes proxy geometries that are a set of opaque particles. The number of the particles is not in proportion to that of volume cells, but in inversely proportional to the square of the particle radius. If we determine an appropriate radius, the number of the particles can be reduced so that it can fit the GPU memory. This fitting is mandatory for interactive rendering. To develop a particle rendering algorithm, we revisited a brightness equation in the volume rendering algorithm and reconsider the definition of opacity which is usually derived from a user-specified transfer function. We define a density function of emissive opaque particles. According to the density function, we generate particles in a given volume dataset and project them onto an image plane. Because an opaque particle is used, no visibility sorting is required and the fusion of different volumes and surfaces becomes very easy to be realized. In order to render the time-varying volume data, we also develop a time-varying visualization framework. With this frame work, the large-scale time-varying data can be visualized in a real time, so that user interaction can be realized to analyze the visualization results more efficiently. To verify the efficiency, we apply our system to the large-scale blood flow dataset. This is a large-scale time-varying data from the medical simulation. The experimental results and the user feed backs show the efficiency of our system.

The rest of this paper is organized as follows: in section 2, previous researches related to our work are presented, and we also make a brief introduction of the large-scale blood flow dataset used in our system. In section 3, we make a detailed explanation of our proposed particle-based rendering system. The application results are showed in section 4. Section 5 gives the discussion on the application results. The conclusion is described in section 6.

2 Background and Datasets

2.1 Related Works

There is a big need for the fusion of different objects in many visualization fields especially for the medical field. That is because it is desirable and advantageous to show the different objects and analyze the relationship between them [7].

Since the fusion visualization for the medical domain has very important application, there are many approaches proposed in this domain. Baum et al. [7] has proposed a fusion view to fuse the different data measured from CT (computed tomography), MRI (magnetic resonance imaging), PET (positron emission tomography) and so on. The fusion result can provide a detailed analysis for the measured data. However, the measured data are 2D images, for the simulation data such as the blood flow data used in this paper, the fusion cannot be realized by this system. Prckovska et al. [8] also develop a multi-field visualization framework to fuse the measured results from DTI (diffusion tensor imaging) and HARDI (high-angular resolution diffusion imaging), which is also based on the 2-dimensional image. 2D image based fusion visualization can also be found in other related works, which cannot fit the needs of the fused visualization for 3D volume objects and semi-transparent surfaces.

As for the fused visualization for the 3D objects, how to sort the multiple objects and fuse the together comes to be a main challenge. Generally, surface-based visualization techniques, such as isosurfaces, sectional slices, and boundary faces, are useful in understanding the geometrical structure of a scalar field. Aaron et al. [9] proposed a volume ray-casting technique using peak-finding, which can integrally render the volumes and the isosurfaces extracted from the volumes, and confirmed the effectiveness of the technique by rendering several structured grid datasets. However, since this system use the ray casting rendering method, it needs to store the whole data into GPU. If the data size of the volumes and surfaces (such as the case of blood flow datasets) is over the GPU memory size, these data cannot be visualized. Other approaches of fused visualization for volume and opaque isosurface rendering can be found in [10] [11] and a transparent rendering technique of semi-transparent multi-isosurfaces [12] have also been proposed. All of these methods cannot render the large-scale data with the data size over the GPU memory.

To make a fused visualization with an efficient sorting and handle a large-scale data, recently utilizing proxy geometries that are a set of opaque particles have been proposed. Koyamada et al. proposed the particle-based volume rendering (PBVR) method [13] [14] which uses tiny particles as rendering primitives. Because this method only need to project the generated opaque particles, it does not require any sorting and is applicable to large-scale data. In our opinion, this sorting-free method can also be applied to fuse different objects by simply merging the generated particles together.

2.2 Datasets

The blood flow dataset is a big data from a numerical simulation performed on the K computer by Sugiyama et al. [5]. The K computer is a distributed-memory supercomputer system, which includes 80,000 computer nodes [3]. Each computer nodes contains an eight-core CPU SPARC64TMVIIIfx with a 2 GHz clock frequency and a set of 16 GB memory. As a result, the output data has a very high resolution that 3,072×640×640. It contains the volume data of red blood cell, platelet and velocity vector. The whole datasets contain 100 time steps. For each time step, the data size reaches about 20 GB for the red blood cell volume, platelet volume.

With this large-scale blood flow dataset, our main goal is to confirm the detailed movement of the red blood cells and platelets, and also the interactivity of them. This raises a requirement to fuse the different volumes of red blood cell and platelet in the visualization result. Sugiyama et al perform the LSV [6] rendering method on the K computer to observe the detailed motion of red blood cells and platelets. To fuse these objects, they change the volume data into isosurfaces but not to fuse the original volume. Such an approach is very hard to observe the contents inside the red blood cell and also hard to change the opacity. Moreover, it takes about 7 minutes to render one image on the K computer. This rendering speed makes the interactive visualization be very difficult to be realized.

3 Proposed Method

In this paper, we use the particle-based rendering (PBR) to visualize the large-scale time-varying volume data. Because this particle-based rendering use the opaque particles, the fusion of different objects and the handling of large-scale data become possible. We also developed a time-varying visualization framework. With this framework, we can visualize the large-scale time-varying data in a real time, so that user interaction can be realized to analyze the visualization results more efficiently.

3.1 Particle-Based Rendering (PBR)

Particle-based rendering technique is a rendering technique based opaque particles in the object space. The original version is proposed by Koyamada et al. [1] [13] [14] [15]. In this technique, a set of opaque particles is generated from a given 3D scalar field based on a user-specified transfer function. The final image is then generated by projecting these particles onto the image plane. The particle projection does not need to be in order since the particle transparency values are not taken into account. During the projection stage, only a simple depth-order comparison is required to eliminate the occluded particles. The algorithm is listed as following.

Assuming that the volume data is a set of light-emitting cloud particles, the brightness B at the eye position can be solved numerically as follows [2]:

$$B_0 = \sum_{i=1}^n c_i \times \left(\alpha_i \prod_{j=1}^{i-1} (1 - \alpha_j) \right) \quad (1)$$

Here, a viewing ray is evenly subdivided into n segments, and c_i and α_i represent luminosity and opacity values at the i -th sampling point, which is a central point of the interval $[t_{i-1}, t_i]$. Usually, the opacity is specified through a transfer function, which is set by user. In the density emitter model, the opacity α_k in the k -th ray segment is defined as:

$$\alpha_k = 1 - \exp \left(- \int_{t_k}^{t_{k-1}} \pi r^2 \rho(\lambda) d\lambda \right) \quad (2)$$

Here, ρ and r represent the number of particles in the unit volume and the radius of a particle, respectively. Since the Poisson distribution is assumed for the number of particles in the density emitter model, the opacity describes the possibility that more than one opaque particle exists along the ray segment. If we assume that the density function is constant in the segment, and that the ray segment length can be described as $\Delta t = t_{k-1} - t_k$, we have:

$$\alpha_k = 1 - \exp(-\pi r^2 \rho \Delta t) \quad (3)$$

From Equation (3), the opacity can be generally expressed as:

$$\alpha_k = 1 - \exp(-\pi r^2 \rho \Delta t) \quad (4)$$

As a result, the particle density used in the particle generation can be estimated using the radius, an opacity value in the user-specified transfer function, and the ray-segment length used in the ray-casting. From Equation (4), we have:

$$\rho = \frac{-\log(1 - \alpha)}{\pi r^2 \Delta t} \quad (5)$$

With this particle generation function, O-PBR is composed of three parts (Figure 1):

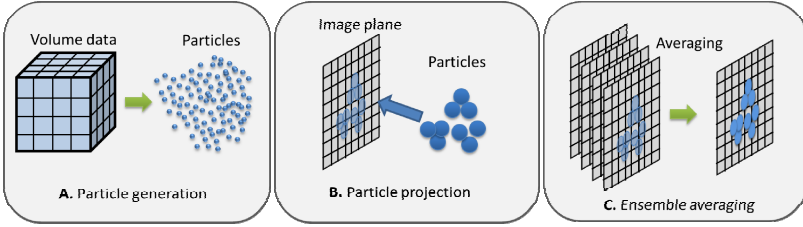


Fig. 1. The three steps of PBR: particle generation, particle projection, ensemble average

Step 1. Particle generation: A set of particles is internally generated for each volume dataset using the density distribution function (5) from a user-specified transfer function. The generation process is done in a cell-by-cell manner.

Step 2. Particle projection: For the second step, the generated particles are then projected onto the image plane to create a rendered image for the volume dataset. At the same time, the calculation of the particle size and the shadow processing are also performed by using the normal vector.

Step 3. Ensemble average: This process means that for the group of particles generated by using different random numbers, the particle projection process is performed multiple times, and the generated images are superimposed on each other to obtain the average. The multiple times is called the repetition level. In general, a larger repetition level can provide a higher image quality but needs more computational resources.

We can achieve a level-of-detail (LOD) control by setting different repetition level. Generally, a larger repetition level can provide a better image quality but needs more computational resources (Figure 2).

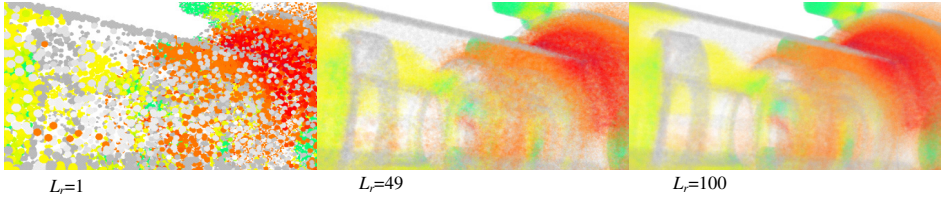


Fig. 2. The image quality of the pump data in an enlarged view obtained by using PBR (L_r : repetition level)

With this PBR method, because the projection of opaque particles does not need any visibility sorting, a high-speed rendering can be realized. When we need to fuse the different volumes, we only need to merge the different particles generated from these volumes together and project them to the image plane (Figure 3). As a result, our PBR is very suitable for the fused visualization of large-scale volume data.

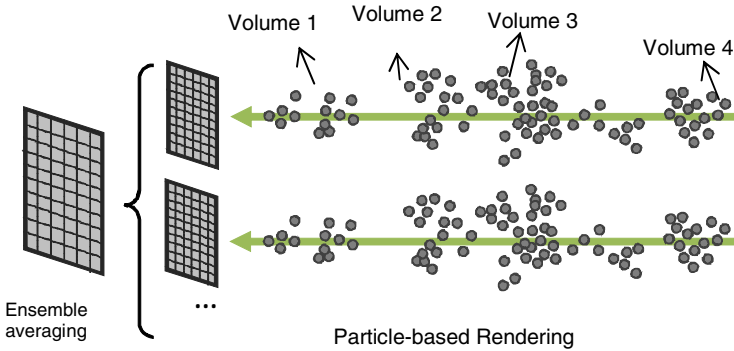


Fig. 3. Fused visualization with particle-based rendering

3.2 Time-Varying Visualization

With the particle-based rendering, we also developed a time-varying visualization framework. With this framework, we can visualize the large-scale time-varying data in a real time, so that user interaction can be realized to analyze the visualization results more efficiently.

As the pre-process, we first need to generate particle data from different volume data or surface data (e.g. the red blood cell volume and platelet volume). Using the given transfer function, we generate particles from the time-varying data. In every time step, particles are repeatedly generated and saved as one file.

Before we launch the rendering animation, we first need to load the particle data for different objects. These data are loaded to CPU memory so that there is no need to read data from the hard disk during the animation. In the rendering process, GPU projects these particles to the image plane depending on the number of repeat levels.

And the higher repeat level can provide a more high-quality image. At the process flow (Figure 4), firstly the particle data is loaded to the CPU memory before the animation is launched. The particle data of time step 0 is rendered to the image plane, so that the user can get an initial image of the time-varying data. As we begin the animation, our system transfers the particle data to GPU memory and these data are rendered step by step in regular intervals. At certain time step t , the particle data of previous step $t-1$ that has been rendered by GPU would be deleted from GPU memory. And the particle data of current time step t is transferred to the GPU memory and rendered to the image plane. After the rendering of the time step t ended, the same process would be performed to time step $t+1$. By repeating this until the last time step n , we can obtain the animation of visualization result.

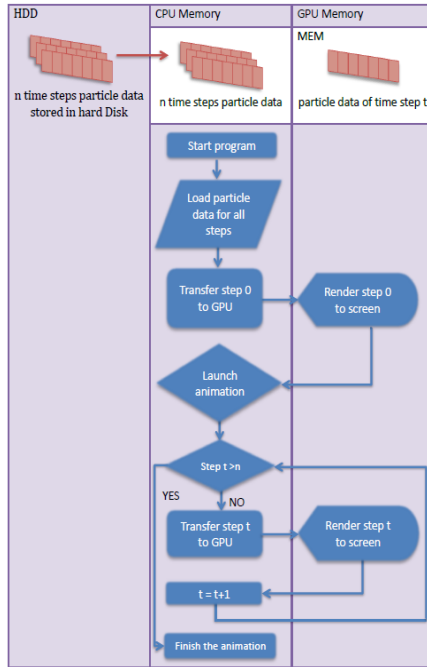


Fig. 4. Process Flow Diagram of the Animation

4 Application

In this section, we show the application of our system to the large-scale blood flow datasets. This experiment is conducted with an Intel Core i7-2820QM CPU (2.3 GHz), an NVidia GeForce GTX580M 2 GB GPU, and 16 GB of system memory. The operating system used in this experiment is Ubuntu 12.04 LTS. In the experiment, we take 10 time steps from the original data into the experiment. We measure the particle generation time, show the rendering image, and get the user feedbacks to confirm the effectiveness of our system.

As the pre-process, the whole time step particle data are generated from different objects of red blood cell volume and platelet volume. With a repetition of 15, each time step cost about 115s to generate particles. By rendering these particle data, we can obtain the animation of the time-varying unstructured grid dataset (Figure 5). For each time step, it cost About 1.2s as the rendering time. Moreover, because our system makes the rendering in real time, we can zoom in or zoom out during the rendering process. This can be very helpful to the detailed analysis (Figure 6).

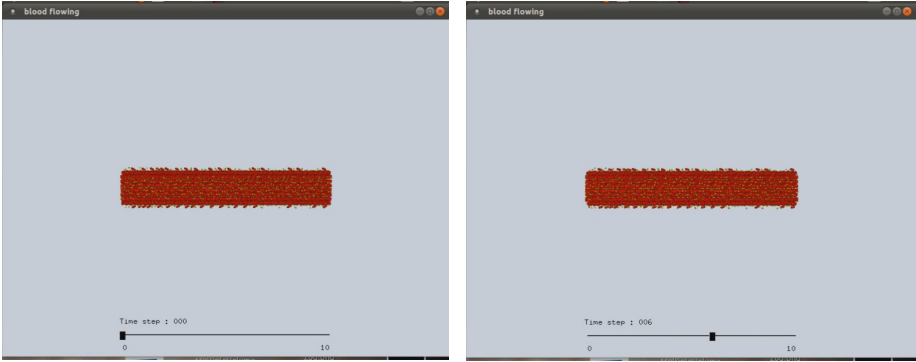


Fig. 5. The rendering image during the animation

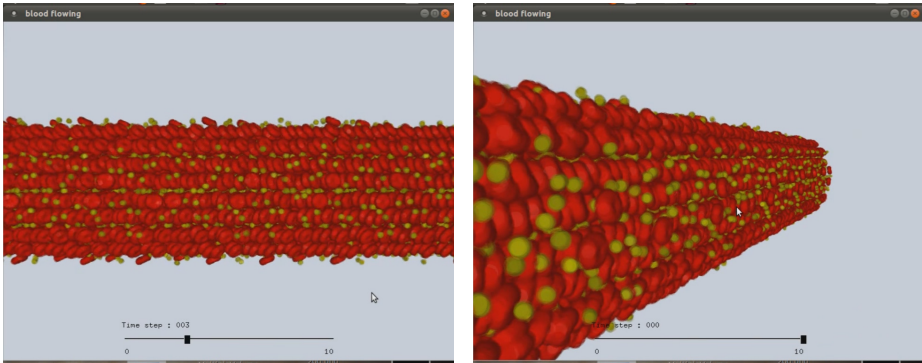


Fig. 6. During the rendering process, we can zoom in or zoom out and also change the view point to get detailed analysis.

We also show this system to some domain experts and get user feedbacks from them. The main feedbacks are summarized as following:

1. The interactive visualization for the large-scale blood flow data is possible on a normal computer. This is very helpful for the visual analytics. In the previous work, the visualization for this data needs to be performed with a super computer.
2. The fused visualization for the red blood cell volume and platelet volume is very helpful to know the positional relation of them. This is very important to analyse some blood diseases such as deformable vesicle problem.

3. The whole view for the entire data and detailed analysis for the enlarged local part is provided. This is very helpful to analyse the interactive motion of red blood cells and platelets.
4. The image quality is also good enough to perform the visual analysis.
5. The pre-process: particle generation process costs a little long time.

From the above experimental results we can see the different objects: red blood cell volume and platelet volume are fused clearly. Our system can also render the time varying data efficiently with a rendering time about 1.2s for each time step. This is much faster than the previous by Sugiyama et al. [5]. With this system, the interactive visual analytics is possible with even a normal computer. The user feedbacks of 1, 2, 3 and 4 also confirm that our system is very efficient to analyze the interactive motion of red blood cells and platelets, and the positional relation of them. The image quality of the particle-based rendering method is also good enough to perform the analysis.

However, there are also some disadvantages of our system. First, as commented in the user feedbacks 5, the particle generation process costs a little long time (about 115s for each time step). The main reason to cost so much time is that we need to generate particles in cell by cell manner for the volume data, and such a process can cost much time. In our future work, we would like to implement more efficient particle generation method. Moreover, the edition for transfer function is very time costly. That is because when we edit the transfer function, we need to regenerate particles. In our future work, we plan to develop a regeneration-free PBR so that when we change the transfer function, the rendering result could also be changed in real time. After that, we plan to add the user interface for the transfer function edition.

5 Conclusion

In this paper, we have proposed a fused visualization system to visualize the large-scale blood flow datasets with Particle-based Rendering. Because the rendering methods used in this system does not need any visibility sorting, it can handle a large-scale volume datasets, and the fusion of different objects is also easy to be realized. In order to render the time-varying volume data, we also developed a time-varying visualization framework. With this frame work, we can visualize the large-scale time-varying data in a real time, so that user interaction can be realized to analyze the visualization results more efficiently. To verify the efficiency, we applied our system to the large-scale blood flow dataset. This is a large-scale time-varying data from the medical simulation. The experimental results and the user feed backs show the efficiency of our system.

The video of our system can be found as following link:

<https://dl.dropboxusercontent.com/u/30566727/LSMS%26ICSEE%202014.mp4>

Acknowledgments. This work was supported by Japan Society for the Promotion of Science (JSPS) KAKENHI Grants-in-Aid for JSPS Fellows (Grant Number 26·837), and was partially supported by the Ministry of Education, Culture, Sports, Science and Technology (MEXT), Grat-in-Aid for Data Integration and Analysis System

(DIAS), Grant-in-Aid for Research Programs on Climate Change Adaptation (RECCA) and by the Japan Science and Technology Agency (JST), A-STEP project ("The research and development of fusion visualization technology", AS2415031H).

References

1. Kawamura, T., Sakamoto, N., Koyamada, K.: A Level-of-Detail Rendering of a Large-Scale Irregular Volume Dataset Using Particles. *Journal of Computer Science and Technology* 25(5), 905–915 (2010)
2. Sabella, P.: A Rendering Algorithm for Visualizing 3D Scalar Field. *Computer Graphics* 22(4), 51–58 (1988)
3. Yonezawa, A., Watanabe, T., Yokokawa, M., Sato, M., Hirao, K.: Advanced Institute for Computational Science (AICS) – Japanese national high-performance computing research institute and its 10-Petaflops supercomputer “K”. In: *Proc of SC 2011, State of the Practice Reports 2011*, p. 2063366 (2011)
4. Sugiyama, K., Ii, S., Takeuchi, S., Takagi, S., Matsumoto, Y.: A full Eulerian finite difference approach for solving fluid-structure coupling problems. *Journal of Computational Physics* 230, 596–627 (2011)
5. Sugiyama, K., Kawashima, Y., Noda, S., Ii, S., Koyama, H., Takagi, S., Matsumoto, Y., Himeno, R.: Massively parallel computing of novel fluid-structure interaction solver on the K computer. In: *Proc. of High Performance Computing Symposium 2013, IPSJ-HPCS2013050*, Tokyo, Japan (January 2013)
6. LSV:Large Scale Visualization, http://www.csrp.riken.jp/application_h_j.html
7. Baum, K.G., Helguera, M., Krol, A.: Fusion Viewer: A New Tool for Fusion and Visualization of Multimodal Medical Data Sets. *J. Digit. Imaging*. 21(Suppl. 1), 59–68 (2008)
8. Prckovska, V., Peeters, T.H.J.M., Van Almsick, M., ter Haar Romeny, B., Vilanova i Bartoli, A.: Fused DTI/HARDI Visualization. *IEEE Transactions on Visualization and Computer Graphics* 17(10), 1407–1419 (2011)
9. Knoll, A., Hijazi, Y., Westerteiger, R., Schott, M., Hansen, C., Hagen, H.: Volume Ray Casting with Peak Finding and Differential Sampling. *IEEE Transactions on Visualization and Computer Graphics* 15(6), 1571–1588 (2009)
10. Rottger, S., Kraus, M., Ertl, T.: Hardware-Accelerated Volume And Isosurface Rendering Based on Cell Projection. In: *Proceedings of IEEE Visualization 2000*, pp. 109–116 (2000)
11. Marroquim, R., Maximo, A., Farias, R., Esperança, C.: Volume and Isosurface Rendering with GPU-Accelerated Cell Projection, *Computer Graphics Forum*, Vol. *Computer Graphics Forum* 27(1), 24–35 (2008)
12. Kipfer, P., Westermann, R.: GPU Construction and Transparent Rendering of Iso-Surfaces. In: *Proc. of Vision, Modeling and Visualization 2005*, pp. 241–248 (2005)
13. Koyamada, K., Sakamoto, N., Tanaka, S.: A particle modeling for rendering irregular volumes. In: *Proc. Int. Conf. Computer Modeling and Simulation (UKSIM 2008)*, Cambridge, pp. 372–377 (2008)
14. Sakamoto, N., Kawamura, T., Koyamada, K.: Improvement of particle-based volume rendering for visualizing irregular volume data sets. *Comput. Graph.* 30(1), 34–42 (2010)
15. Sakamoto, N., Koyamada, K., Saito, A., Kimura, A., Tanaka, S.: Multi-volume rendering using particle fusion. In: *IEEE VGTC Pacific Visualization Symp. 2008*, Kyoto (2008)

The Research on Agent-Based Simulation Oriented to Emergency Management

Zhichao Song, Yuanzheng Ge, Hong Duan, and Xiaogang Qiu

College of Information System and Management, National University of Defense Technology,
Changsha, Hunan P. R. China, 410073
song_zhichao@139.com

Abstract. Emergencies always bring about lots of huge harm to people and are very difficult to be forecasted. Therefore, researches on emergency management have been hot to find the ways to reduce their devastating effect on human beings. This paper proposed one method using agent-based simulation to research emergency management according to ACP (Artificial Societies, Computational Experiments, Parallel Execution) approach. Firstly, the structure of a simulation system oriented to emergency management was analyzed and designed. Then a simulation system oriented to public health emergency management was constructed to study the transmission of infectious diseases. Finally, two experiments were carried out based on the system.

Keywords: Agent, Emergency management, ACP, Simulation system, Transmission of infectious diseases.

1 Introduction

An emergency is a sudden serious event which can or may do lots of harm to society and requires immediate actions, such as a nature disaster, an accident, a public health event and a society security event [1]. Emergencies always take place out of people's expectation and can always exert a devastating effect on human beings. What's more, a large-scale emergency will give rise to a series of other ruinous disasters. Therefore researches on emergencies have become hot issues. G. Kou et al. [2] proposed an efficient disaster assessment expert system, which integrates fuzzy logic, survey questionnaire, Delphi method and multi-criteria decision making (MCDM) methods. X.L. Zhang [3] gave a time series analysis and a spatial analysis to study a unidirectional dense crowd. Y.Z. Ge and W. Duan et al [4, 5, 6] researched public health emergencies using simulation methods. All the researchers try to prevent or control emergencies through their work. Whereas we also clearly realize that emergencies cannot be cleared up and what we have already known about them is so little that it is hard to prevent or control them. What we can do now is to focus on the development and evolvement of emergencies after they take place. When we have learned more about it, scientific actions would be taken to protect ourselves and reduce the harm that emergencies bring to us.

Traditionally, researches on the development and evolvement of emergencies are mainly based on the analysis of history data and questionnaires. For some emergencies which often happened in the past, we can give an estimate for the development of such events in the coming period after they take place. Management can be scientifically adopted to control the emergencies and reduce the harm to human beings. However, for most emergencies, traditional methods cannot meet our demands very well for exact analysis and estimation about emergencies' development. Researchers hope to get access to more information about emergencies and find their development rules. However, it is so hard to collect such information in most cases. What's more, experiment, as a quite common and effective way to achieve more useful information in physics or chemistry researches, always cannot be conducted for researches on emergencies in our real world. Now with the development of computer technology, researchers can collect data about emergencies by taking simulation experiments. As F.Y. Wang [7] said, social computing has become a new research field, and the agent-based simulation method for emergency management has been accepted by many researchers [4, 5, 6]. In the simulations, they can observe the developing process of emergencies and find out the optimum management strategy.

This paper studies the simulation oriented to emergency management and the construction of the simulation system according to ACP approach [8]. The remainder of this paper is organized as follows: in Section two, some basic theories are introduced; the structure and construction design of the emergency-management-oriented simulation system is given in Section three; based on the idea introduced in Section three, a simulation system oriented to public health emergency management is constructed in Section four to study the transmission of infectious diseases; in Section five, some infectious diseases' transmission experiments are taken in the simulation system; Section six gives the conclusions.

2 Basic Theory

2.1 Agent-Based Simulation

Agent-based simulation is an effective method to study complex systems, which relies on the interaction among large numbers of agents and derives macro-phenomena from the interacting process [9]. Agent is actually the abstract model extracted from the real system. With the attributes related to the issue we focus on, an agent can make its own decisions and take some interactive actions. More phenomena may appear when large numbers of agents interact with each other so that a complex system can be studied much more deeply. Therefore, the agent-based simulation method usually needs to define the individual agents, extract the attributes and the activities from the real system in the first place. Then the rules that drive agents to interact with each other need to be designed and the system can be executed by the interactions among agents [10].

2.2 ACP Approach

The ACP (Artificial Societies, Computational Experiments, Parallel Execution) approach, in which artificial societies are for modeling, computational experiments are for analysis and parallel execution is for control [7], was proposed by F.Y. Wang [8] in 2004 to provide a way to address complex system issues. As emergencies can usually be regarded as complex systems, the ACP approach is very suitable for emergency management researches [6]. The main idea of this approach (Fig. 1) is modeling on the real world and constructing an artificial society in computers. Then emergency models and management measure models can be loaded in this artificial society and the system runs driven by the models and the parameters of the management models such as the control measures' styles, intensity or frequency which will be updated by comparing simulation results and users' expected results. At last, an optimization management measure can be found and emergencies can be controlled more scientifically.

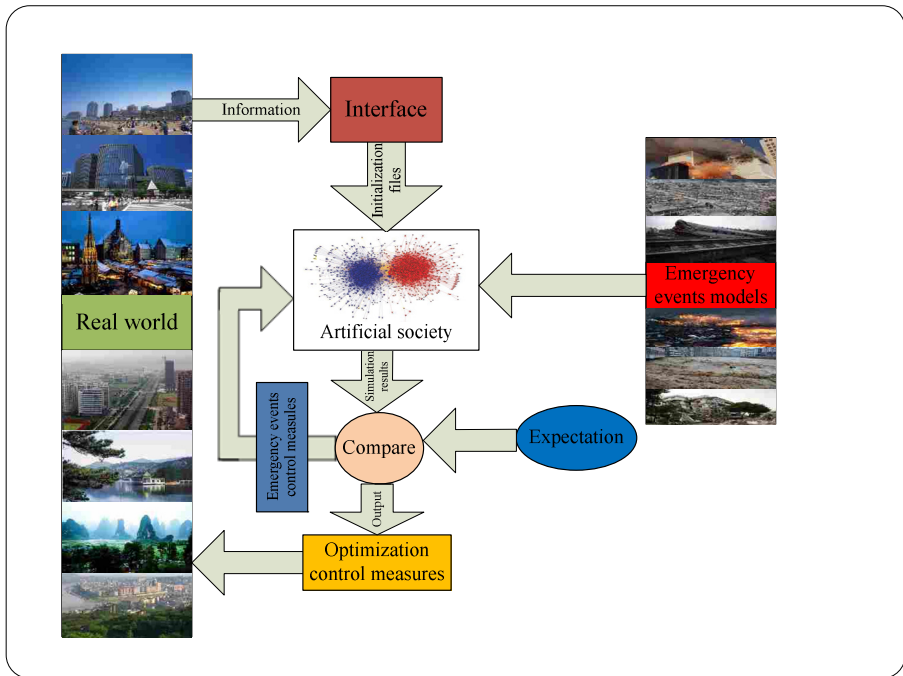


Fig. 1. ACP approach

The artificial society method, the core of the ACP approach was proposed by the Rand Company to research the effect on the society from the information technology. This method aims to bring a virtual laboratory for researchers to study social questions by the means of taking experiments. The main idea of the artificial society method is to simulate individuals in our human society. Then computing experiments can be taken in computers using these artificial individual models and some interesting

phenomena might emerge from their interaction. Therefore, the artificial society is actually an agent-based simulation system and we can use this method to research the system behavior or phenomena.

2.3 Complex Network Models

In recent years, complex network theories have been widely used in the computer science field, society field and information technology field etc. Particularly since the small-world [11] property and the scale-free [12] character of networks are found, the complex network models have become a very useful tool to research complex systems. In social science the complex network models can be used to describe the relationships among human beings and many phenomena can be learned through these models. The common complex network models include regular networks, random networks and scale-free networks etc.

Regular networks are one kind of simple complex network models, in which nodes connect with each other according to some rules. There are three common regular network models: globally coupled network, nearest-neighbor coupled network and star coupled network (see Fig. 2). Any of the models can represent one kind of relationships among human beings. Globally coupled network in which all the nodes connect to each other is the simplest one of the three and can be used to describe family relationship, classmate relationship and so on. Nearest-neighbor coupled network model can describe that human beings prefer communicating with adjacent ones and represent the social relationships among people roughly. Star coupled network can describe the relationship between a center person and the others, for example the teacher-students relationship and singer-fans relationship.

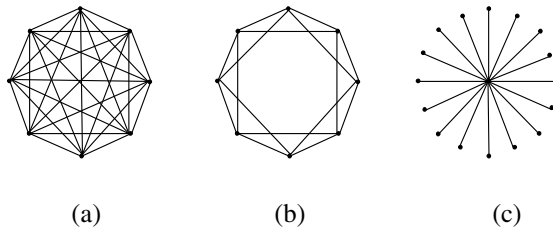


Fig. 2. Regular network models: (a) globally coupled network, (b) nearest-neighbor coupled network, (c) star coupled network

The random network model was proposed by two Hungarian mathematicians, Paul Erdős and Rényi [13], in which every two nodes connect with each other with a probability. This network model is much closer to the true life than regular networks. We can use it to describe more human beings' relationships and some simple issues can be learned by this model. However, man has his own mind and will not communicate with others randomly. What's more, people's desires to communicate with others are different. Therefore, social relationships among human beings described by random network model are still not exact enough.

Scale-free character is another important discovery after the small-world property [11] of networks. Barabási and Albert [12] found that the relations among the links in the internet can form a network, of which the degree distribution does not follow Poisson distribution but shows a heavy-tail phenomenon. Lots of scientists in other fields also discovered the-rich-get-richer phenomenon in so many other relationships. The network formed by these relationships is called the scale-free network. According to Barabási's researches, this phenomenon that very few nodes have especially many attachments and most nodes' attachments are quite few is caused by the growing number of nodes and the node's preferential choice of which node to attach to.

3 Design of the Emergency-Management-Oriented Agent-Based Simulation System

The simulation system in this paper is designed for emergency management researches. It is mainly composed of individual agent models, interaction models for agents, emergency models and management measure models. The individual agent models are mainly used to describe human beings' attributes and the interaction models define the activities' rules for agents. The emergency models and management measure models are respectively the abstraction of emergencies and management measures.

In the emergency-management-oriented simulation system, an agent is the abstract representation of an individual to describe his states and behaviors in computers. Though each individual himself is a huge complex system with so many attributes, what we focus on are only the properties related to emergency management researches. Therefore, this paper designs the agent's attributes, including agent's ID, physical states, psychological states, social relationships list and other properties. Agent's ID is just the identifier for the agent. Physical states and psychological states are the objects on which the emergency management researches focus, and also the input information to drive agents to finish their activities. The Social relationship list is to provide the interactive objects for every agent.

The interaction among human beings is usually a very important factor in the development and evolvement of emergencies. For example, infectious diseases always spread in crowds through contact and a panic also transmits among human beings through their communication. Therefore, the interaction should be considered in emergency management researches. Here we have designed the interaction models. Our life experiences tell us that interactions among human beings do not happen randomly. If interaction appears between two persons, there must be some relationship between them. For example, we communicate with our families and friends much more frequently than with strangers. Therefore, we can use social relationships to design the interaction rules and different complex network models which can describe social relationships would be used in the interaction models design. Social relationship list can be completed according to the network models and the probabilities of an agent interacts with other agents in its social relationship list can also be set.

The emergency models describe the emergencies we want to research, in which the impact mechanism on human beings or environment needs to be considered. Similar to the agent modeling, we need not care about all the aspects concerning emergencies but just those which can bring harm when emergencies happen. Therefore, the disaster elements and the disasters' evolving process should be extracted and modeled. The emergency model is mainly composed of these two parts.

The purpose of this emergency-management-oriented agent-based simulation is to explore the change of the physical states and psychological states when different management measures are adopted in different emergencies by simulating human beings' behaviors in computers. According to the simulation results, the optimum management measures can be found. Therefore, emergency management models should be constructed and the protection mechanism of these measures should be abstracted so that the models can control the emergencies in the simulation.

4 Construction of the Public-Health-Emergency-Management-Oriented Simulation System

According to the design of the emergency-management-oriented agent-based simulation system, we have constructed a public-health-emergency-management-oriented simulation system (see Fig. 3) to study the transmission of infectious diseases. Diseases which spread in crowds by the air such as influenza H1N1 can be researched in this system.

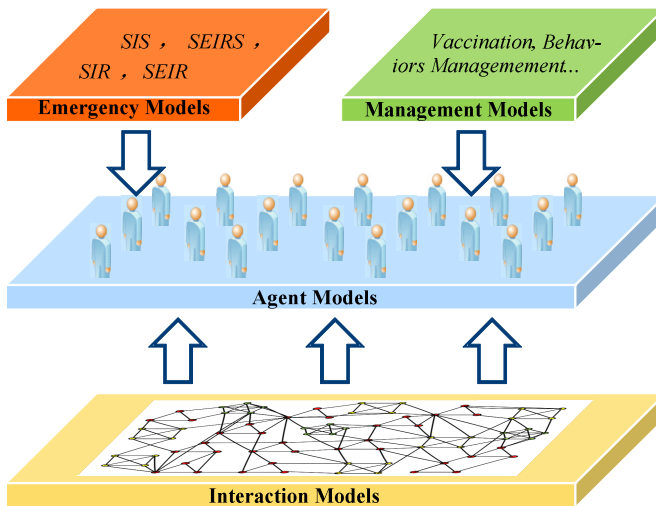


Fig. 3. Structure of the public-health-emergency-management-oriented simulation system

The simulation system has 3000 agents, among which 1440 agents belong to three-person families, 960 agents belong to four-person families and 600 agents belong to five-person families. The attributes of agents have two parts. One is the physical state

properties, including susceptible, latent, of emerging symptoms, recovering, recovered and dead. The other one is agent’s social relationship list produced by interaction models.

Because the susceptible are quite inclined to be infected with the diseases spreading in crowds by the air during their contact with infected persons, we can use the complex network models which represents social relationships among human beings to design the interaction model. To describe the social relationships among agents more exactly we constructed a social relationship network model which integrates the ideas of globally coupled network, random network and scale-free network. Then the interaction model for every agent is designed according to this social relationship network. The constructing process of the social relationship network is shown in Fig. 4 and the degree distribution of the network mentioned above is shown in Fig. 5. The design of the interaction models is as follows.

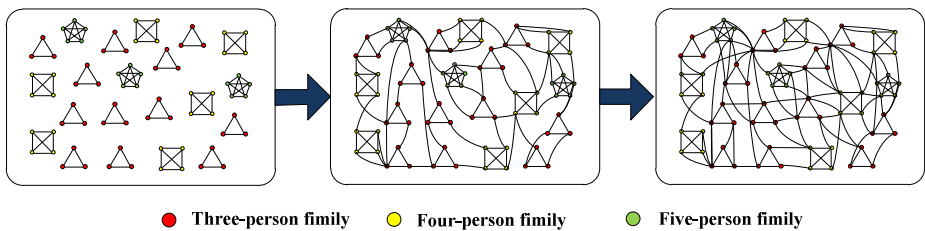


Fig. 4. The constructing Process of the agents’ social relationship network model (The left figure shows the relationships among family members, the middle figure is the network created by randomly connecting agents based on their family relationships, and the right figure shows agents’ preferential attachments based on the relationships the agents already have.)

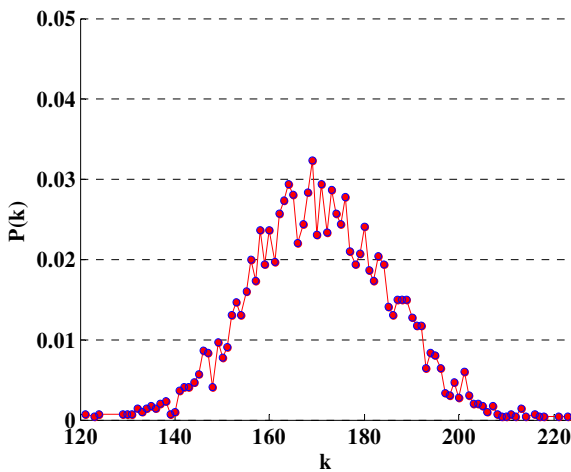


Fig. 5. Degree distribution of the social relationship network

- Social relationships among family members are similar and the probabilities they contact with each other are also similar, so this kind of relationships can be described by globally coupled network model.
- People usually have some good friends beyond their family and this kind of relationships is also an important factor to the transmission of infectious diseases. To construct these relationships, agents are attached to other agents out of their families randomly at the probability 0.04 in this paper.
- According to the scale-free character of the networks, if a person has relatively more good friends or family members he will have more social relationships. Though this kind of relations is not categorized into good friendship, people still contact with them all the time. Therefore, according to the idea of the preferential attachment in the scale-free networks we judged for every agent whether he has the weak ties with the other agents by the probability $P = \exp(-1) * N(i) / n$, in which $N(i)$ is the number of social relationships one agent already has; n is the total number of all agents and P is the probability.
- When every agent's social relationships are constructed, the probability of contact between two agents in every simulation step is set by $P' = \exp(-1) * [N(i) + N(j)] / (2n)$, in which $N(i)$ and $N(j)$ are respectively the number of the two agents' relationships and n is also the number of all agents.

For the transmission of infectious diseases in the public-health-emergency-management-oriented simulation system, the emergency models are actually the infectious diseases transmission model. What's more, the diseases which spread in crowds by the air can be described by dynamic models such as SIS, SIR, SEIR and SEIRS [14, 15, 16, 17]. The main idea of these models is to divide people into several categories according to the periods that their physical states belong to. S means susceptible period; E means latent period; I means symptoms-emerging period and R means recovered period. In different periods, the infecting probabilities are different. Therefore, the transmission simulation model of infectious diseases can be built according to these dynamic models. The time that different stages last for, the infecting probabilities in corresponding stages and the death rate, which are considered in the model, can be set in the simulation.

Vaccination and behavior management are two common measures adopted to control the spread of infectious diseases. Thus the management model in the system mainly includes the protecting ability of vaccines, an agent list recording the IDs of agents that take the vaccine, the time when an agent takes the vaccine and the rules to restrict human beings' behaviors.

5 Experiments and Results

In the public-health-emergency-management-oriented simulation system, we assumed one disease which infects human beings by the air and two transmission experiments about the disease were taken. The settings of the simulation experiments are as follows:

- For this disease, people only in symptoms-emerging period can infect others. The infecting probability is 0.2. If a person takes vaccine, the infected probability can be decreased to 0.1.
- The latent period follows Weibull distribution $W(8,2)$ and the longest time is seven days. The symptoms-emerging period starts when symptoms appear and ends when an infected person accepts treatments in hospital, and it follows Uniform distribution $U(0,2)$.
- Once a person accepts treatments in hospital, he usually cannot infect other people. Thus infection during this period is not considered in this paper.
- The initially infected person is chosen from the agents randomly.
- In this paper, we assumed that this disease can be cured and the death rate is 0. What's more, whoever is recovered can never be infected.

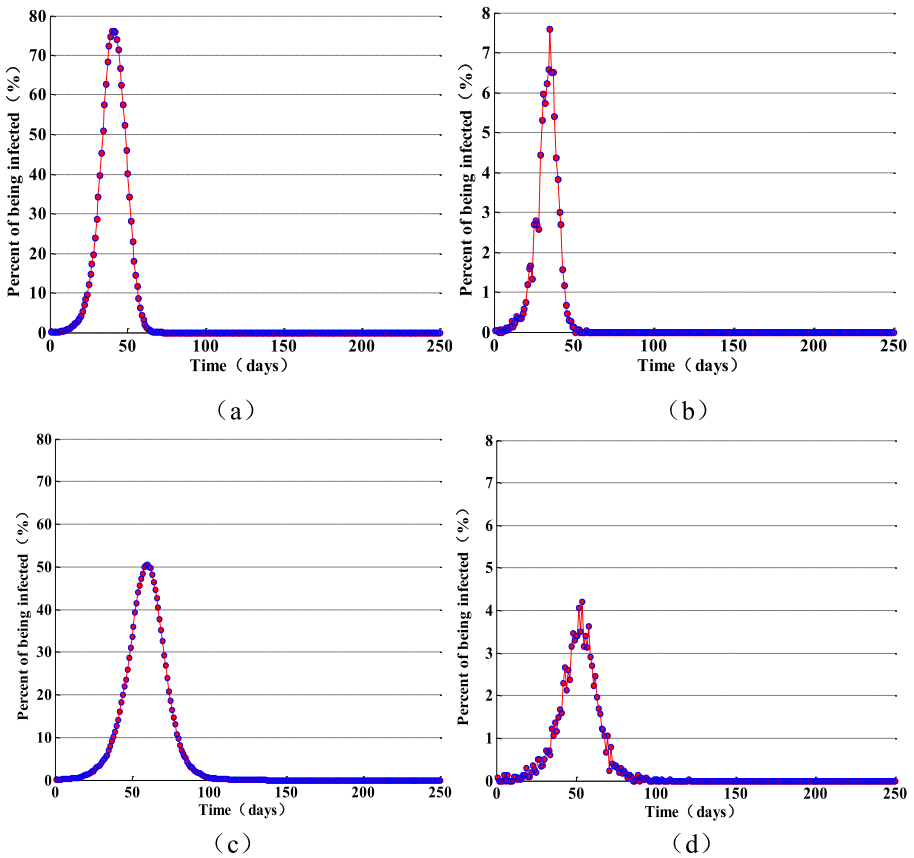


Fig. 6. Simulation experiment results (Figure (a) and figure (b) are respectively the percent of persons who are sick and newly infected every day when nobody takes any measures to protect themselves; Figure (c) and figure (d) are respectively the percent of persons who are sick and newly infected every day when all the people take vaccines.)

Based on the settings above we used the SEIR model [15] and took an epidemic transmission experiment under two conditions that nobody takes any measures to protect themselves and all the people have taken vaccines at the beginning of the simulation. The experiment results are shown in Fig. 6.

From the figures we can find that when vaccines are taken, the number of persons who are sick and newly infected every day is much smaller compared with when nobody takes any measures to protect themselves. However, on such condition, the transmission duration is much longer but the total number of the infected is similar. There are two reasons for it. On one hand, the infecting rate of the infectious disease is so high and the vaccine can only supply finite protection for human beings. It means that the infecting rate is not decreased that much by the vaccine and the disease can still spread in crowds slowly. On the other hand, because the infected persons can get immune to this disease after being cured, the transmission will come to an end when the infected are all cured. It can be concluded that as some vaccines cannot supply enough protection for human beings, if people do not change their behaviors and decrease the probabilities to contact with others, almost all the persons would still be infected when one disease with a high infecting rate breaks out. Therefore, people’s behavior management should also be considered to decrease their probabilities to contact with each other besides the vaccination and to control of the transmission of infectious diseases better.

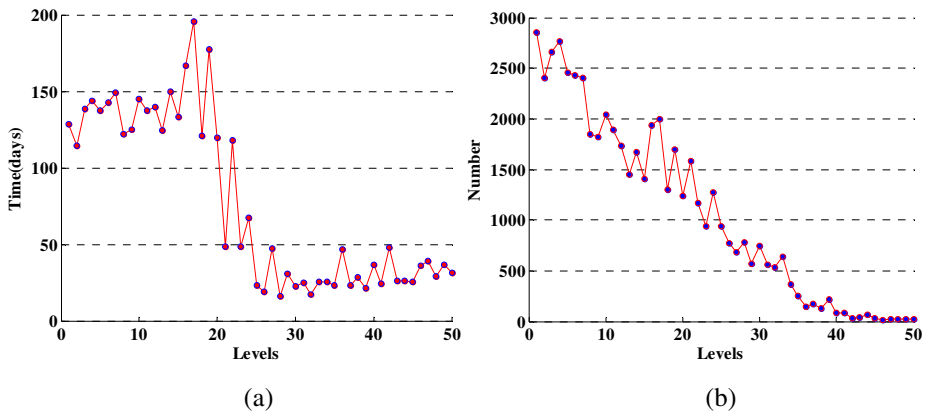


Fig. 7. Experiment results when people’s behaviors are restricted in different degrees (Figure (a) shows the relation between duration of the transmission and control levels and figure (b) shows the relation between the number of infected persons and control levels.)

Actually people will not only take vaccines but also reduce their contact with others when an infectious disease breaks out. What’s more, the government will also take some measures to decrease people’s contact with others. For example, the Chinese government called on schools, malls and some other public facilities to be closed to fight with SARS in 2006. The measures can slow down the transmission of the disease, but will disturb humans’ normal life and lead to a lot of losses. To learn more about the influence of this assumed infectious disease can make when people’s

behaviors are restricted in different degrees, we set the contact probability by $P^{\wedge} = \exp(-1) * [N(i) + N(j)] / [(2 + 0.1 * \text{deg})n]$, in which $N(i)$ and $N(j)$ are respectively the number of relationships the two agents have; n is the total number of agents; and deg is the degrees of the management strength. The bigger the degree is, the lower the possibility of the agents to interact with each other is smaller. In our experiment, people were restricted in fifty different degrees and $\text{deg} = 1, 2, 3, \dots, 50$.

In Fig. 7 duration of the transmission and the total number of the infected at the fifty different control levels are shown, in which y-axis shows the duration of the transmission and the number of the infected, and x-axis shows the control levels. The bigger the number in x-axis is, the lower the probability people contact with each other is. From Fig. 7 (b) we can see that the number of infected persons decreases as the management gets more stringent. In Fig. 7 (a) the transmission duration climbs up when people's contact probability is slightly reduced but it obviously drops down when people's interaction probability decreases to some degree. However, the duration turns flat when the probability continues to decrease. When an infectious disease breaks out, we always hope that the duration is short and the number of the infected persons is small. However, the stricter the management is, the heavier economic losses that are inflicted on the society are. Therefore, we can only take some appropriate management measures to restrict people's contact with others and the simulation system can help us to make a scientific choice.

6 Conclusion

This paper researches emergency management by the agent-based simulation method. According to the ACP approach, the emergency-management-oriented simulation system was designed and a public-health-emergency-management-oriented simulation system to research the transmission of infectious diseases was realized. Two simulation experiments were taken using this system. From the results we have got some simple conclusions: when the infectivity of a disease is too strong and vaccines cannot supply human beings with enough protection, contact behaviors among people should be restricted to slow down the spread of the disease. At the same time, we have also validated the feasibility of the simulation method for emergency management researches, and the simulation results are very useful to make a scientific decision to reduce the harm from emergencies. We will do more researches in two directions in the future. Firstly environment models will be considered and the relationships among people and environments will be learned. Secondly the social relationship network model for agents will be improved to make it more exact.

References

1. Zheng, K., Shu, X., Yuan, H., Jin, S.: on Classification Method of Network Public Opinion Triggered by Incidents. *Computer Applications and Software* 27, 3–5 (2010)
2. Kou, G., Ergu, D., Shi, Y.: An Integrated Expert System for Fast Disaster Assessment. *Computer & Operations Research* 42, 95–107 (2014)

3. Zhang, X.L., Weng, W.G., Yuan, H.Y., Chen, J.G.: Empirical study of a unidirectional dense crowd during a real mass event. *Physica A: Statistical Mechanics and its Applications* 392, 2781–2791 (2013)
4. Ge, Y., Song, Z., Qiu, X., Song, H., Wang, Y.: Modular and Hierarchical Structure of Social Contact Networks. *Physica A: Statistical Mechanics and its Applications* 392, 4619–4628 (2013)
5. Duan, W., Cao, Z., Qiu, X., Cui, K., Zheng, X.: Heterogeneous and Stochastic Agent-Based Models for Characteristic Analysis of Super Spreaders in Infectious Diseases. *IEEE Intelligent Systems* 28, 18–25 (2013)
6. Duan, W., Cao, Z., Wang, Y., Zhu, B., Zeng, D., Wang, F.Y., Song, H.: An ACP Approach to Public Health Emergency Management: Using a Campus Outbreak of H1N1 Influenza as a Case Study. *IEEE Transactions on Systems, Man, and Cybernetics—Part A: Systems and Humans* 43, 1028–1041 (2013)
7. Wang, F.Y.: Toward a Paradigm Shift in Social Computing: The ACP Approach. *IEEE Intelligent Systems* 22, 65–67 (2007)
8. Wang, F.: Artificial Societies, Computational Experiments, and Parallel Systems: A Discussion on Computational Theory of Complex Social-Economic Systems. *Complex System and Complexity Science* 1, 25–35 (2004)
9. Epstein, J.M.: *Growing Artificial Societies: Social Science from the Bottom Up*. Brookings Institution Press (1996)
10. Wooldridge, M., Jennings, N.R.: *Intelligent Agents: Theory and Practice*. *The Knowledge Engineering Review* 10, 115–152 (1995)
11. Newman, M.E.: The Structure and Function of Complex Networks. *SIAM Review* 45, 167–256 (2003)
12. Barabási, A.L., Albert, R.: Emergence of Scaling in Random Networks. *Science* 286, 509–512 (1999)
13. Erdős, P., Rényi, A.: On the Evolution of Random Graphs. *Publ. Math. Inst. Hung. Acad. Sci.* 5, 17–61 (1960)
14. Kermack, W.O., McKendrick, A.G.: Contributions to the Mathematical Theory of Epidemics—I. *Bulletin of Mathematical Biology* 53, 33–55 (1991)
15. Li, M.Y., Muldowney, J.S.: Global Stability for the SEIR Model in Epidemiology. *Mathematical Biosciences* 125, 155–164 (1995)
16. Kermack, W.O., McKendrick, A.G.: Contributions to the Mathematical Theory of Epidemics—II. The Problem of Endemicity. *Proceedings of the Royal Society of London. Series A* 138, 55–83 (1932)
17. Cooke, K.L., Van Den Driessche, P.: Analysis of an SEIRS Epidemic Model with Two Delays. *Journal of Mathematical Biology* 35, 240–260 (1996)

A Research on Human Cognitive Modeling in Rumor Spreading Based on HTM

Xiangchen Li^{1,2}, Xi Chen^{1,2}, and Wei Wang^{1,2}

¹ School of Automation, Huazhong University of Science and Technology, Wuhan, China

² Image Processing and Intelligent Control Key Laboratory of Education Ministry of
China, Wuhan, China

leonmoriaty@163.com, chenxi@mail.hust.edu.cn

Abstract. As a sociological phenomenon, rumor spreading has been widely researched by sociologists and other fields' scholars. How do people generate those strange thinking about the rumor? This paper, from artificial intelligence view, focuses on an algorithm based on Hierarchical Temporal Memory (HTM) to simulate human cognitive process of generating rumors from individual heterogeneous living experience. Comparison with classical Bayesian Networks, our algorithm could effectively and really simulate human cognitive process of rumors, and in accordance with some typical psychology effects proved by sociologists and psychologists.

Keywords: HTM, Rumor spreading, Human cognitive process, Individual heterogeneous, Psychology effects, Bayesian Networks.

1 Introduction

Rumor spreading plays a significant role in a variety of human affairs [1]. The spread of rumors can shape the public opinion in a country [2], and cause panic in a society during wars and disease outbreaks. It is valuable for us to explore the rumors' inner spread mechanism.

At present, the scholars have done many researches about general social rumors in information science, and have made some progress and achievements. M.Nekovee [2] introduced a general stochastic model for the spread of rumors, and derived mean-field equations that described the dynamics of the model on complex social networks. Kawachi [3] introduced four models for the transmission of a constant rumor, which were classified according to whether the population was closed or not and whether the rumor was constant or variable. And he also considered a rumor transmission model with various contact interactions, in which rumor recursion was conjectured as a major challenge to mathematical models of rumors [4]. But most researches in information science consider rumor transmission as an example of social contagion processes. Just like the classical model of rumor spreading introduced many years ago by Daley and Kendall [5]. The main problem of those models is that they ignore the heterogeneity of individuals.

Some new models and methods are proposed to solve this problem recently. Kim and Bock [6] focused on the effect of rumor recipient's emotions to the behavior of spreading online rumors. Other scholars studied the opinion leader's impact on network public opinion [7]. The study of the impact of authorities' media indicated that whether authority's voice is effective depend on the credibility and audience rating of authorities' media [8]. The way concerned the individual heterogeneity is to subdivide the population into more detailed classifications based on a particular aspect. As every individual is different in the rumor spreading and many factors affect the behavior of spreading, we still need a way to model the generation of every different individual's thinking which influence the spread of rumors.

Actually, it is the individual cognition which dominates the behavior of rumor spreading. Through learning of knowledge and personal experience, people formed their own cognitive style. People predict and judge the development of things according to their own cognitive style. When people spread their unconfirmed view as fact, the rumors emerge. Thus the study of individual cognitive model is very significant to the exploration of individual rumor spread behavior. There are many techniques to build artificial intelligent machines which have the ability to cognitive. Neural-network techniques take as their starting point a highly-simplistic view of how the brain operates. And neural networks generally require a large amount of data to train and often struggle with over-fitting. Another class of techniques is probabilistic models. Bayesian Networks[9] employ a directed acyclic graph as the basic structure on which the independence assumptions about probability distributions are specified.

In humans, the cognitive and recognize capabilities are largely performed by the neocortex. Through evolution, biology has discovered a set of assumption about how the neocortex to learn about the world [10]. This set of assumption can be summarized as hierarchy in time and space. Hierarchical Temporal Memory (HTM) is a technology modeled on how the neocortex performs these functions [11]. Through replicating the structural and algorithmic properties of the neocortex, HTM has the ability to build machines that approach human level performance for many cognitive tasks. HTM has a broad application in many fields, such as pattern recognition, control, attention and forward prediction.

In Section 2, we propose an individual cognitive model for rumor spreading based on the extended HTM model. In Section 3, we propose a method to transform the messages about rumor or real earthquake events into binary code. After that, some experiments were conducted to test the performance of the extended HTM system. Then, this paper will consider another probability based systems, Bayesian Network (BN). The comparison section compares BN algorithm to HTM in more detail.

2 Method

2.1 Hierarchical Temporal Memory (HTM)

HTM developed by Numenta, Inc.[12] is a recent form of artificial intelligence. Hierarchical Temporal Memory models the functioning of the human brain. An HTM network is organized as a tree-shaped hierarchy of nodes.

HTM has two modes: training mode and inference mode. During the training mode, the information is passed into a spatial pooler at first. In the spatial pooler, the novel input vector is evaluated for similarity to other vectors that have already been stored. The vector is stored as a new coincidence if it is beyond the defined range. Then the coincidence is passed to a temporal pooler. In temporal pooler, the coincidences consist in a sequential manner as input data. The output of each node is a temporal coincidence which is stored and evaluated in a similar manner to the spatial pooler. During inference, HTM receives novel input vector and determines how close it is to all stored patterns. Finally, HTM selects one of stored patterns which have the highest closeness value measured to the input pattern as the result.

In HTM models, all nodes perform a same learning algorithm with a spatio-temporal vector as output, differing only on the type of input vectors that they process. This network is hierarchical in both space and time. But the top node is different because it does not emit output vectors and it does not perform temporal aggregation of the data. The top node infers through similarity measurements the proper category during inference.

2.2 The Extended HTM Model

The extended HTM model which has an extended top node in the network has been used prominently and successfully in sign language recognition [13] and gaze gesture recognition [14]. It has been developed in order to solve the multivariable time-series problems whose instances develop over time. Typical HTM algorithm is appropriate for problems such as image recognition. These problems consist of instances whose spatial configuration is fully represented at any time instant. As a rumor event consists of sequences of messages over time as a whole, typical HTM model is not available. So Rozado extended the typical HTM paradigm to solve problems where instances unfold over time. In these problems, at any given time, t , the complete representation of a sign is not available. Rumor recognition is one of those problems. For example, when someone just receives the single message which says “A mudslide disaster will happen in YaAn”, he can’t judge whether it is a rumor or not. But if he already knew the news that YaAn had an earthquake recently and torrential rain is sweeping YaAn, he may choose to believe the message is not a rumor.

So in our work, the extended HTM model is applied. Its modification of a binary HTM system concerns the network’s top node. The traditional top node in HTM network clusters the input vector to some categories at any given time. The extended HTM top instead, stores sequences of input vectors from the traditional top node in the so-called ‘sequential pooler’ and maps a whole sequence to a specific category, not just the individual elements. Each element of the sequence is a spatio-temporal configuration pattern of messages about rumor at any given time. And the whole sequence serves enough information as the message evolves over time.

The particular topological arrangement of the extended HTM has been proved to be more effective, and the top node could figure out more distant or elusive dependencies. Topologically, the extended top node sits at the top of HTM network, receiving its inputs from a traditional top node. Fig.1 shows an exemplary topology of HTM network used for rumor recognition. Each node in the bottom levels corresponds to a part

of the rumor message. This particular topological arrangement responds to the HTM theoretical requirement of clustering in the bottom levels with a high degree of local correlation.

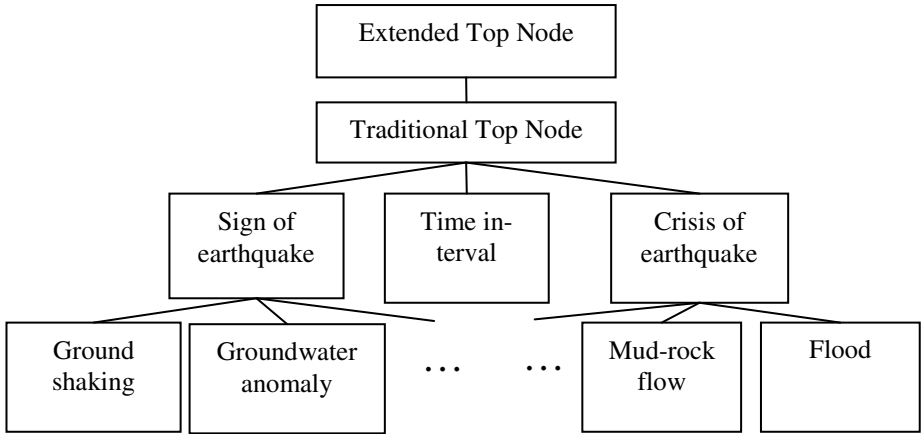


Fig. 1. Exemplary topology of the HTM network used for rumor recognition

Traditional top node receives binary vectors representing the rumor message at one moment active in the nodes underneath in the hierarchy and maps these incoming vectors to categories. The extended top node instead stores sequences of incoming vectors in an abstraction of the rumor message sequences and maps whole sequences to single categories. In [13]and [14], the similarity measurements between sequences carried out using the Needleman-Wunsch algorithm that employs dynamic programming for sequence alignment.

St:	0	0	0	1	1	0	1	0
Sp1:	0	1	0	1	1	0	0	0

	St	0	0	0	1	1	0	1	0
Sp1	0	0	0	0	0	0	0	0	0
0	0	3	3	3	2	1	3	2	3
1	0	2	2	2	6	5	4	6	5
0	0	3	5	5	5	4	8	7	9
1	0	2	4	4	8	8	7	11	10
1	0	1	3	3	7	11	10	10	9
0	0	3	4	6	6	10	14	13	13
0	0	3	6	7	6	9	13	12	16
0	0	3	6	9	8	8	12	11	15

Fig. 2. An example of the sequence alignment calculated with the Needleman-Wunsch

Fig.2 shows a sequence alignment calculated with the Needleman-Wunsch algorithm for two sequences of rumor. The scores in the matrix are calculated according to:

$$M(i, j) = \max \begin{cases} M(i-1, j-1) + s(SA_i, SB_j) \\ M(i-1, j) + g \\ M(i, j-1) + g \end{cases} \quad (1)$$

The external row and column in the matrix represent 2 example sequences encoding the whole spatio-temporal structure of a rumor, which is made up by a series of results of traditional HTM model. A system to score matches, mismatches and gaps is used to calculate the sequence alignment matrix. In (1), g represents the gap cost according to the scoring scheme used, in Fig.2 $gap=-1$. The score of $s(SA_i, SB_j)$ is according to whether element i in sequence A match with element j in sequence B or not.

$$s(SA_i, SB_j) = \begin{cases} 3, & \text{match} \\ -3, & \text{mismatch} \end{cases} \quad (2)$$

According the scores calculated by the way above, the extended top node can cluster the rumor message sequences into categories as a whole. Actually this is also a method realized the overall cognitive on a series of the rumor message. Base on this method, the extended HTM model can simulate the whole process that people receive information related to the rumors in succession and eventually make their own judgment.

3 Experiments and Result Analysis

In HTM models, no matter the traditional models or those with extended top node, message passing from children nodes to parent nodes is implemented using binary vectors, containing just 1s and 0s in each element. As the earthquake rumors frequently appear and attract high attention, we choose this special kind of social rumors for research. We collected about 80 earthquake rumors events, and a large amount of real seismic event related information. Through the summarizing and analysis of these messages, some characteristics of the seismic information can be found. They always have the same structure, which consists of two parts: the signs and the crisis.

In our work, we collected a total of 46 kinds of earthquake warning signs. Due to the different warning signs may appear in one message, so at least 46 bits are needed to represent all of these earthquake warning signs. After that, some more bits are needed to represent the indicators associated with these anomalies, include intensity, duration and frequency. We use 3 bits to represent each indicator, and it increases from 000 to 111 to represent the degree deepening. Then we could use a binary vector with 55 bits to represent a sign of an earthquake message. And by the same method, the crisis part of the earthquake message could be transformed into binary code.

So in this way, we can transform a message into a binary vector. For example, the message that "Due to the ground shaking happened just now, it seems that there will be a tsunami in the next few hours which will cause a large number of casualties" could transform to a vector as shown in the Fig.3

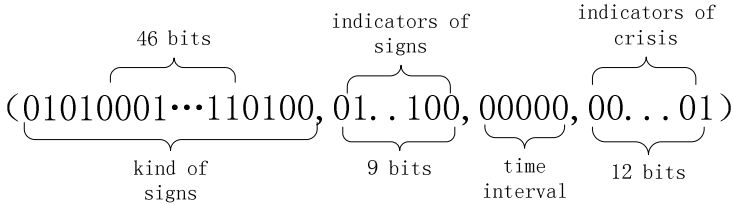


Fig. 3. An example of how to transform a message about the earthquake to a vector

We have to use sequences of vectors to fully describe a rumor. Take the Japanese earthquake happened on 2011.3.11 for example, there were many signs appeared successively. On March 9, earthquakes occurred many times. And on March 11, the electron density in ionospheric above the earthquake focus increased ten percent than the surrounding area. In this event, we have to use two vectors to describe the earthquakes and the increased electron density respectively, because they didn't occur at a same time point. The message sequence is the main data form needed to be deal with. This is the main reason why we use the extended HTM model.

In this work, we can't simply say system's judgment is right or wrong. The so-called recognition accuracy is also meaningless. Whether the system's result can reflect the rumors spread rules discovered by sociologists is our judgment standard. In the field of sociology and psychology, there are a large number of research results of the rumor spreading. Psychologists have proposed many psychological effects which could be felt in the process of rumor spreading. So we set up three kinds of experimental scenario to illustrate the HTM system is in line with the three common social psychology effects, which are primacy effect, repetition effect and the effect of public authority, respectively.

3.1 Primacy Effect

Given a list of items to remember, we will tend to remember the first few things more than those things in the middle. This was named primacy effect by Solomon Asch [15]. The order of the information occurred affects individual cognitive judgment. The first remembered experience has the biggest influence on the individual judgment. So we took an experiment like this: the HTM system was trained by 17 messages, including 4 real earthquake events and 13 rumors. And then, let the system to judge whether the news that after the earthquake just happened in Yushu, Yinchuan would have an earthquake because the magnetic anomalies and the bad weather occurred frequently was a rumor. The result shows that the HTM system thinks there is only 18.1% chance of an earthquake. This suggests that the individuals with rich experience about rumor produce a first impression like "see anomalies, but no earthquake". So when they receive the news about magnetic anomalies and the bad weather, they still trend to believe it is a rumor about earthquake. The system can fully embody the primacy effect in the process of individual cognition.

3.2 Repetition Effect

Repetition effect is derived from the Goebbels effect. A lie repeated one thousand times will be the truth, this is the repetition effect. We took another experiment about this psychological effect. Firstly, the HTM system was also been trained by the same 17 messages which had been used in the experiment of primacy effect. We use a sequence of messages as the test input of HTM system. These messages are repeating the same contents, which said that Yinchuan has occurred magnetic anomalies and the bad weather frequently so there would be an earthquake soon. At this time, the HTM system thinks there is a 67.7% chance of an earthquake. Although the result does not show a high probability, but from that we can obviously find the effect of the repetition to individual cognition. Even the individuals with rich experience would make a mistake when they receive the same rumor message from the people who they believe and respect.

3.3 Effect of Public Authority

Effect of authority refers to the phenomenon that in the process of social public opinion evolution, the opinions of the pundits tend to play a decisive role. The government departments and the earthquake research institute play a role of authority. So we can carry out the following experiment which was based on the first two experiments to verify the effect of public authority. The 17 messages which were used in the experiment of primacy effect, and the 4 messages which were used as test input in the experiment of repetition effect, added up to a total of 21 messages, were used as the training input in HTM systems. In this situation, the system can simulate the people who have rich experiences and knowledge of earthquake and received some repetition rumors about earthquake recently. And then, we input the test message which was issued by the government said that there wouldn't be an earthquake happening as the rumors said before. At this time the HTM system gave a result with 57.8% chance that it is a rumor. Although this is not a high probability, considering the effect of repetition at the same time, it may be a situation closer to the reality.

Through this a series of experiments we can see the HTM can well simulate the individual's judgment of rumors. And in the following chapter, the comparison between the HTM and another probability based systems, Bayesian Network (BN), has been taken.

4 Compare with BN

The design of a BN requires the design of a causal relationship network. But in the research of rumor spreading, there is no consensus on the design of a causal relationship network. So we had to use the simplest way of design, Naive Bayesian Network, which is shown in Figure 6 for this application. Every kind of the signs mentioned above in the Data part is a factor that affect whether believe the rumor. And they are mutually independent and do not affect each other. This design has some disadvantages, which will be introduced in more detail later.

And another difference between these two algorithms is that in contrast to the Bayesian Network implementation, the input to HTM is at a much lower level and comes directly from the real world. For example, in this application, BN just learn that if there is a meteorological abnormal appeared before an earthquake, but at the same time, the HTM system can distinguish a meteorological abnormal into 7 more detailed kinds as mentioned before, just like the long drought, hail in the summer, and so on.

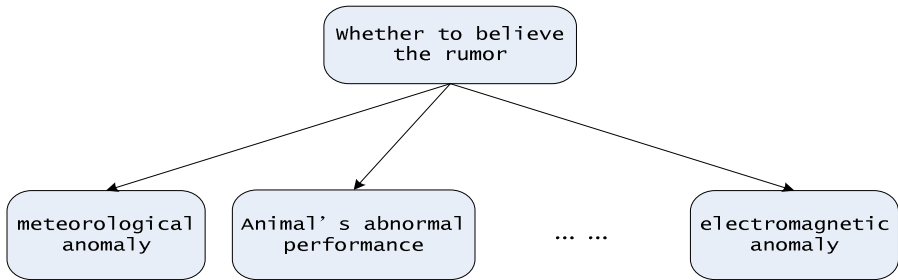


Fig. 6. The causal relationship network of BN used in the rumor recognition

We tried to take the same three experiments about psychological effects which has been describe in the section 4, and compare the BN’s result to the HTM. But we found that it was hard to achieve.

Firstly, in the experiment of repetition effect, the test input should be a sequence of messages, which includes some repetition messages of a same rumor. But the BN system can’t process the message sequence. It only has the ability to deal with a separate message at one time. So it can’t simulate the situation that one person get many messages at the same time, and the messages are not verified authenticity, so we can’t solve this problem by the way to treat those messages as training inputs. So one of the extended HTM’s advantages is it can deal with such a situation and get a reasonable result.

Secondly, in the experiment of effect of public authority, if we use the same training samples set, the BN system would think that earthquake will not occur with a 100% sure, which is a unreasonable result. Appear such result is made by the design of causal relationship network in BN. In the current causal relationship network applied in our BN system, whether there is a message issued by authorities or not is a kind of independent factors which affect the final result immediately. The situation that earthquake still happened when authorities said it wouldn’t is not occurred in our training samples, so the BN system will be convinced that earthquake will not occur when it received the message issued by authorities, and ignore the influence of other factors. But in real society, even if there is a public authority effect, the public will not fully believe what the authorities say immediately. If we want to get a more reasonable result though BN, the more reasonable causal relationship network about rumor is needed. But it is difficult to sociologists and psychologists. Of course, we can change the training samples set to solve this problem. In March 2009, many small earthquakes happened in Italy, and it cause the rumor that there would be a big earthquake

spreading. Then scientists said it would not have a strong earthquake. But unfortunately, on April 1, a magnitude 6.3 earthquake happened and killed 309 people. If we add this message in the training samples, and with the other experiment set unchanged, the BN system will get a result with 91.3% certain to believe that it is a rumor. We can find that even a more comprehensive training set is provided for the BN, the result is still very radical. So this is why we choose HTM to do this work.

The last point, even in the experiment of primacy effect, which the BN system can deal with under the same condition to HTM system, the result of BN is the probability of earthquake will happen is only 8.5%. As mentioned before, BN is designed at a higher level than HTM. This is the main reasons why BN performs a higher probability to believe the message is a rumor, because BN does not include the more detailed signs, which is actually the more difficult part of this application. It is more difficult to infer the result when the distinction between the input information becomes more detailed. And on this point, the HTM system is more similar to human cognitive style. For example, many survivors of the Tangshan earthquake have a deep memory of the hot weather before the earthquake; they may choose to believe another earthquake will happen when they meet the same hot weather again. The other kinds of meteorological abnormal would not have such effect. BN in this application is not able to distinguish those kinds of the meteorological abnormal, but HTM system has the ability.

5 Conclusion

This paper described the implementation of a rumor identification system implemented on the extended HTM platform. The comparison between this method and BN has been done. In comparing them at the design level, BN is designed from a much higher level and requires more help from the sociologist to give the causal relationship between the rumors spreading. HTM takes in the information from the real world, and its standard architecture and algorithm already provide a reasonably good accuracy. Some other experiments in this article proved HTM algorithm could build a system in accordance with some typical psychology effects. Based on this, HTM can help the sociologist to find more potential rules of rumors spreading in turn. This is the main reasons why HTM algorithm is applied in our work.

References

1. Galam, S.: Modeling rumors: the no plane Pentagon French hoax case. *J. Physica A: Statistical Mechanics and Its Applications* 320, 571–580 (2003)
2. Nekovee, M., Moreno, Y., Bianconi, G., et al.: Theory of rumour spreading in complex social networks. *J. Physica A: Statistical Mechanics and its Applications* 374(1), 457–470 (2007)
3. Kawachi, K.: Deterministic models for rumor transmission. *J. Nonlinear Analysis: Real World Applications* 9(5), 1989–2028 (2008)
4. Kawachi, K., Sek, I.M., Yoshida, H., et al.: A rumor transmission model with various contact interactions. *J. Journal of Theoretical Biology* 253(1), 55–60 (2008)

5. Daley, D.J., Kendall, D.G.: Stochastic rumours. *J. IMA Journal of Applied Mathematics* 1(1), 42–55 (1965)
6. Kim, J.H., Bock, G.W.C.: A Study On The Factors Affecting The Behavior Of Spreading Online Rumors: Focusing On the Rumor Recipient's Emotions. In: PACIS 2011 Proceedings, pp. 98–104 (2011)
7. Watts, D.J., Strogatz, S.H.: Collective dynamics of 'small-world' networks. *J. Nature* 393(6684), 440–442 (1998)
8. Zhao, L., Wang, Q., Cheng, J., et al.: The impact of authorities' media and rumor dissemination on the evolution of emergency. *J. Physica A: Statistical Mechanics and its Applications* 391(15), 3978–3987 (2012)
9. Murphy, K.P.: *Dynamic Bayesian networks: representation, inference and learning*. D. University of California (2002)
10. Numenta, Inc.: *Hierarchical Temporal Memory Comparison with Existing Models* (2007)
11. George, D., Jaros, B.: *The HTM learning algorithms* (2007), <http://numenta.com>
12. Hawkins, J., George, D.: *Hierarchical temporal memory: Concepts, theory and terminology*. J. Whitepaper, NumentaInc (2006)
13. Rozado, D., Rodriguez, F.B., Varona, P.: Extending the bioinspired hierarchical temporal memory paradigm for sign language recognition. *J. Neurocomputing* 79, 75–86 (2012)
14. Rozado, D., Rodriguez, F.B., Varona, P.: Low cost remote gaze gesture recognition in real time. *J. Applied Soft Computing* 12(8), 2072–2084 (2012)
15. Asch, S.E.: Forming impressions of personality. *J. The Journal of Abnormal and Social Psychology* 41(3), 258 (1946)

Knowledge Based Modeling Method of Artificial Society Oriented to Emergency Management

Peng Zhang, Laobing Zhang, Zongchen Fan, and Xiaogang Qiu

College of Information System and Management, National University of Defense Technology,
Changsha, Hunan, P.R. China, 410073
Zhangpeng_yes@163.com

Abstract. Emergency management (EM) involves wide public concern over the recent years, and many researchers begin to quantitatively analyze the internal mechanism. We put forward a method to study EM by artificial society and computational experiment. The motivation of our research is to transform the emergency knowledge to simulation models, which support the computational experiment oriented to EM. Combined the ontology modeling and meta-modeling, we clarify the domain concepts oriented to EM, and establish the meta-models with GME tools. We also study the model transformation and code generation, which can realize the model semantic interoperability and support model execution. In the end, we provide a case and construct the artificial scenario oriented to public security emergency management (PSEM) based on EM meta-models.

Keywords: Emergency management, meta-modeling, public security, artificial society.

1 Introduction¹

Public security is especially important for building harmonious society. Many researchers tries to study the characters, forming reasons and spreading mechanisms of emergency by data mining, information fusion and data analyzing [1]. However, it shows shortages in analyzing and interpreting the internal mechanism of EM, so we try to solve the problems in the way of simulation. Constructing artificial society and doing computational experiment is a good approach to study the complex social system and individual behavior [2].

However, domain models are always developed based on different platforms and standards, which present high demands to reliability, expansibility and reusability [3]. It needs a standard method to guide the development process of modeling and simulation. It's possible that all models could operate coordinately and solve the complex practical problems.

¹ This work was supported in part by National Nature and Science Foundation of China under Grant No. 91024030.

Model-Driven Engineering (MDE) is a recent trend in software engineering whose main proposal is to focus on models rather than on computer programs [4]. Domain specific modeling (DSM) is always the appropriate choice to construct the modeling environment in a convenient manner. The domain specific modeling language (DSML) is the key element to construct the modeling environment, and meta-modeling is the common ways to establish the DSML [5].

This paper attempts to transform the domain knowledge space to the model architecture space, which aims at establishing the modeling environment oriented to EM. We can build simulation models based on meta-models, which can accelerate the accumulation of domain knowledge and improve the reliability of modeling [6].

2 Artificial Society and Model Architecture Oriented to EM

2.1 The Framework of Artificial Society and Computational Experiment

Professor Wang Fei-yue proposes the theory of ACP [2], namely artificial society, computational experiment and parallel execution. The artificial society is the foundation of ACP theory, and computational experiment is the approach to study the real system. Parallel execution is the goal of ACP, which keeps the real system and simulation system parallel running. We can do some experiment on the parallel system and guide the evolution of the visual world.

Artificial society provides the environment to do computational experiment oriented to EM. In artificial society, each individual has social network and behavior schedule. They can interact with each other and simulate the operation of the social system. And the operation state can be changed by adding intervention, for example, loading emergency event and control measures. We can foster the virtual society and adjust the individual behavior by injecting dynamic data obtained from real society. The simulation result is significant for the real system, which can guide us to take emergency measures to avoid bad situation.

2.2 The Model Architecture Oriented to EM

Artificial social system contains a list of basic models, such as individual model, environment model, social network model and intervention model. Individual is the basic element of artificial society, which is always autonomous and adaptive. The environment provides the basic operation condition of computation experiments, such as location, temperature and humidity. The social network describes the relationship between individuals. The development of models must be modular and follow certain norms, which can be assembled, interoperable and reusable.

Individual is the most active element in artificial society, which can interact with each other and promote the evolution of the artificial society. We must analyze the individual social characters, and design its general structure, including basic attributes and behaviors. For large scale agent based simulation, schedule is used to simulate the daily routine of individuals. Organization is also designed to simulate the group behavior, such as government and policemen.

Environment is the indispensable part of artificial society. The environment models include the physical environment entities, climate module, traffic module, culture module and so on. Physical environment provides the space where individuals are active in, such as school, government and hospital. Usually, Environment entities must contain the geography location (longitude and latitude), function, and capacity.

Society networks depict the relationship of individuals, which are the basic condition of individual communication. In artificial society, multilayer social networks are introduced including family network, classmate network, neighborhood network and co-worker network. These social networks are called strong links, which describe the steady relationships among individuals. While some relationships are always established temporally in special condition, which are called weak links.

Intervention models can break the balance of the artificial society, which can be classified into emergency model and measure model. Emergency model can affect or change the individual running state, which may lead to bad direction of the artificial society. While measure models can revise the states and maintain the orderly operation of artificial society.

3 The Transformation from EM Knowledge to Simulation Model

3.1 EM Knowledge and Its Representation

Material resource and EM knowledge are all indispensable to take emergency measures when incident occurs. It's a key for the decision maker to master relevant information and knowledge to make informed decision. EM knowledge may contain emergency plans, laws, cases, literatures and professional knowledge, which are usually stored in the form of files, bylaws and workflows. Totally, there are two types of EM knowledge as shown below [5].

- Emergency prevention knowledge: (know-what, how) it contains not only the emergency characters, transmission manner and development trend, but also the possible prevention methods;
- Emergency response knowledge: (know-who, where, when) it contains not only the response measures and basic skills, but also the potential manpower and material resource when taking emergency measures.

Knowledge representation is the process of knowledge encoding, and well-formed knowledge can be disposed by computer. As shown below, there are several methods of knowledge representation in the artificial intelligence field [6].

- Logical method: first logic language can express the simple concepts and relationships.
- Production method: "if...then..." clause can express the rules, which may generate new knowledge.
- Semantics network: vector graph describes the links of domain knowledge, and each node represents a domain concept.

- Framework description method: the frame consists of many slots and facets, which can describe the relation between concepts.
- Bayesian method: probability is used to describe the reliability, which can express uncertainty knowledge.
- Ontology method: ontology clarifies the basic concepts and relationships, which can be consistently understanding and shared.

EM knowledge is the foundation of modeling and simulation oriented to EM, which can be converted into models, data and algorithms. It's significant to share EM knowledge and build up the artificial society, which may support computational experiment and simulation application according to different motives, goals and application layers.

3.2 The Transformation from EM Knowledge into Simulation Models

Domain simulation is widely used in all walks of life, such as system analysis and decision making [7]. Simulation is also called as computational experiment in social simulation based on artificial society. Emergency knowledge can be divided into tacit knowledge and explicit knowledge [8]. Tacit knowledge usually includes methods and experiences, which are usually non-coding. While explicit knowledge is codified in the form of files, graph papers, specification and other mediums. As shown in the Fig.1, tacit knowledge can guide the simulation process, while explicit knowledge can be converted into model, data and design schema. Then we can gain the new knowledge of EM by domain simulation, which can support situation analyzing, decision making and emergency response.

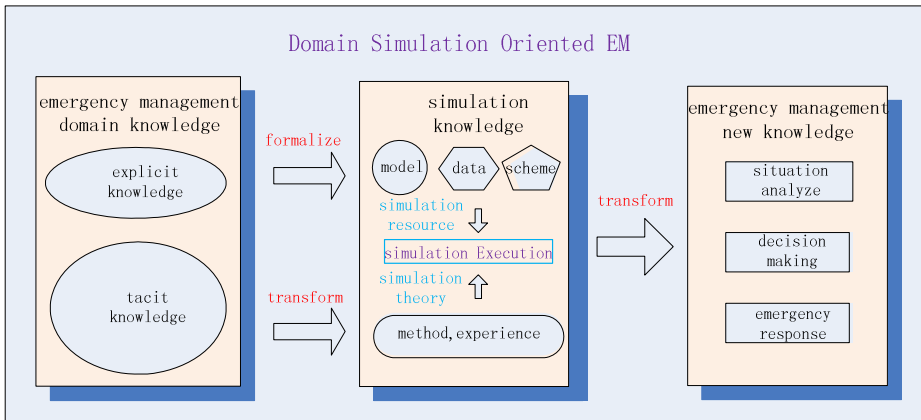


Fig. 1. Domain simulation oriented to EM

As shown in the Fig.2, we can analyze the domain knowledge and establish the domain ontology oriented to EM. Then we can build up the meta-models, which are considered as the domain special modeling language (DSML). Domain knowledge,

conceptual models and meta-models system can all reflect the characteristics of the system. Though meta-models can't be executed directly, it can be transform into simulation model easily by code generation or model transformation.

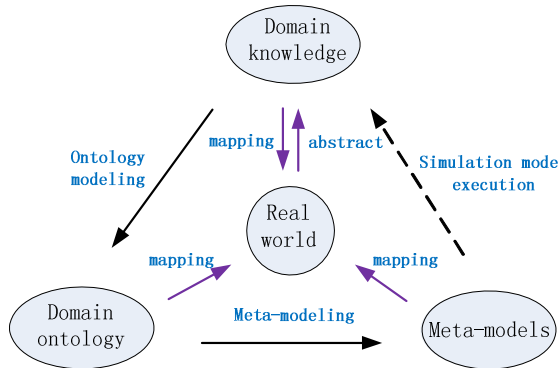


Fig. 2. The relationship of domain knowledge, ontology and meta-models

4 Ontology Modeling in PEMS

Public security emergency management (PSEM) puts main attention on the common scientific problems, including the cause, outbreak and development of emergency. There are three indispensable elements in the emergency, including emergency event, bear disaster body and emergency management [9]. The bear disaster body will change its state under strange force, and lead to subsequence event. The main task of the emergency management is to study the laws and characters of disaster, and take interventions to release the loss.

4.1 Domain Analysis

Nowadays, internet provides us so many conveniences along with a lot of potential dangers, so network security is worth watching. Information dissemination plays an important role in many emergency events, which can transmit emotion and attitude. The motivation of our work is to explore the effect of rumor diffusion in the evolution process of emergency event, and establish the meta-models to support the domain modeling oriented to EM.

PSEM refers to multi disciplines and domain, such as information, psychological and behavior. When incident occurs, the key information and elements form the information space, which will spread to the public by network, newspaper and TV; Receiving information, people will have their own opinions, views and emotions, and form the psychological space; People will display some behavior or take some action driven by psychological factors, which may also affect the development trend of the event.

There are 4 types of main models in the artificial society, namely population, environment, emergency events and intervention measures. Population includes individuals and organizations, and individuals may belong to multi organizations at the same time. Environment contains network opinion model, culture model and communication model. Network opinion usually represents the emotion, attitude and belief in the network. People may have their own opinions which can be shared in special network. Culture model tries to explore the relationships between the culture and individual behavior. Communication model is the carrier of information dissemination, which is especially important for the development of the event. Public security event model describes the event process and development trend, which can affect the state of environment and population.

4.2 Establish the Domain Ontology Oriented to EM

Ontology defines the core concepts and properties of the domain. The modeling primitive of ontology are concepts, relations, functions, axioms and instances, which can be express as $O=\{C, R, F, A, I\}$. Ontology contains semantic information, which can be shared and reuse.

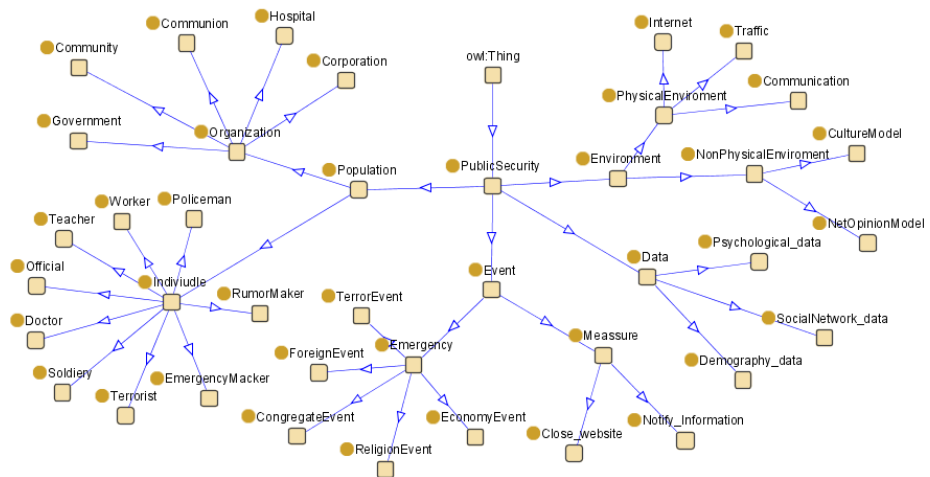


Fig. 3. The ontology tree of PSEM

We can clarify the ontology scope and gain the information by a variety of ways, such as books and domain experts. Ontology can express the semantic information of knowledge, and it's useful to knowledge management and knowledge retrieving. There are two main ways to construct the ontology: reuse the existing ontology or build new ontology.

Protégé 2000 is an open source tool to build ontology, which can edit basic classes, subclass, attributes and instances. It supports extension, and all conceptual models can be stored in the database. As shown in the Fig.3, the main elements of PSEM include population, environment, event, statistics data and emergency material. And the core concepts in the process of information dissemination are listed as follows.

- Individual: the basic unit of the artificial society, which can interact with each other and adapt to the environment.
- Organization: it's a social group made up of individuals, which usually have the same faith, benefit and opinion.
- Social network: it defines the relationship between individuals, which may be in multi-layer social networks.
- Behaviors: it defines the action sequence of population in artificial society, including daily activities and interacting with each other.
- Environment: it includes physical environment and non-physical environment. The former includes buildings, roads and workplaces. The latter includes the culture environment and communication network.
- Event: it defines a group of actions and rules which can affect the behavior of individuals and operation state of artificial society.
- Information: it contain information content and information attitude, which can be changed according to the predefined attitude of individual.

Ontology integrates the distributed knowledge and provides us a knowledge map of EM, which shields the complex internal logic. It should expand the semantic information and provide the access interface to other applications. Then we can establish the meta-models or models, which can support the simulation execution or problem resolving.

5 Meta-modeling Oriented to PSEM

5.1 Establish the Meta-models of PSEM

Generic Modeling Environment (GME) provides us the integrated environment of building domain special modeling language. GME is based on graphic symbol and OCL constrain language [10], which makes use of the computer technology such as finite state machines (FSM), signal flow (SF) and logic circuits. We can build meta-models on the platform to integrate domain knowledge. Meta-model is the basic unit of DSML, which can be combined, reused and shared easily. Based on the ontology tree of PSEM, we can establish meta-models. The meta-models of PSEM are composed of four parts: environment, population, emergency and intervention. Population includes individual and organization, and environment includes physical environment and nonphysical environment.

Taking the population view as an example, models, atoms and connections of the system are listed in the Fig.4. Every individual has the basic attributes and methods. The basic attributes of individual include population type, gender, age, ethnic, education background and so on. Psychological attributes include attitude, emotion and character. The activities of agent include offline activities and online activities. Mental activities contain affective sensation, affective computing and decision making. Organization also has the similar information and behavior, which can represent the whole characters of group individuals. Additionally, the relationship between individuals and organizations are also described in the figure.

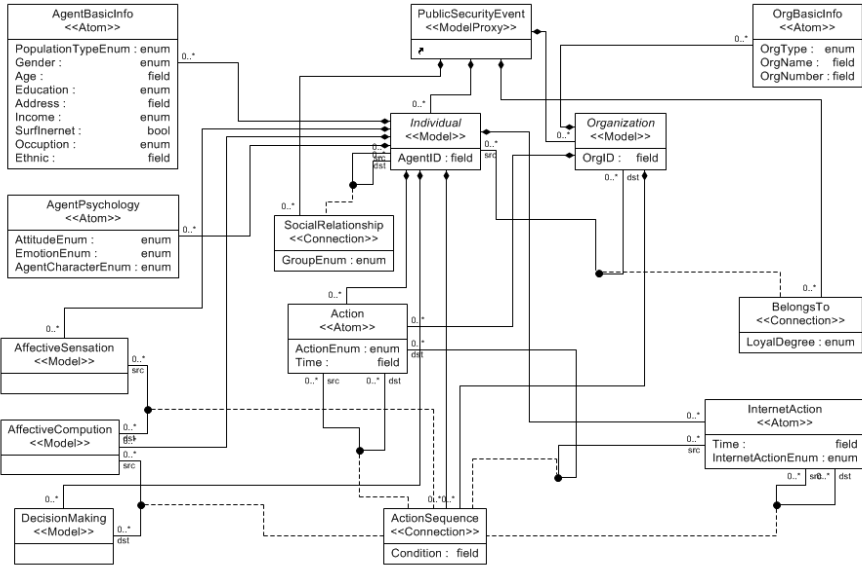


Fig. 4. Meta-models of the population view

Meta-models extract the essence of model entities, which can help us come to an agreement or understanding about some phenomenon. Domain knowledge and semantic information can be reused in the forms of meta-models. We can build DSML based on meta-models and accelerate the development of simulation models.

5.2 Construct the Artificial Scenario Based on Meta-models

Domain specific modeling (DSM) is a system modeling method oriented to special domain, which try to represent the modeling elements in the manner of graphic or texture. DSM supports abstract language and needs less work to describe the details. The core concepts of DSM can describe the domain problems and support problem resolving. Meta-models can be combined and reused in DSM, so we can make use of meta-models to construct the artificial scenario of PSEM.

As shown in the Fig.5, the artificial scenario depicts the evolvement of the religion collide event. All elements are described by meta-models, which includes evil strength (terrorist, terror organization and rumor maker) and justice strength (government, policeman, official and so on). Rumor maker takes the important role in the process of event development, and internet is the main channel of rumor diffusion. Social cultures and network opinions are also the main factor which can impact the development of the emergency event. In the process, we should release timely information on the internet, and all social forces should take part in the EM conducted by the government. Although some details cannot be display on the scenario, meta-models can describe the inter mechanism of artificial society and main strength in the EM process.

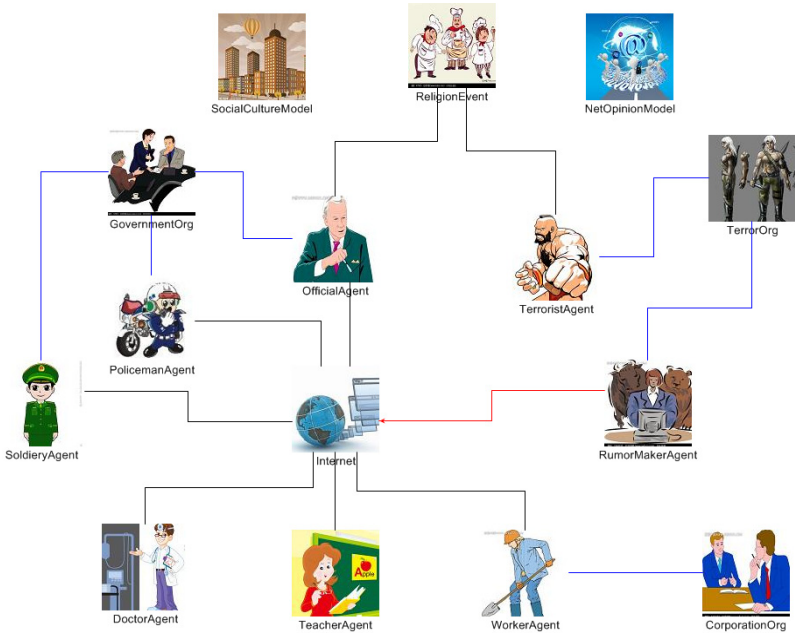


Fig. 5. Initial scene of artificial society oriented to PSEM

5.3 Model Transformation

We can transform the meta-models into simulation models by domain modeling and model transformation. Modeling transformation is based on the fact that different formalized models are just the different view of same phenomenon. The semantic information may lose in the process of transformation, so we must ensure that meta-models must contain enough modeling structure and details.

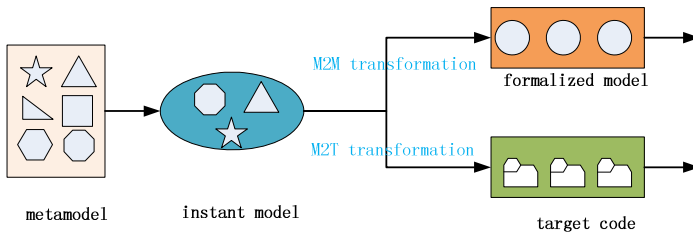


Fig. 6. Two ways of model transformation

As shown in the Fig.6, there are two kinds of model transformation, namely model to model transformation (M2M) and model to text transformation (M2T). In one hand, we can transform the meta-models to formalized models with typical modeling pattern by GREAT package, which can be driven by simulation engine. In the other hand, we can transform the meta-model to target code or dynamic library, which can be used by other application programs.

Code models contain the attributes, methods and model interfaces, which can support simulation execution. We can use meta-models to build instance models described in graphic manner, and generate target code automatically based on the graphic model. We can study the rumor spreading and agent behavior based on code model, and gain new knowledge about EM by data mining and analyzing.

6 Conclusion

This paper studies the construction of artificial society oriented to EM and proposes a knowledge-based modeling method. The contribution of our work is that we provide an approach to convert EM knowledge to simulation models. Combined with the technology of ontology modeling and meta-modeling, we establish the model architecture of artificial society oriented to EM. We can get the simulation models by code generation and model transformation. However, there are some details need to be improved in the future work, such as the mapping between ontology and meta-models. Additionally, the semantic loss in the process of model transformation also needs to be considered.

References

1. Epstein, J.M.: *Growing Artificial Societies: Social Science from the Bottom Up*. Brookings Institution Press (1996)
2. Wang, F.: *Artificial Societies, Computational Experiments, and Parallel Systems: A Discussion on Computational Theory of Complex Social-Economic Systems*. *Complex Systems and Complexity Science* 1, 25–35 (2004)
3. Duan, W., Cao, Z., Wang, Y., Zhu, B., Zeng, D., Wang, F.Y., Song, H.: *An ACP Approach to Public Health Emergency Management: Using a Campus Outbreak of H1N1 Influenza as a Case Study*. *IEEE Transactions on Systems, Man, and Cybernetics–Part A: Systems and Humans* 43, 1028–1041 (2013)
4. Juan, V., Esperanza, M.: *A framework for model-driven development of information systems: Technical decisions and lessons*. *The Journal of Systems and Software* 85, 2368–2384 (2012)
5. José, R.H., Jesús, G.M., Juan, A.B.: *A domain-specific language for context modeling in context-aware systems*. *The Journal of Systems and Software* 86, 2890–2905 (2013)
6. Zhiyang, J., Y. S., Y. J.: *A Framework of Knowledge Management Systems for Tourism Crisis Management*. *Procedia Engineering*, 29, pp. 138–143 (2012)
7. Nicolas, P., Jacky, A., Isabelle, C.W.: *An MDA approach to knowledge engineering. Expert System with Applications* 39, 10420–10437 (2012)
8. Antonio, D.N.: *An MDA-based Approach to Crisis and Emergency Management Modeling*. *International Journal on Advances in Intelligent Systems* 5(1) (2012)
9. Enrico, F.: *A domain specific language approach for agent-based social network modeling*. In: *IEEE/ACM International Conference on Advances in Social Networks Analysis and Mining*, pp. 607–611 (2012)
10. Vanderbilt University: *GME[EB/OL]* (2005), <http://www.isis.vanderbilt.edu/Projects/gme>

A Kinetic Modeling for Radiotherapy Mechanisms with Gene-Environment Network (GEN) Framework

Jin-Peng Qi¹, Jie Qi¹, Fang Pu², and Ying Zhu³

¹ College of Information Science & Technology, Donghua University,
Shanghai P.R. China, 201620

² Informationization Office, Donghua University, Shanghai, P.R. China, 201620

³ Hunter New England Health, Royal North Shore Hospital, NEW South Wales, Australia
{qipengkai, jieqi, pufang}@dhu.edu.cn,
ying.zhu@hnehealth.nsw.gov.au

Abstract. Radiotherapy is a comprehensive method, in which the main factor that determines success in clinical radiotherapy is radiation dose. It is necessary to make the most of mathematical theories to investigate the complicated mechanisms how P53-dependent regulation pathways govern cell survival and apoptosis at molecular level. In this work, we develop an integrated method for modeling Tumor Radiotherapy System (TRS) based on Kinetic Theory of Active Particle (KTAP) and Gene-Environment Network (GEN), and then explore the dynamics of integrated TRS through correlated subsystems, and inner mechanism of cell fate decision under radiotherapy. The inner mechanisms of radiotherapy are investigated at both molecular and systematic levels, including the stochastic kinetics of DNA damage generation and repair, switch-like Ataxia Telangiectasia Mutated (ATM) activation, oscillation of P53-Mouse Mouble Minute 2 homolog (MDM2) negative feedback loop, and outcome of tumor cell degradation and genome stability under radiotherapy.

Keywords: Radiotherapy, Ion Radiation (IR), P53, Kinetic Theory of Active Particle (KTAP), Gene-Environment Network (GEN), Modeling.

1 Introduction

Cancer, like many other diseases, results from a complex interplay of genetic and environmental risk factors [1]. It is important to study the potential genetic and environmental risk factors together in order to understand the mechanisms of underlying aetiology [2]. Radiotherapy is a comprehensive method, which plays a major role in cancer treatment. The main factor determining success in clinical radiotherapy is radiation dose. Low doses are ineffective, whereas if it is possible to give a very large total radiation dose then, in principle, any tumor can be (locally) controlled, but it will bring unavoidable damage to the normal cells adjacent to the tumor [2]. Upon acute radiotherapy, recent experiments have shown that the tumor suppressor P53 and its cofactors play a crucial role in determining the outcome of tumor cell degradation [3,4]. Therefore, it is necessary to make the most of mathematical theories to investigate the

complicated mechanisms that P53-dependent regulation pathways govern cell survival and apoptosis, and outcome of tumor radiotherapy at molecular level as well.

Recently, Gene-Environment Network (GEN) model has been widely investigated by using the KTAP methods [5-15]. GEN can describe not only the stochastic interactions between genes and environmental cofactors at molecular level, but also the systematic dynamics of integrated system in response to external environment perturbations [7,14]. Therefore, GEN model is widely used in different research areas, e.g., cellular repair mechanisms under acute IR perturbations [14], Lung Cancer Etiology with selected gene/region in measures of environmental exposure [12,15], as well as cellular fate decision by gene cofactors in [3,14,16-18]. As a novel mathematical framework, KTAP can model the overall bio-system by evolution equations corresponding to the dynamics of all elements [19,20]. Based on KTAP approach, the biological activities are regarded as dynamics of mutual interactions among molecule particles within different subsystems. Then, the evolution of overall system is represented by distribution function over discrete states of all their elements in the integrated system [19-21]. Currently, KTAP has been applied into some areas in social and life sciences, e.g. modeling vehicular traffic flow [8], social behaviors of interacting individuals [11], as well as multi-cellular systems and tumor-immune system competition [10,13].

Here, based on KTAP method and GEN model, we develop a kinetic framework of integrated TRS with three subsystems and explore a complicated mechanism of cell cycle arrest and apoptosis under radiotherapy. By numerical simulations, we investigate the dynamics of correlated subsystems in TRS framework. It includes the stochastic process of DNA damage generation and repair, damage detection of ATM switch activation, pulses of P53-MDM2 oscillator, cell cycle arrest and apoptosis mechanisms induced by alternative activation of P21 and Bax signal pathways, as well as outcome of tumor cell degradation and genome stability during the first and second phase of radiotherapy. Especially, we analyze the simulation results obtained from our TRS framework, and thus find an optimal outcome of radiotherapy from different therapy strategies.

2 Method

2.1 Overview of TRS Framework

Radiotherapy, is one of the main tumor therapy, acts via the induction of DSBs to DNA, and triggers the cellular self-defense mechanism to induce apoptosis of cancerous cells via programmed cell death [1]. Under radiotherapy, DSBs induced by acute IR can trigger the binding of the sensor protein kinase ATM into the nascent DNA ends, subsequently increase the kinase activity of ATM [16]. As a nuclear transcription factor, P53 can be activated by ATM activation, and then regulate downstream genes and their signal pathways. The active P53 indirectly induces cell cycle arrest to repair DNA damage, and then cell apoptosis eliminates abnormal cells with genome damage or deregulated proliferation. Especially, these properties may modulate the activity of certain anticancer agents [15].

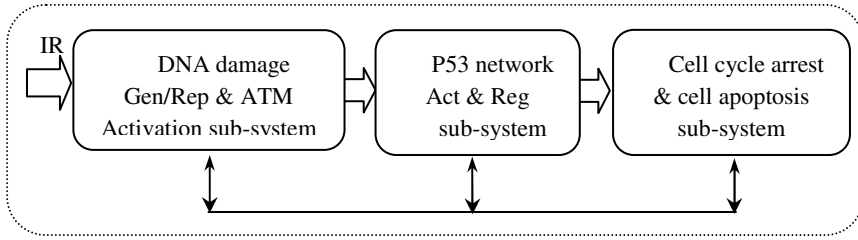


Fig. 1. The scheme of the integrated TRS framework. It is composed of three correlated subsystems: DNA damage generation & repair and ATM activation, P53 network activation and regulation, as well as cell cycle arrest & apoptosis. Each subsystem includes active molecular particles of several populations with different discrete states.

We propose an integrated framework of TRS to explore sophisticated mechanisms of cell fate decision under tumor radiotherapy (see Fig.1). The framework is composed of three subsystems: DNA damage generation, repair and ATM activation subsystem, P53 network activation and regulation subsystem, and tumor cell cycle arrest and apoptosis subsystem. By means of KTAP method and GEN model, the mutual interactions between molecular particles and environmental co-factors may modify either the state or the number of molecular in each subpopulation by proliferation/destruction phenomena [20]. Especially, the dynamic kinetics of integrated TRS is dealt as the results of mutual interactions among correlated molecular particles in different subsystems. Because the intrinsic mechanisms of radiotherapy are complicated, the limited vital genes and mutual interactions with environmental cofactors are involved into our integrated TRS framework.

2.2 DSB Generation, Repair and ATM Activation

The first module in the TRS framework tries to represent the stochastic kinetics of DNA repair and ATM activation in response to acute IR from outside (see Fig.2). Upon acute IR perturbation, DSBs, the typical form of DNA damage, occur stochastically. Fortunately, self-repair mechanism in a normal cell can fix this genome damage. RP, a repair enzyme, can be quickly recruited to bind into the nascent DNA ends, form the DSB-protein Complexes (DSBCs). DSBs are specifically detected by the Ataxia-Telangiectasia-Mutated (ATM) kinase. As a main signal source of DNA damage, DSBCs can trigger the switch-like kinetics of ATM activation through intermolecular phosphorylation [22].

Generally, most of the resulting DSB can be fixed by self-repair mechanism in a normal cell. During the DNA repair process, repair mRNA transcription and repair protein (RP) generation are prompted under mutual interaction of DSB with repair gene and repair mRNA, respectively. As RP is available, they are quickly recruited to break sites, and synthesize DSBC after RP combining into DSB. The rDSBCs is dealt as main signal to stimulate ATM activation, whereas, mDSBCs and remained DSBs are dealt as toxins in a cell, which can seriously weaken genome stability and cellular

viability, even lead to abnormal and cancerous eventually [14,22]. Meantime, ATM, a detector of DNA damage, is activated by DSBC signal transferred from DNA repair kinetics [22]. ATM converts from inactive ATM_d to ATM_m , and further to transform into ATM^* under positive interaction with rDSBC particles. In fact, ATM activation is a reversible kinetics, i.e., ATM_m can convert into ATM_d , and ATM^* can transform into ATM_m reversibly. The total concentration of ATM including ATM_d , ATM_m and ATM^* is assumed constant because it mainly undergoes posttranslational modifications after DNA damage. The dimerization rate of ATM is much larger than its undimerization rate, so that ATM dimers are predominant in unstressed cells [3,14].

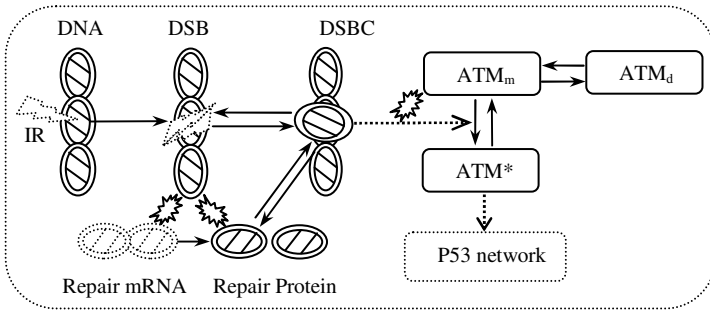


Fig. 2. The schematic diagram of DSB generation, repair, and ATM activation subsystem. It is composed of three subpopulations: DNA, DNA repair enzyme, and ATM. (Arrow-headed solid lines refer to state transition, and arrow-headed dotted lines stand for promotion of state transition, respectively. Bombing icons indicate the mutual interactions between two kinds of molecular particles.)

2.3 P53 Network Subsystem

As an important tumor suppressor, active P53 is very low in unstressed cell. Upon DNA damage, the dynamic equilibrium of P53-MDM2 feedback loop is impaired by ATM-dependent phosphorylation of P53 and MDM2, and then P53 is activated [22].

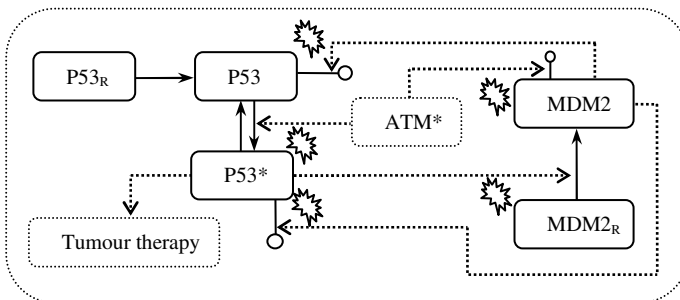


Fig. 3. The scheme of P53 network subsystems. It mainly includes P53-MDM2 negative feedback loop.

To eliminate lethal genome damage or deregulated proliferation, the level of active P53 can increase quickly in some minutes, while the first cellular apoptotic event occurs in a few hours in some cell types [18]. In the P53 network subsystem, we mainly consider the P53-MDM2 negative feedback loop (see Fig.3). Under continuous effect of damage signal from ATM activation module, the phosphorylation of P53 is prompted by positive interaction between P53 and ATM* molecular [22]. Meanwhile, the degradation of MDM2 is also accelerated by negative interaction between MDM2 and ATM* particle. In addition, the expression of MDM2 is triggered by positive interaction of MDM2 with P53* molecular. In order to avoid the over-expression of P53, the concentration of P53* can be depressed by MDM2, a P53-specific ligase and antagonist of P53. Thereafter, the expected oscillation dynamics will occur in the P53-MDM2 negative feedback loop [22].

2.4 Tumor Therapy Subsystem

The cofactors of P53 are vital in the choice of cell fate between survival and apoptosis [3,18]. In this work, tumor therapy subsystem mainly considers the P21-dependent cell cycle arrest and Bax-dependent apoptosis signal pathways (see Fig.4). In terms of the extent of DNA damage, the P53-dependent regulation pathways can make a reliable decision between survival and death [3,4,18]. Specifically, the active P53 sustains a moderate level for repairable damage in the first phase of radiotherapy, and thus cell cycle arrest pathway is triggered indirectly by the low level of P53*. On the other aspect, as for irreparable damage in the second phase of radiotherapy, a high level of P53 evokes Bax-dependent apoptosis pathway [1,3,18].

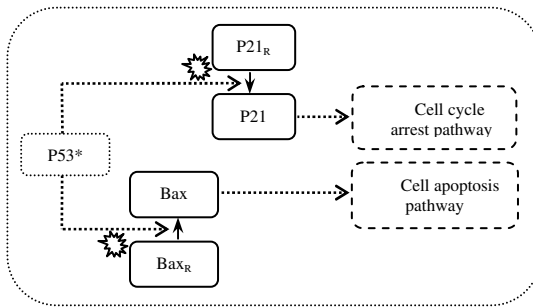


Fig. 4. The scheme of tumor therapy subsystem. It is composed of the kinetics of cell cycle arrest and apoptosis initiated by P21 and Bax signal pathways, respectively.

In the first phase of radiotherapy, we assume that the mechanism of cell cycle arrest is initiated directly by P53-dependent P21 signal pathway, then blocks tumor cell proliferations and promotes DNA damage repair directly. Under repairable DNA damage, P21 is activated by positive interaction with the low level of P53*. Then, the damaged cell undergoes transient cell cycle arrest period. Thus, the process of DNA repair is accelerated indirectly by prompting RP generation and the growth of tumor

cell mass is suspended until DNA damage is fixed [1,3,17,18]. On the other hand, we assume that the apoptosis mechanism is triggered directly by P53-dependent Bax regulation pathway, and fulfils tumor cell degradation directly. As for irreparable DNA damage in the second phase of radiotherapy, the Bax-dependent regulation pathway is activated by positive interaction with the high level of P53* molecular. Thus, tumor cell is degraded directly by Bax-oriented apoptosis mechanism without intermediate steps between CytoC release and Casp3 activation [3,17,18]. In addition, we deal that the number of toxins remained in a tumor cell can decrease the genome stability directly. Thus, the indicators such as, the number of RP available, toxins, tumor cell mass, and genome stability, etc, can analyze the outcomes of tumor radiotherapy under different therapy strategies further.

3 Results and Discussion

By using the platform of Matlab.7, the dynamic kinetics of TRS are investigated, including stochastic kinetics of DNA repair, switch-like ATM activation, oscillations of P53 network activation, and alternative mechanism between cell cycle arrest and apoptosis during the first and second phase of radiotherapy, and then, the outcome of radiotherapy is analyzed roughly under 5Gy IR circumstance. In the following parts, f_x refers to the concentration of molecular particle type x in a cell.

3.1 DSB-Protein Complexes (DSBCs) Synthesis and ATM Activation

Under continuous 5Gy IR, the resulting DSBs occur stochastically under external interactions with constant IR cofactor (Fig.5, a). Due to the limitation of cellular self-repair capability, the number of toxins, including intact DSB and disrepair part of DSBCs (mDSBC), increases quickly after the concentration of remaining DSB, f_{RDSB} , overtaking threshold T_{RDSB} at about 600 time-scales (Fig.5, b).

As an indicator of DSB repair process, the numbers of Repair Protein (RP) available and correct repair part of DSBCs (rDSBC) syntheses begin to decrease quickly after about 600 time-scales, i.e., the capability of cellular self-repair mechanism keeps decreasing (Fig.5, c). Meanwhile, ATM is very sensitive and reliable to damage signal from DSBC synthesis module. After mutual interaction with rDSBC molecular, ATM is activated from inactive ATM monomer (ATM_m), and phosphorylated ATM monomer (ATM^*) rapidly rises to a high plateau after about 30 time-scales, and keeps dynamic equilibrium until the damage is efficiently repaired (Fig.5, d, and e). The simulations above indicate that rDSBCs turn on the switch-like ATM activation after RP combining into damage sites, and f_{RP} is vital factor to decide the capability of cellular self-repair. On the other hand, toxins remaining in a cell, a by-product of radiotherapy, can negatively affect a series of cellular activities, and thus decrease genome stability further.

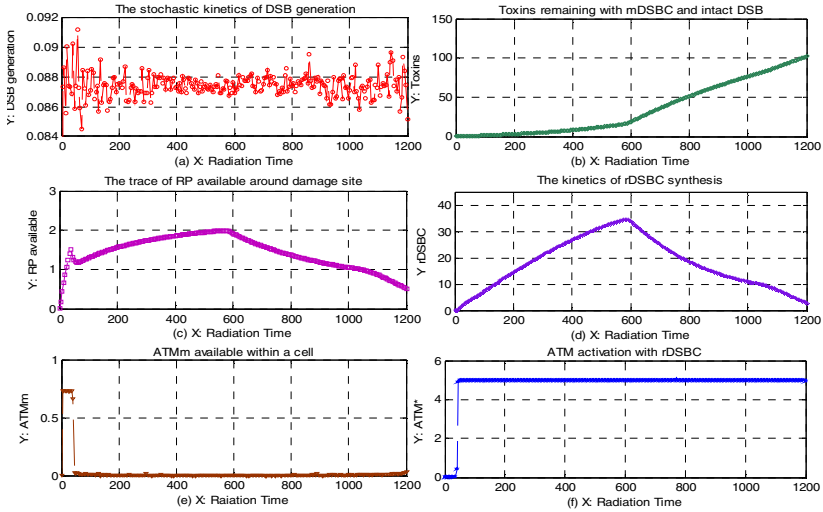


Fig. 5. The kinetics of DSB synthesis and ATM activation under IR=5Gy. (a) Stochastic trace of DSB generation. (b) Toxins remaining, including both intact DSB and mDSBC. (c) RP available around damage sites. (d) rDSBC synthesis after RP binding into DSB. (e) ATM_m decreasing during and after ATM activated from ATM_m. (f) Switch-like ATM activation from ATM_m after positive interaction with rDSBC.

3.2 Oscillations of P53 Network Activation

P53 network is very complicated and helpful for exploring the dynamics of key molecular particles in TRS framework. The oscillations of P53-MDM2 negative feedback loop are important clues to investigate inner mechanism of cellular response to DNA damage [16,22]. Upon positive interaction with ATM* molecular, P53-MDM2 oscillator is initiated by the activated ATM to generate periodic pulses between P53 and MDM2. The number of these pulses is determined by the duration of ATM in the saturation state.

In response to ATM activation, the saturation trace of P53 mRNA transcription provides continuous signal resource to P53-MDM2 oscillator (Fig.6, a). During and after positive interaction with ATM* and negative interaction with MDM2, f_{P53} and f_{P53^*} increase quickly and keep high level with similar periodic pulses (Fig.6, b and c). Meanwhile, upon the positive interaction with activated P53 (P53*) and negative interaction with ATM* molecular, MDM2 is activated from MDM2 mRNA with similar periodic pulses (Fig.6, d and e). These oscillations between P53 and MDM2 have similar periods of about 400 time-scales with different phases and swings, and the first pulse is slightly higher than the second one, and then tends to dynamic equilibrium (Fig.6, f). These simulations above plausibly suggest that cellular self-defensive mechanisms are initiated by damage signal transferring from outer environment.

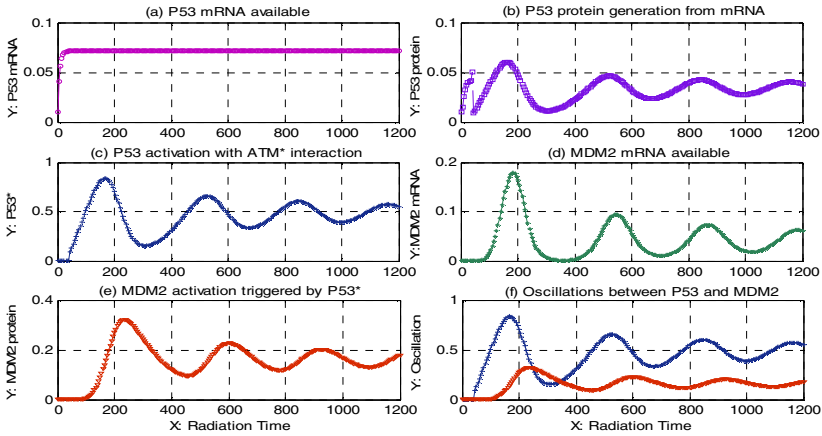


Fig. 6. The oscillations of P53 network activation under IR=5Gy. (a) Switch-like trace of P53 mRNA available upon damage signal from ATM*. (b) Pulses of inactive P53 protein available during and after P53 activated, and (c) P53* activated under positive interaction with ATM*, and negative interaction with MDM2. (d) Pulses of MDM2 mRNA available, and (e) MDM2 activated under positive interaction with P53*, and negative interaction with ATM*. (f) Oscillations of P53-MDM2 negative feedback loop.

3.3 Outcomes of Tumor therapy

During the first phase of radiotherapy, the activated P53 keep low level in response to repairable DNA damage, and thus P21 is activated from P21 mRNA after positive interaction with P53* molecular, and f_{P21} reaches climax at about 600 time-scales (Fig.7, a and b). Meantime, tumor cell mass keeps relatively low level before 600 time-scales, because of the mechanism of cell cycle arrest induced by P21-oriented signal pathway. However, during the second phase of IR=5Gy radiotherapy, f_{P21} decreases sharply and tends to zero after about 600 time-scales, because f_{RDSB} over-takes the threshold T_{RDSB} that a cell can repair maximally (Fig.7, b).

Although Bax can be activated from Bax mRNA under the positive interaction with low level of P53* (Fig.7, c and d), f_{Bax} cannot take over the threshold T_{Bax} that the mechanism of apoptosis can be initiated. Therefore, tumor cell cannot be degraded, and thus the concentration of tumor cell mass, $f_{T_{Mass}}$, keeps increasing dramatically (Fig.7, e). As a result, the genome stability keeps decreasing and tends to zero, due to toxins increasing within tumor cell (Fig.7, f). The results above indicate that the outcomes of radiotherapy under 5Gy strategy are not encouraged, because P53-dependent Bax signal pathways cannot initiate the expected mechanisms of apoptosis for degrading tumor cell.

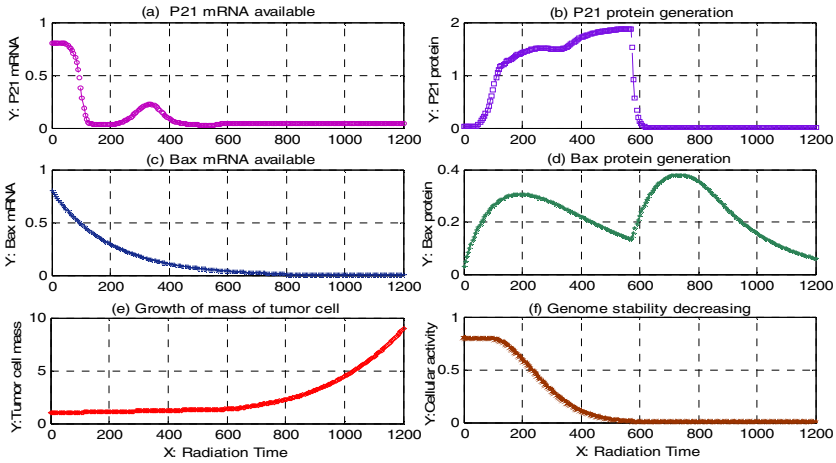


Fig. 7. The outcomes of tumor radiotherapy under IR=5Gy strategy. (a) P21 mRNA available during and after P21 protein translated from P21 mRNA. (b) P21 protein generation under positive interaction with P53*. (c) Bax mRNA available during and after Bax protein transformed from Bax mRNA. (d) Bax protein generation after positive interaction with P53*. (e) Dynamics of tumor cell mess growth, and (f) decreasing genome stability against continuous therapy time.

4 Conclusions

Our work presents the whole process of radiotherapy from DSB generation to tumor cell degradation upon acute IR at both molecular and systematic levels. By using KTAP method and GEN model, the integrated TRS framework with three subsystems are proposed to investigate the complicated mechanisms of tumor radiotherapy. The TRS framework exhibits a series of dynamics from molecular to systematic levels: stochastic process of DSB generation and repair, damage detection of ATM switch, dynamic pulses of P53-MDM2 oscillator, alternative mechanisms of cell cycle arrest and apoptosis triggered by P21 and Bax signal pathways. The outcomes of TRS framework show that tumor cell cannot be efficiently degraded and genome stability cannot be maintained effectively if IR is too low. It is because the mechanism of cell cycle arrest and apoptosis cannot be initiated in the first and second phase of radiotherapy. Especially, our TRS framework can be used to further explore inner mechanisms of tumor radiotherapy from molecular to systematic level, and provide some hints and clues to design more efficient strategies for tumor radiotherapy.

Acknowledgments. This paper is supported by National Natural Science Foundation of China (No.61104154), and the Fundamental Research Funds for the Central Universities.

References

1. Perez, C., Brady, L.: Principles and practice of radiation oncology. *Journal of Pediatric Hematology/Oncology* 21, 560 (1999)
2. Karlsson, M., Weber, W.: Therapeutic synthetic gene networks. *Current Opinion in Biotechnology* 23, 703–711 (2012)
3. Zhang, X.P., Liu, F., Wang, W.: Two-phase dynamics of p53 in the DNA damage response. *Proceedings of the National Academy of Sciences* 108, 8990–8995 (2011)
4. Kim, J., Lee, S.-D., Chang, B., Jin, D.-H., Jung, S.-I., et al.: Enhanced antitumor activity of vitamin C via p53 in cancer cells. *Free Radical Biology and Medicine* 53, 1607–1615 (2012)
5. Bellomo, N., Forni, G.: Looking for new paradigms towards a biological-mathematical theory of complex multicellular systems. *Mathematical Models and Methods in Applied Sciences* 16, 1001–1029 (2006)
6. Bellouquid, A., Delitala, M.: *Mathematical modeling of complex biological systems: a kinetic theory approach*. Springer (2006)
7. Caspi, A., Moffitt, T.E.: Gene–environment interactions in psychiatry: joining forces with neuroscience. *Nature Reviews Neuroscience* 7, 583–590 (2006)
8. Cercignani, C., Gabetta, E.: *Transport Phenomena and Kinetic Theory*. Springer (2007)
9. Bellomo, N., Delitala, M.: From the mathematical kinetic, and stochastic game theory to modelling mutations, onset, progression and immune competition of cancer cells. *Physics of Life Reviews* 5, 183–206 (2008)
10. Bellomo, N., Forni, G.: Complex multicellular systems and immune competition: New paradigms looking for a mathematical theory. *Current Topics in Developmental Biology* 81, 485–502 (2008)
11. Bertotti, M.L., Delitala, M.: Conservation laws and asymptotic behavior of a model of social dynamics. *Nonlinear Analysis: Real World Applications* 9, 183–196 (2008)
12. Brazzoli, I.: From the discrete kinetic theory to modelling open systems of active particles. *Applied Mathematics Letters* 21, 155–160 (2008)
13. De Angelis, E., Lods, B.: On the kinetic theory for active particles: A model for tumor–immune system competition. *Mathematical and Computer Modelling* 47, 196–209 (2008)
14. Qi, J., Ding, Y., Zhu, Y., Wu, Y.: Kinetic theory approach to modeling of cellular repair mechanisms under genome stress. *PloS one*. 6, e22228 (2011)
15. Yu, K., Wacholder, S., Wheeler, W., Wang, Z., Caporaso, N., et al.: A Flexible Bayesian Model for Studying Gene–Environment Interaction. *PLoS Genetics* 8, e1002482 (2012)
16. Cuddihy, A., Bristow, R.: The p53 protein family and radiation sensitivity: Yes or no? *Cancer and Metastasis Reviews* 23, 237–257 (2004)
17. Ribeiro, D., Pinto, J.: An integrated network-based mechanistic model for tumor growth dynamics under drug administration. *Computers in Biology and Medicine* 39, 368–384 (2009)
18. Zhang, X., Liu, F., Wang, W.: Regulation of the DNA damage response by p53 cofactors. *Biophysical Journal* 102, 2251–2260 (2012)
19. Bertotti, M.L., Delitala, M.: From discrete kinetic and stochastic game theory to modelling complex systems in applied sciences. *Mathematical Models and Methods in Applied Sciences* 14, 1061–1084 (2004)
20. Bellomo, N.: *Modeling complex living systems: a kinetic theory and stochastic game approach*. Springer (2008)
21. Deutsch, A., Dormann, S.: *Cellular automaton modeling of biological pattern formation*. University of Bielefeld, Germany Birkhäuser, Boston (2004)
22. Ma, L., Wagner, J., Rice, J.J., Hu, W., Levine, A.J., et al.: A plausible model for the digital response of p53 to DNA damage. *Proceedings of the National Academy of Sciences of the United States of America* 102, 14266–14271 (2005)

Identification of MIMO Neuro-fuzzy Hammerstein Model with Noises

Li Jia¹, Xunlong Li¹, and Min-Sen Chiu²

¹Shanghai Key Laboratory of Power Station Automation Technology,
Shanghai University, Shanghai 200072, China

²Department of Chemical and Biomolecular Engineering,
National University of Singapore, Singapore, 117576, Singapore
jiali@staff.shu.edu.cn

Abstract. A novel identification algorithm for neuro-fuzzy based MIMO Hammerstein system with noises is presented in this paper. A special test signal that contains independent separable signals and uniformly random multi-step signal is adopted to identify the MIMO Hammerstein system. As a result, it can circumvent the problem of initialization and convergence of the model parameters discussed in the existing iterative algorithms used for identification of MIMO Hammerstein model. Moreover, least square method based parameter identification algorithms of dynamic linear part and static nonlinear part are proposed to avoid the influence of noise. Example is used to illustrate the effectiveness of the proposed method.

Keywords: Correlation analysis method, neuro-fuzzy system, MIMO Hammerstein process, separable signals, process noises.

1 Introduction

The Hammerstein model is a block-oriented nonlinear model consisting of the cascade structure of a static nonlinear element followed by a dynamic linear element. It has been shown that such a model can efficiently represent and approximate many industrial processes. For example, pH neutralization processes [1], heat exchangers [2], [3], distillation columns [4], [5], dryer process [6], polypropylene grade transition [7], and continuous stirred tank reactor (CSTR) [8] have been modeled with Hammerstein model. Various system identification methods have been extended to identify the Hammerstein model. Considering immeasurable intermediate variables in the Hammerstein model, the synchronous method and the separate step method are two different ways to identify the static nonlinear element and the dynamic linear element of the Hammerstein model [9]. The synchronous method identifies the parameters of the Hammerstein model by directly constructing a hybrid model of the static nonlinear element and the dynamic linear element, such as over-parameterization method [10], [11], subspace method [12], modulation function method [13] and direct identification method [14]. The separate step method decouples the identification problems of the dynamic linear element and the static nonlinear element by estimating

the immeasurable intermediate variables, such as iterative method [15], separable least squares method [16], stochastic method [17], blind identification method [18], frequency domain method [19] and multi-signal based method [20].

Few papers addressed the MIMO Hammerstein model. Motivated by the previous works, a novel identification method for neuro-fuzzy based MIMO Hammerstein model with process noises by using the correlation analysis method is presented in this paper. We employ the extended version of Bussgang’s theorem [21] for MIMO Hammerstein system. The property of the separable signal of MIMO system is analyzed further. Moreover, the conditions how Bussgang’s theorem can be used for the identification of the generalized MIMO Hammerstein model are given. In this work, a special test signal is adopted to identify the Hammerstein process with process noises, resulting in the identification problem of the linear model separated from that of nonlinear part. The signal satisfies the following conditions: 1) it contains independent separable signals, such as binary signal, sine signal and Gaussian signal; and 2) it contains a uniformly random multi-step signal. As a result, the identifications of the linear model and the static nonlinear function are carried out independently by using the separable input signals. And the effects of the process noises can be avoided.

The rest of this paper is organized as follows. The MIMO Hammerstein process identification problem and neuro-fuzzy based MIMO Hammerstein model with process noises are given in Section 2. A correlation analysis and neuro-fuzzy based identification method is presented in Section 3. Simulation examples are given in Section4, followed by the concluding remarks given in Section 5.

2 Neuro-fuzzy Based MIMO Hammerstein Model with Process Noises

The MIMO Hammerstein process can be formulated by the following equations:

$$\begin{aligned}
 \mathbf{v}(k) &= \mathbf{f}(\mathbf{u}(k)) \\
 \mathbf{w}(k) &= \mathbf{v}(k) + \boldsymbol{\eta}(k) \\
 \mathbf{y}(k) &= \frac{\mathbf{B}(z)}{\mathbf{A}(z)}\mathbf{w}(k) + \mathbf{e}(k)
 \end{aligned}
 \tag{1}$$

where $\mathbf{u}(k) \in \mathbb{R}^m$ and $\mathbf{y}(k) \in \mathbb{R}^n$ denote the process input and output at the k -th sampling instant, respectively, $\mathbf{v}(k) \in \mathbb{R}^m$ and $\mathbf{w}(k) \in \mathbb{R}^m$ represent the corresponding noise-free and disturbed internal variables, $\boldsymbol{\eta}(k) \in \mathbb{R}^m$ and $\mathbf{e}(k) \in \mathbb{R}^n$ are white noises independent of $\mathbf{u}(k)$, $\mathbf{A}(z) = \mathbf{I} + \sum_{i=1}^{n_A} \mathbf{A}_i z^{-i}$ and $\mathbf{B}(z) = \sum_{j=1}^{n_B} \mathbf{B}_j z^{-j}$ are the $n \times n$ and $n \times m$ matrix polynomials, respectively, with z^{-1} being the backward-shift operator $z^{-1}\mathbf{y}(k) = \mathbf{y}(k-1)$, n_A and n_B are integers related to the model order, \mathbf{I} always

denotes the identity matrix of compatible dimension. The static nonlinearity of the Hammerstein process is $\mathbf{f} = [f_1, \dots, f_m]^T$, where $f_r : \mathbb{R}^m \rightarrow \mathbb{R}$, $r = 1, \dots, m$.

In this paper, the MIMO Hammerstein process is identified by a neuro-fuzzy based MIMO Hammerstein model, in which the nonlinearity of the process is represented by a neuro-fuzzy based MIMO model and the linear dynamics by a MIMO ARX model.

The static nonlinearity is approximated by a four layer neuro-fuzzy system which integrates the Takagi-Sugeno fuzzy system and the radial basis function (RBF) based feed forward network into a connection structure. The neuro-fuzzy system consists of four layers. The first layer is input layer. Nodes in this layer just transmit the input variables to the next layer directly. The second layer is the membership function layer that receives the signals from the input layer and calculates the membership of the input variable. Gaussian membership function is used in this layer. The third layer is the rule layer. The number of the nodes in this layer represents the number of fuzzy rules. The last layer is the output layer. All consequence weights are fully connected to the output node in which defuzzification is performed. The r -th output of the neuro-fuzzy system is then given by:

$$\hat{v}_r(k) = \hat{f}_r(\mathbf{u}(k)) = \sum_{l=1}^L \Phi_l(\mathbf{u}(k)) d_{r,l} \quad (2)$$

where

$$\Phi_l(\mathbf{u}(k)) = \frac{\mu_l(\mathbf{u}(k))}{\sum_{l=1}^L \mu_l(\mathbf{u}(k))}$$

where $\mu_l(\mathbf{u}(k)) = \exp\left(-\sum_{r=1}^m \frac{(u_r(k) - c_{r,l})^2}{\sigma_l^2}\right)$ is the Gaussian membership function,

$c_{r,l}$ and σ_l are respectively the center and width of the membership function, $d_{r,l}$ is the corresponding weight of the neuro-fuzzy system, L is the total fuzzy rules.

3 Identification of Neuro-fuzzy Based MIMO Hammerstein Model

A special test signal is adopted to identify the Hammerstein process, resulting in the identification problem of the linear model separated from that of nonlinear part. The signal satisfies the following conditions: 1) it contains independent separable signals, such as binary signal, sine signal and Gaussian signal; and 2) it contains a uniformly random multi-step signal. As such, the identifications of the liner model and the static nonlinear function are carried out independently by using the separable input signals. This section presents the identification procedure for the proposed neuro-fuzzy based MIMO Hammerstein model in detail. For simplicity, all signals are assumed to have zero mean. It should be noted that the assumption is reasonable. Owing to the

deviation variables employed in constructing the MIMO Hammerstein model, the static nonlinearities satisfy $w_r(k) = 0$, $r = 1, \dots, m$. It means that the nonlinear mapping of a given steady state vector of process input, \mathbf{u}_s , gives the corresponding steady state vector of \mathbf{w}_s .

Theorem 1: For a $m \times n$ Hammerstein process with noises described in Eq. 1, if the input signals are independent separable, there exists a matrix \mathbf{B}_0 such that the following equation holds.

$$R_{\mathbf{w}\mathbf{u}}(\tau) = \mathbf{B}_0 R_{\mathbf{u}}(\tau), \quad \forall \tau \in \mathbb{Z} \quad (3)$$

where

$$R_{\mathbf{w}\mathbf{u}}(\tau) = \begin{bmatrix} E(w_1(k)u_1(k-\tau)) & \cdots & E(w_1(k)u_m(k-\tau)) \\ \vdots & \ddots & \vdots \\ E(w_m(k)u_1(k-\tau)) & \cdots & E(w_m(k)u_m(k-\tau)) \end{bmatrix}$$

$$R_{\mathbf{u}}(\tau) = \begin{bmatrix} E(u_1(k)u_1(k-\tau)) & \cdots & E(u_1(k)u_m(k-\tau)) \\ \vdots & \ddots & \vdots \\ E(u_m(k)u_1(k-\tau)) & \cdots & E(u_m(k)u_m(k-\tau)) \end{bmatrix}$$

$$\mathbf{B}_0 = \begin{bmatrix} E(v_1(k)u_1(k)) & \cdots & E(v_1(k)u_m(k)) \\ \vdots & \ddots & \vdots \\ E(v_m(k)u_1(k)) & \cdots & E(v_m(k)u_m(k)) \end{bmatrix} \begin{bmatrix} E(u_1(k)u_1(k)) & \cdots & E(u_1(k)u_m(k)) \\ \vdots & \ddots & \vdots \\ E(u_m(k)u_1(k)) & \cdots & E(u_m(k)u_m(k)) \end{bmatrix}^{-1}$$

A. Identification of the dynamic linear part

As discussed above, the identification of the linear dynamic part can be completely separated from that of nonlinear static part by using the independent separable signals. In this paper, the correlation analysis algorithm is adopted to estimate the parameters of the linear model.

As described in Section 2, the linear dynamics of a MIMO Hammerstein process can be rewritten as follow

$$\mathbf{y}(k) = -\sum_{i=1}^{n_A} \mathbf{A}_i \mathbf{y}(k-i) + \sum_{j=1}^{n_B} \mathbf{B}_j \mathbf{w}(k-j) + \sum_{i=1}^{n_A} \mathbf{A}_i \mathbf{e}(k-i) + \mathbf{e}(k) \quad (4)$$

Multiply both sides of above equation by $\mathbf{u}(k-\tau)$ and then compute the mathematical expectations, we have

$$R_{\mathbf{y}\mathbf{u}}(\tau) = -\sum_{i=1}^{n_A} \mathbf{A}_i R_{\mathbf{y}\mathbf{u}}(\tau-i) + \sum_{j=1}^{n_B} \mathbf{B}_j R_{\mathbf{w}\mathbf{u}}(\tau-j) + \sum_{i=1}^{n_A} \mathbf{A}_i R_{\mathbf{e}\mathbf{u}}(\tau-i) + R_{\mathbf{e}\mathbf{u}}(\tau) \quad (5)$$

As the process noise $\mathbf{e}(k)$ is independent of process input $\mathbf{u}(k)$, we get $R_{\mathbf{e}\mathbf{u}}(\tau) = \mathbf{0}_{n \times m}$, and then

$$R_{\mathbf{y}\mathbf{u}}(\tau) = -\sum_{i=1}^{n_A} \mathbf{A}_i R_{\mathbf{y}\mathbf{u}}(\tau-i) + \sum_{j=1}^{n_B} \mathbf{B}_j R_{\mathbf{w}\mathbf{u}}(\tau-j) \tag{6}$$

Thus, we can use the correlation analysis method [22] to estimate the parameters of the dynamic linear part. Here set $\tau = 1, 2, \dots, P$ ($P \geq n_a + n_b$). And we can get

$$\boldsymbol{\theta} = \mathbf{R}\boldsymbol{\Psi}^T (\boldsymbol{\Psi}\boldsymbol{\Psi}^T)^{-1} \tag{7}$$

where $\boldsymbol{\theta} = [\hat{\mathbf{A}}_1, \hat{\mathbf{A}}_2, \dots, \hat{\mathbf{A}}_{n_a}, \hat{\mathbf{B}}_1, \hat{\mathbf{B}}_2, \dots, \hat{\mathbf{B}}_{n_b}] \in \mathbb{R}^{n \times (n \times n_a + m \times n_b)}$ is the estimated model parameters, and

$$\mathbf{R} = [R_{\mathbf{y}\mathbf{u}}(1), R_{\mathbf{y}\mathbf{u}}(2), \dots, R_{\mathbf{y}\mathbf{u}}(P)] \in \mathbb{R}^{n \times (m \times P)}$$

$$\boldsymbol{\Psi} = \begin{bmatrix} -R_{\mathbf{y}\mathbf{u}}(0) & -R_{\mathbf{y}\mathbf{u}}(1) & -R_{\mathbf{y}\mathbf{u}}(2) & \cdots & -R_{\mathbf{y}\mathbf{u}}(P-1) \\ \mathbf{0}_{n \times m} & -R_{\mathbf{y}\mathbf{u}}(0) & -R_{\mathbf{y}\mathbf{u}}(1) & \cdots & -R_{\mathbf{y}\mathbf{u}}(P-2) \\ \vdots & \vdots & \vdots & & \vdots \\ \mathbf{0}_{n \times m} & \mathbf{0}_{n \times m} & \mathbf{0}_{n \times m} & \cdots & -R_{\mathbf{y}\mathbf{u}}(P-n_a) \\ R_{\mathbf{u}}(0) & R_{\mathbf{u}}(1) & R_{\mathbf{u}}(2) & \cdots & R_{\mathbf{u}}(P-1) \\ \mathbf{0}_m & R_{\mathbf{u}}(0) & R_{\mathbf{u}}(1) & \cdots & R_{\mathbf{u}}(P-2) \\ \vdots & \vdots & \vdots & & \vdots \\ \mathbf{0}_m & \mathbf{0}_m & \mathbf{0}_m & \cdots & R_{\mathbf{u}}(P-n_b) \end{bmatrix} \in \mathbb{R}^{(n \times n_a + m \times n_b) \times (m \times P)}$$

B. Identification of the static nonlinear part

Based on the entire training data, the process of identifying the neuro-fuzzy based model is to estimate the parameters of $c_{r,l}$, σ_l and $d_{r,l}$, which is a nonlinear optimization problem. In this paper, the antecedent parameters, $c_{r,l}$ and σ_l are estimated by a clustering algorithm [23], [24]. The main results are concerned with the estimation of the consequent, $d_{r,l}$ by least square algorithm. As a result, the proposed method can avoid the problems of initialization and convergence of the model parameters, which are usually resorted to trial and error procedure in the existing iterative algorithms used for the neural network or fuzzy system based identification of Hammersstein model.

After the parameters $\hat{\mathbf{A}}_i, \hat{\mathbf{B}}_j, c_{r,l}$ and σ_l have been identified, we proceed with the estimation of the consequent parameter $d_{r,l}$. We get

$$\mathbf{y}(k) + \sum_{i=1}^{n_A} \mathbf{A}_i \mathbf{y}(k-i) = \sum_{j=1}^{n_B} \mathbf{B}_j \mathbf{v}(k-j) + \xi(k) \tag{8}$$

where $\xi(k) = \sum_{j=1}^{n_B} \mathbf{B}_j \boldsymbol{\eta}(k-j) + \sum_{i=1}^{n_A} \mathbf{A}_i \mathbf{e}(k-i) + \mathbf{e}(k)$. Thus, we have

$$\mathbf{y}(k) + \sum_{i=1}^{n_A} \hat{\mathbf{A}}_i \mathbf{y}(k-i) = \sum_{j=1}^{n_B} \hat{\mathbf{B}}_j \hat{\mathbf{f}}(k-j) + \xi(k) \tag{9}$$

Thus

$$\mathbf{h}(k) = \mathbf{W}\boldsymbol{\psi}(k) + \xi(k) \tag{10}$$

where

$$\mathbf{h}(k) = \mathbf{y}(k) + \sum_{i=1}^{n_A} \hat{\mathbf{A}}_i \mathbf{y}(k-i)$$

$$\mathbf{W} = [\mathbf{W}_1, \mathbf{W}_2, \dots, \mathbf{W}_{n_B}] \in \mathbb{R}^{n \times (n_B \times L)}$$

$$\mathbf{W}_j = \mathbf{B}_j \mathbf{D}, \quad j = 1, \dots, n_B$$

$$\mathbf{D} = \begin{bmatrix} d_{1,1} & \cdots & d_{1,L} \\ \vdots & \ddots & \vdots \\ d_{m,1} & \cdots & d_{m,L} \end{bmatrix}$$

$$\boldsymbol{\psi}(k) = [\boldsymbol{\psi}_1(k), \boldsymbol{\psi}_2(k), \dots, \boldsymbol{\psi}_{n_B}(k)]^T \in \mathbb{R}^{(n_B \times L) \times 1}$$

$$\boldsymbol{\psi}_j(k) = [\Phi_1(\mathbf{u}(k-j)), \Phi_2(\mathbf{u}(k-j)), \dots, \Phi_L(\mathbf{u}(k-j))]^T \in \mathbb{R}^{L \times 1}.$$

Thus, we can get the estimation of \mathbf{W} by using the least square algorithm

$$\mathbf{W}_{LS} = \left[\sum_{k=1}^N \mathbf{h}(k) \boldsymbol{\psi}^T(k) \right] \left[\sum_{k=1}^N \boldsymbol{\psi}(k) \boldsymbol{\psi}^T(k) \right]^{-1} \tag{11}$$

We can obtain

$$\mathbf{W}_{LS} = \mathbf{W} + \left[\sum_{k=1}^N \xi(k) \boldsymbol{\psi}^T(k) \right] \left[\sum_{k=1}^N \boldsymbol{\psi}(k) \boldsymbol{\psi}^T(k) \right]^{-1} \tag{12}$$

As $\xi(k)$ is a linear combination of white noises with zero means, we have

$$\begin{aligned} E(\mathbf{W}_{LS}) &= E(\mathbf{W}) + E \left(\left[\sum_{k=1}^N \xi(k) \boldsymbol{\psi}^T(k) \right] \left[\sum_{k=1}^N \boldsymbol{\psi}(k) \boldsymbol{\psi}^T(k) \right]^{-1} \right) \\ &= \mathbf{W} + \left[\sum_{k=1}^N E(\xi(k)) \boldsymbol{\psi}^T(k) \right] \left[\sum_{k=1}^N \boldsymbol{\psi}(k) \boldsymbol{\psi}^T(k) \right]^{-1} \\ &= \mathbf{W} \end{aligned} \tag{13}$$

That is to say, \mathbf{W}_{LS} is the unbiased estimation of \mathbf{W} .

4 Example

Consider the following SISO Hammerstein process, [25]:

$$\begin{aligned}
 w(k) &= 2 \tanh u(k) - 2 \exp(0.1u(k)) + 2 + \eta(k) \\
 y(k) &= \frac{bz^{-1}}{1+az^{-1}} w(k) + e(k) \\
 \theta_1 &= [a, b]^T = [-0.8, 0.6]^T
 \end{aligned}
 \tag{35}$$

where $e(k)$ and $\eta(k)$ are white noises with zero means and independent of the process input $u(k)$.

Define the noise-to-signal ratios as $\delta_{ns1} := \sqrt{\frac{\text{var}[\eta(k)]}{\text{var}[w(k) - \eta(k)]}} \times 100\%$

and $\delta_{ns2} := \sqrt{\frac{\text{var}[e(k)]}{\text{var}[y(k) - e(k)]}} \times 100\%$.

The binary input signals with $u(k) = 0$ or $u(k) = 3$ are chosen as separable input signals to identify the linear element while random multi-step signals with uniform distribution between $[0, 3]$ to identify the nonlinear element. The simulation results showed that the proposed identification method can give a better approximation of the dynamic linear element. The static nonlinear element is estimated by using the random multi-step signals as process inputs. The static nonlinear function and that of the neuro-fuzzy based model are compared in Fig. 1. It is clear that the neuro-fuzzy based model has very accurate approximation of the actual nonlinearity.

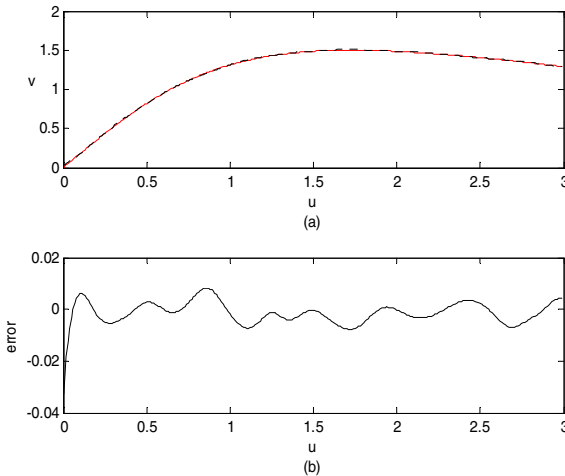


Fig. 1. Static nonlinear function: (a) actual (red solid line) and estimated (black dotted line) process of $f(u)$; (b) prediction error of $f(u)$

5 Conclusion

We employ the extended version of Bussgang's theorem for MIMO Hammerstein system, and a novel identification method for neuro-fuzzy based MIMO Hammerstein model with noises by using the correlation analysis method is presented in this paper. A special test signal is adopted to identify the Hammerstein process, resulting in the identification problem of the linear model separated from that of nonlinear part. Example shows the effectiveness of the proposed method.

Acknowledgments. Supported by National Natural Science Foundation of China (61374044), Shanghai Science Technology Commission (12510709400), Shanghai Municipal Education Commission (14ZZ088), Shanghai talent development plan.

References

1. Smith, J.G., Kamat, S.K., Madhavan, P.: Modelling of PH process using wavenet based Hammerstein model. *J. Process Control* 17, 551–561 (2007)
2. Zhang, H.T., Li, H.X., Chen, G.R.: Dual-mode predictive control algorithm for constrained Hammerstein systems. *International Journal of Control* 81, 1609–1625 (2008)
3. Lakshminarayanan, S., Shah, S.L., Nandakumar, K.: Identification of Hammerstein models using multivariate statistical tools. *Chem. Eng. Sci.* 50, 3599–3613 (1995)
4. Biagiola, S.I., Figueroa, J.L.: Identification of uncertain MIMO Wiener and Hammerstein models. *Computers & Chemical Engineering* 35, 2867–2875 (2011)
5. Bhandari, N., Rollins, D.: Continuous-time Hammerstein Nonlinear Modeling Applied to Distillation. *AIChE. Journal* 50, 530–533 (2004)
6. Rollins, D.K., Bhandari, N., Bassily, A.M., Colver, G.M., Chin, S.T.: A continuous-time nonlinear dynamic predictive modeling method for Hammerstein processes. *Ind. Eng. Chem. Res.* 42, 860–872 (2003)
7. He, D.F., Yu, L.: Nonlinear predictive control of constrained Hammerstein systems and its research on simulation of polypropylene grade transition. *Acta Automatica Sinica* 35, 1558–1563 (2009)
8. Naeem, O., Huesmana, A.E.M.: Non-linear model approximation and reduction by new input-state Hammerstein block structure. *Computers & Chemical Engineering* 35, 758–773 (2011)
9. Jia, L., Li, X.L.: Identification of Hammerstein Model: Review and Prospect. *Control Theory & Applications* 31, 1–10 (2014)
10. Bai, E.W.: An optimal two-stage identification algorithm for a class of nonlinear systems. *Automatica* 34, 333–338 (1998)
11. Ding, F., Chen, T.: Identification of Hammerstein nonlinear ARMAX systems. *Automatica* 41, 1479–1489 (2005)
12. Gómez, J.C., Baeyens, E.: Subspace-based identification algorithms for Hammerstein and Wiener models. *European Journal of Control* 11, 127–136 (2005)
13. Square, D.B., Heinz, U.: Identification of nonlinear continuous-time Hammerstein model via HMF method. In: *Proceedings of the 36th Conference on Decisions & Control*, pp. 2990–2995. IEEE, New York (1997)

14. Li, J.H., Ding, F.: Maximum likelihood stochastic gradient estimation for Hammerstein systems with colored noise based on the key term separation technique. *Computers & Mathematics with Applications* 62, 4170–4177 (2011)
15. Bai, E.W., Li, D.: Convergence of the iterative Hammerstein system identification algorithm. *IEEE Transactions on Automatic Control* 49, 1929–1940 (2004)
16. Bai, E.W.: Identification of linear systems with hard input nonlinearities of known structure. *Automatica* 38, 853–860 (2002)
17. Krzyzak, A., Partyka, M.A.: Global identification of nonlinear Hammerstein systems by recursive kernel approach. *Nonlinear Analysis* 63, 1263–1272 (2005)
18. Vanbeylen, L., Pintelon, R., Schoukens, J.: Blind maximum likelihood identification of Hammerstein systems. *Automatica* 44, 3139–3146 (2008)
19. Jing, X.J.: Frequency domain analysis and identification of block-oriented nonlinear systems. *Journal of Sound and Vibration* 330, 5427–5442 (2011)
20. Sung, S.W.: System identification method for Hammerstein processes. *Industrial & Engineering Chemistry Research* 41, 4295–4302 (2002)
21. Bussgang, J.J.: Crosscorrelation functions of amplitude-distorted Gaussian signals. In: *Technical Report 216*, MIT Research Laboratory of Electronics, Cambridge, Massachusetts (1952)
22. Hu, S.S.: Identification of parameters of MIMO systems by correlation analysis. *Acta Aeronautica et Astronautica Sinica* 11, 400–404 (1990)
23. Jia, L., Chiu, M.S., Ge, S.S.: A noniterative neuro-fuzzy based identification method for Hammerstein processes. *Journal of Process Control* 15, 749–761 (2005)
24. Jia, L., Shi, J.P., Chiu, M.S.: Fuzzy neural model with global convergence for batch process. *Information and Control* 38, 685–691 (2009)
25. Jia, L., Yang, A.H., Chiu, M.S.: Auxiliary model recursive least square algorithm based multi-signal identification of Hammerstein model. *Journal of Nanjing University of Science and Technology* 38, 34–39 (2014)

A Virtual Simulation and Driver Evaluation Platform for Smart Wheelchairs

Li Liu, Jingchuan Wang, and Weidong Chen

Department of Automation, Shanghai Jiao Tong University,
and Key Laboratory of System Control
and Information Processing, Ministry of Education of China, Shanghai 200240, China
{130329004, jchwang, wdchen}@sjtu.edu.cn

Abstract. Driver training system for disabled and elderly people to use electric wheelchairs has an important role for their independent mobility. In this paper a simulator platform of smart wheelchairs is presented for driver training and evaluation. Based on the smart wheelchair, integrated with kinematics, dynamics, sensors, and the 3D model of real wheelchairs and environment, it is implemented in Gazebo and ROS. The sensors include an encoder, a laser range finder and a set of Kinect. Without nursing staff's company, the user could complete driver training and assessment procedures by himself. Experiments verify that this platform can be used as a valid tool for driver training and evaluation.

Keywords: Simulation platform, smart wheelchair, electric wheelchair, driver training, driving skill evaluation.

1 Introduction

Many people, especially, for the disabled and elderly people which are hard to operate a manual wheelchair, have to rely on electric wheelchairs to complete their daily navigation tasks. Electric wheelchairs are conceived to increase the mobility of individuals with mobile dysfunction and enable them to live more independently [1]. The enhancement of independent mobility by electric wheelchairs can also help with rebuilding people's confidence of social skills. However, enough driving skills are required to ensure them operating wheelchairs safely and smoothly.

Similar to vehicle driving training, the traditional driving training for electric wheelchairs should be guided and accompanied by nursing staff for safety reasons. It will cost large manpower and material resources. In addition, how to evaluate the driving effect of electric wheelchair is also the focus of many rehabilitation experts' research. Paper [2] and [3] proposed a detailed test and evaluation standard for driver training and evaluation. However, these assessments are evaluated by subjective indexes with manual class statistics, without automatic evaluation system. Virtual system based on the real smart wheelchair could provide driver training safely without nursing staff's company. Due to the sensors embedded, it could also evaluate the driving effect

automatically. On the other hand, smart wheelchairs have been developed in a number of research labs over the past decades [4][5][6][7]. The development and simulation platform for smart wheelchairs can meet the demands for shortening the development cycle of a new algorithm and reducing the costs of experiments.

A virtual reality based 3D simulator for wheelchairs was presented in paper [8]. However, the simulator only works in 2D world, without dynamics and 3D sensor models. An interactive wheelchair rehabilitation training system was developed in paper [9]. It adjusted the relative position of wheelchair on the screen according to the rotation speeds of wheelchairs' wheels. Nevertheless, the system only takes kinematics into consideration, which is very rough in nature. In paper [10] and [11], a simulation engine and a 2D/3D viewer was described. It was able to test and validate control algorithms for intelligent wheelchairs. It created a mixed reality environment which achieved an interaction between the real and virtual worlds. However, for this simulator was not integrated with the physical engine and there were only be modeled 2 types of subjects: walls and robots, its collision checking was limited by these two types and the collision scene could not be simulated. Another limitation is that it only includes proximity sensors and excludes encoders which are widely used in speed and position calculations.

Integrating kinematics, dynamics, sensors, and the 3D models of wheelchair and world, a comprehensive platform for both driver training and evaluation of electric wheelchairs is presented in this paper. It realistically mimics the characteristics of smart wheelchairs which have been developed before. Integrated with various sensors, it could record the process data during training and give the evaluation results finally. Based on the simulation platform, the training and evaluation standards and procedures for electric wheelchair drivers are also proposed in this paper. Compared with the real electric wheelchair, experiments show that the simulation platform for driving training and evaluation has similar functions and consistent results.

2 System Structure

2.1 Presentation of the Structure

The smart wheelchair is mostly refitted from the traditional electric wheelchair. Based on the commercial electric wheelchair, it is equipped with encoder, laser range finder (LRF), Kinect, smart motion controller and on-board computer. As a two-wheel differential-drive mobile platform, it is driven by motor, and simultaneously effected by the external force action such as friction and gravity. Encoder is used to calculate the speed and position of wheelchair in smart motion controller. LRF could obtain the 2D information of environments. Kinect could obtain the image and cloud information. The data from both LRF and Kinect are proceeded in on-board computer.

Fig.1 provides an overview of simulation platform architecture compared with smart wheelchairs which has been developed before [12]. The environment, wheelchair body, sensors, actors and joystick as the interface between users and wheelchair, are included in Hardware Layer. Based on these hardware devices, the models are built in Model Layer. Joystick as the main interface between user and wheelchair is not modeled in

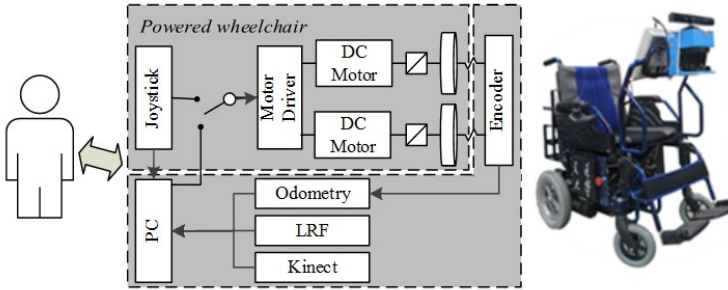


Fig. 1. Hardware Structure of Jiaolong Smart Wheelchair

Model Layer, the Human in the Loop method would be used in this platform. That is to say, users could operate the joystick of the real electric wheelchair to control the virtual platform. In order to simulate different effects of different environments and users, based on the models of encoder and wheelchair body, the Kinematics and Dynamics models are established in Abstract Layer. In Interface Layer, control command and sensor data from Kinect, LRF and Odometry are open for algorithm design of smart wheelchairs. In order to achieve good psychological sense of immersion, GUI displays the simulation scene intuitively. Users could set parameter configuration quickly by modifying the XML file. Fig.2 shows the data structure for the main interface.

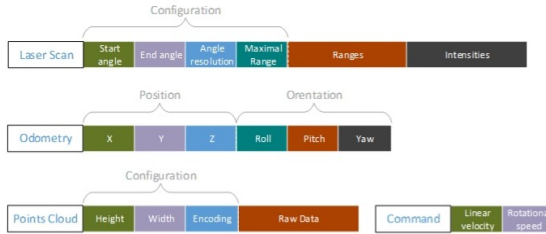


Fig. 2. Data Structure for the Main Interface

Fig.3 shows the driver training structure and GUI of simulation platform. This platform combines a real joystick and a projector. The real-time signal from joystick which is manipulated by users, is gathered and proceeded by simulation platform. According to the response calculation in Abstract Layer, the scene will be displayed to users by projector in first-person view. In order to simulate the actual driving situation, the driving data such as manipulation, movement trajectory and collision times is recorded to analyze the user’s driving habits and proficiency and to evaluate the user’s driving skills.

The implementation of this platform makes use of Gazebo [13][14] and ROS[15]:the calculations of dynamics and sensors are vastly based on the physical engine ODE and rendering engine OGRE in Gazebo; and the automatic evaluation system is implemented in ROS. The modules excluding GUI are dynamically loaded, and can be



Fig. 3. Driver Training Structure, GUI of Simulation Platform

modified or replaced conveniently according to the specified simulated wheelchair (especially sensors). Since the smart wheelchairs are ever-changing, a platform whose code is not available may not work in such situations. Following the open source principles established by Gazebo and ROS, this platform is completely open, and maintains a simple API for developers and a friendly GUI for end users.

2.2 Models

2.2.1 Models of Wheelchair and Environments

Cycle time for all processes including rendering and dynamics is 1 ms. In order to simulate the actual scene, both static and dynamic characteristics of the real world are modeled. The static characteristics refer to stationary objects such as furniture, doors and walls. Described in the COLLADA format [16], these objects are composed of complex shapes and materials with transparency and texture. Some popular 3D modeling software including Google Sketch Up and 3D Studio Max are used to synthesize them in a same scene.

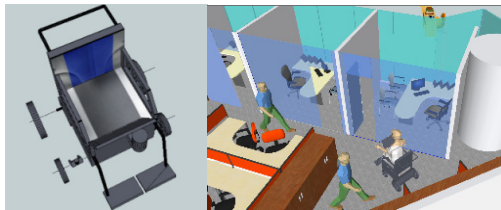


Fig. 4. Model of Wheelchair and Environment

As the dynamic characteristics, random pedestrians are modeled in the scene, and their behavior is roaming with obstacle avoidance. As is shown in Fig.5, the controller generates a polar distribution of obstacles, and after normalization of the distribution, it is regarded as the distribution of the pedestrian moving direction. When the distance to an obstacle is less than a certain value, the pedestrian controller changes the pedestrian moving direction based on this distribution.

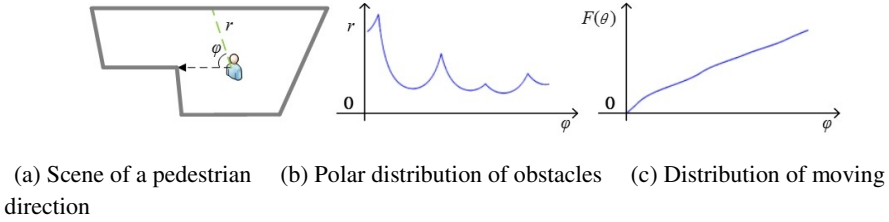


Fig. 5. Operating Principle of the Controller for Pedestrian

2.2.2 Models of Sensors

The real wheelchair mainly contains three sensors which are encoder, LRF, Kinect. In order to simulate the sensors' actual working situation, it's necessary to analyze the principle of sensors and build the error model of the sensors.

Encoder is typically used to in robot speed and position calculations, using the LPP(Lines Per Period) method, which takes the number of pulses per unit time as the speed. Generally speaking, if the assembly error was ignored, the mathematical measuring model is as the following:

$$\hat{\omega} = \frac{2n\pi}{N\rho\Delta T} \stackrel{def}{=} \frac{n}{C\Delta T} \tag{1}$$

Where, ΔT is the measurement cycle, n is the number of pulses in the ΔT , ρ is the transmission ratio between the wheel and encoder, N is encoder line number. Further is:

$$\hat{\omega}_k = \frac{1}{C\Delta T} (\text{floor}(C\theta_k) - \text{floor}(C\theta_{k-1})) \tag{2}$$

Where, ω is the angular speed of the wheel, θ the angle of wheel, floor the rounded down function.

Last formula reflects the measuring principle of the encoder, and the error source caused by discretization.

LRF is similar to sonar sensors and its ranging principle is TOF (Time of Fly), namely by calculate the flight time to measure the distance from the transducer to the obstacles. Since the speed of light is too fast, resulting in large direct measurement error by calculating the flight time, so the current general approach is based on the phase difference to calculate the flight time indirectly.

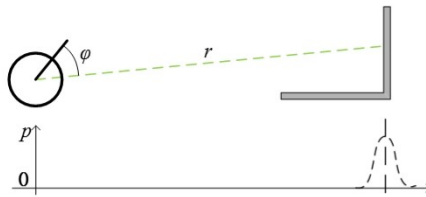


Fig. 6. Principle Diagram of LRF

According to the above analysis, LRF can be simplified to that it emits the rays in the direction φ to measure the distance r to the nearest obstacle, which is shown in Fig.6. Starting angle, end angle and angular resolution of LRF are respectively stood for φ_{\min} , φ_{\max} and $\Delta\varphi$, then the measuring model $(\varphi, \hat{r}), \varphi \in \{\varphi_i | \varphi_i = n\Delta\varphi + \varphi_{\min}, \varphi_i \leq \varphi_{\max}\}$ would satisfy the following :

$$\begin{cases} \hat{r} = r + \delta r \\ r = f(\varphi + \delta\varphi) \end{cases} \tag{3}$$

Where, $f(x)$ is the accurate measuring value of the nearest obstacle in the direction x , which is implemented by the ray algorithm in the simulation platform. $\delta\varphi$ is white noise whose mean is zero and variance is μ_φ . δr is the ranging error, divided into two parts of glint error and white noise, then we have :

$$\begin{cases} \delta r = x + v \\ T\ddot{x}(t) + \dot{x}(t) = \varepsilon(t), \varepsilon \sim N(0, \mu_\varepsilon) \end{cases} \tag{4}$$

Where, x is glint error that satisfies the Gauss-Markov model, v is white noise whose mean is zero and variance is μ_v .

Kinect measuring principle of depth is depicted in the Fig.7, with its mathematical representation described as :

$$\begin{cases} Z_k = \frac{Z_0fb}{fb + Z_0d} \\ X_k = -\frac{Z_k}{f}x_k, \\ Y_k = -\frac{Z_k}{f}y_k \end{cases} \tag{5}$$

Where, (X_k, Y_k, Z_k) is the coordinates of the measured point k , z_0 is the depth of the reference plane, f the focal length of the infrared camera, b the base length, d the observed disparity in image space, and (x_k, y_k) is the origin coordinates of point k in the image plane.

By the geometric relationships:

$$d = \sqrt{x_k^2 + y_k^2} \tag{6}$$

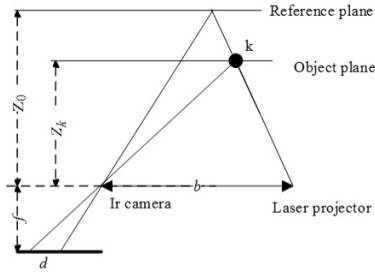


Fig. 7. Principle Diagram of Kinect

To facilitate the analysis, assuming that x_k and y_k both satisfy the normal distribution with the mean zero and they are independent of each other. Then the error propagation model of Kinect is depicted as:

$$\begin{cases} \delta Z_k = -\frac{z_0}{d\eta^2}(x_k \delta x_k + y_k \delta y_k), \eta = 1 + \frac{Z_0 d}{fb} \\ \delta X_k = -\frac{z_0}{fd\eta^2}((x_k - \eta d) \delta x_k + y_k \delta y_k) \\ \delta Y_k = -\frac{z_0}{fd\eta^2}(x_k \delta x_k + (y_k - \eta d) \delta y_k) \end{cases} \quad (7)$$

Where, δx_k and δy_k are the error of x_k and y_k respectively.

3 Training, Assessment and Evaluation

3.1 Driving Training

For users who do not have relevant experience, they need specific training before driving the electric wheelchair. The designed training should meet requirement in real situation, which includes following basic operations of electric wheelchair:

- 1) Driving electric wheelchair for 10m distance in the corridor of 1.5m wide;
- 2) Driving electric wheelchair backward for 2m, docking at specific position, ensure its posture difference with target is less than 0.3m and angle difference is less than 20°.
- 3) Complete 90° right-angled turn while driving electric wheelchair forward.

The three training tasks above cover electric wheelchair operations like start-up, docking, back off, make turns and .etc. The training could be sequential one by one or repeat any tasks which have been completed before. Certification is given once all training tasks completed, with consumed time recorded.

The training could be conducted on simulation platform or real electric wheelchair (e.g. Fig.8). Theoretically, there should be no difference between the two approaches, as long as the training aids on simulation platform ensures same driving experience as real electric wheelchair. In addition, training on simulation platform is lower cost, safer and even could be conducted without professional support.



Fig. 8. Three Training Tasks on simulation platform or real electric wheelchair

3.2 Assessment

The assessment objective is to verify how about the user’s skill of driving a wheelchair. There are no standards for wheelchair driving skills evaluation, therefore we have designed a standard by:

- 1) Consulting 6 wheelchair researchers (with 2yr+ relevant experience) for assessment direction;
- 2) Referring to others relevant research;
- 3) Survey to wheelchair users for common tasks and challenges in their usage of wheelchairs.

The designed assessment standards include two parts: **Task Description** and **Indicators**. The **Task Description** defines assessment scenario and tasks in details, and the **Indicators** quantitatively analyze how well each task is completed.

A. Assessment Tasks

The assessment standards include three tasks, as shown in Table 1.

Table 1. Assessment Tasks of Wheelchair Driving

No.	Tasks	Description
1	Driving in corridor (without obstacle)	Along with a corridor which is 100m long and 2.5m wide, testee drives wheelchair from starting point to destination (should strictly follow designated route).
2	Passing through narrow door	Testee drives wheelchair from the posture parallel with a door which is 1m wide and without obstacles in 2m around it, and pass through it.
3	Driving in narrow space	In a narrow space with furniture (average in 1.5m width), testee drives wheelchair from designated starting point to destination.

Fig.9 shows the examples of three assessment tasks, which are all frequent tasks in testees' daily life, also challenges of wheelchair control. For instance, the users often need to precisely control the wheelchair’s position and posture, such as docking to lift button or furniture. This is exactly the first task - Docking.

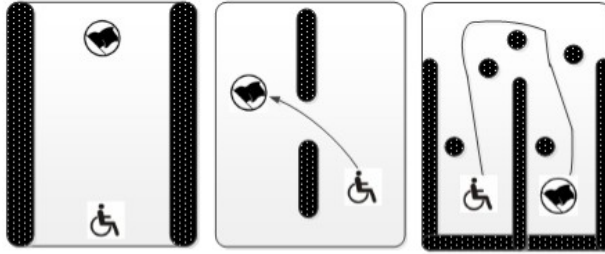


Fig. 9. Three Assessment Tasks

Similar to training, the driving assessment could be conducted on either simulation platform or real wheelchairs. Fig.10 illustrates assessments scenario on simulation platform and real wheelchair under the same indoor environment.



Fig. 10. Examples of Assessment Tasks

4 Experiments and Analysis

4.1 Procedure

21 testees (17 males and 4 females) without electric wheelchair driving experience joined this experiment, age at 20.25 ± 2.14 years old. All testees have good eye-sight and nimble hands, one of them has vehicle driving experience. The testees were equally divided into three groups (A, B, C), for driving training on simulation platform or real electric wheelchair or none. There are three testees having two-year electric wheelchair driving experience, who were named D group as comparison for A, B, C:

- 1) Group A: 7 testees conducted driving training on simulation platform;
- 2) Group B: 7 testees conducted driving training on real wheelchair;
- 3) Group C: 7 testees did not conduct training;
- 4) Group D: 3 testees already with two-year electric wheelchair driving experience did not conduct training.

After training completed, all groups were assessed on simulation platform, for tasks listed in chapter 4.2, and all indicators were calculated.

4.2 Driving Assessment Experiments on Simulation Platform

To quantitatively evaluate user's driving process, this paper proposed indicators as **Time Cost** (t), **Count of Collision** (n_c), **Smoothness** (s)^[5], **Fluency** (f)^[5] and **Driving Trajectory Precision**, etc. The driving assessment results on simulation platform is shown in Fig.11. Driving efficiency of trained group A and B is significantly higher than untrained group C, while no significant difference proven between group A and B. In fact, there is no significant difference among the four groups statistically (lowest $p=0.85^*$).

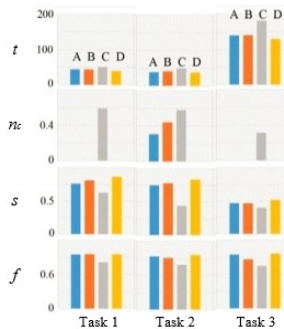


Fig. 11. Driving Assessment Results on Simulation Platform

5 Conclusion

This paper presented a simulator platform of smart wheelchairs for driver training and evaluation, which is integrated with sensors, and 3D models of the wheelchair and world. The software structure is proposed with the analysis of the hardware of smart wheelchairs, followed by a detail modeling for sensors and world. The platform is implemented in Gazebo and ROS. Besides, the driver training and evaluation standards, procedures and experiments of electric wheelchair are proposed in this paper. So in the simulator platform, the user could complete driver training and assessment procedures by himself without nursing staff's company. Experiments show the effectiveness of the proposed simulator platform, and it can be used for driver training and evaluation.

Acknowledgments. This work is partly supported by the National High Technology Research and Development Program of China under grant 2012AA041403, the Natural Science Foundation of China under grant 61175088, and the Research Fund for the Doctoral Program of Higher Education of State Key Laboratory of Robotics and System (HIT) under grant 20100073110018.

References

1. Ding, D., Cooper, R.A.: Electric powered wheelchairs. *IEEE Control Systems* 25(2), 22–34 (2005)
2. Hasdai, A., Jessel, A.S., Weiss, P.L.: Use of a computer simulator for training children with disabilities in the operation of a powered wheelchair. *American Journal of Occupational Therapy* 52(3), 215–220 (1998)
3. Tsui, K.M., Feil-Seifer, D.J., Mataric, M.J., et al.: Performance evaluation methods for assistive robotic technology. In: *Performance Evaluation and Benchmarking of Intelligent Systems*, pp. 41–66. Springer, US (2009)
4. Rebsamen, B., Guan, C., Zhang, H., et al.: A brain controlled wheelchair to navigate in familiar environments. *IEEE Transactions on Neural Systems and Rehabilitation Engineering* 18(6), 590–598 (2010)
5. Li, Q., Chen, W., Wang, J.: Dynamic shared control for human-wheelchair. Cooperation. In: *2011 IEEE International Conference on Robotics and Automation (ICRA)*, pp. 4278–4283. IEEE (2011)
6. Levine, S.P., Bell, D.A., Jaros, L.A., et al.: The NavChair assistive wheelchair navigation system. *IEEE Transactions on Rehabilitation Engineering* 7(4), 443–451 (1999)
7. Simpson, R., LoPresti, E., Hayashi, S., et al.: The smart wheelchair component system. *Journal of Rehabilitation Research and Development* 41(3B), 429–442 (2004)
8. Niniss, H., Nadif, A.: Simulation of the behaviour of a powered wheelchair using virtual reality. In: *3rd International Conference on Disability, Virtual Reality and Associated Technologies*, pp. 9–14 (2000)
9. Lin, C.S., Chang, C.C., Chen, W.L.: Design and application of an interactive wheelchair training system. *Biomedical Engineering: Applications, Basis and Communications* 20(06), 377–385 (2008)
10. Braga, R.A.M., Malheiro, P., Reis, L.P.: Development of a realistic simulator for robotic intelligent wheelchairs in a hospital environment. In: Baltes, J., Lagoudakis, M.G., Naruse, T., Ghidary, S.S. (eds.) *RoboCup 2009*. LNCS, vol. 5949, pp. 23–34. Springer, Heidelberg (2010)
11. Braga, R.A., Petry, M., Reis, L.P., et al.: IntellWheels: modular development platform for intelligent wheelchairs. *Journal of Rehabilitation Research and Development* 48(9), 1061 (2011)
12. Liao, W., Chen, W., Wei, Z., Zhang, W., Wang, J., Li, K.: An Open-Source Development and Simulation Platform for Smart Wheelchairs. In: Lee, J., Lee, M.C., Liu, H., Ryu, J.-H. (eds.) *ICIRA 2013, Part I*. LNCS, vol. 8102, pp. 295–306. Springer, Heidelberg (2013)
13. Wang, Y., Chen, W.: Hybrid map-based navigation for intelligent wheelchair. In: *2011 IEEE International Conference on Robotics and Automation (ICRA)*, pp. 637–642. IEEE (2011)
14. Koenig, N., Howard, A.: Design and use paradigms for gazebo, an open-source multi-robot simulator. In: *2004 IEEE/RSJ Proceedings of the Intelligent Robots and Systems, IROS 2004*, vol. 3, pp. 2149–2154. IEEE (2004)

15. Gazebo, <http://gazebosim.org>
16. Robot Operating System (ROS), <http://www.ros.org/wiki>
17. COLLADA - Digital Asset and FX Exchange Schema, <http://collada.org>
18. Hahnel, D., Burgard, W., Fox, D., et al.: An efficient FastSLAM algorithm for generating maps of large-scale cyclic environments from raw laser range measurements. In: Proceedings of the 2003 IEEE/RSJ International Conference on Intelligent Robots and Systems (IROS 2003), vol. 1, pp. 206–211. IEEE (2003)
19. Wang, Y., Chen, W., Wang, J., et al.: Improved particle filter localization in crowded environments for mobile robots. *Jiqiren (Robot)* 34(5), 596–603 (2012) (in Chinese)

Research of Damage Imaging Algorithm in Plate Based on Signal Magnitude*

Cong Luo¹, Peijiang Li^{1,2}, Xiaojin Zhu^{1,**}, and Fei Deng³

¹ School of Mechatronic Engineering and Automation, Shanghai University, Shanghai, 200072, P.R. China

² School of Information Engineering, Quzhou College of Technology, Zhejiang, 324000, P.R. China

³ School of electronic and Information Engineering, Ningbo University of Technology, Zhejiang, 315211, P.R. China
mgzhuxj@shu.edu.cn

Abstract. Lamb wave damage imaging is one of the hot spots for structural health monitoring (SHM), as for the structural damage location like plate, this paper proposes an ellipse positioning method based on signal magnitude. By this method for the intersection of more groups of elliptical trajectories through defects, the intersection point is the defect; and defect signal amplitude is larger, the higher the image pixels. Through the arrangement of sensor network on Al plate, excite and receive Lamb wave. And the difference between the damage signal and reference signal is damage-scattered signal. Then to solve the envelope of signal with Hilbert transforms which can be used to locate the damage. Experimental results show that, error of the defects positioning algorithm in aluminum plate is small, imaging result is intuitive and clear. And the experimental data verified the effectiveness of the algorithm.

Keywords: Structural health monitoring, Lamb wave, Ellipse positioning, Signal amplitude imaging.

1 Introduction

Structural health monitoring (SHM) technology is a process for engineering structure damage detection and health characteristics analysis[1,2]. Lamb wave used to detect the health of structure is one of the most methods used in the SHM technology[3]. Its principle is: When the Lamb wave propagation in structures, if there are any structural damage or defects such as cracks, holes which will affect the spread of the Lamb wave; and cause the phase change of direction[4]. Using health signals when structure

* This research is supported by the National Nature Science Foundation of China (No.11202137, No.51175319), and key program of Shanghai Municipal Education Commission (No.13ZZ075).

** Corresponding author.

is nondestructive as the reference signal, then compare the signal when the plate is defective with reference signal, so you can highlight the defect signal; and then use a variety of engineering algorithm to locate and identify defect or damage[5]. At present there are many kinds of structural damage detection methods, four kinds of damage location methods commonly used: four arc positioning method[6], ellipse positioning method[7], hyperbolic positioning method[8] and signal amplitude method[9]. The signal amplitude method is an imaging technology based on the amplitude of signal. When collected signal containing defect information, the greater the amplitude difference between the collected signals and the original signal, the more obvious defect features[9]. But when the guided wave spread in the whole plate, the aliasing of the echo of the boundary causes the defect signal is submerged, so it is easy to produce misjudgment[10]. Ellipse positioning method is simple and practical, it can determine the possible defect area only according to the change of signal amplitude, then probably deduced defect imaging area.

This study combines the advantages of the signal amplitude method and ellipse positioning method, proposed an ellipse localization algorithm based on signal amplitude imaging. Using the sensor array to test the aluminum sheet, the algorithm displays the defects in the plate in form of image intuitively. Besides, the positioning error of the algorithm is smaller.

2 Principle of Positioning Algorithm

2.1 Analysis of Signal Propagation

Detection model diagram is shown in Figure 1. The circular area in figure represents piezoelectric sensor, which not only can be used as load excitation signal drives, but also can be used as sensors which accept guided wave signals, and irregular area in figure represents damage or defects. Choose one of the piezoelectric elements as drive, then exerted an excitation signal. The diagnostic wave occurs on the surface of the structure through the drive, that is guided wave begin to spread. There are many different acoustic wave propagation paths in the structure [11]. Guided wave propagation will produce the change of direction and phase, etc. Real lines shown in the figure are signal paths without damage, the wave packet contains no damage information; dotted lines shown in the figure are signal paths which arrive sensor after damage reflection. For the damaged signal, the differential signal of before and after

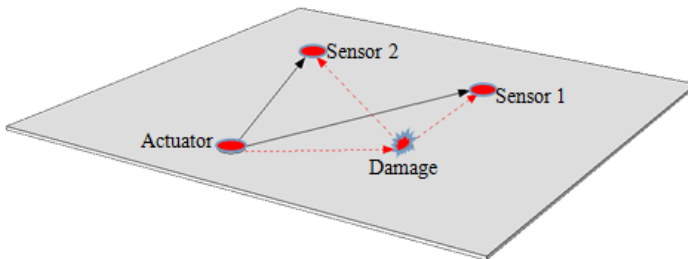


Fig. 1. Path of signal propagation

the damage can highlight the characteristics of them, so as to remove extraneous signals; then through the analysis of the corresponding signal processing, estimates about injury come out by using the relationship among damage reflection echo signal, speed and time. Therefore, damage propagation path can be defined as the processes that drive generate elastic waves which spread in the plate, and arrive at the sensor after damage reflects directly.

2.2 Ellipse Positioning Technology

When detect the plate structure use Lamb waves, the received signals are composed of a plurality of echo. As shown in Fig.1, Actuator is actuator while Sensor1 is sensor. Assuming that the echo is caused by defects, Damage in Fig.1, and the path of signal propagation, L which is AD + DS₁, can be expressed as:

$$L = L_{AD} + L_{DS1} = c_g \times t_{A-D-S1} \tag{1}$$

Where c_g is the group velocity of Lamb wave, t_{A-D-S1} is the time that diagnostic wave from the actuator to damage, and then to the sensor, the time determine the value of L in Eq.1. The group velocity of Lamb wave in aluminum plate can be obtained by solving the Lamb wave equation[12]. After the value of L is determined, all conditions meet the definition of an ellipse. If the position of actuator and sensor located are used as the two foci of the ellipse respectively, the coordinate of damage is on this elliptical track. However, there is no way to determine the coordinate of damage with only one ellipse. So add at least one set of sensors, and draw another ellipse based on the relationship of the signal, then the intersection of this two ellipses is the coordinate of damage. But two ellipses have multiple intersections through geometric analysis, so it can't locate the coordinate of damage precisely.

As shown in Fig.2, four group sensor signals of experiment were used in this paper, and four elliptical tracks which via the coordinate of damage were drawn. It can be seen from the diagram that region where damaged can be located after the number of the ellipse via the damage increased. And the more group of sensors, the higher positioning accuracy.

2.3 Imaging of Signal Magnitude

Assume that the signals captured via an actuator-sensor pair before and after the presence of damage in a structure are $f^0(t)$ and $f(t)$, respectively, so the damaged scattered wave can be expressed as in Fq.2.

$$r(t) = f(t) - f^0(t) \tag{2}$$

Assuming that an active sensor network which consisted with N piezoelectric elements, the group velocity of the Lamb wave for identification is c_g , the coordinate

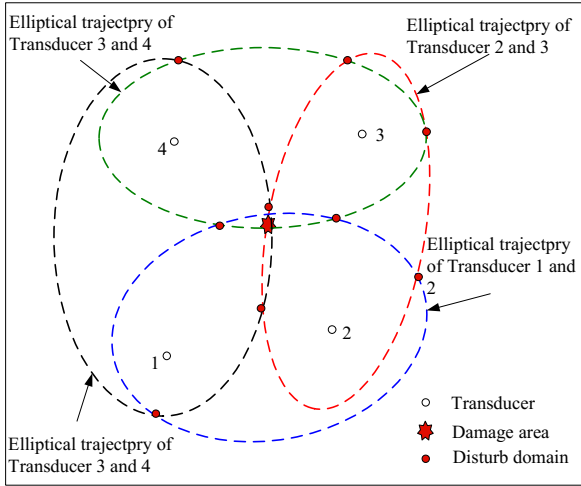


Fig. 2. Network of sensors

of the center of damage is (x, y) , then the time, t , for the diagnostic wave to travel from the i^{th} actuator (x_i, y_i) to the damage (x, y) , and then to the j^{th} sensor (x_j, y_j) can be expressed as in Eq.3:

$$t = \frac{\sqrt{(x-x_i)^2 + (y-y_i)^2} + \sqrt{(x-x_j)^2 + (y-y_j)^2}}{c_g} \tag{3}$$

where $(i, j = 1, 2, \dots, N, i \neq j)$.

In the imaging method with signal magnitude, the value at pixel (x, y) is calibrated by $r(t)$. That is to say, this value is a function about the x, y and t , as shown in Eq.3. Geometrically, pixel defined by Eq.3 fall on the ellipse whose two foci are the actuator and sensor. All pixels which produce the same arrival time will locate on one ellipse. There are many elliptical trajectories like this which is calibrated by $r(t)$, and the area with the highest value is possible damage location.

For the sensor network of N piezoelectric elements, there are $N_p = N(N-1)$ actuator-sensor paths totally. Then the value, $I(x, y)$, at each pixel (x, y) of the image can be defined as:

$$I(x, y) = \frac{1}{N_p} \sum_{k=1}^{N_p} r_k(t, x, y) \tag{4}$$

where $(k = 1, 2, \dots, N_p); (i, j = 1, 2, \dots, N, i \neq j)$, $r_k(t, x, y)$ represents the damage-scattered wave signal acquired by the k^{th} actuator-sensor path. Eq.4

indicate the polymerization of images created by all the available actuator-sensor paths, which is one kind of image fusion algorithms for obtaining a resulting image. Through changing (x, y) in Eq.4, the values of all pixels within the inspection area can be set up. The value will become obvious when damage exists at a specific pixel. The location of damage will be highlighted by the pixels with maximum values in the image after image fusion.

3 Experiment Study

3.1 Equipment and Subject of Experiment

Equipment is shown in Fig.3. First, to generate the excitation signal by the function generator, the signal is amplified, filtered by the RF power amplifier before it is exerted on transmission sensor, actuator. And actuator will produce Lamb wave which received by the receiving sensor after a certain distance spread in the plate, then the wave will be processed by a computer via the Digital Phosphor Oscilloscope. The dimension of Experimental aluminum plate is $700\text{mm} \times 500\text{mm} \times 3\text{mm}$. The location of actuator-sensor and damage is shown in Fig.4, the damage is the hole of 10mm. Their coordinates are (200,130), (470,120), (480,380), (210,390) and (370,250), the unit of coordinates are mm while the coordinate origin is lower left corner of aluminum plate. Based on the forward and inverse piezoelectric effect of piezoelectric, a series of actuator-sensor PZT array were arranged in the detection region of aluminum plate, and then to extract a damage-scattered signal from a plurality of angles in the manner of scanning which to select a piezoelectric as actuator one by one and others are selected as sensors.

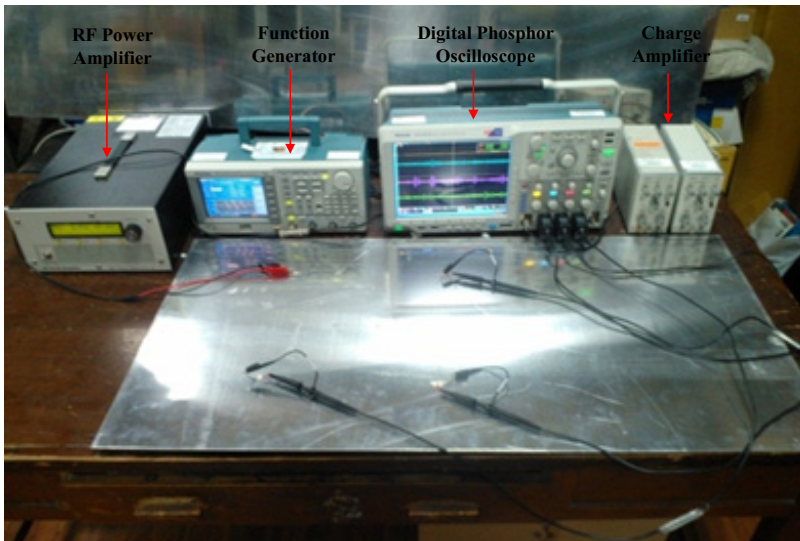


Fig. 3. Equipment of experiment

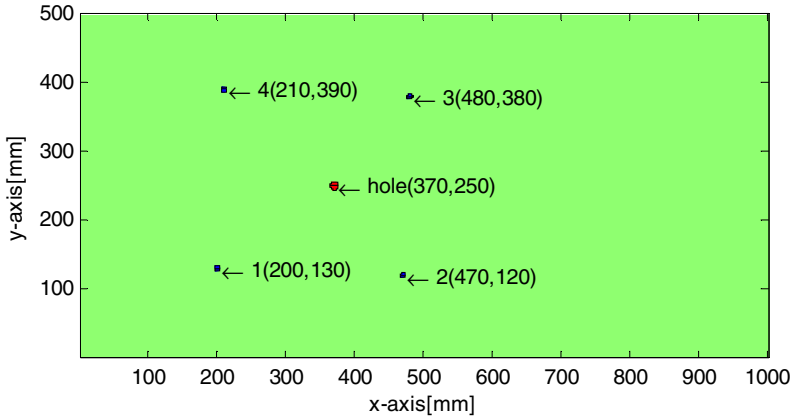


Fig. 4. Subject of experiment

3.2 Excitation Signal

Considering the analysis of Lamb wave propagation is complex, and also need to determine the arrival time of the wave packet, so the excitation signal applied to the actuator is a sine wave signal modulated by hanning window, as shown in Fq.5:

$$u(t) = A \left[\frac{1}{2} - \frac{1}{2} \cos\left(\frac{2\pi f_c}{n} t\right) \right] \sin(2\pi f_c t) \tag{5}$$

where A is the magnitude of signal, f_c is the center frequency of signal, and n is the number of wave peaks. The selected A of the signal is 10V, f_c is 160 kHz, and n is 5. The excitation waveform in time and frequency domain is shown in Fig.5.

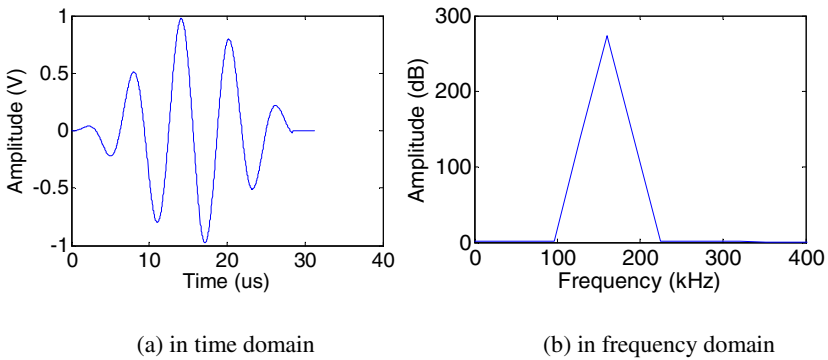


Fig. 5. The excitation waveform with five peaks and 160kHz central frequency: (a) in time domain and (b) in frequency domain

3.3 Analysis of Experimental Results

As shown in Table 1, six groups of signals were collected in the experiment. When PZT1 is used as actuator, PZT2, PZT3 and PZT4 are used as sensors; when PZT2 is used as actuator, PZT3 and PZT4 are used as sensors; and when PZT3 is used as actuator, PZT4 is used as sensors. Seen the distribution of sensors from Fig.2, when PZT1 is used as actuator, PZT3 is used as sensor, and PZT2 is used as actuator, PZT3 is used as sensor, the hole is near to the connection of them. In this situation, the accuracy of damage localization will be lower, so the hole must keep away from the connection of them. Through the above analysis, Pair 1-4 of six groups is useful in this experiment.

Table 1. Groups of the PZT array

Pair	Actuators	Sensors
Pair1	PZT1	PZT2
Pair2	PZT1	PZT4
Pair3	PZT2	PZT3
Pair4	PZT3	PZT4
Pair5	PZT1	PZT3
Pair6	PZT2	PZT4

The excitation signal, as shown in Fig.5(a) is applied on the actuator continuously, a typical guided wave signal is received on the sensor environment, as shown in Fig.6. The signal received by sensor have too much noise in Fig.6, so first of all, the signal must be processed using mathematical methods, such as to filter signal with wavelet transform, signal normalization, to solve the envelope of signal with Hilbert transforms and so on. According to the principle of Fig.2, four group signals were extracted by PZT 1-4 in experiment.

As discussed in Eq.2, damage-scattered signal was equal to the difference between the after the signal which is processed and the reference signal. Seen from Fig.7, they are the four damage-scattered signals. As shown in Fig.6, the whole response can be divided into two parts clearly: waves with damage and the boundary reflected echo. The boundary reflected echo is the interference wave, so it must be filtered out. As shown in Fig.8, after filtering out the interface wave, the remains are waves with damage.

After scattered wave is extracted from Lamb wave, to solve the envelope of signal with Hilbert transforms, as shown in Fig.8. As discussed in Eq.4, the result of imaging with the envelope of damage-scattered wave can show the damage in aluminum plate. The imaging result of each actuator-sensor are shown in Fig.9, the damage is on the elliptical arc with highest pixel. Seen from Fig.9, the ellipse of each pair drawn in this experiment via the location of the hole; because the excitation signal have five peaks in time domain, the final image result will be interfered. In order to improve the accuracy of damage localization, the method in this experiment is using four ellipses which via damage with groups of actuator-sensor signal. The fusion of four imaging results is the final damage imaging of aluminum plate, as shown in Fig.10.

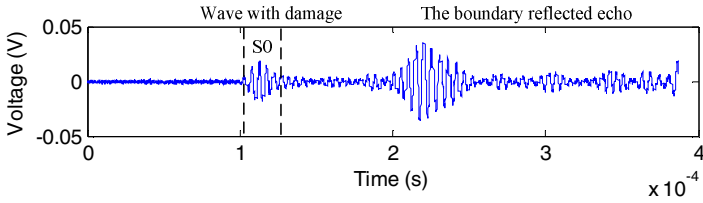


Fig. 6. Typical signal collected by PZT

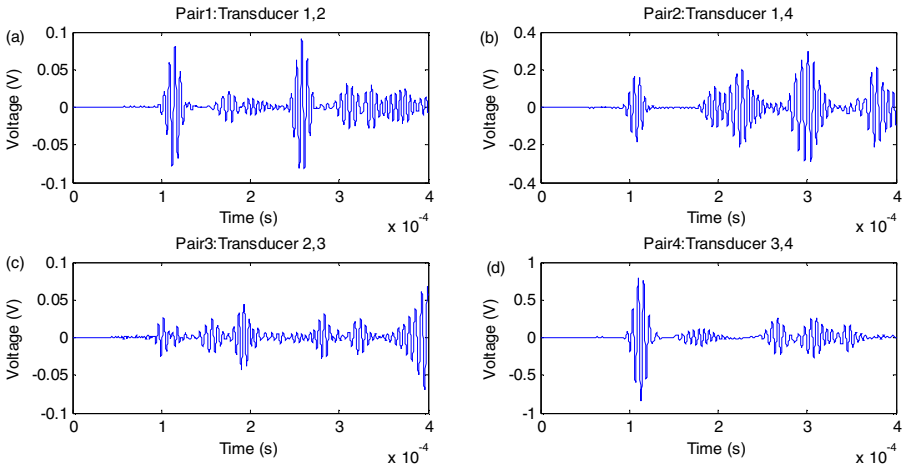


Fig. 7. Scattered waves sensed by PZT pair 1-4

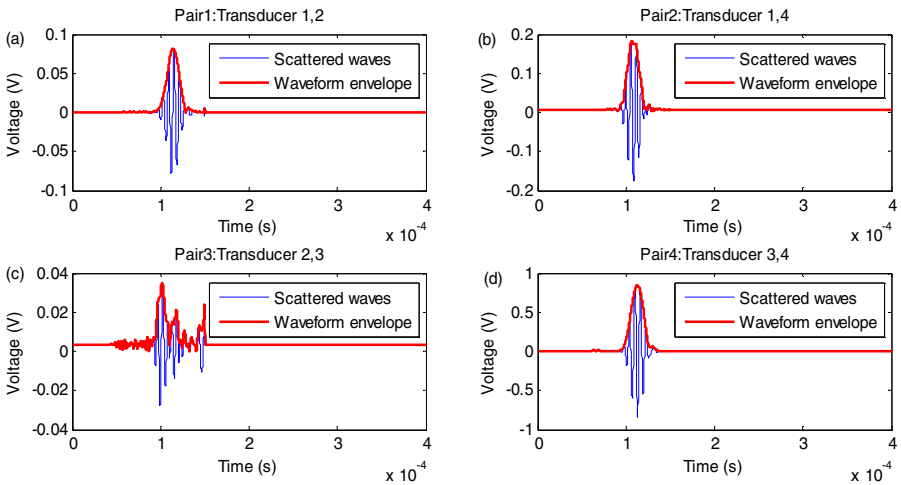


Fig. 8. Separated scattered waves by PZT pair 1-4

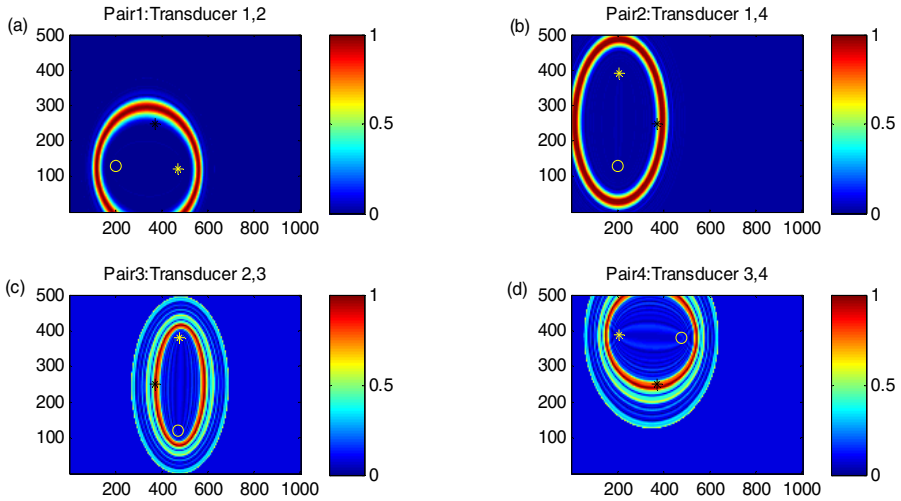


Fig. 9. The damage imaging results for each PZT pair

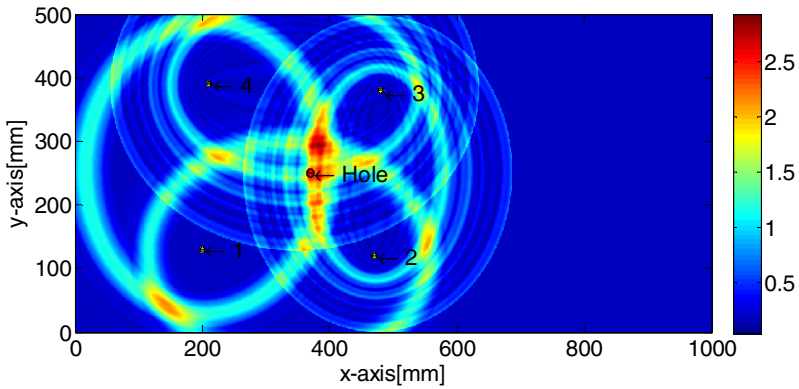


Fig. 10. Damage imaging result of sensor network

4 Conclusion

This paper proposed an ellipse positioning algorithm based on the amplitude of signal, realize the reconstruction of plate damage imaging, which is the expansion and improvement of signal amplitude imaging and ellipse localization algorithm. Experimental results show that, compared with the traditional Ellipse positioning algorithm and amplitude imaging, this method not only maintain the accuracy and fast characteristic of the geometric positioning method, but also can characterize the region and the extent of damage clearly and accurately. It is conducive to promoting ellipse positioning method for study of large-size damage and the combination of

geometric method and image method. Besides, it is easy to implement, not need additional equipment and resources, and less demanding on equipment for data computing and processing. At the same time, it lays a foundation for further analysis of the use of Lamb wave to detect more complex damage in plate.

Acknowledgments. This research is supported by the National Nature Science Foundation of China (No.11202137, No.51175319), and key program of Shanghai Municipal Education Commission (No.13ZZ075), Shanghai University “11th Five-Year Plan” 211 Construction Project and Shanghai Key Laboratory of Power Station Automation Technology.

References

1. Magalhães, F., Cunha, A., Caetano, E.: Vibration based structural health monitoring of an arch bridge: from automated OMA to damage detection. *Mechanical Systems and Signal Processing* 28, 212–228 (2012)
2. Liang, Z.B., Sheng, M.L., Hu, Y.R.: Multi-Stage Health Diagnosis for Concrete Cable-Stayed Bridge Based on EWMA Control Chart. *Applied Mechanics and Materials* 246, 903–907 (2013)
3. El Guerjouma, R., Bentahar, M., Thomas, J.H., et al.: Non Destructive Evaluation and Structural Health Monitoring of structural materials by means of nonlinear acoustics and acoustic emission. *Acoustics 2012 Nantes* (2012)
4. Karpenko, O.Y., Haq, M., Khomenko, A., et al.: Lamb Wave Based Monitoring of Delamination Growth in Mode I and Mode II Fracture Tests. In: *Fracture and Fatigue*, vol. 7, pp. 33–43. Springer International Publishing (2014)
5. Huang, P.Y., Kurasch, S., Alden, J.S., et al.: Imaging atomic rearrangements in two-dimensional silica glass: Watching silica’s dance. *Science* 342(6155), 224–227 (2013)
6. Shi, Z.S., Li, R., Wang, H.Y.: Research on Maneuvering Trajectories Optimization in Bearings-Only Localization for Single Observer. *Advanced Materials Research* 433, 5946–5950 (2012)
7. Oyerman, A., Amar, A.: An extended spherical-intersection method for acoustic sensor network localization with unknown propagation speed. In: *2012 IEEE 27th Convention of Electrical & Electronics Engineers in Israel (IEEEI)*, pp. 1–4. IEEE (2012)
8. Hu, N., Cai, Y., Zhu, G., et al.: Characterization of damage size in metallic plates using Lamb waves. *Structural Health Monitoring* 11(2), 125–137 (2012)
9. Ben, B.S., Yang, S.H., Ratnam, C., et al.: Ultrasonic based structural damage detection using combined finite element and model Lamb wave propagation parameters in composite materials. *The International Journal of Advanced Manufacturing Technology* 67(5-8), 1847–1856 (2013)
10. Su, Z., Ye, L., Lu, Y.: Guided Lamb waves for identification of damage in composite structures: A review. *Journal of sound and vibration* 295(3), 753–780 (2006)
11. Yan, C., Li, R., Li, H., et al.: Research on damage detection of large generator stator insulation using guided wave. In: *2013 IEEE Conference on Electrical Insulation and Dielectric Phenomena (CEIDP)*, pp. 1153–1156. IEEE (2013)
12. Tan, Y., Cai, L., Peng, B., et al.: An Investigation of Structural Damage Location Based on Ultrasonic Excitation-Fiber Bragg Grating Detection. *Advances in Acoustics and Vibration* (2013)

DES Algorithm Realization in Asynchronous Circuit Using Four-Phase Bundled-Data

Jingjing Liu, Guanghai Chen^{*}, Shiwei Ma, Weimin Zeng, and Mingyu Wang

School of Mechatronic Engineering & Automation, Shanghai Key Laboratory of Power Station
Automation Technology, Shanghai University, NO.149, Yanchang Rd.
200072 Shanghai, China
chghua@shu.edu.cn

Abstract. In order to reduce the power consumption of the DES algorithm circuit, this paper designs an asynchronous pipeline based on the four-phase handshake protocol, and realizes the pipeline in the round to satisfy the several rounds operations. The design has been implemented by free Balsa or non-free Tangram language and fabricated with 0.18 μm CMOS process. Both the asynchronous design and its synchronous are embedded into the contactless smart card chip. Compared with the synchronous circuit, the result shows that the power consumption is reduced by 40%, and the average current consumption of DES asynchronous circuits is cut down from 2.9 mA to 0.5mA.

Keywords: symmetric algorithm, synchronous circuit, asynchronous circuit, power.

1 Introduction

Symmetric ciphers are sometimes called traditional cryptographic algorithms, the encryption key can be derived from the decryption key, and vice versa. In most symmetric algorithms, such as DES (Data Encryption Standard) algorithm, the encryption and decryption keys are the same. The hardware implementation of the DES algorithm is usually used the synchronous circuit, which is based on global clock synchronization. All the sub-circuits communicate normally with the circuit modules by the sync pulse. Currently more than 90% of the circuits are synchronous, and a variety of commercial electronic design automation software basically supports synchronous circuits. But Asynchronous circuit does not have clock synchronization, and its basic principle is to "request", "response" signal for handshake mechanism to establish normal communication between the circuit blocks.

First of all, the principle of DES symmetric algorithm is explained, and then the protocols of asynchronous circuits are described in detail. Pros and cons of synchronous and asynchronous circuits are also compared. Finally, this paper uses four-phase asynchronous circuits in bundled data protocol to achieve DES algorithm.

^{*} Corresponding author.

After achieving these typical symmetric DES algorithms, it is clear that asynchronous circuits have self-evident advantages in term of power consumption and operational speed upon synchronous circuits.

2 DES Algorithm

DES algorithm was developed by IBM in 1975, two years later, it was adopted as a standard. To achieve the objective of the encryption algorithm, the following four points must be taken into consideration:

- 1) High quality data leakage is protected.
- 2) Due to its high complexity, cracking cost is large.
- 3) The security of DES algorithm only depends on encryption key.
- 4) To achieve economical benefits and operate efficient, DES algorithm is suitable for a variety of different applications.

At present in China, DES algorithm is widely used in the fields of POS, ATM, magnetic smart cards (IC card), gas stations, highway toll stations, etc., In order to achieve confidentiality between smart card and the reader, DES algorithm is chosen.

The approach to DES algorithm has three parameters: Key, Data and Mode. Key is 64bits, it is the work key of DES algorithm. Encrypted and Decrypted Data is also 64bits, Mode is the work way of DES algorithm, either encryption or decryption.

The plaintext block M is replaced by m_0 through an initial permutation IP , and $m_0=(L_0,R_0)$, L_0 and R_0 both are 32bits.As shown in Fig.1 the whole process is completed after 16 rounds, and the middle process is mix and mash process.

In each round, key is shifted to 1 bit, and then selects 48bits from 56bits. Replacement will be extended by an extension of the right half of the data into 48bits and restoration by an XOR operation into a new 32-bit data at the time of its

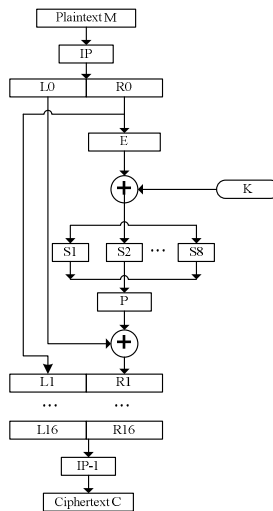


Fig. 1. DES algorithm principle

replacement. This four-step operation constitutes a function f . Then, through another XOR operation, the output data of function f with the remaining data yield a new result, and also original right half is shifted to left part. This operation is repeated 16 times to realize DES algorithm.

DES Encryption and decryption are applied by the same algorithm. The only difference is the order of the key. In DES encryption order key used is $K_1, K_2, K_3 \dots K_{16}$. While in DES decryption, the key order is $K_{16}, K_{15}, K_{14} \dots K_1$.

3 Design Principle of Asynchronous Circuit

Asynchronous circuits can be traced back from mid 1950s^[2], in late 1990s, educational institutions have research on it, and industry launched a chip using asynchronous circuit design for various real world applications, such as mentioned in [3], in 1998, the company of Philips successfully developed a series of 80C51 microcontroller-based commercial baseband chip debut.

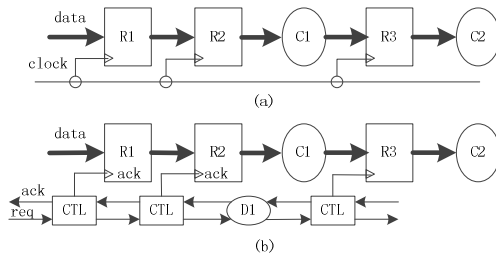


Fig. 2. (a)synchronous circuit; (b)asynchronous circuit

As shown in Fig.2, handshake signals (Req and Ack) between adjacent register are used to replace the clock of synchronization circuit, which must be complied with certain handshake protocol. In order to better understand the mechanism of asynchronous circuits, the way of original architecture design is abandoned, and the applications and operation of asynchronous circuits are considered.

In asynchronous circuits design, it must grasp the hand signals and data signals as a whole, treated as a channel or a link. The data stored in the register as a token, and the value of the data is treated as a tag of this token. In the Fig.2, exchanging of data will be regarded as the token stored in the register is passed into a combinational logic circuit. Combinational logic is transparent to the handshake signal, and has no effect on the handshake signal. It is only the input channel used for token processing, after processing it, and then the token is sent to the output channel.

3.1 The Basic Unit of Asynchronous Circuits

In synchronous circuits, the clock signal used to indicate a certain point in time is stable and correct. Signal can be stable between synchronous clocks, has the same changes with the corresponding circuit signal, and does not affect the performance of

the synchronous circuit. Unlike the synchronous circuit, asynchronous circuits do not have the clock synchronization. In many cases, request value of the signal is maintained, and the conflict between the signals is avoided.

All of the circuits are nearly composed of different basic gates or units (including the feedback loop). If the output of one gate unit is changed, the output of the other gate units will be changed accordingly. But in the actual circuit design, due to lack of synchronous clock, asynchronous circuit should keep the original values as much as possible. Under the certain conditions, the base cell gate of asynchronous circuit with value hold function is required, thus the control signal of asynchronous circuits can be transmitted accurately.

Comparison of AND-OR gates in synchronous circuit shows: if the output of OR gate is 0, only both the inputs are changed from 1 to 0. If the output of OR gate is 1, it is difficult to assume either single input is converted from 0 to 1 or both inputs are converted from 0 to 1. From the output, the input can be determined. OR gate responds when all inputs are 0, while AND gate responds when all inputs are 1.

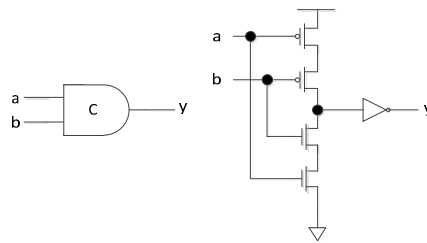


Fig. 3. Muller C-element: its symbol and circuit

Unit circuit in asynchronous circuit responds all inputs into 0 or 1 at the same time. Fig. 3 is a Muller C-element, a good state maintaining unit. It can be seen from Table 1, when the Muller C-element inputs are 0, the output is also 0; When the inputs are 1, its output is also 1, output is unchanged when different input combinations are applied. This means that when Muller C element output in asynchronous circuit is changed from 1 to 0, its inputs are 0. When output is changed from 0 to 1, its inputs are also 1. Extending the feature to all the asynchronous circuit relies on the handshake mechanism, it's clear that whenever output is changed from one state to the other, its inputs are also changed, without un-certainty states in the middle, and the important role of Muller C-element in asynchronous circuits is shown in Table 1.

Table 1. Muller C-element truth table

a	b	y
0	0	0
0	1	Cost reserved
1	0	Cost reserved
1	1	1

3.2 Agreement of Asynchronous Circuits

Asynchronous circuit protocols can be divided into two protocols, bundled-data protocol and dual protocol [4]. If handshake signal is introduced in it, no matter it's rising or falling edge, then protocol is divided into four-phase and two-phase handshake protocol. Since these handshake protocols determine the realization of asynchronous circuits, in DES asynchronous circuits, only four-phase bundled data protocol is used. So only four-phase bundled data protocol is described.

In Fig.4 (a), the black dot represents that the data sender is the active part, Active part is the master, and decides to communicate. Bundled data refer to the data signal using normal Boolean algebra, and are independent from the response and request signals.

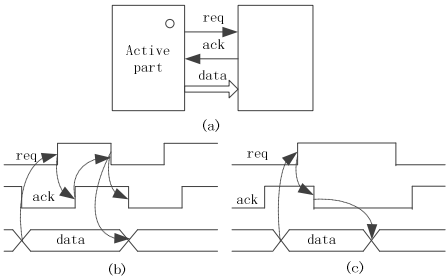


Fig. 4. (a) bundled-data channel; (b) four-phase bundled-data protocol; (c) two-phase bundled-data protocol;

In Fig.4 (b), the request and response signals also use Boolean algebra to encode the control signal. Four-phase refers to the number of data transceiver actions in the process of communication:

- 1) The sender sends data when the request signal is set high
- 2) The receiver accepts the data, and sets the response signal high;
- 3) The sender will request to set signal low (The transmitted data cannot be guaranteed to be correct at this time).
- 4) The receiver will answer signal is set low (At this point the sender can initiate a data transfer).

Four-phase bundled data protocol is equivalent to a handshake agreement, it has too much zero transition state to cause unnecessary processing time, and consumes extra power. In Fig.4(c), the two-phase protocol can overcome the shortcomings of four phase protocol. In the two-phase protocol, the request and response signal indicate the edge of the transfer, unlike the four phase protocol which does not distinguish between from 1 to 0 and from 0 to 1, as long as there is a jump behavior, it means there are events (request and response). Under the ideal conditions, the two-phase protocol circuit is faster than the four-phase protocol circuit, but the control circuit is more complex, and it is difficult to make absolute judgment which one is more efficient. The four-phase and two-phase protocols have been established in the data sender that the data transfer is initiated by the sender, which is called as push

channel. Similarly, if the data transmission is initiated by the data terminal (send request signal), it will be called as pull channel, then the correct transmission of data is confirmed by the response signal of the sender to the receiver. Then the push-channel and four-phase bundled data protocol are used in this paper.

3.3 Comparison of Synchronous and Asynchronous Circuits

1) Avoid the clock skew.

Due to the different transmission paths of clock tree, the clock phase difference is faced in the synchronous circuit. The phase difference of clock needs to be processed by static timing analysis tool and automatic layout tool, while it is not necessary in asynchronous circuits.

2) Low power consumption.

Since the synchronous clock is used in synchronous circuit, even the clock is not required in the module, which is also flipped, and consumes extra power. While the load of clock tree in synchronous circuit is very large, so a great drive capability of the clock tree is needed, and extra energy consumption will be caused. These problems are easily avoided in the asynchronous circuits.

3) Better electromagnetic compatibility.

Though the edge of the clock is to synchronize the circuit, at the clock edge, the transistor will be turned on at the same time. The high harmonics electromagnetic radiations in this clock frequency are caused. Since the synchronization of asynchronous circuits, the spectrum distribution of asynchronous circuit is an average, and is helpful for application of asynchronous circuits in the wireless radio frequency communication.

4) Module reuse is better.

After designing a module in synchronous circuit, the module must be run at a given frequency of circuit system. When this module is applied to other higher frequency of circuit system, there are two behaviors, one is to use multiple clock domains in the new circuit system; other is to design the modules to fit the higher rate. The asynchronous circuit does not have such situation. It only requires improvement in the performance of the most active part of the module. Modification of module interface is not required because the mechanism of asynchronous circuits determines that it is "on demand" operation.

Asynchronous circuits also have some shortcomings. For example, the support for automation circuit design software is still very inadequate. Due to lack of global clock synchronization, when one of these channels is clogged, leads deadlock of entire circuit easily. Asynchronous circuit simulation and testing tools also needed to be improved.

4 Implementation of Asynchronous Circuits in DES Algorithm

Because of the lack of support for commercial circuit software in asynchronous circuits, the Manchester University UK developed integrated tools using Balsa

language to design DES asynchronous circuits. Based on Balsa language, asynchronous circuit description is compiled into protocol elements, and has the appropriate interface with the commercial circuit software.

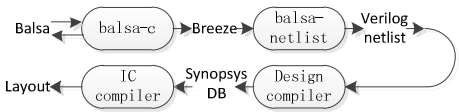


Fig. 5. The design flow for DES asynchronous circuit

It can be seen from Fig.5, the Balsa language is used to describe the DES algorithm, and then balsa-c commands are used to generate an intermediate file namely Breeze. The asynchronous circuit handshake protocol is depicted in this file, which can be determined by the bundled data protocol with four-phase or other asynchronous circuits protocol. The balsa-netlist command is used to develop the netlist with verilog language and back-end design of synchronization circuit. For example, production of chip technology library and Design Compiler tools together, SMIC 0.18um library is used to synthesize the protocol, so gate-level netlist is generated. Finally layout is generated by using automatic placement and routing.

IP transformation of DES algorithm principle is as under:

```

-- IP procedure
-- internal channel
import [balsa.types.basic]
type dword is 64bits
type word is 32bits
procedure IP (input data_in:dword; output data_l:word; output data_r:word) is
variable x_in : dword
variable x1, x2 : word
variable b0,b1, ..., b62, b63 : bit
channel chan1, chan2: dword
begin
loop
    data_in -> x_in;    -- Input communication
    b0:=(data_in as array 64 of bit)[58];
    b1:=(data_in as array 64 of bit)[50];
    ...
    b62:=(data_in as array 64 of bit)[15];
    b63:=(data_in as array 64 of bit)[7];
    x:={b0,b1,...,b62,b63};
    x1:=(x as array 32 of bit)[0:31];
    x2:=(x as array 32 of bit)[32:64];
    data_l <- x1 || data_r <- x2 -- Output communication
end
end

```

In this Program, "-" indicates annotation, and "..." indicates omitted, as IP transformation of DES algorithm is converted according to a certain regularity, it needs to write 64 syntax lines at a 64-bits, program code is too long, so stopped here, but it is not omitted in the actual application.

5 Analysis and Results Comparison

Because the DES algorithm in synchronous and asynchronous circuit is implemented as two internal modules in entire non-contact smart card, it cannot measure the computing time of DES algorithm directly. So the non-contact communication interface (ISO/IEC 14443 TYPEA Protocol [6]) is measured to get the operation time. Then the speed of two arithmetic operations are compared, from sending DES algorithm configuration instructions until receiving the interval computation time of DES algorithm from the non-contact smart card. As shown in Fig.6

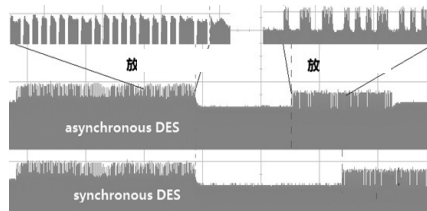


Fig. 6. Calculation time comparison between asynchronous and synchronous DES design

During power consumption analysis, using the DES synchronous and asynchronous circuits netlist generated by Synopsys DB document for gate-level simulation, and generates a waveform file, the waveform files can be read by Synopsys PTXT tool, which compares the power consumption analysis. As seen from Table 2 of this paper using asynchronous circuits to achieve significantly low power consumption, the average consumption reduction is about 40%, the peak power consumption reduction is 65%, running time is faster up to 30%, but the chip area is almost increased 20%.

Table 2. The comparison of DES synchronous circuit and DES asynchronous circuit

DES	Synchronous clock	Asynchronous clock	Philips Research ^[7]
Design language	Verilog	Balsa	Tangram
Computing time	5.77ms(3.39MHz)	3.91ms	N/A
AVG power	1.48mw (1.8V)	0.897mw (1.8V)	1.25μs and 12nJ (3.3V)
Peak power	6.77mw (1.8V)	2.15mw (1.8V)	N/A
Area(Gate)	5627	6777	3250

EEPROM technology library of SMIC 0.18um with four metal layers and polycrystalline is used. Area in Table 2 represents results that comprehensive area is divided by standard cell area of two-input NAND gate which is also called equivalent cell Gates. In this paper, DES asynchronous circuits can be implemented by free Balsa or non-free Tangram language, while Philips Research^[6] achieved only by free Balsa language (employing a five-metal 0.35um process). The average current consumption of DES asynchronous circuits is cut down from 2.9 mA to 0.5mA, but the effective gate number nearly has been doubled.

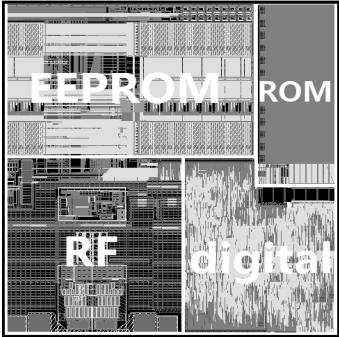


Fig. 7. The layout of the contactless smart card chip

Non-contact smart card chip photographs are showed in Fig.7, including the binding antenna RF modules, 2k byte EEPROM, 8-bit MCU and digital portions of synchronous and asynchronous DES module with size 1.2mmX1.5mm.

6 Conclusion

In order to reduce the power consumption of the DES algorithm circuit, an asynchronous pipeline based on the four-phase handshake protocol is designed in the paper, and the pipeline in the round is realized to satisfy the several rounds operations. The design has an advantage in power and speed consumption (including peak power and average power), which are very advisable for requirements in chip designing. Although the IC area will be increased, power consumption is reduced by 40%, and the average current consumption of DES asynchronous circuits is cut down from 2.9 mA to 0.5mA. Moreover, the area percentage of logic circuits in the entire chip including ROM, RAM and other analog circuits is not considerable large, so the increment in the logic circuit area has little effect on the entire chip area.

Acknowledgments. This work was financially supported by the Shanghai Science and Technology Foundation (13510500400) and the Shanghai Educational Commission Foundation (12ZZ083).

References

1. FIPS PUB 46-3, Data Encryption Standard (DES), January 15, 1977. Reaffirmed (1999)
2. Muller, D.E., Bartky, W.S.: A theory of asynchronous circuits. In: Proceedings of an International Symposium on the Theory of Switching, Part I, Cambridge, April 1957, pp. 204–243. Harvard University Press (1959), The annals of the computation laboratory of Harvard University
3. Nowick, S.M., Josephs, M.B., van Berkel, C.H.: Proceedings of the IEEE Special issue on Asynchronous Circuits and Systems, vol. 87(2), pp. 219–222 (February 1999)
4. Chris, J.M.: Asynchronous Circuit Design, pp. 205–255. Copyright 2001 by John Wiley & Sons, Inc.
5. Edwards, D., Bardsley, A., Janin, L., et al.: Balsa: A Tutorial Guide. The University of Manchester, Version V3.5 (2006)
6. International standard ISO/IEC 14443, International Standardization Organization (November 2008)
7. Kessels, J., Kramer, T., Besten, G.D., Peeters, A., Timm, V.: Applying Asynchronous Circuits in Contactless Smart Cards. In: Proceedings of the Sixth International Symposium on Advanced Research in Asynchronous Circuits and Systems, ASYNC (2000)
8. Chandramouli, R., Kharrazi, M., Memon, N.D.: Image steganography and steganalysis: Concepts and practice. In: Kalker, T., Cox, I., Ro, Y.M. (eds.) IWDW 2003. LNCS, vol. 2939, pp. 35–49. Springer, Heidelberg (2004)
9. Mittelholzer, T.: An information-theoretic approach to steganography and watermarking. In: Pfitzmann, A. (ed.) IH 1999. LNCS, vol. 1768, pp. 1–16. Springer, Heidelberg (2000)

Integrated Neurofuzzy-JITL Model and Its Application in Batch Processes

Zhao Fu and Li Jia

Shanghai Key Laboratory of Power Station Automation Technology,
Shanghai University, Shanghai 200072, China
jiali@staff.shu.edu.cn

Abstract. In this paper, an integrated neurofuzzy-JITL model is proposed for batch processes. The neurofuzzy is employed to build a global model with its excellent extrapolating ability while Just-in-Time Learning (JITL) is used to build the local ARX model due to its good local dynamic modeling ability. In addition, Simulated Annealing (SA) algorithm is adopted to obtain the optimal weights of two models. As a result, the integrated model has better global generalization ability and higher accuracy. Lastly, the effectiveness of the presented integrated neurofuzzy-JITL model is verified by example.

Keywords: Batch process, neurofuzzy, JITL, integrated model, simulated annealing (SA) algorithm.

1 Introduction

Batch process is the main production mode in fine chemical engineering and biopharmaceuticals. It means that in a batch of the process, limited materials was added into one or more batch process or semi-batch process units to get limited products[1]. Since batch process inherent complicated mechanism, a series of problems will be met in the modeling, such as: ①unequal process length; ②dynamic process variable characteristic; ③ slow time-varying characteristics; ④ multimodal production process; ⑤non-Gaussian and serious nonlinearity[2]. So the research on mechanism model is very hard. At the same time, the flexibility of batch process decides that the processed products may be changed at any time. So there is no time to do enough experiments for model identification [3].

With the rapid development of information technology, the storing, detecting, collecting and processing of industrial data becomes more and more convenient. Every day, a large number of factories generate and store mass data of process and equipment, which imply the information of internal mechanism, process changes and equipment operation[4]. How to get effective usage of the data to serve production optimizing becomes a research hotspot in control field. As is known, the neural network has high mapping ability to approximate a nonlinear system in any precision and fuzzy system can built a model with expert knowledge to fix a complicated

system which is hard to describe conveniently. In order to make better use of these two technology for modeling, a neurofuzzy model which can both optimize rules and membership functions for the fuzzy component and enforce the self-control ability for the neural network component was proposed by [5]. At the same time, a new data-based method with self-adaptive ability for local modeling named JITL gains extensive attention and is applied in batch process modeling soon after it appears. JITL can build a local linear model with the most similar dataset selected from historical database to get an accurate prediction for process output[6][7]. But JITL also faces some problems such as high accurate modeling samples requirement and difficult model parameters selection. A strategy which can automatically update the database was applied to enhance the self-learning ability of JITL was proposed by [8]. And also CSF(cumulative similarity factor) and LOOCV(leave one out cross validation) algorithm were introduced to build an adaptive parameter selection strategy for system computation load reduction by[9].

Considering that in the batch process, neurofuzzy cannot be applicable for each process modality as a global modeling method and JITL shows a poor extrapolating ability as a local linear modeling method when its historical database is insufficient[10]. How to make their respective advantages complementary to each other has very important practical significance. In this paper, an integrated Neurofuzzy-JITL model with weighted output is proposed to gain both good extrapolating ability and modal adaptive capacity. The model weight coefficient is optimized by SA algorithm and the effectiveness is verified by examples.

2 Integrated Neurofuzzy-JITL Model

In this paper, $k(k=1,2,\dots,K)$ and t_f denote the k -th batch and end time of one batch, respectively. In the k -th batch, the input and output of the t -th time are represented by $u_k(t)$ and $y_k(t)$. For the convenience of research, suppose that one batch is divided into T equal intervals, namely $t=1,2,\dots,T$. Thus, the input sequence of the k -th batch is $U_k=[u_k(1),\dots,u_k(T)]^T$ and the corresponding output sequence is $Y_k=[y_k(1),\dots,y_k(T)]^T$ [11].

Since these two models has their own advantages and disadvantages, this paper considers to build an integrated model for advantages complementation. In the proposed model, each output of each submodel was assigned a fixed weight to get a more accurate system output. The output of batch process can be predicted by:

$$\hat{y} = \lambda \hat{y}_{JITL} + (1 - \lambda) \hat{y}_{NFM} \quad (1)$$

where \hat{y}_{JITL} denotes the output of JITL model, \hat{y}_{NFM} denotes the output of Neurofuzzy model. \hat{y} is the output of integrated model, $\lambda \in (0,1)$ is the weighting coefficient. The integrated model structure can be showed by Fig. 1.

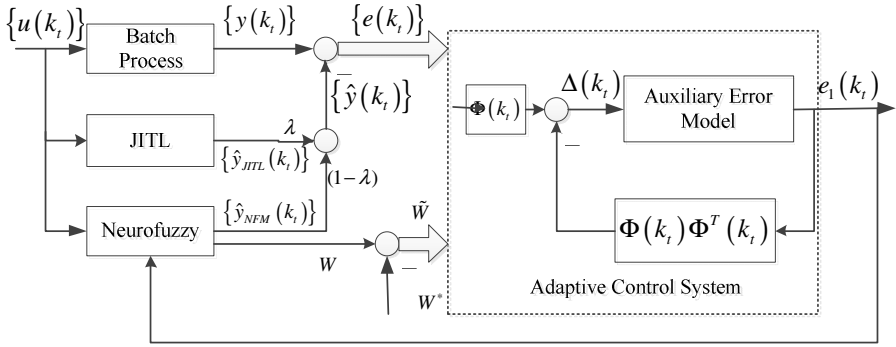


Fig. 1. The proposed integrated model

2.1 JITL Model

In the proposed integrated model, a JITL is used to build system’s local linear model. The concrete structure is showed in Fig. 2.

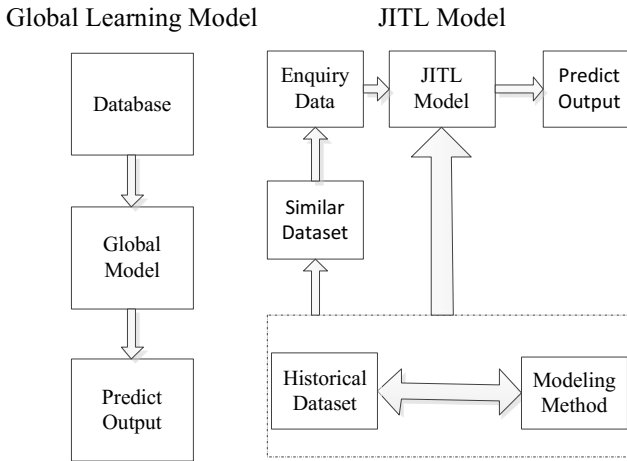


Fig. 2. The JITL structure

$$d(x_q, x_i) = \sqrt{\sum_{j=1}^{m_1+m_2} (x_{qi} - x_{ij})^2} \tag{2}$$

$$\cos(\theta_i) = \frac{\Delta x_q^T \Delta x_i}{\|\Delta x_q\|_2 \|\Delta x_i\|_2} \tag{3}$$

$$s_i = \mu \sqrt{e^{-d^2(x_q, x_i)}} + (1 - \mu) \cos(\theta_i) \text{ , if } \cos(\theta_i) \geq 0 \tag{4}$$

where $\Delta x_q = x_q - x_{q-1}$, $\Delta x_i = x_i - x_{i-1}$, $\mu \in [0, 1]$ is the weight coefficient, $s_i \in [0, 1]$ denotes the similarity between current input sample x_q and historical database sample x_i .

- (1) If $\cos(\theta_i) < 0$, the angle between Δx_q and Δx_i is really huge, and it means that these two sample has low similarity and should be abandoned.
- (2) If $\cos(\theta_i) \geq 0$, the angle between Δx_q and Δx_i is tiny, and it means that these two sample has high similarity and should use (4) to calculate the similarity index[12].

When the similarity index s_0 and domain data sample number k are set, all the data sample in historical database which has the similarity index large than s_0 will be selected and sorted in descending order. The JITL will choose the first k data to build a local ARX model:

$$\hat{y}_{jitl_{k,i}} = \alpha_1 u_{k,i-1} + \dots + \alpha_{m_1} u_{k,i-m_1} + \beta_1 y_{k,i-1} + \dots + \beta_{m_2} y_{k,i-m_2} \tag{5}$$

where $i = 3, 4, \dots, T$. Denote $\Theta = [\alpha_1, \dots, \alpha_{m_1}, \beta_1, \dots, \beta_{m_2}]$, formula (5) can be denoted as follow:

$$\hat{y}_{jitl_{k,i}} = \Theta x_{k,i} \tag{6}$$

As in different operation condition, the density of satisfied data will be completely different. So a fixed sample number k cannot meet the modeling accuracy requirement. To get higher modeling accuracy, this paper set a domain for k and use LOOCV to choose the best k [13].

2.2 Neurofuzzy Model

In this paper, a Neurofuzzy is proposed to identify batch process as follows.

$$\hat{y}_k(t+1) = f_{NFM}(x_k(t)) \tag{7}$$

where $x_k(t) = [y_k(t), y_k(t-1), \dots, y_k(t-n_y+1), u_k(t), u_k(t-1), \dots, u_k(t-n_u+1)]^T$, $\hat{y}_k(t+1)$ is the predicted output of the $t+1$ -th time of the k -th batch, and n_y and n_u are integers related to the model order. Then the predicted output sequence of the k -th batch is

$$\hat{Y}_k = [\hat{y}_k(1), \dots, \hat{y}_k(T)]^T \tag{8}$$

The proposed Neurofuzzy model contains five layers. The first layer is the input layer, which contains $n_y + n_u$ neurons. The second layer is fuzzy layer and has $(n_y + n_u) \times N$ neurons, in which N denotes the number of fuzzy IF-THEN rules and each neuron in this layer represents a membership function. The third layer is the rule layer and contains N neurons. The fourth layer is the fuzzy decision layer with two neurons. Finally, the fifth layer is output layer. The output of the Neurofuzzy model is given by:

$$Output = \frac{\sum_{j=1}^N w_j \mu_j(x_k(t))}{\sum_{j=1}^N \mu_j(x_k(t))} = \frac{\sum_{j=1}^N w_j \cdot \exp\left(-\sum_{i=1}^{n_y+n_u} \frac{(x_k(t,i) - c_{ji})^2}{\theta_j^2}\right)}{\sum_{j=1}^N \exp\left(-\sum_{i=1}^{n_y+n_u} \frac{(x_k(t,i) - c_{ji})^2}{\theta_j^2}\right)} \tag{9}$$

where $\mu_j(x_k(t))$ denotes Gaussian radial basis function, and θ_j and c_{ji} are width and centre, respectively. w_j is the j -th consequence of fuzzy rule which can be defined as follow:

$$w_j = \alpha_0^j + \sum_{i=1}^M \alpha_i^j x_i(t) \tag{10}$$

where $\alpha_i^j (i = 0, 1, 2, \dots, M, j = 1, 2, \dots, N)$ denotes consequence parameters[14]. For the convenience of follow discussion, define the following variables:

$$\Phi = [\varphi_1, \varphi_2, \dots, \varphi_N] \tag{11}$$

$$\varphi_j = [1, x_1, \dots, x_M] \bar{\mu}_j(x(k_t)) \tag{12}$$

$$\bar{\mu}_j(x(k_t)) = \frac{\mu_j(x(k_t))}{\sum_{j=1}^N \mu_j(x(k_t))} \tag{13}$$

Then the output of Neurofuzzy can be denoted as:

$$\hat{y}(k_t + 1) = \Phi W \tag{14}$$

A clustering algorithm in our previous work is employed to estimate the antecedent parameters of N , c_{ji} and θ_j . Then the task of this work is to identify the parameters of $w = \{w_1, w_2, \dots, w_N\}$. To get better output performance, the auxiliary error is introduced in Neurofuzzy training. The structure of Auxiliary error is showed in Fig. 3.

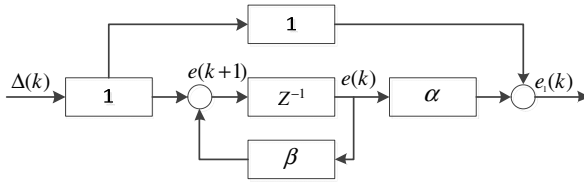


Fig. 3. The auxiliary error structure

Auxiliary error model can be denoted as follow:

$$e_1(k) = \frac{\alpha e(k) + \Phi(k)W(k) - y(k+1)}{1 + \Phi(k)\Phi^T(k)} \tag{15}$$

where α is a constant..

The predicted output of Neurofuzzy can be described by following equations:

$$\hat{y}(k_i + 1) = \beta e(k_i) + \Phi(k_i)W(k_i) - \Phi(k_i)\Phi^T(k_i)e_1(k_i) \tag{16}$$

$$\Delta(k_i) = \Phi(k_i)\tilde{W}(k_i) - \Phi(k_i)\Phi^T(k_i)e_1(k_i) - d(k_i) \tag{17}$$

where $\tilde{W}(k_i) = \hat{W}(k_i) - W$ and β is a constant.

Therefore, the auxiliary error model is given as follows:

$$e(k_i + 1) = \beta e(k_i) + \Delta(k_i) \tag{18}$$

$$e_1(k_i) = \alpha e(k_i) + \Delta(k_i) \tag{19}$$

And then the Neurofuzzy weight coefficient can be modified by[5]:

$$\Delta W(k) = -\Phi^T(k)e_1(k) \tag{20}$$

$$\hat{W}(k+1) = \hat{W}(k) + \Delta W(k) \tag{21}$$

So the output of integrated model is:

$$\begin{aligned} \hat{y} &= \lambda \hat{y}_{JITL} + (1 - \lambda) \hat{y}_{NFM} \\ &= \Theta X + \Phi W \end{aligned} \tag{22}$$

2.3 Integrated Model Weighting Coefficient Training

As weight coefficient is extremely important for the proposed integrated model, in this paper, simulated annealing algorithm is introduced to optimize the weight coefficient.

Simulated annealing(SA) is a generic probabilistic heuristic algorithm for global optimization problem. It was independently presented by Kirkpatrick in 1983, and by Cerny in 1985. In the real physical annealing, solid is heated until it melts and then it

starts cooling with a proper annealing schedule until it reaches the least energy state. If the initial temperature is not high enough or cooling process is too fast, there can be a deformation in the solid at the end of cooling. SA possess an advantage over other heuristic algorithms for its easy implementation and excellent performance for optimization problems[15]. The flow chart of SA algorithm is showed in Fig. 4.

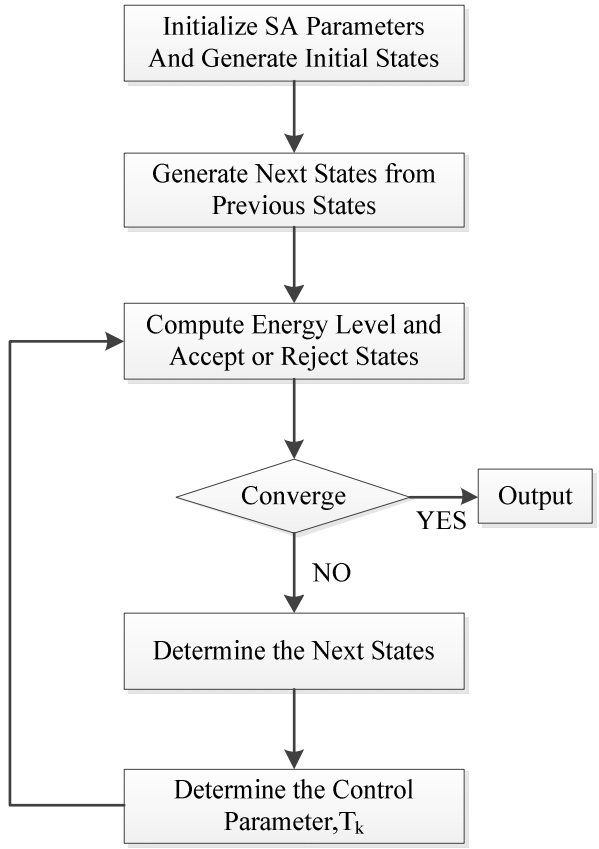


Fig. 4. Flow chart of SA algorithm

As is shown in Fig 4, the concrete operation steps of SA can be described as follows:

- Step 1.** Set the initial temperature: $T_{initial}$ and generate the initial solution x .
- Step 2.** Calculate the objective function value.
- Step 3.** Refresh the temperature with cooling schedule. If the temperature reaches termination point, then stop iteration and output the optimization results.
- Step 4.** Generate a new solution and calculate the corresponding objective function value.

Step 5. Acceptance criterion: Store the new solution when it get a better performance or meet the fixed acception probability.

Step 6. Go to step 3.

3 Illustrative Example

One typical continuous stirred tank reactor (CSTR) is considered to illustrate the proposed algorithm, in which a first-order irreversible exothermic reaction $A \xrightarrow{k_1} B \xrightarrow{k_2} C$ takes place. This process can be described by the following dynamic equations

$$\begin{aligned}\dot{x}_1 &= -k_1 \exp(-E_1/T)x_1^2 \\ \dot{x}_2 &= k_1 \exp(-E_1/T)x_1^2 - k_2 \exp(-E_2/T)x_2\end{aligned}\quad (23)$$

where x_1 and x_2 are respectively the reactant concentration, T denotes reactor temperature[17].

In this simulation, $k_1 = 4000$, $k_2 = 6.2 \times 10^5$, $E_1 = 2500$, $E_2 = 5000$. T is normalized by using $T_d = (T - T_{\min}) / (T_{\max} - T_{\min})$, in which T_{\min} and T_{\max} are respectively 298 (K) and 398 (K). $x_1(0) = 1, x_2(0) = 0$. T_d is the control variable and is bounded by $0 \leq T_d \leq 1$, and $x_2(t)$ is the output variable.

To identify the proposed integrated model, a nominal trajectory of the input are derived firstly, and then independent random signal with uniform distribution between $[0,1]$ are used to simulate 270 input-output data for training purpose. To illustrate the prediction capability of the proposed integrated model, another 20 batches are generated for validation purpose and mean square error(MSE) is introduce as an evaluation index:

$$MSE = \sqrt{\frac{1}{N} \sum_{i=1}^N (y_i - \hat{y}_i)^2}\quad (24)$$

With experience and a certain numbers of testing, the iteration number is set as 6000, clustering algorithm similarity is set as 0.88, similarity weight is set as 0.95, k min is set as 10, k max is set as 40 and weighting coefficient $\lambda = 0.63$. Then the Neurofuzzy get a rule number of 8 and a output MSE of 2.3×10^{-5} , the JITL has the MSE of 2.2×10^{-5} and the integrated model has the MSE of 1.2×10^{-5} , the output error is also showed in Fig. 5 and Fig. 6.

To simulate the inside disturbance, the parameters of batch process are varied at different instants of time. The inside disturbance can be added are as follow:

$$E_1 = E_1 + \Delta_{E_1}$$

$$E_2 = E_2 + \Delta_{E_2}$$

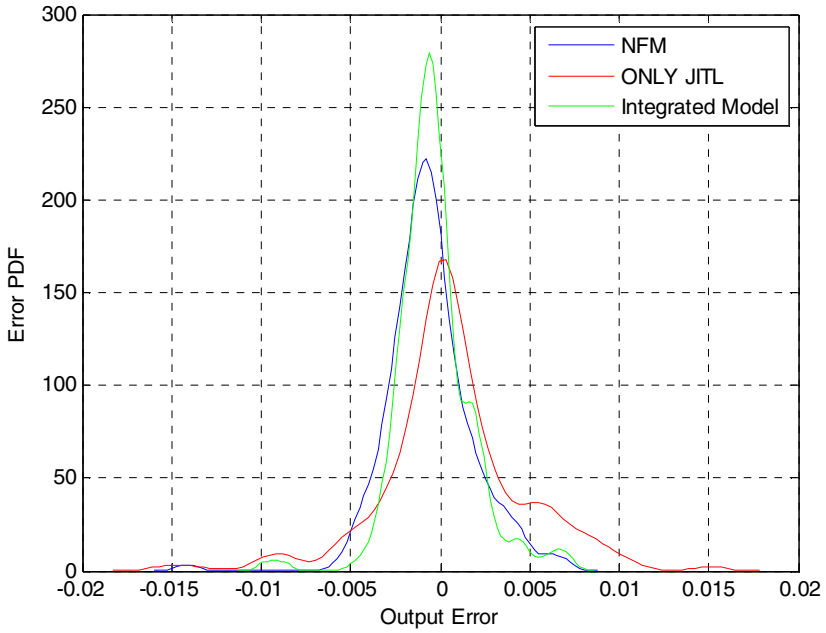


Fig. 5. Modeling error PDF of testing data

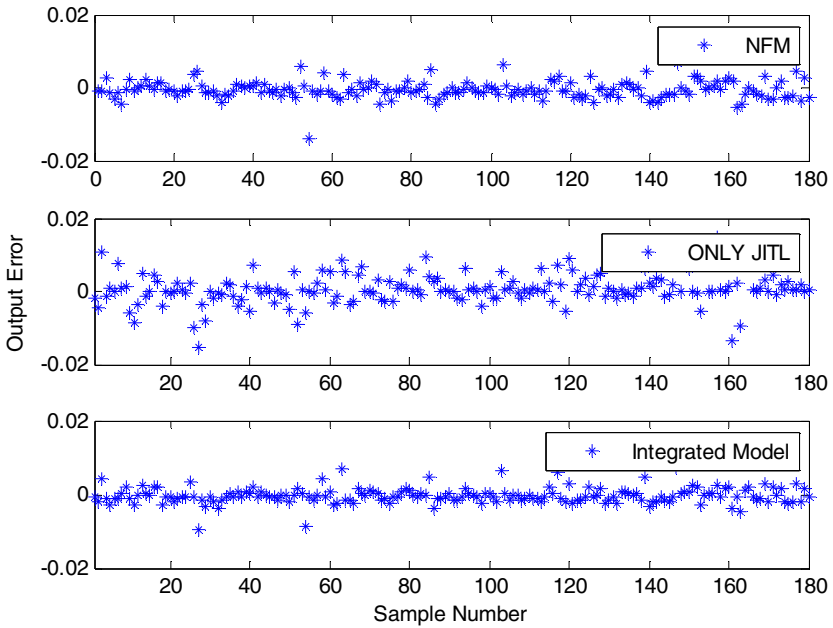


Fig. 6. Modeling error of testing data

Where Δ_{E_1} and Δ_{E_2} are 15% Gaussian white noise of E_1 and 8% Gaussian white noise of E_2 respectively. Result also shows that the integrated model can preserve a better predictive performance than both Neurofuzzy and JITL with inside noise.

Table 1. MSE of different Gaussian white noise

Method	JITL	Neurofuzzy	Integrated Model
MSE	1.18×10^{-4}	9.50×10^{-5}	8.39×10^{-5}

4 Conclusion

In this paper, an integrated modeling method was proposed to build a model with Neurofuzzy and JITL. The new model can suit the modalities of batch process and keep a good extrapolating ability when facing data insufficient. SA algorithm is also introduced to optimize the weight coefficient for the proposed model. Examples illustrate the proposed method yields better predictive performance than its counterparts.

Acknowledgments. Supported by National Natural Science Foundation of China (61374044), Shanghai Science Technology Commission (12510709400), Shanghai Municipal Education Commission (14ZZ088), Shanghai talent development plan.

References

1. Yang, Z.C.: Batch process in chemical engineering-principle, technology and equipment. Chemical Industry Press, Beijing (2001)
2. Zhao, C.H., Wang, F.L., Yao, Y., Gao, F.R.: Phase-based statistical modeling, online monitoring and quality prediction for batch process. *Acta Automatic Sinica* 36, 366–374 (2010)
3. Lu, L.Y., Wang, F.L., Gao, F.R.: Statistical modeling and online monitoring of batch processes. *Acta Automatic Sinica* 32(3), 400–410 (2006)
4. Hou, Z.S., Xu, J.X.: On data-drive control theory: the state of the art and perspective. *Acta Automatic Sinica* 35, 650–666 (2005)
5. Jia, L., Shi, J.P., Chiu, M.: Research on fuzzy neural model with global convergence for batch process. *Information and Control* 38, 683–691 (2009)
6. Atkeson, C.G., Moore, A.W., Schaal, S.: Locally weighted learning. *Artif. Intell. Rev.* 72, 643–658 (1999)
7. Bontempi, G., Birattari, M., Bersini, H.: Lazy learning for local modeling and control design. *Int. J. Control* 11, 11–73 (1999)
8. Pan, T.H., Li, S.Y.: Optimal control for nonlinear system based on lazy learning. *Control and Decision* 22, 26–29 (2007)
9. Xiong, F.Q., Gui, W.H., Yang, C.H.: Integrated prediction model of iron concentration in goethite method to remove iron process. *Control and Decision* 27, 329–334 (2012)
10. Jia, L., Cao, L.M., Chiu, M.: Modeling error PDF shape based data-drive model for batch process. *Chinese Journal of Scientific Instrument* 33, 1505–1512 (2012)

11. Cheng, C., Chiu, M.: Nonlinear process modeling based on just-in-time learning and angle measure. In: Palade, V., Howlett, R.J., Jain, L. (eds.) KES 2003. LNCS, vol. 2773, pp. 1311–1318. Springer, Heidelberg (2003)
12. Yi, L., Gao, Z.L.: Just-in-Time kernel learning with adaptive parameter selection for soft sensor modeling of batch process. *Industrial & Engineering Chemistry Research* 51, 4313–4327 (2012)
13. Jia, L., Shi, J.P., Chiu, M.: Research on fuzzy neural model with global convergence for batch process. *Information and Control* 38, 683–691 (2009)
14. Tan, S.H., Hao, J.B., Vandewalle, J.: Efficient identification of RBF neural net models for nonlinear discrete-time multivariable dynamical systems. *Neurocomputing* 9, 11–26 (1995)
15. El-Naggar, K.M., AIRashidi, M.R., AIHajri, M.F., AI-Othman, A.K.: Simulated Annealing algorithm for photovoltaic parameters identification. *Solar Energy* 86, 266–274 (2012)
16. Jia, L., Yang, T., Chiu, M.: An integrated iterative learning control strategy with model identification and dynamic R-parameter for batch processes. *Journal of Process* 23, 1332–1341 (2013)
17. Ray, W.H.: *Advanced Process Control*. McGraw-Hill, New York (1981)

MongoDB Improves Big Data Analysis Performance on Electric Health Record System

Wei Xu¹, Zhonghua Zhou¹, Hong Zhou², Wu Zhang¹, and Jiang Xie^{1,*}

¹ School of Computer Engineering and Science, Shanghai University

² Shanghai University Hospital

{xw, zzh2, zhouhong, wzhang, jiangx}@shu.edu.cn

Abstract. Electronic Health Record system has been widely used in different occasions such as hospitals, health welfare institutions and education institutions. However, the data structures of health information are usually very complicated and unstructured. It is hardly to deal with the health data for the general relational databases. We build a Nosql-based EHR system named Shanghai University Electronic Health Record System (SHU-EHR) for health data management and analysis with MongoDB. The experiments demonstrate that the performance of SHU-EHR is far better than the SQL-based EHR system.

Keywords: Electronic Health Record, Nosql, MongoDB.

1 Introduction

An electronic health record (EHR) is a systematic collection of electronic health information about an individual patient or population [1]. With the development of information technology, EHR system becomes more and more popular in hospitals, health welfare institutions and education institutions. Investigators contributed themselves to EHR system [2-4] and many EHR systems are developed by commercial companies such as Cerner [5], Mckensson [6], eClinicalWorks [7], Allscripts altenahealth [8] etc. However, most of the EHR systems are built on SQL database which can hardly handle big data in short time.

MongoDB [9-10], which is written in C++, is an open-source document database rather than a traditional relational database. It is the leading NoSQL database so far. Different with SQL databases, MongoDB provides weak consistency guarantees so that it has better performance in big data management and analysis than SQL database. Some people have used MongoDB in different areas [11-13].

Shanghai University Electronic Health Record System (SHU-EHR) is a Nosql-based EHR system that is built on MongoDB. It includes 13 different types of student health data such as physical examination records, medical records, and so on. This paper introduces the architecture, database component and data synchronization

* Corresponding author.

method of SHU-EHR. Two experiments are conducted on SHU-EHR to compare the performance of SQL database and MongoDB database.

2 Architecture

The basic architecture of SHU-EHR is introduced. SHU-EHR adopts .NET MVC framework and Entity Framework so as to keep maintainability. Figure 1 shows the basic architecture.

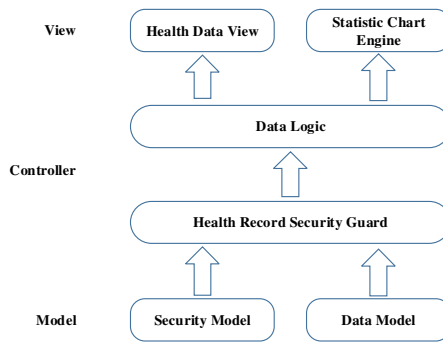


Fig. 1. Architecture of SHU-EHR

SHU-EHR is mainly consists of three parts. The model part includes two main parts which are the security model and the data model. The security model is one of the most important parts of SHU-EHR, because the health record of each person is very private. This model is in the kernel of SHU-EHR, which is used to keep all the health data safe. The data model is built to maintain all the 13 different types of health records. This model can keep the data in a uniformed format so that the data can be easily shared.

The middle part of SHU-EHR is controller. This part handles all the data logic and user requests. The health record security guard is the basic component of the controller. All the requests are protected by this component and the user access logs are recorded by the security core. The data logic part dispatches all the requests to different controller instances and process query, computational requests.

On the top, it is the view part. Health data view displays all the data details of 13 different kind of health records. Statistic chart engine is used to show computational results with various data charts such as line chart, bar chart, pie chart and polar chart. With the help of chart engine the system data managers and department leaders can easily understand the whole health conditions.

3 Mixture Database

SHU-EHR uses mixture database. Figure 2 shows the database architecture of SHU-EHR. The security model and the data model in section 2 are mapped to different

databases. The security model is mapped to the SQL database because SHU-EHR implements the Microsoft ASP.NET Identity which is stable, reliable and security. The data model is mapped to the Nosql database that can make queries and calculations much faster.

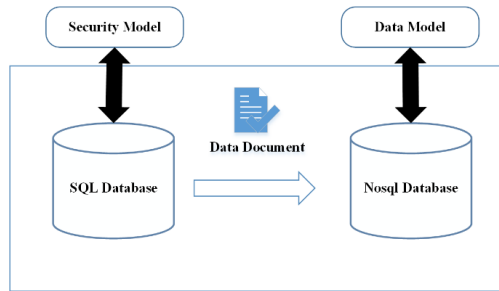


Fig. 2. Mixture Database of SHU-EHR. SHU-EHR uses two different kinds of databases. The SQL database is used for user roles identification and the Nosql database is used for data storage and data query.

3.1 SQL Based Component

The SQL database of SHU-EHR plays the key role for security reasons. This database includes the user authority information, system configuration, system logs and the original health data. The user authority module implies the Microsoft ASP.NET Identity model which includes profile support, OAuth integration and works with open web interface for .NET (OWIN) [14]. With the help of this module, SHU-EHR offers many useful data interfaces and web APIs for different occasions.

The other security information is the system configuration and running logs. System configuration controls the whole system and the running logs traces user operations. Both of these information are all stored in the SQL database. Usually these information should not be accessed by the normal user.

For some reason, the original data are firstly stored in the SQL database and then SHU-EHR transfers the data to Nosql database. Figure 3 shows the SQL database component of SHU-EHR.

3.2 Nosql Based Component

The Nosql database of SHU-EHR is showed in figure 4. This database stores two kinds of data, the users' health data and the data statistic results. Because most of the query requests are about user data and the statistic results that are high-dimension and with complex relationships, it is difficult for SQL databases to response in a short time when it comes to big data. MangoDB can address this problem.

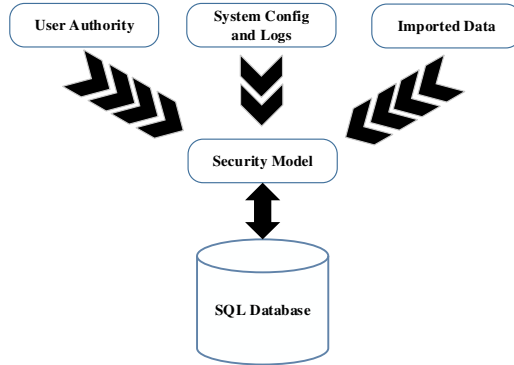


Fig. 3. SQL database component of SHU-HER

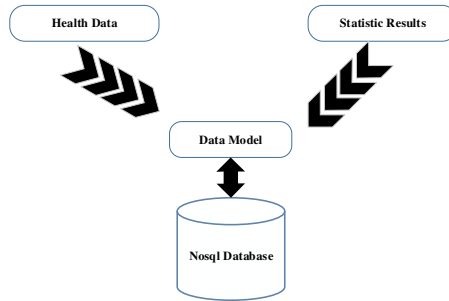


Fig. 4. Nosql database component of SHU-EHR

3.3 Multi Databases Synchronization

The health data in the Nosql database are imported from SQL database. SHU-EHR has two different interfaces for data synchronization. One is the synchronous interface, which is used to synchronize user health information as soon as new data is inserted into SQL database. If the synchronous interface load failed, the unloaded data will be handled by the asynchronous interface. When the system is free, the asynchronous interface reloads the unloaded health data. All the data are defined as SHU-HER health record object and then transferred in the uniform format between SQL and Nosql databases. At the same time, the user access log and data transfer logs are stored into Nosql database by synchronous interface. Figure 5 shows the two interfaces.

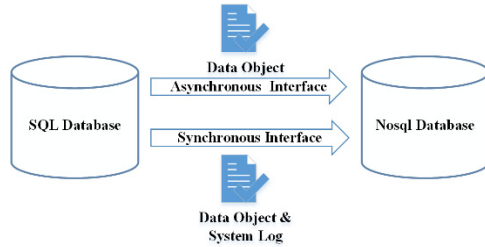


Fig. 5. Data synchronization of SHU-EHR

4 Experiments

In this section we conduct two experiments with the same health data to compare query performance and statistic performance of SQL database and Nosql database. The SQL database is Microsoft SQL Server v11.00.2100 and the Nosql database is MongoDB v2.4.9. Both of the experiments are conduct on the same computer with 4GB memory, Intel core i3 3.4GHz dual-core processor and Windows 8.1 operating system.

4.1 Query Performance

Table 1. Data Query Performance between SQL and Nosql Databases

Data Number	SQL Time(ms)	Nosql Time(ms)
5K	179.3558	4.0036
10K	306.2019	4.0027
20K	633.4176	6.0043
50K	1255.828	5.0045
100K	3026.469	5.0036
200K	6065.009	6.0046
500K	20148.33	7.0043
1000K	N/A	8.0056

Table 1 displays the query performance of these two different databases. We searched the top 10 records of the total data. As the number of total data increases from 5000 to 1000000, SQL database query time increases by over 100 times (from 179ms to 20148ms), while the MongoDB query time only increase by 2 times (from 4ms to 7ms). Figure 6 shows the same results of the query performance comparison. Because the difference of the two query time is too large, and the query time of MongoDB is almost zero, the y-axis of this figure is converted by equation 1.

$$y = 10 \log(\text{Query Time}). \quad (1)$$

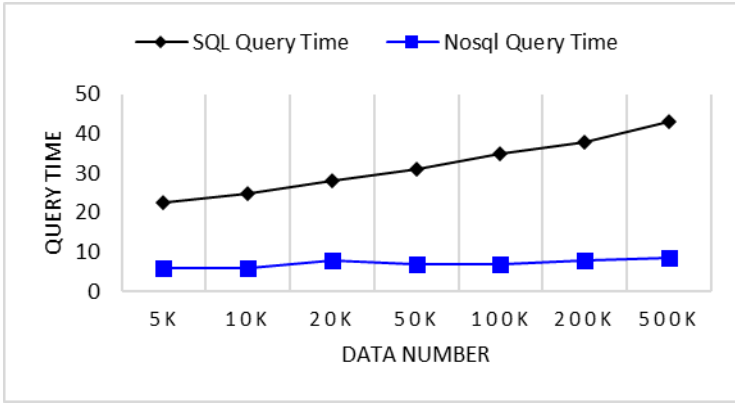


Fig. 6. Query performance between SQL and Nosql Databases

Table 2. Calculation Performance between SQL and Nosql Databases

Data Number	SQL (ms)	Nosql (ms)
5K	269	300.7302
10K	341.0455	154.1017
20K	805.5341	296.1966
50K	1325.8772	490.3232
100K	2570.7013	989.6535
200K	8056.3307	1935.2803
500K	15198.039	4342.87
1000K	N/A	7919.1565

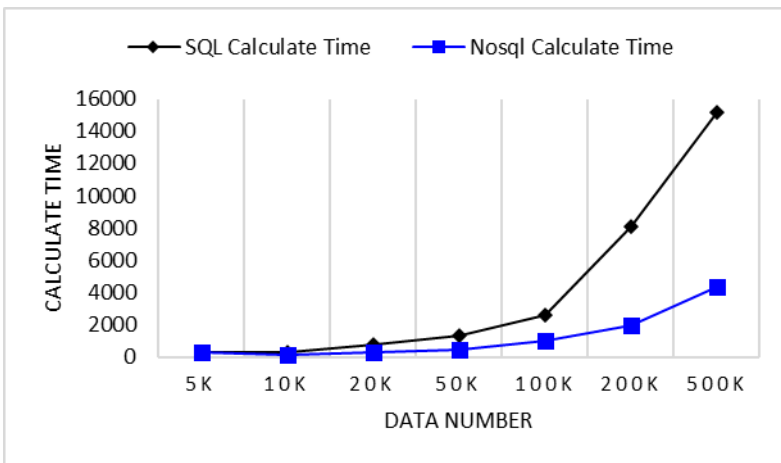


Fig. 7. Calculation performance between SQL and Nosql Databases

4.2 Statistic Performance

Table 2 shows the calculation time of the two databases. In this experiment we compute the record number of 10 different groups. When the data is small, the two databases have the same performance. However, when the amount of the records increases, the computing time of SQL database increases much faster than Nosql database. Figure 7 displays the experiment result of the statistic performance of SQL and MangoDB.

5 Conclusion

Using MongoDB in SHU-EHR greatly improves both query and statistic performance of the system. Thanks to MongoDB, SHU-EHR offers many APIs for big data analysis with MongoDB data analysis methods. Investigators who are not familiar with system coding can easily use SHU-EHR for big health data analysis.

Acknowledgements. This research is partially supported by the Specialized Research Fund for the Doctoral Program of Higher Education [SRFDP 20113108120022], the Key Project of Science and Technology Commission of Shanghai Municipality [No. 11510500300], and the Major Research Plan of NSFC [No. 91330116].

References

1. Gunter, T.D., Terry, N.P.: The emergence of national electronic health record architectures in the United States and Australia: models, costs, and questions. *Journal of Medical Internet Research* (2005)
2. Lowry, S.Z., Quinn, M.T., Ramaiah, M., et al.: Technical evaluation, testing and validation of the usability of electronic health records. *National Institute of Standards and Technology* (2012)
3. Baron, R.J., Fabens, E.L., Schiffman, M., et al.: Electronic health records: just around the corner? Or over the cliff? *Annals of Internal Medicine* (2005)
4. Tang, P.C., Ash, J.S., Bates, D.W., et al.: Personal health records: definitions, benefits, and strategies for overcoming barriers to adoption. *Journal of the American Medical Informatics Association* (2006)
5. Cerner, <http://www.cerner.com/>
6. McKesson, <http://www.mckesson.com/>
7. eClinicalWorks, <http://www.eclinicalworks.com/>
8. Allscripts altenahealth, <https://www.allscripts.com/international1.html>
9. MongoDB, <https://www.mongodb.org/>
10. Truica, C.O., Boicea, A., Trifan, I.: CRUD Operations in MongoDB. *Adv. Intel. Sys. Res.*, 41 (2013)
11. Cogean, D.I., Fotache, M., Greavu-Serban, V.: Nosql in Higher Education. A Case Study. In: *Int. Conf. Inform. Econ.* (2013)

12. Yang, J.H., Ping, W.Y., Liu, L., Hu, Q.P.: Memcache and MongoDB based GIS Web Service. In: Second International Conference on Cloud and Green Computing / Second International Conference on Social Computing and its Applications, Cgc/Sca 2012 (2012)
13. Dykstra, D.: Comparison of the Frontier Distributed Database Caching System to NoSQL Databases. In: International Conference on Computing in High Energy and Nuclear Physics 2012, Chep 2012 (2012)
14. ASP.NET Identity, <http://www.asp.net/identity>

Survey of Multi-sensor Image Fusion

Dingbing Wu¹, Aolei Yang¹, Lingling Zhu², and Chi Zhang²

¹ Shanghai Key Laboratory of Power Station Automation Technology
School of Mechatronic Engineering and Automation
Shanghai University

149 Yanchang Road, Shanghai, China

² Ningbo Institute of Materials Technology & Engineering, Chinese Academy of Sciences
hanbing0821@126.com, aolei.yang@gmail.com,
zhull_7627@163.com, zhangchi@nimte.ac.cn

Abstract. The paper presents multi-sensor image fusion and its relevant framework and technical characteristics. The image fusion is divided into three level fusions: pixel level, feature level and decision level. It mainly discusses the image fusion algorithm at all levels of fusion, and then makes the summary and comparison of these algorithms. Since the high-level algorithms are related to some relevant practical applications of the image fusion, it is in general difficult to be summarized. So this paper also presents some typical algorithms of the feature and decision levels from the perspective of the applications, to provide the necessary summary of the high level image fusion algorithm. Further, the three levels of implementation schemes are described, followed by the comparison and summary for the image evaluation criteria of the fusion method. Some problems and future directions about the multi-sensor image fusion are finally given.

Keywords: Multi-sensor image fusion, image fusion classification, neural network image fusion, decision level fusion, fusion evaluation criteria.

1 Introduction

Multi-sensor image fusion is to adopt specific algorithms for combining two or more source images into new image information, which is more suitable for human visual perception, or for computer subsequent processing to meet the requirement of applications, such as image segmentation, feature extraction, and target identification. Through the image fusion technology, we can effectively improve the reliability of the system and the utilization efficiency of image information. From the early 1980s, the research of the multi-sensor image fusion has triggered widespread interest in the world, since it has a wide range of applications in automatic target recognition,

¹ This work was supported by the Science and Technology Commission of Shanghai Municipality under “Yangfan Program” (14YF1408600), the Shanghai Municipal Commission of Economy and Informatization under Shanghai Industry-University-Research Collaboration Grant (CXY-2013-71). Corresponding author: Aolei Yang, email: aolei.yang@gmail.com

computer vision, remote sensing, robotics, medical image processing, military applications and other fields [1-5], for example, infrared image and visible light image fusion can better help the helicopter pilot for navigation, and computed tomography (CT) and magnetic resonance imaging (MRI) are implemented to investigate the anatomy and function of the body in both health and disease, which could provide reliable information for clinical diagnosis [3-6].

The multi-sensor image fusion is generally divided into three level fusions: the pixel level, the feature level and the decision level. Most of the image fusion algorithms are based on the pixel level fusion which is the main fusion algorithm, and the fusion algorithm on the feature and decision levels are much less mentioned in the literature. However, for the high-level image fusion including the feature and decision levels, the corresponding problems of the image fusion are more complex, and the fusion methods of the system are more ambiguous. For example, the feature level image fusion method is in general associated with specific applications, which has rich meanings, and can be used in various applications of the image processing [4-6].

In this paper, the multi-sensor image fusion is divided into three levels depending on our thoughts. The algorithm of the pixel level was presented in detail, and some typical image fusion algorithms in the feature and decision levels are reviewed from the view of application to provide the necessary summary of the high level image fusion algorithm. Specifically, for the pixel algorithms, the classification and comparison of the pixel level algorithm are in detail presented, followed by the summaries of the fusion algorithms on the feature level and decision level.

This remainder of the paper is organized as follows. Section 2 outlines the principles of image fusion technology and architecture, technical features and image fusion classification methods, Section 3 presents a number of specific embodiments of the various methods and features, reviews some of the key issues of image fusion technology, and depicts some typical algorithms of the feature and the decision levels from the perspective of practical applications. Section 4 presents the image fusion evaluation criterion. The paper finally points out some problems and future directions about the multi-sensor image fusion.

2 Theory and Characteristics of Image Fusion

2.1 Image Fusion Classification

The image fusion requires preliminary pretreatment, which includes several aspects: alignment, calibration, removing noise, etc. After completing the pretreatment, the image fusion can generally be divided into three levels: pixel level, feature level and decision level fusion, which is shown in Fig.1.

A. Pixel level fusion

The pixel level fusion belongs to the lower level of fusion which directly fuses the image pixels information. Currently, most researches focus on this level. It fuses on the layer of the original image data collected from the imaging sensors. It is the highest accuracy level data fusion in spite of its lowest level image fusion. It can provide the details are that the other levels do not have, but a large amount of information

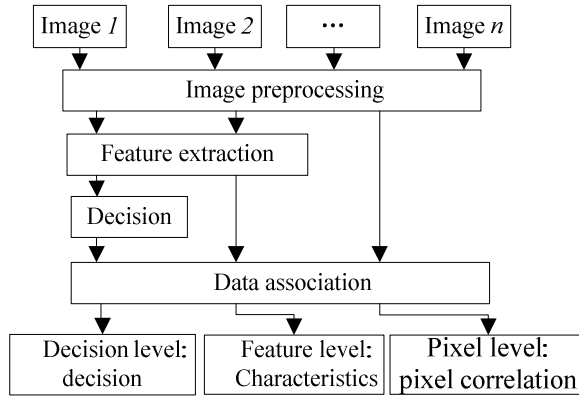


Fig. 1. Three levels image fusion

need be processed. The pixel level fusion called data level fusion is the basis of the high-level image fusion.

B. Feature level fusion

The feature level image fusion extracts feature information from each imaging sensor, and comprehensively analyzes and processes this information. During the fusion, the purpose of application and the scene of the multi-sensor image fusion are closely related to specific form and the feature information. Through the feature level image fusion, the related information is extracted from the original image, and it increases the credibility of the feature information, eliminates the false features, and creates a new composite feature, etc. The feature level image fusion is middle level for the preparation of the decision level fusion. Its advantage is of achieving considerable information compression, and being convenient for real-time processing. Since the extracted feature is directly related to decision analysis, the fusion result can furthest support to decision analysis in the high level fusion.

C. Decision level fusion

The decision level fusion can be simply described as: (1) classify and identify the feature information of each image, (2) form the corresponding results, (3) make the further fusion process. It is a higher level of information fusion, and the fusion results will provide the basis for controls or decisions. Therefore, the decision level fusion must combine with specific application and demand characteristics. Because the feature directly affects the final result, we should selectively use the feature information to achieve the fusion purpose. The input information is all kinds of features, and the output results are about decision descriptions, so the decision level fusion is with the characteristics of the minimum data size and strong anti-jamming.

Tab.1 shows the comparison of the different fusion levels performance characteristics. From the table and the previous description, we can see that the pixel level fusion is the most important and most fundamental multi-sensor image fusion methods, which can obtain a large amount of information and the best fusion performance [4-8].

Table 1. Comparison of image fusion levels and performance

Features \ Levels	Pixel level	Feature level	Decision level
Information content	maximum	medium	minimum
Information loss	minimum	medium	maximum
Fault tolerance	the worst	medium	the best
Immunity	the worst	medium	the best
Dependence of the sensor	maximum	medium	minimum
Method difficulty	hardest	medium	the easiest
Pretreatment	minimum	medium	maximum
Classification performance	the best	medium	the worst
Open systems	The worst	medium	the best

2.2 Characteristics of Multi-sensor Image Fusion Technology

The cost of the multi-sensor image fusion is less than that of single sensor, and it gets more or precise target information. The system has the following characteristics: (1) information redundancy: the confidence of the same scene target information may be different for the multi-sensor, but the image fusion will improve the overall target confidence. When a part of sensors are abnormal or damaged, it is also able to improve the system robustness (trustworthiness); (2) information complementary: the information complementary is achieved from the multi-sensor fusion to make the system getting scenery features, which is not able to be achieved using the single sensor (enlarge the spatial overlapping); (3) enlarge time overlapping: in a long time, the single sensor and the multi-sensors are capable of getting multiple information with a long time overlapping; (4) higher cost performance: as increasing of the number of sensors, the increasing cost of the system is less than its increasing information [1-8].

3 Image Fusion Methods

3.1 Pixel Level Image Fusion

Currently, the pixel level fusion methods have been more deeply studied. There are many kinds of image fusion algorithms, but the pixel level fusion can be broadly divided into two categories: (1) image fusion based on space domain and (2) image fusion based on transform domain. The significant differences between them are: the former directly fuses the pixels; the latter firstly transforms the image, and the object of fusion is then transformed coefficient instead of pixel values itself. The fusion coefficient may come from several or even all the original space pixel value which is obtained by the result of some transformation. The fusion process is shown in Fig.2.

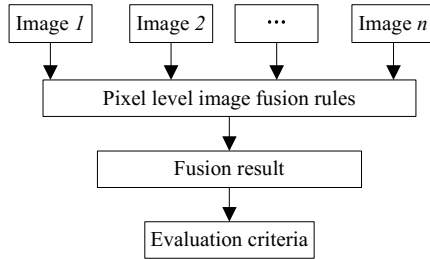


Fig. 2. Pixel level image fusion flow

3.1.1 Image fusion algorithm based on space domain

1) Linear Weighting

The linear weighting method is a simple image fusion method, which is to directly make the weighted stacking for corresponding pixels of the original images. If $A_k(i, j)$ represents the grey value of the k^{th} image at the corresponding position (i, j) , the fusion image $B_k(i, j)$ can be then obtained by the following formula:

$$B_k(i, j) = \sum_{k=1}^n W_k(i, j) A_k(i, j) \tag{1}$$

$$\sum_{k=1}^n W_k(i, j) = 1 \tag{2}$$

The advantages of the linear weighting method are that its concept is simple and it is suitable for real-time processing. The drawback is that the fusion image contains strong noise, especially, when the gray difference of the fusion image is significant, it may appear obvious splicing trace and poor visual effect.

2) Component Substitution (CS)

The component substitution algorithm is also called false color fusion algorithm. The most representative algorithm is the intensity-hue-saturation (IHS) transform, where “I” represents density or brightness information, “H” represents chrominance information, and “S” represents saturation information. Although the IHS transform is very important false color fusion algorithm, it is just suitable for three band color image transformation. However, the current imaging systems, i.e. satellite imaging system, could provide far more than three bands. The latest IHS research, the related improvement and discussion to the spectral distortion can refer to the recent literature [2-4].

3) Probability Statistical Model Method

There are many kinds of methods are based on probabilistic statistical model, such as Bayesian estimation theory, Markov random field theory [4-6], etc. The probability and statistics theory is needed to establish the corresponding optimization model, and the expectation maximization or simulated annealing algorithm can be used to solve the problem.

3.1.2 Image fusion algorithm based on transform domain

The transform domain image fusion algorithms include the Discrete Cosine Transform (DCT) and the Fast Fourier Transform (FFT), etc. However, the most important one is based on multi-scale and multi-resolution, such as Wavelet Transform (WT),

Lifting Wavelet Transform (LWT), Discrete Wavelet Transform (DWT), Ridgelet Transform, Pyramid Decomposition, etc. Currently, this category obtains unprecedented success in all kinds of the image fusion practical applications. The most prominent characteristics are that these algorithms have fast computing capabilities to satisfy a large number of practical systems. 3.1.3 Other image fusion algorithm

In recent years, there are some other image fusion algorithms in this field, such as Gradient-based multi-resolution image fusion method, which is based on the system transfer function theory and is established on basis of fusion decomposition model. It is significantly different from the multi-scale decomposition fusion algorithm. While also image fusion algorithm is based on ICA [7]; PDE-based approach to three-dimensional seismic image fusion algorithm [8]; total variation-based image fusion algorithm [9]; image fusion algorithm based on geometry [10]; and in recent years based on joint sparse representation theory and the theory of Compressive Sensing(CS) image fusion algorithm [11], [12]. These algorithms are based on broader basis theories, and they expand the meaning of image fusion itself.

3.2 Feature Level Image Fusion

The feature level algorithm is divided into two steps: target extraction and target feature fusion. In complex conditions, it is difficult to effectively extract the image target feature, which is a hot research area in this field, so the feature level fusion is more dependent on the target feature whether to correctly obtain. When getting the correct target feature, all classification algorithms, such as support vector clustering, fuzzy clustering, and neural network algorithm, can be directly used to fuse the image feature.

1) Joint Statistical

When multi-sensor information is used for classification and decision, we need some type of discrimination scale, and need compare the sensed environment with the known feature. The joint statistics can be used to quickly and efficiently classify the unknown sample probability density function.

2) Constrained Gauss-Markov Estimate

The covariance matrix is used to storage and to restrain relevant information, and can be used as the fundamental geometric reasoning database.

3) Extended Kalman Filter

The Extended Kalman filter can be effectively adopted to make the image registration and then implement the feature layer fusion. It also can reduce the uncertainty of the object location when appearing environment and sensor noise.

4) Neural Network Image Fusion

The characteristics of artificial neural network: inherent parallel structure and parallel processing, distribution storage knowledge, fault tolerance, self-adaptability, etc. Network knowledge representation and acquisition process will be completed at the same time, so the execution speed can be accelerated. Additionally, the image noise exists inevitably in the real world, and even some information may be missing. In this case, the neural network fusion method can also reason in a reasonable way. After the neural network is trained, each image pixel is divided into several classes

during image fusion, so that each image pixel has a membership function vector group. At present, most of the neural network is implemented by simulations, and digital signal processing chips and the relevant software are employed to simulate the parallel compute [13-17].

3.3 Decision Level Image Fusion

The decision level fusion is a joint decision-making process and is more reliable than single sensor. Currently, the main problems of the decision level fusion: due to the time-varying characteristics of the environment and target, the prior knowledge is difficult to obtain. Simultaneously the enormous knowledge base and the design requirement of the object-oriented system hinder the theory and technology development of the decision level fusion. The main decision level image fusion methods are based on the cognitive model algorithm, which needs to use expert system and relational database to analyze fusion judgment. The fusion algorithms on this level are mainly based on Bayes inference, evidence reasoning, neural networks, support vector machines and fuzzy integral fusion algorithm [7-11], etc.

1) Bayesian estimation

The bayesian estimation provides method which assembles sensor information in probability theory rule. The bayesian estimation is based on Bayes' rule basal technology.

2) Fuzzy Logic

The fuzzy logic is a class of multi-valued logic. The reasoning process uncertainty of the multi-sensor fusion can be directly represented by assigning real values for each proposition and operator from 0.0 to 1.0. The uncertainty model of the fusion process is then generated, as well as the subsequent consistency reasoning.

3) Dempster-Shafer (D-S)

The dempster-shafer (D-S) reasoning method: it is the bayesian approach extension, which uses probability interval and uncertainty interval to firm the likelihood function under the assumption of more evidence. The evidence theory can deal with uncertainty which is caused by unknown factors. Here, the belief function rather than probability is considered as a measure, bounding some event probability to establish trust function without explanation precise probability which is difficult to obtain. When constraints limit is strict probability, which becomes probabilistic theory. When evidence is relevant, we may consider using D-S theory promotion methods [18-21].

4 Performance Evaluation of Multi-sensor Image Fusion Method

The performance evaluation of the image fusion effect is an important and meaningful research aspect, that is, how to evaluate the fusion effect or how to evaluate the image fusion quality. Although it is an important step in the image fusion, there still lack systematic evaluation methods. In the literature, the image fusion evaluation mainly consists of the two subjective and objective evaluation methods.

4.1 Subjective Evaluation of Image Quality Fusion

If a person is an image observer, the meaning of the image quality mainly includes two aspects: one is the image fidelity, and another is the image intelligibility. Over many years, people always want to seek quantitative measurement method about the image fidelity and intelligibility to be a criterion of image quality and image design system. Since a human visual system is not fully understood and a quantitative description method about people's psychological factors is not generated, these issues should be resolved in the future.

4.2 Objective Evaluation of Image Quality Fusion

In order to overcome the human visual system, mental status, knowledge background and other uncertainty factors, we mostly use the objective evaluation criterion in the actual evaluation of the fusion effect. Objective evaluation determines and compares the pros and cons of various fusion methods through the calculation of fusion image statistical parameters [19-22].

In order to quantitatively evaluate the effect and quality of the fusion image, assuming the two source images of participating into the fusion are A , B , its image size is $M \times N$, and the fusion image F can be generated through the fusion treatment, several parameters are defined as follows:

1) Entropy

Image entropy is an important index of image information richness, and the entropy value shows how much the image average information is. The greater the entropy value of the fusion image is, the richer the information about the fusion image is, and the better the quality of the image fusion is.

2) Average Gradient

The average gradient can sensitively reflect the expression ability of image tiny details contrasts. It can be not only used to evaluate image clarity, but also reflects the image tiny detail contrasts and texture transform features.

3) Standard Deviation (SD)

The SD reflects the discrete case of the image gray level relative to the average gray level, and it can be used to compare the size of image. If the SD is large, the image grayscale distribution is dispersed, and the image contrasts is big, so more information can be achieved. If the standard deviation and the image contrasts are small and the hue is homogeneous, we do not see too much information.

4) Cross Entropy

The cross entropy called the relative entropy is generally adopted to represent the difference between the two images. The smaller the cross-entropy is, the smaller the image difference is.

5) Correlation Coefficient

The correlation coefficient called similarity measure reflects the relevance of two images. After image fusion, it can reflect the spectrum information of the multispectral image to judge the retention capacity of the fused image spectrum.

4.3 Combination of Subjective and Objective Methods

The combination of subjective and objective quality evaluation method is an important index of the fusion image quality evaluation. It is the combination of artificial intelligence and expert systems fusion method to evaluate the effect [30]. This method does not require the ideal image, and does not take full account of the human visual characteristics. It can quantitatively evaluate the fusion image retaining much significant information (such as variance, contrast and edge information, etc.). It is a practical, effective and versatile method of the image fusion quality evaluation.

5 Conclusions

In this paper, the multi-sensor image fusion is divided into three levels, which are made relatively systematic analyze and compare. This paper makes a systematic summary about the algorithms of the pixel, the feature and the decision levels from a large number of literatures. For lots of the pixel algorithms, the classification and comparison of the pixel level algorithm is presented in detail. Facing numerous the feature level and decision level algorithms, we list some typical algorithms for everyone's reference.

The involved image fusion technology is very extensive, and it is restricted by time and conditions, so there is a lot of intensive detail work need to be continued in the future:

1) Although there are many kinds of the image fusion methods, researchers do not think there is recognized standard and mature theory to support particular type image fusion. For the specific type image fusion, we need to develop corresponding unified mathematical model and integration framework.

2) In this paper, we study the objective evaluation methods are just some commonly evaluation methods, to avoid subjective evaluation of one-sidedness on some level. There are so many image fusion evaluation methods and standards, however, for the specific image fusion, the uniform evaluation criteria becomes an urgent problem to be studied.

3) The rapid image fusion can be achieved by the optimization algorithm and reducing the algorithm complexity. The improvement of the fusion effect often sacrifices the calculation speed and the algorithm complexity. The rapid and simple algorithm is the foundation of practical applications, so it is necessary to optimize the algorithm and study the fast algorithm.

References

1. Mahmood, A., Tudor, P.M., Oxford, W.: Applied Multi-dimensional Fusion. *Computer Journal* 50(6), 646–659 (2007)
2. Gholipour, A., Kehtarnavaz, N., Briggs, R.: Brain Functional Localization: A Survey of Image Registration Techniques. *IEEE Transactions on Medical Imaging* 26(4), 427–451 (2007)

3. Chikr, M., Mezouar, E., Taleb, N., Kpalma, K.: An IHS-based Fusion for Color Distortion Reduction and Vegetation Enhancement in IKONOS Imagery. *IEEE Transactions on Geoscience and Remote Sensing* 49(5), 1590–1602 (2011)
4. John Nisha Anita, S., John Moses, C.: Survey on Pixel Level Image Fusion Techniques. In: *International Conference on Emerging Trends in Computing, Communication and Nanotechnology*, pp. 141–145 (2013)
5. Xu, M., Chen, P.H., Varshney, K.: An Image Fusion Approach Based on Markov Random Fields. *IEEE Geosci. Remote* 49(12), 5116–5127 (2011)
6. Mignotte, M.A.: Multiresolution Markovian Fusion Model for the Color Visualization of Hyper Spectral Images. *IEEE Transactions on Geoscience and Remote Sensing* 48(12), 4236–4247 (2010)
7. Nedeljko, C., David, B., Nishan, C.: Region-based Multimodal Image Fusion Using ICA Bases. *IEEE Sensors Journal* 7(5), 743–751 (2007)
8. Sorin, P., Lavialle, O., Donias, M.: A PDE-based Approach to Three-dimensional Seismic Data Fusion. *IEEE Transactions on Geoscience and Remote Sensing* 46(5), 1385–1393 (2008)
9. Kumar, M., Dass, S.: A Total Variation-based Algorithm for Pixel-level Image Fusion. *IEEE Transactions on Image Processing* 18(9), 2137–2143 (2009)
10. Mark, A., Davenport, B., Hegde, C.: Joint Manifolds for Data Fusion. *IEEE Transactions on Image Processing* 19(10), 2580–2594 (2010)
11. Yu, N., Qiu, T.S., Wang, A.Q.: Image Features Extraction and Fusion Based on Joint Sparse Representation. *IEEE Journal of Selected Topics in Signal Processing* 5(5), 1074–1082 (2011)
12. Wan, T., Qin, Z.C.: An Application of Compressive Sensing for Image Fusion. *International Journal of Computer Mathematics* 4, 1–16 (2011)
13. Rong, W., Fanliang, B., Hua, J., et al.: A Feature-level Image Fusion Algorithm Based on Neural Networks. In: *2007 1st International Conference on Bioinformatics and Biomedical Engineering, Wuhan*, pp. 821–824 (2007)
14. Kong, A., Zhang, D., Kamel, M.: Palmprint Identification Using Feature-level Fusion. *Pattern Recognition* 39(3), 478–487 (2006)
15. Ross, A., Govindarajan, R.: Feature Level Fusion Using Hand and Face Biometrics. *Biometric Technology for Human Identification II* 57(79), 196–204 (2005)
16. Kong, A., Zhang, D., Kamel, M.: Palmprint Identification Using Feature-level Fusion. *Pattern Recognition* 39(3), 478–487 (2006)
17. Wu, K.X., Wang, C.H., Li, L.H.: Image Fusion at Pixel Level Algorithm is Introduced and the Evaluation Criteria. In: *International Conference on Educational and Network Technology*, pp. 585–588 (2010)
18. Qian, T., Veldhuis, R.: Threshold-optimized Decision-level Fusion and Its Application to Biometrics. *Pattern Recognition*, 823–836 (2009)
19. Dawoud, A., Alam, M.S., Bal, A.: Target Tracking in Infrared Imagery Using Weighted Composite Reference Function-based Decision Fusion. *IEEE Transactions on Image Processing* 15(2), 404–410 (2006)
20. Huan, R., Pan, Y.: Decision Fusion Strategies for SAR Image Target Recognition. *IET Radar Sonar&Navigation* 5(7), 747–755 (2011)
21. Yi, W., Wei, C., Yi, M.S.: Multi-sensor Decision Level Image Fusion Based on Fuzzy Theory and Unsupervised FCM. In: *Proceedings of the SPIE-The International Society for Optical Engineering*, pp. 62000–62007 (2006)
22. Kong, W.W.: Multi-sensor Image Fusion Based on NSST Domain I2CM. *Electronics Letters* 49(13), 802–803 (2013)

An Novel Quality Classification for Ring Die Pellet*

Kun Zhang^{1,2}, Minrui Fei^{2,**}, Jianguo Wu³, and Peijian Zhang³

¹ School of Electronics, Electrical Engineering and Computer Science,
Queen's University Belfast, United Kingdom

² School of Mechatronic Engineering & Automation, Shanghai University,
Shanghai Key Laboratory of Power Station Automation Technology, Shanghai

³ School of Electrical Engineering, Nantong University, Nantong, Jiangsu 226019
mrfei@staff.shu.edu.cn

Abstract. Ring die granulator is a high energy consumption and complex system. Conventional method for improvement the quality of pellets is detected by human sense offline. Aimed to lowness of efficiency and bigness of error, a novel strategy is present for the intelligence quality classification. By means of machine vision, after extract the feature, the pellet edge images are captured based canny algorithm, and the quality classification can be accuracy got by FSVM. Real pellet images are conducted to prove the effect. Compared with other methods by the simulation, the present approach has apparent advantages. The result of the present work implied that, the present method can be applied to auto quality detection and the classification results can be used as the feedback signals in controller to update the parameters to control the ring die granulator well.

Keywords: Ring die pellet, edge detection, canny algorithm, FSVM, quality classification.

1 Introduction

Ring die granulators are widely used in feed processing area and the installed capacity of hoop standard granulators can reach 100MW and see details in literature [1]. In such a situation, under the premise of ensuring the quality of granulation, how to improve reduce consumption must be considered. At present in our country, ring die granulators are used mostly by manual control with the low quality outcome. It is difficult to control well not only the granulator structure like a “black box”, which he measurements of the granulator are too limited but also the characteristics: coupling, nonlinear, large time delay. More details in literature [2]. To control the “black box” well and improve the quality, engineers detect and analyse the product offline, and with the analysis results, they has known how to adjust the parameters of input

* This work is supported by Key Project of Science and Technology Commission of Shanghai Municipality under Grant No. 14JC1402200, by Nantong Research Program of Application Foundation under Grant BK2012030, and by China Scholarship Council program under Grant No. 201406890060.

** Corresponding author.

temperature and motor current. But it comes to the low quality rate for the long time analysis.

In this paper, a novel strategy by means of machine vision and machine learning is present for the intelligence quality classification. The machine vision is to extract the feature and capture the edge image based on canny algorithm. In addition, a FSVM method is used to classify the pellets. The computer simulation results are presented to verify the feasibility of the method. With the good performance of the result can be used as the feedback signals in controller to adjust the control parameters in future.

This paper is organized as follows. In Section 2, we analysis the structure of ring die granulator. In Section 3 we investigate canny edge detection method for capture the image. In Section 4 we introduce FSVM for classification. In Section 5 we conduct experiments to compare two classification methods. Section 6 concludes this work.

2 Analysis the Stricture of Ring Die Granulator

Fig.1 presents the structure of ring die granulator and more details in literature [3]. The supplies of the hopper are sent to the conditioner by feeder which is controlled by inverter), the heat steam and water are as inputs, and the conditioner can make the supplies reach the right temperature and moisture. Condition is the pre-work of granulation which is closely related to the quality of the product. The key of the control is to balance the output temperature of the conditioner.

Where 1-rack; 2-magnet; 3-blanking chute; 4- loop die; 5-press roll; 6-feed motor; 7-feed reducer; 8-hopper; 9-blanking gate; 10-electric steam flow control valve; 11-electric level flow control valve; 12- temperature sensor; 13-feeder; 14-conditioner; 15-condition reducer ; 16-condition motor; 17-main gearbox; 18-main motor of granulation.

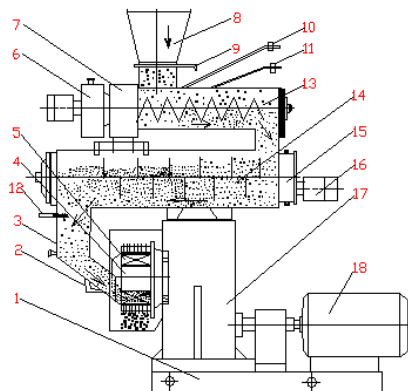


Fig. 1. Schematic diagram of ring die granulator

3 Edge Detection and Feature Extraction

3.1 Canny Edge Detection Algorithm

Edge is one of the most important characteristics of machine vision, which present part areas significantly changes. The edges are chosen as the main features for detection can reduce over information and maintain the shape information. In an historical paper, Marr and Hildreth [4] introduced the theory of edge detection and described a method for determining the edges using the zero-crossings of the Laplacian of Gaussian of an image. Haralick [5] determined edges by fitting polynomial functions to local image intensities and finding the zero-crossings of the second directional derivative of the functions. and Shyu [6] in which edge contours were represented by parametric curves that fitted to high-gradient image pixels with weights proportional to the gradient magnitudes of the pixels.

In image edge detection, traditional algorithms have mentioned cannot satisfy the performance of suppress noise and edge precise positioning. i.e., smooth filtering not only reduce the noise but also improve the uncertainty of edge precise positioning.

Among the edge detection methods proposed so far, the Canny edge detector is the most rigorously defined operator and is widely used. The popularity of the Canny edge detector can be attributed to its optimality according to the three criteria of good detection, good localization, and single response to an edge.

Canny pointed out following three rules to analysis the edge detection.

1) signal-to-noise ratio (SNR) rule

Edge error detection rate should be as low as possible, and the false edges. i.e., SNR should be as large as possible, because of the larger the output SNR the low the error rate. The SNR can be described in formula (1).

$$SNR = \frac{\left| \int_{-\sigma}^{+\sigma} G(-x) f(x) dx \right|}{n_0 \left[\int_{-\sigma}^{+\sigma} f^2(x) dx \right]^{\frac{1}{2}}} \quad (1)$$

Where $f(x)$ is the impulse response within $[-\sigma, +\sigma]$. $G(x)$ is the edge. n_0 is the root mean square value of Gaussian noise.

2) precision position rule

to detect the real edge, in mathematics, Loc in filtering function should be as large as possible. The Loc can be described in formula (2)

$$Loc = \frac{\left| \int_{-\sigma}^{+\sigma} G(-x) f'(x) dx \right|}{n_0 \left[\int_{-\sigma}^{+\sigma} f'^2(x) dx \right]^{\frac{1}{2}}} \quad (2)$$

Where $G(-x)$ 、 $f'(x)$ is first derivative of $G(-x)$ and $f(x)$.

3) single edge response rule

To same edge the responses should be as low as possible, i.e., one response to each single edge. The average distance is max value of filter to edge response, and can be described in formula (3).

$$d_{\max} = 2\pi \left[\frac{\int_{-\sigma}^{+\sigma} f'^2(x) dx}{\int_{-\sigma}^{+\sigma} f''^2(x) dx} \right]^{\frac{1}{2}} \approx kW \tag{3}$$

The implementation of the Canny edge detector [7,8] follows the steps below.

- 1) Smooth the image with an appropriate Gaussian filter to reduce desired image details. Gaussian function is as following.

$$H(x, y) = \exp\left(-\frac{x^2 + y^2}{2\sigma^2}\right) \tag{4}$$

$$G(x, y) = f(x, y) * H(x, y) \tag{5}$$

Where $f(x, y)$ is image matrix.

- 2) Determine gradient magnitude and gradient direction at each pixel.

$$H_1 = \begin{vmatrix} -1 & -1 \\ 1 & 1 \end{vmatrix} \text{ and } H_2 = \begin{vmatrix} 1 & -1 \\ 1 & -1 \end{vmatrix}$$

$$\varphi_1(x, y) = f(x, y) * H_1(x, y)$$

$$\varphi_2(x, y) = f(x, y) * H_2(x, y)$$

$$\varphi(x, y) = \sqrt{\varphi_1^2(x, y) + \varphi_2^2(x, y)} \tag{6}$$

$$\theta_\varphi = \tan^{-1} \frac{\varphi_2(x, y)}{\varphi_1(x, y)} \tag{7}$$

- 3) If the gradient magnitude at a pixel is larger than those at its two neighbours in the gradient direction, mark the pixel as an edge. Otherwise, mark the pixel as the background.
- 4) Remove the weak edges by hysteresis thresholding.

3.2 Feature Extraction

These images are firstly segmented by PCNN and labelled, and then morphologically processed to extract the approximate locations and contours. Patel [9] introduce an approach by twenty-nine features, including ten appearance features, twelve colour features and seven fitting features. in our work, we choose three appearance features for feature extraction, which are length, wide, area and gray level . Because of over and lower than average, the pellet is below standard. Fig.2 is sum of the each feature extraction.

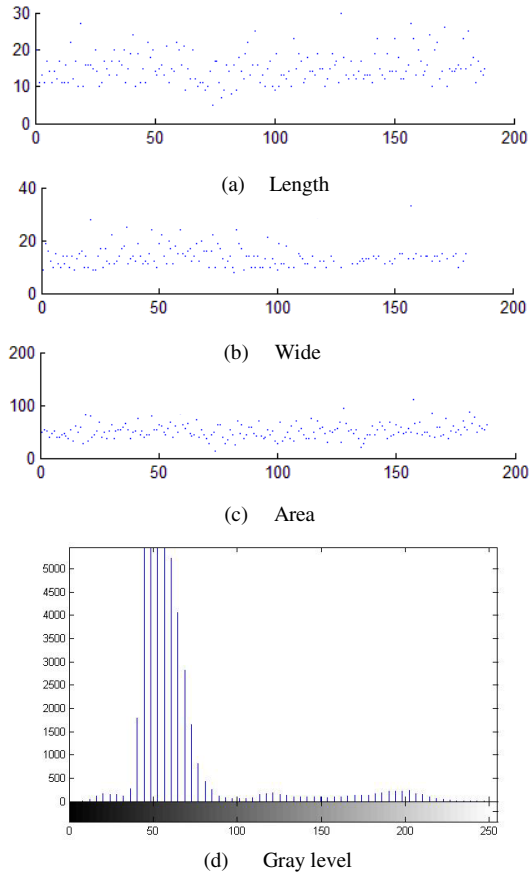


Fig. 2. Four features of pellet

4 FSVM Model

Recently, fuzzy support vector machine (FSVM) has been a hot tool for data classification [10-12]. Its basic idea is to map data into a high dimensional space and find a separating hyper plane with the maximal margin.

Given training data $x_i \subseteq R^n, i = 1 \dots l$ in multiple classes, and a vector of labels $y \in R^m$ such that $y_i \in \{-1, 1\}$, SVM solves a quadratic optimization problem:

$$\begin{aligned} & \min \frac{1}{2} \omega^T \omega + C \sum_{i=1}^l \xi_i & (8) \\ & \text{Subject to } y_i(\omega^T \phi(x_i) + b) \geq 1 - \xi_i \\ & \xi_i \geq 0, i = 1, \dots, l \end{aligned}$$

Where C is the penalty parameter of the error term, ξ_i is the measure of error in the SVM and we usually call it slack variable.

For classification prognostics problem, it is often that the training points and the measured point. So a fuzzy membership associated with each training point is used. For multivariate time series after phase space reconstruction, we make the vector if fuzzy membership is,

$$\begin{aligned} s_i &= [s_{11}^i, s_{21}^i, \dots, s_{m1}^i, s_{12}^i, s_{22}^i, \dots, s_{m2}^i, \dots, s_{uv}^i, \dots, s_{mv}^i]^T & (9) \\ & u = 1, 2, \dots, m, v = 1, 2, \dots, n \end{aligned}$$

Where m is the embedding dimension and n is the number of parameters. We make the fuzzy membership s_{uv}^i be a function of (p, η, m, u, v) .

$$s_{uv}^i = f(p, \eta, m, u, v) \tag{10}$$

Where p the position of the point in the multivariate is input samples and η is lower bound of fuzzy memberships. For one of n parameters. We make the last point be the most important and choose its fuzzy membership is 1, and make the first point of m_i input points be the least important and its fuzzy membership is η . By applying the boundary conditions, we can get the multivariate fuzzy membership function is,

$$s_{uv}^i = \eta_i + (1 - \eta_i) \left(\frac{p_{uv} - p_{1v}}{m_v} \right)^2 \tag{11}$$

Then, we can reconstruct function (8) as

$$\min \frac{1}{2} \omega^T \omega + C \sum_{i=1}^l s_i \xi_i \tag{12}$$

Here training vectors x_i mapped into a higher (maybe infinite) dimensional space by the function ϕ . FSVM finds a linear separating hyper plane with the maximal margin in this higher dimensional space. For any testing instance x , the decision function is

$$f(x) = \text{sgn}(\omega^T \phi(x) + b) \tag{13}$$

Furthermore, $K(x_i, x_j) \equiv \phi(x_i)^T \phi(x_j)$ is called the kernel function. Literature [13] introduces some favourite kernels.

- Linear: $K(x_i, x_j) = x_i^T x_j$
- Polynomial: $K(x_i, x_j) = (\gamma x_i^T x_j + r)^d, \gamma > 0$
- RBF: $K(x_i, x_j) = \exp(-\gamma \|x_i - x_j\|^2), \gamma > 0$
- Sigmoid: $K(x_i, x_j) = \tanh(\gamma x_i^T x_j + r)$

RBF kernel has better performance in self-study than other kernels, but the parameters of RBF kernel are very important. There are two parameters in RBF kernel: the penalty parameter C and the kernel parameter γ . The optimization (C, γ) will make the FSVM have the best performance.

After model is trained by solving the above optimization problems, the classification of performance can be evaluated by cross validation.

5 Experiment and Result

We take three experiments to verify the performance of this intelligence quality classification. These experiments were carried out on an Intel dual-core 3.0GHz PC with 4 GB RAM. The first two of the computations were performed with Matlab 7.0, and the third experiment was performed with visual studio 2010.

Our first experiment is to compare three edge detection algorithms: Canny algorithm, Sobel algorithm and Prewitt algorithm, so that only the better one is used for classification analysis. For this comparison, we take an original pellets picture Fig.3 (a) as the template. Fig.3 (b) is canny algorithm, Fig.3 (c) is sobel algorithm. Results show that canny algorithm is significantly more accuracy than others. A right threshold is important to detection. Fig. (4) is an example of error result cause of the bad threshold. In Fig.4 (a) there are six pellets, while two of them are nearby and the other four are separated. In Fig.4 (b) with the wrong threshold, canny cannot detect the middle two and mix as a single. In Fig.4 (c) canny algorithm can clearly detect all of them with the right threshold.

The second experiment is to testify the accuracy of classification. The samples are collected in this study with the help of a company in Shandong Province. Before doing experiments, data sets are scaled. With training, validation, and testing data together, we scale each feature to $[0, 1]$.

Many methods can optimize operating parameters. Compare with these methods, genetic algorithm with a lot of advantages, such as spend less time in optimizing. Genetic algorithm is given to optimize operating parameters..

Encoding parameters and population initialization: the parameters of FSVM model are represented by a chromosome composed of float number code which can avoid decoding and coding repeatedly.

The construction of fitness function: the fitness function is the unique information and plays a critical role to measure GA's performance.

Selection operation: based on the fitness function, compare the best chromosome A of the old generation and the best chromosome B of the new generation, the worst chromosome of the new generation is replaced by A if B is better than A, and B is replaced by A if A is better than B. the selection method can avoid the drawback of high fitness chromosome occupies population quickly in early stage.

Offspring forms a new population in the next generation and replaces the old population. The evolutionary process proceed until stop conditions are satisfied and then the best chromosomes are presented as a solution.

Given 100 samples to train and get the best parameters of SVM. Fig.5 is the result of searching best parameters.Fig.6 is the test result of classification.

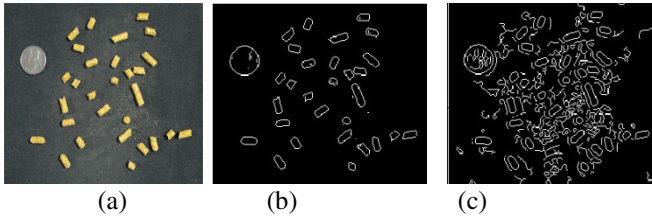


Fig. 3. compare with three edge detection algorithms

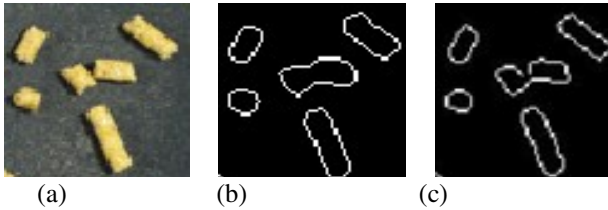


Fig. 4. Detail detection

We can draw the conclusion from table.1 that FSVM has obvious advantages not only training time is competitive but also the classification accurate rated is proved.

The third experiment combine canny algorithm and FSVM algorithm with visual C#. Fig.7 is the main interface with two parts. The left side is ActiveX interface. The right side is visual interface. The process of auto classification is as following.

The first step is to load image. To obtain a high speed to deal with image, we read out only a part of the image sensor as large as 640×600 pixels. The second step is to local the detection area. The third step is to analyze the image and list all the information including area, length, wide, and RGB. The fourth step is to set the qualified pellet parameters by expert experience. The fifth step is to screen the qualified pellet and label it. Fig.8 is the result of qualified pellet classification. In this picture, there are thirty three pellets and fifteen are classified to good. In manual vision inspection fourteen are good. Comparison with manual vision inspection, the result is satisfied.

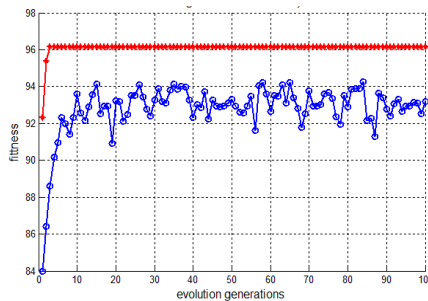


Fig. 5. Result of CV-accuracy based on genetic algorithm

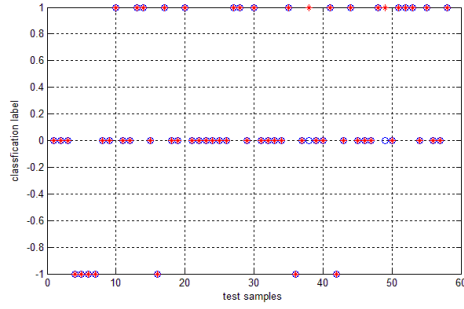


Fig. 6. Test result of classification

Table 1. Comparison among four classification algorithm

algorithm	188 samples		739 samples	
	accuracy	Train time	accuracy	Train time
FSVM	96.816%	6.3 s	98.154%	12.2 s
SVM	93.227%	7.6 s	95.483%	15.3 s
ANN	91.348%	8.9 s	93.383%	17.9 s
RIPPER	87.235%	11.3 s	91.492%	20.5 s

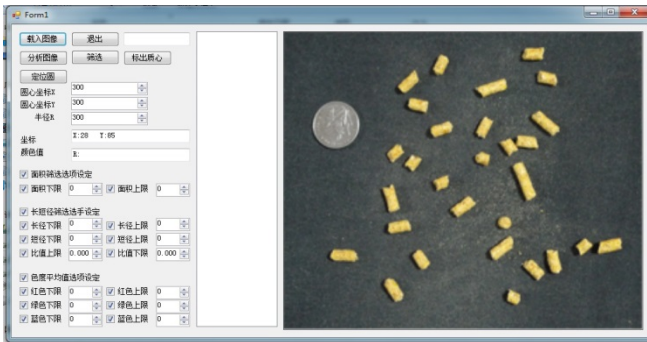


Fig. 7. Interface of auto classification



Fig. 8. Classification result

6 Conclusions and Future Work

A new method base on canny edge algorithm and FSVM for classify the pellet quality is presented. The method employs canny edge algorithm to detect the edge of each pellet, and FSVM to classify the pellet into three parts. Experiments on real images show that the proposed method is the effectiveness in searching the defect of pellet. This method has more competed than other algorithm. However, our method is more sensitive to changes in light and training time is too long which cannot meet with online needs. The feature can extend to the colour, so that we can classify the wet and dry pellets. In future, after perfection of these works, with these kinds of information the engineers can revise control parameters to adjust the input temperature valve and main motor current and control the granulator well.

References

1. Li, Y.C., Wan, Z.S.: Factors Affedting Quality and Granulation Property of Pellet Feeds. *J. Anhui Agri Science* 39(10), 5929–5930 (2011)
2. Zhang, K., Fei, M.R., Zhang, P.J., Wu, J.G., Hu, Z.J.: Application Study on Intelligent Control of a Class of Time Delay Systems with Parameter Uncertainty. *Chinese Journal of Scientific Instrument* 35(6), 1394–1401 (2014)
3. Zhang, K., Wu, J.G., Zhang, P.J.: Study on the Control System of the Hoop Standard Granulator Based on the Expert System. *Computers and Applied Chemistry* 29(10), 1249–1252 (2012)
4. Marr, D., Hildreth, E.: Theory of edge detection. *Proc. Roy. Soc. London B* 207, 187–217 (2010)
5. Haralick, R.: Digital Step Edges From Zero Crossing of Second Directional Derivatives. *IEEE Trans. Pattern Anal. Mach. Intell.* 6, 58–68 (2011)
6. Goshtasby, A., Shyu, H.L.: Edge Detection by Curve Fitting. *Image Vision Comput.* 13(3), 169–177 (2005)
7. Mokrzycki, W.: Canny Edge Detection Algorithm Modification. In: *Computer Vision and Graphics - International Conference*, pp. 533–540 (2012)
8. Varadarajan, S.: A Distributed Psycho-visually Motivated Canny Edge Detector. In: *IEEE International Conference on Acoustics, Speech, and Signal Processing*, pp. 822–825 (2010)
9. Patel, K.K.: Machine Vision System: A Tool for Quality Inspection of Food and Agricultural Products. *Journal of Food Science and Technology* 49(2), 123–141 (2012)
10. Diao, Z.H., Zhao, X.Y., Guo, S.L.: A New SVM Multi-class Classification Algorithm Based on Balance Decision Tree. *Control and Decision* 1, 151–154 (2010)
11. Chang, C.C., Lin, C.J.: LIBSVM: A library for support vector machines. *ACM Transactions on Intelligent Systems and Technology* 2(27), 117–127 (2011)
12. Zhu, Z.A., Chen, W., Wang, G., Zhu, C., Chen, Z.: Parallel Primal Gradient Descent Kernel SVM. In: *Proceedings of the IEEE International Conference on Data Mining* (2009)
13. Chang, Y.W., Hsieh, C.J., Chang, K.W., Ringgaard, M., Lin, C.J.: Training and Testing Low-degree Polynomial Data Mappings Via Linear SVM. *Journal of Machine Learning Research* 11, 1471–1490 (2010)

Stereo Matching for Binocular Underwater Images Using SURF Operator and Epipolar Restriction

Nengjun Wang¹, Bin bin Peng¹, Daqi Zhu^{1*}, and Pengfei Xu²

¹Laboratory of Underwater Vehicles and Intelligent Systems, Shanghai Maritime University, Haigang Avenue 1550, Shanghai, 201306, China

²Underwater Engineering Institute, China Ship Scientific Research Center, Wuxi 214082, China
zdq367@aliyun.com

Abstract. The stereo matching algorithm of binocular underwater images based on SURF (Speeded Up Robust Features) operator and epipolar restriction is presented. With complex underwater environment, epipolar restriction is introduced to solve the impact of refraction. Fast hessian-matrix detector is used to detect the interest points and the SURF descriptor is used to describe the points' features. Euclidean distance and epipolar restriction are used for features matching to simplify the calculation. The method has better performance than traditional algorithm on computing efficiency and matching accuracy.

Keywords: Stereo matching, Speeded Up Robust Features (SURF) operator, epipolar restriction, underwater image processing.

1 Introduction

Stereo matching is the most complex and the most difficult part in stereo vision. Its proposition is determined the corresponding relationship of pixels in different spatial image on the same scene to search corresponding points on the images. Stereo matching algorithms in common use can be divided into two main categories, local and feature-based matching [1]. Local methods consider each pixel in isolation of others, and they take advantage of the relevance of gray information between local windows to get pixels matched. In rich details area, local methods can reach higher accuracy. With window-based techniques a trade-off has to be made with respect to the window size and in occlusion, distortion, and lack of texture area, local techniques may lead to false matching [2]. Local methods typical implemented by Kanade T [3] and Quan L [4], Quan L's methods studies local growth stereo matching algorithm, the method is based on regional segmentation, although it can obtain dense disparity map, but the selective of seeds is more complex, some extent improve the performance of matching, but still consuming much time.

Feature-based matching techniques have significant applications in 3D reconstruction, target recognition and other domains. Feature-based matching techniques extract points, lines or edges features etc. on the image pairs to search corresponding points, feature-based matching techniques do not depend on the gray, insensitive to noise,

great robustness to light intensity, geometric distortion and high accuracy. David Lowe [5] proposed scale invariant feature transform (SIFT) in 1994, which has very excellent property on features extracting. SURF is the improvement of SIFT, compared with SIFT, SURF consumes less time. Hence our method is based on SURF to satisfy the request of real time computing.

This paper mainly studies how to extract and match features on the images obtained by underwater vehicle. While underwater imaging itself poses many potential challenges, the harsh environment lends itself to turbidity, making it far more difficult to observe features in sufficient details [6]. Considering this, we utilize SURF algorithm [7], one has to strike a balance between the speed and performance, reducing the descriptor's dimension and complexity, while keeping it sufficiently distinctive. First, the image is preprocessed and 'interest points' are selected at distinctive locations in the image, such as corners, blobs, and T-junctions. Next, the neighborhood of every interest point is represented by a feature vector. Finally, the descriptor vectors are matched between different images with epipoalr curves. This restriction could reduce search area from the whole image to a curve, not only cut down the error probability, but also increase computing efficiency.

The remaining part of this paper we first briefly introduce our method in the second section, on the basis of this, epipolar geometry and SURF algorithm are introduced in the third section, then experiment is presented to compare the performance our method with traditional method, at last, we conclude our experiment.

2 Images Obtain and Matching Algorithms

Two cameras installed on underwater vehicle to obtain images. We assume cameras' focus and other parameters are invariant. Our camera model is UWC-325/p/e of Outland Technology. Cameras were already Precalibrated [8]: Scale factors in the x, y coordinate directions, the pixel skew and pixel coordinates of the principal point. These parameters are the intrinsic parameters of the camera. Zhang's calibration method [9] is used to figure out camera's other extrinsic parameters. Our remaining work includes: image calibration, 'interest point' detection and matching. Algorithm procedure shows as follows (Fig 1):

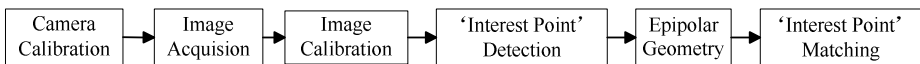


Fig. 1. Algorithm procedure

Fig 2(a) and 2(b) show images obtained by underwater vehicle after preprocessing and calibration. Then have feature points matched with SURF algorithm based on epipoalr geometry.

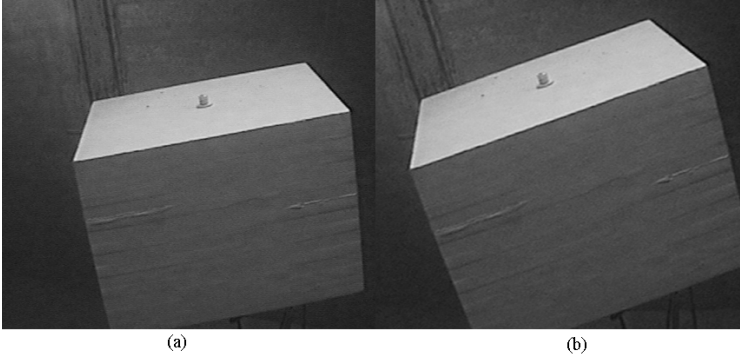


Fig. 2. Images after preprocessing and calibration

2.1 Epipolar Geometry

Almost all stereo algorithms rely on epipolar geometry to reduce the search space when locating matching pixels. Under epipolar geometry, given a point x_1 in one image and its corresponding point x_2 in the other image, the fundamental matrix F imposes the epipolar restriction [10]:

$$x_2^T F x_1 = 0 \tag{1}$$

This equation restricts our correspondence search from two dimensions to just one dimension, we only need to search the corresponding point of one image on the epipolar lines on the other image, which would reduce our computational complexity. When it comes to underwater images, we must take refraction into consideration. The amount of bending caused by traveling from one medium to another can be found using Snell’s Law [11]:

$$n_1 \sin \theta = n_2 \sin \phi \tag{2}$$

where n_i is the refraction index of medium i and θ, ϕ are angle of incidence and angle of refraction. Our cameras are placed inside a waterproof container filled with air, so $n_1 = 1$, also we neglected the glass window between air and water for easy operation. As the model shows in Fig 3, cross section of a camera system centered at V and under the influence of a planar refractive interface. By reference the paper of Jason [2], with Snell’s Law, we can conclude that:

$$[n^2 (d^2 + u^2) - u^2] (x - u)^2 - u^2 z^2 = 0 \tag{3}$$

where $x = \|M_{proj} - M\|$ and $z = \|M_{proj}\| - d$, $n = n_2 / n_1$, u is the distance between point projection Q on the refraction interface and O , when projecting points into the camera, the only unknown is u .

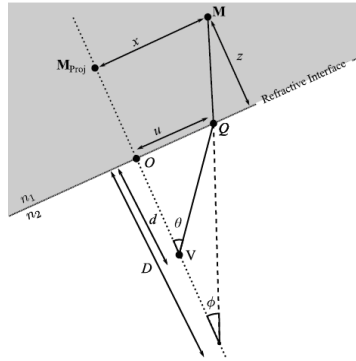


Fig. 3. Planar refractive interface

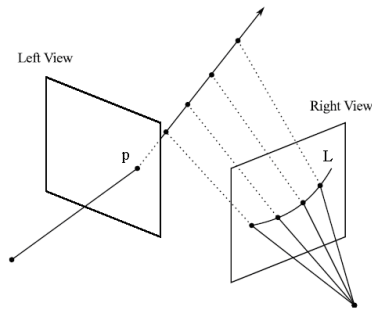


Fig. 4. A feature point and its corresponding epipolar curve

Equation (3) has four roots in u , but only one root is meaningful. Once we have projected M onto the refraction interface to obtain Q , then we can find the actual image point for M , then we can get the new epipolar curve instead of a straight line in normal epipolar geometry. As figure shows in Fig 4, a feature in the left view and its corresponding epipolar curve in the right view. In traditional non-refractive epipolar geometry this curve is actually a straight line. The nonlinear effect of refraction warps this line into a curve. In one image point p corresponding to the other image is on the curve L . Before apply epipolar geometry constraint matching feature points, we get the images calibrated to ensure they meet the epipolar constraint. This allows us to map rays and points to and from global space to each of the cameras' local coordinate systems, which are prepared for 3D reconstruction.

Next we would match features points on images with epipoalr restriction in SURF algorithm, which would cut down computational complexity, correspondingly improve the efficiency and reduce computing time to ensure real time matching, now we simply discuss SURF algorithm.

2.2 SURF Algorithm

The SURF detector is based on the determinant of the hessian matrix [7]. We can calculate the Hessian matrix $H(x, \sigma)$, as function of both space $x = (x, y)^T$ and scale σ :

$$H(x, \sigma) = \begin{bmatrix} L_{xx}(x, \sigma) & L_{xy}(x, \sigma) \\ L_{xy}(x, \sigma) & L_{yy}(x, \sigma) \end{bmatrix} \quad (4)$$

Here $L_{xx}(x, \sigma)$ refers to the convolution of the second order Gaussian derivative $\partial^2 g(\sigma) / \partial x^2$ with the image at point $x = (x, y)^T$ and similarly for L_{yy} and L_{xy} . These derivatives are known as Laplacian of Gaussians. Gaussian second order partial derivatives in y -direction and xy -direction, and our approximations thereof using box filters show in Fig 5(a). Bay [7] proposes the following formula as an accurate approximation for the Hessian determinant using the approximated Gaussians:

$$\det(H_{approx}) = D_{xx} D_{yy} - (0.9 D_{xy})^2 \quad (5)$$

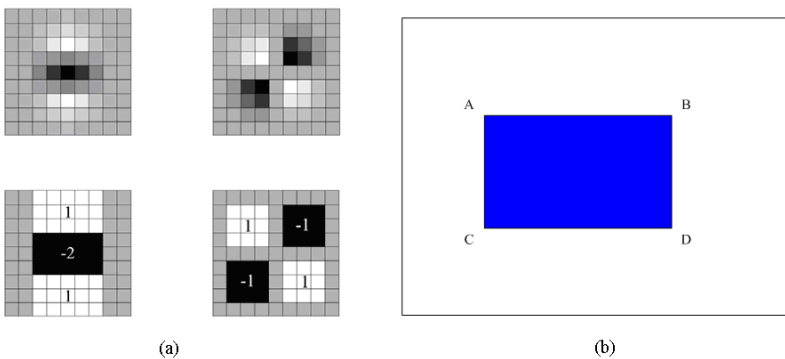


Fig. 5. (a) Gaussian second order partial derivatives. (b) Area computation using integral images.

At the same time the use of an intermediate image representation known as the ‘Integral Image’ [12]. Given an input image I and a point $(x, y)^T$ the integral image I_{Σ} is calculated by the sum of the values between the point and the origin. Formally this can be defined by the formula:

$$I_{\Sigma}(x, y) = \sum_{i=0}^{i \leq x} \sum_{j=0}^{j \leq y} I(x, y) \quad (6)$$

If we consider a rectangle bounded by vertices A, B, C and D as in Fig 5(b), the sum of pixel intensities is calculated by:

$$\Sigma = A + D - (C + B) \quad (7)$$

Since computation time is invariant to change in size this approach is particularly useful when large areas are required. SURF makes good use of this property to perform fast convolutions of varying size box filters at near constant time.

The responses are weighted with a Gaussian centered at the interest point. In keeping with the rest the Gaussian is dependent on the scale of the point and chosen to have standard deviation 2.5σ . The dominant orientation is selected by rotating a circle segment covering an angle of $\pi/3$ around the origin. At each position, the x and y responses within the segment are summed and used to form a new vector. The longest vector lends its orientation the interest point. The sketch map is illustrated in Fig 6(a).

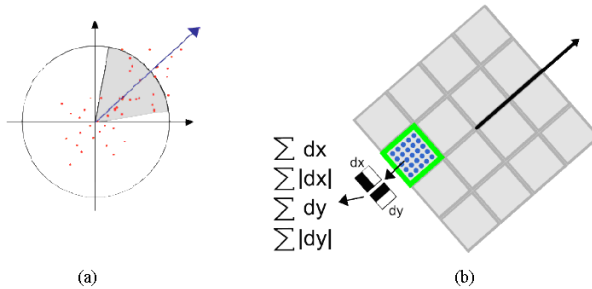


Fig. 6. (a) Determines of the dominant orientation. (b) Descriptor Components.

$$v_{subregion} = [\sum dx, \sum dy, \sum |dx|, \sum |dy|] \quad (8)$$

The first step in extracting the SURF descriptor is to construct a square window around the interest point. The descriptor window is divided into $4 * 4$ regular sub regions. Therefore each sub region contributes four values to the descriptor vector leading to an overall vector of length $4 * 4 * 4 = 64$. The descriptor components show in Fig 6(b), the green square bounds one of the 16 sub regions and blue circles represent the sample points at which we compute the wavelet responses.

3 Experiment

Now we have calibrated cameras and processed images show in Fig 2(a) and Fig 2(b). With epipolar restriction, we can narrow down searching area on a curve of each feature point. SURF describes the length and orientation of each point. We use multi-dimensional vector space's Euclidean distance as the matching criteria [13]. Specific processes are follows:

Step 1: take one feature point x_1 as original the feature point shows in Fig 2(a), compute the Euclidean distance D_i ($i=1,2,3,\dots$) between original feature point and the corresponding point on the epipoalr curve in the other image. We suppose the minimum of distances D_i away from the original feature point is the corresponding feature point of x_1 , if the value less than the threshold, assume the point is the corresponding points of x_1 , denote it as x_2 , then go to step 2, else get next feature point matched and exclude x_1 .

Step 2: take x_2 in Fig 2(b) as original feature point, repeat step 1, figure out the corresponding point x_3 in Fig 2(a).

Step 3: if $x_1=x_3$, consider that x_1 and x_2 successfully matched, else exclude it.

Fig 7 shows the matching result without epipolar restriction, In Fig 7, notice that details in the magnified portion, many matching lines are cross together, a lot of features are mismatched. In Fig 8, most of feature points are correctly matched with epipolar restriction, achieving better matching effects.

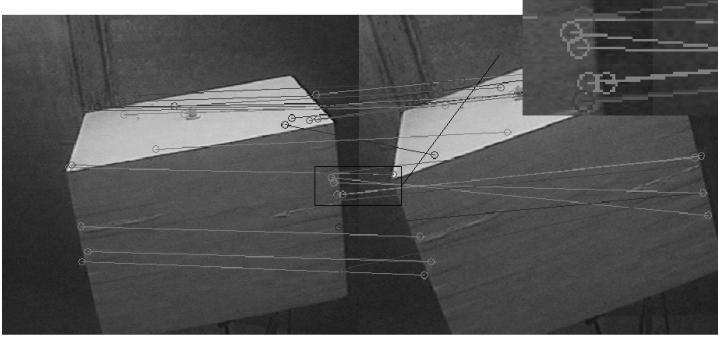


Fig. 7. Matching without epipolar restriction

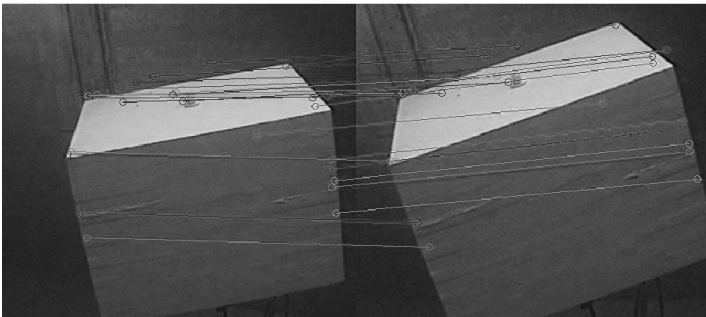


Fig. 8. Matching with epipolar restriction

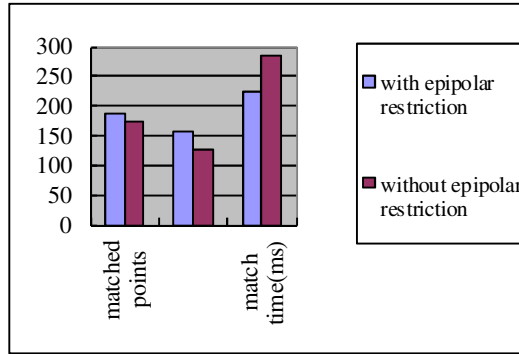


Fig. 9. Comparison of with/without epipoalr restriction

Groups images collected in different environment and get those images matched, then analyze kinds of information compare to conventional SURF algorithm. Our algorithm has great performance than the conventional algorithm, the table 1 shows the performance in Table 1.

Table 1. Comparison of matching information with epipolar restriction and without epipolar restriction

matching information	with epipolar restriction	without epipolar restriction
matching points	186	173
correct matching points	157	104
match time(ms)	324.57	405.76

From experiments we can conclude that: SURF algorithm has great performance in the details, with epipolar restriction, more feature points get correctly matched, the percentage of correct matching points is over 84%, while without epipolar restriction the number is around 60%, and consuming less computing time, our method saves 20% time more than the old technique, achieve the request of real time matching for 3D reconstruction.

4 Conclusion

Stereo matching have very important effect in three-dimensional reconstruction and robot navigation, against to the drawback in existing algorithm, we make the use of epipolar restriction to improve computing efficiency and increase the accuracy of matching. The results show that our method can get feature points matched quick enough to satisfy the request of real time matching.

Acknowledgments. This project is supported by the Creative Activity Plan for Science and Technology Commission of Shanghai (13510721400) and the Innovation Program of Shanghai Municipal Education Commission (13ZZ123).

References

1. Cao, M., Zhang, G., Chen, Y.: Stereo matching of light-spot image points in light pen in binocular stereo visual. *Optik* 125, 1366–1370 (2014)
2. Jason, G.: Underwater Stereo Matching and its Calibration. University of Alberta (2011)
3. Kanade, T., Okutomi, M.: A stereo matching algorithm with an adaptive window: Theory and experiment. *IEEE Trans. Pattern Anal.* 16, 920–932 (1994)
4. Lhuillier, M., Quan, L.: Match propagation for image-based modeling and rendering. *IEEE Trans. Pattern Anal.* 24, 1140–1146 (2002)
5. Lowe, D.G.: Distinctive image features from scale-invariant keypoints. *Int. J. Comput. Vision* 60, 91–110 (2004)
6. Kocak, D.M., Dalglish, F.R., Caimi, F.M., Schechner, Y.Y.: A focus on recent developments and trends in underwater imaging. *Mar. Technol. Soc. J.* 42, 52–67 (2008)
7. Bay, H., Ess, A., Tuytelaars, T., Gool, L.V.: Speeded-up robust features (SURF). *Comput. Vis. Image Und.* 110, 346–359 (2008)
8. Hata, K., Etoh, M.: Epipolar geometry estimation and its application to image coding. In: 1999 International Conference on Image Processing, pp. 472–476. IEEE Press, New York (1999)
9. Zhang, Z.: A flexible new technique for camera calibration. *IEEE Trans. Pattern Anal.* 22, 1330–1334 (2000)
10. Haupt, R.L., Cote, M.: Snell’s law applied to finite surfaces. *IEEE Trans. Antenn Propag.* 41, 227–230 (1993)
11. Hartley, R., Zisserman, A.: Multiple view geometry in computer vision. Cambridge University Press (2003)
12. Baumberg, A.: Reliable feature matching across widely separated views. In: IEEE Conference on Computer Vision and Pattern Recognition, pp. 774–781. IEEE Press, New York (2000)
13. Peng, H., Wen, Y., Zhai, R.: Stereo matching for binocular citrus images using SURF operator and epipolar constraint. *Computer Engineering and Applications* 47, 157–160 (2011)

Seedling Image Segmentation and Feature Extraction under Complicated Background

XiaYan Lu, Xin Li, YuShen Chai, and Xiang Li

School of Mechatronics Engineering and Automation, Shanghai University,
Shanghai 200072, China
su_xinli@aliyun.com

Abstract. Vision system is applied to automated transplanter to increase the productivity in greenhouse. How to separate the seedlings from complicated background and extract the features of them are the two key technologies. Traditional segmentation algorithms based on threshold (Otsu), edge (ES) and region growth (RG) were contrasted in this paper. These segmentation methods are seriously interfered by disturbances. In view of the disadvantages existed in the present algorithms for seedling image segmentation, an improved segmentation algorithm based G-channel region growth (GRG), which utilized G-channel pixel values only, is proposed. Morphological filter was applied to remove noises existed in the binary image segmentation. Then, four kinds of features of seedling leaves image were extracted through this algorithm. Error rates of Eggplant segmentation were 0.48, 0.52, 0.44 and 0.04 for Otsu, ES, RG and GRG respectively, which indicates that the GRG algorithm for seedling image segmentation is better than others. In addition, parameters of seedlings present a correlation and the consistency of average gray value (AGV) can be an indicator for subsequent recognition. The results show that the goals of optimizing operation time and separating leaves unbroken are achieved in this paper.

Keywords: Vision system, seedling image segmentation, morphological filter, feature extraction.

1 Introduction

Machine vision is a rapid, nondestructive and real-time inspection technology. Automated transplanter based on machine vision have been realized in greenhouse to transplant healthy seedlings from high-density to low-density trays which reduce the labor costs and improve the production efficiency [1], [2]. Assessing the quality of seedlings through computer vision is a key technology in the system of automated transplanter. How to segment objects from the background precisely and extract features represented seedlings to sort plants correctly have been studied for many years and many algorithms concerned computer-based image-processing systems are proposed and improved by researchers.

Tai, Ling, and Ting [3] developed a machine vision system which employed leaf area obtained from grey-level information to detect the absence of leaves and empty

cubes to improve the quality of transplanted seedling trays. The identification of empty cubes exhibited a 95% success rate. Urena, Rodriguez, and Berenguel [4] developed an automatic system which uses a color camera to capture image trays as well as an image-processing system to identify the seedlings and their leaf area for seed germination monitoring. By calculating the germination percentage (GP) associated with leaf area to estimate the degree of the seedlings. Chien and Lin [7] developed a non-destructive measurement method by incorporating two side-view images with a top-view image to extract and reconstruct the three-dimensional structure of selected vegetable seedlings, and thus to improve the accuracy of the leaf estimation. The average relative errors of total leaf estimation for cabbage and broccoli seedlings were reduced to 1.6% and 4.9%. Jun, Jiang and Huan [1] developed an image-processing method for the measurement of the leaf area of vegetable seedlings and to determine seedling quality for automated transplanting. A segmentation map was obtained by reducing the level of over segmentation and the identification accuracy greater than 95%. However only setting the area threshold to distinguish the bad from the good plugs is a deficiency of the method, and the improved watershed segmentation algorithm proposed in this paper is time-consuming which influence the real-time of the vision system for automated transplanter.

Although leaf area is an important parameter influencing productivity among many useful indicators of seedling, and leaf shape has been used extensively to identify various plants and agricultural products [8]. However, Zheng etc. [5] reviewed image feature extraction techniques and highlighted that assessing performance of food products can be improved by combining a larger number of features, such as color, size, shape and texture. Costa etc. [6] reviewed and emphasized the relevance of morphological features of agricultural products for several aspects of product quality evaluation. Muhammad [9] developed an algorithm which inspected the bending, nodes of leaves and stem diameter of seedlings from their images and then to grade and sort them as the initial task of the grafting robot. Extracting a large set of relevant features of seedlings can improve the performance of evaluating seedling quality.

The goal of this work is to develop an improved algorithm that could optimize the real-time performance of the visual system and to extract other relevant characters of seedling besides leaf area to extend the capability for estimating seedling quality of computer-based image-processing system. This paper is organized as follows: several traditional algorithms for image segmentation and optimized method are described in the part of methodology; the extraction of features of seedling leaves is also described in this part. Then experimental data are presented in the third part to illustrate the advantage of the improved algorithm. And the purpose of this paper is proved to achieve at last.

2 Segmentation and Extraction

2.1 Image Analysis Process

Among the components of the automatic transplanting system, machine vision is a key technology which consists of a CCD camera, a frame grabber board, and image processing software working on an industrial computer, etc. [10]. Computer vision

technology as a non-touch measuring method has changed the traditional detection methods which may damage the objects such as seedlings by contacting. It replaced the eyes of people to acquire amounts of information from image and liberated workers from the tedious and heavy works at the same time. Figure 1 shows the image processing of machine vision system. This system was used to detect seedling's condition in the plug tray, identify empty cells and estimate whether suitable to transplant. The evaluating performance of machine vision distinctly influences the capability of transplanter.

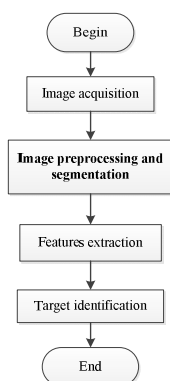


Fig. 1. The image processing of machine vision system

Image segmentation is an important part of image analysis process and attracts many concerns of researchers. Its aim is to extract information, such as humans, cells, cars, etc., from a certain kind of images. The extraction has to be reliable and robust to be able to meet the demands of the application. Three traditional algorithms were contrasted and an optimized segmentation method was developed following.

The characteristics of target, such as morphological characters, textural properties and color features, are calculated by the vision system to serve as inputs of next control system (such as PLC) to complete the operation of automated transplant. Seedlings quality has many evaluation indexes. The area, average color, perimeter and center coordinate of leaves detected through machine vision system were selected as the quality indicators in this paper.

2.2 Image Acquisition and Pre-processing

The shapes of tomato, cucumber, eggplant and pepper (generally holding two or three pieces of leaves) are similar in their seedling period, while the same vegetables seedling in different growth stages are unlike in shapes and colors. So eggplant (Fig2-a) and lettuce (Fig2-b), apparently unlike in shapes in different growth stages, were studied in this study. Figure 2 shows the top-view seedling images of eggplant and lettuce which were acquired under normal fluorescent lighting in greenhouse by camera. The seedling vegetables were raised automatically in trays fitted with soil for subsequent transplanting. The images with a resolution of 640×480 were captured in RGB (24 bit)

format, so every pixel in the image is represented by the combination of three values (corresponding to red, green and blue colors) between 0 and 255 (8-bit codification), and transferred to the industry computer to process by the image-processing program. The image-processing system worked on a Core i3 computer and was developed using Visual C++ under the Microsoft Windows operating system. The basic image-processing functions in the program, such as image acquisition and display, were supported by the OpenCv library.

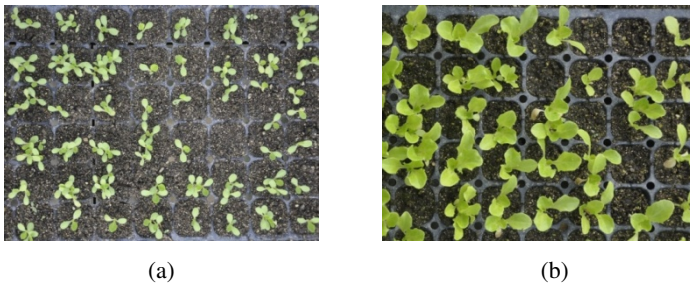


Fig. 2. Eggplant (a) and lettuce (b) images analyzed in this paper

The acquired image mainly comprised of two parts: objectives (seedling leaves) and background (root-growth medium and plug tray). To obtain the features of objectives, seedling leaves should be segmented from the background firstly. However, the images captured by camera usually hold some noises caused by light reflective or halation. To remove these effects, spatial filtering techniques were applied before image segmentation. Compared with smoothing filtering and median filtering, the latter is better in reducing noise and brings fewer distortions. 3×3 median filter was applied in the image-processing program to reduce effects of noises. Each pixel of the source image was replaced with the mid-value of its 3×3 adjacent-area pixels, so the filtered picture could be determined through the following formula:

$$f(x, y) = \underset{(s,t) \in S_{xy}}{\text{median}}\{g(s, t)\}, \quad (1)$$

Where $g(s, t)$ represents an element of a 3×3 two-dimensional array, and S_{xy} represents the 3×3 adjacent-area of (x, y) .

2.3 Image Segmentation

Following image acquisition and filtering, the seedling was then extracted from the background. There are now a wide variety of image segmentation algorithms, some considered general purpose and some designed for specific classes of images. These methods can be classified as: edge detection schemes, threshold segmentation schemes and region growing schemes.

2.3.1 Traditional Segmentation Algorithms

Some representative segmentation algorithms, such as Otsu method (proposed by Otsu in 1979), schemes based on Canny edge detector (ES) and seeded region growing method (SRG), were applied to separate the leaves in figure 2 from the background. Otsu's method utilizes the shape information of the image histogram to select automatically a threshold value for image segmentation. The advantages of Otsu's method are small amount of computations and time-saving. It also possesses apparent superiority in handling images whose gray level of object and background distribute obviously. However, because of light impact, the gray information of part background is similar to the object, these pixels are possibly classified as the foreground pixels.

Segmentation can also be completed by detecting edges of various regions. Edge-based methods [17] assume that the pixel properties, such as intensity, color, and texture, should change abruptly between different regions. Canny operator [16] proposed by Canny in 1986 was used to detect edges in this paper. It possesses the capacity of immunizing noises and utilizes two thresholds to detect edges and connect cracked lines. However, segmentation results would be over-segmentation when the background was complex (was showed in Fig5-b).

Seeded region growing (SRG) is one of the hybrid methods proposed by Adams and Bischof [18]. It starts with assigned seeds, and grow regions by merging a pixel into its nearest neighboring seed region. Although the similar objects (seedling leaves) could be separated into individual regions from background by SRG, the operation time of multi-dimensional space (RGB color space or $YCbCr$ color space) was long and complicated.

As shown in the figure 5 (a), acquired using Otsu segmentation method, plug tray was judged as seedling leaves. The result of segmentation will affect the accuracy of recognition. Figure 5 (b) shows the segmentation result using scheme based on canny edge detector and figure 5 (c) is obtained utilizing SRG. It's obvious to see that image (b) was over-segmentation and the pixels around the image were easily recognized as seedling leaves. Although the region growth method improved the performance of segmentation (was showed in Fig5-c), there were also a few background pixels judged as objectives, and this method was time-consuming and could not meet the real-time performance of vision system.

2.3.2 G-channel Region Growth (GRG) Segmentation

To extract the seedling leaves from background accurately, an improved segmentation algorithm based on region growth was presented in this section in terms of the specific classes of seedling images. It's the core concept of region growth method to select the pixels adjacent to and similar with seed points as the next growth points beginning to grow from a set of seed points, until developing a cluster of single linkage closed regions. Growing criteria and termination criteria are the keys for this algorithm. Supposing (x, y) represents a seed point, to determine whether the four pixels (the up, down, left, right side of seed point) adjacent to seed point are seed points can be described by the following formula:

$$Q = \begin{cases} TRUE, & |D(x, y)| < T \\ FALSE, & else \end{cases}, \quad (2)$$

Where $|D(x, y)|$ represents the absolute difference between seed point and its adjacent domain pixels and T represents a threshold of pixel value. And termination criterion can be defined as finding no more seed points.

In the RGB 3-channels pictures, the pixels of G-channel contain the most information of seedling leaves. Several indices were studied and tested in the paper of Woebbecke [11], the 2g-r-b index was found to be successful in identifying weeds and the G-channel image was emphasized in the application for seedling segmentation. The histograms of the RGB image presented in figure 2 (a) were showed in figure 3, and the three curves with different colors are respectively the statistics of pixel number in each channel of the RGB image. Apparently, the difference of two peak values of the green curve representing the statistical properties of pixels in G-channel image was big, which was easy to segment.

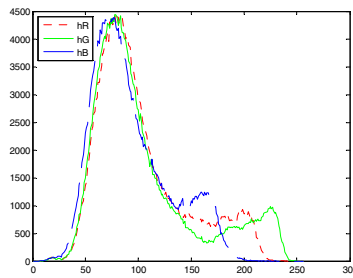


Fig. 3. The histograms of the RGB image presented in Fig.2 (a) (pixel value on the horizontal axis , number of pixel value on the vertical)

Therefore, regardless of the red and blue color information of the RGB format image, the G-channel image was selected as the input image for this improved algorithm. The threshold T in the expression (2) was automatically calculated based on the average gray value M and the background gray value B , and the threshold of T is defined as:

$$T = a * |M - B|, \tag{3}$$

Where a is a factor to meet the segmentation of seedlings in different growth stages.

Then, the seeds start to grow. A binary image would be obtained when the growth end. Supposing $G(x, y)$ represents the gradient of adjacent pixels, $Dis(x, y)$ represents the absolute difference between seed point and one of its adjacent domain pixels, and (x, y) represents the pixels coordinate of initial image. Scanning and segmenting the whole image, the picture will be divided into three major regions: S , A , and E , which denote the area of seeds, objects and edge accordingly. The relationship is as follows:

$$\begin{cases} G(x, y) < T \cap Dis(x, y) < T & , (x, y) \in S \\ G(x, y) < T \cap Dis(x, y) \geq T & , (x, y) \in A \\ G(x, y) \geq T & , (x, y) \in E \end{cases} \tag{4}$$

Equation 4 is the growing criterion of GRG. Two growing directions were applied to distinguish the background and object by contrasting $Dis(x, y)$ with T . The algorithm consists of three steps: (1) calculating the threshold T , (2) searching for seed point, and (3) full image region growing, (4) judge whether complete growth. A flowchart of the algorithm is shown in figure 4.

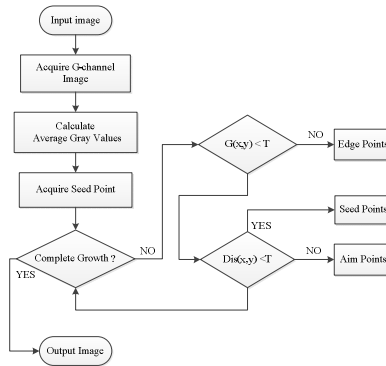
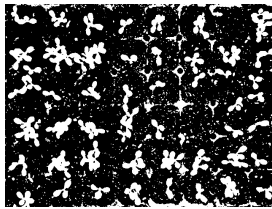


Fig. 4. Flowchart of GRG

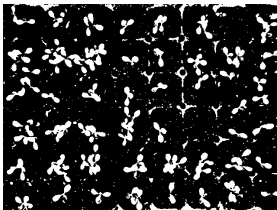
Figure 5 (d) shows the segmentation result of eggplant seedling image using GRG. Obviously, the seedling leaves of eggplant were isolated from the background accurately. Compared with other binary images, there is no plug tray judged as objects and noises around the picture caused by edge detection were also fixed.



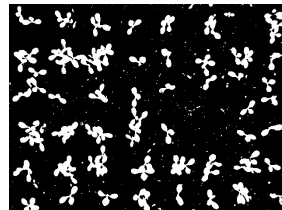
(a)



(b)



(c)



(d)

Fig. 5. Segmentation results using Otsu method (a), Canny edge detector (b), region growth (c) and GRG (d)

2.3.3 Morphological Operation

A few noises still existed in the binary image after segmentation through GRG. And morphological filter was applied to remove the noises. As the area of noises in the image (Fig.6 a) is much smaller than the seedlings', to eliminate noises without affecting seedling leaves, area of each connected region was counted firstly. Then the noises were removed with a certain area threshold. Supposing $A_{(x,y)}$ represents the area of connected region in which the coordinate (x, y) located and T represents the value of the area threshold. The output binary image removed noises could be acquired by the following formula:

$$f(x, y) = \begin{cases} 0, & A_{(x,y)} < T \\ 1, & A_{(x,y)} \geq T \end{cases} \quad (5)$$

$f(x, y)$ represents pixel values of output binary image. And the picture removed noises through morphological filter was showed in figure 6 (b). Then features such as calculation of the perimeter and the area of seedling leaves can be extracted based on the image for subsequent processing.

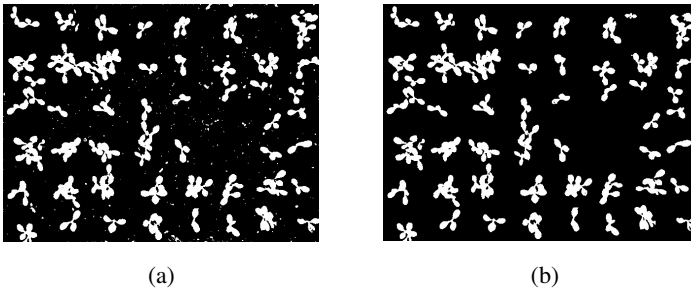


Fig. 6. (a) binary image before morphological operation, (b) binary image after morphological operation

2.4 Features Extraction

To evaluate the quality of seedlings efficiently, various features were extracted from the image. Characters such as area, perimeter, coordinate, etc. were used to assess seedlings in many papers. However, the average gray value of leaves in the G-channel image is also an important indicator. And experimental data of average gray value also showed a consistency in the paper. The methods of calculating these features were described in this section.

2.4.1 Area Calculation

The leaf area of seedlings in each cell was calculated after seedlings were segmented from the background. As the image is made up of pixels, pixel number of each connected region corresponding to seedling leaves was counted to denote the area in many published papers and was also selected as a characteristic parameter of seedling image in this paper. To

actually represent the area of seedling leaves a proportional constant (w in the equation 6) was used to transform the pixel number getting close to reality.

$$A_i = w * N_i \quad (6)$$

Equation 6 determined the leaf area of the seedlings. Where $1 \leq i \leq n$ (n represents the total number of connected regions), and N_i represents the pixels number of connected region i .

2.4.2 Perimeter

Freeman chain code was applied to describe the edge of each region. Scan exhaustively the image and find out all the clusters firstly. Chain code for a region could be obtained by following steps:

Step 1: located the first white point at the top-left corner of the region.

Step 2: search for the next edge pixel in clockwise direction from the first point got in step 1, and the orientation from the previous point to the next one is coded with digit 0 to 7 (represents eight directions).

Step 3: stop searching when search out the first white pixel again and output the chain code.

A connected seedling leave perimeter could be determined by the following formula:

$$L = \sum_{i=1}^n \left[1 + \frac{\sqrt{2}-1}{2} (1 - (-1)^{e_i}) \right] \quad (7)$$

Where n represents the number of edge pixels for a region and e_i ($1 \leq i \leq n$) represents the freeman chain code.

2.4.3 Center Coordinate and Average Gray Value (AGV)

The center of the component was obtained by calculating each boundary coordinate in the component region. (x, y) (the center coordinate of the region) could be determined by the following expression:

$$\begin{cases} x = \frac{1}{n} \sum_{i=1}^n x_i \\ y = \frac{1}{n} \sum_{i=1}^n y_i \end{cases} \quad (8)$$

And the average gray value of the component was obtained by calculating each pixel value in the component region of G-channel image. Equation 9 shows the relationship between average color P and pixel value g_j . n represents the pixel number of a connected region attained by segmenting.

$$P = \frac{1}{n} \sum_{j=1}^n g_j \quad (9)$$

3 Experiments and Analysis

An image-processing program was realized to verify algorithms mentioned in this article. Loading the image into this program and separating seedling leaves from the background by GRG, the marked image showed in figure 7 output from the software. As can be seen in figure 7, single seedlings labeled with red sign are detected precisely, while more than one seedlings grown in a tray and connected together or leaves grown out of their own cell, overlapping the borders of other leaves are regarded as one. The dense seedlings are not fit for subsequent growth and should be judged as ‘bad’ in the process of recognition.

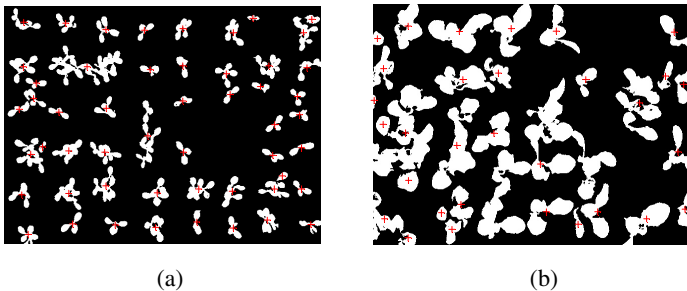


Fig. 7. Marked binary images of eggplant (a) and lettuce (b)

It is important to assess whether one algorithm produces more accurate segmentations than another [13]. To date, many evaluation methods that have been proposed in the literature [12], [14], such as subjective evaluation, supervised evaluation. In this paper, the superiority of GRG was illustrated from two perspectives of time-consuming and error rate.

The error rate was calculated to indicate the performance of segmentation and was defined as:

$$E_p = \frac{|n - N|}{N}$$

n is the number of connected regions obtained through the image-processing program, and N is the practical number acquired manually. The better of the performance of segmentation, the lower of E_p . Supposing that every plug trays holds one seedling ideally, and seedlings linked together in a hole are regarded as one seedling. Especially, seedlings separated distinctly in a hole are counted two or more. Based on that criterion, the number of seedling in image showed Fig.2 (a) is 50, and the other is 30 counted manually. Calculated the error rates of different algorithm for eggplant and lettuce and showed them in table 1. We can see that the error rate of optimized algorithm is apparently improved than others. Experimental data of GRG also indicate that seedling number obtained automatically is close to practical number.

Table 1. Error rate of different segmentation algorithms

	Eggplant	Lettuce
Otsu	0.48	0.52
ES	0.52	0.46
RG	0.44	0.26
GRG	0.04	0.02

Less time-consuming is another advantage of GRG by contracting traditional region growth. Operation time of different algorithms for eggplant and lettuce was showed in table 2.

Table 2. Operation time of different segmentation algorithms

	Eggplant	Lettuce
Otsu	29ms	22ms
ES	571ms	565ms
RG	2609ms	2589ms
GRG	1619ms	1690ms

As we can see from table 2, computing time of GRG was shortened by about 1 second comparing with RG and the execution time performance was significantly improved. Although the performance of Otsu and ES were better in terms of time, the segmentation results could not meet requirements for subsequent processing and they were susceptible to noises and not suitable for images with complex background.

Table 3. Features achieved by GRG

Region Number	Coordinate	Area	Perimeter	AGV
1	(39,31)	786	229.7	192
2	(125,33)	701	207.7	195
3	(203,46)	898	251.0	203
4	(283,48)	478	146.4	210
5	(360,46)	774	184.9	204
6	(462,54)	929	223.9	203
7	(503,23)	167	67.6	200
8	(606,53)	1199	279.0	199
9	(621,26)	372	87.8	187

Characteristics of leaves are also extracted by the program and table 3 shows four kinds of features of seedling leaves located the first row in the image showed Fig.7 (a). The vertical coordinates of center points in each component are near while the horizontal coordinates range from 0 to 640. And the region with large area also holds a great perimeter. It's worth mentioning that the seedling leaves' average gray values obtained by this program show a good consistency and can be a significant indicator for assessing the quality of seedlings and subsequent recognition.

4 Conclusion

An image segmentation algorithm based on region growth was developed to separate seedling leaves from background for the vision system used in automated transplanter. Before segmentation, median filter was utilized to smooth the image. Then three traditional segmentation methods were tested for seedling leaves separation. The binary images obtained through those algorithms holds amounts of noises and were over-segmentation. Based on these disadvantages, an optimized segmentation algorithm was proposed to solve those problems and binary images acquired by GRG showed that there was no plug tray judged as objects and noises around the picture caused by edge detection were also fixed. However, this algorithm suits to certain kind of pictures, such as showing in the beginning (as showed Fig 2). So the future research will focus on the robustness performance of the method. Morphological filter was then applied to remove noises still existed in the image without affecting seedling leaves. Following segmentation and filtering, features such as areas, perimeters, coordinates and AGVs were extracted to represent seedlings' quality. Besides leaf area which was used to evaluate seedling quality in many published papers, the perimeter of leaves also performed a correlation with leaf area and character of AGV showed a consistency according to experimental results. Testing two kinds of vegetable grown in different stages, AGV with a low error rate and little operation time shortened by about 1 second was proved to be better than other algorithms.

References

1. Tong, J.H., Li, J.B., Jiang, H.Y.: Machine vision techniques for the evaluation of seedling quality based on leaf area. *J. Biosystems Engineering* 115(3), 369–379 (2013)
2. Gao, F., Yu, L., Lu, S.Q., et al.: Status quo and development trend of facility agriculture in foreign countries. *Journal of Zhejiang Forestry College* 26(2), 279–285 (2009)
3. Tai, Y.W., Ling, P.P., Ting, K.C.: Machine vision assisted robotic seedling transplanting. *Transactions of the ASAE* 37(2), 661–667 (1994)
4. Urena, R., Rodríguez, F., Berenguel, M.: A machine vision system for seeds germination quality evaluation using fuzzy logic. *Computers and Electronics in Agriculture* 32, 1–20 (2001)
5. Zheng, C., Sun, D., Zheng, L.: Recent developments and applications of image features for food quality evaluation and inspection – a review. *Trends in Food Science & Technology* 17(12), 642–655 (2006)
6. Costa, C., Antonucci, F., Pallottino, F., Aguzzi, J., Sun, D., Menesatti, P.: Shape analysis of agricultural products: A review of recent research advances and potential application to computer vision. *Food and Bioprocess Technology* 4(5), 673–692 (2011)
7. Chien, C.F., Lin, T.T.: Non-destructive growth measurement of selected vegetable seedlings using orthogonal images. *Transactions of the ASAE* 48(5), 1953–1961 (2005)
8. Yonekawa, S., Sakai, N., Kitani, O.: Identification of idealized leaf types using simple dimensionless shape factors by image analysis. *Trans. ASAE* 39(4), 1525–1533 (1996)
9. Ashraf, M.A., Kondo, N., Shiigi, T.: Use of Machine Vision to Sort Tomato Seedlings for Grafting Robot. *Engineering in Agriculture, Environment and Food* 4(4), 119–125 (2011)

10. Tong, J.H., Jiang, H.Y., Wei, Z.: Development of Automatic System for the Seedling Transplanter Based on Machine Vision Technology. In: 2012 IEEE International Conference on Computer Science and Automation Engineering, vol. 2, pp. 742–746 (2012)
11. Woebbecke, D.M., Meyer, G.E., VonBargen, K., Mortensen, D.A.: Color indices for weed identification under various soil, residue, and lighting conditions. *Transactions of the ASAE* 38(1), 259–269 (1995)
12. Zhang, Y.J.: A survey on evaluation methods for image segmentation. *J. Pattern Recognition* 29(8), 1335–1346 (1996)
13. Lee, J.S., Yang, M.C.K.: Threshold selection using estimates from truncated normal distribution. *IEEE Transactions on Systems, Man and Cybernetics* 19(2), 422–429 (1989)
14. Hui, Z., Jason, E.F., Sally, A.G.: Image segmentation evaluation: A survey of unsupervised methods. *Computer Vision and Image Understanding* 110(2), 260–280 (2008)
15. Adams, R., Bischof, L.: Seeded region growing. *IEEE Transactions on Pattern Analysis and Machine Intelligence* 16(6), 641–647 (1994)
16. Canny, J.F.: A computational approach to detection. *IEEE Trans. Pattern Analysis. Mach. Intell.* 8, 679–698 (1989)
17. Basak, J., Chanda, B.: On edge and line linking with connectionist model. *IEEE Transactions on System, Man, and Cybernetics* 24(3), 413–428 (1994)
18. Adams, R., Bischof, L.: Seeded region growing. *IEEE Transactions on Pattern Analysis and Machine Intelligence* 16(6), 641–647 (1994)

Survey of Indoor Positioning Technologies and Systems*

Lingling Zhu, Aolei Yang**, Dingbing Wu, and Li Liu

Shanghai Key Laboratory of Power Station Automation Technology, School of Mechatronic Engineering and Automation, Shanghai University, Shanghai 200072, China.
{zhull_7627, liulildu}@163.com, aolei.yang@gmail.com,
hanbing08021@126.com

Abstract. This paper presents the state-of-the-art of the leading indoor positioning technologies and systems. The positioning technology is classified into the active positioning system and the passive positioning system, which are presented respectively in detail, including wireless local area network, radio frequency identification, Bluetooth, inertial navigation, and magnetic field positioning. Additionally, the advantages and disadvantages of various indoor positioning technologies and systems are analyzed, as well as the positioning accuracy, applicability, and working principle. Particularly, in order to better understand them, the key performance parameters of the mentioned technologies and systems are finally compared using a table.

Keywords: Indoor positioning, active positioning, passive positioning, inertial navigation system.

1 Introduction

With the rapid development of the mobile Internet, data and multimedia services are increased rapidly. The demand of positioning and navigation is increasing day by day [1]. Especially in complex indoor environments, the indoor position of the mobile terminal i.e. its owner, facilities and goods, is generally needed to be determined in real-time. These complex indoor environments include airport halls, exhibition halls, warehouses, supermarkets, libraries, underground car parks and other environments. The indoor positioning system is to locate and track an object within buildings or closed environment, and these systems are based on the principle of radio waves [2], optical tracking, magnetic field or ultrasonic technology etc. The technology of positioning and tracking the object is the basis for many applications on monitoring and activity recognition. For example, in the supermarket, through obtaining the relevant position information of the consumers and target commodities, the supermarket is able to provide the services of the route guidance and the intelligent shopping guide.

* This work was supported by the Science and Technology Commission of Shanghai Municipality under “Yangfan Program” (14YF1408600), the Shanghai Municipal Commission of Economy and Informatization under Shanghai Industry-University-Research Collaboration Grant (CXY-2013-71).

** Corresponding author.

The indoor positioning system can be specially employed for guiding the rescuers to search the building and rescue the trapped personnel quickly when a sudden disaster happens. In addition, the position technology can be used in hospital, i.e. the patient's monitoring and the management of the medical equipment. So, it is necessary and important to apply the indoor positioning technology and system into people's lives.

It is well known that global positioning system (GPS) is the most widely used satellite-based positioning system and it provides location-based services, such as navigation, tourism and so on [3]. However, GPS is not suitable in indoor positioning due to a variety of obstacles. For solving the indoor positioning problems, many solution technologies are proposed in literatures [4, 5]. In this paper some popular indoor positioning technologies and systems are presented, i.e. wireless local area network (WLAN) [6], radio frequency identification (RFID) [7, 8], Bluetooth technology, inertial navigation system (INS) [9], magnetic field positioning technology, etc.

This paper classifies the indoor positioning systems into the active system and passive system, and reviews the state-of-the-art of the leading indoor positioning technologies. The passive system is that the position is estimated by measuring the received signal or video process. Most solutions of passive system based on the triangulation and multiple points positioning technology, and they use light, ultrasonic or radio signal, which can represent the position information of the object. These technologies include WLAN/WIFI, RFID, Bluetooth technology. The active system means that the tracked target carries electronic devices or tags, which can transmit its signal to a management station calculates the position by using a certain positioning algorithm. They include INS, magnetic field positioning technology, etc.

Further, some basic measuring principles are also presented in this paper, such as time of arrival (TOA)[10, 11], time difference of arrival (TDOA)[12], angle of arrival (AOA)[13, 14], received signal strength indication (RSSI)[15, 16]. It provides a qualitative overview for these positioning technologies and offer quantitative comparison for these systems or solutions, as well as analysis and comparison for their performances.

The remainder of the paper is organized as follows. Section 2 shows four kinds of basic measuring principles. In Section 3, the passive indoor positioning systems are presented. In section 4, the active indoor positioning systems are presented. The paper finally compares the various positioning systems and technologies.

2 Basic Measuring Principle

Geometric positioning technology is used for calculating target's position through measuring the geometry relationship between the target and beacon nodes, the typical technologies are TOA, TDOA, AOA, RSSI and the integration of above.

2.1 Time of Arrival (TOA)

The principle of TOA is to measure the arrival time between the mobile target and the at least three known beacon nodes, and multiplies the signal speed to calculate the distances between the target and beacon nodes. Then taking the beacon nodes as the centers of circles, the distances between target and beacon nodes as the radius of

circles, the intersection of circles is the coordinate of the mobile target. As shown in Fig.1.

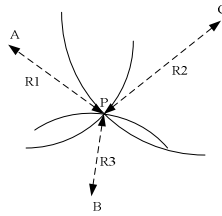


Fig. 1. Positioning based on TOA measurements

A simple method uses geometrical to calculate the intersection of the circles of TOA. The position of the target can also be calculated by minimizing the sum of squares of nonlinear cost function, i.e., least-squares algorithm [17, 18]. It assumes that mobile terminal at (x_0, y_0) , transmits a signal at time t_0 , N base stations are located at $(x_1, y_1), (x_2, y_2), \dots, (x_N, y_N)$, and receives signal at time t_1, t_2, \dots, t_N . As a performance indicator, the cost function can be represented by

$$F(x) = \sum_{i=1}^N \alpha_i^2 f_i^2(x) \tag{1}$$

Where α_i is chosen to reflect the reliability of the signal, which received at the measuring unit i , and $f_i(x)$ is given by

$$f_i(x) = c(t_i - t) - \sqrt{(x_i - x)^2 + (y_i - y)^2} \tag{2}$$

In equation (2), c is the speed of light, and $x = (x, y, t)^T$. This function form for each measurement unit $i = 1, \dots, N$, choosing the proper x, y and t can make the $f_i(x)$ zero. So the position estimation is determined by minimizing the function $F(x)$.

2.2 Time Difference of Arrival (TDOA)

The TDOA is to determine the relative position of the mobile target by computing time difference of the signal arrival at many measurement units. TDOA positioning method does not require strict time synchronization between the mobile target and beacon nodes.

The TDOA positioning algorithm is usually achieved by the target simultaneously transmits the radio signal to two beacon nodes. Due to the different distances between target and two beacon nodes, which can be obtained through the known signal propagation speed multiplies the received signal' TDOA, the position of the target can be determined by Hyperbola, which the two beacon nodes as focal points, the difference of the distances is $v \cdot \Delta t$. In addition, measuring the location of the mobile target need at least three beacon nodes, as shown in Fig.2.

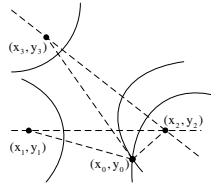


Fig. 2. Positioning based on TDOA measurements

TDOA measurement can be constituted by a set of hyperbolic equations. So the position estimation of the mobile target can be obtained by these hyperbolic equations.

$$\begin{cases} \sqrt{(x_2-x_0)^2 + (y_2-y_0)^2} - \sqrt{(x_1-x_0)^2 + (y_1-y_0)^2} = v \cdot \Delta t_{21} \\ \sqrt{(x_3-x_0)^2 + (y_3-y_0)^2} - \sqrt{(x_1-x_0)^2 + (y_1-y_0)^2} = v \cdot \Delta t_{31} \end{cases} \quad (3)$$

The formula (3) is the TDOA from target to each beacon node. The optimal solution of the equations is the coordinate of the target. Due to the equations are nonlinear, the corresponding algorithms are required for solving the nonlinear equations [19].

2.3 Angle of Arrival (AOA)

In AOA, mobile target transmits wireless signal to the beacon nodes. The signal' AOA is measured by antennas on the beacon nodes, and the coordinate of mobile target is calculated by the principle of geometry. In two-dimensional space, at least two signal' AOA of the beacon nodes are needed for calculating the position of the mobile target. Based on the line direction of the signal arrival angle θ_1, θ_2 respectively, the target position is the intersection of them. But in this technology the positioning accuracy is not high, thus the improved method used antenna arrays is proposed in [20].AOA technology may use at least two known reference points (M,N) and two measured angles θ_1, θ_2 to calculate the 2-D location of the target P , as shown in Fig.3.

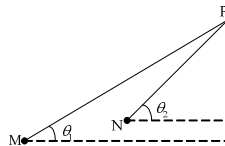


Fig. 3. Positioning based on AOA measurement

2.4 Received Signal Strength Indication (RSSI)

Principle of RSSI positioning method is that the signal receiver measures the received power P_r , the distance between nodes is calculated by using a transmission loss formula (4). The coordinate of the mobile target is calculated by using triangular method,

which depends on measuring the distances between target and at least three beacon nodes.

Assuming that the signal is from free space to the receiver and the distance between them is expressed by d . There are no obstacles between transmitter and receiver, and the signal transmits along a straight line. The relationship between received power P_r and transmitted power p_t is given by (4),

$$P_r = \frac{P_t G_t \lambda^2}{(4\pi d)^2} \quad (4)$$

where p_t is the power of the transmitting signal, G_t is the product of the gain of transmitting antennas and receiving antennas, λ is the signal wavelength, d is the distance, P_r is given as RSSI values in the wireless receiving chip. The distance d can be calculated by measuring the RSSI values and combined with the known P_t, G_t, λ . In addition, theoretical and empirical patterns are used to calculate the difference of the signal strength between the transmitter and the receivers for positioning estimation, as shown in Fig. 4.

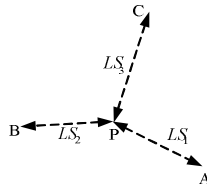


Fig. 4. Positioning based on RSSI, where LS1, LS2, and LS3 denote the measured path loss

Due to the appearance of severe multipath fading and shadow in indoor environment, path loss model is not always suitable. The parameters in these models thus need field measurement. A novel tracking system based on the development of RSSI is proposed in [21], this system is designed for wireless sensor network (WSN) system, and it can transmit data with a high transmission rate.

3 Passive Indoor Positioning

The vast majority of indoor positioning estimation systems track the mobile target by measuring the signal from transmitter to the receivers. The systems use the geometric positioning technology to calculate the position of the mobile target. This section focuses on some main passive positioning systems such as WLAN/WIFI, RFID, Bluetooth.

3.1 WLAN/WIFI

WLAN (Wireless Local Area Network, IEEE 802.11 standard, is a radio frequency technology for data transmission system; WIFI aims to improve the interoperability

between products of wireless network based on IEEE 802.11 standard. WIFI is held by the Wi-Fi Alliance. In simple terms WIFI is a kind of wireless network technology, in the past connected through a computer network, and now through radio network) can be used to estimate the location of mobile device within this network. Indoor positioning system based on WLAN consists of three main parts: wireless network terminal, WLAN hotspots in fixed-location and position platform. For the system facilities, WLAN system is divided into two stages: offline database and real-time position.

In offline database stage, the main work is to determine the sampling points according to certain distance in the WLAN signal coverage area, and forming a network with evenly distribution sample points. At each sampling point measures all visible hotspots' signal strength values, MAC address and the coordinates of sampling points, these information as a record is saved in a database. The database information corresponding to these sampling points is called the location fingerprint.

In real-time positioning stage, the wireless network terminal is used to measure the signal strength of the visible WLAN hotspots, which is compared with the recorded data location in the fingerprint database, to consider the sampling points with maximum similarity as the positioning result. From a machine learning perspective, location fingerprinting can be viewed as training the computer to learn the rule between signal strength and location, and then carry out the reasoning and judgment.

WLAN indoor positioning has attracted more and more research on cost effectiveness and reasonable positioning accuracy [22]. Existent positioning methods all focused on establishing more accurate relationship between the received signal strength (RSS) and the physical locations, however, the deployment of the access points (APs) are ignored. Thus an optimized method of APs is presented in [23], to improve WLAN positioning accuracy. The sparse nature of location finding makes the theory of compressive sensing (CS) desirable for the accuracy of indoor positioning base on RSS from WLAN Aps. An accurate indoor positioning system based on RSS is proposed in [24], this system used compressive sensing for solving the minimization problem and making the sparse signal recovery from a small number of noisy measurements.

3.2 RFID

RFID technology uses radio frequency communication to exchange data and subsequently make the identification and positioning. The location of the positioning tags is calculated by the signal strength between known tags and readers. The system is composed by three main parts: RFID tags, readers and miniature antennas between the tags and the readers. When tags obtain energy and power-on reset within the range of the electromagnetic field, the readers emit electromagnetic field with fixed-frequency. By this time the dormant tags are activated, and the identification code information is modulated into the carrier, which is emitted by the antennas to support the readers' identification.

An overview of RFID-based localization and tracking technology is presented in [25], this technology include tag-based (e.g., LANDMARC) technology, reader-based (e.g., reverse RFID) technology, transceiver-free technology, and hybrid approaches. These technologies mainly use the readily available resource of radio signal strength

information or RSS change information to locate the mobile target. An enhanced method is proposed in [26], this method estimated the indoor position accurately by an RFID reader antenna based on passive RFID tags.

3.3 Bluetooth

Bluetooth positioning technology locates object by measuring the signal strength. It is a short-distance wireless transmission technology with low power consumption. Bluetooth technology is mainly used in small area positioning with a single floor or warehouse. Bluetooth indoor positioning technology has advantages, such as small volume, easy to integrate in PDA, PC and mobile phone, so it is easy to spread. Theoretically, users hold the integrated Bluetooth mobile terminal devices, as long as the Bluetooth of device turned on, the position of the object can be tracked by Bluetooth positioning system. Using Bluetooth positioning technology as short distance positioning, which easier to detect the devices and the signal transmission and not affected by the LOS. The problem lies in the Bluetooth devices are expensive, but for a complex spatial environment, stability of the Bluetooth system poorly, and easy influenced by noise signal.

An indoor positioning module is comprised of a Bluetooth beacon deployment and Bluetooth devices, which integrated in the mobile phone used to track the position. It is possible to view the employees' locations on a graphical interface in [27], which also provided room-level accuracy for applications of worker protection and automatic alarm dispatch.

4 Active Indoor Positioning

Some applications could be developed use active positioning systems, such as INS is a self-contained navigation technology. Based on the measurements of INS which are provided by accelerometers and gyroscopes, the INS could track the position and orientation of the mobile target. In addition, magnetic field positioning is also an active positioning technology, it uses the magnetic field disturbance for indoor positioning and not require deploy the infrastructure in advance.

4.1 Inertial Navigation System

Inertial navigation system is an autonomous system that provides position information based on the measurement of inertial sensors and dead reckoning (DR) principle, using INS to calculate the attitude and angular velocity. The current position of the target is obtained by knowledge of its previous position. Under the initial conditions given, the first integration of acceleration provides velocity and the second integration gives position. However, performing the integrations caused drift with time, which can lead to accumulation error without bound. So INS is unsuitable for accurate positioning with a period of time.

INS is a kind of electronic device provides the estimation of position, velocity and orientation from an inertial measurement unit (IMU). If the initial position and orientation are known, then the position, orientation and velocity of the mobile platform are

continually updated by DR without external reference positions. The advantages of INS are that it has short term accuracy, low cost and allows high sampling rates.

Due to the accurate navigation in minimally invasive surgery, many methods have been used to track the position and orientation of instruments in the operating room. A sub-problem of using integrated inertial and magnetic sensing for tracking the attitude (orientation) of surgical instruments is considered in [28]. A navigation method based on the traditional INS technology is presented in [29].

4.2 Magnetic Field Positioning

The principle of geomagnetic fluctuations could be used to estimate the position of the mobile target. Engineers in Finland designed a Smartphone application and named it IndoorAtlas [30]. According to different specific fluctuations emitted by indoor concrete and steel structure, the orientation of earth's magnetic field can be detected. Due to non-uniform magnetic field environments lead to different observed values of the magnetic field. So the different observed values rely on the different path. IndoorAtlas use this fact to determine the position of mobile target. Engineers obtained inspiration from the homing pigeons, and it used the Earth's magnetic field for positioning. The engineers used digital signal processing technology to develop new indoor navigation solution. Users only need to upload the indoor layout to IndoorAtlas, and then used application to record target's geomagnetic field in different directions for navigation. These geomagnetic data will be recorded and uploaded to IndoorAtlas. Other people can use recorded geomagnetic to calculate the indoor positioning, its accuracy can reach 0.1 m to 2 m. This smartphone application is a software-only positioning system, which does not require additional wireless access points and other external hardware base.

5 Conclusions

According to the study based on the current mainstream indoor positioning technologies and systems, the advantages and disadvantages are analyzed for each indoor positioning technology and system. Table 1 lists the comparison of performances on various indoor positioning.

Table 1. Overview of comparison between various indoor positioning systems

Technologies	Accuracy	Coverage	Cost	NLOS performance
WLAN	m	20m-50m	Medium	Good
RFID	dm-m	1m-50m	Low	Good
Bluetooth	m	10m-15m	Medium	Good
INS	1%	10m-100m	Medium	Good
Magnetic	0.1m-2m	1m-20m	Low	Good

From the table we can see all kinds of indoor positioning technologies have the difference in accuracy, applicable scope and cost. Thus depending on the performance requirement for design and selection, the different applications of indoor positioning technologies are needed by different occasions. At the same time, the research on

indoor positioning technologies gradually to multiple complementary directions, these technologies learn from each other by different theories, policies and network topologies to achieve the optimal solution. In a word, the indoor positioning technology with the characteristics of low cost, low complexity, high accuracy is needed for further study.

References

1. Deng, Z.L., Yu, Y.P., Yuan, X., Wan, N., Yang, L.: Situation and Development Tendency of Indoor Positioning. *China Communications*, 42–55 (2013)
2. Gu, Y.Y., Lo, A.: A Survey of Indoor Positioning Systems for Wireless Personal Networks. *IEEE Communications Surveys and Tutorials* 11, 13–32 (2009)
3. Hua, T.Y., Hong, N.L., Gu, M.: Recent research and Applications of GPS-based Monitoring Technology for High-rise Structures. *Structural Control and Health Monitoring* 20, 649–670 (2012)
4. Deak, G., Curran, K., Condell, J.: A Survey of Active and Passive Indoor localization systems. *Computer Communications* 35, 1939–1954 (2012)
5. Cruz, C.C., Costa, J.R., Fernandes, C.A.: Hybrid UHF/UWB Antenna for Passive Indoor Identification and Localization Systems. *IEEE Transactions on Antennas and Propagation* 61, 354–361 (2013)
6. Meng, W.X., He, Y., Deng, Z., Li, C.: Optimized Access Points Deployment for WLAN Indoor Positioning System. In: *IEEE Wireless communications and Networking Conference*, pp. 2457–2461 (2012)
7. Saab, S.S., Nakad, Z.S.: A Standalone RFID Indoor Positioning System Using Passive Tags. *IEEE Transactions on Industrial Electronics* 58(5), 1961–1970 (2011)
8. Park, S.H., Hashimoto, S.J.: Autonomous Mobile Robot Navigation Using Passive RFID in Indoor Environment. *IEEE Transactions on Industrial Electronics* 56, 2366–2373 (2009)
9. Xiao, W.D., Ni, W., Yue, K.T.: Integrated Wi-Fi Fingerprinting and Inertial Sensing for Indoor Positioning. In: *Indoor Positioning and Indoor Navigation (IPIN)*, pp. 1–6 (2011)
10. Geng, Y.H., He, J., Deng, H.K., Pahlavan, K.: Modeling the Effect of Human Body on TOA Ranging for Indoor Human Tracking with Wrist Mounted Sensor. In: *Wireless Personal Multimedia Communications*, pp. 1–6 (2013)
11. Shen, J.Y., Molish, A.F., Salmi, J.: Accurate Passive Location Estimation Using TOA Measurements. *IEEE Transactions on Wireless Communications* 11, 2182–2192 (2012)
12. Ho, K.C.: Bias Reduction for an Explicit Solution of Source Localization Using TDOA. *IEEE Transactions on Signal Processing* 60, 2101–2114 (2012)
13. Huang, X.J., Guo, Y.J.: Frequency-Domain AoA Estimation and Beamforming with Wideband Hybrid Arrays. *IEEE Transactions on Wireless Communications* 10, 2543–2553 (2011)
14. Luo, Y.J., Law, C.L.: Indoor Positioning Using UWB-IR Signals in the Presence of Dense Multipath with Path Overlapping. *IEEE Transactions on Wireless Communications* 11, 3734–3743 (2012)
15. Blumrosen, G., Hod, B., Anker, T., Dolev, D., Rubinsky, B.: Enhancing RSSI-Based Tracking Accuracy in Wireless Sensor Networks. *ACM Transactions on Sensor Networks* 9, article 29 (2013)
16. Daiya, V., Ebenezer, J., Murty, S.A.V.S., Raj, B.: Experimental Analysis of RSSI for Distance and Position Estimation. In: *IEEE International Conference on Recent Trends in Information Technology*, pp. 1093–1098 (2011)

17. Kanaan, M., Pahlavan, K.: A Comparison of Wireless Geolocation Algorithms in the Indoor Environment. In: IEEE Wireless Communications and Networking Conference, vol. 1, pp. 177–182 (2004)
18. Fang, B.: Simple Solution for Hyperbolic and Related Position Fixes. IEEE Transactions on Aerospace and Electronic Systems 26, 748–753 (1990)
19. Torrieri, D.: Statistical Theory of Passive Location Systems. IEEE Transactions on Aerospace and Electronic Systems 20, 183–197 (1984)
20. Rose, R., Zorn, S., Goetz, A., Fischer, G., Weigel, R.: A New Technique to Improve AoA using Dual Polarization. In: European Microwave Conference, pp. 420–423 (2011)
21. Wang, G., Chen, H.Y.: An Importance Sampling Method for TDOA-Based Source Localization. IEEE Transactions on Wireless Communications 10, 1560–1568 (2011)
22. Sharp, I., Yu, K., Hedley, M.: On the GDOP and Accuracy for Indoor Positioning. IEEE Transactions on Aerospace and Electronic Systems 48, 2032–2051 (2012)
23. Meng, W.X., He, Y., Deng, Z., Li, C.: Optimized Access Points Deployment for WLAN Indoor Positioning System. In: IEEE Wireless Communications and Networking Conference, pp. 2457–2461 (2012)
24. Feng, C., Au, W.S., Valaee, S., Tan, Z.H.: Received-Signal-Strength-Based Indoor Positioning Using Compressive Sensing. IEEE Transactions on Mobile Computing 11, 1983–1993 (2012)
25. Ni, L.M., Zhang, D.: RFID-BASED Localization and Tracking Technologies. IEEE Wireless Communications (2011)
26. Uchitomi, N., Inada, A., Fujimoto, M., Wada, T., Mutsuura, K., Okada, H.: Accurate Indoor Position Estimation by Swift-Communication Range Recognition (S-CRR) Method in Passive RFID systems. In: International Conference on Indoor Positioning and Indoor Navigation, IPIN (2010)
27. ZONITH: <http://www.zonith.com/products/ips/> (last accessed 21, 2011)
28. Ren, H.L., Kazanzides, P.: Investigation of Attitude Tracking Using an Integrated Inertial and Magnetic Navigation System for Hand-Held Surgical Instruments. IEEE/ASME Transactions on Mechatronics 17, 210–217 (2012)
29. Bird, J., Dale, A.: Indoor Navigation with Foot-Mounted Strapdown Inertial Navigation and Magnetic Sensors. IEEE Wireless Communications, 28–34 (2011)
30. Finland Team uses Earth's Magnetic Field for Phone Indoor Positioning System, <http://phys.org/news/2012-07-finland-team-earth-magnetic-field.html>

Robust H_∞ Control for Discrete-Time Systems with Uncertain Packet Dropouts Probabilities

Ying Zhou¹, Chenjie Ma¹, Jiangnan Cao¹, and Qiang Zang²

¹ College of Automation, Nanjing University of Posts & Telecommunications, Nanjing 210003, China

² School of Information and Control Engineering, Nanjing University of Information Science & Technology, Nanjing 210044, China

Abstract. For a class of discrete-time system with both measurement data and control data missing, a decentralized state feedback H_∞ controller design is studied in this paper. The packet dropouts are modeled as a Bernoulli random binary switching sequence with an unknown conditional probability distribution that is assumed to be in an interval. An observer-based controller is proposed to make the closed-loop system exponentially stable in the sense of mean square and achieve the prescribed H_∞ performance. Sufficient conditions are derived for the existence of controller. A numerical example is also provided to demonstrate the validity of the proposed design scheme.

Keywords: Packet dropouts, unknown conditional probability, linear matrix inequalities, H_∞ control.

1 Introduction

With the advances in network technology, more and more control systems have appeared whose feedback control loop is based on a network. These kinds of control systems are called networked control systems (NCS) [1]. Owing to the data communication errors in network and the temporarily disabled sensor, packet dropouts and transmission time delay usually occur, which can degrade the system performance and even make the system unstable. There have been significant research efforts on the design of controllers and filters for system with packet dropouts. There are two main approaches to handle packet dropouts. One approach is to replace the packet dropouts with an estimated value[2], and the other approach is to view packet dropouts as “zero”[3], such as Markov chains[4], Bernoulli binary switching sequence[5], [7], and so on. Random packet dropouts have been the focus of several research studies in the last few years. In some of these studies, only sensor data dropouts are studied [4], [8], while others consider the state-feedback and combine sensor and control delay and dropouts together [6]. In [4], a robust fault detection method is proposed for NCS with uncertain missing measurements probabilities. The robust H_∞ control problem is investigated for stochastic uncertain discrete time-delay systems with missing measurements in [5].

In [8], an observer-based H_∞ controller is designed for NCS with missing measurements, where the missing measurements are assumed to obey the Bernoulli random binary distribution.

The most existing research treats the packet dropouts' probability as a known constant, however due to the environmental factors, the packet dropouts probability usually keeps varying and can not be measured exactly. In [3] the robust control problem of the discrete-time system with measurement data loss is studied, where the packet dropouts are modeled as a Bernoulli random binary switching sequence and an interval is used to describe the measurement data loss probability.

In this paper, robust H_∞ control for discrete-time systems with uncertain packet dropouts probabilities, where an interval is used to describe the packet dropouts probability which satisfies the Bernoulli random binary switch sequence. There exist both measurement loss and control data loss in the systems considered in this paper. The sufficient conditions for the existence of the controller based on state observer are given through the method of linear matrix inequality (LMI). The proposed controller can make the closed-loop systems mean square exponential stable and satisfy prescribed H_∞ performance.

2 Problem Formulation

The network can be modeled as a switch that opens and closes in a random manner as shown in Fig 1. When a switch is open, its output is held at the previous value and the data packet is lost.

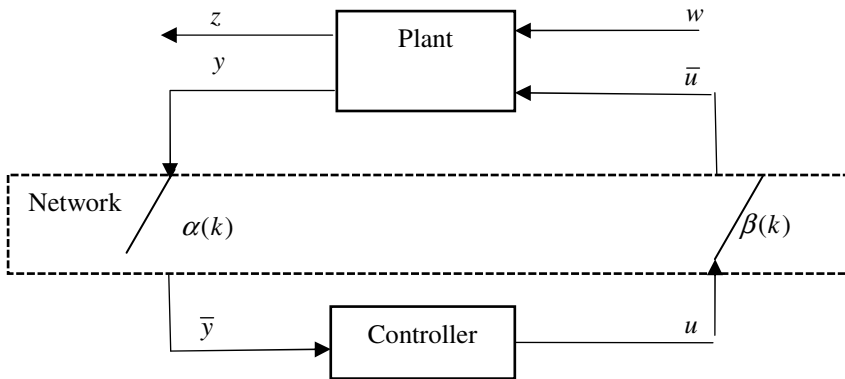


Fig. 1. NCS schematic with packet dropouts. $\alpha(k), \beta(k)$ are Bernoulli random variables, \bar{y} is the measured data which received by the controller, \bar{u} is the control data which received by the actuator.

Consider the following system controlled through a network

$$\begin{cases} x(k+1) = Ax(k) + B\bar{u}(k) + E\omega(k) \\ y(k) = C_1x(k) + F\omega(k) \\ z(k) = C_2x(k) + D\omega(k) \end{cases} \tag{1}$$

where $x(k) \in R^n$ is state vector, $\bar{u}(k) \in R^m$ is the control signals received by actuator, $\omega(k) \in R^l$ is the external disturbance which meets L_2 -norm bounded, $y(k) \in R^p$ is the output vector, $z(k) \in R^q$ is controlled output vector respectively, and A, B, C_1, C_2, D, E, F are known and real matrix with proper dimension.

Design the controller based on observer as follows

$$\begin{cases} \hat{x}(k+1) = A\hat{x}(k) + B\bar{u}(k) + L(\bar{y}(k) - \hat{y}(k)) \\ \hat{y}(k) = C_1\hat{x}(k) \\ u(k) = K\hat{x}(k) \\ \bar{u}(k) = \beta(k)u(k) \\ \bar{y}(k) = \alpha(k)y(k) \end{cases} \tag{2}$$

where $\hat{x}(k) \in R^n$ is state estimation vector, $\hat{y}(k) \in R^p$ is observer output vector, $\bar{y}(k) \in R^p$ is measurement output, $u(k) \in R^m$ is controller output signal, $L \in R^{n \times p}, K \in R^{m \times n}$ are observer gain and controller gain respectively, $\alpha(k), \beta(k)$ are Bernoulli random variables with uncertain probabilities

$$Prob\{\alpha(k) = 1\} = E\{\alpha(k)\} = \bar{\alpha}, Prob\{\beta(k) = 1\} = E\{\beta(k)\} = \bar{\beta} \tag{3}$$

where $\bar{\alpha}, \bar{\beta} > 0$ are unknown and denote the occurrence probability of the packet dropouts. Without loss of generality, we assume

$$\bar{\alpha} \in [\alpha_{min}, \alpha_{max}], \bar{\beta} \in [\beta_{min}, \beta_{max}], 0 < \alpha_{min}, \beta_{min} \leq \alpha_{max}, \beta_{max} \leq 1 \tag{4}$$

where $\alpha_{min}, \beta_{min}$ are the lower limits and $\alpha_{max}, \beta_{max}$ are the upper limits of the probabilities respectively. Choose

$$\alpha_0 = \frac{\alpha_{min} + \alpha_{max}}{2}, \alpha_1 = \frac{\alpha_{max} - \alpha_{min}}{2}, \beta_0 = \frac{\beta_{min} + \beta_{max}}{2}, \beta_1 = \frac{\beta_{max} - \beta_{min}}{2} \tag{5}$$

we can obtain another expressions about $\bar{\alpha}, \bar{\beta}$ as follows

$$\left. \begin{cases} \bar{\alpha} = \alpha_0 + \alpha_1 \bullet \Delta\alpha \\ |\Delta\alpha| \leq 1 \end{cases} \right\} \left. \begin{cases} \bar{\beta} = \beta_0 + \beta_1 \bullet \Delta\beta \\ |\Delta\beta| \leq 1 \end{cases} \right\} \tag{6}$$

Throughout this paper, following assumption is introduced for (2).

Assumption 1: Random variables $\alpha(k)$, $\beta(k)$ were independent of each other.

Define $e(k) = x(k) - \hat{x}(k)$, and from (1) and (2) we can get the closed-loop system as follows

$$\begin{cases} e(k+1) = (A - LC_1)e(k) + (1 - \alpha(k))LC_1x(k) + E\omega(k) - \alpha(k)LF\omega(k) \\ x(k+1) = (A + \beta(k)BK)x(k) - \beta(k)BK e(k) + E\omega(k) \\ z(k) = C_2x(k) + D\omega(k) \end{cases} \quad (7)$$

The objective of this paper is to design the controller (2) for the system (1), such that the closed-loop system (7) satisfies following requirements:

1. When $\omega(k) = 0$, the closed-loop system (7) is exponentially mean-square stable.
2. Under zero initial conditions, the controlled output $z(k)$ of the closed-loop system (7) can satisfy the following H_∞ performance metrics as follows

$$\sum_{k=0}^{\infty} E\{\|z(k)\|^2\} < \gamma^2 \sum_{k=0}^{\infty} E\{\|\omega(k)\|^2\} \quad (8)$$

where $\gamma > 0$ is a given scalar.

Remark 1: The packet dropouts probability usually keeps varying and can not be measured exactly. However it can be estimated by a value region shown as (5) which is much more practical. In (5), $\alpha_{max} = 1, \beta_{max} = 1$ mean that no packet dropouts, and $\alpha_{max} = 0, \beta_{max} = 0$ mean that packets are lost completely.

3 Main Results

Lemma 1. For any parameter $\xi > 0$, matrices G, F, E with appropriate dimensions, if $EE^T \leq I$, then

$$GEF + F^T E^T G^T \leq \xi GG^T + \xi^{-1} F^T F \quad (9)$$

Lemma 2. Let $V(x(k))$ be a Lyapunov functional. If there exist real scalars $\lambda \geq 0, \mu > 0, \nu > 0$ and $0 < \psi < 1$ such that

$$\mu \|x(k)\|^2 \leq V(x(k)) \leq \nu \|x(k)\|^2, E\{V(x(k+1)/x(k))\} - V(x(k)) \leq \lambda - \psi V\|x(k)\|^2 \quad (10)$$

then the sequence $x(k)$ satisfies

$$E\{\|x(k)^2\|\} \leq \frac{V}{u} \|x(0)^2\| (1-\psi)^k + \frac{\lambda}{u\psi} \tag{11}$$

At first, for the case of system (1) without disturbance, i.e., $\omega(k) = 0$, we have the following theorem.

Theorem 1 The closed-loop system (7) with $\omega(k) = 0$ is exponentially mean-square stable if there exist positive definite symmetric matrices $P_1 \in R^{n \times n}, P_2 \in R^{n \times n}$ and gain matrix L, K satisfying

$$\begin{bmatrix} -P_2 & * & * & * & * & * & * & * & * & * \\ 0 & -P_1 & * & * & * & * & * & * & * & * \\ (1-\alpha_0)LC_1 & A-LC_1 & -P_1^{-1} & * & * & * & * & * & * & * \\ \xi_1^{-1} \frac{LC_1}{2} & \xi_1^{-1}(A-LC_1) & 0 & -P_1^{-1} & * & * & * & * & * & * \\ A+\beta_0BK & -\beta_0BK & 0 & 0 & -P_2^{-1} & * & * & * & * & * \\ \xi_2\beta_1BK & -\xi_2\beta_1BK & 0 & 0 & 0 & -P_2^{-1} & * & * & * & * \\ \xi_2^{-1}(A+\frac{BK}{2}) & -\xi_2^{-1}\frac{BK}{2} & 0 & 0 & 0 & 0 & -P_2^{-1} & * & * & * \\ nBK & -nBK & 0 & 0 & 0 & 0 & 0 & -P_2^{-1} & * & * \\ \xi_1\alpha_1LC_1 & 0 & 0 & 0 & 0 & 0 & 0 & 0 & -P_1^{-1} & * \\ mL C_1 & 0 & 0 & 0 & 0 & 0 & 0 & 0 & 0 & -P_1^{-1} \end{bmatrix} < 0 \tag{12}$$

where $\alpha_0(1-\alpha_0) = m^2, \beta_0(1-\beta_0) = n^2$, and $\xi_1 > 0, \xi_2 > 0$ are arbitrary given constants.

Proof. Consider following Lyapunov functional

$$V(k) = e^T(k)P_1e(k) + x^T(k)P_2x(k) \tag{13}$$

where $P_1 \in R^{n \times n}, P_2 \in R^{n \times n}$ are the positive definite symmetric matrices. when $\omega(k) = 0$, we have

$$\begin{aligned} & E\{V(k+1)/V(k)\} - E\{V(k)\} \\ &= [(A-LC_1)e(k) + (1-\bar{\alpha})LC_1x(k)]^T P_1[(A-LC_1)e(k) + (1-\bar{\alpha})LC_1x(k)] \\ &+ [(A+\bar{\beta}BK)x(k) - \bar{\beta}BKe(k)]^T P_2[(A+\bar{\beta}BK)x(k) - \bar{\beta}BKe(k)] \\ &+ \bar{\beta}(1-\bar{\beta})[BK(x(k)-e(k))]^T P_2[BK(x(k)-e(k))] \\ &+ \bar{\alpha}(1-\bar{\alpha})[LC_1x(k)]^T P_1[LC_1x(k)] \\ &- e^T(k)P_1e(k) - x^T(k)P_2x(k) \end{aligned} \tag{14}$$

Substitute (6) into (14), we get

$$\begin{aligned}
 & E\{V(k+1)/V(k)\} - E\{V(k)\} \\
 &= [(A - LC_1)e(k) + (1 - \alpha_0)LC_1x(k)]^T P_1[(A - LC_1)e(k) + (1 - \alpha_0)LC_1x(k)] \\
 &+ (-\alpha_1\Delta\alpha)x^T(k)(LC_1)^T P_1[(A - LC_1)e(k) + \frac{LC_1}{2}x(k)] \\
 &+ (-\alpha_1\Delta\alpha)[(A - LC_1)e(k) + \frac{LC_1}{2}x(k)]^T P_1(LC_1)x(k) + m^2x^T(k)(LC_1)^T P_1(LC_1)x(k) \\
 &+ [(A + \beta_0BK)x(k) - \beta_0BKe(k)]^T P_2[(A + \beta_0BK)x(k) - \beta_0BKe(k)] \\
 &+ \beta_1\Delta\beta(x(k) - e(k))^T (BK)^T P_2[Ax(k) + \frac{BK}{2}(x(k) - e(k))] \\
 &+ \beta_1\Delta\beta[Ax(k) + \frac{BK}{2}(x(k) - e(k))]^T P_2(BK)(x(k) - e(k)) \\
 &+ n^2(x(k) - e(k))^T (BK)^T P_2(BK)(x(k) - e(k)) - e^T(k)P_1e(k) - x^T(k)P_2x(k)
 \end{aligned} \tag{15}$$

where $\alpha_0(1 - \alpha_0) = m^2$, $\beta_0(1 - \beta_0) = n^2$. And by virtue of Lemma 1, we have

$$\begin{aligned}
 & E\{V(k+1)/V(k) - V(k)\} \\
 &\leq [(A - LC_1)e(k) + (1 - \alpha_0)LC_1x(k)]^T P_1[(A - LC_1)e(k) + (1 - \alpha_0)LC_1x(k)] \\
 &+ \xi_1^{-2}[(A - LC_1)e(k) + \frac{LC_1}{2}x(k)]^T P_1[(A - LC_1)e(k) + \frac{LC_1}{2}x(k)] \\
 &+ \xi_1^2\alpha_1^2x^T(k)(LC_1)^T P_1(LC_1)x(k) + m^2x^T(k)(LC_1)^T P_1(LC_1)x(k) \\
 &+ [(A + \beta_0BK)x(k) - \beta_0BKe(k)]^T P_2[(A + \beta_0BK)x(k) - \beta_0BKe(k)] \\
 &+ \xi_2^{-2}[Ax(k) + \frac{BK}{2}(x(k) - e(k))]^T P_2[Ax(k) + \frac{BK}{2}(x(k) - e(k))] \\
 &+ \xi_2^2\beta_1^2(x(k) - e(k))^T (BK)^T P_2(BK)(x(k) - e(k)) \\
 &+ n^2(x(k) - e(k))^T (BK)^T P_2(BK)(x(k) - e(k)) \\
 &- e^T(k)P_1e(k) - x^T(k)P_2x(k) \triangleq \eta_1^T(k)\Lambda_1\eta_1(k)
 \end{aligned} \tag{16}$$

where $\xi_1 > 0$, $\xi_2 > 0$ are arbitrary given constants, and According to the Schur complement lemma, (12) implies $\Lambda_1 < 0$, and we obtain

$$\begin{aligned}
 & E\{V(x(k+1))|V(x(k))\} - V(x(k)) \leq x(k)^T \Lambda_1 x(k) \\
 &\leq -\lambda_{\min}(-\Lambda_1)x(k)^T x(k) < -\alpha x(k)^T x(k)
 \end{aligned} \tag{17}$$

where $0 < \alpha < \min\{\lambda_{\min}(-\Lambda_1), \lambda_{\max}(P_1, P_2)\}$. Definite $\sigma = \lambda_{\max}(P_1, P_2)$, we get

$$E\{V(x(k+1))|V(x(k))\} - V(x(k)) \leq -\alpha x(k)^T x(k) \leq -\frac{\alpha}{\sigma} V(x(k)) \triangleq -\psi V(x(k)) \tag{18}$$

where $\psi = \frac{\alpha}{\sigma} \in (0, 1)$.

By Lemma 2, the closed-loop system (7) is exponentially mean-square stable. This completed the proof.

For the case of system (7) with disturbance, i.e., $\omega(k) \neq 0$, we have the following theorems.

Theorem 2. The closed-loop system (7) is exponentially mean-square stable and achieves the prescribed H_∞ performance if there exist positive definite symmetric matrices $P_1 \in R^{n \times n}, P_2 \in R^{n \times n}$ and gain matrices L, K satisfying

$$\begin{bmatrix}
 -P_2 & * & * & * & * & * & * & * & * & * & * & * \\
 0 & -P_1 & * & * & * & * & * & * & * & * & * & * \\
 0 & 0 & -\gamma^2 I & * & * & * & * & * & * & * & * & * \\
 (1-\alpha_0)LC_1 & A-LC_1 & E-\alpha_0 LF & -P_1^{-1} & * & * & * & * & * & * & * & * \\
 \frac{\xi_1 LC_1}{2} & \xi_1(A-LC_1) & \xi_1(E-\frac{LF}{2}) & 0 & -P_1^{-1} & * & * & * & * & * & * & * \\
 A+\beta_1 BK & -\beta_1 BK & E & 0 & 0 & -P_2^{-1} & * & * & * & * & * & * \\
 \xi_2 \beta_1 BK & -\xi_2 \beta_1 BK & 0 & 0 & 0 & 0 & -P_2^{-1} & * & * & * & * & * \\
 \frac{\xi_2^{-1}(A+\frac{BK}{2})}{2} & -\frac{\xi_2^{-1} BK}{2} & \xi_2^{-1} E & 0 & 0 & 0 & 0 & -P_2^{-1} & * & * & * & * \\
 nBK & -nBK & 0 & 0 & 0 & 0 & 0 & 0 & -P_2^{-1} & * & * & * \\
 \xi_1 \alpha_1 LC_1 & 0 & \xi_1 \alpha_1 LF & 0 & 0 & 0 & 0 & 0 & 0 & -P_1^{-1} & * & * \\
 mL C_1 & 0 & mL F & 0 & 0 & 0 & 0 & 0 & 0 & 0 & -P_1^{-1} & * \\
 C_2 & 0 & D & 0 & 0 & 0 & 0 & 0 & 0 & 0 & 0 & -I
 \end{bmatrix} < 0 \tag{19}$$

where $\gamma > 0$ is a given parameter and $\xi_1 > 0, \xi_2 > 0$ are arbitrary given constants.

Proof When $\omega(k) = 0$, inequality (19) is equivalent to (12). From Theorem 1 the closed-loop system (7) is exponentially mean-square stable.

When $\omega(k) \neq 0$, choose the Lyapunov functional as

$$V(k) = e^T(k)P_1 e(k) + x^T(k)P_2 x(k) \tag{20}$$

Through the method of theorem 1, we can also get

$$E\{V(k+1)/V(k) - V(k)\} + E\{z^T(k)z(k)\} - \gamma^2 E\{\omega^T(k)\omega(k)\} \leq \eta_2^T(k)\Lambda_2\eta_2(k) \tag{21}$$

Based on the Schur complement, inequality (22) implies $\Lambda_2 < 0$, then we get

$$E\{V(k+1)/V(k) - V(k)\} + E\{z^T(k)z(k)\} - \gamma^2 E\{\omega^T(k)\omega(k)\} < 0 \tag{22}$$

Now summing (22) from 0 to ∞ with respect to k yields

$$\sum_{k=0}^{\infty} E\{z^T(k)z(k)\} < \gamma^2 \sum_{k=0}^{\infty} E\{\omega^T(k)\omega(k)\} + E\{V(0)\} - E\{V(\infty)\} \tag{23}$$

Since the system (7) is exponentially mean-square stable, under the zero-initial condition it is straightforward to see that

$$\sum_{k=0}^{\infty} E\{z^T(k)z(k)\} < \gamma^2 \sum_{k=0}^{\infty} E\{\omega^T(k)\omega(k)\} \quad (24)$$

This completed the proof.

It should be noted that matrix inequality (19) is not a linear matrix inequality and difficult to be solved. For this, we have following Theorem 3.

Theorem 3. The closed-loop system (7) is exponentially mean-square stable and achieves the prescribed H_∞ performance if there exist positive definite symmetric matrices $P_1 \in R^{n \times n}$, $P_2 \in R^{n \times n}$ and gain matrices M, N satisfying the following LMI

$$\begin{bmatrix} -P_2 & * & * & * & * & * & * & * & * & * & * & * \\ 0 & -P_1 & * & * & * & * & * & * & * & * & * & * \\ 0 & 0 & -\gamma^2 I & * & * & * & * & * & * & * & * & * \\ (1-\alpha_0)MC_1 & P_1A-MC_1 & P_1E-\alpha_0MF & -P_1 & * & * & * & * & * & * & * & * \\ \xi_1^{-1} \frac{MC_1}{2} & \xi_1^{-1}(P_1A-MC_1) & \xi_1^{-1}(P_1E-\frac{MF}{2}) & 0 & -P_1 & * & * & * & * & * & * & * \\ P_2A+\beta_0BN & -\beta_0BN & P_2E & 0 & 0 & -P_2 & * & * & * & * & * & * \\ \xi_2^{-1}\beta_1BN & -\xi_2^{-1}\beta_1BN & 0 & 0 & 0 & 0 & -P_2 & * & * & * & * & * \\ \xi_2^{-1}(P_2A+\frac{BN}{2}) & -\xi_2^{-1}\frac{BN}{2} & \xi_2^{-1}P_2E & 0 & 0 & 0 & 0 & -P_2 & * & * & * & * \\ nBN & -nBN & 0 & 0 & 0 & 0 & 0 & 0 & -P_2 & * & * & * \\ \xi_1^{-1}\alpha_1MC_1 & 0 & \xi_1^{-1}\alpha_1MF & 0 & 0 & 0 & 0 & 0 & 0 & -P_1 & * & * \\ mMC_1 & 0 & mMF & 0 & 0 & 0 & 0 & 0 & 0 & 0 & -P_1 & * \\ C_2 & 0 & D & 0 & 0 & 0 & 0 & 0 & 0 & 0 & 0 & -I \end{bmatrix} < 0 \quad (25)$$

where $\gamma > 0$ is a given parameter and $\xi_1 > 0, \xi_2 > 0$ are arbitrary given constants,

$$P_2B = BP, M = P_1L, N = PK \quad (26)$$

Proof. Through left-and-right multiplying (19) by

$$diag\{I, I, I, P_1, P_1, P_2, P_2, P_2, P_2, P_1, P_1, I\} \quad (27)$$

Define $P_2B = BP, M = P_1L, N = PK$, then the matrix inequality (25) is equivalent to (19). From Theorem 2, we can conclude that the closed-loop system (7) is exponentially mean-square stable and achieve the prescribed H_∞ performance. This completed the proof.

4 Simulation Example

Consider the system parameters are as follows

$$A = \begin{bmatrix} -0.29 & 0.35 \\ -0.43 & 0.25 \end{bmatrix} B = \begin{bmatrix} -0.32 & 0.41 \\ 0.33 & 0.26 \end{bmatrix} C_1 = \begin{bmatrix} 0.17 & -0.23 \\ 0.33 & -0.22 \end{bmatrix} C_2 = \begin{bmatrix} 0.10 & -0.45 \\ 0.20 & -0.33 \end{bmatrix}$$

$$D = \begin{bmatrix} -0.26 & 0.14 \\ 0.42 & 0.42 \end{bmatrix} E = \begin{bmatrix} -0.23 & 0.32 \\ 0.43 & 0.31 \end{bmatrix} F = \begin{bmatrix} -0.20 & 0.50 \\ 0.30 & 0.43 \end{bmatrix}$$

Assume $\bar{\alpha} \in [0.4, 1]$, $\bar{\beta} \in [0.5, 1]$, we can get $\alpha_0 = 0.7, \alpha_1 = 0.3, \beta_0 = 0.75, \beta_1 = 0.25$. Choose $\xi_1 = \xi_2 = 2$ and $\gamma = 0.3$, we can obtain the gain matrices as follows

$$K = \begin{bmatrix} -0.0201 & 1.3005 \\ 0.1624 & -0.2099 \end{bmatrix}, L = \begin{bmatrix} -0.1809 & 0.0200 \\ 0.7107 & 0.5670 \end{bmatrix}$$

Choose the disturbance input $\omega(k) = 0.01 \begin{bmatrix} \sin(k) \\ \sin(k) \end{bmatrix}$. The initial state values

$x(0) = \begin{bmatrix} -1 \\ 1 \end{bmatrix}$ and $\hat{x}(0) = \begin{bmatrix} 0 \\ 1 \end{bmatrix}$, the system state variables is shown in Fig.2. It can be

verified that $\sum_{k=0}^{\infty} E\{\|z(k)\|^2\} < \gamma^2 \sum_{k=0}^{\infty} \{\|w(k)\|^2\}$.

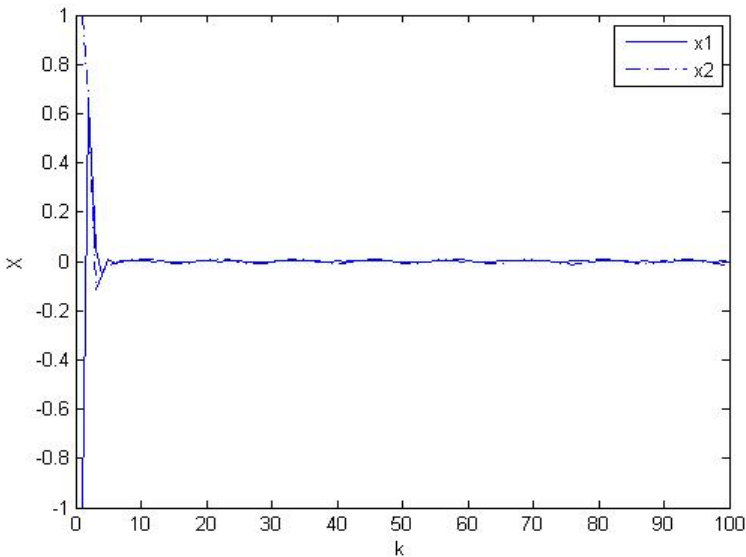


Fig. 2. The state response of the closed-loop system. x is the state of system, k is the discrete time.

5 Conclusions

In this paper, the robust H_∞ controller has been designed for a class of discrete-time system with uncertain packet dropouts probabilities. The random packet dropouts are modeled as a stochastic variable satisfying a Bernoulli distributed with uncertain probabilities. Sufficient conditions for the existence of an observer-based controller is presented via LMI, and the designed controller enables the closed-loop system to be exponentially mean-square stable and achieve the prescribed H_∞ performance.

Acknowledgements. This work is supported by National Natural Science Foundation of China (61104103; 61304089; 51177019); Natural Science Foundation of Jiangsu Province of China (BK2011826; BK20131000); Open Project of Key Laboratory of Measurement and Control of Complex Systems of Engineering, Ministry of Education, Southeast University (MCCSE2012A07).

References

1. Tipsuwan, Y., Chow, M.Y.: Control methodologize in networked control system. *Control Engineering Practice* 10(11), 1099–1111 (2003)
2. Chen, Y.M., Huang, H.C.: Multisensor data fusion for manoeuvring target tracking. *International Journal of Systems Science* 32(2), 205–214 (2001)
3. Wang, W., Yang, F.W., Zhan, Y.Q.: Robust H_2 state estimation for stochastic uncertain discrete-time system with missing measurements. *Control Theory and Applications* 25(3), 439–445 (2008)
4. Wang, B.F., Guo, G.: State estimation for discrete-time systems with Markovian time-delay and packet loss. *Control Theory and Applications* 26(12), 1331–1336 (2001)
5. Ruan, Y.B., Wang, W., Yang, F.W.: Fault detection filter for networked systems with missing measurements. *Control Theory and Applications* 26(3), 291–295 (2009)
6. Zhang, J., Bo, Y.M., Lv, M.: Fault detection for networked control systems with delays and data packet dropout. *Control and Decision* 26(6), 933–939 (2011)
7. Wang, Z.D., Yang, F.W., Ho, D.W.C., Liu, X.H.: Robust H_∞ control for networked systems with random packet losses. *IEEE Transactions on Systems, Man, and Cybernetics, Part B* 37(4), 916–924 (2007)
8. Seiler, P., Sengupta, R.: An H_∞ approach to networked control. *IEEE Transaction on Automation Control* 50(3), 356–364 (2005)

Effect of Environment on Prey-Predator Systems with Numerical Simulation*

Qing Fang¹ and Xiao-Yu Zhang^{2,**}

¹ Department of Mathematical Sciences
Faculty of Science, Yamagata University
Yamagata 990-8560, Japan
fang@sci.kj.yamagata-u.ac.jp

² Department of Mathematics
College of Science, Beijing Forestry University
Beijing 100083, China
xyzhang@bjfu.edu.cn

Abstract. In this paper, we are concerned with effect of environmental parameters on the Rosenzweig-MacArthur model with the Holling type II functional response. We introduce attenuated functions of the carrying capacity and hunting parameters, respectively, and investigate how the population densities behave when environmental quantities change. The Hopf bifurcation diagrams are obtained by numerical simulation.

1 Introduction

The Rosenzweig-MacArthur model in the form of

$$\begin{cases} \frac{dp}{dt} = r \left(1 - \frac{p}{K}\right) p - f(p)z, \\ \frac{dz}{dt} = k_1 f(p)z - d_1 z \end{cases} \quad (1)$$

is usually used to describe the behavior of prey-predator system, where p and z denote the population densities of the prey and the predator, respectively. r denotes the intrinsic growth rate, and K denotes the carrying capacity of the prey. k_1 and d_1 denote the increasing rate and the mortality rate of the predator, respectively. The function $f(p)$ represents the Holling type II functional response defined by

$$f(p) = \frac{bp}{c+p}, \quad (2)$$

where b and c denote the maximum foraging rate and the half saturation constant, respectively.

* The author is supported by National Natural Science Foundation of China, Tian Yuan Foundation under grant No.11326223.

** Corresponding author.

When we choose the carrying capacity K as the parameter, it is known that as K increases, the population dynamics of (1) is destabilized. That is, a coexisting equilibrium of (1) becomes unstable and a stable periodic orbit (prey-predator limit cycle) appears through the Hopf bifurcation.

The ecosystem around us is always changing due to activities of human beings enforced to natural environment like destructive actions. These activities sometimes makes other animals could not live as before so that it is necessary to investigate how the population densities behave when environmental quantities change.

2 Time-Dependent Carrying Capacity Effect

By introducing an attenuated function of the carrying capacity $k(t)$, we consider the prey-predator system of the following form

$$\begin{cases} \frac{dp}{dt} = r \left(1 - \frac{p}{k(t)} \right) p - f(p)z, \\ \frac{dz}{dt} = k_1 f(p)z - d_1 z, \end{cases} \quad (3)$$

in which we consider the following two kinds of positive decreasing functions

$$k(t) = (k_0 - \beta)e^{-\lambda t} + \beta \quad (4)$$

and

$$k(t) = -\frac{k_0 - \beta}{2} \tanh\left(\frac{t - \eta}{\lambda}\right) + \frac{k_0 + \beta}{2}. \quad (5)$$

(4) shows that the environment is destructed gradually while (5) implies that the environment is destructed rapidly. We note that k_0 is the initial carrying capacity before attenuation, β is the minimal carrying capacity at the final stage of attenuation, λ is a constant denoting the sharpness of attenuation and η is the level of switching effect denoting the period of attenuation.

The numerical simulations of (3) for which (4) is used show that at the beginning stage of attenuation, the solutions p and z continue oscillations. But when $k(t)$ goes near K^H , the amplitudes of the solutions p and z become smaller and smaller so that the solutions behave like stable coexistent states for a long time. But at eventually the predator decades to the state near extinction.

The behavior of (3) by using (5) is also simulated, which is the case when a natural disaster with large scale takes place. The solutions p and z oscillate usually before the time when the carrying capacity decreases rapidly at one moment and then go to extinction.

3 Hunting Effect

There are many complex factors affecting the carrying capacity together with other quantities such as the intrinsic growth rate. Here we introduce hunting effect to the Rosenzweig-MacArthur model (1) and investigate how the behavior of the solutions change.

$$\begin{cases} \frac{dp}{dt} = r \left(1 - \frac{p}{K}\right) p - f(p)z - \omega_1 \frac{K}{K^H} p, \\ \frac{dz}{dt} = k_1 f(p)z - d_1 z - \omega_2 \frac{K}{K^H} z, \end{cases} \tag{6}$$

where the hunting parameters $\omega_1 \geq 0$ and $\omega_2 \geq 0$ are constants denoting the hunting effect of the prey and the predator, respectively.

The system (6) can be considered as one in which the intrinsic growth rate and the carrying capacity for the prey are reduced, while the death rate for the predator is raised, since the system can be reformed as

$$\begin{cases} \frac{dp}{dt} = \left(r - \omega_1 \frac{K}{K^H}\right) \left(1 - \frac{rp}{\left(r - \omega_1 \frac{K}{K^H}\right) K}\right) p - f(p)z, \\ \frac{dz}{dt} = k_1 f(p)z - \left(d_1 + \omega_2 \frac{K}{K^H}\right) z. \end{cases}$$

Numerical results show that when $K > K^H$, although the system (1) has prey-predator limit cycle with large amplitude, the limit cycle of the system (6) gets smaller amplitude as the hunting parameters appear (refer to Fig. 1). And when the hunting parameters get large, the solutions of the system (6) converge to equilibria. This implies that the hunting parameters have stabilized effect for the prey-predator systems. But the Hopf bifurcation point is not always getting large as the hunting parameters get large.

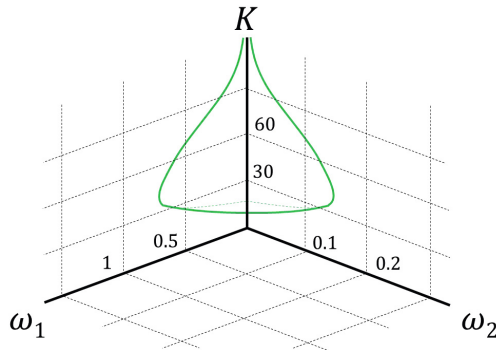


Fig. 1. Hopf bifurcation diagram of (6) with the green surface. The part of K axes is where there are period solutions, and the opposite part is where there are equilibria.

References

1. Alekseev, V.R., De Stasio, B.T., Gilbert, J.J.: *Diapause in Aquatic Invertebrates: Theory and Human Use*. Kluwer Academic (2007)
2. Bazykin, A.D.: *Nonlinear Dynamics of Interacting Populations*. World Scientific (1998)
3. Cheng, K.: Uniqueness of a limit cycle for a predator-prey system. *SIAM J. Math. Anal.* 12, 541–548 (1981)
4. Hastings, A.: *Population Biology: Concepts and Models*. Springer, New York (1998)
5. Hofbauer, J., Sigmund, K.: *Evolutionary Games and Population Dynamics*. Cambridge University Press (1998)
6. Hoppensteadt, F.C., Izhikevich, E.M.: *Weakly Connected Neural Networks*. Springer, New York (1997)
7. Kuwamura, M., Chiba, H.: Mixed-mode oscillations and chaos in a prey-predator system with dormancy of predators. *Chaos* 19, 043121 (2009)
8. Kuwamura, M., Nakazawa, T., Ogawa, T.: A minimum model of prey-predator system with dormancy of predators and the paradox of enrichment. *Journal of Mathematical Biology* 58, 459–479 (2009)
9. Kuznetsov, Y.A.: *Elements of Applied Bifurcation Theory*, 3rd edn. Springer (2004)
10. Meiss, J.D.: *Differential Dynamical Systems*. SIAM, Philadelphia (2007)
11. Murray, J.D.: *Mathematical Biology II Spatial Models and Biomedical Applications*, 3rd edn. Springer, New York (2003)
12. Murray, J.D.: *Mathematical Biology I An Introduction*, 3rd edn. Springer, New York (2002)
13. Neubert, M.G., Klepac, P., van den Driessche, P.: Stabilizing dispersal delays in predator-prey metapopulation models. *Theoret. Population Biol.* 61, 339–347 (2002)
14. Turchin, P.: *Complex Population Dynamics*. Princeton University Press (2003)
15. Rosenzweig, M., MacArthur, R.: Graphical representation and stability conditions of predator-prey interaction. *American Naturalist* 97, 209–223 (1963)
16. Sugie, J., Saito, Y.: Uniqueness of limit cycles in a Rosenzweig-MacArthur model with prey immigration. *SIAM J. Appl. Math.* 72, 299–316 (2012)

Author Index

- Ai, Yutao 121
- Billham, Mark 215
- Bu, Rui-Rui 39, 50, 91
- Buchanan, Fraser 215
- Cai, Jiyuan 129
- Cao, Jiangnan 410
- Chai, YuShen 387
- Chen, Duanduan 170
- Chen, Guanghua 329
- Chen, Lanlan 33
- Chen, Weidong 307
- Chen, Xi 268
- Chiu, Min-Sen 298
- Deng, Fei 319
- Ding, Weilong 178
- Ding, Yongsheng 101
- Ding, Zhiguo 160
- Du, Dajun 160
- Du, Zhou 62
- Duan, Hong 256
- Fan, Huimin 234
- Fan, Shengli 109
- Fan, Zongchen 278
- Fang, Qing 420
- Fei, Minrui 160, 368
- Feng, Zhonggang 198
- Fu, Zhao 339
- Gao, Ting 39
- Ge, Yuanzheng 256
- Gong, Jing 39, 50, 91
- Gu, Xingsheng 137
- Gutmann, Greg 13
- Hao, Kuangrong 101
- Hao, Zhonghua 82
- He, Liangfei 1
- Hong, Haifa 62
- Hu, Chen 178
- Hu, Zhifa 150
- Inoue, Daisuke 13
- Jia, Li 298, 339
- Jiang, Gangyi 109
- Jiang, Rui 101
- Kakugo, Akira 13
- Kang, Hong-Xuan 188
- Kitajima, Tatsuo 198
- Konagaya, Akihiko 13
- Kosawada, Tadashi 198
- Koyamada, Koji 246
- Lennon, Domhnall 215
- Li, Peijiang 319
- Li, Qihong 226
- Li, Tieyan 234
- Li, Xiang 387
- Li, Xiangchen 268
- Li, Xin 387
- Li, Xunlong 298
- Liu, Fei 150
- Liu, Hao 188
- Liu, Jinfen 62
- Liu, Jingjing 329
- Liu, Jinlong 62
- Liu, Li 307, 400
- Liu, Zhongmin 234
- Lu, Rong 234
- Lu, XiaYan 387
- Luo, Cong 319
- Lv, Xiaomeng 209
- Ma, Chenjie 410
- Ma, Shiwei 82, 329
- Max, Nelson 178
- McAfee, Marion 215
- Mei, Yuqian 170
- Müller-Eschner, Matthias 170
- Nakamura, Takao 198
- Nie, Sheng-Dong 39, 50, 91
- Peng, Bin bin 378
- Pu, Fang 288

- Qi, Jie 288
 Qi, Jin-Peng 288
 Qian, Yi 62
 Qiu, Xiaogang 256, 278

 Ren, Shuang 226
 Ren, Yanyun 129
 Rong, Qiguo 226

 Sakamoto, Naohisa 246
 Sato, Daisuke 198
 Shao, Hui 72
 Shao, Yong 121
 Shen, Kai 137
 Shu, Shiyu 101
 Song, Chunting 1
 Song, Zhichao 256
 Sun, Qi 62
 Sun, Yanjun 62

 Tu, Dawei 72

 Umezu, Mitsuo 62, 198

 Wang, Jingchuan 307
 Wang, Ming 209
 Wang, Mingyu 329
 Wang, Nengjun 378
 Wang, Qian 1, 62
 Wang, Wei 268
 Wang, Xiao-Fei 39, 50, 91
 Wang, Yigang 109
 Wang, Yuan-Jun 91
 Wei, Lisheng 23
 Wen, Jiarui 82
 Whitaker, Darren A. 215
 Wu, Dingbing 358, 400
 Wu, Fuli 178
 Wu, Jianguo 368
 Wu, Shengxi 137

 Xie, Jiang 350
 Xu, Pengfei 378

 Xu, Sheng 160
 Xu, Wei 350
 Xu, Wen-Shan 188
 Xu, Yulin 209

 Yang, Aolei 358, 400
 Yang, Banghua 1
 Yang, De-Zhou 188
 Yang, Lei 129
 Yang, Ming 150
 Ye, Liang 234
 Ye, Qiang 137
 Yin, Bao-Shu 188
 Yu, Mei 109

 Zan, Peng 121
 Zang, Qiang 410
 Zeng, Weimin 329
 Zhang, Chi 358
 Zhang, Jian 33
 Zhang, Kun 368
 Zhang, Laobing 278
 Zhang, Ning 129
 Zhang, Peijian 368
 Zhang, Peng 278
 Zhang, Wu 350
 Zhang, Xiao-Yu 420
 Zhang, Xudong 72
 Zhang, Yunyuan 1
 Zhao, Fan 82
 Zhao, Jie 121
 Zhao, Kun 246
 Zhao, Qijie 72
 Zhao, Yu 33
 Zhou, Hong 350
 Zhou, Shengwen 23
 Zhou, Ying 410
 Zhou, Zhonghua 350
 Zhu, Daqi 378
 Zhu, Lingling 358, 400
 Zhu, Xiaojin 319
 Zhu, Ying 288
 Zou, Junzhong 33